Dissertation
submitted to the
Combined Faculties for the Natural Sciences and for Mathematics
of Ruperto-Carola University of Heidelberg, Germany
for the degree of
Doctor of Natural Sciences

Put forward by

Master of Science: Friederike Bock

born in Gardelegen (Germany)

Oral examination: 29.11.2017

Measurement of Direct Photons and Neutral Mesons in Small Collisions Systems with the ALICE Experiment at the LHC

Referees: **Prof. Dr. Johanna Stachel**
Prof. Dr. Stefanie Hansmann-Menzemer

Abstract

The Quark-Gluon Plasma (QGP), a strongly interacting state of matter in which quarks and gluons are deconfined, is hypothesized to have existed merely a few micro-seconds after the Big Bang. This state can be studied experimentally in heavy ion collisions at the current high-energy particle accelerators, like the Large Hadron Collider (LHC). However, recently the size of the collision system, which is required to create a QGP has been been put into question and many measurements suggests that this might even be possible in high multiplicity pp or p–Pb collisions. The research carried out in this thesis focuses on the study of direct photons and neutral mesons in pp collisions at $\sqrt{s} = 2.76$ TeV and p–Pb collisions at $\sqrt{s_{\rm NN}} = 5.02$ TeV with the ALICE detector at the LHC. The neutral pion and η meson have been reconstructed in their two photon decay channels. For that up to four different reconstruction methods have been pursued within this thesis, out of which two are entirely new within ALICE, exploiting the full photon detection capabilities of ALICE. Like this the neutral pion spectra could be measured up to transverse momenta of 40 GeV/c in pp collision and a new level of precision could be reached for identified particle measurements in p–Pb collisions at $\sqrt{s_{\rm NN}} = 5.02$ TeV. For pp collisions new high precision inputs for the determination of the fragmentation functions for neutral pions and η mesons are provided and the current models are compared to the obtained results. For p–Pb collisions a small suppression can be observed beyond 4 GeV/c with respect to an interpolated pp reference at the same center-of-mass energy. It is investigated further through the comparison with various models and results from other identified particles, in order to test whether another ansatz, taking into account only cold nuclear matter effects, would yield a similar suppression. For the direct photons three partially independent reconstruction techniques are presented, two of which are entirely new in ALICE, as well as, their combined results for in minimum bias pp and p–Pb collisions. The combination of the results yields a significant direct photon excess in p–Pb collisions beyond 6 GeV/c, which is in agreement with the predicted excess from prompt photons in this collision system. Below these momenta and for pp collision at $\sqrt{s} = 2.76$ TeV upper limits on the possible direct photon production can be provided. In this region a possible thermal photon signal of $2 - 3\%$ cannot be excluded within the current uncertainties.

Zusammenfassung

Es wird vermutet, dass wenige Mikrosekunden nach dem Urknall ein Quark-Gluon-Plasma (QGP) existiert hat. Dieses ist ein Zustand der Materie in dem Quarks und Gluonen frei bewegen und interagieren können. Experimentell kann dieser Zustand in Schwerionenkollisionen an den derzeitigen Hochenergie Beschleunigern untersucht werden, wie zum Beispiel dem Large Hadron Collider (LHC). Allerdings wird in letzter Zeit hinterfragt, wie gross das Kollisionssystem sein muss um ausreichend Teilchen und Energie zu enthalten um ein QGP kreieren zu können. Einige Messungen weisen darauf hin, dass ein solcher Zustand bereits in pp oder pPb Kollisionen, in denen viele Teilchen erzeugt wurden, vorherrschen könnte. Diese Dissertation befasst sich vorranging mit der Untersuchung der Produktion von Photon und neutralen Mesonen in pp Kollisionen bei $\sqrt{s} = 2.76$ TeV und p–Pb Kollisionen bei $\sqrt{s_{\rm NN}} = 5.02$ TeV mit Hilfe des ALICE Detektors am LHC. Die neutralen Pionen und η Mesonen wurden in ihrem Zwei-Photonen Zerfallkanal rekonstruiert. Dafür wurden bis zu vier verschiedene Rekonstruktionsmethoden verfolgt, von denen zwei zum ersten Mal innerhalb von ALICE benutzt wurden. Damit wird das gesamte Potential zur Rekonstruktion von Photonen in ALICE ausgeschöpft. Dies erlaubt die neutralen Pionen Spektren in pp Kollisionen bis zu transversalen Impulsen von 40 GeV/c zu extrahieren. Desweiteren konnte eine neue Stufe der Präzession für die Messung von identifizierten Teilchen in p–Pb Kollisionen bei einer Schwerpunktsenergie von $\sqrt{s_{\rm NN}} = 5.02$ TeV erreicht werden. Diese neu erlangten, sehr präzisen, Daten bezueglich der π^0 und η Produktion in pp und p–Pb Kollisionen werden helfen, den Parameterraum der Fragmentationsfunktionen besser einzuschränken. Innerhalb dieser Arbeit wurden sie zu den neuesten theoretischen Berechnungen und Modellen verglichen. Darüber hinaus kann in p–Pb Kollisionen oberhalb von 4 GeV/c eine leichte Unterdrückung der Produktion von neutralen Pionen im Vergleich den erwarteten Werten in pp Kollisionen festgestellt werden. Dafür wurden die pp Spektren bei der gleichen Schwerpunktsenergie über eine Interpolation der gemessenen Spektren bei anderen Schwerpunktenergien berechnet. Die Unterdrückung wurde weitergehend untersucht um zu verstehen, ob auch andere Modelle ohne Erzeugung eines Quark-Gluon-Plasmas die erhaltenen Werte reproduzieren könnten. Zur Extraktion der direkten Photonen in pp und p–Pb Kollisionen wurden drei teilweise unabhängige Methoden präsentiert, wovon zwei innerhalb von ALICE vollkommen neuartig waren. Des weiteren wurde die Kombination dieser Techniken erläutert. Die kombinierten Ergebnisse erlauben die Extraktion eines direkten Photonenspektrums oberhalb von 6 GeV/c in p–Pb Kollisionen. Bei diesen transversalen Impulsen stimmen die Vorhersagen zur Produktion von prompten Photonen mit den gemessenen Daten überein. Unterhalb dieser transversalen Impulse konnten nur Obergrenzen für die direkte Photonen Produktion ermittelt werden. Gleiches gilt auch für pp Kollisionen. Allerdings kann in dieser Region ein direktes Photonen Signal, in der Grössenordnung von 2-3%, auf Grund der Fehler nicht ausgeschlossen werden.

Contents

1. Introduction

"In science, too, it is impossible to open up new territory unless one is prepared to leave the save anchorage of established doctrine and run the risk of a hazardous leap forward."

Werner Heisenberg (1971), "Physics and Beyond: Encounters and Conversations" (p.70), New York, Evanston & London: Harper & Row, Publishers Inc.

"Wirkliches Neuland in einer Wissenschaft kann wohl nur gewonnen werden, wenn man an einer entscheidenden Stelle bereit ist, den Grund zu verlassen, auf dem die bisherige Wissenschaft ruht, und gewissermaßen ins Leere zu springen."

Werner Heisenberg (1972), "Der Teil und das Ganze" (S. 101), München, Piper.

When we are children, the world around is full of wonders and every day we are amazed by what nature can do. What machines make possible and how our parents can understand all these things. When we grow older we realize, however, that many of the things, which our parents explained so confidently, are actually not as simple as they let it seem. Thus we learn to understand, that the simplest explanation is not always the correct one and that there are many levels of understanding the truth. Everyone of us then chooses to which level we want to understand the world around us and its different aspects. For many people the answers provided by our teachers and parents are sufficient and thus they stop asking questions.
A few people, however, never loose their curiosity and hunger for knowledge. These are the people, who become scientists. They leap into the unknown to advance their respective fields and try to reestablish solid ground, where non existed before. These are the people whom I admire, because they have the courage, not only to ask the difficult questions, but also to make an attempt of answering them. Similar to ships of famous explorers of the 15^{th} and 16^{th} century, experiments serve as the vessels to fill the blank spots in the maps of science.
The Large Hadron Collider (LHC), has been build to fill in some of the blanks, which remain for particle physicists, like:

- How our universe has been created and how it evolved afterwards to the miraculous world we see all around us.
- What our world is made of and how these building blocks interact with each other.

Even though, these questions are located at opposite ends of the observation horizon, both can be studied in the experiments carried out at the LHC. For that purpose, within the LHC different particles can be brought to collision with center-of-mass energies of up to 14 TeV for pp and up

to $\sqrt{s_{\mathrm{NN}}} = 5.5$ TeV per nucleon pair for heavy ions. These conditions offer new possibilities to test the current theoretical concepts. Among them the production mechanisms of the Higgs boson or searches for other unknown or unexpected particles. In addition, to these rather well defined states, which we hope to observe in pp collisions, it is expected that a strongly coupled state of matter is created in heavy ion collision, the quark-gluon plasma. This plasma should have existed shortly after the big bang, as well, and thus will allow us to study the evolution of matter shortly after the big bang in the LHC experiments.
One of these experiments is the ALICE (A Large Ion Collider Experiment) experiment, at which this thesis has been carried out. The focus of the design of the experimental apparatus has been the capability to handle large charged-particle densities. Furthermore, it is of utmost importance, that these particles can also be identified down to very low momenta. Which allows us to study the produced medium in all its aspects. The production of a quark-gluon plasma can not be claimed based on one observation alone, but it requires a coincidence of many different observations all pointing towards its existence. Among them, is the possibility to change its size and maybe even switch it off completely. Thus within ALICE not only Pb–Pb collisions are studied in great detail, but also smaller collision systems are investigated, like pp and p–Pb collisions. Ideally those would serve as control probes for the Pb–Pb measurements. It has been shown recently, however, that even in these systems a quark-gluon plasma might be created.
This thesis will try to advance the understanding of the smaller systems in that aspect, using the direct photons, neutral pions and eta mesons as probes of a possible quark-gluon plasma production in pp collisions at $\sqrt{s} = 2.76$ TeV or p–Pb collisions at $\sqrt{s_{\mathrm{NN}}} = 5.02$ TeV. In order to do this the full capabilities of ALICE to reconstruct photons have been exploited and the photons are either reconstruction within the electro-magnetic calorimeters or via the photon conversion reconstruction (PCM). The neutral pions and η mesons will be reconstructed in their two-photon decay channels using a maximum of four different reconstruction techniques using different combinations of photons from the three different photon detection techniques. The structure of the thesis is as follows: After this short introduction, a theoretical overview together with the current state of knowledge from the experimental point of view will be presented (Chapter 2). Afterwards, a short overview of the experimental setup is given (Chapter 3). It is followed by the description of the data sets and selection criteria for the photons entering the different analyses (Chapter 4). Then the reconstruction of the neutral mesons in the two considered collision systems will be explained in detail (Chapter 5). The results on the direct photon reconstruction will be described in Chapter 6 together with an overview of the reconstruction methods. The thesis is concluded by a summary.

2. Theoretical Background and Current State of Knowledge

This chapter is dedicated to a brief overview of the theoretical background and the current theoretical understanding of high multiplicity pp, p–A and A–A collisions. The focus will lie on the results obtained from the LHC experiments and their implications for the physics under investigation later on in this thesis. As such only a small subset of the possible Quark-Gluon Plasma (QGP) signatures are discussed. Where appropriate the history of these measurements and the parallel developments at RHIC will be outlined, however.

2.1. The Standard Model and Quantum Chromodynamics

In the late 1960s S. L. Glashow [1], A. Salam [2, 3] and S. Weinberg [4] conceived the Standard Model (SM) of particle physics, a gauge Quantum Field Theory (QFT) combining the quantum field theories of the electro-weak and strong interactions. The model describes the constituents of matter as well as their interactions. Its fundamental particles are the quarks (u, d, c, s, t, b) and leptons (e, ν_e, μ, ν_μ, τ, ν_τ), each organized in three generations, and the four gauge bosons mediating the fundamental forces (γ, g, Z^0, $W^\pm$). This work was awarded with the Nobel Prize in Physics in 1979 after tremendous success in predicting the formation of by then unknown particles, with their properties.
The electro-weak (EW) theory on its own offers a unified description of the electro-magnetic and weak interaction among particles, formulated on their own in Quantum Electrodynamics (QED) and Quantum Flavordynamics (QFD), respectively. It explains how a quark can change into another quark or lepton into another lepton (flavor changes). Its force carriers are the photon (γ) for the electro-magnetic and the Z^0 and $W^\pm$ boson for the weak force.
Quantum Chromodynamics (QCD) characterizes the strong interaction, the fundamental force describing the interaction between quarks and gluons (g), its mediators. According to QCD, the quantum number of color plays the role that the charge plays in the electromagnetic interaction. Contrary to the other forces, the mediators carry color charge themselves and as such can interact with each other. All bound states of quarks and gluons have to be colorless. The combinations, which have been observed in experiments are: 3 quarks with different colors (baryons), 3 anti-quarks with different anti-colors (anti-baryons) or one quark and one anti-quark carrying color and anti-color (mesons). Additional combinations have been predicted [5] and are currently being searched for in various experiments [6, 7], however no convincing evidence has been presented for their existence up to now. Further information can be found in various reviews [8–12].
The Lagrange density of QCD is given by

$$\mathcal{L} = \sum_q \overline{\psi}_q \gamma^\mu (i\partial^\mu - g_s A_q^\mu \frac{\lambda_a}{2})\psi_q - \sum_q m_q \overline{\psi_q}\psi_q - \frac{1}{4}\sum_a F_a^{\mu\nu} F_{\mu\nu,a}. \tag{2.1}$$

The ψ_q represents the quark field, g_s is the effective strong charge and A_q^μ is a gluon field, while the λ_a are the Gell-Mann matrices. The gluon field strength tensor $F_a^{\mu\nu}$ can be expressed as:

$$F_a^{\mu\nu} = \partial^\mu A_a^\nu - \partial^\nu A_a^\mu + i g_s f_{abc} A_\mu^b A_\nu^c \tag{2.2}$$

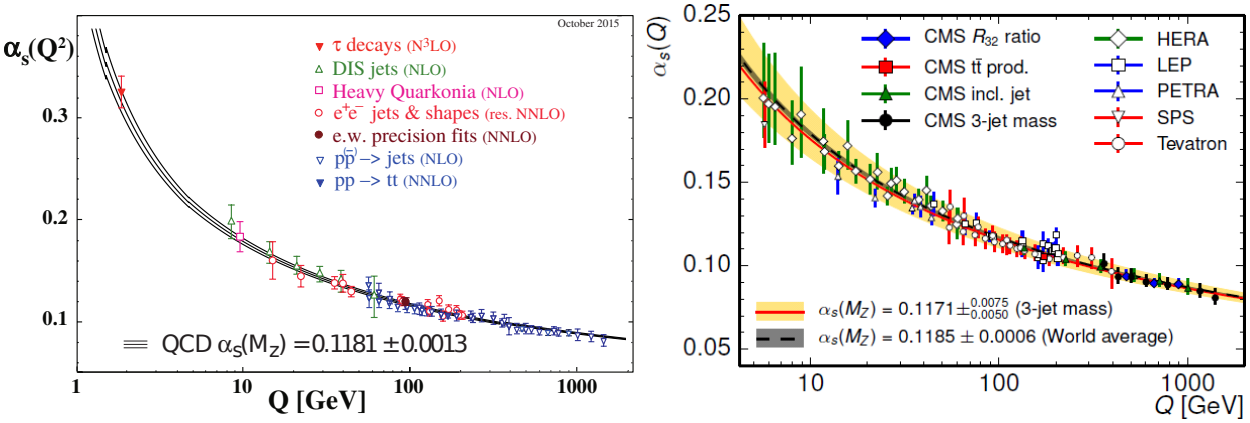

Figure 2.1.: Latest results on α_s from various sources including the recent measurements on the jet properties from CMS [13, 15, 16].

The last term represents the gluon self interaction.
For massless particles the QCD Lagrangian is invariant under the exchange of left- and right-handed components of the quark spinor, which is called *chiral symmetry*. As the quarks have masses, this symmetry is explicitly broken. However, even for massless quarks, the strong force would give rise to a so-called *chiral condensate*, which is not invariant under exchange of right- and left-handed fermions. Thus, the chiral symmetry of the QCD Lagrangian is spontaneously broken. This leads to the existence of massless *Goldstone bosons*, which can be identified with the octet of the lightest mesons (π^0, $\pi^\pm$, $K^\pm$, K^0, $\overline{K}^0$, η). These mesons on their own acquire mass due to the explicit breaking of chiral symmetry.
The coupling strength g_s of QCD can be expressed as $\alpha_s = g_s^2/4\pi$. The value of α_s cannot be predicted by QCD but needs to be determined from experiments. It is much larger than the coupling constant in QED ($\alpha_{em} \simeq \frac{1}{137}$) and varies as a function of momentum transfer (Q). Therefore, it is often referred to as the running coupling constant of QCD. The dependence of α_s on Q in leading order can be expressed by

$$\alpha_s(Q^2) \approx \frac{12\pi}{(33 - 2N_f)\ln\frac{Q^2}{\Lambda^2}}. \tag{2.3}$$

where N_f is the number of quark flavors and Λ is the QCD scaling parameter, which was experimentally determined to be about 200 MeV. Equation 2.3 does not hold if $Q^2 \simeq \Lambda^2$.
The current reference value of α_s at the Z pole mass is $\alpha_s(m_Z^2) = 0.1186 \pm 0.0013$ [13, 14], which corresponds to a relative uncertainty of $\approx 1\%$, making it the least precisely known fundamental constant in nature by several orders in magnitude. Figure 2.1 [13, 15, 16] shows two compilations of world data on α_s as a function of the momentum transfer. The left plot shows the compilation currently used for the world average based on 6 different techniques. The right plot includes recent measurements from the CMS collaboration on various jet and top properties, leading to a factor two improvement in the accuracy of α_s in the world average. However, to measure α_s with much better accuracy ($< 0.01\%$) high precision future e^+e^- colliders with very large Z and W samples will be needed.
The phenomenological potential between a quark and its anti-quark can be approximated by:

$$V_s = -\frac{4}{3}\frac{\alpha_s}{r} + kr, \tag{2.4}$$

where r is the radial distance between the quarks. At small radii the first term is dominant and equivalent to a Coulomb-like interaction. With increasing r the potential grows linearly, thus at some point it is energetically more favorable to create a new quark-anti-quark pair (a meson) from a vacuum. As a consequence of this behavior at long-distances no single quark has been observed

in nature, which is called *confinement*. In the limit of high momentum transfer, on the other hand, the coupling strength decreases and particles behave as if they were free. This is called *asymptotic freedom* of QCD at short distances and high energies.
Collisions of highly energetic hadrons can be classified in two categories:

(i) Elastic collisions, without a modification of the initial state particles beyond their momentum,

(ii) Inelastic collisions, where the hadrons are either exited or even broken up and the freed energy is used to create new particles.

The latter can be further subdivided into soft, low momentum transfer, and hard, high momentum transfer, interactions. As already described, hadrons are non static composite objects, thus it is necessary to take their substructure and its time dependence into account when calculating scattering cross sections. However, it has been found that for hard processes the interaction time scale $(1/Q)$ is much smaller than the characteristic time scale on which fluctuations occur. Meaning that the hard probe takes an instantaneous snapshot of the hadrons structure at a characteristic resolution, given by $\sim 1/Q$. Thus, the internal structure of the hadrons (or long-wavelength structure) is independent of the hard interaction itself and the terms can be calculated independently, which is known as factorization theorem [17, 18]. Using this, the interaction cross section can be written as a convolution of a non-perturbative Parton Distribution Function (PDF) and the perturbatively calculable partonic scattering cross section, with the factorization scale (μ_F) as 'user-defined' devision line between the two processes. The parton density functions ($f_{i/h}(x, \mu_F^2)$) for a certain parton i in a hadron of type h reflect the effective density of that parton at a momentum fraction x_i of the hadrons momentum, probed at the respective factorization scale μ_F. These non-perturbative functions cannot be calculated from first principles. They can, however, for instance be derived from Deep Inelastic Scattering (DIS) [19–21] or Drell-Yan data [22, 23] assuming the aforementioned factorization scheme and that the cross section is independent of the choice of μ_F. This is formalized in the DGLAP[1] equation [24–26], which can be used to evolve the respective PDF from one perturbative resolution scale to another.
Perturbative QCD (pQCD) calculations can describe the interactions with high momentum transfer together with the initial and final state radiation rather well. These calculation are mostly done to Leading Order (LO) with the inclusion of corrections due to single gluon emission, called Next-to-Leading Order (NLO). To describe the data even better most calculations by now include second or even third order corrections, referred to as NNLO/N^{2}LO and N^{3}LO, as it can be seen for the calculation of α_s in [13]. In addition to these hard interactions among the quarks and gluons of the initial hadron, low momentum particles can be produced in these collisions, which build the so-called *underlying event*.
Regardless of the scattering process, all final-state partons undergo a non-perturbative hadronization process to form the colorless particles observed in nature. The high momentum partons hadronize in a spray of lower momentum particles, so-called *jets*. This process is called fragmentation and includes final-state radiation of the parton as well as the hadronization process itself. Similar to the PDFs the fragmentation process can be considered independent from the actual scattering process and factorizes as well. The Fragmentation Functions (FF) (D_f) for a hadron f has the same non-perturbative nature as the PDFs and needs to be determined from data for each final state hadron and initial parton pair.
Although the Standard Model is a renormalizable theory and the predictions extracted from this theory are self-consistent and well reproduced by experimental data, it still leaves some unexplained phenomena. These are mainly related to energies and distances, where the gravitational force, which can be described by general relativity, plays a role and gravitons, the force carriers of that force, should emerge. Therefore, it is seen as an effective field theory in the context of modern

[1] Dokshitzer-Gribov-Lipatov-Altarelli-Parisi

field theories. For high energy physics, however, these gravitational effects are rather small and therefore they can be neglected in the calculations. Not all particles included in the Standard Model were known when it was invented. The significant successes for the predictions made by the model were:

1973: the observation of neutral currents [27]

1974: the observation of the J/ψ [28, 29]

1983: the discovery of the $W^{\pm}$ and Z^0 bosons [30]

1994: the observation of the top quark [31, 32]

2000: the observation of the τ neutrino [33]

2012: the observation of the Higgs boson [34, 35]

The existence of the last missing piece, a scalar particle called Standard Model Higgs boson, has been experimentally verified in 2012 by the ATLAS[2] and CMS[3] experiment at the LHC[4]. It is a manifestation of the mechanism [36–41] that breaks electroweak symmetry in the SM and gives mass to all massive elementary particles. During the past two centuries limits on the Higgs boson mass had been set indirectly by global fits to electroweak results [42] and directly by searches at the LEP[5] [43], the Tevatron [44–47] and the LHC [48], leaving a very narrow mass window for a low-mass Higgs between 116 GeV/c^2 and 127 GeV/c^2. In July 2012 the two big experimental collaborations at the LHC finally announced the discovery of a new neutral boson with a mass of 126 GeV/c^2, which is consistent with a Standard Model Higgs boson. The main focus of the experimental collaborations researching the standard model Higgs boson since then has been precise determination of the properties of the observed scalar, such as its precise mass [49], its couplings to other bosons and ferminons [50] and its spin [51–53]. All of which have been found to be consistent with the standard model predictions.

2.2. The Quark-Gluon Plasma

An interesting consequence of the idea of asymptotic freedom in QCD is that at very high energies and baryon densities hadronic matter dissolves into its constituents. This deconfined state of matter is referred to as QGP, and is expected to have existed from about 10 picoseconds to 10 microseconds after the Big Bang. In this state, both gluons and quarks ideally behave like free particles.
It has been shown theoretically, that for non-vanishing quark masses ($0 < m_q < \infty$) and a vanishing baryo-chemical potential ($\mu_B = 0$), the phase-transition from normal matter into a quark gluon plasma can be characterized as a rapid cross over, rather than a first order phase-transition [54]. Nonetheless it is possible to define a common crossover point T_c by looking at the order parameters $L(T)$, corresponding to the deconfinement measure derived from the Polyakov-loop [55–57], and $\langle\psi\bar{\psi}\rangle(T)$, the effective quark mass, and their susceptibilities χ_L and χ_M. Both order parameters show a sharp temperature variation for all quark masses around a common T_c, defining the pseudo-critical temperature of the system [58]. For $\mu_B > 0$, meaning an excess of baryons over antibaryons, first calculations show that the phase transition remains a rapid cross over until μ_t of a tricritical point and then turn into a first order phase transition [59–61]. A schematic view of the QCD phase diagram of hadronic matter including the QGP can be seen in Figure 2.2. However, to be able to

[2] A Toroidal LHC Apparatus (ATLAS)
[3] Compact Muon Solenoid experiment (CMS)
[4] Large Hadron Collider (LHC)
[5] Large Electron Positron Collider (LEP)

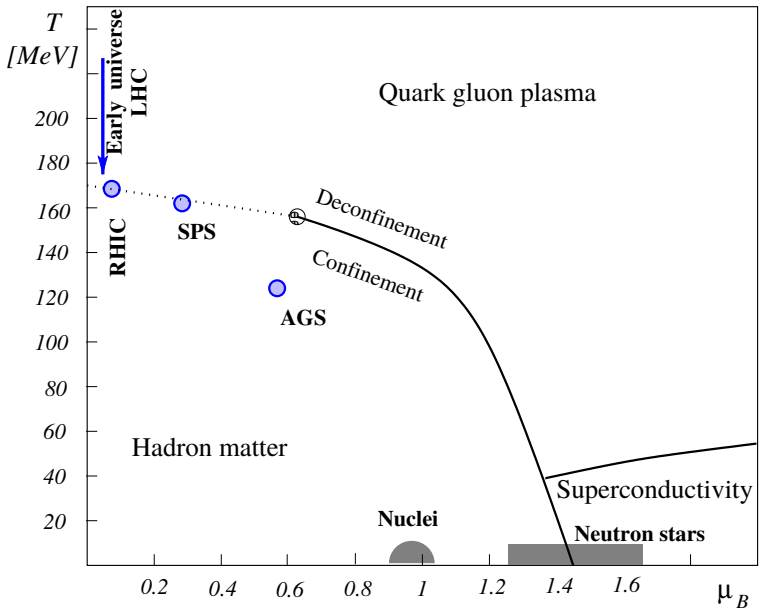

Figure 2.2.: Schematic QCD phase diagram in the $T - \mu_B$ plane, taken from [64]. At low T and μ_B nuclear matter shows confinement and hadrons determine the number of degrees of freedom. On the other hand, at higher T a phase transition to a deconfined quark-gluon plasma with restored chiral symmetry is predicted by lattice QCD. The phase diagram might exhibit a critical point at about $\mu_B \sim 700$ MeV. At higher densities more exotic phases can be reached, e.g. states in very dense neutron stars. In this figure the chemical freeze-out conditions for RHIC, SPS and AGS are indicated as well. The LHC will contribute to measurements at low μ_B, but very high temperatures. The blue arrow illustrates how matter is supposed to have evolved after the Big Bang and before chemical freeze-out at LHC.

talk about temperatures and phases the system needs to consist of a large number of degrees of freedom. Moreover, it has to reach local equilibrium, so that quantities like pressure, temperature, energy and entropy density can be defined and their relations be studied. A consequence of these requirements is that the lifetime of the system has to be significantly larger than the inverse rate of interactions, to allow enough interactions among particles to drive the system towards an equilibrium state [62, 63].

Already in the 1960s, Rolf Hagedorn discovered, by detailed investigations of hadronic matter, that there is a limiting temperature of 140 MeV for hadronic systems. The advances in Lattice QCD (LQCD) calculations, which are non-perturbative calculations of QCD on a space-time lattice allowing to calculate the interactions in the region of low momentum transfer, lead to more precise values of $T_c \sim 150 - 160$ MeV at vanishing baryon chemical potential $\mu_B \approx 0$ [65–68]. Depending on the number of included quarks, their respective masses, their interaction potentials as well as the spacing of the lattice in LQCD calculations the critical temperature and other calculated properties of the system vary. Figure 2.3 shows the results of two groups [67, 68] for the energy density (ϵ) divided by T^4 as a function of the temperature. Both groups find similar values for T_c of (152 ± 5) MeV and (154 ± 9) MeV, respectively. In the left plot of Figure 2.3 the results for different lattice spacings are shown in addition, which are in good agreement and allow for an extrapolation to the continuum as shown and done for the right plot of the same figure. Furthermore, the calculations remain below the Stefan-Boltzmann limit of a non interacting gas of massless quarks and gluons. In addition to the normalized energy density ϵ/T^4, the normalized pressure ($3p/T^4$) and entropy density ($3s/4T^3$) are also shown on the right and found to be consistent with calculations from the Statistical Hadronisation Model (SHM), which successfully describes the hadronic equation of state at low temperatures [69], in their region of validity.

In general it is believed that the majority of collisions of protons or electrons do not produce high enough particle densities to create a quark-gluon plasma. Heavy-ion collisions, on the other hand,

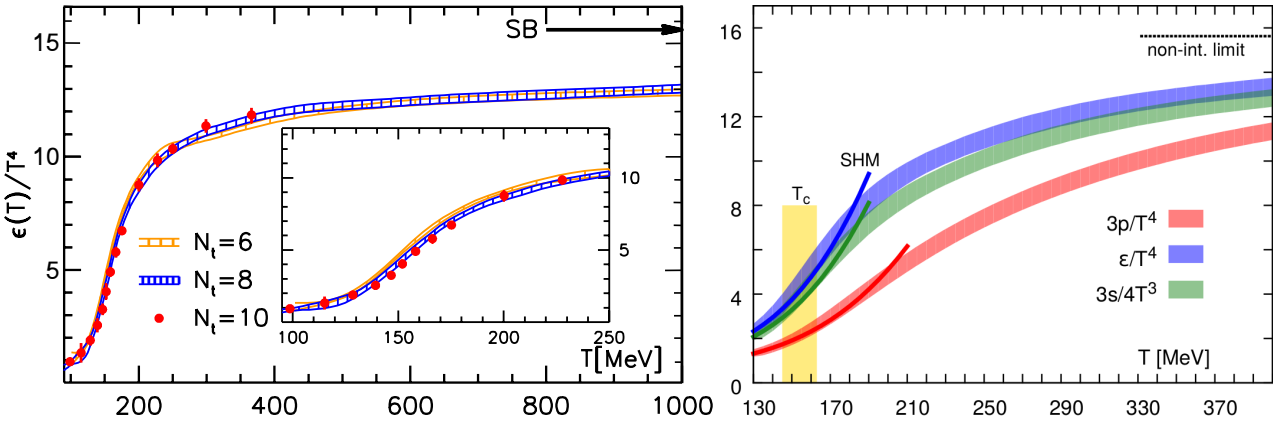

Figure 2.3.: Left: Normalized Energy density as a function of the temperature calculated with lattice QCD for different compositions for different lattice spacings [67]. Right: The normalized energy density (ϵ), pressure (p) and entropy density (s) from LQCD in the continuum limit [68] compared to the calculations from the SHM models [69].

seem to be a good candidate for the production of a QGP state, at least if the energy of the colliding nuclei is large enough. The first calculations considering a QGP were, however, performed in order to explain an excess in the di-lepton spectrum at intermediate invariant masses in pp collisions at ISR[6] energies and performed rather well [70].
Since 1986, high energy heavy-ion collisions have been produced in different laboratories, starting with the AGS[7] at BNL[8] and the SPS[9] at CERN[10]. These experiments started with rather low energies of $\sqrt{s_{\mathrm{NN}}} = 4.6$ and 17.2 GeV per colliding nucleon pair. Figure 2.2 shows that at the SPS at least an intermediate state between the hadron gas and the quark-gluon plasma had been reached already. Continuing with this research, the Relativistic Heavy Ion Collider (RHIC) was built at BNL, which reached $\sqrt{s_{\mathrm{NN}}} = 200$ GeV GeV per nucleon pair, giving very clear indications for the creation of a quark-gluon plasma. The LHC at CERN provides energies that are up to a factor 30 larger than RHIC energies. The fireball is then expected to contain tens of thousands of gluons and quarks and should exceed the critical temperature for the phase transition several times. Both facilities do not only offer to collide heavy nuclei (Pb, Au), but also smaller systems like pp, p–Pb, d–Au and lighter nuclei, like Al and Cu for instance, in order to provide rigorous testing of the system size dependence of the formation of a QGP.
To measure signatures of the QGP, one first has to define event classes for heavy-ion (A–A) collisions. One of the criteria to define such classes is the collision *centrality*: an event selection related to the *impact parameter* b (the distance between the colliding nuclei perpendicular to the beam axis). However, this parameter is experimentally not accessible, but it can be determined via multiplicity measurements and model fits to these distributions. In very central events (e.g. $0-5\%$ of the nuclear inelastic cross-section) two ions collide head-on and the QGP is expected to be formed. Going to more peripheral events (e.g. $> 70\%$ centrality), on the other hand, the quark-gluon plasma phase either only lasts very shortly and in a small volume or is non existent and thus the collisions look more like a superposition of multiple pp collisions. Quantitative estimates of the collision centrality are given by the number of participating nucleons N_{part}, binary nucleon-nucleon collisions N_{coll} or spectators $N_{\mathrm{spec}} = 2A - N_{\mathrm{part}}$ (where A is the mass number of the initial nuclei). These quantities can be related to the impact parameter via Glauber Model calculations [71]. For instance, the mean number of collisions $\langle N_{\mathrm{coll}} \rangle$ can be derived from the nuclear overlap function

[6] Intersecting Storage Rings (ISR) at European Organization for Nuclear Research (CERN), Geneva, Switzerland
[7] Alternating Gradient Synchrotron (AGS)
[8] Brockhaven National Laboratory (BNL), Brookhaven, United States
[9] Super Proton Synchrotron (SPS)
[10] European Organization for Nuclear Research (CERN), Geneva, Switzerland

T_{AA} and the inelastic cross section of nucleon nucleon collisions σ_{NN}^{inel}:

$$\langle N_{\mathrm{coll}} \rangle = \langle T_{\mathrm{AA}} \rangle \; \sigma_{\mathrm{NN}}^{inel} \tag{2.5}$$

While this classification is rather intuitive for A–A collisions, it is less obvious in case of pp or p–A collisions and can be rather understood as subdivision of the observed events according to their number of successive quark pair interactions. Meaning that a proton traversing the center of Pb-ion for instance has a larger probability to interact with the partons of the Pb-ion, leading to a larger number of participating partons and thus a larger probability to create a quark gluon plasma. Similar to A–A collisions the classification is done using particle multiplicities in different detectors, however, for the smaller systems correlations induced by the hadronization process itself and their fluctuations play a larger role and thus the distinction is not as clear [72]. This introduces a strong dependence on the experimental setup and the multiplicity measure used for the classification, which needs to be modeled in the theory calculations.

2.3. Selected Signatures of the Quark-Gluon Plasma

The equilibrium state of the QGP cannot be observed directly in heavy-ion collisions, as it has a lifetime of the order of 10^{-23}s [62]. However, several distinctive signatures can be observed in the experiment, a selection of these is given here [54, 62, 64, 73].

2.3.1. Global Event Properties

By investigating the characteristics of the majority of the particles at low momentum (p_{T} below a few GeV/c), often referred to as "soft particles", we can access the global event properties, which allow insights into the state and dynamical evolution of the bulk matter created in A–A and p–A collisions. These global event properties include multiplicity distributions, yields and transverse-momentum spectra of unidentified and identified particles.

Multiplicity Distributions

The basic first global observable to be discussed is the average multiplicity of charged particles per unit (pseudo)rapidity $\mathrm{d}N_{\mathrm{ch}}/\mathrm{d}y$ ($\mathrm{d}N_{\mathrm{ch}}/\mathrm{d}\eta$). It can be measured with a limited amount of statistics and is thus usually the first publication at a new center of mass energy. In addition, this variable is needed to constrain the model predictions and large extrapolations versus $\sqrt{s}$ are normally challenging as many different effects have to be considered. During the design phase of the LHC the predictions for the particle density ranged from 1000 to above 8000 particles per unit in rapidity, due to the large extrapolation which was necessary from Sulphur beams at $\sqrt{s} = 20$ GeV to Pb–Pb beams at $\sqrt{s_{\mathrm{NN}}} = 5.5$ TeV at the LHC. The uncertainties of the predictions were reduced by including the measured data from RHIC to $\mathrm{d}N_{\mathrm{ch}}/\mathrm{d}\eta = 1500$-$4000$ [74]. The final value, measured by the three LHC experiments taking part in the heavy-ion program, in very central Pb–Pb collisions (0-5%) at $\sqrt{s_{\mathrm{NN}}} = 2.76$ TeV is $\mathrm{d}N_{\mathrm{ch}}/\mathrm{d}\eta \approx 1600$ [73, 75–77], while it increases to ≈ 1950 at $\sqrt{s_{\mathrm{NN}}} = 5.02$ TeV in the same centrality class [78]. The evolution of $\mathrm{d}N_{\mathrm{ch}}/\mathrm{d}\eta$ [11]

[11] The rapidity y of a particle is defined as

$$y = \frac{1}{2} \ln \left(\frac{E + p_z}{E - p_z} \right), \tag{2.6}$$

where E is the energy of the particle and p_z the longitudinal momentum relative to the beam axis. In high energy collisions the rapidity is often replaced by the pseudo-rapidity η in the limit, where $p \gg m$:

$$\eta = -\ln \left[\tan \left(\frac{\theta}{2} \right) \right] = \frac{1}{2} \ln \left(\frac{|\vec{p}| + p_z}{\vec{p} - p_z} \right) \approx y, \tag{2.7}$$

where θ is the polar angle relative to the beam axis.

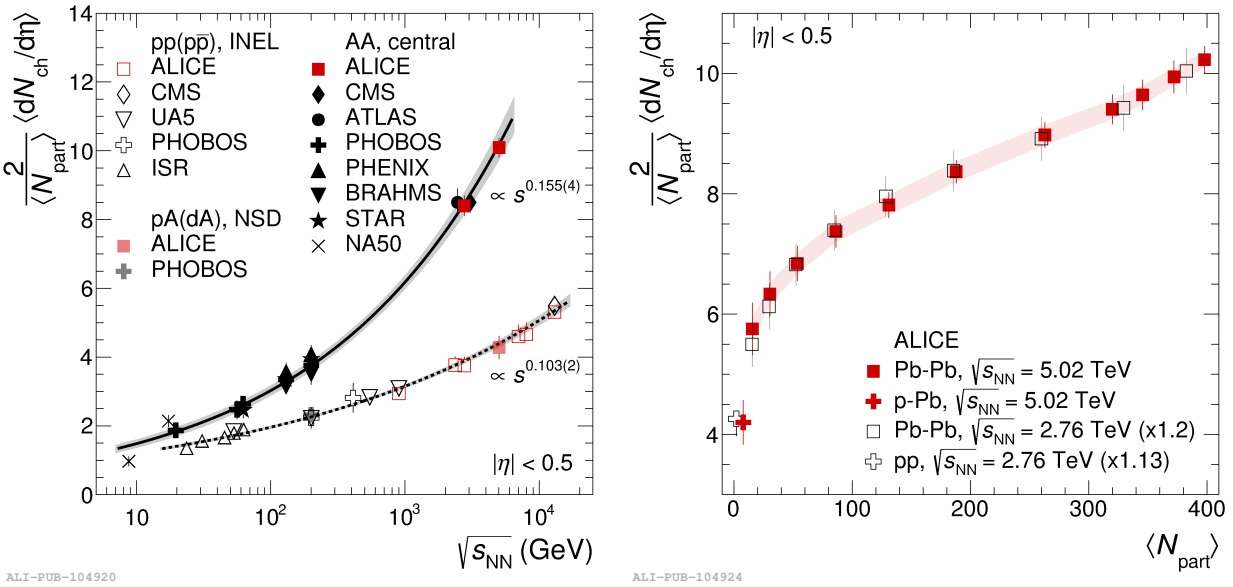

Figure 2.4.: Left: Average charged particle pseudo-rapidity density per participant pair as a function of $\sqrt{s_{\mathrm{NN}}}$for central A–A, p–A and pp collisions [78]. The dependence of the center of mass energy (s) of the heavier systems can be described by a function proportional to $\sqrt{s_{\mathrm{NN}}}^{0.155}$ (solid line), while the minimum bias results of the lighter systems fall on a common function proportional to $\sqrt{s_{\mathrm{NN}}}^{0.103}$ (dashed line). The shaded bands reflect the uncertainty of the power-law dependence.

versus the center-of-mass energy per participant pair is shown in Figure 2.4. In this representation central A–A clearly follow a common dependence of the center of mass energy, while p–A and pp collisions follow a different one. Comparing the same quantity as a function of the average number of participants for different collisions systems and energies shows a close to linear increase for $\langle N_{\mathrm{part}}\rangle > 60$ and a strong drop below that. Suggesting the onset of a different particle production mechanism in the regime below $\langle N_{\mathrm{part}}\rangle = 60$, which comes to a saturation above that value.
The average particle density can be related to a rough estimate of the initial energy density ϵ by the Bjorken formula [79]

$$\epsilon \geq \frac{\mathrm{d}E_{\mathrm{T}}/\mathrm{d}\eta}{\tau_0 \pi R^2} = 3/2\langle E_{\mathrm{T}}/N\rangle \frac{\mathrm{d}N_{\mathrm{ch}}/\mathrm{d}\eta}{\tau_0 \pi R^2} \tag{2.8}$$

where τ_0 is the formation time of the system, R is the nuclear radius and $E_{\mathrm{T}}/N \approx 1$ GeV is the transverse energy per emitted particle. The value for $\mathrm{d}N_{\mathrm{ch}}/\mathrm{d}\eta$ measured by the LHC experiments therefore leads (at $\tau_0 = 1$ fm/c) to an initial energy density of about $12.5-15$ GeV/fm^3 for central Pb–Pb collisions at $\sqrt{s_{\mathrm{NN}}} = 2.76$ TeV, which can also be derived from the measured transverse energy distributions [80, 81]. This is roughly three times higher than at top RHIC energy [82–85].

Identified Particle Spectra

The particle production at low transverse momenta as explained earlier is a non-perturbative process, which cannot be calculated directly from first principles in QCD, thus the particle spectra and ratios in event generators are adjusted to the data of pp and $\mathrm{e^+e^-}$ collisions using a large number of parameters. In heavy-ion collisions, on the other hand, can be described by statistical/thermal [69, 86–88] and hydrodynamical models [74, 89, 90]. These models derive their particle composition from the hadronization at the QGP phase boundary ("chemical freeze-out"), or close to it. While the spectral shape reflects the conditions at the later"kinematic freeze-out" [73].
The particle production of a single species in pp or $\mathrm{e^+e^-}$ collisions at low transverse momentum ($p_{\mathrm{T}} <$ few GeV/c) can be described by an exponentially decreasing function, similar to black body

radiation at a certain temperature. At higher p_{T}, however, it follows a power-law like behavior, reflecting the dominance of hard QCD scattering and fragmentation processes. In A–A collisions, on the other hand, there seems to be an ordered motion amongst the emitted hadrons in the soft part of the momentum spectrum [91, 92], which is referred to as collective flow. In contrast to pp collisions the particles do not follow a random thermal motion anymore but a strong correlation between the position of a particle and its transverse momentum can be observed. This flow arises in a strongly interacting medium in the presence of local pressure gradients [73]. Recently similar effects have been seen in very high multiplicity pp or central p–A collisions and are under investigation from the theory side as well.
As the flow pattern depends on the initial conditions of the collisions, it is classified in terms of the azimuthal angle φ with respect to the reaction plane. The uniform (i.e. φ-independent) component is called *radial flow*. It can be extracted by fitting the transverse-momentum spectra with a "Blast-wave" fit [93]; however, the fit values need to be taken with caution as they highly depend on the particle types which have been included as well as the momentum range in which they have been fitted.
Preliminary transverse-momentum spectra for identified π^+, K^+, p, Ξ and Ω for central Pb–Pb collisions can be seen in Figure 2.5(left) [73,94] compared to a boost-invariant hydrodynamic model with and without rescattering in the hadronic phase [89]. The published results for pions, protons, kaons and cascades can be found in [95, 100] and [96], respectively. The spectral shape differs significantly from the pp results as seen in [95]. For protons, the characteristic mass-dependent blue-shift, generated by the radial flow, leads to a flattening of the spectrum between 0.5 and 1.5 GeV/c and to a harder spectrum at high p_{T}, leading to $\mathrm{p}/\pi \approx 0.9$ at 3 GeV/c in central Pb–Pb collisions. The hydrodynamical calculations are each normalized to the particle species, to be able to compare the shapes, as the absolute particle yields and ratios are an external input to the hydrodynamical models discussed here. The pure hydrodynamical model (full line) can be improved by the inclusion of final-state rescattering (dashed line), calculated by the URQMD [101, 102] transport code, coming closer to the data due to the higher radial flow. Both models, however, fail to describe the spectral shape above 2 GeV/c for pions, kaons, and protons indicating a progressive decoupling of high momentum particles from the thermalized bulk [73]. Whereas they describe spectra of the cascades to much higher p_{T}, indicating the mass ordering of the radial flow and later decoupling of these particles from the thermalized bulk.
The right plot of Figure 2.5 shows the measured spectra for the same particles species [97, 98] in $0-5\%$ central p–Pb collisions at $\sqrt{s_{\mathrm{NN}}} = 5.02$ TeV together with the K^0_S and Λ measurements [99] within the same centrality class. In addition the global Blast-wave fit shown, which describes the spectra well at low transverse momenta for all particle species, also indicates a common radial flow in central p–Pb collisions.
The results of simultaneous Blast-wave fits to the transverse-momentum spectra of $\pi^{\pm}$, $\mathrm{K}^{\pm}$ and $\mathrm{p}/\bar{\mathrm{p}}$ for different centralities and collisions systems are shown in Figure 2.6. It can be seen that the two parameters T_{kin} (kinetic freeze-out temperature) and $\langle\beta_T\rangle$ (average radial flow velocity) are strongly correlated in all collision systems. Contrasting the pp and p–Pb results with the ones from Pb–Pb collisions reveals a higher kinetic freeze-out temperature but a similar average radial flow velocity as in peripheral Pb–Pb collision. These together with the possibility to describe the spectra with hydrodynamic calculations [103, 104], are strong indicators for a collective motion in central p–Pb collisions and very high multiplicity pp collisions, which could be caused by the formation of small QGP droplets and their successive hadronization in the respective collision systems [103].

Integrated Identified Particle Yields

While the transverse-momentum spectra of identified particles contain the information about the collective expansion of the fireball, the integrated yields carry the information about the process of

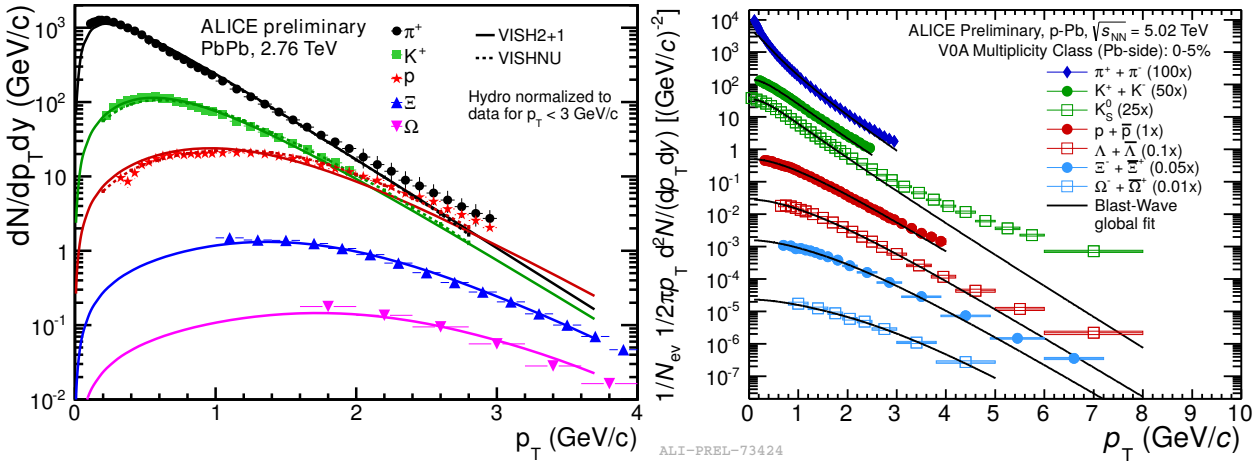

Figure 2.5.: Left: Comparison of the preliminary results on identified transverse-momentum spectra for central Pb–Pb collision at $\sqrt{s_{\mathrm{NN}}} = 2.76$ TeV measured by the ALICE collaboration [73, 94–96] and scaled results from a boost-invariant hydrodynamic model with (VISHNU, dashed lines) and without (VISH2+1, full lines) rescattering in the hadronic phase [89]. Right: Invariant transverse momentum spectra for various identified particles measured by ALICE compared to their global Blast-wave fit in 0-5% central p–Pb collisions at $\sqrt{s_{\mathrm{NN}}} = 5.02$ TeV [97–99].

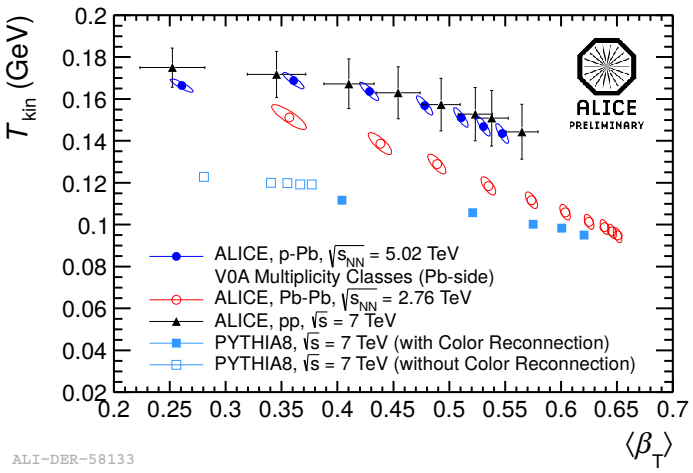

Figure 2.6.: Results from a simultaneous "Blast-wave"-fit to the identified spectra (π K, p) for different centralities in Pb–Pb, p–Pb and pp collisions measured by ALICE.

hadron production itself. Figure 2.7 shows the particle ratios obtained at different center of mass energies and collisions systems from pp collisions at the highest RHIC energy to most central Pb-Pb collisions at $\sqrt{s_{\mathrm{NN}}} = 2.76$ TeV measured by ALICE. When integrating the transverse momentum spectra of the respective particles, an extrapolation to 0 p_{T} and infinite p_{T} has to be performed according to some reasonable functional shape. For the results presented here Blast-wave fits were used at low transverse momenta in the heavier systems and Levy-Tsallis fits for pp collisions and high transverse momenta. While the unmeasured region at high p_{T} can be neglected in general the contribution at low p_{T} can reach up to 20-30%, leading to larger systematic error for the spectra covering a smaller transverse momentum reach due to detection limitations.
The left plot of Figure 2.7 indicates that there is no strong energy dependence of the particle ratios in pp at the respective energies, except for the multi-strange baryons and the p/π, all of which have large systematic or statistical error bars at the lower center of mass energies. Changing the collision system from pp to p–Pb and Pb–Pb, as shown in the right plot, there seems to be an enhancement in the production of particles containing strange quarks, which is emphasized strongest for the

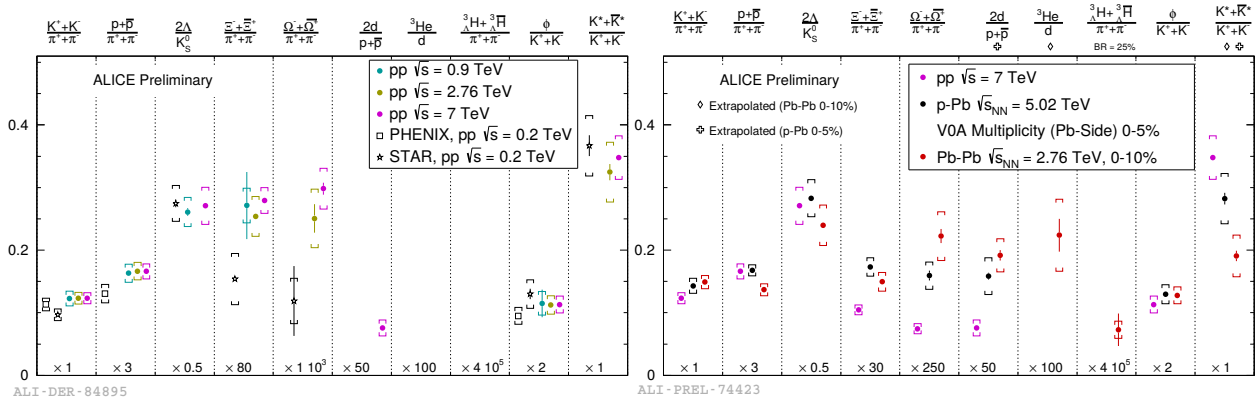

Figure 2.7.: Particle ratios for different particle species in pp collisions at different center of mass energies measured by ALICE, together with the respective ratios from pp collisions at $\sqrt{s_{\mathrm{NN}}}$= 200 GeV at RHIC (left) and from p–Pb and Pb–Pb collisions at the LHC (right) [105].

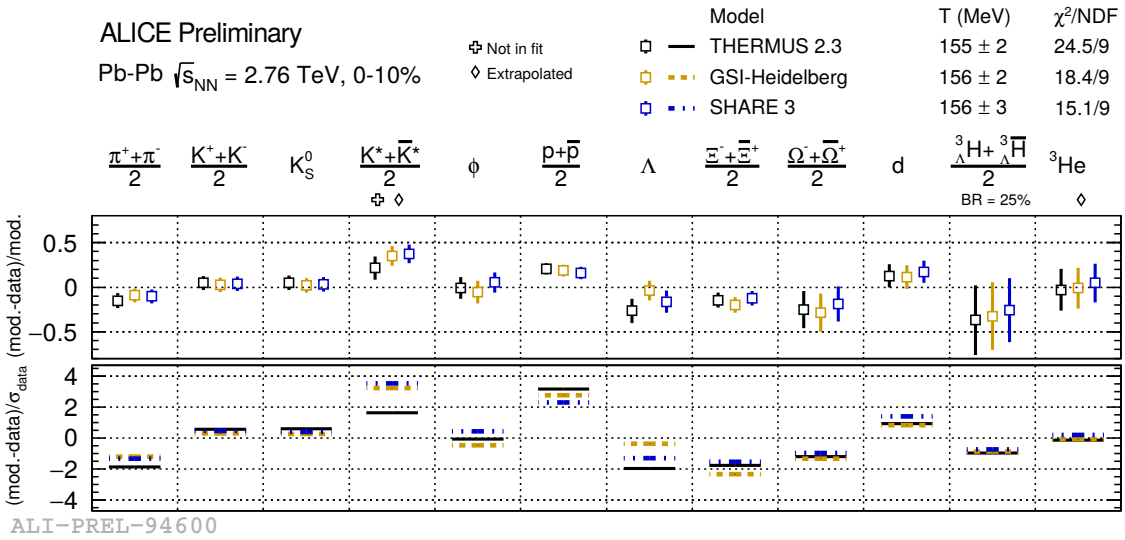

Figure 2.8.: Integrated identified particle yields in 0-10% central Pb–Pb collisions at $\sqrt{s_{\mathrm{NN}}}$ = 2.76 TeV measured by ALICE [105] compared to a thermal model fit [69], THERMUS 2.3 [106] fit and a SHARE 3 [107] fit.

multi-strange baryons with respect to the charged pions. Additionally, the production of the nuclei compared to the proton is enhanced with respect to pp collisions.

The particle production in heavy-ion collisions at lower $\sqrt{s_{\mathrm{NN}}}(2-200$ GeV) is well described by SHM models [69, 86, 87, 106, 107]. These models assume that all particle species are created in thermal (and/or chemical) equilibrium. The only free parameters being: the chemical freeze-out temperature T_{ch}, the baryon potential μ_B, and the volume V. The inclusion of additional free parameters, like the strangeness suppression factor γ_s to account for the difference to the grand-canonical thermal expression, allows the description of lighter collision systems as well [108, 109]. In order to extract these four free parameters a thermal fit to the integrated yield at midrapidty $\mathrm{d}N/\mathrm{d}y$ in central Pb–Pb or pp collisions has been performed. The results are shown in Figure 2.8. While the fit to lower energy data yielded a temperature between $160-170$ MeV, with a value of 164 MeV predicted for LHC, the best fit to the data for central Pb–Pb collisions gives a temperature of 156 ± 2 MeV. However, none of the two can describe all particle ratios simultaneously. Excluding the proton yield from the fit increases the temperature to about 160 MeV but leads to an even larger tension for the protons. This tension could have been there at lower energies already, if the larger relative errors at RHIC are taken into account for the comparisons. A possible explanation

for the significant deviation might be the interactions in the hadronic phase with a particularly large cross-section for antibaryon-baryon annihilation [110].
Similar fits to earlier pp data at $\sqrt{s} = 7$ TeV show that γ_s decreases from $0.9 - 1$ in A–A to $0.5 - 0.6$ in pp collisions, while the temperature range stays constant, ranging from 154 MeV to 170 MeV [111, 112]. However again the model cannot reproduce the proton yields with 170 MeV regardless of the volume, while for 154 MeV the multi-strange ratios are underestimated.

2.3.2. Anisotropic Flow

As nuclei are composed out of partons clustered in protons a collision of two nuclei cannot have an isotropic shape perpendicular to the beam axis. To first order this overlap region has an almond like shape, where its size and excentricity changes depending on the impact parameter. This spatial asymmetry translates into anisotropic pressure gradients in the created medium, leading to an anisotropic expansion of the medium, called *flow* [113]. The flow pattern can be quantified by analyzing the particle production in the transverse plane with respect to the reaction plane, which is defined by the shorter axis of the almond. The asymmetry in this distribution can be decomposed into Fourier components [114]

$$E\frac{\mathrm{d}^3N}{\mathrm{d}^3p} = \frac{1}{2\pi}\frac{\mathrm{d}^2N}{p_\mathrm{T}dp_\mathrm{T}dy}\left(1 + 2\sum_{n=1}^{\infty}\nu_n\cos\left[n(\varphi - \Psi_n)\right]\right), \tag{2.9}$$

where E is the energy of the particle, $p_{(T)}$ its (transverse) momentum, y the rapidity, φ the azimuthal angle of the particle and Ψ_n the azimuthal orientation of the reaction plane. Within the colliding nuclei, however, the partons are inhomogeneously distributed, which causes large density fluctuations in the overlap region, dissolving the idealized almond shape. The resulting different geometrical shapes give rise to higher order Fourier (or flow) coefficients (ν_n). They are p_T, y and centrality dependent and can be calculated using Equation 2.10.

$$\nu_n(p_\mathrm{T}) = \langle\cos\left[n(\varphi - \Psi_n)\right]\rangle. \tag{2.10}$$

The ν_n provide insights into the hydrodynamic evolution of the plasma and allow estimates on the shear viscosity η/s of the produced medium. The first harmonic ν_1 is called directed flow, which is largest close to beam rapidity [115]. Before 2005 mainly the largest remaining component ν_2, referred to as elliptic flow, was considered, as it can be directly linked to the almond shape of the initial spatial geometry. With the higher precision data available from the experiments at RHIC and LHC the extraction of the higher order flow coefficients and combinations of these are getting more and more important to distinguish effects caused by the initial conditions and the evolution or properties of the plasma. The sensitivity to these variables varies depending on the order n. Several experimental methods are available for the measurement of the ν_n as well as the symmetry plane angles, detailed discussions can be found in [91, 92, 116–121].
Bounds on the shear viscosity can be extracted either by comparing the momentum dependent flow parameters to results of viscous hydrodynamical calculations with different η/s or by fitting the centrality dependence of the p_T-integrated value of these flow coefficients. The accuracy of this can be improved by taking into account as many Fourier coefficients as possible as well as their correlations [120]. Results from SPS and RHIC [91, 92] showed that the ν_2 increases with increasing $\sqrt{s_\mathrm{NN}}$, reaching at top RHIC energy a value, which is compatible with the prediction by hydrodynamics for an almost "perfect fluid" [82–85, 132].
The latest results on the harmonic decomposition of two-particle correlations measured by the ALICE collaboration [122] can be seen in Figure 2.9, similar results where obtained by the other LHC [117, 119, 133–135] and RHIC experiments [136]. While the elliptic flow as a function of p_T is very similar to the one measured at RHIC, the momentum-integrated flow increases by 30%, supporting the hydrodynamical prediction that the transport properties do not change significantly

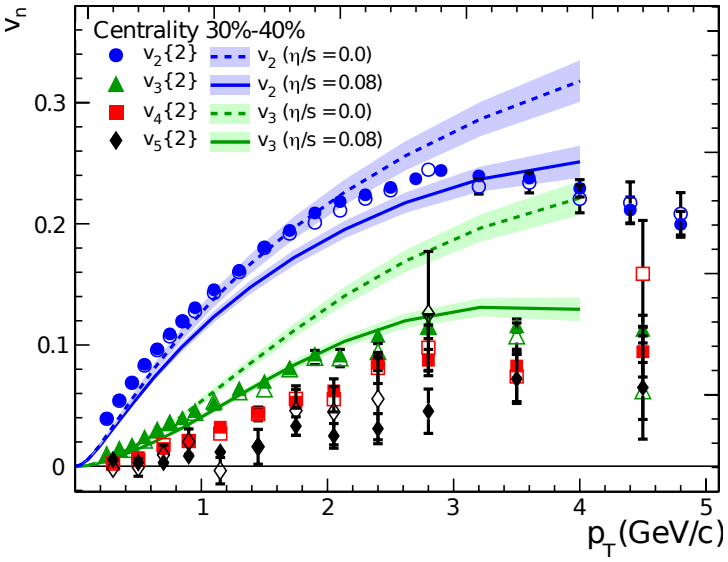

Figure 2.9.: ν_2, ν_3, ν_4, ν_5 as a function of transverse momentum for 30-40% central Pb–Pb events at LHC measured by ALICE compared to hydrodynamical calculations with different shear viscosities (η/s) [122]. The full and open symbols are for $\Delta\eta > 0.2$ and $\Delta\eta > 1.0$, respectively.

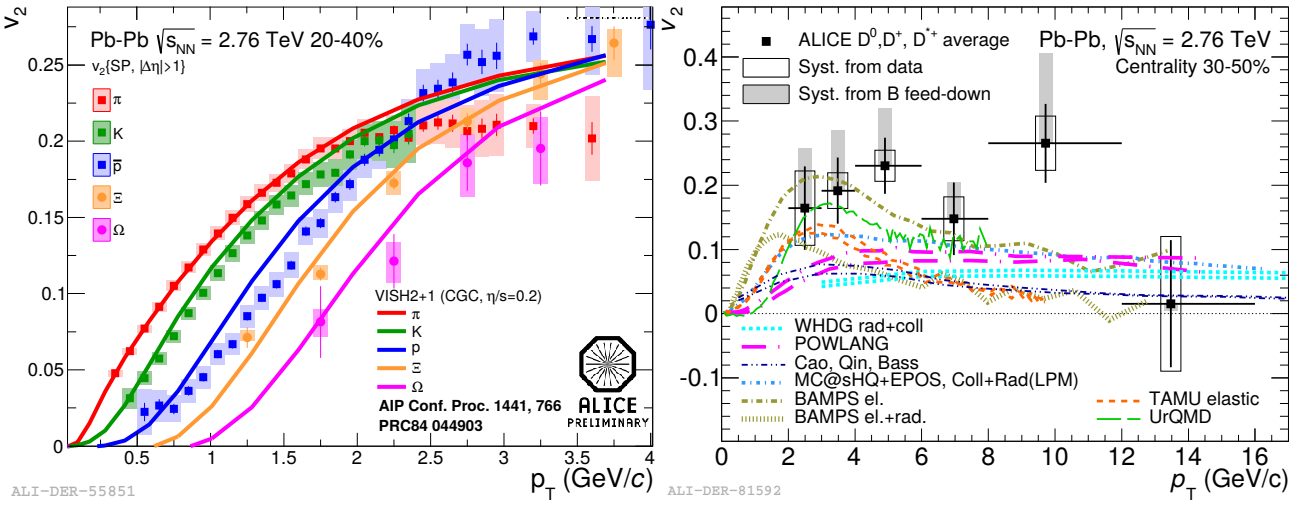

Figure 2.10.: Left: ν_2 as a function of transverse momentum for low momentum π, K, $\bar{p}$, Ξ and Ω together with the corresponding hydrodynamical calculation [123, 124]. Right: ν_2 as a function of transverse momentum for various D-mesons [125] together with various theoretical calculations [126–131].

between RHIC and LHC energies. Moreover, the access to higher harmonics allows to constrain the shear viscosity to $4\pi\eta/s \leq 2$ [90], regardless of the initial conditions. Nevertheless, none of the currently used initial-state models can describe all experimental flow observations simultaneously. Similar conclusions have been drawn from the latest RHIC results [137, 138]. Exploiting in addition to the ν_n the correlations between event-by-event fluctuations of amplitudes of anisotropic flow harmonics allow to gain excess to the temperature dependence of η/s as well as distinguish different initial conditions [120].

While correlations in general can be explained by many different effects, like the hadronization process itself for instance, a splitting of all flow coefficients according to the mass of the particles would indicate a collective motion. Thus, the measurement of identified-particle flow is one of the most stringent tests of the collective-flow interpretation of the azimuthal anisotropies. In Figure 2.10 the latest results from ALICE are shown for light particles [123] and for D-mesons [125] together with different hydrodynamical calculations. The mass splitting, which is also seen for

higher order ν_n's, can be understood taking into account that the collective radial flow does not equalize the particle momenta, but their velocities. Thus, the flow asymmetry for higher-mass particles manifests itself at higher momenta. This effect can be well reproduced by hydrodynamic models up to intermediate transverse momenta. For p_{T} above 1.5 GeV/c the pion and kaon predictions deviate from the data, while the hydrodynamical curves follow the data for baryons up to 3 GeV/c. This different behavior for mesons and baryons, also seen at RHIC [82–85, 132], has been attributed to quark recombination or coalescence [139–143]. An alternate explanation is that the low momentum flow is dominated by the contribution from single quarks and as such scales with the number of valence quarks. While this assumption has been confirmed by the RHIC data, it does not seem to hold for LHC energies.
The result of ν_2 for prompt D-mesons is consistent with the unidentified charged particle ν_2 at high p_{T}. This can be explained by either elliptic flow or the path length dependence of heavy-quark energy loss, which will be explained in the next section.
Recently the same techniques used to extract ν_n in heavy ion collisions have been applied to smaller collision systems (pp, p–Pb, d–Au, p–Au, ^{3}He–Au) in various multiplicity classes. Surprisingly nonzero ν_2 and ν_3 can be extracted for most of the multiplicity classes [144, 145], as it can be seen in Figure 2.11(left) measured by CMS for unidentified charged hadrons. The magnitude of ν_2 at the same average track density decreases going from Pb–Pb to pp collision but rises going from low multiplicity to high multiplicity events. As these measurements are based on two particle correlations they could be interpreted as correlations due to the initial hard collision, however a similar magnitude in ν_2 is seen for 4,6 and even 8 particle correlations using the cumulants technique [144], indicating that they really originate from a common motion of many particles and with that most likely a common source. While the ν_2 is different between Pb–Pb and p–Pb collisions at the same average multiplicity the ν^3 seems to be consist among these two systems, only the high statistics results from pp collisions at $\sqrt{s} = 13$ TeV, which can be explained by its dependence on the initial conditions, which are dominated by the presence of the Pb-nuclei in the heavier systems.
The transverse momentum dependence follows the characteristic patterns seen also in A–A, as it can be seen in Figure 2.11(right, top) for the results from PHENIX versus transverse momentum for p–Au, d–Au and ^{3}He–Au [146] compared to Super hybrid mOdel simulatioN for relativistic heavy-Ion Collisions (SONIC) [147]. Furthermore, recent hydro calculations can reproduce this behavior assuming a small QGP droplet in the smaller systems [147, 149], establishing the interpretation of the existence of a short-lived and small medium in pp and p–A collisions as well.
In addition it has been found that similar to A–A the ν_2 exhibits the characteristic mass splitting, further strengthening the assumption of the existence of a quark gluon plasma in high multiplicity pp and p–A collisions. Figure 2.11(right, bottom) shows the ratio of ν_2 in central and peripheral p–Pb collisions at $\sqrt{s_{\mathrm{NN}}} = 5.02$ TeV for charged hadron, pions, kaons and protons [148]. Within this representation the effect of the mass splitting is enhanced as the strength of ν_2 for the various particles depends on multiplicity, getting stronger in central p–Pb collisions with respect to peripheral collisions. Similar results were obtained for pp collisions at $\sqrt{s} = 13$ TeV by the CMS collaboration for K^0_s and Λ [144].

2.3.3. Suppression of Particle Production and Nuclear Suppression Factor (R_{AA} and R_{pA})

A key observable for the QGP is the nuclear suppression factor R_{AA} or R_{pA} for A–A and p–A collisions, respectively, which quantifies the modification of particle yields due to medium effects. If heavy-ion collisions could be interpreted as a superposition of many binary collisions of the individual nucleons the value for R_{AA} would be equal to unity at high p_{T} ($p_{\mathrm{T}} \geq 2$ GeV/c). This is

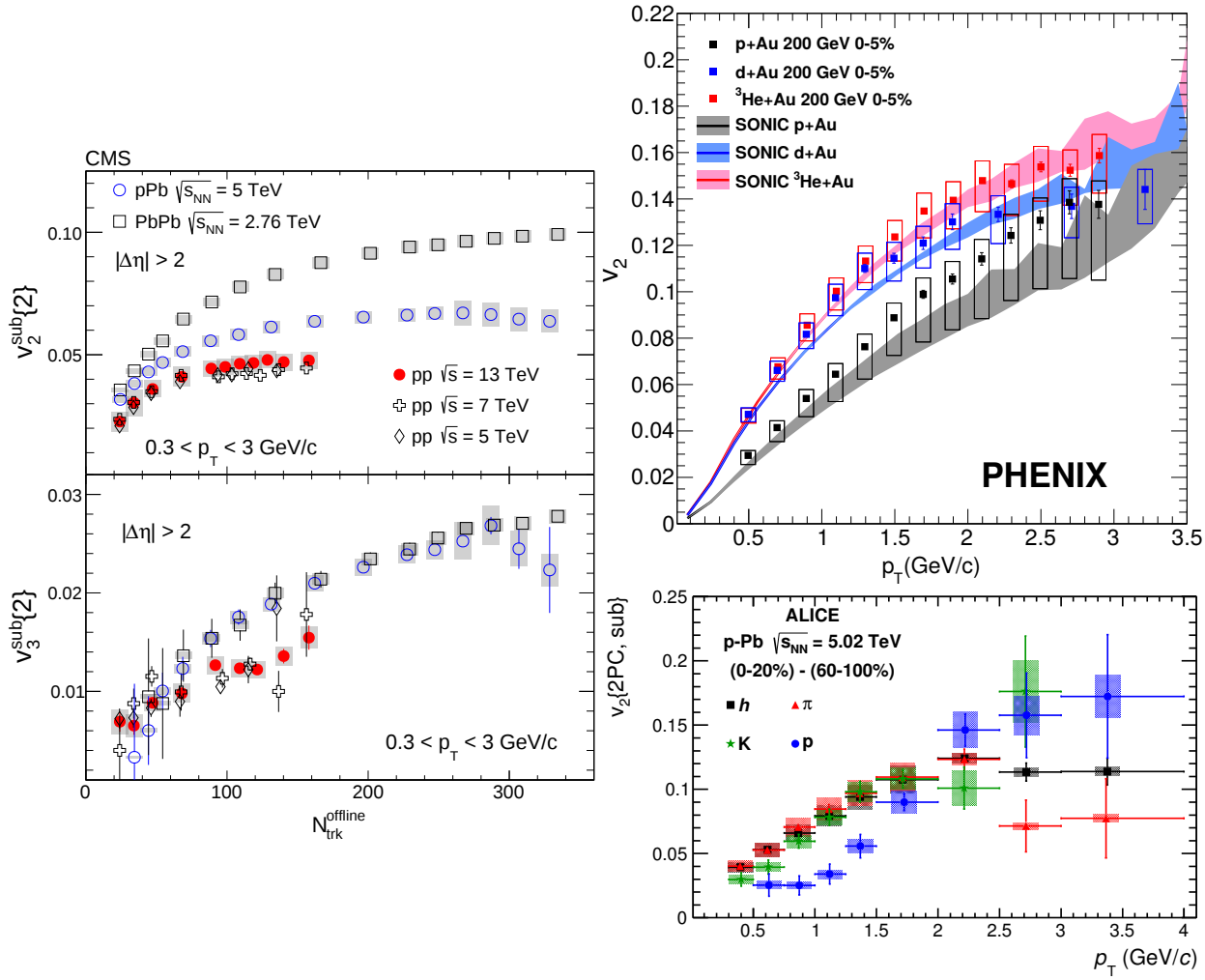

Figure 2.11.: Left: Average multiplicity dependence of ν_2 and ν_3 in Pb–Pb, p–Pb and pp collisions at various collisions energies at the LHC measured by CMS using two particle charged hadron correlations with the sub-event technique [144]. Right top: Elliptical flow (ν_2) as a function of p_T for different collisions system at $\sqrt{s_{NN}} = 200$ GeV measured by the PHENIX experiment [146] and compared to hydro calculations using SONIC [147]. Right bottom: Ratio of ν_2 in central and peripheral p–Pb collisions at $\sqrt{s_{NN}} = 5.02$ TeV for charged hadron, pions, kaons and protons [148].

called binary scaling. The R_{AA} is defined as

$$R_{AA}(p_T) = \frac{\frac{1}{N_{evt}^{AA}} d^2N^{AA}(p_T)/d\eta dp_T}{\langle N_{coll}\rangle \frac{1}{N_{evt}^{pp}(p_T)} d^2N^{pp}/d\eta dp_T}, \tag{2.11}$$

where N_{evt}^{xx}, with $xx = AA$ or pp, is the number of events and $d^2N^{xx}/d\eta dp_T$ is the double differential yield of a certain particle type in heavy-ion and pp collisions respectively. $\langle N_{coll}\rangle = \langle T_{AA}\rangle \sigma_{NN}^{inel}$ was defined in Equation 2.5. The same holds for the R_{pA} exchanging the respective A–A yields and $\langle T_{AA}\rangle$ by the ones measured and calculated for the p–A system.

However, binary scaling is not only broken due to final state effects occurring in A–A collisions which are related to collisional or radiative energy loss of partons. It can be broken by initial-state effects as well, like the Cronin effect, radial flow or the modification of the nuclear PDFs with respect to nucleon PDFs. Until recently it was assumed that only the initial-state, or cold-nuclear matter, effects should be seen in p–A collisions, taking into account the previously discussed observations this might not be true. The magnitude of the final state effects, on the other hand, should be larger in the heavier system and in more central p–A collision.

The increase of transverse momentum (k_{T}) for the incident partons due to multiple scattering on their path through the nucleus A is referred to as Cronin effect [150]. It can be understood as the projectile partons acquiring an extra transverse momentum (k_{T}) while traveling through the nucleus, which contributes to an increase of the transverse momentum of the produced hadron. Consequently the R_{pA} increases at low transverse momenta, while for higher p_{T} this extra k_{T} broadening becomes a negligible fraction of the measured p_{T} and therefore the R_{pA} will approach unity again. The Cronin effect can be quark mass and number dependent, thus can look different for different particle species.
An additional cold nuclear matter effect is the modification of the parton density distributions in nuclei with respect to those in the free nucleon. These nuclear modifications depend on the fraction x of the hadron momentum carried by the parton, the momentum scale Q^2, and the mass number of the nucleus. The PDFs of heavy nuclei (nPDFs) can be related to the ones for the proton via:

$$f_i^A(x, Q^2) = R_i(A, x, Q^2) f_i^p(x, Q^2) \tag{2.12}$$

where R_i is a functional representation of the modification with respect to the parton distribution for the proton f_i^p. These functions vary for valence quarks, sea quarks and gluons [151]. Depending on the collision energy, a different region of x and Q^2 is probed and one speaks of shadowing or anti-shadowing, a depletion or enhancement respectively of the parton densities with respect to the free parton. These effects lead to a different shape of the R_{pA} as well as of the R_{AA} at different energies, not necessarily allowing any statement on the existence of final state effects.
The final state effects can be categorized in two main contributions: the energy loss due to scattering on other partons and the radiation of gluons in the medium. The first one is called collisional energy loss and dominates at low energies, whereas the latter represents gluon bremsstrahlung, which is dominating at high energies. Both mechanisms lead to the reduction of the parton energy when traversing a strongly interacting medium. Which translates into a reduction in the average momentum of the produced hadron and therefore into a reduction of the yield at high p_{T} with respect to pp-collisions. Owing to the power-law shape of the initial p_{T} spectrum for $p_{\mathrm{T}} > 3$ GeV/c, a modest reduction in the parton energy leads to a significant decrease in the hadron yield. A simple model for describing the radiative energy loss due to gluon radiation is the BDMPS approach [152, 153]. In this approach the mean energy loss depends only on the Casimir factor C_R, the length L of the particle traveling through the medium and the transport coefficient $\hat{q}$. It can be described by:

$$\langle \Delta E \rangle \propto \alpha_s \, C_r \, \hat{q} \, L^2 \tag{2.13}$$

By introducing a dependence on L^2 the non-abelian structure of QCD is taken into account as well as quantum interference effects. Depending on the exact model the power of L can vary, however. The Casimir factor reflects the different weightings for the interaction vertices: 3 for a gluon-gluon interaction and 4/3 for a quark-gluon interaction. Finally, the transport coefficient $\hat{q}$, which describes the average transverse momentum transfer per path length, is related to the medium properties and the gluon density, allowing an indirect measurement of the medium energy density.
It is necessary to disentangle the final and initial state effects to quantify the influence of the QGP on the measured particles. This might be realized by a measurement of p–A collisions at the same energy as the A–A collisions in order ascertain the magnitude of the initial-state effects to first order. The current results on the charged hadron R_{pA} for p–Pb collisions at $\sqrt{s_{\mathrm{NN}}} = 5.02$ TeV measured by ALICE [154] are shown in the left plot of Figure 2.12. It shows no suppression for high momenta ($p_{\mathrm{T}} > 2$ GeV/c), which indicates that the strong suppression in Pb–Pb collisions at the LHC is mainly due to intial-state effects. Similar results have been obtained by the other LHC experiments [155, 156]. Looking at the R_{pA} more differentially versus charged particle multiplicity [72], reveals a strong dependence on the different multiplicity estimators due to fluctuations and other correlations. This complicates the interpretation of the R_{pA} using these multiplicity classes.

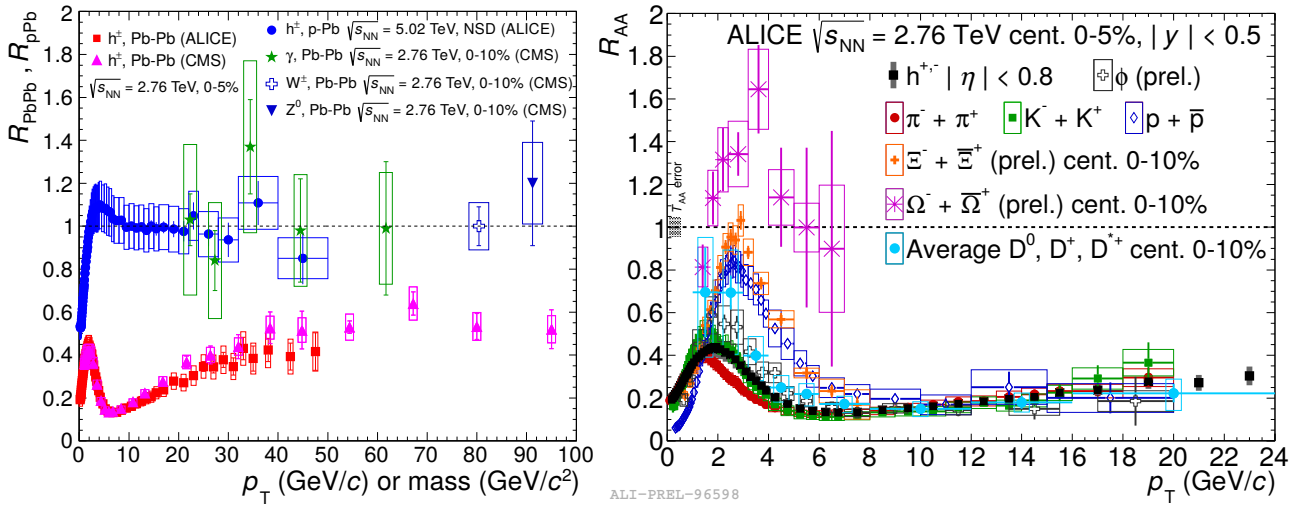

Figure 2.12.: Left: Comparison of the charged hadron nuclear modification factor R_{AA} (R_{pA}) for Pb–Pb collisions at $\sqrt{s_{\mathrm{NN}}} = 2.76$ TeV [157, 158] and p–Pb collisions at $\sqrt{s_{\mathrm{NN}}} = 5.02$ TeV [154]. In addition the nuclear modification factors for isolated photons [159], the Z^0 [160] and the $\mathrm{W}^{\pm}$ [161] are shown. Right: Nuclear modification factor R_{AA} as a function of p_{T} for a variety of particle species [95, 162–164].

Currently no uniform definition of centrality has been agreed upon by the different experiments, requiring the theorist to model the centrality selection criteria applied by the different experiments. The nuclear suppression factor is a general quantity and can be built for all particle types, giving access to different properties of the medium. The fastest measurement for new collision energies is usually the charged hadron R_{AA} since it does not require particle identification and only the p_{T} reach is statistically limited. For Pb–Pb collisions at $\sqrt{s_{\mathrm{NN}}} = 2.76$ TeV the ALICE collaboration was the first of the LHC experiments to publish this measurement after only few days of data taking in 2010 [165]. If no pp-reference is available at the respective center of mass energy it is usually interpolated or extrapolated from the measurements available at the energies closest to the desired s using simple power-law scaling. This procedure is not optimal and can introduce biases, which are non negligible, thus it is desired to take data at the same center of mass energy as the Pb–Pb or p–Pb run. While for the first publication no such reference was available, an updated result has been released including the measured reference [157]. Additionally, the other LHC experiments participating in the Pb–Pb running have published their results [158, 166], confirming the ones initially obtained by ALICE but extending the transverse momentum range by about a factor 10.

A partial compilation of the R_{AA} and R_{pA} results from LHC is shown in the left plot of Figure 2.12. The rise in the R_{AA} for most central Pb–Pb collisions for $p_{\mathrm{T}} > 7$ GeV/c was never observed in such a significant way, although there were indications from the π^0 data measured by PHENIX [167]. The CMS measurement extends the p_{T} reach up to 100 GeV/c with charged hadrons and 300 GeV/c with jets, giving a better chance to differentiate between the different theoretical predictions. The R_{AA} is lower by a factor 2 for $\sqrt{s_{\mathrm{NN}}} = 2.76$ TeV than for the measured charged-particle spectrum at RHIC, though the shape agrees. Increasing the center of mass energy by another factor 2 at the LHC shows a similar transverse momentum dependence as well as a similar suppression [155]. Within the QGP the strong force dominates over the electro-weak interaction, due to the smaller coupling strength of the electo-weak interaction. Therefore, any particle traversing the plasma will mainly experience the strong force. Direct photons or the gauge bosons ($\mathrm{W}^{\pm}$, Z^0), however, will not be influenced by the plasma to first order, therefore their yields should fulfill binary scaling at high transverse momenta. They provide an ideal control probe and should show an R_{AA} of unity at high p_{T}. The direct photons have been measured at RHIC and yielded the expected result [168], although latest results show a slight deviation from unity [169] for the highest p_{T} bins. The first attempts to measure the control probes at LHC were presented by the CMS [159–161] and ATLAS

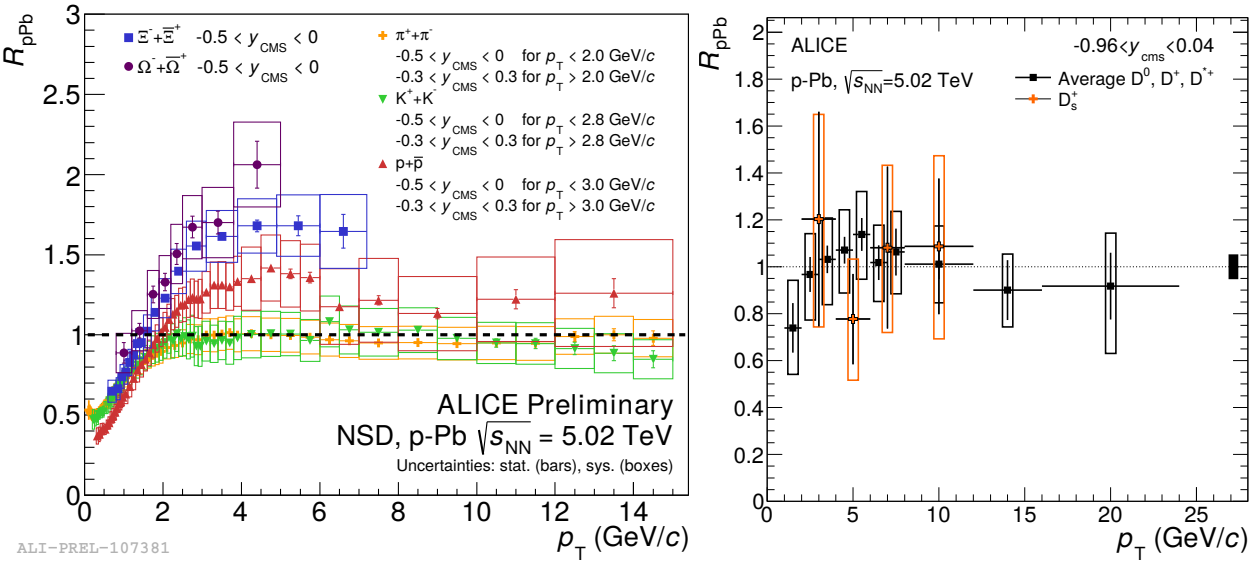

Figure 2.13.: Nuclear modification factor R_{pA} versus transverse momentum for identified light particles and cascades (left) [97, 154, 162], as well as D-mesons (right) [199] measured by the ALICE experiment at $\sqrt{s_{\mathrm{NN}}} = 5.02$ TeV p–Pb collisions at the LHC.

collaborations [170–172]. A selection of these are shown alongside the charged hadron measurements in the left plot of Figure 2.12. The measurements agree with unity within the error bars. These are the first measurements of the Z^0 and W-bosons in Pb–Pb collisions and their respective suppression factor [160].
Although the charged-particle spectra allow to distinguish between different models, identified particles and jets need to be measured in addition as they probe different properties of the medium. They give access to the energy density and the quark content or the quark multiplicity. Measurements exist for a variety of identified particles: light particles [95, 163, 173, 174], cascades [162], heavy flavor particles [164, 175], quarkonia [176–183] and jets [184–187]. Some of the first measurements on identified particle R_{AA} are shown in right plot of Figure 2.12. Surprisingly, even the heavier quarks, as shown by the R_{AA} of prompt D mesons, are almost as strongly suppressed as the inclusive charged particles. This seems contrary to the prediction that gluons, which are the main source of inclusive charged particles at LHC, should suffer twice as much energy loss as light quarks. Moreover, their energy loss should be less due to the mass dependence of radiation ("dead-cone" effect [188]). From the data it seems that the mass dependence is weaker than expected from radiative energy loss, and above $p_{\mathrm{T}} \approx 8$ GeV/c the suppression is universal for all particles. In order to further distinguish the initial and final state effects, the identified particle R_{pA} has been measured for NSD p–Pb collisions at $\sqrt{s_{\mathrm{NN}}} = 5.02$ TeV for light flavor particles [97, 99, 189], cascades [162], heavy flavor mesons [190], quarkonia [191–195] and jets [196–198]. A selection of identified particle R_{pA} results from ALICE is shown in Figure 2.13. The light flavor particles, as well as the D-mesons agree with unity for $p_{\mathrm{T}} > 6$ GeV/c, the cascades however exhibit a strong enhancement at low transverse momenta, and it is unclear whether their R_{pA} will agree with unity when going to higher momenta. The same enhancement is seen for the spectra and particle ratios, as discussed earlier.

2.3.4. Photon Signals

As discussed earlier, the dominant force in the QGP is the strong interaction, meaning photons, only interacting electromagnetically, can leave the plasma nearly unmodified. As such, they carry the information about the conditions of their production outside of the plasma, being much less

affected by the medium and the following stages of the collisions than hadronic probes.
In heavy-ion collisions photons can be produced at different stages of the collisions. For pp collisions, on the other hand, the photon production is traditionally separated in three different categories: direct photons, fragmentation photons and photons, which are produced by decays subsequent to the collision. As the distinction between direct photons and fragmentation photons is rather arbitrary, they are often summarized as prompt photons. Their production is dominated by the $2 \rightarrow 2$ processes, like $q + g \rightarrow q + \gamma$, $\bar{q} + q \rightarrow g + \gamma$, which can be calculated using pQCD at next-to-leading order with sufficient precision above $p_{\mathrm{T}} = 3 - 4$ GeV/c.
For these interaction the produced quark or gluon will most likely hadronize inform of a jet. While this jet subsequently loses some of its energy in the medium the γ will leave it unchanged, thus providing a measure for the initial energy of the partonic collision. Using these kind of events, it is possible to probe the PDF as well as obtain a direct measurement of jet quenching. The magnitude of the modification to the jet will depend not only on the transport coefficient, but on the path length of the jet in the QGP as well. Thus, measurements of the correlation function of direct photons and jets, as well as their energy imbalance, should lead to a better understanding of the properties of the medium. Recently the first measurements on these observables from the LHC have been presented [159,170,200], showing a significant decrease in the number of jets produced in coincidence with a γ with $p_{\mathrm{T}} > 60$ GeV/c, with respect to the same measurement in pp collisions. However, no significant broadening of the azimuthal correlation of the photon and the jet can be observed.
For A–A collisions, however, there are additional sources of photons: the medium contributions which are discussed in detail in [201]. These contributions include:

- **Jet-Photon Conversion**
  This source of photons is similar to the initial hard scattering, being induced by jets crossing the hot medium and undergoing annihilation or QCD Compton scattering. Thus, their p_{T} distribution should be very similar to the one of hard processes. As a result of the larger gluon density in the QGP it will, however, be dominated by the gluon-channel (Compton scattering). Additionally, the high p_{T} photons will preferably be emitted at the early stages of the QGP phase when the density and temperature are largest.

- **Bremsstrahlung Photons**
  Annihilation and Compton radiation are not the only processes producing photons in the medium, they can also be produced by bremsstrahlung while scattering on the quarks and gluons forming the medium. While this process has a larger cross-section than the jet-photon conversion, the photons normally only carry a small fraction of the initial jet energy. Therefore, jet-conversion dominates the in medium production if folded with the steeply falling jet spectrum.

- **Thermal Photons**
  Similar to black-body radiation these photons are emitted from a thermally equilibrated phase, which can be the QGP phase or the hot hadronic phase following the QGP in heavy ion collisions. Their production rate and shape is governed by the temperature at which the photon was emitted. Therefore the photons which are produced by the quark-gluon plasma carry information on the thermodynamical state of the medium at the moment of their production. As the QGP is expanding after the initial collision and cooling while doing so, thermal photons are emitted at various temperatures and it is experimentally not possible to extract the initial temperature of the QGP directly. Only an effective temperature, deduced from an exponential fit can be reported, which includes this blue-shift. Thermal photons should dominate the photon spectrum below a transverse momentum of about 3 GeV/c, depending on the initial collision energy.

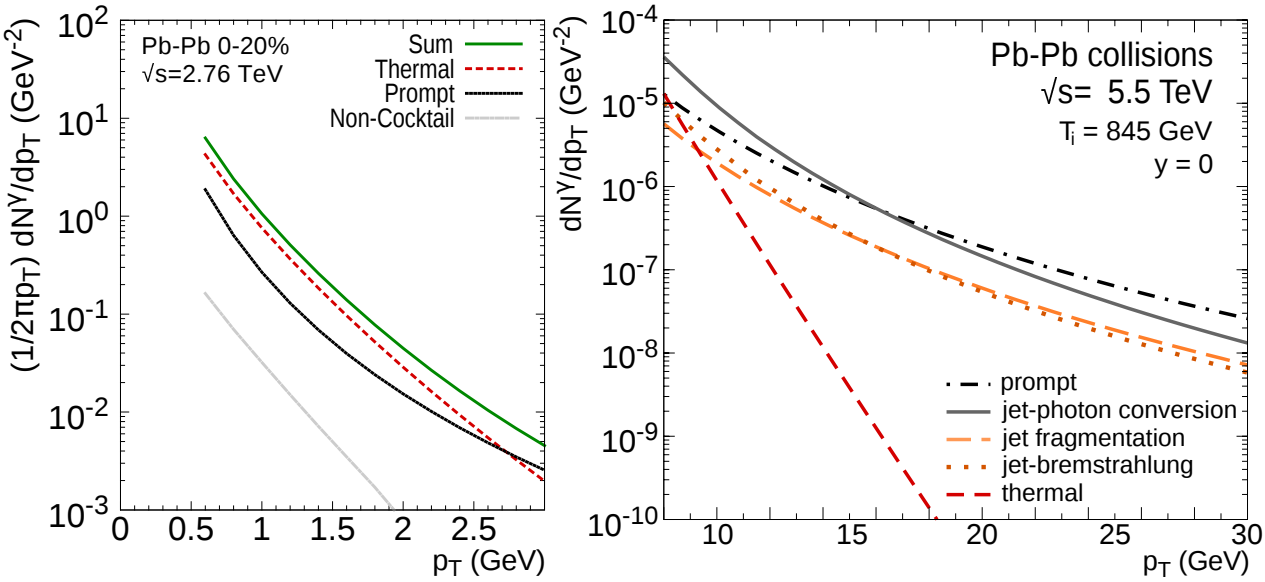

Figure 2.14.: Sources of photons in central Pb–Pb collisions at $\sqrt{s_{\mathrm{NN}}} = 2.76$ TeV (left) and $\sqrt{s_{\mathrm{NN}}} = 5.5$ TeV (right) at the LHC at midrapidity. The different contributions at low transverse momenta (left) are the thermal photons (red dashed line), the prompt photons (black solid line) and photons which are not included in the experimental electromagnetic cocktails (grey solid line). For higher momenta (right) the prompt contribution is further split into jet-photon conversions (grey solid line) and photons originating from the initial nucleus-nucleus collision (black dashed-dotted line). Additionally, the jet fragmentation and jet bremstahlungs photons are show (orange lines), as well as the thermal photon component (red dashed line) at this center of mass energy. The plots adapted from [202] and [201], respectively.

The expected yield versus transverse momentum for the different sources is shown in Figure 2.14 for Pb–Pb collisions at $\sqrt{s_{\mathrm{NN}}} = 2.76$ TeV [202] (left) and $\sqrt{s_{\mathrm{NN}}} = 5.5$ TeV [201] (right). At high transverse momentum, shown here for $\sqrt{s_{\mathrm{NN}}} = 5.5$ TeV, the direct photon spectrum will be dominated by prompt photons and those from jet-photon conversions. As the detailed separation of the two contributions depends on an arbitrary length scale, recent calculations sum them as prompt photons, as shown here for the calculation at $\sqrt{s_{\mathrm{NN}}} = 2.76$ TeV. For RHIC energies even the jet-photon conversion component would be sub-dominant above $p_{\mathrm{T}} \approx 4$ GeV/c and only below that the modification of the spectral shape due to the presence of a QGP can be seen. Photon production via jet bremsstrahlung or fragmentation in the plasma turns out to be weak, it is approximately a factor 3 below the jet-photon conversion contribution. Consequently, the efforts of calculating this contribution within the currently applied frameworks have subsided.
The thermal contribution on the other hand is small at high transverse momenta but rises strongly towards very low momenta, becoming the dominant source below $p_{\mathrm{T}} = 3$ GeV/c. Similar results have been obtained by various theoretical collaborations for collisions at LHC and RHIC [64, 202–206]. However, each of them is using slightly different photon production rates and mechanisms in the QGP and the hot hadron gas phase, leading to differences in the predicted yields of factors of up to 10.
The thermal photons at low momentum are of particular interest, as they could give a hint about the temperatures in the plasma. Experimentally in order to obtain the direct-photon spectrum the background from meson decays needs to be subtracted. One of the most promising methods for measuring the thermal photons is the measurement of the direct-photons via the subtraction method in combination with the double ratio method [207]. In this case the direct-photon signal (γ_{dir}) is extracted by subtracting the meson-decay photon spectrum (γ_{dec}), which is dominated by the photons originating from π^0 and η decays, from the inclusive photon spectrum (γ_{inc}),

Equation 2.14.

$$\gamma_{\mathrm{dir}} \quad = \quad \gamma_{\mathrm{inc}} - \gamma_{\mathrm{dec}} = \left(1 - \frac{\gamma_{\mathrm{dec}}}{\gamma_{\mathrm{inc}}}\right) \times \gamma_{\mathrm{inc}} \tag{2.14}$$

The expected photon decay spectrum is obtained from a electromagnetic cocktail simulation, which is based on the yield parametrization of mesons with photon decay branches. Where the dominant sources are the π^0 ($\sim 80-85\%$) and the η ($\sim 10-15\%$). As input for the calculation all available measured identified particle spectra are used and the unknown particle yields are obtained by m_{T}-scaling [208]. In order to reduce the systematic uncertainties, the ratio $\frac{\gamma_{\mathrm{decay}}}{\gamma_{\mathrm{inc}}}$ is calculated as:

$$R_\gamma = \frac{\gamma_{\mathrm{inc}}}{\gamma_{\mathrm{decay}}} = \frac{\gamma_{\mathrm{inc}}/\pi^0}{\gamma_{\mathrm{decay}}/\pi^0_{\mathrm{param}}} \tag{2.15}$$

By using the same sample of photon candidates to create the meson spectra and the inclusive photon spectra further uncertainties cancel out [207, 209]. The first measurements of the direct-photons at low p_{T} in Pb–Pb collisions at LHC were presented at Quark Matter 2012 [210, 211] for $0-40\%$ central events. As this measurement is very sensitive to small variations in the neutral pion yield, the publication of the more differential results versus centrality was only possible after having been confirmed by an independent measurement using another photon detection technique within ALICE, as well as the publication of the neutral pion yields themselves [173]. The final results from ALICE [212], as shown in Figure 2.15, are a combination of two fully independent results using different photons detection techniques, increasing the precision even further. The double ratio shows a centrality dependent enhancement for low momenta ($p_{\mathrm{T}} < 3$ GeV/c) going from about 5% in peripheral to $\sim 13\%$ in most central collisions. While the enhancement in peripheral collisions is compatible with 1, the significance of the direct photon signal for $0.9 < p_{\mathrm{T}} < 2.1$ GeV/c in central Pb–Pb collisions is 2.6σ. At high transverse momenta the measurements are in agreement with the expectations from N_{coll} scaled pQCD NLO predictions [213,214] in all centrality classes, in particular when using the nuclear Parton Density Functionss (nPDFs) as input to the JETPHOX calculations [215]. Exponential fits to the resulting direct photon spectra in 0-20% and 20-40% Pb–Pb collisions yield effective temperatures of $T_{\mathrm{eff}} = (297 \pm 12^{\mathrm{stat}} \pm 41^{\mathrm{syst}}$ MeV and $T_{\mathrm{eff}} = (410 \pm 84^{\mathrm{stat}} \pm 140^{\mathrm{syst}})$ MeV, respectively. Comparing the measurements to the various theory calculations shows that these tend to underestimate the most probable value of the yield in almost all transverse momentum bins for 0-20% central Pb–Pb collisions by about a factor 1.5-2, while most of them are still in agreement within the given 1σ systematic errors.
A similar analysis at RHIC yielded $T_{\mathrm{eff,RHIC}} = 221 \pm 19^{\mathrm{stat}} \pm 19^{\mathrm{syst}}$ MeV for 0-20% central Au-Au-collisions at $\sqrt{s_{\mathrm{NN}}} = 200$ GeV [168, 217], which indicated by comparison to a hydrodynamic calculation an initial temperature of the QGP that exceeds the critical temperature T_c. However, recent theory calculations fail to describe those excess yields for different centralities to better than a factor two [202–205, 216, 218–222]. Furthermore, recent measurements at the same $\sqrt{s_{\mathrm{NN}}}$ by the STAR collaboration report a smaller excess yield [223], which is in agreement with the theoretical expectations within about 1σ.
While the photon spectra carry a lot of information about the initial temperatures of the QGP, they do not provide insight to the evolution of medium. To gain access to this information the Fourier coefficients of the direct photons have to be measured. This is done using a similar Ansatz as for the direct photon spectra: By measuring the inclusive photon ν_n and subtracting the expected ν_n from decay photons taking into account their relative abundances through the R_γ, according to Equation 2.16.

$$\nu_2^{\gamma,\,\mathrm{dir}} = \frac{R_\gamma \nu_2^{\gamma,\,\mathrm{inc}} - \nu_2^{\gamma,\,\mathrm{dec}}}{R_\gamma - 1}\,. \tag{2.16}$$

The first measurements of ν_2 and ν_3 for direct photons by the PHENIX collaboration [224, 225] report a similar magnitude in both quantities as seen for the charged hadrons and pions. Having

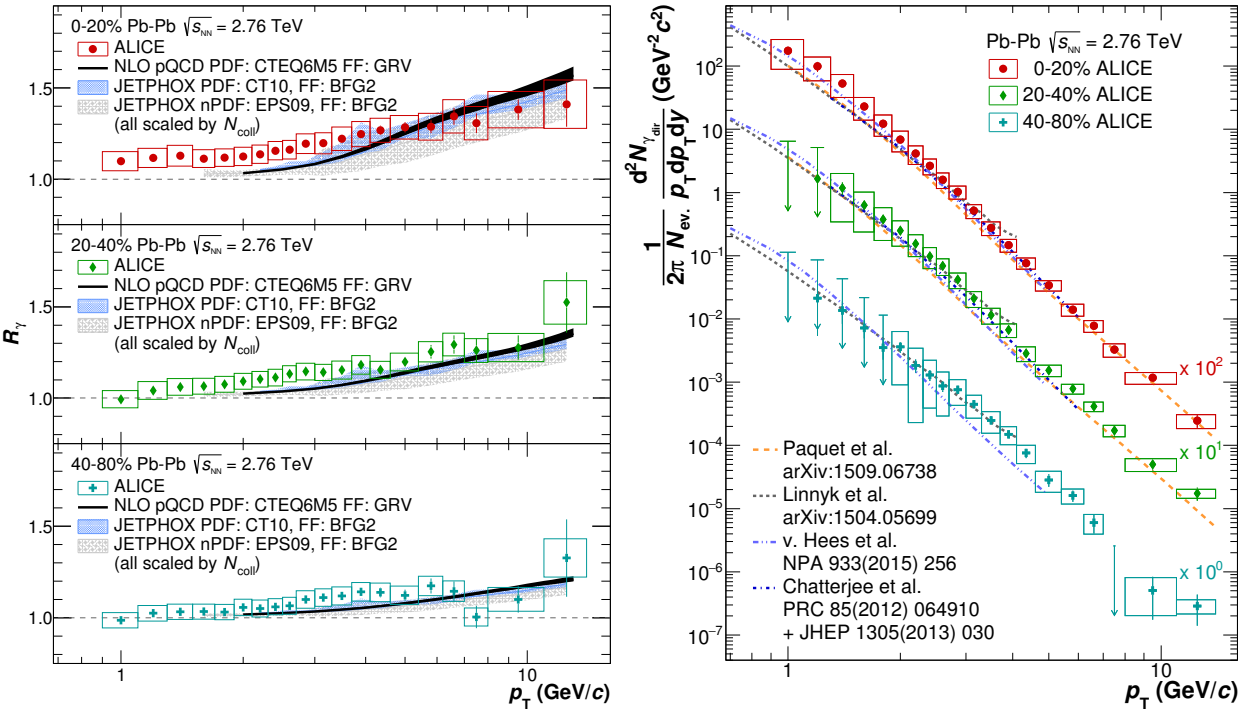

Figure 2.15.: The left plot shows the direct-photon double ratio and the right plot the direct-photon invariant yield in Pb–Pb collisions at $\sqrt{s_{\rm NN}}$ = 2.76 TeV for 0-20%, 20-40% and 40-80% central events [212]. The results are compared to theoretical expectations from NLO pQCD, JETPHOX and a variety of thermal photon predictions [204–206, 216]. While the data follow the expectations above $p_{\rm T} > 5$ GeV/c, the central value below that is underestimated by the calculations including thermal photons by about 50-100% depending on transverse momentum and the respective calculation.

in mind the effective temperatures obtained from the spectra at the same center of mass energy, the two results seemingly contradict each other and lead to the so called *'direct photon puzzle'*:

> *Theoretically it does not seem possible to model at the same time the large excess yield at low transverse momenta, requiring large temperatures and early production times, while still reproducing the ν_n results pointing to a later production time, as the ν_n needs to develop first [204, 206].*

A possible solution for this contradiction is the introduction of a long and hot hadronic gas phase and fairly high photon emission rates at the cross over temperature between the hadronic and QGP phase [202, 205, 216]. Other possible contributions could be a strongly anisotropic distribution of primordial photons, strong magnetic fields or strongly fluctuating initial conditions [219]. A similar result was obtained measuring the ν_2 of direct photons for 0-40% Pb–Pb collisions at the LHC [226, 227]. Due to the larger statistical and systematic errors, however, no strong tension between the experimental results and the theoretical calculations can be observed.
If a thermal photon signal could be measured for the smaller collision systems (high multiplicity pp, p–A) as well this would strongly support the interpretation of the origin of the observed collective being a QGP droplet. Thus, the strength of such possible signals was calculated recently with the free parameters of the hydro calculation adjusted to match the observed hadronic yields and Fourier coefficients for unidentified and identified particles [103]. Their results are depicted in Figure 2.16. The effect is quantified with respect to minimum bias pp collisions as the $R_{\rm pA}$ and shows a strong enhancement for $p_{\rm T} < 2$ GeV/c and central p–A collisions. While this enhancement offers exciting prospects, the extraction of the direct photons in p–A collisions proves to be challenging. As the double ratio (R_γ) according to the same predictions will not exceed 2-3%, which is very close to the sensitivity limit of the current photon extraction techniques.

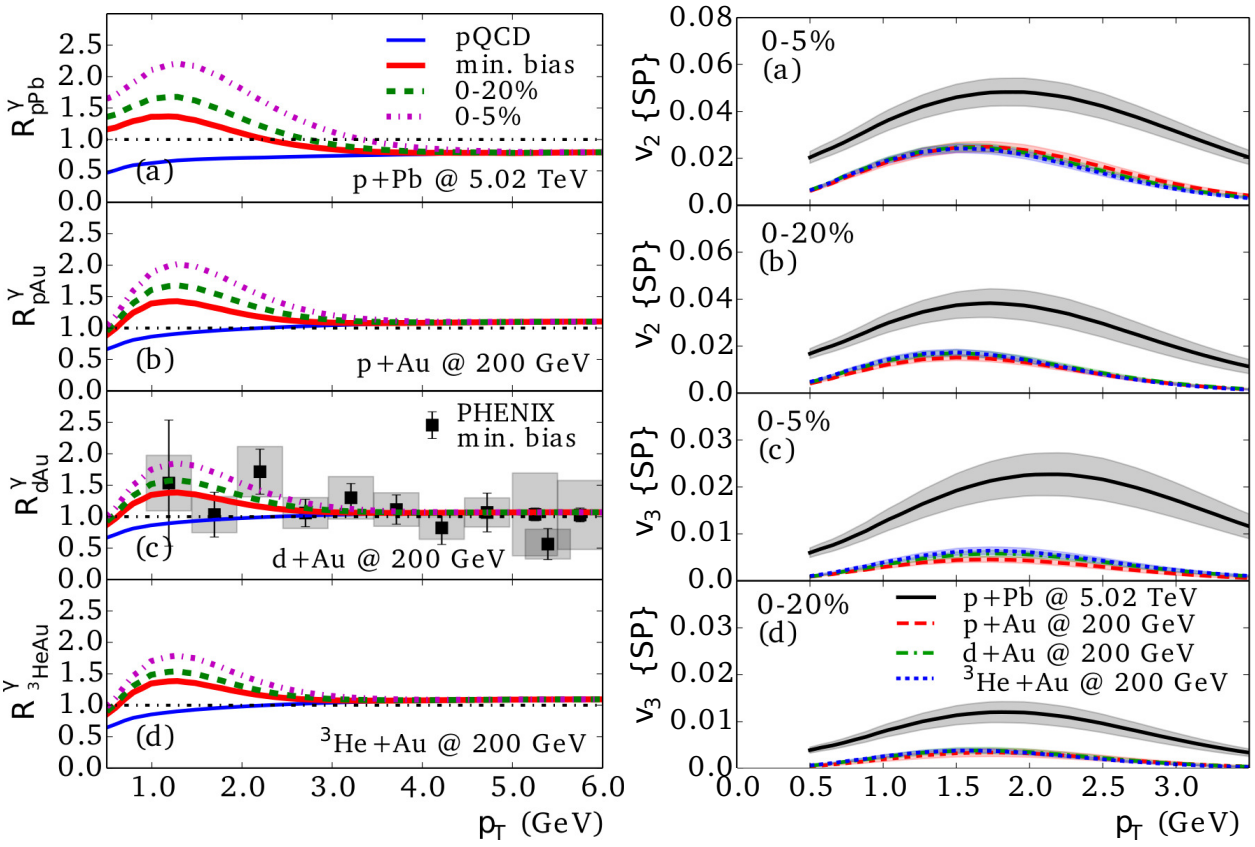

Figure 2.16.: Left: Predictions of the direct photon nuclear suppression factor (R_{pA}) for different collision systems and centralities. Additionally, the R_{dAu} of direct photons for minimum bias d–Au collisions at $\sqrt{s_{\mathrm{NN}}} = 200$ GeV [228] is shown in the appropriate panel. Right: Corresponding ν_2 (top panels) and ν_3 (bottom panels) for central collisions (0-5% and 0-20%) of the respective p–A system. The plots are adapted from [103].

Nonetheless the PHENIX collaboration managed to extract a direct photon signal for minimum bias d–Au collisions at $\sqrt{s_{\mathrm{NN}}} = 200$ GeV [228], which is in agreement with the predictions as shown in Figure 2.16(left).
From the same hydrodynamical calculations the Fourier coefficients (ν_2 and ν_3) could be extracted yielding about half the strength of the respective quantities as seen for the charged hadrons. Studies within this framework showed that in particular the direct photon ν_2 has a larger sensitivity to the choice of the thermalization time τ_0 which cannot be determined precisely with the current measurements.

3. Experimental Setup

This chapter will give an overview of the experimental setup used for the analyses presented in this thesis. Before describing the ALICE detector system, a short overview of the accelerator complex at CERN is given. In the consecutive sections the subdetectors of ALICE with a particular focus on the central barrel detectors and their particle identification capabilities will be presented. Afterwards the triggering setup as well as the track and vertex reconstruction are described.

3.1. The Large Hadron Collider

To date the LHC, located at CERN, near Geneva, Switzerland, is the largest and most powerful man-made particle accelerator. Its design was optimized to collide protons up to a center-of-mass energy of $\sqrt{s} = 14$ TeV and heavy ions (eg. Pb, Ar, Si) up to an energy of $\sqrt{s_{\mathrm{NN}}} = 5.5$ TeV per nucleon-nucleon pair [229]. The design luminosity of the LHC is $\mathcal{L} = 10^{34}$ cm^{-2}s^{-1} for colliding protons and $\mathcal{L} = 10^{27}$ cm^{-2}s^{-1} for lead ions. These values were optimized to be able find the Higgs-boson in the suspected mass region of $115 - 145$ GeV/c and explore its properties. Furthermore, the prospects for new physics searches were taken into consideration.
The LHC has been constructed in the existing tunnel of LEP, which was in operation until 2000. It is subdivided in eight main sectors and consists out of 4 major components:

(i) dipole magnets bending the beam on its orbit with a maximum magnetic field of 8.33T,

(ii) quadrupole, sextupole, octupole and decapole magnets focusing the beams,

(iii) acceleration cavities increasing the beam energy and

(iv) two beam pipes with an ultra-high vacuum containing the two beams.

The magnetic field in the dipoles is provided by superconducting magnets which are filled with liquid helium ($T = 4.5$ K) and then cooled to 1.9 K to reach the super-fluid state of helium. To reduce the number of interactions of the beam with the environment, an ultra-high vacuum is kept in the beam pipes reaching a quality of $\sim 10^{-13}$ atm on a total volume of 150 m^3 [229].
As it is not feasible to reach the maximum beam energy of 7 TeV per beam within one single accelerator, it is necessary to accelerate the particles in several steps. Therefore the previous accelerators at CERN were partially upgraded and are used as preaccelerators for the LHC. A schematic overview of the CERN accelerator complex is given in Figure 3.1, together with the accelerator chains used for protons and ions, respectively.
In 2009 the LHC delivered the first collisions of proton beams at injection energy ($\sqrt{s} = 0.9$ TeV). A year earlier a major incident happened, when first attempting to operate the accelerator, which destroyed the magnets of 1/8 of the LHC, and delayed the full startup of the LHC by one year. Due to this accident, and the consecutive discovery of some faulty connections within the magnets, the LHC management decided to only run up to center-of-mass energies of $\sqrt{s} = 8$ TeV until the first long shutdown (LS) in 2013/14 instead of ramping the LHC to its full energy. During which those connections could be repaired. One year after the first collisions at $\sqrt{s} = 0.9$ TeV and the following ramp up to $\sqrt{s} = 7$ TeV a few months later, in November 2010, the LHC experiments reported the successful collection of the first Pb–Pb events produced by the LHC at a center of mass energy of $\sqrt{s_{\mathrm{NN}}} = 2.76$ TeV. Although the design considerations did not explicitly foresee

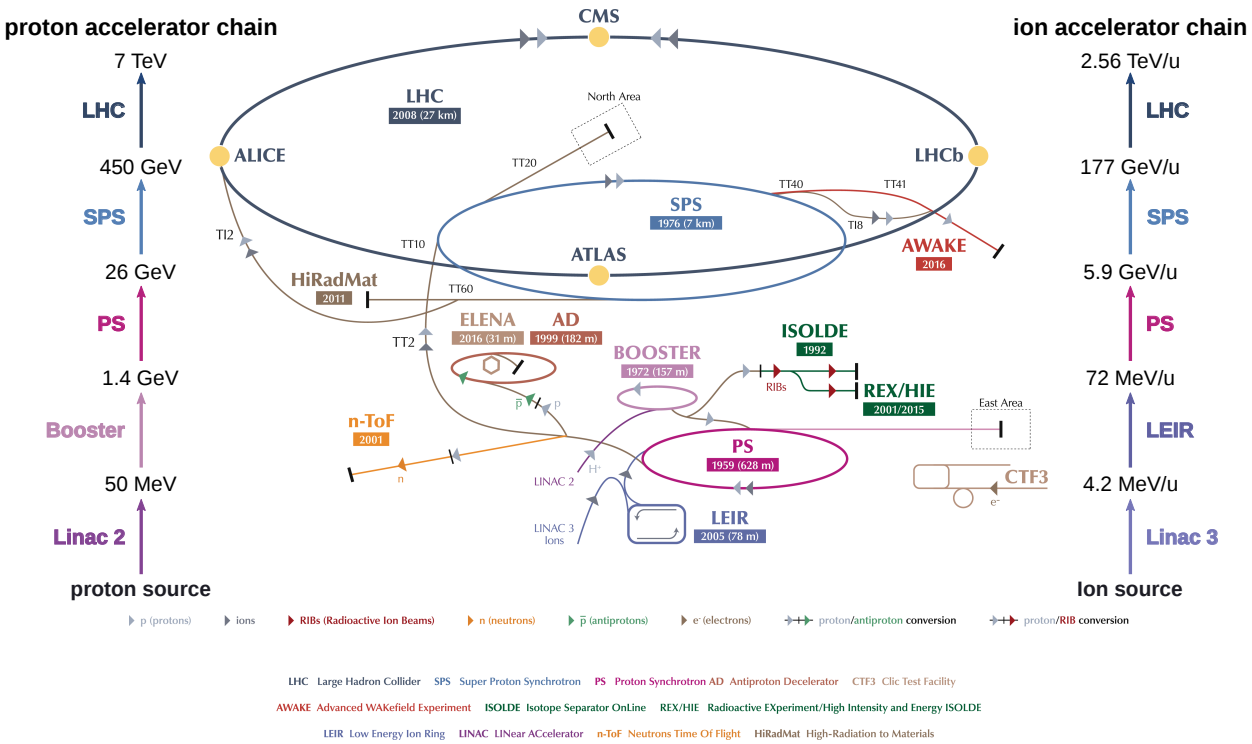

Figure 3.1.: Overview of the CERN accelerator complex and the injection chains used for the LHC with their respective top energies for protons and ions after the respective accelerator. Adapted from [232].

operations as a p–A or A–B collider, their feasibility has been studied [230, 231]. To explore the full potential of the LHC for the heavy ion community a first attempt to operate the LHC as a p–Pb collider has been made in 2012, with an overwhelming success, reflecting the versatility of the accelerator.

The LHC has eight possible interactions points, four of them are equipped with large detector systems as shown in Figure 3.1. ALICE is the only dedicated heavy-ion experiment, it will be described in the next section. The detectors systems of ATLAS (A Toroidal LHC Apparatus) and CMS (Compact Muon Solenoid experiment) where designed as complementary general purpose detectors primarily for pp collisions. Both collaborations focused their physics program for pp collisions on the search for the Higgs-boson and its properties. Additionally their programs include precision measurements of the Standard Model particles and searches for physics beyond the Standard Model, e.g. extra dimensions or super-symmetric (SUSY) particles. Driven by these goals the detector design aimed at the detection of particles with large momenta with a variety of detector techniques as well as a hermetic coverage around the interaction point in order to collect all particles produced in the collisions. Therefore, they installed silicon detectors, transition radiation detectors, large electromagnetic and hadronic calorimeters, as well as large muon detection arrays, covering the full azimuth and nearly the full pseudorapidity range. Although both detectors have not been optimized for heavy-ion collisions, they contribute extensively to the high transverse momentum (p_{T}) analysis in Pb–Pb collisions profiting from their large pseudorapidity coverage as well as their excellent high-rate capabilities and high momentum resolution.

The LHCb (LHC beauty) experiment dedicated its research program to the search for CP-violation in the B-meson system, as well as precision measurements in the charm and beauty quark sector. Both of which will help in the understanding of the asymmetric distribution of matter and antimatter in our universe. As the mesons with open and hidden charm or beauty are highly boosted, the detector has been designed as a one-sided forward detector with an excellent primary vertex resolution, to separate the primary vertex from the decay vertex of the B/D-meson. Furthermore, excellent particle identification is provided by the Ring Imaging Cherenkov detectors (RICHs), the

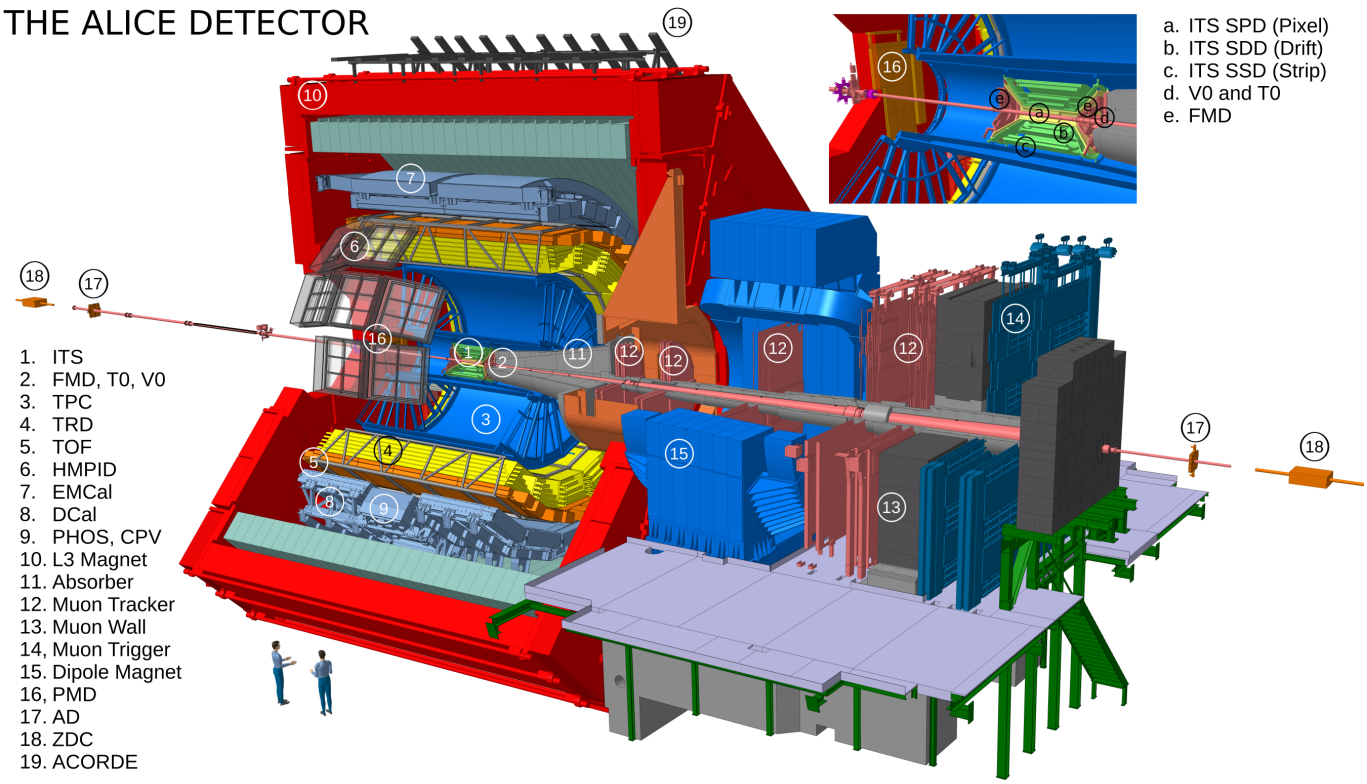

Figure 3.2.: Layout of the ALICE detector system with an insert zooming into the detectors closest to the beam pipe [233] for the Run 2 of the LHC.

electromagnetic and hadronic calorimeters. The tracking, on the other hand, is mainly done using silicon detectors and the muon system. Due to the high occupancy in the detectors initially the LHCb experiment did not take part in Pb–Pb runs. However after their participation in the p–Pb runs in 2012 and 2013, they reevaluated their limits and joined the Pb–Pb campaign in 2015 as well.

3.2. A Large Ion Collider Experiment

The ALICE detector system [234] has been designed as the general-purpose heavy-ion experiment at the LHC. As such the detectors were optimized to handle charged-particle densities up to $\mathrm{d}N/\mathrm{d}y \approx 8000$ at midrapidity. Within ALICE two main detector regions are distinguished:

- the central barrel, measuring hadrons, electrons, positrons and photons, and
- the forward muon spectrometer, consisting of the muon tracker (MCH) and muon trigger (MTR), focusing on the muon detection.

Furthermore, ALICE is equipped with a cosmic ray detector (ALICE cosmic ray detector (ACORDE)) mounted on top of the central barrel. As all analyses presented in this thesis are photon related the muon spectrometer as well as ACORDE will not be discussed any further. A schematic overview of the full experiment in its current state can be found in Figure 3.2.

3.2.1. The Detectors

The unique feature of the ALICE detector system is its focus on particle identification (PID) down to very low p_{T} at midrapidity. As such, the central barrel is equipped with detectors which can provide tracking and PID information for the reconstruction of primary charged particles

Detector	η	φ	$\sigma_{r\varphi}$ [μm]	σ_z [μm]	Specific Resolution
ITS					
SPD 1(2)	$\lvert\eta\rvert < 2$ (1.4)	$0^\circ < \varphi < 360^\circ$	12	100	
SDD	$\lvert\eta\rvert < 0.9$	$0^\circ < \varphi < 360^\circ$	35	25	
SSD	$\lvert\eta\rvert < 0.97$	$0^\circ < \varphi < 360^\circ$	20	830	$\sigma_{\mathrm{d}E/\mathrm{d}x} = 2.0\%$ at low p_T
TPC					
$r \simeq 1.4$ m	$\lvert\eta\rvert < 1.5$	$0^\circ < \varphi < 360^\circ$	1100	1250	$\sigma_{\mathrm{d}E/\mathrm{d}x} = 5.0\%$ (for 160 clusters)
$r \simeq 2.8$ m	$\lvert\eta\rvert < 0.9$	$0^\circ < \varphi < 360^\circ$	800	1100	
TRD	$\lvert\eta\rvert < 0.84$	$0^\circ < \varphi < 360^\circ$	400	2	$\sigma_p/p = 2.5\% \oplus \frac{0.5\%p}{[\mathrm{GeV/c}]}$
TOF	$\lvert\eta\rvert < 0.9$	$0^\circ < \varphi < 360^\circ$			$\sigma_t < 70$ ps
HMPID	$\lvert\eta\rvert < 0.6$	$1.2^\circ < \varphi < 58.8^\circ$			
PHOS	$\lvert\eta\rvert < 0.12$	$220^\circ < \varphi < 320^\circ$			$\sigma_E = 1.12\% \oplus \frac{3.6\%}{\sqrt{E}}$
					$\sigma_{x,y}(\mathrm{mm}) = \sqrt{\left(\frac{3.26}{\sqrt{E[\mathrm{GeV}]}}\right)^2 + 0.44^2}$
EMCal/	$\lvert\eta\rvert < 0.7$	$80^\circ < \varphi < 187^\circ$			$\sigma_E/E(\%) = (1.7 \pm 0.3)^2 \oplus \frac{(11.3\pm0.5\%)^2}{E} \oplus \frac{(4.8\pm0.8\%)^2}{E^2}$
DCal	$0.22 < \lvert\eta\rvert < 0.7$	$260^\circ < \varphi < 327^\circ$			$\sigma_{x,y}(\mathrm{mm}) = 1.5 + \frac{5.3}{\sqrt{E}}$

Table 3.1.: Resolution and detector coverage for the central barrel detectors [234–237]. For energy dependent resolution parameters the energy should be given in GeV.

over a large transverse momentum range (0.1 GeV/c - 100 GeV/c). Each of the subdetectors is designed to distinguish different particle species in different transverse momentum regions and their capabilities are matched such that the combination of all signals complements each other and allows to distinguish electrons, pions, kaons, protons and heavier nuclei from 0.05 GeV/c up to 20 GeV/c.
The central barrel detectors are embedded in the large L3 solenoid magnet, which ALICE inherited from the L3 experiment at LEP, providing a magnetic field of up to 0.5 T. From inside out the detectors are arranged as follows:

- four cylindrical detectors with full azimuthal overage: an Inner Tracking System (ITS), a Time Projection Chamber (TPC), a Transition Radiation Detector (TRD), a Time-Of-Flight detector (TOF),
- an High Momentum Particle Identification Detector (HMPID) with limited azimuthal coverage and
- three electromagnetic calorimeters: EMCal, Photon Spectrometer (PHOS) and Di-jet Calorimeter (DCal), where the latter was installed during the first long shutdown in 2013/14.

The following section gives a brief description of their performance and the respective detector techniques. The resolution parameters for the different subdetectors within the central barrel are given in Table 3.1, as well as their azimuthal and η coverage.

Inner Tracking System (ITS)
The ITS [238,239] is built out of six cylindrical layers of silicon detectors using three different techniques: silicon pixel (SPD), silicon drift (SDD) and silicon double-sided micro strip (SSD). Each technology is used for two layers of the ITS. Its primary design goal was to localize the primary vertex of the interaction and to separate it from secondary vertices, coming from the decays of short lived particles such as B and D mesons. Thus, the number of channels, the position of the layers, as well as their segmentation are optimized for efficient track finding and high resolution, having in mind the anticipated track density of up to $\mathrm{d}N/\mathrm{d}y \approx 8000$ at midrapidity. The innermost radius is determined by the smallest possible distance from the beam pipe ($R_{BP} = 2.94$ cm), while the outermost radius was optimized

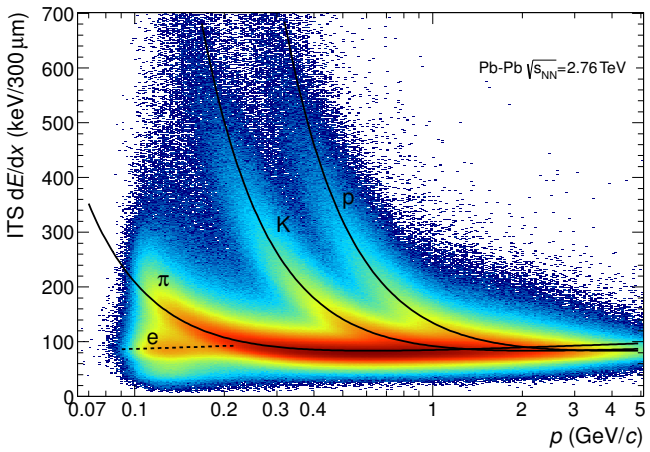

Figure 3.3.: Energy loss measurement ($\mathrm{d}E/\mathrm{d}x$) performed in the outer layers of the ALICE ITS versus momentum measured by the combined tracking of ITS and TPC [235]. The separation of the different particles species (electrons, pions, kaons, protons) can be clearly seen, the black line indicates the theoretical Bethe-Bloch-curves Equation 3.1.

to have the best possible track matching with the TPC. To allow for particle identification in addition to the tracking the four outer layers are equipped with analogue readout, with a dynamic range large enough to provide a $\mathrm{d}E/\mathrm{d}x$ measurement for low-momentum particles. This can help to distinguish electrons, pions, kaons and protons up to $p = 1.5$ GeV/c, as it can be seen in Figure 3.3. The full track reconstruction in the central barrel is a combined ITS, TPC and optionally TRD tracking. In addition to the vertex reconstruction and PID, the ITS can be used for standalone tracking, offering the possibility to fill the dead areas of the TPC. It allows the TPC to track charged particles down to $p_{\mathrm{T}} \approx 100$ MeV/c. The coverage in η and φ as well as the resolution in $r\varphi$ and z, are given in Table 3.1.

Time Projection Chamber (TPC)

The main tracking detector in the central barrel is the TPC [240, 241]. It consists of two main components: the field cage and the read-out chambers located at the end-plates.

A uniform electrostatic field in the gas volume with a total volume of approximately 90 m^3 is provided by a cylindrical field cage. Its active volume spans a radial distance from $R = 84.8$ cm up to $R = 246.6$ cm and covers the full azimuthal angle in a pseudorapidity range of $|\eta| < 0.9$ for full radial track length and $|\eta| < 1.5$ requiring 1/3 of radial track length. The foreseen gas admixture was 85.7% Ne/ 9.5% CO_2 / 4.8% N_2, which had been optimized concerning radiation length (low multiple scattering), low electron diffusion, high drift speed and operational stability. After a year of data taking the nitrogen was removed from the gas mixture for the 2011 data taking campaign, as it did not have the desired impact of more stable operations, leaving a gas mixture of 90% Ne/10% CO_2 for the remainder of the first LHC running period. Electrons emitted close to the central electrode at $Z = 0$ m, have to travel about 2.5 m in Z to the readout chambers at the end of the TPC. The central electrode is operated at 100kV, leading to an electron drift time of about 90 μs using this gas admixture. For the signal readout multi-wire proportional chambers at the end plates are used. The TPC readout is segmented in 18 sectors in φ and 2 chambers per φ-sector in R, which are further split into small pads. Their size is tuned to cope with the expected maximum track density depending on their radial position. It reaches from 4×7.5 mm^2 up to 6×15 mm^2. For the reconstruction of 3D-track points the measured drift time (z-direction) (up to $t \sim 90$ μs) and the position on the cathode pads (x-,y-direction) of the induced signal are used.

Taking into account these 3D-dimensional track points the path of a particle through the

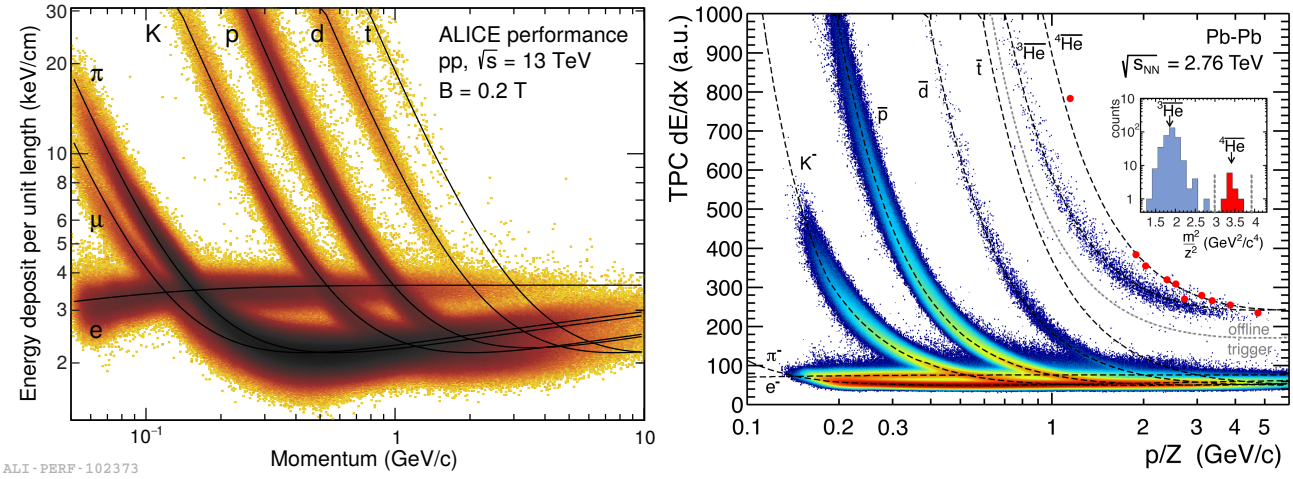

Figure 3.4.: Energy loss measurement $\mathrm{d}E/\mathrm{d}x$ versus momentum p (left) and versus rigidity p/Z, for data taken in pp collisions at $\sqrt{s} = 13$ TeV [13] and Pb–Pb collisions at $\sqrt{s_{\mathrm{NN}}} = 2.76$ TeV [235], respectively. Additionally, the theoretical Bethe-Bloch-Curves according to Equation 3.1 (black lines) for the different particle species are plotted.

detector can be reconstructed and the transverse momentum can be determined based on the curvature of the track. Primary charged particles can be reconstructed within the TPC with a reasonable momentum resolution, if their transverse momentum is larger than 100 MeV/c and smaller than 100 GeV/c. Primary particles with lower momenta will most likely not reach the TPC due to the bending in the magnetic field or do not traverse more than 1/3 of the radial length of the TPC, which is required during the tracking for a reliable reconstruction of the particles. For particles with momenta higher than 100 GeV/c the curvature within the TPC is to small to determine their momenta with enough precision. For secondary particles, which can be produced at larger radii, the low-momentum reach is mainly determined by the accuracy of the tracking algorithm. The current limit for secondary electrons is 50 MeV/c. In addition to the track reconstruction, the TPC provides particle identification for each track through energy loss measurements in the gas. Each particle looses energy while traversing matter through inelastic collions with the electrons bound in the atoms of the material. This energy loss is usually small compared to the total energy of the particle, resulting in the possibility of many such interactions until the particle is stopped. In general two different classes of energy loss can be distinguished:

(i) soft collisions, in which only enough energy is transferred to excite the atom in the target material and

(ii) hard collisions, in which the atoms are ionized.

If the electrons, which are freed by the hard collision, are energetic enough to cause ionization themselves, they are often referred to as δ-electrons. Additionally, particles can loose energy by other mechanisms, like Cherenkov radiation, nuclear interactions, bremsstrahlung or transition radiation, however their magnitude is negligible compared to the previously mentioned processes. The mean energy loss per path length ($\mathrm{d}E/\mathrm{d}x$) for elastic scatterings can be described by the *Bethe-Bloch-formula*:

$$-\frac{dE}{dx} = 4\pi N_A r_e^2 m_e c^2 \rho z^2 \frac{Z}{A}\frac{1}{\beta^2}\left[\frac{1}{2}\ln\left(\frac{2m_e c^2\beta^2\gamma^2 T_{max}}{I^2}\right) - \beta^2 - \frac{\delta}{2}\right]. \tag{3.1}$$

The path length x in the material is usually given in g cm^{-2} or kg m^{-2} and corresponds to the amount of matter transversed. The other parameters are the charge (z) and the velocity (v) of the transversing particle, Avogadro's number (N_A) and the effective ionization potential (I) of the atom species of the medium (roughly $I = 10Z$ eV). Furthermore, Z and A are the

atomic mass numbers of the atoms in the medium.
Figure 3.4(left) shows the $\mathrm{d}E/\mathrm{d}x$ measurement in the TPC for pp collisions at $\sqrt{s} = 13$ TeV versus momentum, taken at $B = 0.2$ T [13]. By reducing the magnetic field primary particles can be reconstructed down to 0.05 GeV/c and electrons, muons and pions can be clearly separated below 0.15 GeV/c. As shown by the black lines, depicting the expected Bethe-Block curves for the different species, it is possible to distinguish kaons, proton, deuterons and tritons at higher momenta from the electron and pion expectations. Above $3-4$ GeV/c, however, the lighter particles start to merge into one band and they can only be identified using statistical methods. The right plot of Figure 3.4 shows the $\mathrm{d}E/\mathrm{d}x$ distribution in Pb–Pb collisions at $\sqrt{s_{\mathrm{NN}}} = 2.76$ TeV versus rigidity (p/Z), highlighting also sample of nuclei produced in those collisions. The first observation of the production of $^4\overline{\mathrm{He}}$ in heavy ion collisions was reported by the STAR collaboration in 2011 [242], and shortly after that confirmed by the ALICE collaboration in Pb–Pb collisions at $\sqrt{s_{\mathrm{NN}}} = 2.76$ TeV [235].
The $\mathrm{d}E/\mathrm{d}x$ resolution of the TPC for tracks with 160 clusters ($\mathrm{d}E/\mathrm{d}x$ measurements) is $\approx 5\%$ [241]. Detailed information on the coverage of the TPC as well as its resolution parameters can be found in Table 3.1.

Transition Radiation Detector (TRD)
Situated outside the TPC the TRD [243] completes the ALICE tracking system in the central barrel. It consists of 6 layers of radiators and multi-wire-proportional chambers (MWPCs) and was designed to improve the tracking at high p_{T} as well as to provide electron identification in the transverse-momentum range of 1 GeV/c to 100 GeV/c. Due to the complex structure of hundreds of surfaces with different dielectrical constants in the radiator, transition radiation (TR) can be emitted in form of X-rays, if a charged particle is traversing the detector with a Lorentz factor (γ) larger than 1000. As the electron is much lighter than any other particle it is more likely to produce a TR-signal, which can then be observed in the high-Z-gas mixture (85% Xe, 15% CO_2) of the MWPCs. In case an X-ray was emitted it is detected on top of the $\mathrm{d}E/\mathrm{d}x$ measurement for that particle, which can be extracted in every MWPC it traverses. Therefore, the TRD is not only capable of separating high-p_{T} pions from electrons but can also provide six additional $\mathrm{d}E/\mathrm{d}x$-measurements for the tracks. Moreover, it is used as trigger detector for high-momentum particles, heavier nuclei as well as jets. For that, the Global Tracking Unit (GTU) evaluates track segments (tracklets) from the TRD online regarding various criteria and returns an L1-trigger signal [235].

Time of Flight Detetector (TOF)
The TOF [244] allows the separation of pions and kaons in the momentum range of $0.5-3.0$ GeV/c, proton identification for $0.5-4.0$ GeV/c and electron identification in pp collisions from $0.3-0.5$ GeV/c, by measuring the time a particle needs to fly from the primary interaction point to the detector. This complements the information accumulated in the TPC and ITS in the momentum regions, where the Bethe-Bloch curves for different particles intersect, and thus only an approximate identification can be made otherwise. The time of flight is measured using Multigap Resistive Plate Chambers (MRPCs) allowing a theoretical time resolution of down to 70 ps. Like the previously discussed inner barrel detectors the TOF covers the full azimuthal angle and a pseudorapidity of $|\eta| < 0.9$. In order to reduce the material budget in front of PHOS, the TOF and TRD sectors infront of the PHOS modules have been removed. In Figure 3.5 the time of flight versus momentum can be seen for particles produced in p–Pb collisions [235] at $\sqrt{s_{\mathrm{NN}}} = 5.02$ TeV. It demonstrates the separation power of the TOF for light particles at low momentum and for heavier particles in the full momentum range. Additionally, the achieved time resolution versus the average number of reconstructed tracks is reported, which is 10 ps larger than the one acchieved during the test beam campaign.

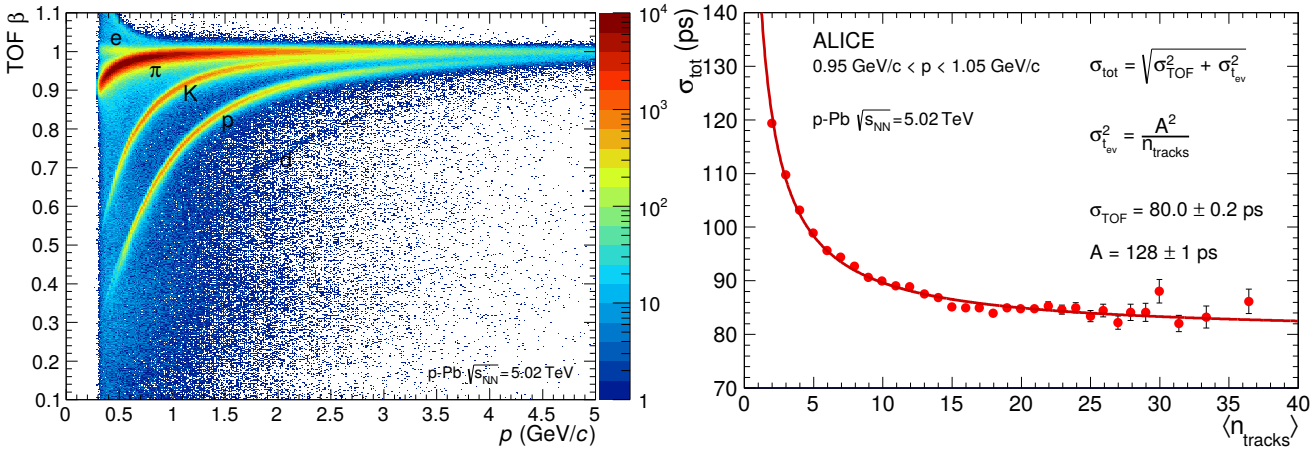

Figure 3.5.: Measured $\beta = \frac{v}{c}$ in the ALICE TOF detector versus momentum for data taken in p–Pb collisions in 2013 [235] (left) and achieved time resolution versus average track multiplicity in this data set (right). This measurement can provide an e/π separation between 0.3 GeV/c and 0.5 GeV/c as well as separation of pions and kaon up to $\sim$ 3 GeV/c and kaons and proton up to $\sim$ 4 GeV/c. Even deuterons can be seen and separated by this measurement from 1 GeV/c up to 5 GeV/c.

High Momentum Particle Identification Detector (HMPID)
The HMPID [245] is a Ring Imaging Cherenkov detector (RICH) consisting of 7 modules, which enhances the already described PID capabilities of ALICE by discriminating π/K and K/p on a track-by-track basis up to 3 GeV/c and 5 GeV/c, respectively. Each of the modules is equipped with a chamber filled with liquid C_6F_{14}, an MWPC filled with CH_4 and pad cathodes covered with a thin photo-sensitive CsI film. Due to a lack of space within the L3-magnet as well as funding limitations it covers only a small pseudorapidity area ($|\eta| < 0.6$) and azimuthal range, reaching from 1.2° to 58.8° in φ.

Photon spectrometer (PHOS)
The PHOS [246, 247] is a high-resolution electromagnetic spectrometer covering a limited pseudorapidity and azimuthal area (see Table 3.1), which is optimized to observe low-p_T photons. This requires a fast response as well as very good position and energy resolution at low p_T. It is comprised out of five modules, each equipped with 3584 lead-tungsten crystals ($PbWO_4$) of 20 X_0 with a granularity of the order of the Moliére radius. For the first data taking campaigns from 2009-2013, however, only 3 out of the 5 modules were installed. As it aims at measuring low p_T photons the material budget in front of the detector has been kept to a minimum. The required timing resolution is achieved by using fast scintillators and preamplifiers, leading to a time resolution of 2 ns. To efficiently distinguish between charged and neutral particles hitting the calorimeter the installation of a Charged-Particle-Veto (CPV) directly in front of the PHOS is foreseen in the future. It is supposed to consist of MWPCs filled with 80% Ar and 20% CO_2 with a cathode-pad readout. The first CPV module was installed during the first long shutdown, together with an additional PHOS module and is currently being tested. It is supposed to have a charged particle detection efficiency of better than 99%, with an impact point resolution of $\sigma_z = 1.54$ mm and $\sigma_{xy} = 1.38$ mm.

Electromagnetic Calorimeter (EMCal) and Di-jet Calorimeter (DCal)
Contrary to the PHOS, the EMCal was designed mainly for the measurement of high p_T objects, allowing ALICE to better reconstruct the neutral components of jets within the acceptance of EMCal. As such, it requires a larger azimuthal and pseudorapidity coverage, compared to the PHOS. It was proposed as a layered lead-scintillator sampling calorimeter with wavelength shifting fibers for light collection, in 2008 [248], covering 107° in azimuth and $|\eta| < 0.7$ in pseudorapidity. In order to enable di-jet studies using full jets in ALICE

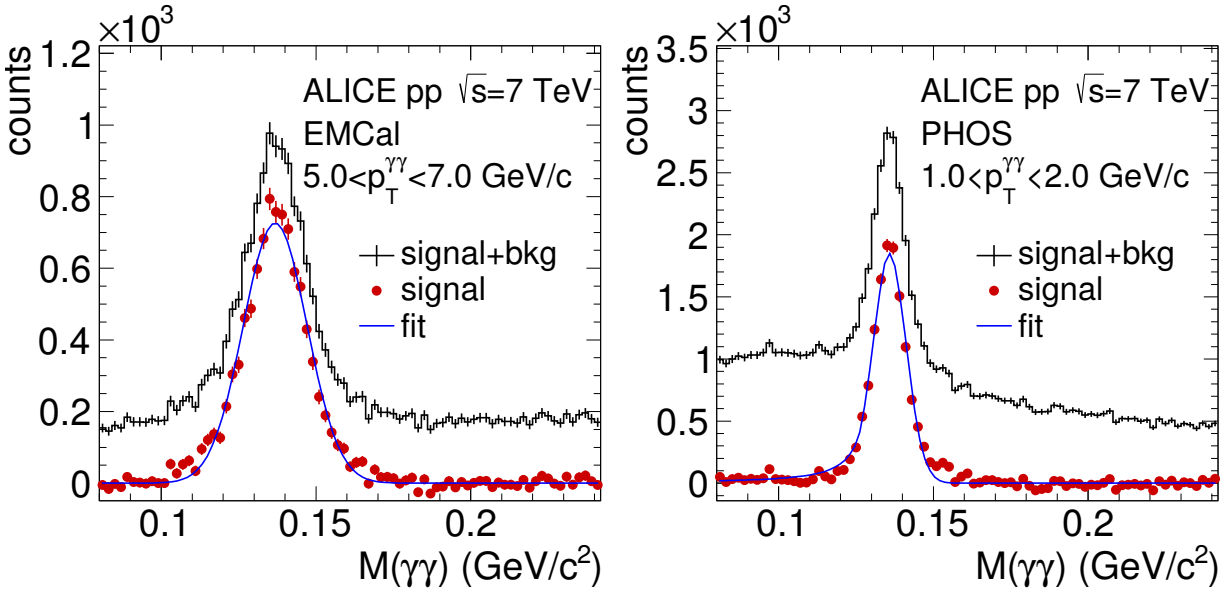

Figure 3.6.: Invariant two-photon mass measured with EMCal (left) and the PHOS (right) [235]. These invariant-mass plots are shown for data taken in pp collisions at $\sqrt{s} = 7$ TeV in one transverse-momentum bin (EMCal $5.0 < p_{\mathrm{T}} < 7.0$ GeV/c and PHOS $1.0 < p_{\mathrm{T}} < 2.0$ GeV/c). The black histograms represent the measured signal and background distributions, the red data point are obtained by subtracting the combinatorial background, calculated using mixed events. The red line represents a Gaussian fit, together with a linear component to account for possible remaining background, to the signal distribution.

as well the project was extended in 2010 to also include the DCal [237], being situated approximately opposite in φ, using the same technology and readout as well as triggering infrastructure. The detectors consist of 12288 and 5376 towers(cells) with a size of about twice the effective Moliére radius $\Delta\eta \times \Delta\varphi = 0.0143 \times 0.0143$ for EMCal and DCal, respectively. Each of the towers can be read out separately and has a depth of 24.6 cm, corresponding to approximately 20 radiation lengths. A physical module is comprised out of 2x2 cells, which in turn are arranged in 10 full-sized (12×24 modules) and 2 one-thirds sized (4×24 modules) supermodules to form the full EMCal. As the DCal is installed around the PHOS its six supermodules will be 1/3 shorter than the EMCal ones, to allow for the PHOS hole at $|\eta| < 0.15$. Furthermore, two one third sized supermodules are installed above the PHOS. The supermodules are installed with a radial distance to the nominal collision vertex of 4.28 m at their closest point. The wavelength shifting fibers are bundled such that the scintillation light from each cell is read out by an 5×5 mm^2 active-area avalanche photodiode. The relative energy resolution of the calorimeter is optimized for high momentum particles and improves with increasing incident energy of the particles, it can be parametrized as given in Table 3.1 [236]. Due to the emphasis on high-p_{T} particles, as well as the larger coverage in η and φ the intrinsic energy resolution of EMCal and DCal is worse than the one of PHOS, which is demonstrated in Figure 3.6 showing the π^0 invariant-mass peaks measured by EMCal (left) and PHOS (right).

Forward Detectors

The forward detectors do not only provide fast level-0 trigger signals based on the charged or neutral particle multiplicity detected in the detectors, but can also help to determine the centrality in p–Pb and Pb–Pb collisions as well as extend the measurement of the particle multiplicities beyond the coverage of the central barrel detectors. These detectors are :

The **V0 detector (VZERO)** [234], consisting out of two arrays of scintillation counters covering large pseudorapidity ranges (VZERO-A $2.8 < \eta < 5.1$ and VZERO-C $-3.7 < \eta < -1.7$). These detectors usually provide an interaction trigger, as well as a very fast multi-

plicity measurement. As such they can be used for the generation of a minimum bias trigger as well as a centrality trigger. Additionally, they are used for the luminosity measurement during the van-der-Meer scans. Furthermore, they often provide reference particle measurements for correlation studies as well as the reaction plane angle in Pb–Pb collisions.
The second forward detector is the **Timing and Trigger detector at ALICE (TZERO)** [234], which provides a detailed primary vertex position measurement as well as the start time for TOF and a wake-up signal for the TRD. In addition its signals can serve as alternate minimum bias triggers. It consists of 24 Cherenkov counters in two arrays, which are placed 73 cm away from the interaction point on the C-side and at 375 cm on the A-side.
An additional charged-particle multiplicity measurement can be supplied by the **Forward Multiplicity Detector (FMD)** [234]. A silicon strip detector covering a pseudorapidity range from $-3.4 < \eta < -1.7$ and $1.7 < \eta < 5$. While similar to the VZERO detectors the FMD detectors can be used to estimate the reaction plane angle as well as the centrality, its slower readout does not allow for it to be used as L0 trigger detector.
The photon multiplicities at forward rapidity can be measured by the **Photon Multiplicity Detector (PMD)** in the pseudorapidity region of $2.3 \geq \eta \geq 3.7$ [234]. Additionally, this detector can be used to estimate the transverse electromagnetic energy and the reaction plane on an event-by-event basis.
The **Zero Degree Calorimeter (ZDC)** [234], which is designed to measure the centrality in heavy-ion collisions based on the measurement of the number of spectators, consist of three detectors: the Zero Degree Neutron Calorimeter (ZN) for neutrons, the Zero Degree Proton Calorimeter (ZP) for protons and the Zero Degree Electromagnetic Calorimeter (ZEM) for measuring the energy of particles emitted at forward rapidity $4.8 < \eta < 6.7$.

3.2.2. The Trigger System

The ALICE detector system was primarily designed to cope with central Pb–Pb collisions, which occur with low rates but very high multiplicities. Driven by these concerns mainly gaseous detectors have been chosen for the detector layout, which leads to a lower maximum interaction rate, which can be inspected in the ALICE detector system. While ATLAS and CMS were designed to cope with approximately 40 MHz collision rates delivered by the LHC in pp collisions, ALICE initially should only be able to handle about 200 kHz of pp collisions [249, 250]. As the different subdetectors have different readout times the ALICE Trigger System (TRG) consists of three trigger levels, the Level 0 (L0) after 1.2 μs after the collision, the Level 1 (L1) after 6.5 μs and the Level 2 (L2) after 88 μs. Such a structure allows for an optimal usage of the available luminosity based on detectors, which can provide a fast decision after a short inspection of the event concerning a specific property.
In order to create the various trigger signals the fast detectors (i.e VZERO, TZERO) provide logical signals depending on a specific measurement (e.g. multiplicity) to the Central Trigger Processor (CTP). There these logical signals are combined by logical operations inside a Field Programmable Gate Array (FPGA) to form the different physics triggers (e.g. minimum bias, centrality) at L0. Afterwards the calculated outputs are propagated to the Local Trigger Units (LTUs) of the different detectors, where they are processed and then forwarded to the Front End Electronics (FEE). As some of the detectors have a relatively long readout time, the L0-trigger signal is needed to initiate the read-out of these detectors. Without it the data of that particular detector is not processed any further. The second trigger level (L1) is introduced to allow detectors with a longer data processing time to provide a trigger signal as well. Additionally, it allows for more complicated operations within the LTUs depending on inputs from other fast detectors or different sectors of the same detector. The third step, the L2 decision, waits for the end of the TPC drift time and the readout of the detector electronics to the optical data links is only initiated, if a positive L2 signal has been received by all detectors.

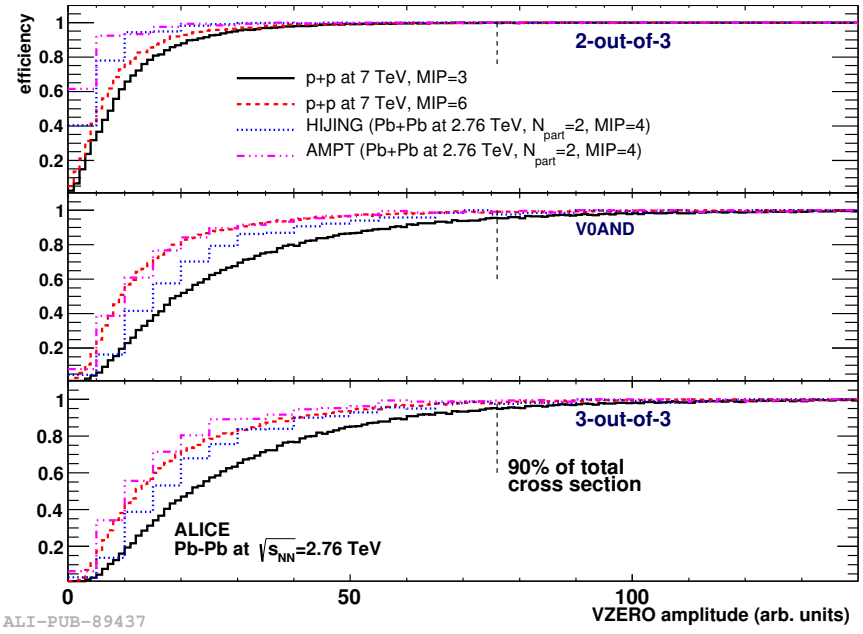

Figure 3.7.: Trigger efficiency for pp and Pb–Pb collisions under the detector conditions for data taken in 2010 [251]. The three different triggers use the VZERO and the SPD as inputs. For the top figure a coincidence of 2 out of the 3 detectors has to be present. This trigger measures the largest fraction of the total cross section. The central plot is a coincidence of V0-A and V0-C (MB_{AND}.), which comes closest to the having NSD events. The last class is the coincidence of all 3 detectors this measures the smallest fraction of the total cross section. All of these classes have very similar efficiencies for heavy-ion collisions and pp collisions as seen by different histograms shown in the panels.

In addition to the aforementioned trigger levels, a very fast interaction trigger can be derived from the interaction masks provided by the LHC together with the multiplicities registered in the TZERO or VZERO. This so called "pretrigger" can also serve as a wakeup signal for the TRD as it arrives less than 100 ns after the interaction.
The data from the detector front end cards is streamed in parallel to the Data Acquisition (DAQ) and the High Level Trigger (HLT), after having received the L2-accept signal. Within the software-based HLT the data volume can be reduced by applying additional trigger conditions or by compressing the complete or partial event information of the subdetectors. This can be achieved by using a farm of up to 1000 multiprocessor computer systems performing an on-line analysis of the collected data. The compressed information from the HLT can replace the information, which was streamed to the DAQ from the detectors, which otherwise would be sent to the storage elements. With increasing interaction rates the data compression and subsequent storage reduction, even for pp collisions became more and more important, thus since 2011 the HLT data compression for the TPC clusters is used by default to reduce the data volume of the raw events.
When the ALICE experiment was conceived the heavy-ion community was mainly interested in so-called minimum bias physics. As indicated by the name, such events should be taken with smallest requirements possible, while avoiding to record empty events. As such they are often based on fast multiplicity detectors, like the VZERO or SPD in case of ALICE, or a coincidence of their signals. Figure 3.7 shows the trigger efficiency for Pb–Pb and pp collisions for different minimum bias trigger conditions depending on the signal registered in the VZERO detectors. The three different trigger classes sample different physics. While the MB_{OR} (2-out-of-3) is closest to having Inelastic (INEL) events, the MB_{AND} (V0AND) measures mainly NSD events, which are biased event further towards non diffractive events when requiring the coincidence of both VZERO detectors and the SPD (3-out-of-3). These minimum bias triggers can be provided very fast and serve as basis for all other triggers. Within the level 0 time frame also the calorimeters and the muon trigger are capable of providing a first trigger response based on the energy deposited in

subsections of the detectors or the coincidence of several sectors of the muon arm. More complex trigger decisions, however, involving the hole sub-detector and various properties of the detected particles are taken at level 1, like the jet triggers in the EMCal and TRD. Such triggers can also be based on rough PID estimates. Examples for these triggers are the γ-jet triggers in the EMCal and DCal, di-electron or nuclei triggers in the TRD or di-muon triggers provided by the MTR.

3.2.3. The ALICE Reconstruction and Analysis Framework

In order to effectively process the data collected by the ALICE detector system a software package has been designed, providing the necessary tools for simulation, reconstruction and physics analysis of the events collected by the ALICE detectors. This framework is split in two components AliRoot [252] and AliPhysics [253]. Both packages are build on top of ROOT [254], a C++ based object-oriented programming tool for physics analysis, maintained and developed at CERN. Each of these packages is subject to different development cycles to adapt to the challenges provided by the physics analysis or detectors.
Within the AliRoot framework various Monte Carlo (MC) generators can be used to simulate full-events or single particles, such as PYTHIA [255–257], PHOJET [258], DPMJET [259], HIJING [260] or AMPT [261], while other can be interfaced using the HepMC format [262]. These generators can create full event records including the kinematic information of every particle which is produced in the interaction, as well as subsequent strong decay products and their relationship to each other. Afterwards the created particles are passed to transport programs like GEANT3 [263], GEANT4 [264] or FLUKA [265], to simulate a realistic detector response based on the detector layout implemented within AliRoot. Within these programs the particles are propagated through the detectors according to their interaction probabilities, taking into account the energy loss due to the interactions with the sensitive and insensitive detector materials. Each interaction within the sensitive detector materials, like the SPD sensors for instance, is stored with its particular time and position as a so-called hit. The hits are later converted into digits taking into account the approximate sensitivity of the electronic read-out, trying to reproduce the actual detector response as closely as possible.
The next steps in the reconstruction, are the same, regardless whether the original data has been collected using the actual detector or simulated. During the first reconstruction step neighboring digits are combined into so-called clusters, assuming they originated from the same particle traversing the detector. In a subsequent step the tracking combines these clusters to the most probable path of the particle through the detectors, which is further described in Section 3.2.4. The full information from the tracks and other reconstruction objects is stored in the Event Summary Data (ESD) output format, which can be further compressed into Analysis Object Data (AOD). Both formats serve as inputs for further physics analysis, which should be implemented within the daily-build AliPhysics-package to guarantee efficient data processing on the world wide LHC computing grid [266, 267].

3.2.4. Track and Vertex Reconstruction

Primary Vertex Reconstruction

The collision vertex, also referred to as primary vertex, is reconstructed within ALICE based on the information provided by the SPD [234]. As a first step reconstructed points in the 2 layers of the SPD, which are close in azimuthal and transverse direction, are paired. Based on their z-coordinates an estimate of the position in z of the primary vertex is calculated using linear extrapolation. The same procedure is repeated in the transverse plane. The resolution in the x and y coordinates is worse than for the z coordinate, as the tracks are bend in the transverse plain due to the magnetic field. Due to the proximity of the two SPD layers their precision suffices, however, to improve the initial estimate of the z coordinate using this information. In case the

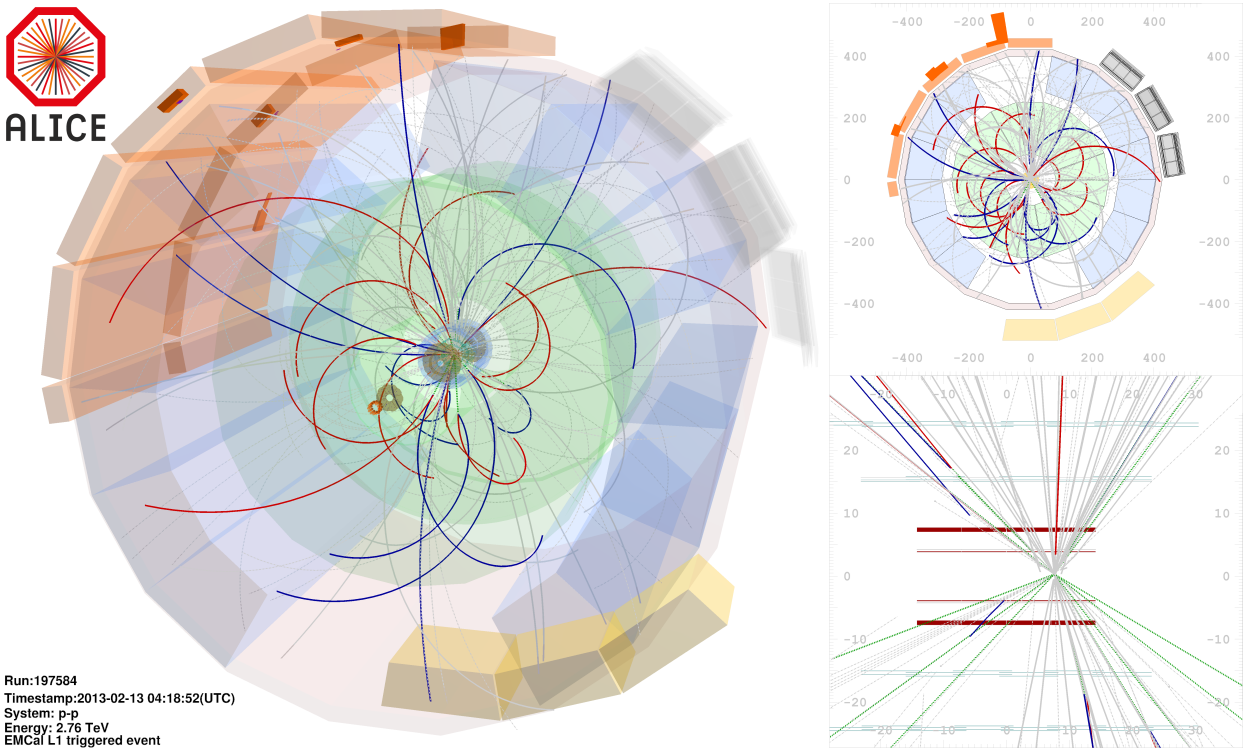

Figure 3.8.: Fully reconstructed event recorded during the pp data taking campaign at $\sqrt{s} = 2.76$ TeV, triggered by the EMCal level 1 gamma trigger. The full three dimensional view of the event is shown on the left, while the projections to the $X-Y$ and $R-Z$ planes are shown on the right in the upper and lower panel respectively. Solid gray lines represent primary charged particles, while the dashed gray lines indicate neutral primary particles and their subsequent decays. Highlighted in particular are photon conversion candidates with the photons displayed as green dashed lines and the conversion products as red and blue solid lines. The information accumulated by the EMCal is shown orange towers, reflecting the energy which could be reconstructed in the respective calorimeter tower.

beam is well focused the estimate of the transverse position can be improved by averaging over several events.
The precision of this measurement strong depends on the number of particles emitted during the collision and thus the charged-particle density at mid-rapidity. Its functional dependence on this quantity can be expressed as

$$\sigma_{z(xy)} = \frac{A}{\left(\sqrt{dN_{ch}/d\eta}\right)^{\beta}} \oplus B. \tag{3.2}$$

Typically values for A are 290(300) μm for the longitudinal (z) and transverse (xy) direction, respectively, with $B \approx 40$ μm and $\beta \approx 1.4$ [234]. As a consequence the z-vertex resolution in pp collisions is limited to about 150 μm, while in Pb–Pb collisions down to 10 μm are feasible. If the remaining misalignment between the SPD layers is reduced, which is reflected in the parameter B. Using the full information of the reconstructed tracks the initial estimates for the primary vertex can be improved even further, in particular in the transverse plane. Therefore, for pp collisions the transverse resolution can be improved to 70 μm and the z-resolution to 110 μm.
An example of a fully reconstructed and visualized event from the 2013 pp data taking period at $\sqrt{s} = 2.76$ TeV can be found in Figure 3.8. The reconstructed primary vertex together with the primary charged (gray solid lines) and neutral (gray and green dashed lines) particles originating from it can be found in the lower right part of the event display. The two innermost ITS layers are indicated as red lines in this view $R-Z$-view of the event.

Track Reconstruction

The track reconstruction in ALICE is performed as a multi-step process by finding and fitting the tracks using Kalman filtering [234,268]. Initially space points close to the end of the TPC are used as seeds for the Kalman filter. For low multiplicity environments those space points are calculated by the center-of-gravity method in the directions of the pad row as well as the time direction. For higher charge densities, however, this method cannot be employed any longer as the clusters start to overlap. Thus, they need to be unfolded in both dimensions to determine their original position. As only a fraction of the particles detected in the experiment come from the collision vertex, the seeding is done twice: once under the assumption that the particle comes from the primary vertex and once assuming that it originated somewhere else within the detector and is hence called secondary particle. In the next step the seeds, starting in the outermost pad-rows of the TPC, are combined with nearby clusters into tracks going inwards to the collision vertex. This procedure is repeated until the innermost pad row of the TPC is reached, each time considering pad rows closer to the primary vertex. A space point is assigned to the respective track if it is close to its trajectory and afterwards the covariance matrix is recalculated. The same procedure is performed assuming the track corresponds to a primary or secondary particle (track), using the previously reconstructed primary vertex as an additional constraint or not.
After having reached the inner boundary of the TPC, the tracks are propagated to the outermost SSD layer using both sets of parameters. Starting from the highest momentum particles the tracks are matched to hits in this outermost layer of the ITS and the same procedure as in the TPC is performed for the five lower layers of the ITS. Due to the larger gaps between the active layers of the ITS compared to the TPC pad rows, it is possible to assign multiple space points to the same track coming from the TPC. In those cases each possibility is calculated separately and the most probable track is stored based on the summed χ^2 values along the track.
Following the combined ITS and TPC fit the Kalman filtering is inverted and the procedure repeated starting from the primary vertex outwards using the already reconstructed tracks as seeds. During this process each cluster track association in the ITS and TPC is revisited and improperly assigned points are removed, while the ones which were missed in the first iteration are added. Then the tracking follows the track beyond the TPC and assigns space points in the TRD, TOF, HMPID and calorimeter towers in the EMCal or PHOS. While most of the outer detectors do not contribute to the momentum fit, the TRD track points can be taken into account if they improve the momentum resolution. Due to the limited acceptance of the TRD this feature has not been used for the data collected during the first LHC run from 2009-2013.
In the final step the Kalman filter is inverted once more and the final track parameters are again calculated twice, assuming the track to be from a primary or secondary particle. Both sets of parameters are stored and the second on can be used for subsequent studies of short-lived particle decays as well as photon conversion.
In order to recover tracks, which went through dead areas of the TPC, all ITS hits which have been attached to a track already can be removed and the remaining space points can be used as input for another iteration of the Kalman filter based solely on ITS information, providing so called ITS standalone tracks.
Figure 3.9 shows the primary track finding efficiency for different detector combinations in pp collisions [234] on the left and for different collisions systems [235] on the right. The track finding efficiency is mainly determined by dead areas of the different detectors. As such it drops from $\approx 95\%$ at 2 GeV/c for the TPC only reconstruction to $\approx 90\%$ for the combined TPC-ITS reconstruction. It reduces even further when requiring the TRD. The transverse momentum resolution on the other hand follows the opposite trend, improving significantly with the inclusion of additional detectors [234]. For high momentum tracks, which bend less within the magnetic field, this inclusion is of particular importance, as in those cases additional track points within the TPC would not help any longer to reliably determine the momentum. Extending the track towards

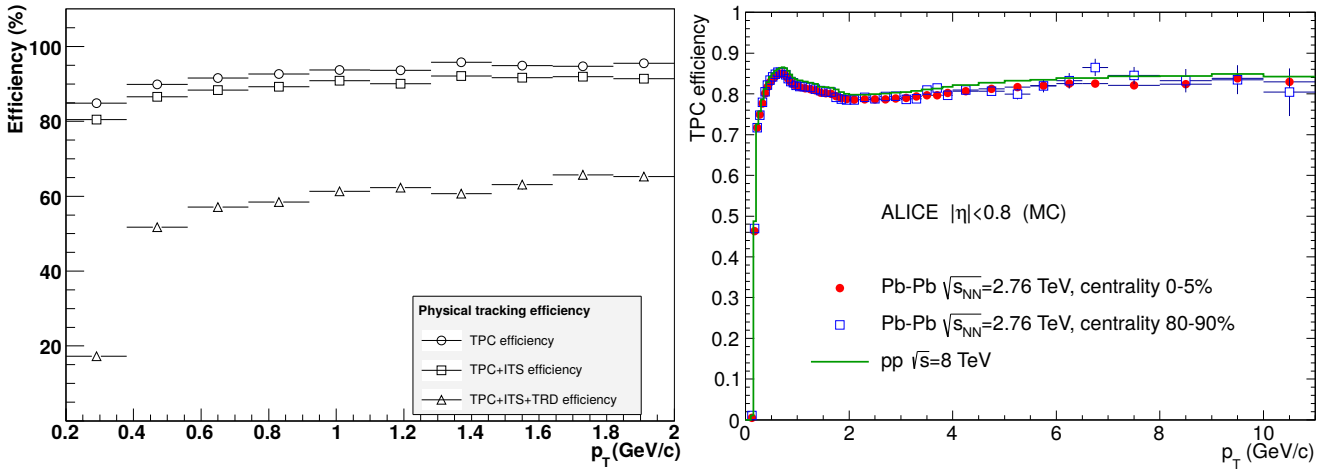

Figure 3.9.: Left: Track finding efficiency for different combinations of tracking detector for pp collisions at low transverse momenta [234]. Right: Track finding efficiency within the TPC for different collision systems using Monte Carlo simulations adjusted to reproduce the data [235].

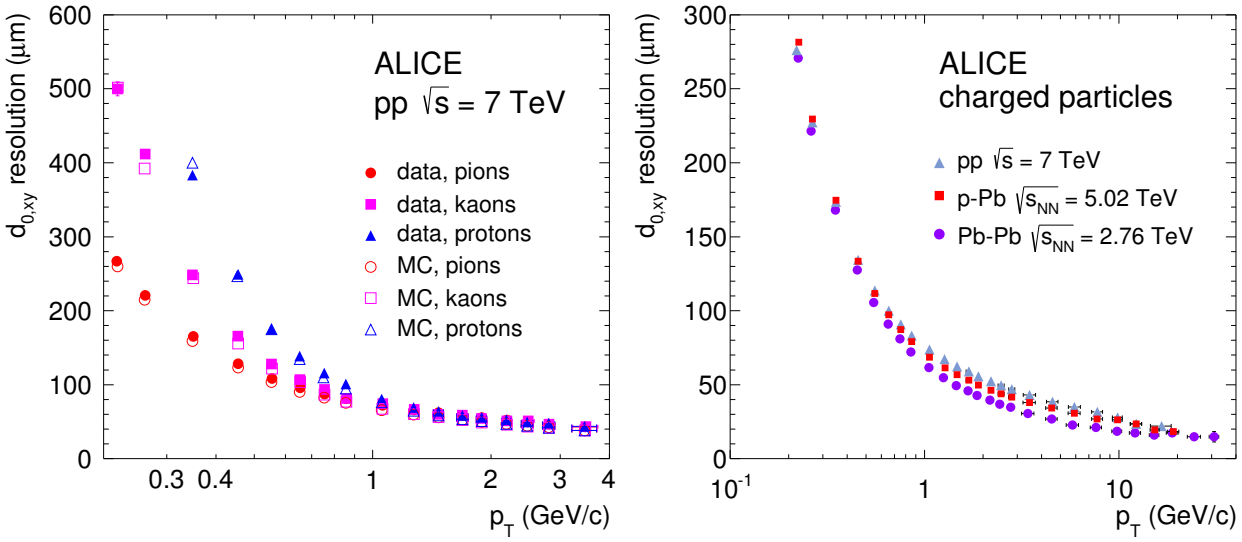

Figure 3.10.: Left: Impact parameter resolution in pp at $\sqrt{s} = 7$ TeV for different particle species as a function of p_{T}. Right: Dependence of the impact parameter resolution on the collision system for unidentified charged particles [235].

the ITS and TRD on the other hand allows to sample a larger fraction of the arc the particle is following, and thus allows to calculate its curvature to a better precision. As seen in the right part of Figure 3.9 the track finding efficiency within the TPC does not significantly depend on the charged particle density within the event. It varies by less than 4% going from pp collisions with an average track density of 7 tracks at midrapidity to central Pb–Pb collisions with about 1600 charged particles at midrapidity.

One of the main parameters to determine the performance of such track finding algorithms in the data is the impact parameter resolution. The impact parameter in this case is defined as the distance between the primary vertex and the track prolongation to the point of closest approach to the primary vertex, as shown by b_1 and b_2 in Figure 3.11. This resolution does not only depend on the accuracy of the track parameters but also on the primary vertex position resolution as well. It can be studied using Monte Carlo simulations and measured data. The results as a function of transverse momentum for different particle species are shown in Figure 3.10(left). Furthermore, the impact parameter resolution for different collision systems for unidentified hadrons is compared in Figure 3.10(right). As it can be seen the impact parameter resolution depends on the particle

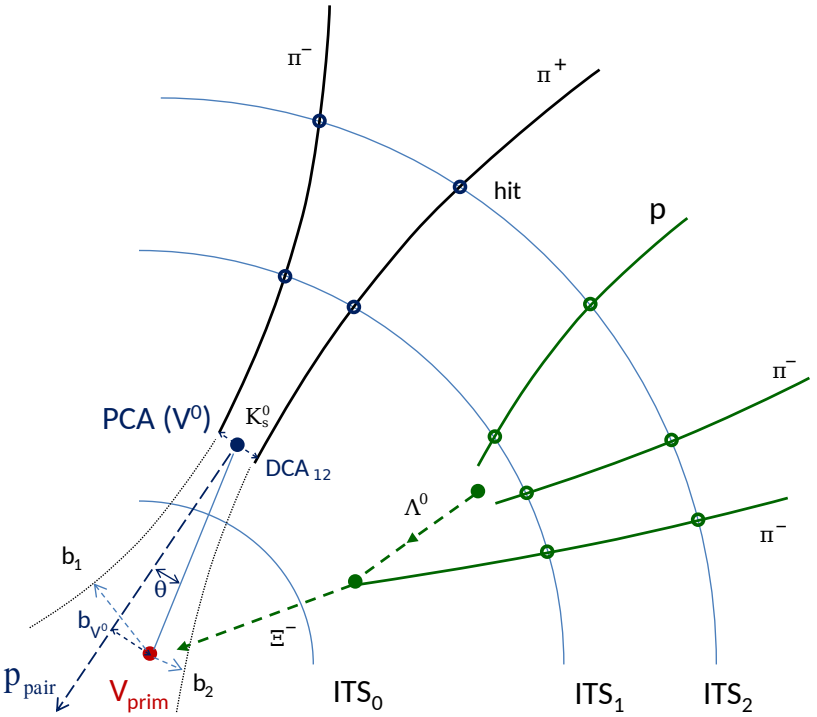

Figure 3.11.: Sketch of the reconstruction of a generic secondary vertex as well as a cascade decay, adapted from [235].

species as well as the transverse momentum and both dependencies are well reproduced within the simulation. The influence of the primary vertex resolution can be deduced from the collision system dependence, which improves for systems with larger multiplicities. In general, however, the impact parameter resolution above 1 GeV/c is better than 80 μm, regardless of the particle species or collision system.

Secondary Vertex Finding

As described earlier not only particles originating from the primary collision leave signals in the detectors. Additional particles can be created by primary particles decaying after a certain distance or via interactions of the primary particle with the detector material itself. The latter are referred to as hadronic interactions.
In particular decays of neutral particles follow a distinct V-topology, shown in Figure 3.11, with the tip of the "V" being the decay vertex (or secondary vertex). Thus, neutral particles decaying into 2 charged particles are often referred to as Unknown Particles (V^0s). Which particles can be reconstructed using this topology depends on the impact parameter resolution of the detector. Most commonly it is used, however, for strange particle decays of K^0_S and Λ, as well as photon conversions into an electron-positron pair in the vicinity of a nucleus.
In general the V^0-finding algorithm uses as input the secondary track sample obtained during the full reconstruction, pairing tracks of opposite charge. In a second step the impact parameter of the track (b_1, b_2) with respect to the primary vertex is calculated, as seen in Figure 3.11. Tracks which would have similar impact parameters as primary tracks are removed from the secondary track sample and the procedure is restarted. Afterwards the distance of closest approach (DCA) of the two secondary tracks is calculated. If this DCA value is above a certain threshold, depending on the distance to the primary vertex and its resolution, the track pair is rejected. In general only secondary track pairs with a DCA$<$ 1 cm are considered further. The remaining track pairs form candidate V^0s, with their point of closest approach (PCA) being the secondary vertex. On these candidates further selection criteria can be applied, like a minimum and maximum radial

distance of the secondary vertex to the primary vertex (0.5 cm$< R_{\mathrm{sec}} <$ 220 cm). Afterwards the momentum of the unknown particle is reconstructed by extrapolating the momenta of both tracks to the PCA and calculating their vector sum at this point. Particles for which the momentum vector (p_{pair}) does not point towards the primary vertex, which can be quantified by $\cos\theta < 0.85$, are rejected from the sample in addition.
In ALICE it is possible to reconstruct V^0s using two different V^0-finding algorithms, the **On-the-fly** and the **Offline V^0** finder. In case of the On-the-fly V^0 finder the reconstruction algorithm is running during the reconstruction, which allows the tracks to be refitted taking into account the secondary vertex as their origin. During this refitting procedure the full cluster information which is attached the respective secondary tracks is reevaluated and clusters might be added or removed accordingly. Afterwards the updated covariance matrix and parameter set for the track pair is stored. The inclusion of the secondary vertex in the Kalman filter allows to improve the position and momentum resolution compared to the Offline V^0 finder, which does the vertex finding after the full tracking is finished. The Offline V^0 finder, however, allows to redo the secondary vertex finding on ESD data without a new reconstruction pass of the full data set.
By modifying slightly the parameters of the V^0 finding algorithm it is possible to reconstruct secondary hadronic vertices as well. In those cases more than two particles can be emitted from the secondary vertex, their charge does not need to cancel and neither does their momentum vector need to point to the primary vertex. Furthermore, a primary charged particle can terminate in this secondary vertex. Within ALICE secondary hadronic vertices are only reconstructed during the analysis if at all.

4. Data Sets and Photon Detection in ALICE

Within this chapter, the different data sets and Monte Carlo simulations are introduced, which have been used for the neutral meson and direct photon analyses presented in this thesis. Furthermore, a general overview of the photon reconstruction within ALICE using the Photon Conversion Method (PCM) and EMCal is given. These reconstructed photons can be combined in the neutral pion and eta meson analysis to derive the invariant yield of those particles. If the neutral mesons have been reconstructed using one photon from each reconstruction technique, the analysis is referred to as PCM-EMC or hybrid analysis, whereas if both have been reconstructed with the same technique the analysis is called PCM or EMC meson analysis, respectively. In addition, the combined residual energy and alignment calibration is described for the photons measured with the EMCal using the neutral pions reconstructed with one photon being reconstructed using PCM. For pp collisions at $\sqrt{s} = 2.76$ TeV the criteria for the merged EMCal cluster (mEMC) analysis are provided, in addition to the cluster selection parameters for the photon analysis, as they largely overlap.

4.1. Data Sets and Monte Carlo Simulations

ALICE has collected data from pp collisions at six different center-of-mass-energies, reaching from $\sqrt{s} = 0.9$ - 13 TeV. In addition, it recorded p–Pb at $\sqrt{s_{\mathrm{NN}}} = 5.02$ and 8.16 TeV as well as Pb–Pb collisions at $\sqrt{s_{\mathrm{NN}}} = 2.76$ and 5.02 TeV. As the detector is not symmetric, the beam direction was inverted for each p–Pb energy once, allowing in particular the forward detectors to investigate the production of particles in the p and Pb going direction to be able to compare the results. The data taking is split in LHC runs (Run 1: 2009-2013, Run 2: 2015-2018) and so-called periods, during which neither the detector, trigger nor beam conditions are changing rapidly. A further splitting into runs within ALICE is applied in addition, as the life time of the beams in the LHC is shorter than our periods and even during one fill of the LHC we might want to change the read-out or trigger configuration of our detector system.
This thesis focuses on the reference measurements in the smaller collisions systems (pp, p–Pb) for the respective spectra measured at the same center-of-mass-energy in Pb–Pb collisions. Only data taken during Run 1 of the LHC are considered in the presented analysis. As such, only pp collisions with $\sqrt{s} = 2.76$ TeV and p–Pb collisions with $\sqrt{s_{\mathrm{NN}}} = 5.02$ TeV will be discussed further in the course of the next chapters. The pp data were collected in March 2011 (LHC11a) and February 2013 (LHC13g), whereas the p–Pb data were taken in January 2013 (LHC13[b-c]).
An offline event selection was applied to reject events, which did not fulfill the central barrel trigger conditions or which were not of physics type (e.g. calibrations events). Furthermore, events assigned to noise or beam-gas interactions were rejected. This selection is called *Physics Selection* (PS). Moreover, the events entering in the analysis have to have a reconstructed primary vertex within $|z_{vtx}| < 10$ cm from the center of ALICE. This vertex can be reconstructed either with global tracks or with SPD tracklets. However, it has to have at least one contributing track or tracklet to the vertex.

trigger	function	typical patch size
level-0 (L0)	enhances number of events with large energy deposit in the EMCal	4x4 towers (in 1 TRU)
level-1 (L1) EGA	enhances number of collected events with large energy deposit in the EMCal	4x4 towers (accross TRU boundaries)
level-1 (L1) EJE	enhances the probability of events with large jet contribution on the EMCal surface	16x16 towers (accross TRU boundaries) 32x32 towers (accross TRU boundaries)

Table 4.1.: Different EMCal subtriggers and their functions [269].

4.1.1. Event and Trigger Selection for pp Collisions at $\sqrt{s}$ = 2.76 TeV

For pp collisions at $\sqrt{s} = 2.76$ TeV, the neutral pion and eta meson have been reconstructed using four different techniques, employing different combinations of the photons reconstructed with the EMCal or PCM. Each of these can require a different subset of detectors and triggers. As such, all analyses involving mesons reconstructed partially within the EMCal are considering a total of six different trigger conditions: the minimum bias (V0OR/INT1, V0AND/INT7) and EMCal trigger conditions (EMC1, EMC7, EG2, EG1). The analyses solely relying on photons reconstructed with PCM, however, only consider the minimum bias sample collected in 2011. Furthermore, in order to maximize the read-out rate ALICE collected data with and without the SDD in the read-out in 2011. In this configuration the calorimeters were only considered for the data stream with the SDD. As the exclusion of the SDD mainly changes the track resolution the full data set (LHC11a) was reconstructed once with the SDD input considered and once without that. So that analyses, which can afford a slightly deteriorated resolution, can take advantage of the improved statistics. Consequently, the analysis purely based on conversion photons uses the reconstruction pass without the SDD and the corresponding Monte Carlo Simulations. The statistics available for the different triggers and reconstruction passes can be found in Table 4.2.
The V0OR (INT1) trigger requires a hit in either SPD or one of the two VZERO detectors, whereas the V0AND (INT7) requires a coincidence of hits in both VZERO detectors. As described in Section 3.2.2 ALICE has two main trigger levels, L0 and L1. At each of these levels the EMCal can provide trigger signals requiring a certain amount of energy deposited in a specific area of the EMCal. Their purpose is described in Table 4.1 [269, 270]. The EMCal level-0 trigger fires about 1.2 μs after the interaction if the energy summed over a sliding window of 4x4 towers (2x2 FastOR) is higher than a threshold above the background noise. The 4x4 towers are required to be inside one Trigger Region Unit (TRU) which corresponds to 8x48 towers (4x24 FastOR) and each full supermodule consists of three TRUs. In order to trigger the readout, it has to be in coincidence with one of the minimum bias triggers. It is referred to as EMC1, EMC7 or EMC8, depending on the underlying minimum bias trigger. The EMCal level-1 triggers fire about 6.2 μs after the interaction. Similar to the L0 trigger, the L1 photon trigger (EGA) compares the energy summed over a sliding window of 4x4 towers to a given threshold, which can be made multiplicity dependent for instance based on the VZERO information. For this L1 trigger, the 4x4 towers can also cross the border to another TRU which increases the effective surface by about one third. The jet trigger (EJE) sums the energy over a patch consisting of 3x3 subregions while one subregion is defined as 8x8 towers and compares it to a threshold, which again can be made multiplicity dependent. Each of these two L1 triggers can run with 2 different fixed thresholds or functions dependent on the multiplicity (EG1, EG2 or EJ1, EJ2) and they can be requesting a coincidence with different minimum bias triggers. For the data considered in this thesis no multiplicity dependent thresholds were used and the triggers were required to fire in coincidence with the INT7 trigger.
Since its start in 2009, the LHC has been constantly increasing the delivered instantaneous luminosity for all experiments. As ALICE can only take data at low interactions rates due to the read-out time of the TPC, both beams at the ALICE interaction point were displaced to reduce the intensity in the crossing region. This setup does not guarantee, however, that only one event

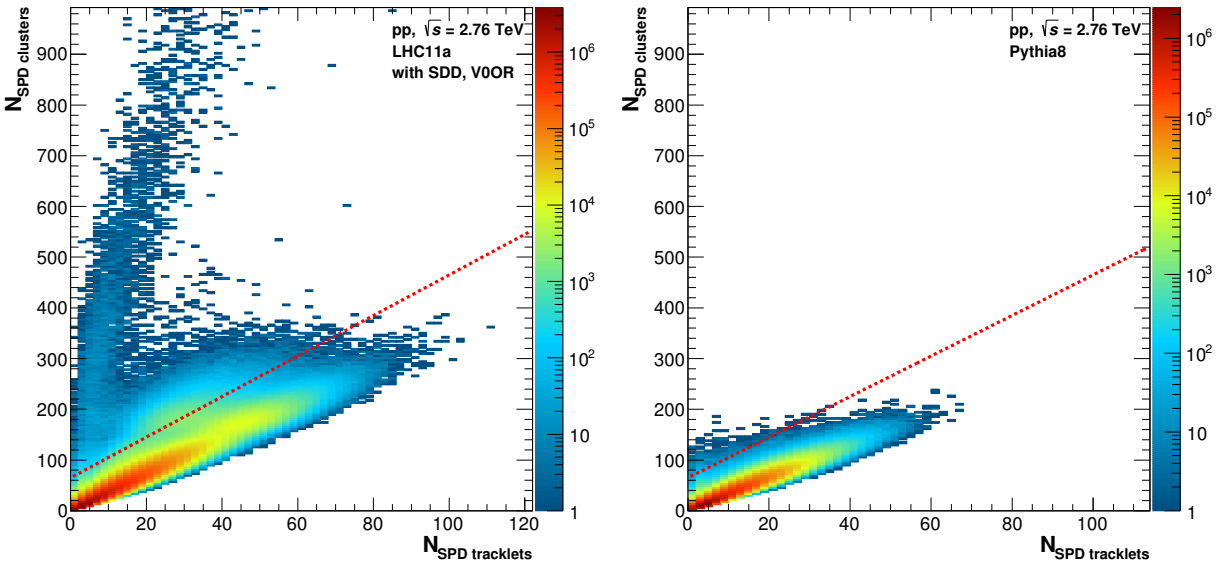

Figure 4.1.: Number of SPD clusters vs. number of SPD tracklets for LHC11a data (left) and Pythia 8 (right). The dotted red line displays the applied cut from Equation 4.1.

is seen at a time in our detectors. Thus, a pile-up rejection, based on the number of reconstructed vertices in the SPD, was included in the analysis. It allows us to reject events which had at least two primary vertices which were more than 0.8 cm apart and could be reconstructed using only tracklets in the SPD. This condition removes more than 75% of the events which contained more than one vertex registered in the same bunch crossing. The fraction of events rejected by this selection criterion depends highly on the beam conditions: the higher the luminosity or the smaller the beam diamond, the larger the fraction of rejected events due to pile up in the SPD.
To further reject background events, an additional cut has been applied to the correlation of SPD tracklets and SPD clusters. If the number of SPD clusters is disproportionally larger than the number of SPD tracklets within an event, it is being regarded as "background event" and as such discarded from the analysis.

$$N_{\text{Clusters}} > 4 \times N_{\text{Tracklets}} + 60 \tag{4.1}$$

This additional condition leads to a total efficiency to reject events containing more than one primary vertex of 92-98% for the periods considered in this analysis. Figure 4.1 shows that correlation for data and Pythia 8 simulations, respectively, the applied cut condition is also displayed using a dotted red line. This condition can be released for the EMCal triggered data, as it is very unlikely to have two events, which would fulfill the trigger conditions in the same bunch crossing. As the SPD showed a particularly large number of unresponsive channels in front of the EMCal for the data taking in 2013, no pile-up rejection was applied for the EMCal triggered data. The small fraction of same-bunch pile-up is later corrected for by the normalization with the trigger rejection factor R_{Trig} for that part of the data.
We normalize our spectra with the following number of events, where Y corresponds to the respective trigger class:

$$N_{\text{norm,evt}} = N_{\text{Y,Vtx},|z_{Vtx}|<10\text{cm}} + \frac{N_{\text{Y,Vtx},|z_{vtx}|<10\text{cm}}}{N_{\text{Y,Vtx},|z_{vtx}|<10\text{ cm}} + N_{\text{Y},Vtx,|z_{vtx}|>10\text{cm}}} N_{\text{Y,no Vtx}}. \tag{4.2}$$

To convert the invariant yield to an invariant cross-section, the measured Lorentz invariant yield needs to be multiplied with the total cross-section for the trigger condition. However, the cross-section for the V0OR cannot be measured directly. First, the total inelastic cross-section and hence the luminosity needs to be measured. Therefore, several van der Meer scans [271], with the V0AND as trigger condition, were performed to study the geometry of the beam interaction region

		norm. Evt. N_{evt}	Trig. Evt. N_{Y}	A_1	A_2	A_3	A_4
pp $\sqrt{s}$ = 2.76 TeV, Data							
LHC11a, w/o SDD, pass 4							
INT1 (V0OR)		5.32e+07	6.67e+07	0.80	0.11	0.09	0.007
LHC11a, w/ SDD, pass 4							
INT1 (V0OR)		2.64e+07	3.29e+07	0.80	0.10	0.08	0.006
EMC1		6.17e+05					
LHC13g, pass 1							
INT7 (V0AND)		1.56e+07	1.97e+07	0.79	0.076	0.017	0.11
EMC7		4.49e+05					
EG2		1.69e+05					
EG1		2.93e+05					
pp $\sqrt{s}$ = 2.76 TeV, MC simulation							
anchored to LHC11a w/o SDD, pass 4							
Pythia 8	LHC12f1a	2.09e+07	2.55e+07	0.82	0.063	0.095	0
Pythia 8 + GA sig.	LHC12i3	1.10e+07	1.19e+07	0.93	0.072	0.00	0
Phojet	LHC12f1b	2.52e+07	3.07e+07	0.82	0.064	0.094	0
anchored to LHC11a w/ SDD, pass 4							
Pythia 8	LHC12f1a	2.09e+07	2.55e+07	0.82	0.063	0.095	0
Phojet	LHC12f1b	2.52e+07	3.07e+07	0.82	0.064	0.094	0
Pythia 8, Jet-Jet	LHC15g1a	3.48e+07	3.15e+07	0.90	0.1	0	0
anchored to LHC13g, pass 1							
Pythia 8	LHC15g2	4.1e+07	5.28e+07	0.78	0.077	0.14	0
Pythia 8, Jet-Jet	LHC15a3a + LHC15a3a_plus	3.57e+07	3.93e+07	0.91	0.093	0	0
p–Pb $\sqrt{s_{\text{NN}}}$ = 5.02 TeV, Data							
LHC13b, pass 3							
INT7 (V0AND)		2.57e+07	2.95e+07	0.874	0.121	0.005	0.006
LHC13c, pass 2							
INT7 (V0AND)		8.00e+07	9.12e+07	0.879	0.116	0.005	0.005
p–Pb $\sqrt{s_{\text{NN}}}$ = 5.02 TeV, MC simulation							
anchored to LHC13[b,c], pass 2/3)							
DPMJet	LHC13b2_efix_p[1-4]	1.13e+08	1.30e+08	0.877	0.120	0.013	<0.001
HIJING + GA sig.	LHC13e7	0.43e+08	0.49e+08	0.881	0.118	0.001	0.002

Table 4.2.: Number of events used in the analysis for the normalization for each data taking period and the corresponding Monte Carlo simulations. In addition, the number of triggers by a certain condition (Y) and the fractions for $A_1 = \frac{\text{Y+Vtx+}|z_{vtx}|<10}{\text{Y}}$, $A_2 = \frac{\text{Y+Vtx+}|z_{vtx}|>10}{\text{Y}}$, $A_3 = \frac{\text{Y+ no Vtx}}{\text{Y}}$ and $A_4 = \frac{\text{Y+Pile-up}}{\text{Y}}$ are given.

in ALICE [272]. The rate $\frac{dN}{dt}$ can then be determined by

$$\frac{dN}{dt} = A \times \sigma_{\text{INEL}} \times \mathcal{L}, \tag{4.3}$$

where A is the acceptance and efficiency for the trigger condition, σ_{INEL} the inelastic cross-section for pp collisions and $\mathcal{L}$ the luminosity. The luminosity for a single proton bunch pair colliding with

$\sqrt{s}$ (TeV)	$\sigma_{\mathrm{MB_{AND}}}$ (mb)	$\mathrm{MB_{AND}}/\mathrm{MB_{OR}}$ measured	simulated	$\sigma_{\mathrm{MB_{OR}}}$ (mb)	$\sigma_{\mathrm{MB_{INEL}}}$ (mb)
2.76	47.73	0.8613 ± 0.0006	$0.863^{+0.02}_{-0.03}$	55.42	$62.8^{+2.4}_{-4.0}\%$(model) $\pm$ 1.2%(lumi)
5.02	51.17				$67.6 \pm 2.5\%$

Table 4.3.: Cross sections for the different triggers and the ratio of the trigger efficiencies for V0OR and V0AND [272–274], if they were available.

Year	Trigger name	Approx. threshold	Sim. threshold ($E_{\mathrm{thr,\,sim}}$) μ_{Trig}	σ_{Trig}	Trigger rejection factor (R_{Trig})	L_{int} (nb^{-1})
2011	INT1	0	-	-	1	0.524 ± 0.010
	EMC1	3.4 GeV	3.43 GeV	0.7 GeV	1217 ± 67	13.8 ± 0.806
2013	INT7	0	-	-	1	0.335 ± 0.013
	EMC7	2.0 GeV	2.01 GeV	0.1 GeV	126.0 ± 4.3	1.19 ± 0.062
	EG2	3.9 GeV	3.9 GeV	0.2 GeV	1959 ± 131	6.98 ± 0.542
	EG1	6.0 GeV	6.0 GeV	0.4 GeV	7743 ± 685	47.1 ± 4.57

Table 4.4.: Approximate trigger threshold and corresponding trigger rejection factor for EMCal triggers, as well as integrated luminosity for minimum bias and various EMCal triggers. In addition, the settings for the trigger mimicking in the full detector simulation are given. The simulated trigger threshold ($E_{\mathrm{thr,\,sim}}$) is drawn from a Gaussian distribution with the mean given by μ_{Trig} and the width by σ_{Trig} on an event-by-event basis.

zero crossing angle can be determined from the beam-profile using

$$\mathcal{L} = f N_1 N_2 / h_x h_y, \tag{4.4}$$

where f is the revolution frequency for the accelerator (11245.5 Hz for the LHC), N_1, N_2 the number of protons in each bunch, and h_x, h_y the effective transverse width of the beam in the interaction region.

Combining this measurement with the trigger efficiency for the V0AND, which can be obtained from Monte Carlo simulations, we arrive at the final inelastic cross section in pp collisions at $\sqrt{s} = 2.76$. To derive the cross-section for the V0OR, we need to simulate or measure in addition the ratio of the different triggers to each other. The resulting cross-sections and ratios are shown in Table 4.3.

For the normalization of the triggered data sets, the enhancement factor resulting from the triggers has to be calculated in addition. This factor is referred to as trigger rejection factor (R_{Trig}). In 2011, only the L0 trigger was used with one threshold (EMC1), while in 2013, one L0 (EMC7) and two L1 triggers (EG1, EG2) with different thresholds were used, as summarized in Table 4.4. The lower L1 trigger threshold in 2013 was set to approximately match the L0 threshold in 2011 for consistency. In case an event was associated with several triggers, the trigger with the lowest threshold was retained. As the thresholds are configured in the hardware via analog values, their transformation into energy values directly depends on the energy calibration of the detector and as such can have slightly different values for different trigger channels. The scaling with R_{Trig} takes into account a combination of the efficiency, acceptance and the downscaling of the respective triggers. In the presented analyses, it is obtained from the ratio R of the number of clusters reconstructed in EMCal triggered events to those in minimum bias events at high cluster energy E, where R should be approximately constant (plateau region). This implicitly assumes that the trigger does not affect the cluster reconstruction efficiency, but only the overall rate of clusters. The description of the EMCal clustering algorithm can be found in Section 4.3, together with the respective selection criteria applied for the different data sets. As the reach in energy is naturally limited for the lower threshold trigger and in particular for the minimum bias trigger the normalization for the higher threshold triggers was done with respect to the next lower threshold

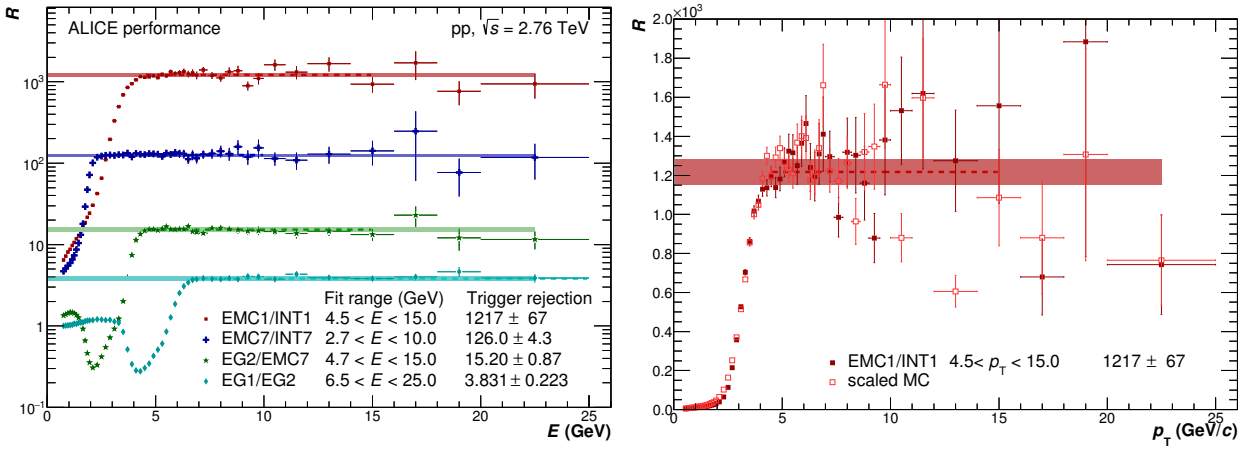

Figure 4.2.: Left: Energy dependence of ratios between cluster spectra for EMC1/INT1, EMC7/INT7, EG2/EMC7 and EG1/EG2. The trigger names INT1 and INT7 denote the minimum bias triggers $\mathrm{MB_{OR}}$ and $\mathrm{MB_{AND}}$ respectively. The trigger names EMC1, EMC7, EG2 and EG1 denote the EMCal triggers at L0 in 2011 and 2013, and the EMCal triggers at L1 in 2013 with increasing threshold. The individual trigger rejection factors and their respective fit ranges in the plateau region are indicated as well. The final rejection factors with respect to the minimum bias trigger are given in Table 4.4. Right: Comparison of energy dependence of the measured EMC1/INT1 cluster spectra ratio and the same quantity obtained with simple trigger emulation on the respective Monte Carlo sample, scaled to the plateau value of the data versus transverse momentum.

in the EMCal or the respective minimum bias trigger if no lower EMCal trigger was available. These individual rejection factors were then multiplied consecutively up to the minimum bias trigger and the final R_{Trig} to the minimum bias trigger is obtained. This procedure significantly reduces the statistical errors associated with the trigger rejection factor and allows for a more precise measurement of the integrated luminosity sampled by the various triggers, which can be calculated by:

$$L_{\mathrm{int}} = \frac{N_{\mathrm{trig}}}{\sigma_{\mathrm{MB}}} R_{\mathrm{trig}}\,, \tag{4.5}$$

where σ_{MB} refers to $\sigma_{\mathrm{MB_{OR}}}$ for 2011 and $\sigma_{\mathrm{MB_{AND}}}$ for 2013. The energy dependence of the ratios between cluster spectra of the relevant trigger combinations (EMC1/INT1, EMC7/INT7, EG2/EMC7 and EG1/EG2) are shown in Figure 4.2. The ratio shows a minimum at low E for EG2/EMC7 and EG1/EG2 at approximately the trigger threshold of the higher energy trigger, while at high E there is a pronounced plateau for every trigger combination. The fitting range for the respective trigger rejection factors is indicated in the plot and the final R_{Trig} is shown as dashed line, surrounded by its systematic uncertainty band, which is obtained by varying the fitting range for the fit to the plateau region. Finally, the values for the average trigger rejection factors above the threshold with respect to the corresponding minimum bias triggers are given in Table 4.4, with their respective uncertainties and the calculated integrated luminosities resulting from these. The statistical uncertainties on R_{Trig} have been treated as systematic uncertainties on the integrated luminosity.

In order to obtain the correction factors for this collision system different Monte Carlo event generators have been used as input for the full detector simulation: **Phojet** [258,275] and **Pythia 6.4, 8.1/2** [255–257]. All of these are general purpose generators for pp collisions and have been tuned based on lower energy experiments or, as for Pythia 8.2, on part of the early data collected by the LHC experiments.

Pythia

In ALICE two different versions of the Pythia library are used, which mainly differ in their implementation language and the level of tuning to the available data. While Pythia 6.4 is still written in Fortran 77, Pythia 8 is implemented in C++. As Pythia 8.1 was supposed to

be used for comparisons with the first LHC data, γp and $\gamma\gamma$ physics are not yet addressed in this version and some intended processes still remain to be implemented.
The event generation in Pythia is optimized for leading order $2 \longrightarrow 1$ and $2 \longrightarrow 2$ hard scattering processes, which by default take the initial states from the CTEQ 5L PDFs [276]. To reproduce the observed low momentum physics also diffractive processes based on Regge Field Theory [277] have been implemented. Furthermore, it is possible to import process level information (or events) via the Les Houches Accord (LHA) and Les Houches Event Files (LHEF) libraries. Both libraries can automatically generate matrix-element code and sample the respective phase space for various processes. As a consequence, the focus of Pythia 8 has shifted towards a good description of the subsequent steps such as the initial and final state parton showers, multiple parton-parton interactions, string fragmentation and decays. For the initial and final state algorithms Pythia relies on a $p_\perp$-ordered evolution and the hadronization is simulated based on the LUND String Model [278]. Unstable particles are decayed according to the information on the decay properties summarized by the particle data group [279].
Similar to nature, Pythia combines a lot of different processes. As such, it has many tunable parameters with significant influence on the generated distributions. This is reflected especially in the low momentum transfer processes. One of these parameters is the connection between low and high momentum processes, which is given by a minimum momentum transfer ($p_{T,\text{cut-off}}$) of 2 GeV/c. The authors of Pythia provide various sets of parameters, so-called tunes, which are optimized to reproduce different measurements at various energies. The most commonly used tunes at LHC energies for Pythia 6 are Perugia 0 or 2011, while Tune 4C or Monash 2013 are preferred for Pythia 8. The latter two were optimized to describe the early LHC measurements as well as lower energy data.
An additional feature of Pythia is the possibility to run it with cuts on the parton momentum ($p_{\text{T,hard}}$). This allows to generate samples with larger statistics for higher transverse momenta without adding particles arbitrarily. Instead, they follow the original compositions and energy distributions but enhance the processes with the respective transverse momentum of the initial hard collision. Those productions need to be weighted in order to correctly describe the spectrum and should not be used below a certain threshold in momentum. The respective weight (ω_{JJ}) can be calculated according to Equation 4.6, using the number of generated events $N_{\text{evt. gen.}}$, the number of trials necessary to obtain an event with the respective $p_{\text{T,hard}}(N_{\text{trials}})$ and the average cross section for those events according to Pythia ($\sigma_{\text{evt.}}$).

$$\omega_{\text{JJ}} = \frac{\sigma_{\text{evt.}}}{N_{\text{trials}/N_{\text{evt. gen.}}}} \tag{4.6}$$

The productions are called Jet-Jet productions within ALICE and are produced in several $p_{\text{T,hard}}$-bins varying in width to sample the full particle production spectrum. As the weights have to be applied on an event-by-event basis, the resulting particle spectra, which are represented by the weighted sum of all $p_{\text{T,hard}}$-bins, can show strong fluctuations depending on the statistics generated in the different bins. Thus, all events which have a single particle $p_{\text{T, part}} > 1.5 p_{\text{T,hard}}$ or a jet with a $p_{\text{T, jet}} > 3 p_{\text{T,hard}}$ are rejected. Those events are very rare and represent most likely a very odd configuration on the generator level.

Phojet
Phojet is a Monte Carlo event generator, which combines the ideas of the Dual Parton Model (DPM) [280] with perturbative QCD to give an almost complete picture of hadron-hadron, photon-hadron and photon-photon interactions at high energies [275]. The Dual Parton Model dominantly describes the soft scattering regime and allows to simultaneously calculate the elastic (i.e. cross sections) and inelastic processes (i.e. multi-particle production) within the same event. As such, the model directly relates the free parameters necessary to describe

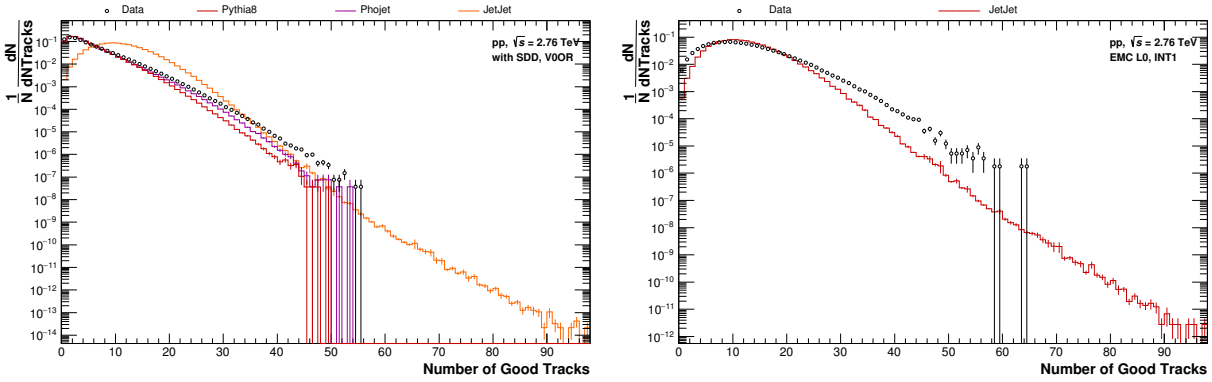

Figure 4.3.: Uncorrected p_{T} integrated charged track multiplicity for the minimum bias (left) and EMCal L0 (right) triggered data collected in 2011 compared to distributions obtained from the corresponding minimum bias and Jet-Jet Monte Carlo simulations. All distributions have been respectively scaled by the number of accepted events.

the cross sections to the multi-particle production.
As for Pythia, the parton showers are governed by the DGLAP evolution equations [281] and the hadronization process follows the LUND fragmentation model.

To judge whether a certain simulation can be used to correct the data, various quantities are compared between the output of the full detector simulation and the data. Many of these, like the PID performance or the EMCal detector response, are mainly driven by the GEANT3 and Aliroot implementation of the respective processes or detector material and are generator independent. Some of them, however, are directly linked to the capability of the generators to reproduced the basic features of the data. The latter are used to exclude certain generators or tunes, when deciding from which Monte Carlo sample the correction factors should be derived. One of the crucial quantities is the p_{T} integrated charged track multiplicity per event, as this quantity is directly linked to the primary and secondary vertex resolution. This is of particular importance for the analysis involving photons reconstructed using the conversion method. It can be found in Figure 4.3 for two different triggers compared to the respective distribution in the reconstructed simulation data. For the minimum bias trigger, the agreement between data and simulations for the pure minimum bias generators is reasonable and the remaining difference can be corrected for by applying event weights to the simulation. The Jet-Jet simulation, on the other hand, shows a very different multiplicity distribution, as by construction events with higher average multiplicity are preferred in these simulations. Thus, it should not be used to correct the minimum bias data, whereas it can be used to correct for instance the EMCal triggered data. For the latter, a similar bias in multiplicity is introduced through the trigger condition.
Even after adjusting the average multiplicity, none of the available generators with their respective tunes can describe simultaneously the soft and hard part of the neutral meson or photon spectrum but all of them can reproduce the spectral shape in a limited transverse momentum range. Consequently, none of them should be preferred over the other and all of the Monte Carlo productions can be used and the resulting correction factors should be compared.
As the detector conditions can change from run to run within ALICE, for instance due to problems in the electronics or different pressures in the gaseous detectors, the key parameters of the detectors to reproduce these features are stored in a central data base. These detector conditions are afterwards emulated in the simulations by using this data base as input for the full detector simulation. Such productions are referred to as anchored Monte Carlo productions, taking into account the statistics in the respective runs in addition. This guarantees the compatibility of data and simulations even if the statistics of several runs or periods is combined. The generation of such anchored full detector simulations is computationally expensive, thus all available full detector simulations with the mentioned generators as input were used and their correction factors

averaged. An overview of the simulations considered for the various data sets, together with their respective statistics can be found in Table 4.2.
Due to the constantly changing detector conditions a detailed multi variable quality assurance (QA) on a run-by-run basis has been performed. During which it was checked whether the performance trends seen in the data for the number of reconstructed conversion photons or calorimeter clusters, number of primary tracks per event and many others were followed by the same run-by run behavior in the simulated data. If the analysis depended on that detector and the run-by-run dependence in simulated and reconstructed data was not the same the affected runs were discarded for the respective analysis. This lead to slightly different set of runs accepted in the different analysis streams.
The reconstruction efficiency of the neutral pion and eta meson in the two photon decay channel depends on various parameters. For instance with which detector the photons have been reconstructed, but also where in that detector the photons are reconstructed and how the energy is shared among the two daughter photons ($\alpha_{\gamma\gamma}$). Triggering with the EMCal can enhance the probability to reconstruct mesons with a certain decay kinematics as they are not measured directly but reconstructed via their decay products. Thus, the trigger conditions have to be simulated as well. In order to do that a simple algorithm to mimic the triggers based on the reconstructed EMCal clusters in the fully anchored detector simulations has been implemented. This algorithm tags an event as triggered if at least one of the reconstructed clusters in the simulated event exceeds the energy $E_{\mathrm{thr,\,sim}}$. This threshold energy is randomly chosen from a Gaussian distribution on an event-by-event basis. The mean of this distribution can be identified with the average minimum trigger energy in the respective triggered data set and the width with the average spread from TRU to TRU in the same data set. The two parameters have been optimized to reproduce the different trigger turn on curves in the data and their exact values for the different triggers can be found in Table 4.4. This algorithm cannot reproduce a possible remaining φ or η dependence of the triggers, which could be introduced by imperfections in the trigger time alignment. However, it reproduces the p_{T} differential distribution with a sufficient accuracy, as it can be seen in the right plot of Figure 4.2.

4.1.2. Event and Trigger Selection for p–Pb Collisions at $\sqrt{s_{\mathrm{NN}}}$ = 5.02 TeV

The event selection for the p–Pb analysis to a large extent coincides with the minimum bias event selection for pp collisions at $\sqrt{s} = 2.76$ TeV. For example, only events triggered by the coincidence of the VZERO detectors have been taken into account. Furthermore, the interaction rates for the periods, which are considered in this analysis, were high enough that an in-bunch pile-up rejection based on the SPD primary vertex separation as well as the hit to tracklet correlation was necessary as well. The in-bunch pile-up conditions rejected about 0.6% of the collected events and had a similar efficiency as for pp collisions. To obtain the invariant yield for the mesons and photons the same event normalization as for pp collisions (Equation 4.2) has been applied. The final numbers are given in Table 4.2 for the respective periods.
The event sample selected by the above-mentioned criteria mainly consists of non single-diffractive (NSD) collisions. However, a small fraction of those NSD collisions is lost due to the limited trigger and primary vertex efficiency. To recover those, the number of collected minimum bias events is divided by the correction factor $96.4\% \pm 3.1\%$ [97, 282]. This correction factor has been obtained from a combination of several Monte Carlo generators to correctly describe not only the non single-diffractive processes but also the single-diffractive (SD) and electromagnetic (EM) interactions with their respective efficiencies [282].
In order to obtain the p_{T}-differential correction factors for the neutral meson and photon analyses two different minimum bias p–Pb event generators were used. The generated events were processed using GEANT3 and reconstructed with the same software version of AliRoot as the data, anchored to the two minimum bias periods of the p–Pb data taking campaign (LHC13[b,c]) in statistics and

detector conditions. The two multipurpose generators utilized for p–Pb collisions are **DPMJet III** [259] and **HIJING** [260].

DPMJet III
DPMJet III represents the merger of all features of the event generators DPMJet II [283,284] and DTUNUC-2 [285,286] into one single code system. As such it is based to a large extend on Phojet, which has been described in Section 4.1.1, and the Dual Parton Model [287].
For the modeling of the high-energy nuclear collisions, DPMJet relies on the Gribov-Glauber multiple scattering formalism as implemented in [288]. This allows to calculate the total, elastic, quasi-elastic and production cross sections for any high-energy nuclear collisions, while the parameters entering the hadron-nucleon scattering amplitude are determined using Phojet.
When simulating inelastic collisions, the afore-mentioned algorithm samples the number of "wounded" nucleons, the impact parameter and the interaction configuration of the wounded nucleon, assuming realistic nuclear densities as well as radii for light nuclei and Wood-Saxon densities otherwise. Phojet on the other hand is used to simulate the subsequent individual hadron(photon,nucleon)-nucleon interactions. Afterwards, the hadronization of the color neutral strings follows the LUND fragmentation model as implemented in Pythia 6.

HIJING
This event generator combines perturbative QCD (pQCD) inspired models for multiple jet production with low p_{T} multistring phenomenology implemented along the lines of the LUND FRITIOF [289,290] model and the Dual Parton Model [280]. As such it allows to study multiparticle production in pp, p–A and A–A collisions. Moreover, the model includes descriptions for multiple minijet production with initial and final state radiation using the Pythia routines and nuclear shadowing of parton distribution functions. For the simulation of multiple collisions in p–A and A–A collisions the Glauber model [71] is used. To study the energy loss in a hot and dense environment a simple jet quenching model has been implemented for heavy ion collisions, where the strength of the suppression can be tuned to reproduce the features seen in the data. This parameter is not the only free parameter and, similar to Pythia, many of the parameters have to be adjusted for every new collision system and energy. In particular the total charged-particle multiplicity needs to be tuned to the measured quantity to correctly reproduce the data.

In the p–Pb analysis DPMJet serves as default generator for ALICE for the anchored Monte Carlo simulations and as such the largest statistics has been generated for this setup. To be able to crosscheck the obtained correction factors, however, a HIJING production has been generated corresponding to about half of the statistics collected in the experiment.
In order to reach higher momenta for the neutral pion and eta meson analysis for the correction factors in the HIJING production, those particles have been embedded following a flat p_{T} distribution on top of the original minimum bias event. To correctly take into account the resolution effects of the detectors, those added signals have been weighted in the analysis to match the fully corrected spectrum. This process has been done iteratively, as the correction factors will change depending on the initial transverse momentum distribution. Additionally, the pure minimum bias part of the simulations was weighted to follow the same transverse momentum distribution. The agreement between the data and the simulations converged within 3-4 iterations. Unfortunately, the added signals and the underlying minimum bias event cannot be fully separated in the EMCal related analysis at the moment, due to the granularity of the EMCal and its software implementation. As such the use of this HIJING simulation for analysis involving the photon reconstruction within EMCal is limited and it should only be used as a cross check or to ascertain a possible systematic uncertainty related to the correction factors obtained using DPMJet.
In addition to the already mentioned criteria, a detailed quality assurance on the detector as well

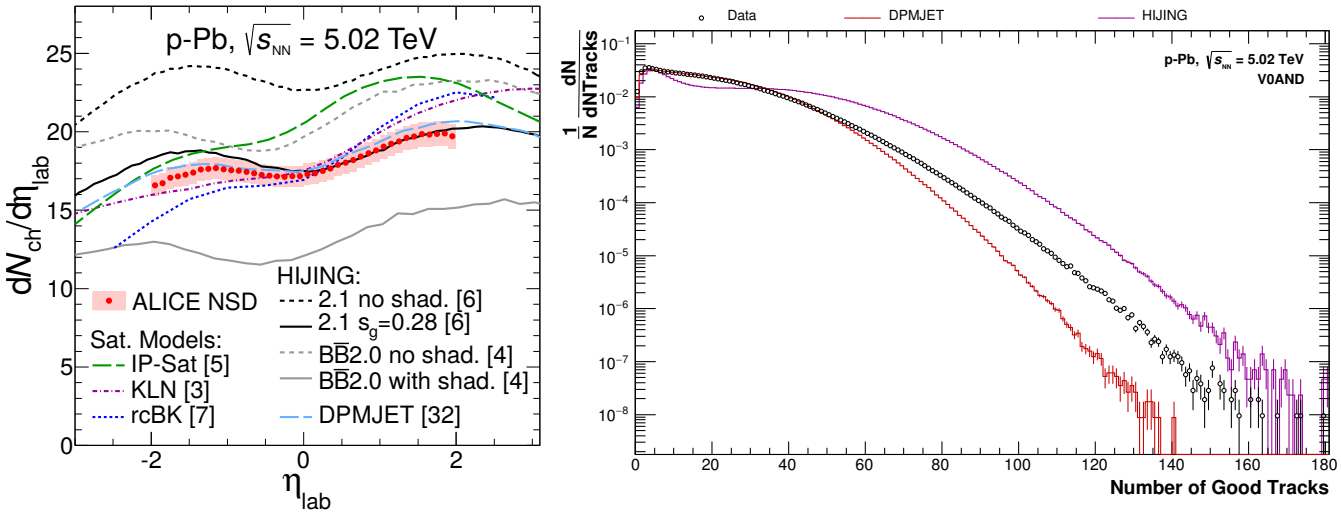

Figure 4.4.: Left: Pseudorapidity density of charged particles measured in NSD p–Pb collisions at $\sqrt{s_{\mathrm{NN}}}$ = 5.02 TeV, compared to various generators and their respective tunes [282]. Right: Uncorrected p_{T} integrated charged track multiplicity for the minimum bias triggered data at the same collision energy compared to distributions obtained from the corresponding minimum bias simulations. All distributions have been respectively scaled by the number of accepted events.

as run level has been performed, similar to the one described for pp collisions. The runs for which a mismatch in the behavior between real and simulated data was observed were excluded from the analysis. The same run list was used by all p–Pb analyses presented in this thesis.
While the average charged-particle multiplicity is well reproduced by the DPMJet and HIJING as seen in Figure 4.4(left), the uncorrected p_{T} integrated charged track multiplicity per event (Figure 4.4(right)) cannot be reproduced within a sufficient accuracy. Consequently, these have been reweighted on an event-by-event basis in the simulations to remove possible biases on the photon reconstruction efficiencies.

4.2. Photon Reconstruction using the Photon Conversion Method (PCM)

	pp, $\sqrt{s}$ = 2.76 TeV	**p–Pb, $\sqrt{s_{\mathrm{NN}}}$ = 5.02 TeV**
Track selection		
Track quality selection	$p_{\mathrm{T}} > 0.05$ GeV/c	
	$N_{\mathrm{TPC\ cluster}}/N_{\mathrm{reconstructible\ clusters}} > 0.6$	
	$\lvert\eta\rvert < 0.9$	
Electron selection		
PCM:	$-4 < n\sigma_{\mathrm{e}} < 5$	
PCM-EMC:	$-4 < n\sigma_{\mathrm{e}} < 5$	
Pion rejection		
PCM:	$n\sigma_{\pi} < 1$ for $0.4 < p < 3.5$ GeV/c,	$n\sigma_{\pi} < 1$ for $p > 0.4$ GeV/c
	$n\sigma_{\pi} < 0.5$ for $p > 3.5$ GeV/c	
PCM-EMC:	$n\sigma_{\pi} < 1$ for $p > 0.4$ GeV/c	
Photon selection criteria		
Conversion point	$\lvert\eta_{V^0}\rvert < 0.9$	
	$5\ \mathrm{cm} < R_{\mathrm{conv}} < 180\ \mathrm{cm}$	
	$\lvert Z_{\mathrm{conv}}\rvert < 240$ cm	
	$0 \leq \lvert\varphi_{\mathrm{conv}}\rvert \leq 2\pi$	
	$\cos(\theta_{\mathrm{point}}) > 0.85$	
Photon quality	$\lvert\psi_{\mathrm{pair}}\rvert < \psi_{\mathrm{pair,\ max}} - \frac{\psi_{\mathrm{pair,\ max}}}{\chi^2_{\mathrm{red,\ max}}}\chi^2_{\mathrm{red}}$,	
	with $\psi_{\mathrm{pair,\ max}} = 0.1$ and $\chi^2_{\mathrm{red,\ max}} = 30$	
Armenteros-Podolanski	$q_{\mathrm{T}} < q_{\mathrm{T,max}}\sqrt{1 - \frac{\alpha^2}{\alpha^2_{\mathrm{max}}}}$,	
	with $q_{\mathrm{T,max}} = 0.05$ GeV/c and $\alpha_{\mathrm{max}} = 0.95$	

Table 4.5.: Criteria for photon candidate selection for PCM. If different cuts are applied for the two different collision systems, they are mentioned in both columns. Otherwise, they are only displayed in the column for pp collisions at $\sqrt{s} = 2.76$ TeV. If the selection criteria in the meson or photon analysis were chosen differently for different analysis streams (*PCM, PCM-EMC*), it is mentioned explicitly in different rows.

Many photons convert within the active and inactive detector material of ALICE. If they converted before having passed more than half of the the TPC ($R_{\mathrm{conv}} < 180$ cm), they can be reconstructed using a secondary vertex finder. Within ALICE two of these algorithms have been implemented, as described in Section 3.2.4. While both can be used for the photon reconstruction, the on-the-fly V^0-finder is better suited as it provides a larger efficiency for the photons in particular at low transverse momentum. Regardless of the employed V^0-finder, in the current reconstruction algorithm no assumption on the mass of the daughter particles is made when reconstruction a V^0. Therefore, no additional geometrical considerations can be applied either. For the analyses presented in this thesis, however, the precision of the reconstructed photon conversion point has been improved by recalculating the position of the secondary vertex under the assumption that the momenta of the decay products are parallel at the point of their creation. This assumption is only valid when attempting to reconstruct photons, as they have no mass. The recalculation procedure is explained in detail in [291, 292] and the resulting spatial resolution in all spatial dimensions can be found in [293].
For the reconstruction of photons with this technique, only tracks from secondary vertices without kinks with a minimum momentum of 0.05 GeV/c were taken into account. Additionally, these

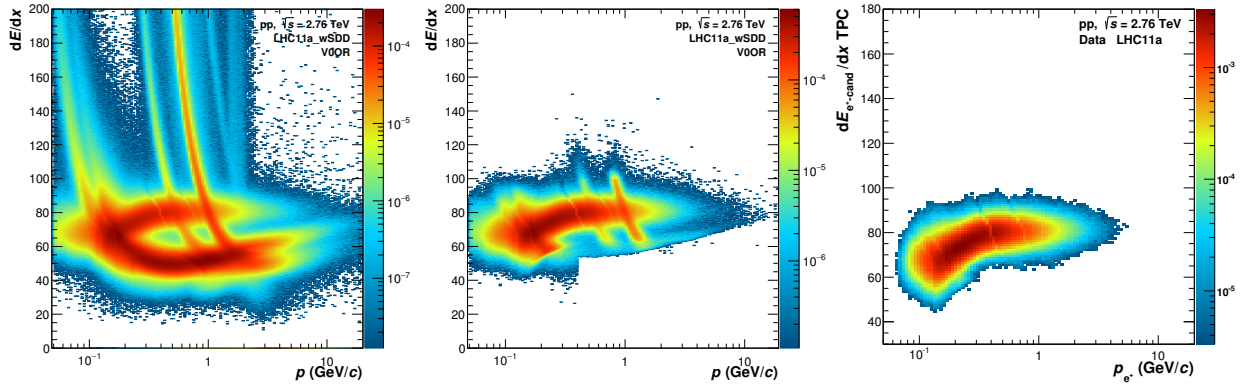

Figure 4.5.: $\mathrm{d}E/\mathrm{d}x$ distribution in the TPC as a function of momentum for all secondary tracks, normalized to the number of events, after the basic track and V^0selection cuts (left), after the particle identification cuts (middle) and after all photon selection criteria have been applied in addition (right) for pp collisions at $\sqrt{s_{\mathrm{NN}}} = 2.76$ TeV. The PID and photon selection criteria correspond to the once chosen for the direct photon and meson analysis based on PCM in combination with the photons reconstructed in EMCal.

tracks had to be reconstructed within the fiducial acceptance of the TPC and ITS and with at least 60% of the reconstructible track points in the TPC. The amount of reconstructible clusters in the TPC varies depending on the position of the conversion point. Thus, no rejection based on a fixed minimum for the number of clusters within the TPC has been applied. On average, more than 100 track points have been associated to each of the legs of the photon, leading to an excellent spatial and kinematics resolution for the electrons. Consequently, the photon momentum resolution is better than 1.5% at low p_{T}, which is driven by the precise determination of the track momenta within the TPC.

In order to further select photons among the remaining V^0's, the associated energy loss measured in the TPC for each track was required to be within $-4(-3) < n\sigma_e < 5$ of the electron expectation, where $n\sigma_X = (\mathrm{d}E/\mathrm{d}x - \langle \mathrm{d}E/\mathrm{d}x_X \rangle)/\sigma_X$ with $\langle \mathrm{d}E/\mathrm{d}x_X \rangle$ and σ_X the average energy loss and resolution for particle X, respectively. The contamination from charged pions was suppressed by excluding all track candidates within a certain $n\sigma_\pi$ of the pion expectation. These cuts differ slightly for different analysis streams involving photons reconstructed with PCM as they have been optimized either with respect to efficiency or purity of the resulting photon sample. The detailed selection criteria for the different analysis streams in pp and p–Pb collisions for the pion rejection can be found in Table 4.5. Comparing the left and middle plot of Figure 4.5 shows the effects of the applied PID selection criteria on the secondary track sample for the TPC $\mathrm{d}E/\mathrm{d}x$. The enhancement of the electrons is clearly visible. The remaining contamination could be partially removed by using the PID capabilities of other detectors like the ITS, TOF or TRD in their applicable kinematic regions. For the analysis presented in this thesis, however, no other PID method has been chosen as it would significantly reduce the reconstruction efficiency of the photons. Leaving the photon sample with a purity of approximately 80% after the secondary track and PID selection has been applied.

To remove combinatorial background from primary electron candidate pairs or Dalitz decays of the π^0 and η, only conversions, which were pointing to the primary vertex and could be reconstructed with a conversion point with $5 < R_{\mathrm{conv}} < 180$ cm within the acceptance of the ITS and TPC were considered ($|\eta| < 0.9$). The photon η is calculated based on the angle between the beam axis and the momentum vector of the particle in the ZR plane without requiring this vector to point to the nominal center of the detector $(X, Y, Z) = (0, 0, 0)$. To remove photons which would be displaced in Z but comply with the η cut mentioned in Table 4.5, a geometrical η cut is defined with respect to the center of the detector in addition. Accordingly, for every V^0 candidate the following condition has to be satisfied:

$$R_{\mathrm{conv}} > |Z_{\mathrm{conv}}| \times ZR_{\mathrm{Slope}} - Z_0, \tag{4.7}$$

where $ZR_{\text{Slope}} = \tan(2 \times \arctan(\exp(-\eta_{\text{cut}})))$, $Z_0 = 7$ cm and the coordinates of the secondary vertices (i.e. $R_{\text{conv}}, Z_{\text{conv}}$) are determined with respect to the nominal center of the detector. For these calculations the spread of the primary vertex position is taken into account through Z_0 only and no additional smearing is applied.
Compared to previous PCM standalone measurements [173], the photon candidate selection criteria were optimized in order to suppress the combinatorial background even further. In particular, a two dimensional selection on the reduced χ^2 of the photon conversion fit and the angle between the plane defined by the conversion pair and the magnetic field ($|\psi_{\text{pair}}|$) was introduced to reduce random e^+e^- pairs. Those two variables (χ^2_{red} & ψ_{pair}) span a plane in which the background and the signal can be easily distinguished. While the combinatorial background is distributed randomly in the whole plane, the signal is concentrated at χ^2/ndf & $|\psi_{\text{pair}}|$ close to 0. Those distributions can be seen in Figure 4.6 for the Monte Carlo background on the left and the true photons on the right for Pythia 8 simulations for pp collisions at $\sqrt{s} = 2.76$ TeV. In order to remove most of the combinatorial background, while still keeping most of the signal, a triangular cut is applied. To avoid errors in the efficiency calculation due to these cuts, it has been verified that the distributions can be reproduced by Monte Carlo simulations. The comparison between data and Monte Carlo for both variables can be seen in Figure 4.7. The distributions are peaked at zero and can be reproduced by the Monte Carlo simulation within reasonable uncertainties. However, they are not matched in the tails, which probably stems from the underestimation of the secondaries in Pythia compared to the data and the out-of-bunch pile-up contribution of photons in the data, which should show up predominantly at large χ^2_{red}.
The remaining K^0_S, Λ and $\overline{\Lambda}$ can be removed from the sample using an elliptical cut in the Armenteros-Podolanski variables [294]: $q_\text{T} = p \times \sin\theta_{\text{mother-daughter}}$ and $\alpha = (p_L^+ - p_L^-)/(p_L^+ + p_L^-)$. In the Armenteros-Podolanski plot, the projection of the momentum of the daughter particle with respect to the mother particle in the transverse direction (q_T) versus the longitudinal momentum asymmetry (α) is shown. The photon daughter particles, due to the negligible mass of the photon, will follow the direction of the mother in the laboratory frame. Thus, the q_T of the real photons is close to zero. Heavier mother particles, however, will have larger q_T which is correlated with their larger opening angle and mass. The symmetry around $\alpha = 0$ depends on the mass difference of the decay products, as such the α distributions of γ and K^0_S decays are symmetric, while the once for the Λ and $\overline{\Lambda}$ are asymmetric.
Figure 4.8(left) shows the Armenteros-Podolanski-Plot for all V^0 candidates after the basic track cuts. Four different distributions are clearly visible: the symmetric distributions of the photons with a q_T close to 0 GeV/c and the K^0_S's with a q_T ranging from $0.1 - 0.23$ GeV/c. Moreover, the asymmetric distributions representing the Λ and $\overline{\Lambda}$ can be identified around $\alpha = \pm 0.7$. The right plot of Figure 4.8 shows the distribution after all photon selection criteria have been applied. The elliptical sharp line with the maxima at $q_\text{T} = 0.05$ GeV/c and $|\alpha| = 0.95$ is caused by the two dimensional q_T cut itself. It can be seen, that only very few Λ and $\overline{\Lambda}$ survive our cuts below this sharp q_T cut, leading to a high purity photon sample. The high purity of the the photon sample is also reflected in the $\text{d}E/\text{d}x$ distribution of the electrons after all cuts, as seen in Figure 4.5(right). By applying the tight photon selection criteria, the otherwise visible π, K, p contamination is removed and the photon sample reaches a purity of at least 98%.

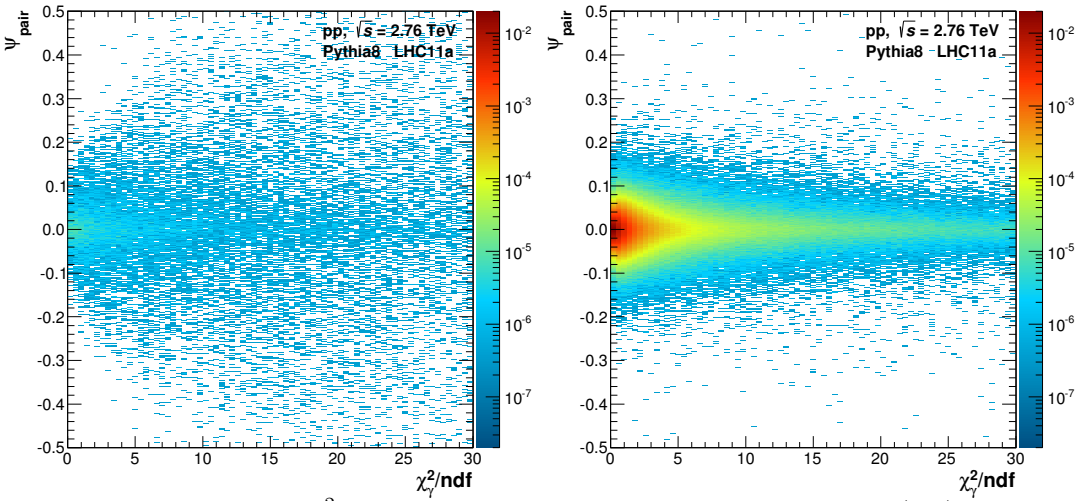

Figure 4.6.: Distribution of the χ^2_{red} versus ψ_{pair} for the combinatorial background (left) and true photons (right) with all cuts applied (except the respective cuts shown) summed over all momenta. The distributions correspond to simulated data using Pythia 8 as generator for pp collisions at $\sqrt{s} = 2.76$ TeV anchored to the data taken in 2011 at the same energy.

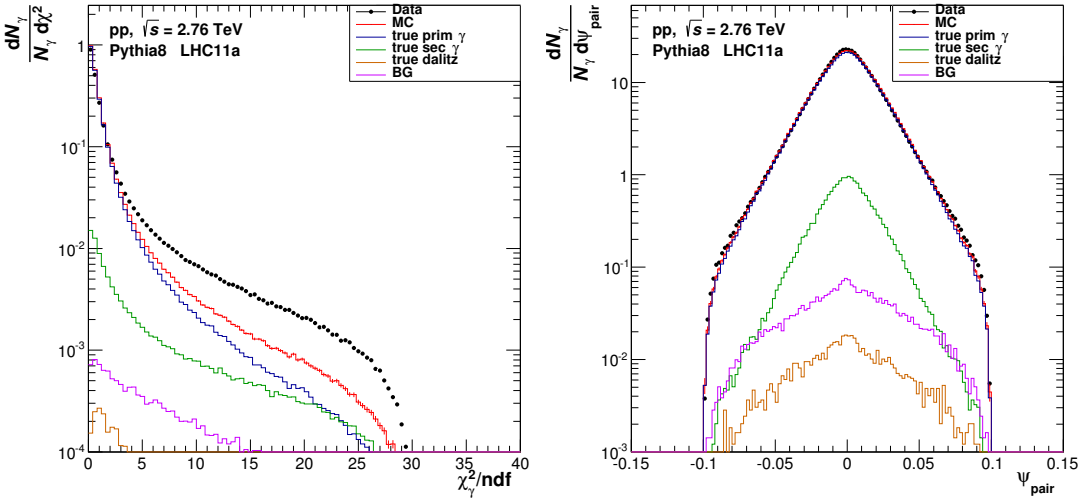

Figure 4.7.: Comparison of the distribution of the χ^2_{red} (right) and ψ_{pair} (left) of the photon candidates for pp collisions at $\sqrt{s} = 2.76$ TeV and the corresponding Pythia 8 Monte Carlo simulation.

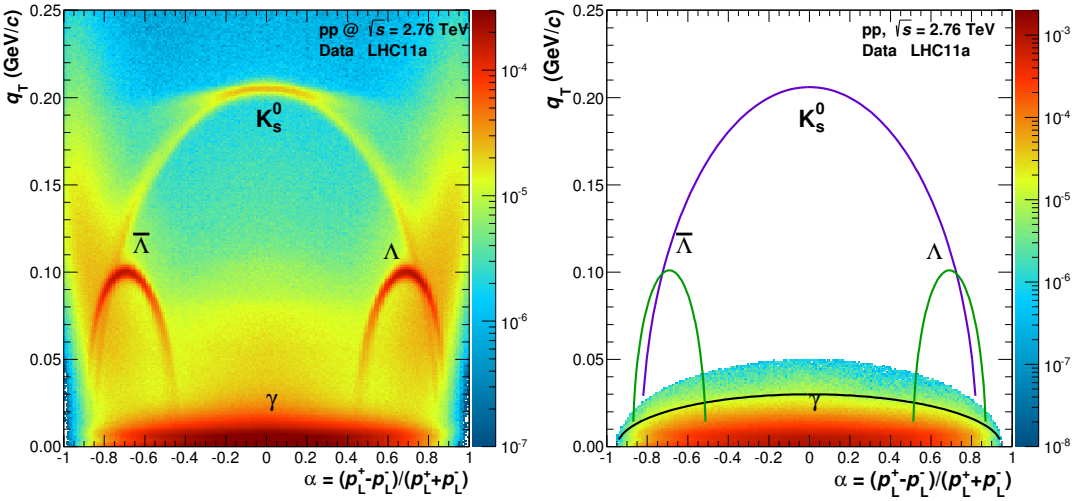

Figure 4.8.: Armenteros-Podolanski-Plot of all V^0 candidates after the basic track and V^0 cuts for pp collisions at $\sqrt{s} = 2.76$ TeV (left) compared to the remaining photon candidates fulfilling all the selection criteria (right).

4.3. Photon Reconstruction using EMCal

	pp, $\sqrt{s}$ = 2.76 TeV	**p–Pb, $\sqrt{s_{\mathrm{NN}}}$ = 5.02 TeV**
Cluster reconstruction		
Minimum cell energy	$E_{\mathrm{cell}} > 0.1$ GeV	
Minimum leading cell energy	$E_{\mathrm{seed}} > 0.5$ GeV	
Cluster energy correction	CCMF	CCRF
Cluster selection		
Selection in η	$\lvert\eta\rvert < 0.67$	
Selection in φ	$1.40\,\mathrm{rad} < \varphi < 3.15\,\mathrm{rad}$	
Minimum cluster energy	$E_{\mathrm{clus}} > 0.7$ GeV	
Minimum number of cells	$N_{\mathrm{cells}} \geq 2$	
Cluster-shape parameter		
PCM-EMC	$0.1 < \sigma^2_{\mathrm{long}} < 0.5$	
EMC	$0.1 < \sigma^2_{\mathrm{long}} < 0.7$	$0.1 < \sigma^2_{\mathrm{long}} < 0.5$
EMC γ_{dir}	$0.1 < \sigma^2_{\mathrm{long}} < 0.32$	
mEMC	$\sigma^2_{\mathrm{long}} > 0.27$	
Cluster time	$\lvert t_{\mathrm{clus}}\rvert \leq 50$ ns (2011)	$\lvert t_{\mathrm{clus}}\rvert \leq 50$ ns
	-35 ns $< t_{\mathrm{clus}} < 30$ ns (2013)	
Cluster–track matching	$\lvert\Delta\eta\rvert \leq 0.010 + (p_{\mathrm{T}} + 4.07)^{-2.5}$	
	$\lvert\Delta\varphi\rvert \leq 0.015 + (p_{\mathrm{T}} + 3.65)^{-2}$	

Table 4.6.: Criteria for photon candidate selection for the EMCal-based methods. If different cuts are applied for the two different collision systems, they are mentioned in both columns. Otherwise, they are only displayed in the column for pp collisions at $\sqrt{s} = 2.76$ TeV. If the selection criteria in the meson or photon analysis were chosen differently for different analysis streams (*PCM-EMC, EMC, mEMC*), it is mentioned explicitly in different rows.

Clusters in the EMCal were reconstructed by aggregating cells with $E_{\mathrm{cell}} > 0.1$ GeV to a leading cell energy with at least $E_{\mathrm{seed}} > 0.5$ GeV, and were required to have only one local maximum. A new cluster is started if during the aggregation the energy of a neighboring cell is larger than that of the already aggregated cell. Within one event, the clustering algorithm always starts with the highest cell energy and afterwards continues with the next highest which has not been used in a cluster yet.

The transfer function from ADC counts for a certain cell to the exact energy in GeV in this cell is obtained from a cell-by-cell π^0 mass calibration combined with the general knowledge of the response of the electronics. For this cell-by-cell calibration clusters with cell A as leading cell are paired with all other clusters in the same event. From the resulting invariant mass distribution, the neutral pion mass peak position was extracted and the transfer function for tower A has been calculated to fix the reconstructed π^0 mass to its nominal mass of 0.134976 GeV/c^2. In this procedure only pairs with a minimum momentum of 2 GeV/c were taken into account and the algorithm was repeated for every channel of the EMCal. While this procedure allows for an average absolute calibration of the detector, it cannot provide an energy depended correction factor. The latter is obtained by adjusting the full GEANT3 simulations to match the data in their response, which is further described in Section 4.3.1.

Calorimeter clusters can be identified with the response of the calorimeter to one or more particles hitting the same area in the calorimeter. In pp collisions a cluster contains on average energy from only 1 particle, while for Pb–Pb at least 2 particles contribute energy to the cluster on average. The probability for those clusters to originate from photons was enhanced by requiring a cluster

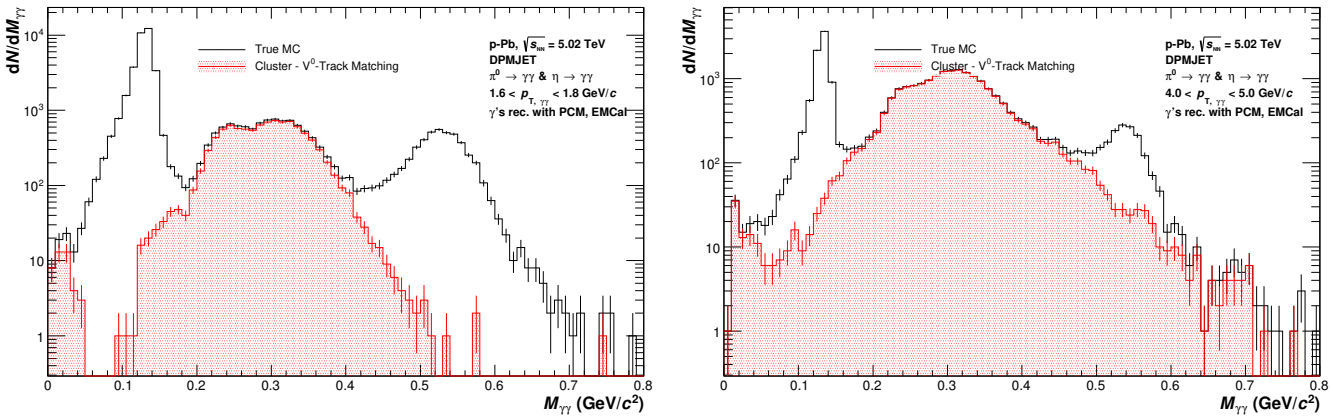

Figure 4.9.: By combining photons from EMCal and PCM, the shown invariant mass histograms are obtained on true Monte Carlo (DPMJET) level. The left and right plots show the invariant masses of the two photons for different transverse momentum ranges: 1.6< $p_{\mathrm{T},\gamma\gamma}$ <1.8 GeV/c and 4.0< $p_{\mathrm{T},\gamma\gamma}$ <5.0 GeV/c. The black distributions represent invariant masses of true meson candidates (π^0 and η, decaying into $\gamma\gamma$) where one photon is measured with EMCal while the other photon converts and is being reconstructed with PCM. Both photons stem from the same mother particle. The red distribution shows the invariant mass spectrum for combinations of one PCM photon with an EMCal photon candidate, which could be matched using the track matching procedure to one of electron legs of the PCM photon.

energy of 0.7 GeV to ensure acceptable timing and energy resolution and to remove contamination from minimum-ionizing ($\lesssim$ 300 MeV) and low-energy hadrons. Furthermore, a cluster had to contain at least two cells to ensure a minimum cluster size and to remove single cell electronic noise fluctuations. Clusters, which could be matched to a track propagated to the average shower depth in the EMCal (at 440 cm) within certain $|\Delta\eta|$ and $|\Delta\varphi|$ criteria that depend on track p_{T} as given in Table 4.6, were rejected to further reduce contamination by charged particles. The track-to-cluster matching efficiency amounts to about 97% for primary charged hadrons at cluster energies of $E_{\mathrm{clus}} > 0.7$ GeV, decreasing slowly to 92% for clusters of 50 GeV. The removal of matched tracks is particularly important for the PCM-EMC method, as otherwise a severe auto-correlation between the clusters originating from one of the conversion electrons and the conversion photon would be introduced. Figure 4.9 shows the two photon invariant mass distribution obtained from DPMJet simulations for different transverse momentum slices in the mother momentum. The black distribution reflects the invariant mass distribution of real photons originating from a meson candidate (π^0 or η) and as such it excludes the combinatorial background from random photon pairs. For all candidates, one of the photons is reconstructed using PCM and one is reconstructed in the EMCal. The auto-correlated pairs strongly distort the shape of the invariant mass distribution between the π^0 and η mass peak region. The red distribution in the same plot reflects the meson candidates, where one photon was reconstructed with PCM and the EMCal photon candidate could be matched using the track matching procedure to one of electron legs of that same PCM photon. That means that the PCM photon is being combined with an EMCal cluster which originated from one of the conversion electron, but was assumed to stem from the primary vertex. The importance of this auto-correlation rises with increasing transverse momentum. Thus, in order to obtain clean invariant mass spectra for the combination of photons reconstructed in PCM and EMCal, the cluster – V^0-track matching procedure is mandatory and implies to be an important step, especially for higher momenta. The standard track matching applied to each conversion leg allowed for the removal of these auto-correlation pairs with an efficiency of more than 99% since the corresponding track was already found.
An additional distinction between clusters from mainly photons, electrons and neutrons is based on their shower shape. The shower shape can be characterized by the larger eigenvalue squared of

the cluster's energy decomposition in the EMCal η–φ plane. It is expressed as

$$\sigma^2_{\text{long}} = 0.5 \left(\sigma^2_{\varphi\varphi} + \sigma^2_{\eta\eta} + \sqrt{(\sigma^2_{\varphi\varphi} - \sigma^2_{\eta\eta})^2 + 4\sigma^4_{\varphi\eta}} \right) \tag{4.8}$$

where $\sigma^2_{xz} = \langle x\, z \rangle - \langle x \rangle \langle z \rangle$ and $\langle x \rangle = \frac{1}{w_{\text{tot}}} \sum w_i x_i$ are weighted over all cells associated with the cluster in the φ or η direction. The weights w_i logarithmically depend on the ratio of the energy of a given cell to the cluster energy, as $w_i = \max(0, 4.5 + \log E_i/E)$, and $w_{\text{tot}} = \sum w_i$ [295].
Nuclear interactions, in particular from neutrons, can create an abnormal signal when hitting the corresponding avalanche photodiodes for the readout of the scintillation light. This signal is localized in one high-energy cell. However, within one read-out card of the EMCal cross-talk can lead to a small signal in the surrounding cells as well. During the clustering algorithm these cells might then be paired and a cluster with more than 95% of the energy contained in 1 cell can be created. By requiring $\sigma^2_{\text{long}} > 0.1$, most of these abnormal clusters can be removed from the sample and with them a large fraction of the contamination from neutrons.
The energy response of electro-magnetic calorimeters to electrons and photons tends to be very similar. Thus, the only distinguishing point among them, if no track could be matched to the cluster, is their elongation, as most of the low-p_{T} electrons will hit the EMCal surface at an angle due to the bending in the magnetic field. The electro-magnetic shower of pure photons, on the other hand, does not follow a preferred direction and as such the clusters will appear round and most of them will be reconstructed with $\sigma^2_{\text{long}} \approx 0.25$. Only late conversions can lead to showers which are elongated beyond this value. Thus, rejecting clusters with $\sigma^2_{\text{long}} > 0.7$ (0.5) for EMC (PCM-EMC) rejects the contamination from late conversion electrons significantly for pp collisions at $\sqrt{s} = 2.76$ TeV. For p–Pb collisions, the shower shape cut was tightened for the mesons analysis purely based on EMCal to only accept clusters with $\sigma^2_{\text{long}} < 0.5$ in order to suppress clusters originating from multiple particles in addition. At very high transverse momenta (> 10 GeV/c), it also rejects part of the contamination from neutral pions for which both photons have been reconstructed within a single cluster. For the direct photon analysis with the EMC reconstruction technique the σ^2_{long} was restricted even more to $\sigma^2_{\text{long}} < 0.32$ in order to increase the purity at lower momenta.
This elongation of the clusters is exploited in the merged cluster analysis, for which only cluster with a $\sigma^2_{\text{long}} > 0.27$ are accepted to enhance the probability of having both photons contributing to the same cluster. The merged cluster analysis is, however, only applicable for cluster momenta beyond $E_{\text{cl}} = 12 - 15$ GeV. Those candidate clusters for the mEMC analysis are referred to as neutral pion candidates and not photon candidates, like for the other analysis streams.
Contributions of clusters from different bunch crossings were suppressed by a suitable selection of clusters within a certain time window around the main bunch crossing. The selected time window depends on the time between bunch crossings and is thus dependent on the data taking period. Finally, some regions of the EMCal were rejected in the analysis to exclude faulty cells from the analysis. A summary of the selection criteria for EMCal photon and neutral pion candidates can be found in Table 4.6.
As an example, the resulting cluster distribution in $\eta - \varphi$ is shown in Figure 4.10 for real and simulated data in p–Pb collisions at $\sqrt{s_{\text{NN}}} = 5.02$ TeV. The distributions are individually scaled to the number of events as well as the average cluster density per cell. As such the distributions can be compared between real and simulated data to validate that both the detector acceptance as well as the local occupancy are well reproduced by the anchored simulations. The $\eta - \varphi$ map also shows that the photon reconstruction efficiency in different φ slices can be very different due to the material in front of the detector. For instance for the data taking in 2011 only 4 EMCal super modules, located at $\varphi > 2.45$, had the TRD installed in front of them. While by 2013 an additional two super modules ($2.1 < \varphi < 2.4$) were covered by TRD super modules. The material added by the installation of the TRD reduces the probability to reconstruct low momentum photons, as approximately half of them will convert within the TRD material and the resulting electrons might

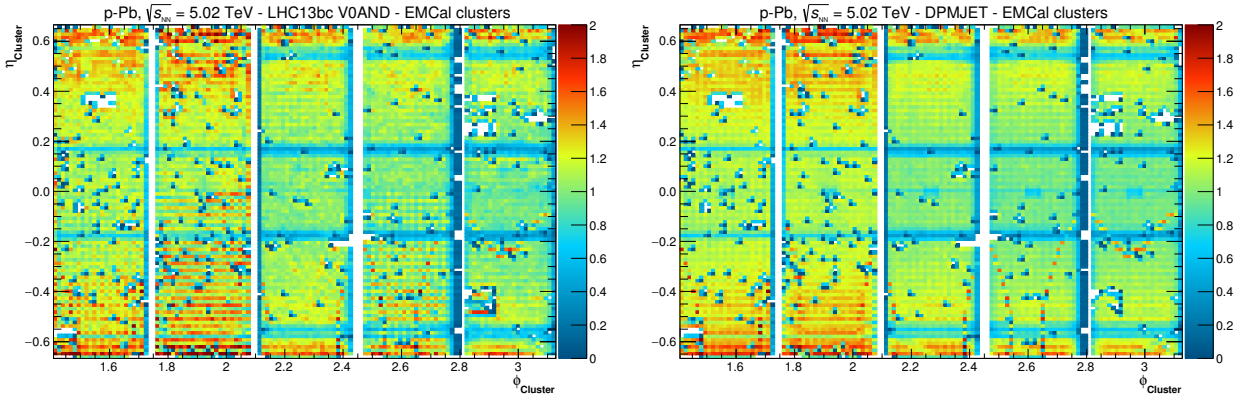

Figure 4.10.: η-φ distributions of EMCal clusters for data collected in p–Pb collisions at $\sqrt{s_{\mathrm{NN}}} = 5.02$ TeV (left) and the corresponding DPMJet simulations (right). The distributions are normalized per event and divided by the average cluster density per cell.

not be reconstructible with the chosen analysis cuts. Consequently, the average cluster density per cell is lower in the region of the EMCal, where TRD modules had been installed in the respective data taking period. Furthermore, it can be seen that the cluster densities increase for higher $|\eta|$, which is well reproduced by the simulations and coincides with the η dependence of the conversion photons in the material up to the outer radius of the TPC.

4.3.1. EMCal Cluster Energy Correction

Instead of using a classical non-linearity correction based on test-beam data, in this analyses an energy calibration based on the measured π^0 peak position in the PCM-EMC analysis channel has been chosen. This technique exploits the good momentum resolution of the PCM photon to derive an improved correction for the relative energy scale, while at the same point correcting for the residual misalignment of the EMCal in the data, which was not included in the simulation.
If only the calibration obtained from the 2010 test beam data would have been used, as for [296], a reasonably good calibration of the energy response of the detector would have been achieved. However, further fine tuning would have been necessary due to slightly modified readout and running conditions of the detector in the analyzed data taking periods compared to the test beam data. Hence, instead of applying two corrections in a row, an independent calibration was developed in the course of this thesis that includes the overall calibration as well as the non-linearity correction, based on the aforementioned comparison of the π^0 peak position in data and Monte Carlo simulations.
The invariant masses of the neutral pion and η meson can be calculated from the energy of their decay photons ($E_{\gamma_{1,/2}}$) and their respective opening angle (θ_{12}) in the laboratory frame via

$$M_{\gamma\gamma} = \sqrt{2E_{\gamma_1}E_{\gamma_2}(1-\cos\theta_{12})}. \tag{4.9}$$

The π^0 and η mesons are reconstructed as excess yield, visible at their respective rest mass, 0.135 GeV/c^2 for the π^0 and 0.548 GeV/c^2 for the η meson. Due to miscalibrations in terms of energy or position of the involved detectors those peaks can, however, be displaced in invariant mass.
To illustrate the initial mismatch between the simulated and real data for EMCal after the channel by channel equilibration the neutral pion mass position reconstructed with the PCM-EMC reconstruction is show in Figure 4.11. The π^0 mass obtained from different fit functions is plotted for the different transverse momentum intervals for p–Pb data and the respective Monte Carlo simulation using DPMJet as event generator. Furthermore, the corresponding ratios of the mass positions in data and Monte Carlo are shown in the same figure. The mismatch is of the order of

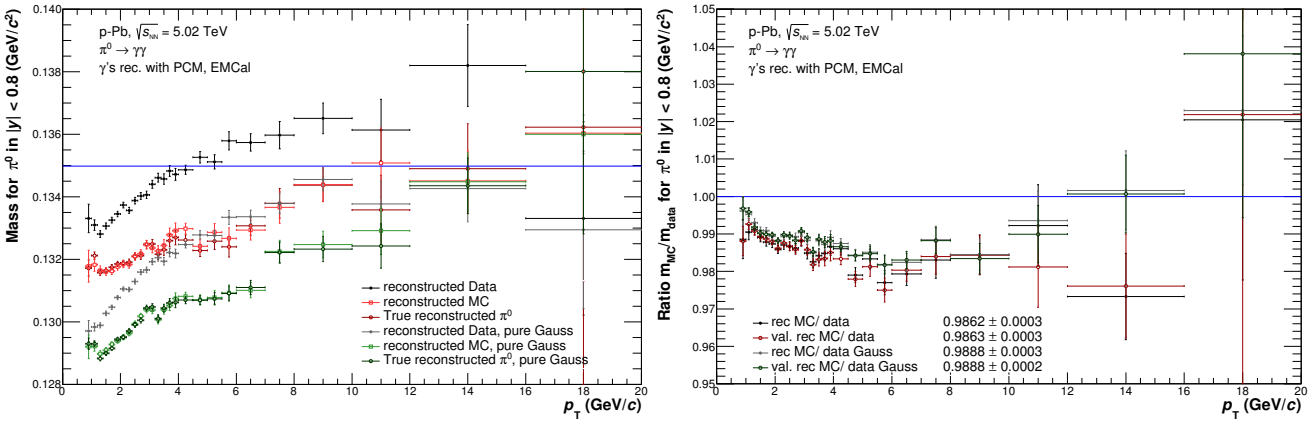

Figure 4.11.: Left: Reconstructed π^0 masses for data, Monte Carlo and validated reconstructed neutral pions in the simulation for p–Pb collisions at $\sqrt{s_{\mathrm{NN}}} = 5.02$ TeV. The meson peaks were fitted using an Gaussian convoluted with an exponential tail on the left side (black, red) or a pure Gaussian distribution (gray, green). Right: Mass ratios for the various fitting options.

1.5%, which corresponds to a $1-2$ MeV displacement of the neutral pion peak. It increases with increasing momentum. A similar behavior was observed for pp collisions at $\sqrt{s} = 2.76$ TeV and for the neutral meson reconstruction involving only photons reconstructed with the EMCal. For the latter the mismatch is however approximately twice as large as it affects both photons.
To obtain the correction function from the PCM-EMC method, the π^0 mass position is obtained in slices of the EMCal cluster energy for data and simulation and its ratio parametrized afterwards. The latter can either be done by directly fitting the ratio of the peak positions in simulated and real data or by fitting the mass positions in data and simulation independently and calculating the ratio thereafter. If the ratio was fitted directly, the correction procedure is referred to as Conv-Calo ratio fit (CCRF), while the correction using directly the mass positions is called Conv-Calo mass fit (CCMF). Prior to the fitting of the peak positions the combinatorial $\gamma\gamma$ below the neutral pion peak was subtracted using mixed event background subtraction binned in the same energy. This was necessary to take out biases on the peak position arising from slightly different slopes of the background in real and simulated data. Details on the event mixing procedure can be found in Section 5.1.1.
The mass position versus energy was fitted either with a power-law like function (m_1) or with an exponential (m_2) function.

$$m_1(E_{\mathrm{cl}}) = p_0 + p_1 E_{\mathrm{cl}}^{p_2} \tag{4.10}$$
$$m_2(E_{\mathrm{cl}}) = p_0 - \exp\left(-p_1 E_{\mathrm{cl}} + p_2\right) \tag{4.11}$$

For the fit of the ratio of the mass positions in simulated and real data an exponential function (f_0) was used as functional form. Alternatively, the ratio of the functions $m_{[1,2],Data}$ and $m_{[1,2],MC}$ was calculated, where the functional form ($m_{[1,2]}$) was chosen such, that it reproduces the data as closely as possible in the different data sets.

$$\text{CCRF:} \quad f_0(E_{\mathrm{cl}}) = p_0 + \exp\left(p_1 + p2E_{\mathrm{cl}}\right) \tag{4.12}$$
$$\text{CCMF:} \quad f_1(E_{\mathrm{cl}}) = \frac{m_{1,Data}}{m_{1,MC}} = \frac{p_0 + p_1 E_{\mathrm{cl}}^{p_2}}{p_3 + p_4 E_{\mathrm{cl}}^{p_5}} \tag{4.13}$$
$$f_2(E_{\mathrm{cl}}) = \frac{m_{2,Data}}{m_{2,MC}} = \frac{p_0 - \exp\left(-p_1 E_{\mathrm{cl}} + p_2\right)}{p_3 - \exp\left(-p_4 E_{\mathrm{cl}} + p_5\right)} \tag{4.14}$$

The obtained correction factor is afterwards applied to the energy of the simulated clusters without modifying the energy of the clusters in the real data. As the relation between the photon energy and the invariant mass is not linear, this procedure has to be repeated until it converges. This is

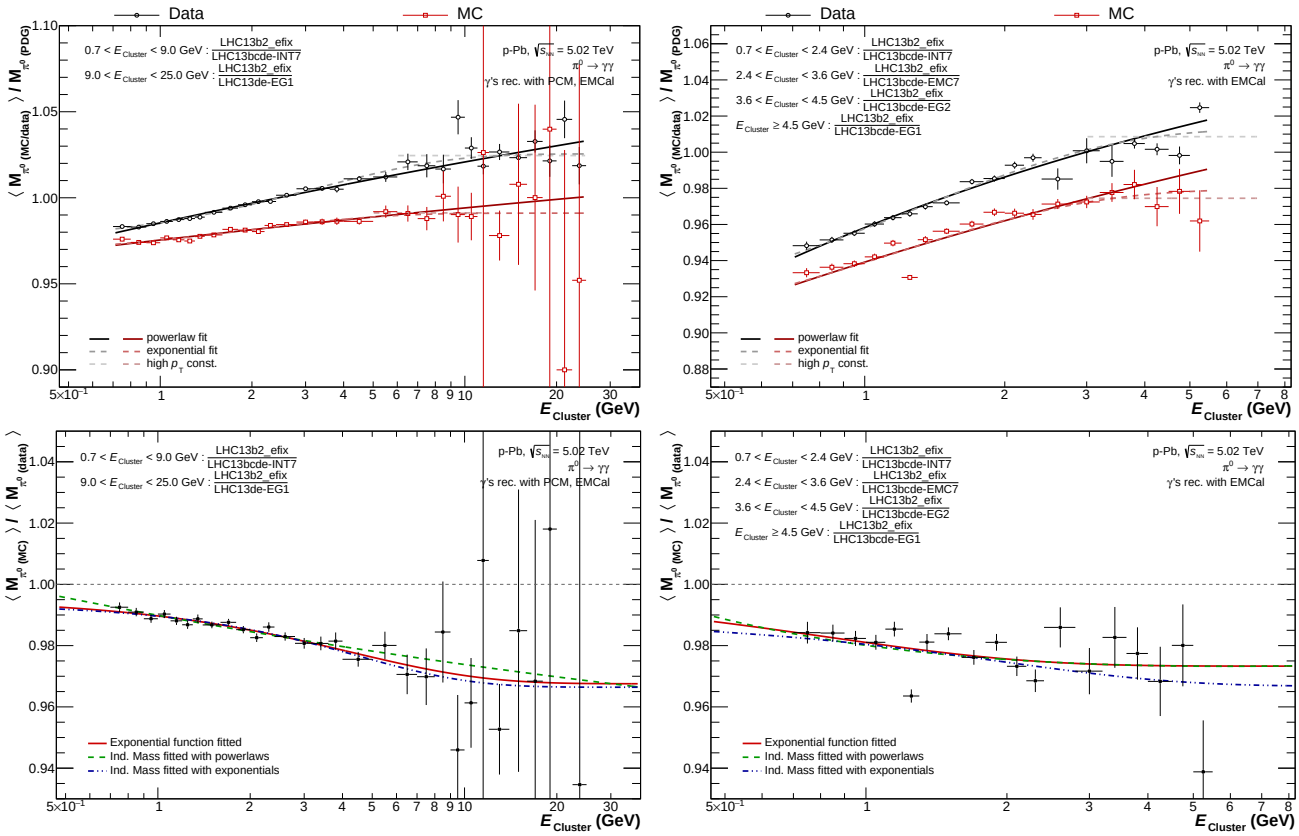

Figure 4.12.: Top: Normalized reconstructed mass positions for the PCM-EMC (left) and EMC (right) reconstruction methods versus the cluster energy (E_{cluster}) used to obtain the Monte Carlo fine tuning functions in the first iteration for the p–Pb data and the respective DPMJet simulation. The black and red points display the real and simulated data, respectively. The black/red lines show the fits according to Equation 4.10 & 4.11 to the mass positions for data and simulation, from which the CCMF and CMF are derived, respectively. Bottom: Ratio of the mass positions in simulation and data together with the exponential fit (red) to the ratio and the resulting correction functions from the ratio of the mass fits (green & blue).

normally reached after 1-2 iterations and the accuracy of the calibration thereafter is only limited by the conversion photon momentum resolution. If the statistics in the simulation in particular at high transverse momenta is insufficient the correction using CCMF is more reliable, while otherwise the direct ratio fitting is preferred due to the reduced number of parameters. As such the default correction of the Monte Carlo energies for p–Pb collisions was chosen to be the CCRF, while for pp collisions at $\sqrt{s} = 2.76$ TeV the CCMF was selected as standard correction method.
Due to the finite energy resolution, the exact functional form of the correction in addition depends on the spectral shape of the respective input spectrum of the neutral pion. Thus, it has to be determined independently for simulations using different event generators.
Alternatively, the correction functions can be obtained using symmetric decays of the neutral pion solely reconstructed with the EMCal. This approach can be referred to as Symmetric Decay Method (SDM) and exploits that for small asymmetries

$$\alpha_{\gamma_1\gamma_2} = \frac{|p_{\gamma_1} - p_{\gamma_2}|}{p_{\gamma_1} + p_{\gamma_2}} < 0.1 \tag{4.15}$$

the relation between the invariant mass and the single photon energy reduces to $M^2_{\pi^0} = 2E^2_\gamma(1 - \cos\theta_{1,2})$, leaving the cluster energy as reference parameter again. Consequently, the same procedures can be applied as for the PCM-EMC calibration. The obtained corrections functions can be referred to as Calo ratio fit (CRF) and Calo mass fit (CMF), fitting either the ratio of the

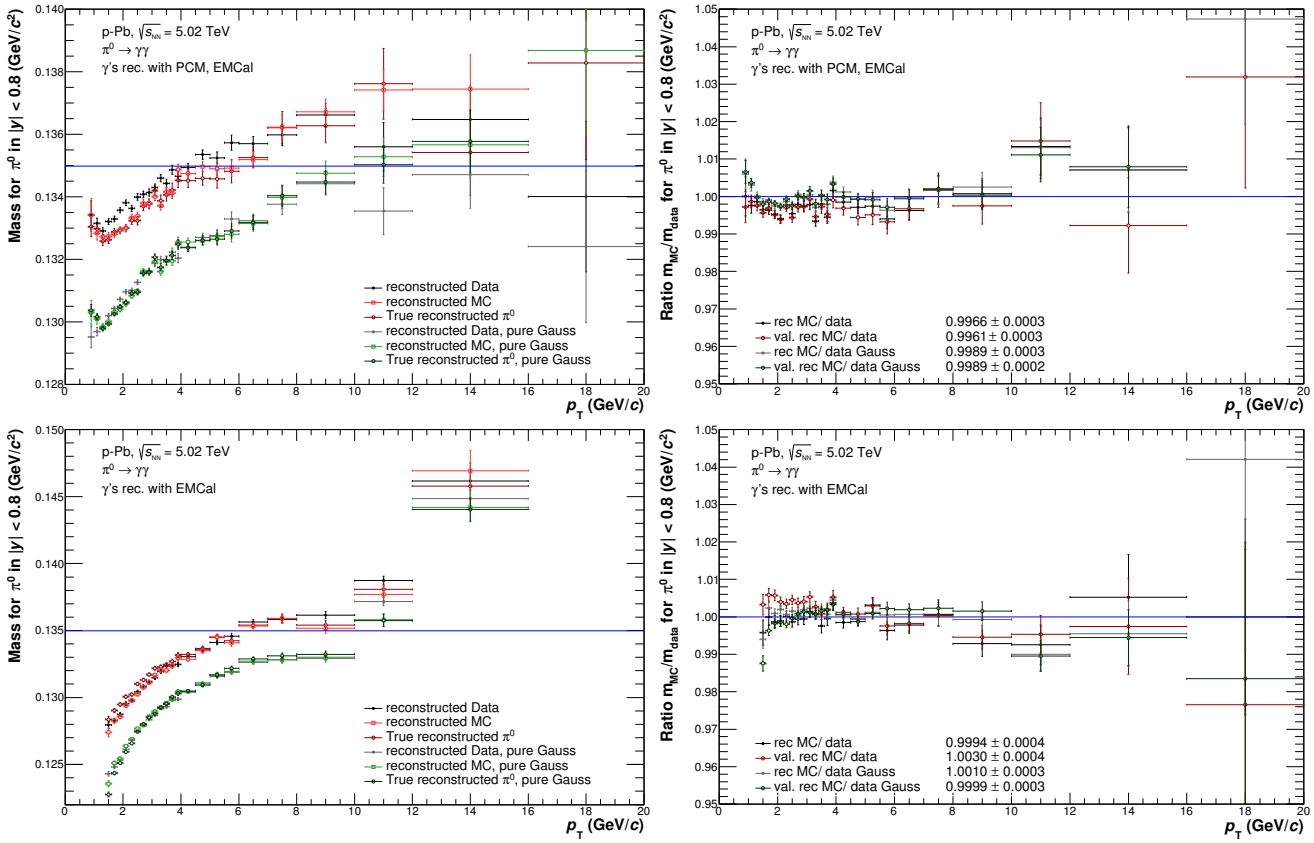

Figure 4.13.: Reconstructed π^0 masses for data, Monte Carlo and validated reconstructed neutral pions in the simulation for p–Pb collisions at $\sqrt{s_{\mathrm{NN}}} = 5.02$ TeV using the PCM-EMC (top left) or EMC (bottom left) reconstruction methods after the CCRF has been applied. The meson peaks were fitted using an Gaussian convoluted with an exponential tail on the left side (black, red) or a pure Gaussian distribution (gray, green). Additionally, the ratios of these mass positions between data and simulation are shown on the right for the different fit options and reconstruction methods.

mass positions or their energy dependence directly. Due to the onset of cluster merging at high transverse momenta ($p_{\mathrm{T},\pi^0} > 6$ GeV/c) and the reduced signal-to-noise ratio at low momenta, the SDM correction procedures are only constrained in a limited energy regime. Therefore, they only serve as alternates to understand the systematic uncertainty which needs to be associated to the Monte-Carlo fine tuning correction.
In Figure 4.12 the starting point of the four different correction methods is shown for p–Pb collisions at $\sqrt{s_{\mathrm{NN}}} = 5.02$ TeV and the corresponding Monte Carlo simulation with DPMJet as event generator. In the upper plots of this figure, the average neutral pion mass position versus cluster energy is displayed for those pions which could be reconstructed in the PCM-EMC (left) and the EMC analysis streams (right). To illustrate the absolute miscalibration of the EMCal, these mass positions are normalized to the rest mass of the neutral pion. The disadvantage of the SDM correction procedure is clearly visible. Even though all available triggers were used for this method, the correction functions could not be constrained beyond $E_{\mathrm{cl}} = 6$ GeV. The PCM-EMC corrections on the other hand could be validated up to cluster energies of 25 GeV in the data. For the PCM-EMC method, the most stringent limit on the precision is represented by the available statistics in the simulation. The ratio of the mass positions in simulation and data for the different methods is shown in the lower part of Figure 4.12 together with the respective correction functions. While the correction functions show a similar behavior in the regions where they are constrained by the data, their extrapolation to lower and higher cluster energies can lead to very different final correction factors. The latter is partially compensated for by the subsequent iterations as described in the previous paragraphs.

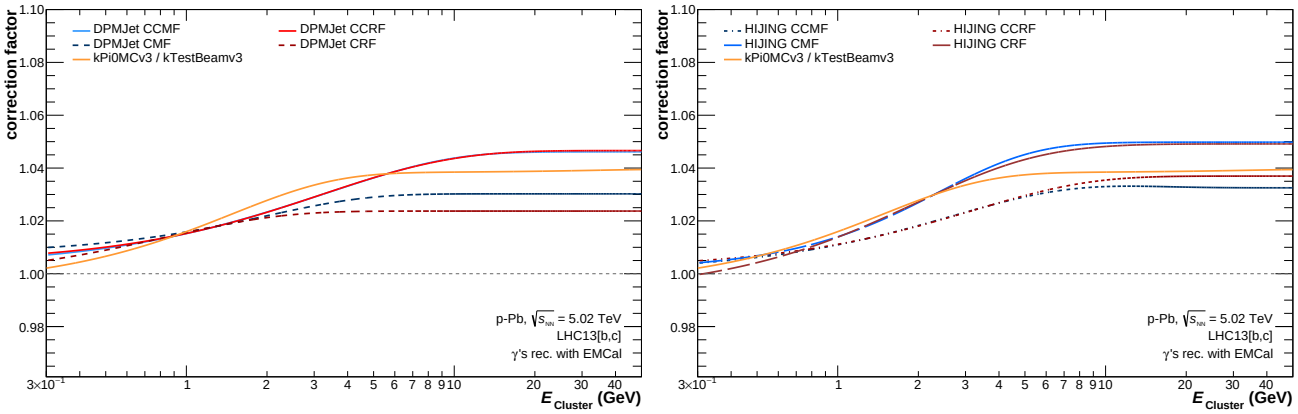

Figure 4.14.: Summary of the obtained Monte Carlo fine tuning correction functions for the simulation using DPMJet (left) and (HIJING) as event generators versus the cluster energy measured in the EMCal. The different corrections functions introduced in this thesis are compared to the one obtained from the test beam and its corresponding simulation shown in orange.

To obtain a more complete picture of the EMCal detector performance, all four final correction functions have been validated using the neutral pions and eta mesons reconstructed with either the PCM-EMC and EMC analysis methods. In Figure 4.13, part of this validation can be found for the p–Pb data set and the corresponding DPMJET simulation using the CCRF correction functions. As it can be seen in the lower plots of that figure, the agreement of the mass positions in data and simulation after the CCRF correction has been applied is better than 0.1%, if both photons have been reconstructed in the EMCal. If one of the photons has been reconstructed using the conversion method, on the other hand, the agreement is slightly worse, as it can be seen in the upper part of the same figure. This is due to a small mismatch in the conversion photon resolution between simulated and real data for that particular data set. By validating all correction functions with both analysis streams for the neutral meson reconstruction, the risk of introducing biases due to mismatches in the tracking resolution is significantly reduced, while still allowing to use the full energy range for the calibration.
The full set of correction factors for the p–Pb data set can be found in Figure 4.14 for the DPMJet (left) and HIJING (right) Monte Carlo simulation. They are compared to the correction function obtained from the test beam campaign in 2010 and its corresponding simulation shown in orange. The correction functions mainly differ in their total magnitude at high cluster energies, while their low energy values are rather well defined, but different from the test beam correction. For DPMJet as well as for pp collisions at $\sqrt{s} = 2.76$ TeV, the correction functions derived from the PCM-EMC method have proven to be more reliable. Consequently, they have been chosen as default Monte Carlo fine tuning functions, while the remaining functions were used to determine the systematic uncertainties.
Comparing these correction factors between HIJING and DPMJet shows the influence of the reduced statistics in the simulation as well as the effect of the different transverse momentum distribution of the original neutral pion spectrum.

5. Neutral Meson Analysis

This chapter is dedicated to the neutral meson analyses in pp collisions at $\sqrt{s} = 2.76$ TeV and p–Pb collisions at $\sqrt{s_{\rm NN}} = 5.02$ TeV.
The new measurement of the π^0 production cross section in pp collisions at $\sqrt{s} = 2.76$ TeV is the result of five analyses using data from various ALICE detector systems and different identification techniques. As explained in the previous chapters, decay photons are either measured directly in the EMCal, the PHOS or via the photon conversion method. The π^0 is reconstructed statistically using the invariant mass technique. At high $p_{\rm T}$, where the decay photons are too close together to be resolved individually, the π^0 can still be measured via the characteristic shape of their energy deposition in the EMCal. Within an earlier publication [173], based partially on the results from my master thesis [293], only the PCM and PHOS were employed to reconstruct photons and hence neutral pions. During the course of this thesis the analysis using the conversion technique has been refined. Additionally, three analyses involving either photons or pions reconstructed within the EMCal have been developed. These statistically independent analyses where *(i)* both photons are individually resolved in the EMCal (EMC), *(ii)* one photon is identified in the EMCal and one is reconstructed via its conversion to e^+e^- (PCM-EMC), and *(iii)* the photon pair's energy is merged in the EMCal (mEMC) were combined with the already existing two analysis using *(iv)* PHOS and *(v)* PCM. The photon reconstruction technique for the PCM and EMC has been explained with the respective selection criteria in Section 4.2 and Section 4.3. The PHOS spectra have been obtained independently and are discussed in [173]. For the EMCal related analyses a total of six different triggers has been exploited, as explained in Section 4.1. This allows an extension of the neutral pion measurement from 12 GeV/c to 40 GeV/c, representing the highest momentum for an identified particle measurement so far. The η meson cross section was previously only available from the PCM standalone measurement with significant statistical errors. Within this thesis those results were refined and the inclusion of the EMC and PCM-EMC methods allows to present the first measurement in the range from 0.6 to 20 GeV/c for the η meson production cross section for pp collisions at $\sqrt{s} = 2.76$ TeV. Furthermore, the η/π^0 ratio has been measured in the same $p_{\rm T}$ range. The discussed results have been recently published in [297].
In order to obtain the neutral meson spectra and nuclear modification factors in p–Pb collisions at $\sqrt{s_{\rm NN}} = 5.02$ TeV, six different invariant mass techniques were used, namely the PCM, EMC, PCM-EMC, PCM-PHOS, PHOS and PCM-Dalitz technique (PCM-Dal). For the latter, the second decay channel of the neutral pion is explored, the $\pi^0 \rightarrow \gamma e^+e^-$ or Dalitz decay, and the real photon is reconstructed using the conversion method. The respective analysis is explained in detail in [298]. During this thesis, mainly the PCM-EMC measurement for p–Pb collisions was carried out. However, significant contributions were made to the PCM [299] and EMC [300] measurements as well. As such, they will be discussed where appropriate. The PHOS analysis was carried out following the prescription given in [173,301] and more details can be found in [302]. For the PCM-PHOS analysis the same strategy as for the PCM-EMC method has been pursued, except that the calorimeter photons have been measured with the PHOS. This analysis also included the same calibration procedure for the PHOSas outlined in this thesis for the EMCal. It is explained in detail in [303]. The neutral pion measurement reaches from 0.3 GeV/c to 20 GeV/c, while the η meson spectrum and nuclear modification factor reach from 0.4 GeV/c to 20 GeV/c, same as the η/π^0 ratio. Due to the smaller acceptance for PHOS and smaller branching ratio for PCM-Dal, these analyses have not been pursued to extract the η meson spectrum.
The first section summarizes the analysis techniques used to obtain the neutral pion and eta

meson spectra in general, including the full correction procedure. Afterwards, the π^0 and η meson invariant cross sections for pp collisions at $\sqrt{s} = 2.76$ TeV are presented along with the procedure how to obtain them from the individual measurements. In addition, the systematic uncertainties of the individual measurements together with the cross correlations among the different measurement techniques are discussed. The obtained spectra will then be compared to the respective next-to-leading order pQCD and Pythia 8.2 calculations. In the last section, the combined π^0 and η transverse momentum spectra as well as the respective nuclear modification factors will be presented for p–Pb collisions at $\sqrt{s_{\mathrm{NN}}} = 5.02$ TeV. Similarly as for the pp results, a detailed discussion of the systematic uncertainties and the combination procedure is contained in that section. Additionally, the interpolation technique to arrive at the pp reference at $\sqrt{s} = 5$ TeV will be discussed together with its uncertainty estimate. The chapter is concluded by a discussion of the impact of p–Pb measurements for the various theoretical models as well as our general understanding of p–Pb collisions.

5.1. Neutral Meson Reconstruction

Neutral mesons decaying into two photons fulfill

$$M_{\gamma\gamma} = \sqrt{2E_{\gamma_1}E_{\gamma_2}(1-\cos\theta_{12})}, \tag{5.1}$$

where $M_{\gamma\gamma}$ is the reconstructed mass of the meson, E_{γ_1} and E_{γ_2} are the measured energies of two photons, and θ_{12} is the opening angle between the photons measured in the laboratory frame, as already described in Section 4.3.1. The photon candidates are then measured either by a calorimeter or by PCM. Neutral meson candidates are obtained by correlating photon candidates measured either by EMC, PHOS or PCM exclusively, or by a combination of them (PCM-EMC). Alternatively, virtual photons (γ^*) originating from the Dalitz decay of the neutral meson have been reconstructed based on primary electron positron pairs and then paired with a PCM photon. With increasing transverse momentum the typical opening angle between the two photons decreases due to the larger Lorentz boost. For the neutral mesons with p_{T} above 5–6 GeV/c, the decay photons become close enough so that their electromagnetic showers overlap in neighboring calorimeter cells of the EMCal. Due to the smaller cell sizes of PHOS this is only happening above 25 GeV/c for the π^0 meson reconstructed with PHOS. For transverse momenta above 15 GeV/c, the EMCal clustering algorithm can no longer efficiently distinguish the individual showers and π^0 mesons can only be measured by inspecting the shower shape of single clusters in the EMCal. This technique will be further referred to as "merged" cluster (mEMC) reconstruction and explained in Section 5.1.2.
To be able to directly compare the reconstruction performances of the various measurement techniques and triggers, the invariant differential neutral meson cross sections or yields were expressed as

$$E\frac{\mathrm{d}^3\sigma}{\mathrm{d}p^3} = \frac{N_{\mathrm{rec}}}{p_{\mathrm{T}}\,\Delta p_{\mathrm{T}}\,\kappa_{\mathrm{Trig}}\,\varepsilon}\,\frac{1}{L_{\mathrm{int}}} \tag{5.2}$$

$$E\frac{\mathrm{d}^3N}{dp^3} = \frac{1}{2\pi}\frac{1}{p_{\mathrm{T}}}\frac{\mathrm{d}^2N}{\mathrm{d}y\mathrm{d}p_{\mathrm{T}}} = \frac{N_{\mathrm{rec}}}{p_{\mathrm{T}}\Delta p_{\mathrm{T}}\varepsilon\kappa_{\mathrm{Trig}}}\frac{1}{N_{\mathrm{evt.}}} \tag{5.3}$$

with the inverse of the normalized efficiency

$$\frac{1}{\varepsilon} = \frac{1}{2\pi\,A\,\Delta y}\frac{P}{\varepsilon_{\mathrm{rec}}}\frac{1}{\mathrm{BR}} \tag{5.4}$$

and integrated luminosity (see Equation 4.5) for pp and p–Pb respectively. The measured cross sections or yields were obtained by correcting the reconstructed meson yield N_{rec} for reconstruction

	pp, $\sqrt{s}$ = 2.76 TeV	**p–Pb, $\sqrt{s_{\mathrm{NN}}}$ = 5.02 TeV**
Invariant Mass Meson Selection Criteria		
rapidity	$\lvert y\rvert < 0.8$	
minimum opening angle		
PCM	$\theta > 5$ mrad	
PCM-EMC	$\theta > 5$ mrad	
EMC	$\theta > 20.2$ mrad	$\theta > 17$ mrad, no common edge of leading cells
mEMC	-	
energy asymmetry	$0 \leq \alpha_{\gamma\gamma} \leq 1$	
Single Cluster Meson Selection Criteria		
rapidity	$\lvert y\rvert < 0.8$	

Table 5.1.: Neutral meson selection criteria for the PCM, PCM-EMC, EMC and mEMC meson reconstruction techniques.

efficiency $\varepsilon_{\mathrm{rec}}$, purity P and acceptance A, efficiency bias κ_{Trig}, integrated luminosity L_{int}, as well as for the p_{T} and y interval ranges, Δp_{T} and Δy, respectively, and the $\gamma\gamma$ or γe^+e^- decay branching ratio BR [13]. The efficiency bias κ_{Trig} is introduced by the calorimeter triggers and thus only had to be taken into account for the pp collisions. Furthermore, for invariant mass methods, the effect of reconstructed photon impurities on the meson purity is significantly reduced due to the subtraction of the combinatorial background, and hence the resulting meson impurities were neglected. For the mEMC method, the π^0 purity correction was obtained from MC simulations tuned to data. In the case of neutral pions, the contribution from secondary $\pi^0 s$ was subtracted from N_{rec} before applying the corrections. The contribution from weak decays was estimated for the different methods by simulating the decays of the $\mathrm{K}^0_{\mathrm{S}}$ $\mathrm{K}^0_{\mathrm{L}}$ and Λ using their measured spectra [95, 97, 99] in the respective collision system, taking into account the reconstruction efficiencies, as well as resolution and acceptance effects for the respective daughter particles for the different detection techniques. The contribution from neutral pions produced by hadronic interactions in the detector material was estimated based on the full detector simulations using GEANT3. Finally, the results were not reported at the center of the p_{T} intervals used for the measurements, but following the prescription in [304] at slightly lower p_{T} values, in order to take into account the effect of the finite bin width Δp_{T}. The correction was found to be less than 1% in every p_{T} interval for the π^0, and between 1–4% for the η meson.

5.1.1. Invariant Mass Analyses

Applying Equation 5.1, the invariant mass distribution is obtained by correlating all pairs of real or virtual photon candidates per event. The neutral meson yields are extracted statistically as an excess yield on top of a combinatorial background at their respective mass positions. Example invariant mass distributions for the analyses pursued within the course of this thesis can be found in Figure 5.1 and 5.2 for the π^0 and η meson respectively for pp collisions at $\sqrt{s} = 2.76$ TeV. Similar distributions for p–Pb can be found in Figure B.13 of Section B.2 for selected transverse momentum bins.
The neutral pion peak is clearly visible around 0.135 GeV/c^2 on top of the combinatorial background. Depending on the reconstruction technique and p_{T} interval, the significance ranges from 2 to 50 (PCM), 8 to 60 (PCM-EMC) and 9 to 75 (EMC). While for the η meson the significance rarely exceeds 10, due to its larger combinatorial background and width. The combinatorial back-

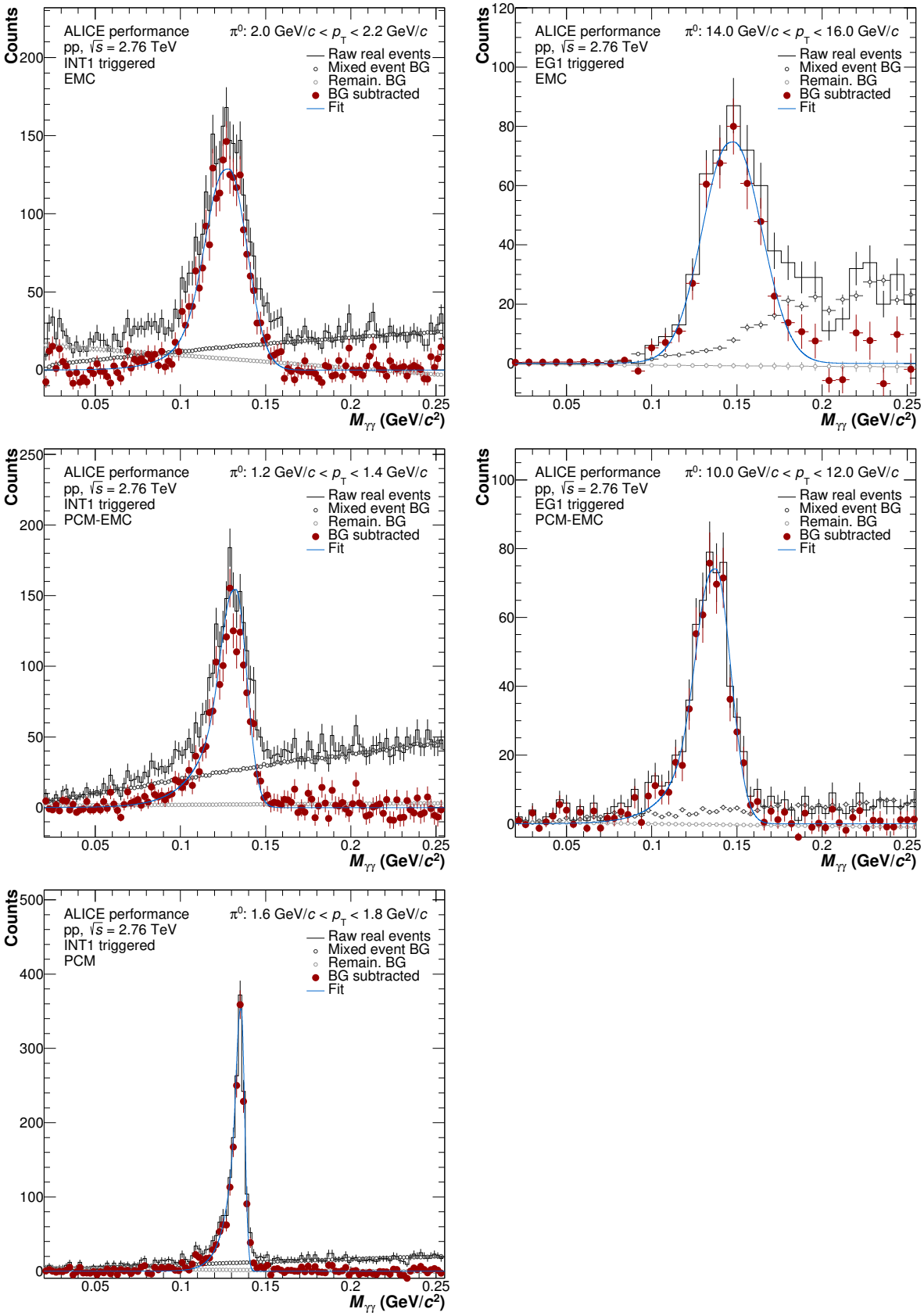

Figure 5.1.: Invariant mass distributions in the π^0 peak region for INT1 (left) and EG1 (right) triggers for the EMC (top), PCM-EMC (middle) and PCM (bottom) methods.

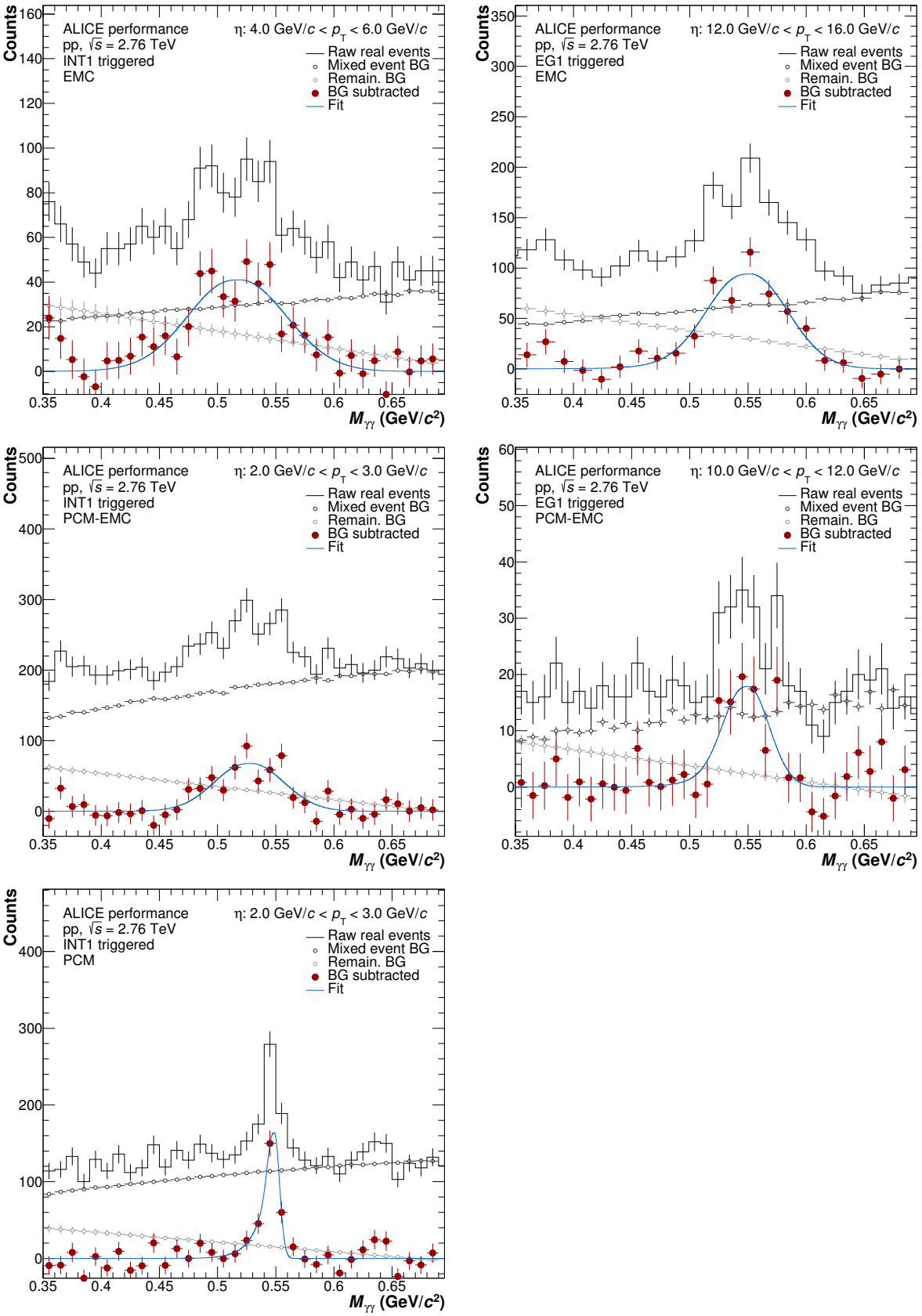

Figure 5.2.: Invariant mass distributions in the η peak region for INT1 (left) and EG1 (right) triggers for the EMC (top), PCM-EMC (middle) and PCM (bottom) methods.

ground was calculated using the mixed event technique [305] using event pools binned by primary vertex position and photon multiplicity. In all analyses a pool depth of 80 photon candidates was used with four bins in photon or charged multiplicity and seven bins in the Z-vertex position of the primary vertex. Each of them was optimized to contain a reasonable amount of statistics, while still reflecting the change in the background shape induced by the respective variation in Z or multiplicity. The fully normalized mixed event is shown as open black points in Figure 5.1 and 5.2.

This technique assumes that all correlations of photon pairs are destroyed by combining photons from different events. The mixed event background has been normalized on the right side of the $\pi^0(\eta)$ peak avoiding the peak region itself. For the same and mixed event di-photon distributions, only pairs with a minimum opening angle (θ_{min}) have been accepted. The choice of the θ_{min} is driven by the spatial resolution of the different methods. For the combination of two EMC photons, for instance, the naive expectation is that they have to be separated by more than a cell width, as the leading cells cannot be in adjoining cells. The closest distance should be very close to a cell diagonal on the EMCal surface (0.02 rad). When translating this distance to θ_{min} between two photons it well, however, be possible to have pairs with smaller opening angles. This is caused by two contributing effects: a) such a large detector can only be built approximately projective in η and φ to the nominal collision vertex and b) the actual collision vertex can move along the beam axis by up to ± 10 cm. These effects can both reduce or enlarge the actual θ_{min} imposed by the clusterization.

As this was only later understood during the analyses of the higher statistics data sets at $\sqrt{s} = 8$ TeV collisions the EMC measurement at $\sqrt{s} = 2.76$ TeV still uses 20 mrad as minimum opening angle, while for the p–Pb EMC analysis it is 17 mrad and it is not allowed that the leading cells share an edge. The exact values of the cuts are given in Table 5.1 for the different methods together with their restrictions in rapidity (y) cuts.

The decay of the π^0 or η meson, however, is not the only source of correlation of photons within an event. Most of the particles will originate from the same initial collision and consequent parton shower. Thus, the mixed event background is only expected to describe the same-event distribution up to a certain degree and an additional residual background needs to be subtracted. The latter will mainly originate from the correlation of photons within the same jet. It has been estimated using a simultaneous fit of the signal and remaining background distribution, assuming that the residual background can be described solely by a linear function. The full functional form of the signal and background after the mixed event background subtraction is given by [306]:

$$y = A \cdot \left(G(M_{\gamma\gamma}) + \exp\left(\frac{M_{\gamma\gamma} - M_{\pi^0(\eta)}}{\lambda} \right) (1 - G(M_{\gamma\gamma}))\theta(M_{\gamma\gamma} - M_{\pi^0(\eta)}) \right) + B + C \cdot M_{\gamma\gamma} \quad (5.5)$$

$$, \text{ with } G = \exp\left(-0.5 \left(\frac{M_{\gamma\gamma} - M_{\pi^0(\eta)}}{\sigma_{M_{\gamma\gamma}}} \right)^2 \right) \quad (5.6)$$

Here G is a Gaussian distribution with the width σ, the amplitude A and the mean position $M_{\pi^0(\eta)}$. The last parameter can be identified with the reconstructed mass position of the corresponding meson. The parameter λ represents the inverse slope of an exponential function, which is disabled for $M_{\gamma\gamma} > M_{\pi^0(\eta)}$ by the Heavyside function $\theta(M_{\gamma\gamma} - M_{\pi^0(\eta)})$. The remaining background is parametrized by the linear function given by B and C as constant and linear part depending on $M_{\gamma\gamma}$, respectively. It is shown in Figure 5.1 and 5.2 with open gray points.

Although the signal fit was merely used to determine the mass position and width of the peak it was necessary to include the left side exponential tail. This tail is caused by different effects for the two photon reconstruction techniques. For the PCM photons it originates from an energy loss due to Bremsstrahlung on the level of the electrons, while for the EMC clusters its is mainly caused by the energy loss of at least one electron due to a late conversion of the original photon in front of the detector. The competing influences from the respective photons on the neutral meson

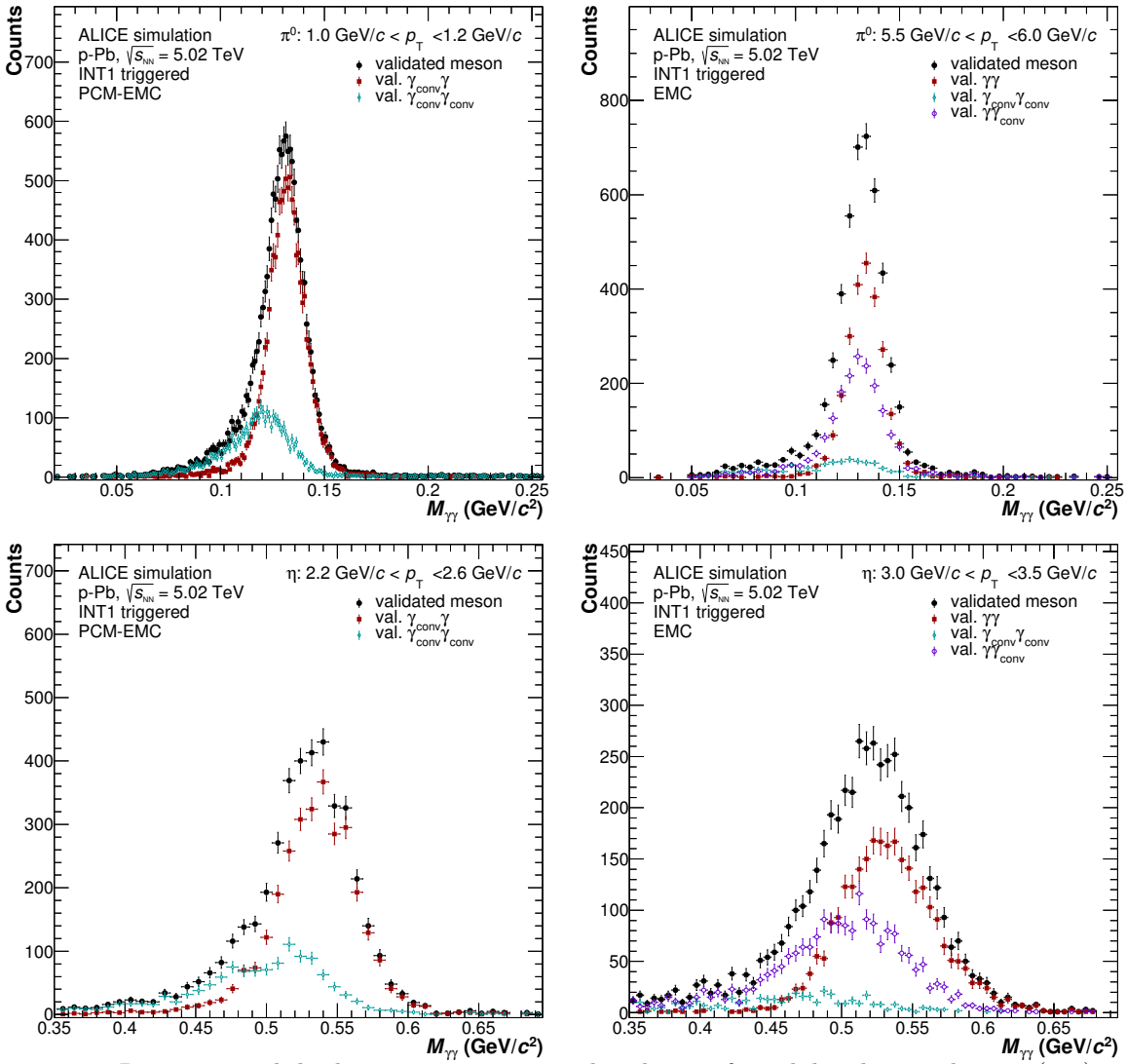

Figure 5.3.: Reconstructed di-photon invariant mass distribution for validated neutral pions (top) and η mesons (bottom) for the PCM-EMC(left) and EMC(right) reconstruction technique in a selected transverse momentum slice for the DPMJet Monte Carlo simulation (black).

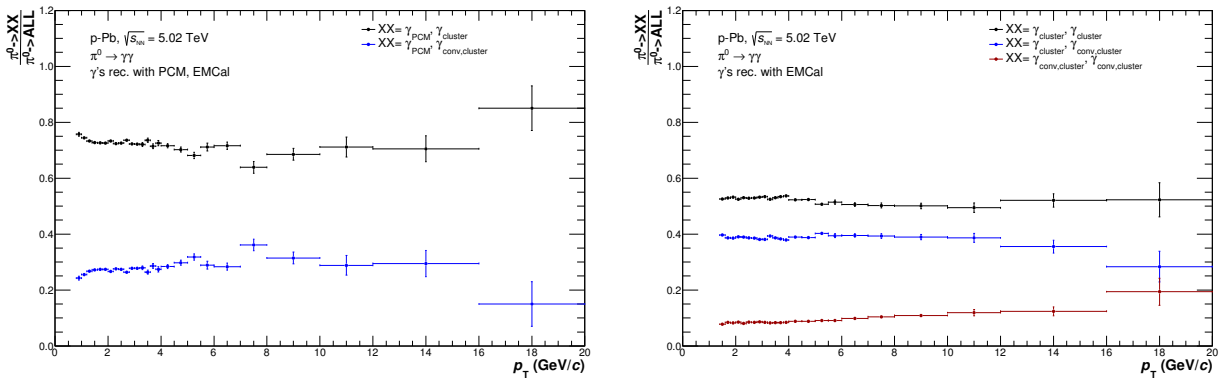

Figure 5.4.: Fraction of yields from different sources contributing to the reconstructed neutral pion yields for PCM-EMC(left) and EMC(right) according to the Monte Carlo simulation. The black dots represent the fraction of the total yield reconstructed with a real photon reconstructed in the EMCal cluster, while the blue show the fraction, where only an electron from a converted photon could be reconstructed in the calorimeter. For the EMC method an additional contribution from double conversions for the EMCal clusters is shown.

peaks are visualized in Figure 5.3 for the PCM-EMC(right) and EMC(left) for the π^0(top) and η(bottom) for p–Pb simulations. While the energy loss due to Bremsstrahlung can be seen for the PCM photon candidates in the red points in the left column, the effect from conversions for EMCal clusters is shown in cyan and violet. If the photon converts in front of the EMCal the cluster does not contain the full energy of the original photon. Furthermore, it is deflected from its original direction, leading to a reduced resolution as well as average mass position for both mesons. This effect increases, if both clusters came from conversions. The three (two) different peaks for the EMC (PCM-EMC) cannot be separated due to the small shift and the initial resolution of EMCal photons. Thus, their superposition appears as an exponential tail at low invariant masses.
The fraction of π^0 candidates reconstructed with different photon reconstruction qualities for the EMC photons is shown in Figure 5.4. It can be seen that, according to the simulation, $\sim 30\%$ of the π^0 candidates reconstructed with PCM-EMC also the second photon converted. Most of these conversions, however, have to occur close to the calorimeter, as otherwise the electron would be deflected too much and the pions would no longer be reconstructed with an invariant mass close to the nominal mass. A similar observation can be made for the π^0 candidates reconstructed with the EMCal alone. Although in this case an additional contribution from both photons converting has to be considered. Furthermore, it is slightly more likely to have earlier conversions entering the sample, as the integration window for the signal is wider than for the PCM-EMC reconstruction.
The results of the signal fits for the average mass position and width for both mesons are shown in Figure 5.5 and 5.6 for pp and p–Pb collisions, respectively. For completeness also the PHOS and PCM-Dal points have been included, they have been taken from [173, 298, 302]. For all reconstruction and collisions systems, the data for both π^0 and η are reproduced by the corresponding anchored Monte Carlo simulations with a precision which is on average better than 0.3% of the meson masses. The neutral pion and η mass positions for the PCM reconstruction approach the respective nominal rest masses for low transverse momenta from higher invariant masses and afterwards remains constant same as for the PCM-Dal reconstruction. In order to achieve this no additional tuning of the mass position was necessary for either data or simulation. For PHOS, however, the neutral pion mass for each data set was calibrated to reproduce the nominal pion rest mass and afterwards the simulation has been tuned to match the newly obtained mass position in the data. If the photon has been reconstructed using the EMCal, no additional correction beyond the channel-by-channel equilibration has been applied to the cluster energy in the data. However, the simulation has been calibrated fully to reproduce the data, as described in Section 4.3.1. The pronounced rise of the mass positions at low momenta can thus be explained by non-linearity effects, while the trend at high momenta can be attributed to shower merging, shower overlaps and decay asymmetries. All of these are enhanced by the employed triggers, as it can be seen when comparing the results for pp and p–Pb.
The width of the neutral meson peaks in pp collisions at $\sqrt{s} = 2.76$ TeV is similarly well described and reflects the expected ordering for the various methods. In particular the peak width of the PCM-EMC reconstruction lies between the respective standalone measurements of PCM and EMC. Furthermore, it is comparable to the PHOS measurement above 7 GeV/c. This illustrates that with reasonable statistics in the respective data set the PCM-EMC method can significantly improve the neutral meson measurements over a large transverse momentum range. A similar ordering of the resolutions can be found for the η meson as well as for the respective measurements in p–Pb collisions. In the latter, however, the tracking resolution for electrons does not seem to be fully reproduced by the simulation leading to a slightly smaller width of the π^0 peaks in the simulations at high transverse momenta for all PCM related measurements. This small mismatch also leads to an offset in the mass positions for PCM of about $0.1 - 0.2\%$ limiting also the calorimeter calibration in its precision for the ConvCalo methods. The offset will be taken into account in the systematic uncertainties of the neutral meson yields. The exact cause of the mismatch between simulation and data could not be identified, yet. Possible reasons are: localized space charges distorting the tracks, a reduced track matching efficiency between the ITS and TPC due to a small

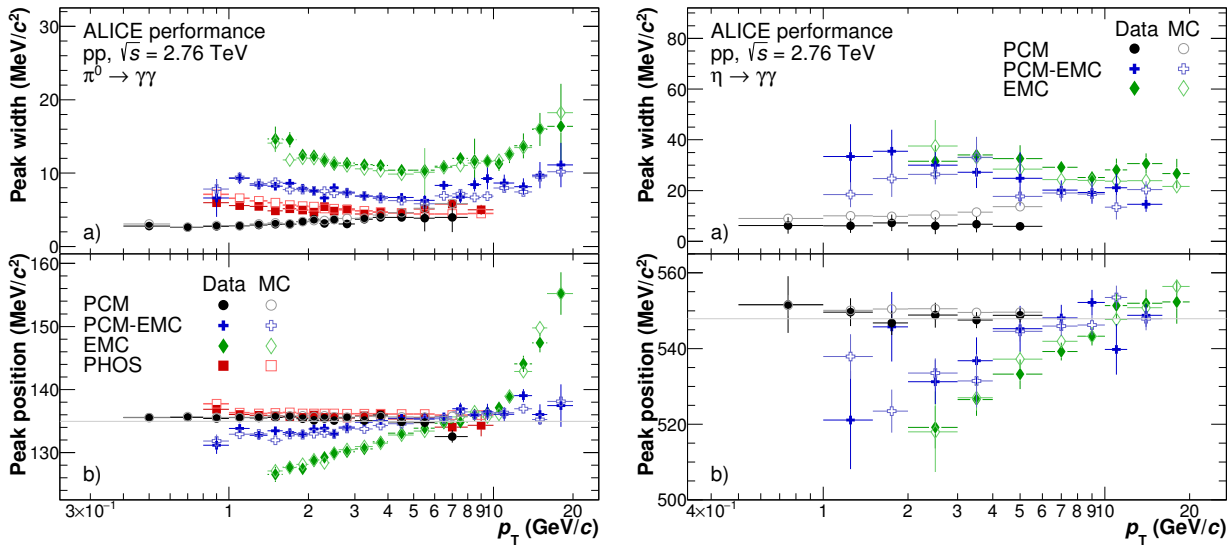

Figure 5.5.: Neutral pion (left) and η meson (right) mass position (bottom) and width (top) for the PCM, PCM-EMC and EMC methods for pp collisions at $\sqrt{s} = 2.76$ TeV [297]. The performance of PHOS for π^0 is taken from [173]. The data are displayed using closed symbols, simulations using open symbols.

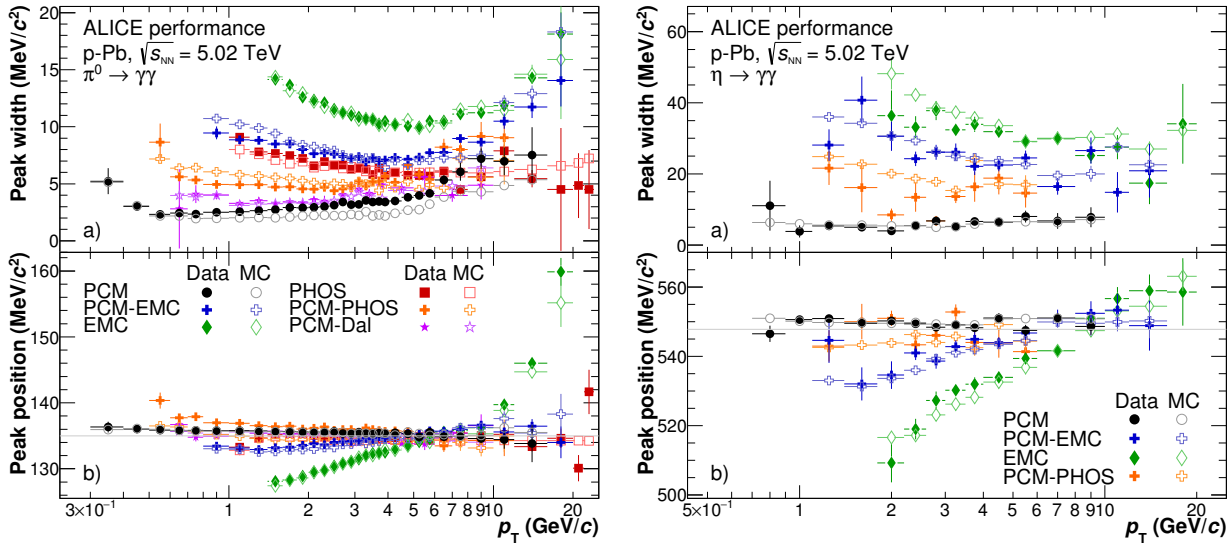

Figure 5.6.: Neutral pion (left) and η meson (right) mass position (bottom) and width (top) for the PCM, PCM-EMC, PCM-Dal, EMC and PHOS methods in p–Pb collision at $\sqrt{s_{\mathrm{NN}}} = 5.02$ TeV. The data are displayed using closed symbols, simulations using open symbols.

misalignment of the detector or minor changes in the TPC gas mixture. None of the above could be identified as single origin and even a convolution of several causes is plausible.
The neutral meson raw yields have been extracted by integrating the fully background subtracted invariant mass distributions around the measured meson peak mass using fixed mass windows. The integration windows for the different reconstruction techniques explored in this thesis have been adjusted based on the average width of the meson peaks and their signal shape. Thus, all of them have been chosen to be asymmetric for both mesons to account for the low mass tail, except the for the η meson reconstructed with EMC. In order to minimize the influence of small remaining mismatches between simulated and real data in the meson peak width, the integration windows have additionally been chosen wide enough to incorporate them. The respective windows applied for the π^0 and η meson using the PCM, PCM-EMC and EMC meson reconstruction techniques can be found in Table 5.2.
Part of the obtained yield for the π^0 meson has been generated by long lived strange particles

reco. technique	π^0	η
PCM	$[M_{\pi^0} - 0.035, M_{\pi^0} + 0.010]$ (GeV/c)	$[M_\eta - 0.047, M_\eta + 0.023]$ (GeV/c)
PCM-EMC	$[M_{\pi^0} - 0.032, M_{\pi^0} + 0.022]$ (GeV/c)	$[M_\eta - 0.060, M_\eta + 0.055]$ (GeV/c)
EMC	$[M_{\pi^0} - 0.050, M_{\pi^0} + 0.040]$ (GeV/c)	$[M_\eta - 0.080, M_\eta + 0.080]$ (GeV/c)

Table 5.2.: Integration windows for the π^0 and η meson invariant mass distributions, where M_{π^0} and M_η are the reconstructed mass positions from the fit.

particle	decay channel	branching ratio	decay length ($c\tau$)
K^0_S	$\pi^0\pi^0$	30.69%	2.6844 cm
K^0_L	$\pi^0\pi^0\pi^0$	19.52%	15.34 m
	$\pi^+\pi^-\pi^0$	12.54%	
Λ	$n\pi^0$	35.80%	7.89 cm

Table 5.3.: Particles considered in the toy model and their respective decay channels, branching ratios and decay lengths.

decaying into neutral pions or hadronic interactions of the primary particles with the detector material. These neutral pions should not be taken into account in the total invariant cross section or yield. As described earlier the correction for secondary neutral pions from hadronic interactions fully relies on the correct implementation of the ALICE detector material in Aliroot and the subsequent particle propagation with GEANT3. This correction strongly depends on p_{T} for the EMC-related methods. It ranges from 1.2% at the lowest p_{T} to 0.1% (0.4%) above 3 GeV/c for the PCM-EMC (EMC) method and is approximately the same in both collision systems. A similar p_{T} dependence is seen for the PCM correction as well, ranging from 1.2% below 0.6 GeV/c to 0.1% above 2 GeV/c.

As light strange particle production is currently not well described by the various Monte Carlo generators, the same approach could not be followed for their contribution to the neutral pion spectrum. Instead the measured $\mathrm{K}^0_{\mathrm{S}}$ and Λ spectra [99, 307] have been parametrized and their decays modeled by a decay algorithm. In general, also the $\mathrm{K}^0_{\mathrm{L}}$ contribution to the neutral pion yield has to be considered. It is, however, heavily suppressed due to its longer decay length, which can be seen in Table 5.3. Nonetheless, it has been simulated assuming the same spectral shape as the $\mathrm{K}^0_{\mathrm{S}}$. The parameterizations of the $\mathrm{K}^0_{\mathrm{S}}$ for pp and p–Pb collisions have been improved at higher transverse momenta by taking into account the charged kaon spectra [95, 97], which according to Pythia simulations should agree with the neutral kaons to the 1-2% level. Beyond the measured transverse momentum range, the spectra in both collision systems have been extrapolated using a Tsallis distribution [308]. The decayer TGenPhaseSpace [254] was used for the corrections of the pp data set implementing the decay channels and branching ratios as described in Table 5.3. For the p–Pb data set, on the other hand, the approach was refined and the Pythia 6 decay algorithm has been used as decayer. In this case, all possible decays leading to a π^0 have been included with the branching ratios listed by the Particle Data Group [13].

Due to their non-negligible decay length, the efficiency and the geometrical acceptance for the secondary π^0's can vary depending on their mother particle and might also be significantly different from that of the primary neutral pions. As such, these correction factors have to be applied to the generated secondary pion spectra and the resulting contribution has to be subtracted from the neutral pion raw yield prior to any further corrections. As an example, the different efficiencies for secondary pions from the considered sources are shown in Figure 5.7 for the PCM-EMC and EMC reconstruction method. These efficiencies do not only contain the pure reconstruction efficiency, but also the respective neutral pion momentum resolution. The latter deteriorates for the EMC reconstruction, if the π^0 is produced close to the calorimeter leading to a seemingly higher efficiency. The resulting relative contribution of the neutral pions from $\mathrm{K}^0_{\mathrm{S}}$ decays to the total reconstructed

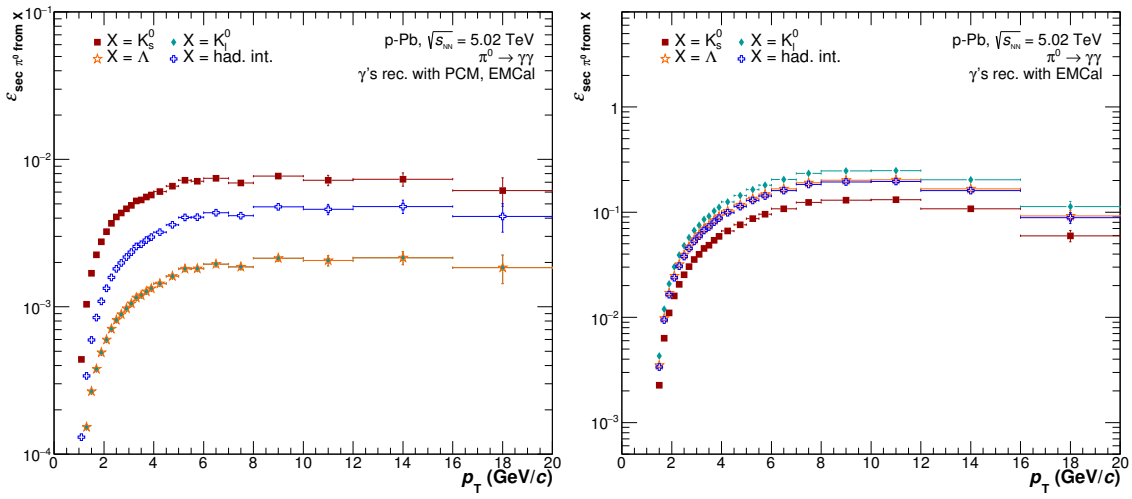

Figure 5.7.: Secondary neutral pion efficiency for π^0 originating from different sources in p–Pb collisions for the PCM-EMC(left) and EMC(right) pion reconstruction techniques.

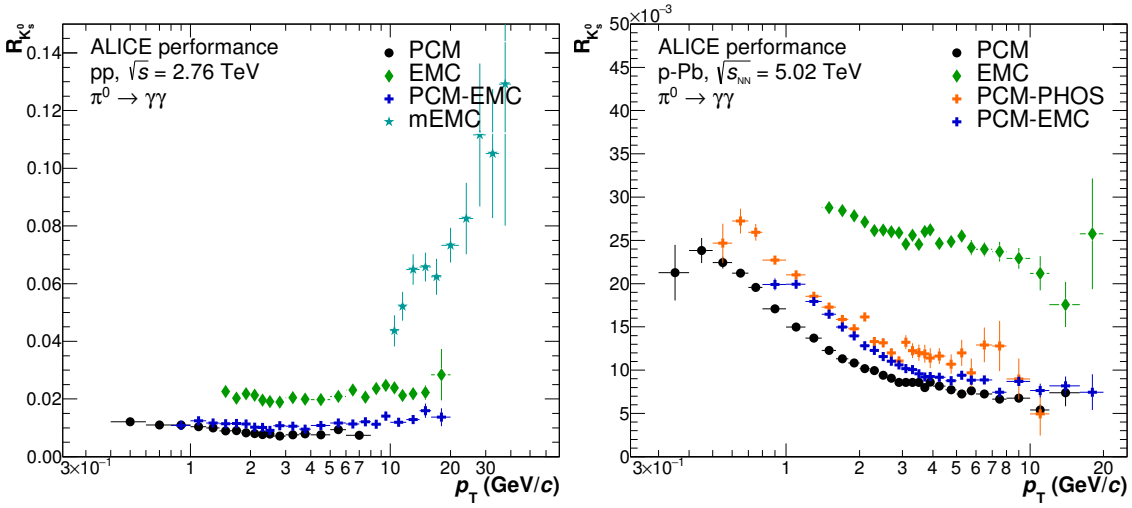

Figure 5.8.: Effective secondary pion correction for neutral pions from K^0_S decays for various methods in pp collisions at $\sqrt{s} = 2.76$ TeV (right) and p–Pb collision at $\sqrt{s_{NN}} = 5.02$ TeV.

pion yield is shown in Figure 5.8 for pp and p–Pb collisions. It shows a strong p_T dependence at low transverse momenta, if at least one of the legs has been reconstructed with the PCM method. This is a consequence of the tight selection criteria forcing the photons to point to the primary vertex. For the PCM neutral pion reconstruction, the contribution drops quickly from about 1.5-2.0% at 0.4 GeV/c to less than 1% at 1.5 GeV/c. The same behavior is observed for the PCM-EMC, however slightly shifted in transverse momentum. At higher momenta, this correction approaches 1%. A weaker transverse momentum dependence is observed for the EMC reconstruction method, reaching a high momentum limit of 2-2.5% of the reconstructed raw yield. Other strange particle decays contribute less than 0.1% to the reconstructed neutral pion yields for all invariant mass methods exhibiting a similar or stronger p_T dependence than the K^0_S contribution.
For the reconstruction of neutral mesons with the PCM method, an additional source of contamination has to be considered: the contribution from mesons from neighboring bunch crossings. This effect stems from the long read-out time of the TPC (92 μs) and the fact that a large fraction of the reconstructed photons has been reconstructed purely based on the TPC information due to the material distribution within the ALICE detector. When reconstructing photons with the conversion method, three categories have to be distinguished when considering out-of-bunch pile-up.

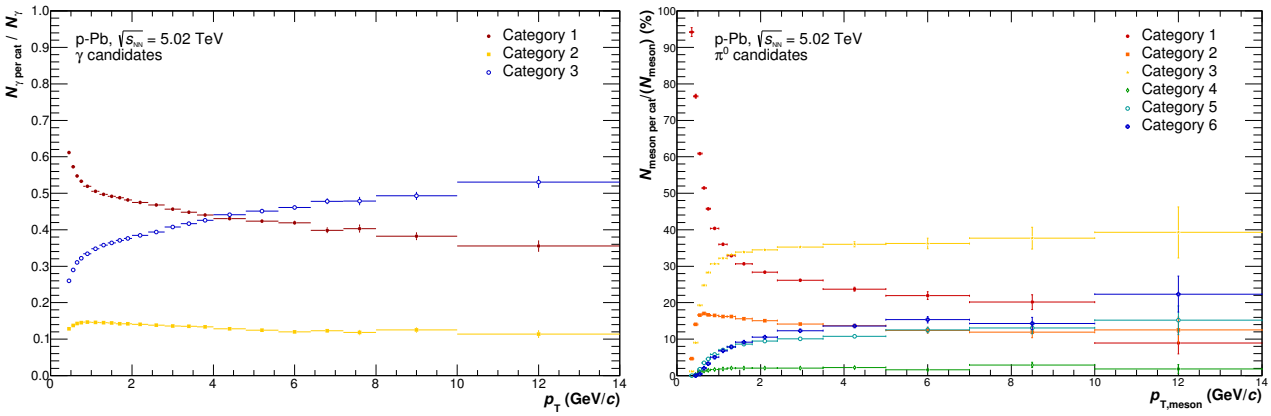

Figure 5.9.: Fractions of photons (left) and neutral pions (right) classified according to their reconstruction qualities regarding the usage of ITS and TPC information with respect to the total reconstructed yield regardless of the category.

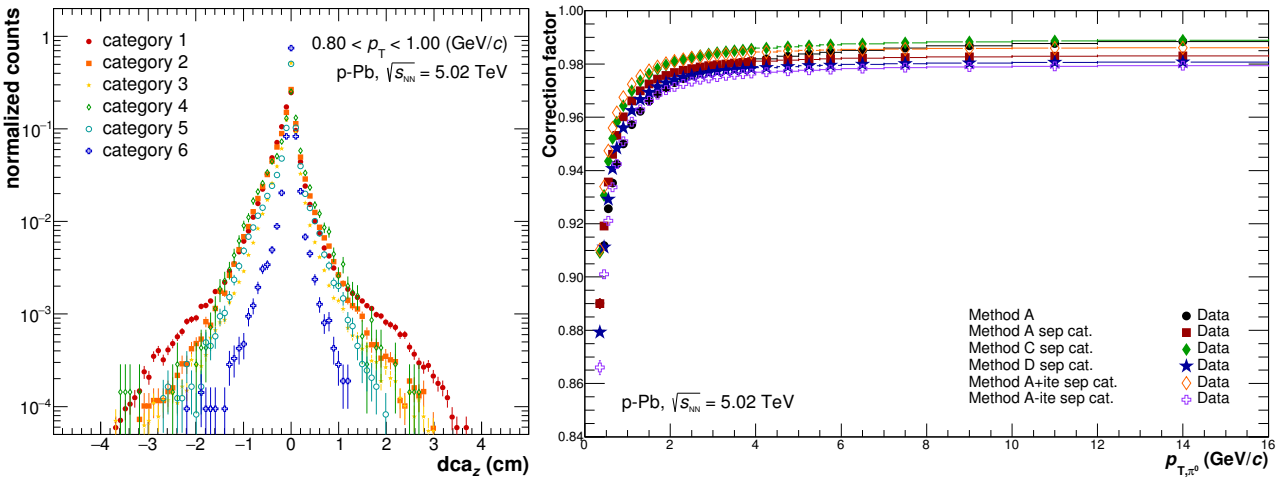

Figure 5.10.: Left: dca_Z distribution of photons from neutral pion candidate for different meson reconstruction categories, with category 1 relying only on TPC information and category 6 containing only photons which could be reconstructed with at least 2 hits on each electron leg. Right: Out-of-bunch pile-up correction factor for neutral pions reconstructed with PCM in p–Pb collisions at $\sqrt{s_{\mathrm{NN}}} = 5.02$ TeV.

(1) Both electrons have been reconstructed purely based on TPC information.

(2) One of the electrons has at least two ITS hits associated to its track.

(3) Both electrons have at least two ITS hits associated to their tracks.

Their contribution to the total photon yields depends strongly on the photon transverse momentum (see left plot of Figure 5.9), as electrons which are produced at low R need to have at least an energy $\sim$ 100 MeV to be reconstructed within the TPC, while those which are created later can have lower momenta and might still be reconstructed. As the ITS provides a more precise time estimate for its clusters, the categories 2 and 3 should not be affected by out-of-bunch pile-up, except if the ITS hits had been associated to the track accidentally. Out of these three photon categories a total of six different combinations for two photons can be built to obtain a neutral meson candidate. Where category 1 contains only combinations where all four electrons had been reconstructed solely based on TPC information and for category 6 all electrons had at least 2 ITS hits associated to each track. The p_{T} dependent fraction of these categories, contributing to the neutral pion yield, can be found in Figure 5.9(right) for p–Pb collisions at $\sqrt{s_{\mathrm{NN}}} = 5.02$ TeV. It shows that category 1, which will be affected most by out-of-bunch pile-up, dominates the π^0 spectrum at low transverse momenta, while its contribution drops to less than 30% beyond 1.5 GeV/c. As such, the correction factor for the out-of-bunch pile-up will be strongest at low momenta and

should then approach a constant smaller value.
As the readout of the TPC is 92 μs, even collisions which are further apart than 1 μs from the triggered collision could contribute to the total meson yield. However, the further the collisions are apart in time, the fewer photons will be reconstructed from the later bunch crossings due to the tight photon quality selection criteria. The removal of this contribution can only be done on a statistical basis as no event criterion has been found which could be used to identify those events without loosing the majority of the collected statistics. To identify the photons and mesons originating from the next bunch crossing we instead rely on the dca_Z distribution of the photons to the measured primary vertex position as a function of transverse momentum. The dca_Z distribution for an average neutral pion transverse momentum of 1.1 GeV/c can be seen in Figure 5.10(left), split into the different meson categories. The dca distribution broadens when decreasing the number of tracks which have ITS clusters associated to it. This broadening can be partially explained by the worsened pointing resolution for tracks which have been created a higher R and can be partially observed in the simulation as well. On the other hand, the Gaussian like structure for category 1 for $dca_Z > 2$ cm, on top of which the expected peak of the dca_Z can be found, is not seen in the simulation and thus has been identified with the contribution associated to out-of-bunch pile-up. Similar Gaussian structures are also observed for the meson categories 2 and 3, but they are suppressed by at least one order of magnitude. The yields of the Gaussian shaped pile-up distributions have been estimated using different methods for each transverse momentum bin and category. Afterwards, the obtained yield for different categories has been summed and then subtracted from the measured meson yields with the PCM method.
The resulting correction factor for p–Pb collisions and its variations, which enter in the systematic error evaluation, are shown in Figure 5.10(right). It ranges from 7.5% at low transverse momenta to 1.5% above 3 GeV/c, while it reaches 20% at low momenta in pp collisions at $\sqrt{s} = 2.76$ TeV due to the higher bunch intensities and smaller bunch spacing. Above 3 GeV/c, the out-of-bunch pile-up contributes about 6% to the neutral pion yield reconstructed with PCM in pp collision at that energy. A similar magnitude and transverse momentum dependence was also observed for the corrections to the η meson raw yields in the respective systems.
After the correction for secondary neutral pions, the remaining primary raw yield of the π^0 and η meson needs to be corrected for detector acceptance and reconstruction efficiency. Both quantities are calculated using all available Monte Carlo simulations for the respective collision systems, regardless of the generator, as mentioned in Section 4.1.
The acceptance for the EMC reconstruction technique was calculated as the fraction of π^0 (η), whose decay photons point to the EMCal surface ($|\eta| < 0.67,\ 1.40\,\text{rad} < \varphi < 3.15\,\text{rad}$), compared to the π^0 (η) generated with $|y| < 0.8$ in the full azimuth. In the case of PCM-EMC, at least one photon was required to point to the EMCal surface, while the other was required to be within the acceptance of the TPC ($|\eta| < 0.9,\ 0\,\text{rad} < \varphi < 2\pi\,\text{rad}$). For the PCM reconstruction, both photons had to be within the TPC acceptance as well as their electron daughters.
In order to obtain the reconstruction efficiencies, the full event MC simulations have been reconstructed and analyzed in the same way as the data. It has been calculated as the fraction of reconstructed mesons compared to those whose decay photons passed the acceptance criteria. Moreover, a second efficiency has been calculated, where each photon is verified using the Monte Carlo information and it has been checked that they originate from the same particle (π^0 or η meson). This is called validated efficiency. For the latter, the contribution from Dalitz decays has been rejected and in general only primary particles are taken into account for the efficiency. The two efficiencies have been compared and it has been found that they agree within 1-5%. The observed offset can be explained by a bias in the background subtraction and thus varies between the different reconstruction techniques. It is strongest for the EMC reconstruction due to the significant low invariant mass tail, which presents itself as a pedestal at low invariant masses. The advantage of the validated efficiency is the possibility to use p_{T} dependent weights for the purely simulated and reconstructed mesons, thus allowing to modify the shape of the input spectra to

recover the proper momentum resolution corrections, which are included in the reconstruction efficiency. This is of particular importance when using simulations with added signals to decrease the statistical error of the efficiency at high momenta, like it is done for the PCM analysis. As these pions and etas have been added to the minimum bias events following a flat p_{T} distribution to enhance the signal statistics at higher transverse momenta. The correction factors for the PCM photons depend mildly on multiplicity as they are coupled to the primary vertex resolution, meaning that the correction factor for very low multiplicities (< 2 primary tracks in the central acceptance) and higher multiplicities is significantly different. The multiplicity dependence however implies as well that even the minimum bias Monte Carlo samples need to be weighted in order to match the multiplicity measured in the data. The correction originating from this is of the order of $1 - 2\%$.
The normalized efficiency ε (see Equation 5.4) as a function of meson p_{T} is shown in Figure 5.11 and 5.12 for the various methods for pp and p–Pb collisions, respectively. Its general functional form for the invariant mass analysis techniques is governed by the phase space in which the mesons can be reconstructed due to the minimum p_{T} or energy cuts imposed on the respective reconstructed photons. For instance at low meson momenta, only symmetric decays can be reconstructed with the PCM, EMC and PHOS reconstruction techniques. This changes when going to higher meson momenta allowing more and more asymmetric decays to be reconstructed, which in turn increases the efficiency. The rise in the normalized efficiency continues until nearly all meson asymmetries can be reconstructed within the given geometrical acceptance. At which point the maximum efficiency for the respective reconstruction technique has been reached. While the increase in the geometrical acceptance can be neglected for neutral pions above 0.6 GeV/c it has to be taken into account for the η meson, due to its larger mass and thus larger opening angle. As such, the total correction factor for the η meson rises slower than that of the neutral pion. If no other effects are interfering both mesons, however, should reach the same plateau value at high enough momenta. For the π^0 reconstruction using the EMC method, ε reaches its maximum of 0.75 (0.6) at 10 GeV/c for pp (p–Pb) collisions. Subsequently, ε drops due to the merging of the two photon clusters on the EMCal surface and is already a factor 5 smaller at 15 GeV/c for meson selection criteria employed in pp collisions. For p–Pb collisions, smaller opening angles have been allowed for the meson reconstruction. Thus, the drop on the efficiency is less pronounced. In the case of the η, the efficiency at 15 GeV/c is not yet affected by the cluster merging due to its higher mass and thus no decrease in ε can be observed. The normalized efficiency of both mesons using the PCM-EMC reconstruction is about a factor 10 smaller than for the EMC case due to the conversion probability of about 9% in the respective rapidity window. This suppression is stronger at lower meson momenta as the conversion probability is lower for low momentum photons, see Figure 6.9. The small decrease of the PCM-EMC reconstruction efficiency at high transverse momenta can be attributed to shower overlaps of the EMC photon with one of the conversion legs and thus a stronger rejection of the EMCal clusters due to the track matching. Relative to the PCM-EMC the ε of the standalone PCM reconstruction is suppressed by another 10% as the conversion probability affects the second photon as well.
The correction factor for the neutral pions in PHOS varies strongly between the two collision systems as a larger number of dead channels was found for the p–Pb data set. In pp collisions at $\sqrt{s} = 2.76$ TeV the correction factor is very similar to that of the PCM-EMC reconstruction, while for p–Pb collisions it is only slightly larger than the PCM correction factor. For the PCM-Dal reconstruction method, the geometrical acceptance and reconstruction efficiency are of a similar order as ε for PCM-EMC, however, the total correction factor is smaller due to the much smaller branching ratio. Thus, the PCM-Dal reconstruction technique has the smallest statistics for the neutral pion reconstruction in p–Pb collisions, while still having a similar accuracy as the PCM standalone method.
As the triggers of the EMCal affect the properties of the reconstructible mesons (i.e. $\alpha_{\gamma\gamma}$) a significant reduction of the reconstruction efficiency below the trigger threshold is expected. However,

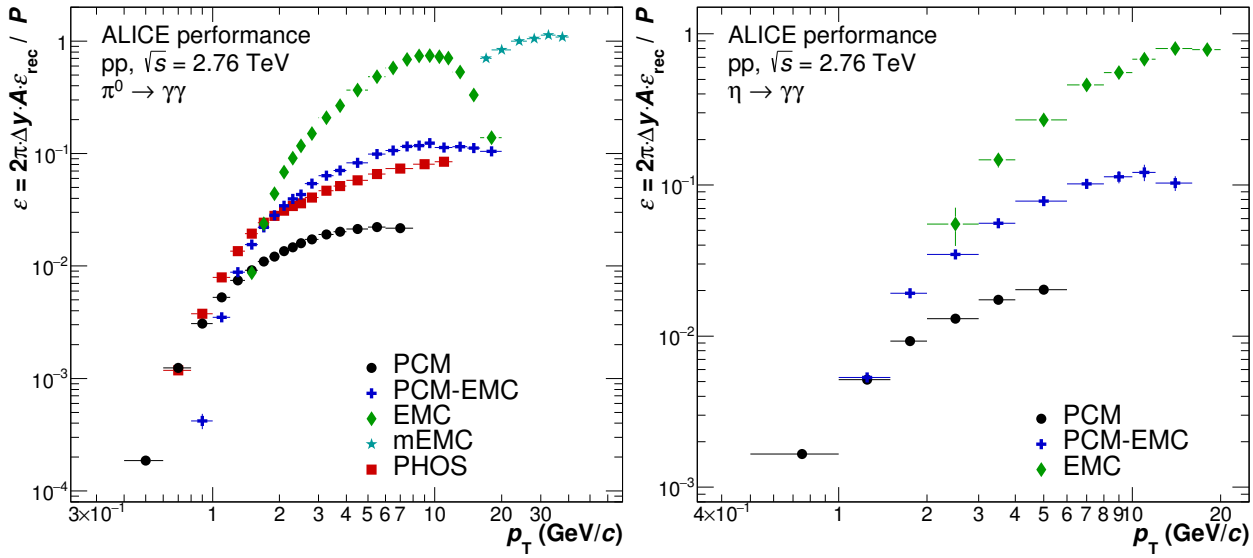

Figure 5.11.: Normalized efficiency for different methods of neutral pion (left) and η meson (right) reconstruction methods for pp collisions at $\sqrt{s} = 2.76$ TeV [297]. The values for PHOS are taken from [173].

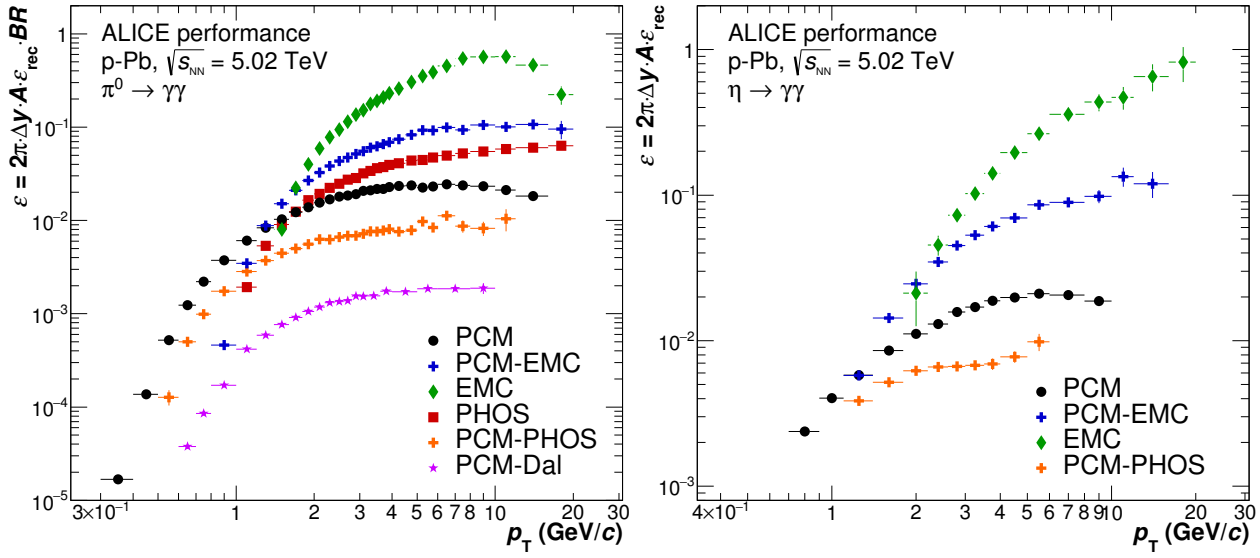

Figure 5.12.: Normalized efficiency for different methods of neutral pion (left) and η meson (right) reconstruction methods for p–Pb collisions at $\sqrt{s_{\mathrm{NN}}} = 5.02$ TeV.

this efficiency bias (κ_{Trig}) has been factorized out for the previously shown plots as it depends on the exact trigger settings. It has been simulated using the trigger emulation, described in Section 4.1.1. Its transverse momentum dependence for different triggers and reconstruction methods for the π^0 and η meson can be seen in Figure 5.13. As expected, κ_{Trig} is significantly below 1 below the trigger threshold for the PCM-EMC and EMC reconstruction methods. However, even above the trigger threshold it only slowly approaches 1 at about twice the trigger threshold. As the PCM photon reconstruction imposes a much lower energy threshold, the asymmetry and opening angle distribution of the reconstructible mesons are wider for the PCM-EMC reconstruction. Furthermore, stronger variations of the efficiency with respect to the asymmetry of the meson decay are expected for this method compared to the EMC reconstruction at the same meson energy. This leads to larger correction factors for PCM-EMC compared to EMC when using the same trigger conditions. Similar arguments hold when comparing κ_{Trig} for the η and π^0 meson. At low p_{T} κ_{Trig} also shows an effect of the trigger on sub-leading particles, for which the efficiency in the triggered events is strongly reduced.

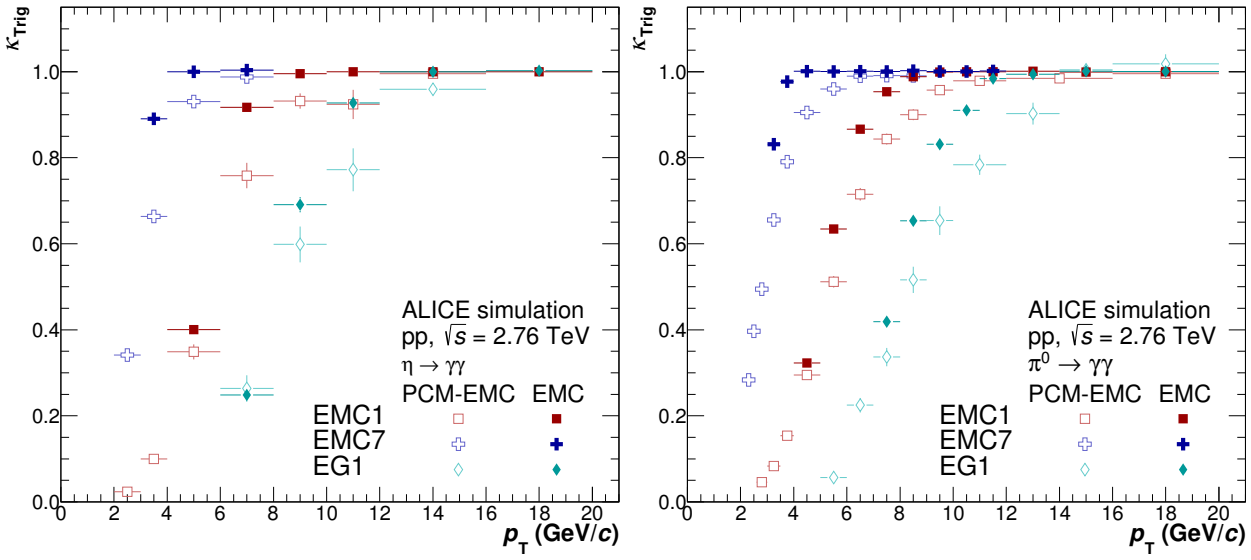

Figure 5.13.: Efficiency bias κ_{Trig} induced by different triggers (EMC1, EMC7 and EG1) for neutral pions (left) and η mesons (right) for PCM-EMC (open symbols) and EMC (closed symbols).

As discussed earlier, six different triggers have been used to obtain the neutral meson spectra in pp collisions at $\sqrt{s} = 2.76$ TeV with PCM-EMC and EMC. After all necessary corrections have been applied to the spectra measured in the individual trigger classes, a combined spectrum for each method is obtained following the Best Linear Unbiased Estimate (BLUE)-algorithm [309–314]. The weighted average of the n individual measurements ($Q_a(p_{\mathrm{T}})$) is obtained by calculating

$$\langle Q(p_{\mathrm{T}})\rangle = \boldsymbol{\omega}^T(p_{\mathrm{T}})\mathbf{Q}(p_{\mathrm{T}}) \tag{5.7}$$

$$= \sum_{a=1}^{n} \omega_a(p_{\mathrm{T}}) Q_a(p_{\mathrm{T}}) \tag{5.8}$$

for each p_{T} slice using the weights ω_a for the different measurement. To each of the individual measurement $Q_a(p_{\mathrm{T}})$ a statistical, systematic and total error can be associated. These are represented by $D_a(p_{\mathrm{T}})$, $S_a(p_{\mathrm{T}})$ and $T_a(p_{\mathrm{T}})$. While the statistical errors among the different triggers are fully uncorrelated, their systematic errors can be partially correlated. Thus, the full 6×6 ($\mathcal{C}$) for each measurement and p_{T} slice has to be calculated. Its coefficients $\mathcal{C}_{ij}(p_{\mathrm{T}})$ for trigger i and j can be calculated according to

$$\mathcal{C}_{ij}(p_{\mathrm{T}}) = \frac{\rho_{ij} S_i(p_{\mathrm{T}})\ \rho_{ji} S_j(p_{\mathrm{T}})}{T_i(p_{\mathrm{T}}) T_j(p_{\mathrm{T}})}, \tag{5.9}$$

where ρ_{ij} represents the fraction of the correlated systematic errors of a trigger i with respect to trigger j. Those ρ_{ij} are momentum dependent. As an example, the ρ_{ij} for the combination of the π^0 PCM-EMC measurements are shown in Figure 5.14(left). The fraction varies from 55% to 95% correlated systematic uncertainty among the different triggers. In most cases, only the systematic error due to the yield extraction has been considered as fully uncorrelated among different triggers, while the remaining systematic error sources have been assumed to be largely correlated. These systematic uncertainties sources are mainly driven by the detector conditions and response, which should only change when switching between runs or periods and not triggers within the same run. The weights have been calculated according to

$$\boldsymbol{\omega}(p_{\mathrm{T}}) = \mathcal{C}^{-1}\mathbf{U}/(\mathbf{U}^T\mathcal{C}^{-1}\mathbf{U}) \quad \text{, with } \mathbf{U} \text{ as unity vector and} \tag{5.10}$$

$$\omega_a(p_{\mathrm{T}}) \equiv \frac{\sum_{b=1}^{n} \mathcal{H}_{ab}}{\sum_{a,b=1}^{n} \mathcal{H}_{ab}} \quad \text{, with } \mathcal{H} = \mathcal{C}^{-1} \text{ and } \mathcal{H}_{ab} \text{ its elements.} \tag{5.11}$$

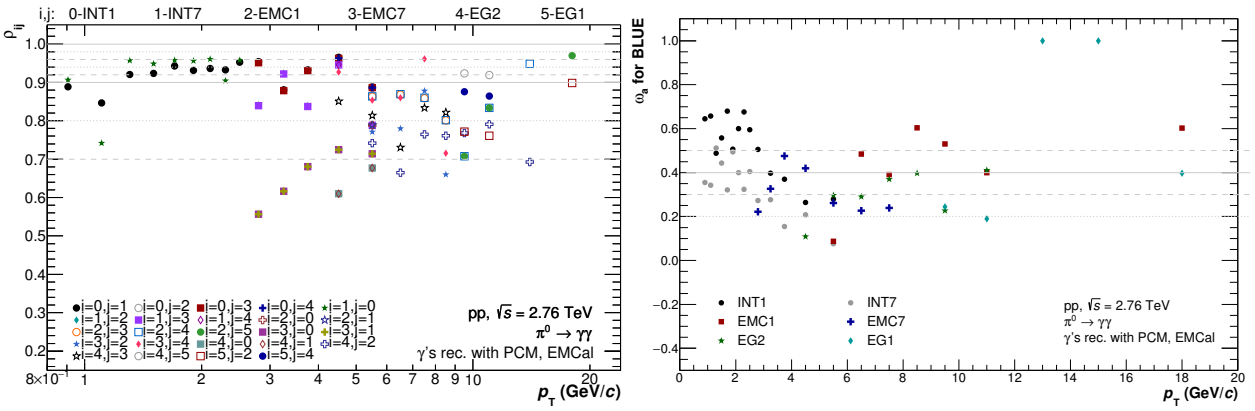

Figure 5.14.: Correlation factors ($\rho_{ij}(p_T)$) among different triggers (trigger (i) and trigger (j)) (left) and resulting weights for different triggers (right) for the neutral pion spectra using the PCM-EMC neutral meson reconstruction for pp collisions at $\sqrt{s} = 2.76$ TeV.

They are shown in Figure 5.14(right) for the π^0 measurement using the PCM-EMC reconstruction, while similar plots for the other reconstruction methods and mesons can be found in Section B.1.1 together with the comparison of the individual spectra obtained for different triggers to a fit of the combined spectrum. As it can be deduced from Figure 5.14(right), the spectra evaluated from EMCal triggered events have only been used in the full combination if the transverse momentum of the meson was at least 1.5 times that of the respective trigger threshold on the photon level. Below this threshold, a more detailed trigger simulation would be needed to also understand fully the biases imposed to the sub-leading particles in these events. For all reconstruction techniques and mesons, the spectra for different triggers agree within 5-15% with each other and in most cases these differences are well within the statistical uncertainties of the individual measurements.

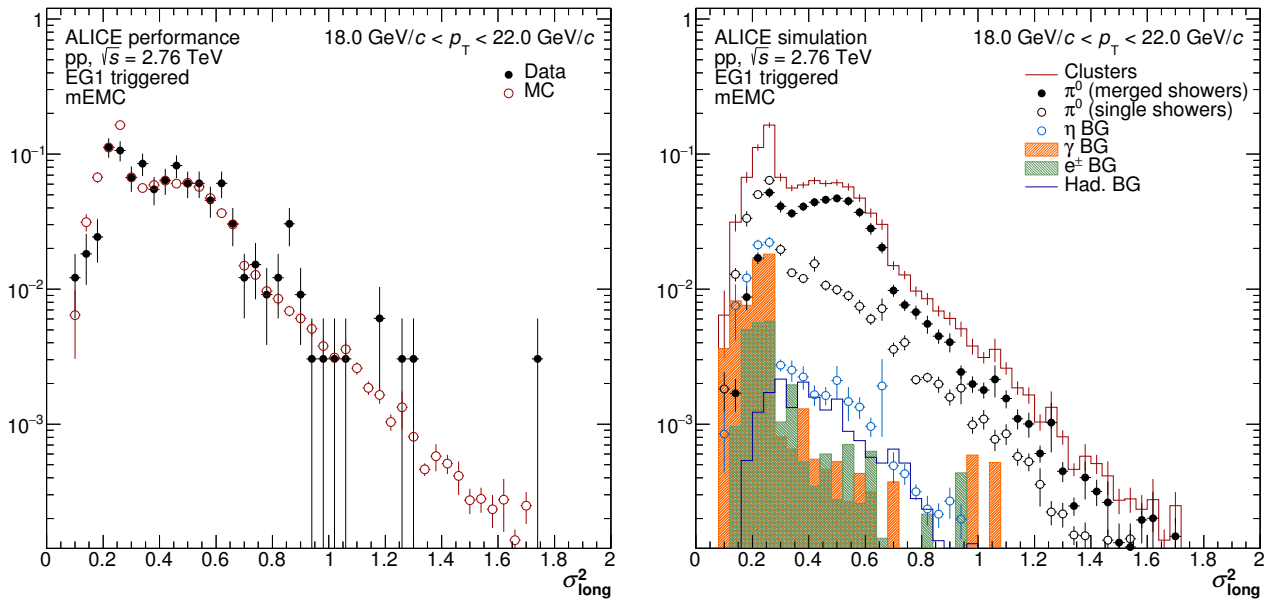

Figure 5.15.: Shower shape (σ^2_{long}) distributions for π^0 candidates with $18 < p_{\text{T}} < 22$ GeV/c compared in data and MC (left), and corresponding signal and background contributions in MC (right).

5.1.2. Single Cluster Analysis

At high p_{T} the showers induced by the two decay photons from a neutral pion merge into a single EMCal cluster, and therefore are unidentifiable in an invariant mass analysis. Hence, for $\pi^0 s$ above 15 GeV/c, we use a different approach, namely to reconstruct and identify $\pi^0 s$ based only on single clusters, exploiting that clusters at high p_{T} mostly originate from merged π^0 decay photons. This analysis technique closely resembles the approaches followed for the reconstruction of long lived particles, like $\pi^{\pm}, K^{\pm}, \gamma$. As such, it relies to a larger degree on the correct description of the physics backgrounds and the detector properties in the simulations than for instance the invariant mass analyses. Consequently, this analysis technique was only explored for the pp data taken at $\sqrt{s} = 2.76$ TeV, as the understanding of the underlying event for p–Pb collisions in the simulations is not yet sufficient to pursue this analysis.

Merged clusters from π^0 decays tend to be more elongated than clusters from photons and electrons, and their deformation is reflected by the shower shape σ^2_{long}, defined in Equation 4.8. The remaining features of the cluster are, however, very similar, thus the same cluster selection criteria have been used as for the invariant mass and photon analysis in the EMCal. They have been listed in Table 4.6. The shower shape distributions of clusters fulfilling these criteria (except the shower shape cut) are shown for data and MC in Figure 5.15 for π^0 candidates. The σ^2_{long} distribution is found to be fairly well described by the MC, in particular for $\sigma^2_{\text{long}} > 0.3$.

For $\sigma^2_{\text{long}} > 0.3$, the dominant contribution to π^0 candidates is from merged π^0 showers. However, the candidates where only one decay product is contributing dominantly for clusters with smaller σ^2_{long}. The main difference between these two categories is the energy resolution of the reconstructed meson candidate. In order to understand the relative importance of the different reconstruction qualities of the meson candidates in different σ^2_{long} regions, the relative fractions of fully merged and only partially reconstructed π^0 candidates are shown in Figure 5.16 for $\sigma^2_{\text{long}} > 0.1$ (left) and $\sigma^2_{\text{long}} > 0.27$ (right). For this study, the candidate clusters were split even further to additionally show the effect from conversion in front of the EMCal. As it can be seen by comparing these two σ^2_{long} regions, the contribution from single photon and electron clusters can be reduced by more than 20% below 30 GeV/c by selecting clusters with $\sigma^2_{\text{long}} > 0.27$. The corresponding transverse momentum resolutions are shown in Figure 5.17 for the different reconstruction qualities (left) and the final sample (right). If the resolution is obtained from a Gaussian fit to the response

(Figure 5.17(right, blue points)) it is better than 5% at high transverse momenta. However, this is only true for part of the sample, as this Gaussian resides on top of a rather wide distribution, which is indicated by the green point in Figure 5.17(right). The latter are calculated directly from the mean and root mean square (rms) of the respective distribution. Furthermore, it can be seen that not only the resolution for partially merged or single particle clusters is worse, but also their mean momentum is shifted significantly, as expected. In order to correct for these effects we have to fully rely on the simulation to model not only the clustering algorithm correctly, but also the material in front of the calorimeter.
As none of the mentioned quantities can be assessed directly in the data at high momenta the quality assessment of the simulation concerning the clustering algorithm has been based on the σ^2_{long} distribution and the distribution of the number of cells for the cluster candidates measured at different cluster energies. Examples of these can be found in Figure 5.15(left) and Figure 5.18. While the σ^2_{long} distributions agree reasonably well the average number of cells in the simulation is one cell lower than in the data, which could indicate either a small discrepancy in the response simulation of the calorimeter or a different average composition of the cluster due to contributions from charged particles for instance.
Neutral pions at high momenta are usually contained in a shower of particles originating from a quark or gluon, so called jets. Consequently, it is very unlikely that only one particle (i.e. π^0) will be seen within the EMCal acceptance. Considering the size of the EMCal cells it can even happen that within one cluster contributions from several particles are registered. This could have a severe impact, particularly within the jet cone, and needs to be corrected for. Thus, it has been tested whether the simulation describes the data reasonably well based on the energy surrounding the merged cluster candidate ($E_{\text{around merged cluster}}$) as well as the number of cells registered around it ($N_{\text{cells around merged cluster}}$). Both quantities have been evaluated for signals contained in a cone of $R < 0.15$ around the merged cluster, while not belonging to the actual cluster. For illustration, the respective quantities can be seen in Figure 5.19 for a selected transverse momentum slice of the data collected with the EGA trigger in pp collisions at $\sqrt{s} = 8$ TeV. For the inspected collision system the statistics was insufficient to draw any conclusions. Thus, the agreement between data and simulation had to be checked for the 8 TeV data set and it is assumed that it does not depend strongly on the collision energy.
The corrections for the geometric acceptance, reconstruction efficiency, and purity were calculated using Monte Carlo simulations, as described in Section 4.1. The resulting correction factor is shown in Figure 5.11 compared to the other neutral pion reconstruction techniques for pp collisions. At high p_{T} the mEMC technique clearly has an advantage due to its larger coverage compared to PHOS, and the exploitation of merging of the π^0 decay photons in the EMCal above 15 GeV/c. For mEMC, also the γe^+e^- channel has been used in the signal definition. In the following paragraphs, the individual components of ε will be explained in more detail for this novel reconstruction technique.
The purity represents the fraction of reconstructed clusters that pass all the selections and are from a π^0 decay. It is defined as

$$P(p_{\text{T}}) = 1 - \sum_{i=0}^{n} c_i(p_{\text{T}}), \tag{5.12}$$

where the c_i are the relative contributions of misidentified particles (i.e. photons, electrons, charged pions) to the reconstructed neutral meson cluster candidates. They are shown in the left plot of Figure 5.20 as function of transverse momentum. The largest contamination in the considered σ^2_{long} window originates from the η meson decay ($\approx 5\%$ after fine-tuning the η/π^0 ratio to the measured value), closely followed by the hadronic background consisting mainly of K^0_{L}, charged pions and neutron or anti-neutrons. The contamination from η mesons rises by about 2% towards higher momenta, while the contamination from the other two sources decrease. Fragmentation photons

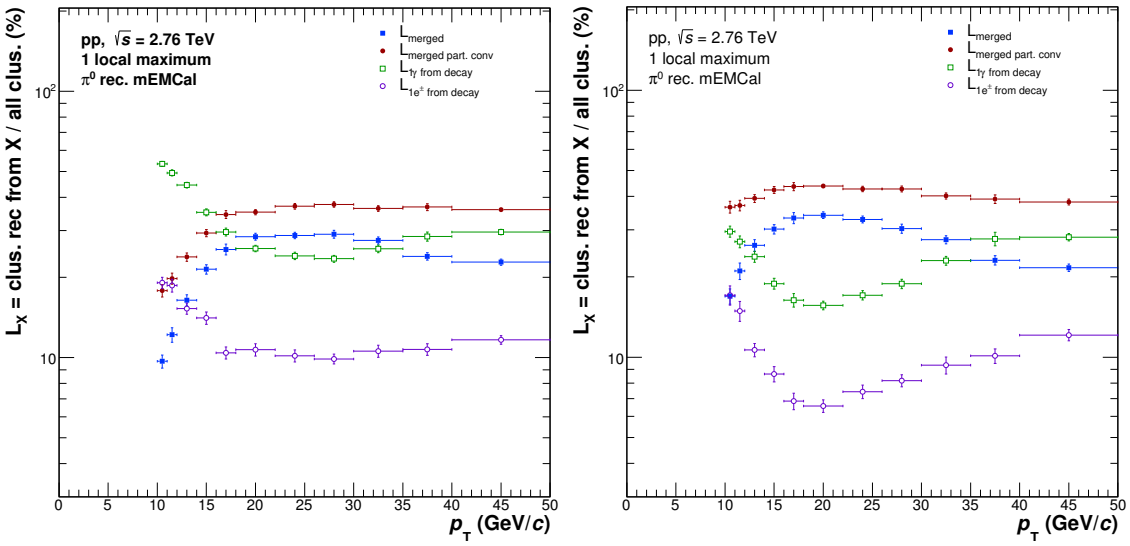

Figure 5.16.: Fraction of different reconstruction qualities for the merged cluster analysis taking into account cluster candidates with $\sigma^2_{\text{long}} > 0.1$ (left) and $\sigma^2_{\text{long}} > 0.27$ (right). It can be seen that the candidates were at least a small fraction of the neutral pion energy is lost due to a conversion dominate the spectrum above 15 GeV/c. They are followed by the fully merged cluster candidates in their strength (blue). For $\sigma^2_{\text{long}} > 0.1$ a significant fraction the merged cluster candidates are single photon (green) or electron (violet) clusters. Their relative strength is reduced when going to higher $\sigma^2_{\text{long}} > 0.27$. However, even then beyond 35 GeV/c their contribution is larger than that of the fully merged clusters.

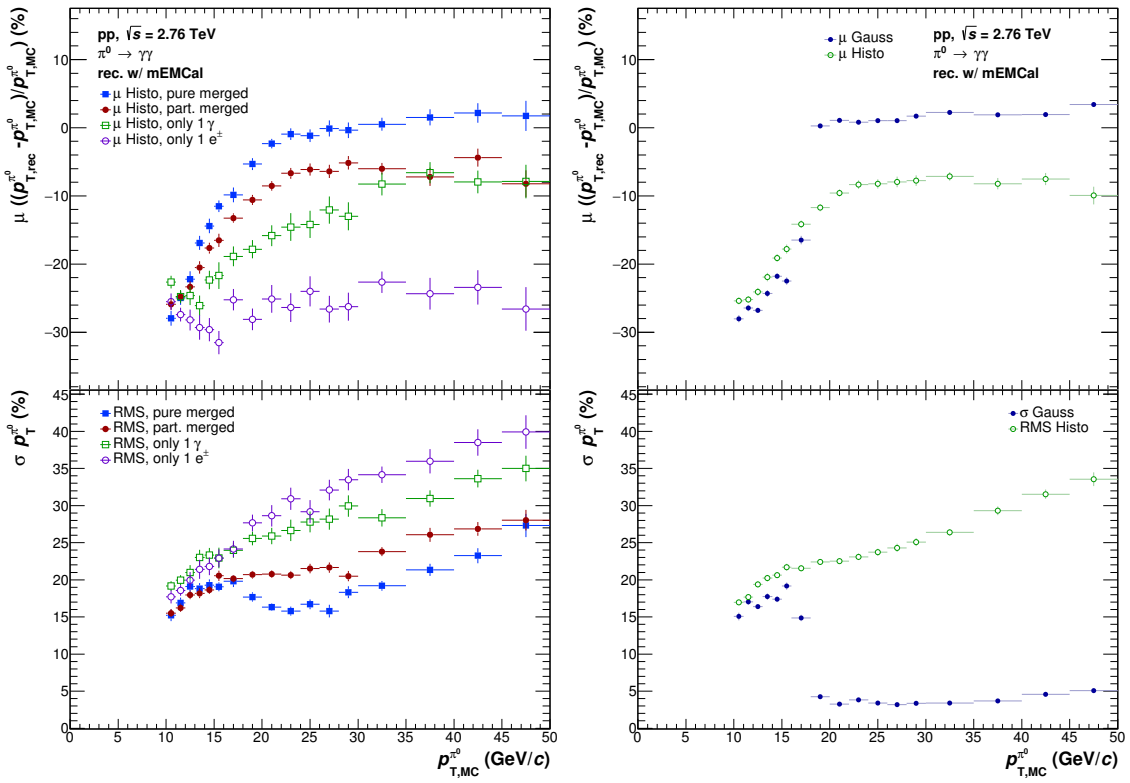

Figure 5.17.: Neutral pion meson momentum shift (upper row) and resolution (lower row) versus momentum for pp collisions at $\sqrt{s} = 2.76$ TeV. Shown here are different techniques to estimate the resolution, based on the summed resolution matrix (left). Given in this case are the values of a Gaussian fit (blue) and the mean and RMS of the histogram, both parameters have to be given as the Gaussian has a significant BG below the peak. In addition, the mean and RMS of each individual component contributing to the signal are given (right).

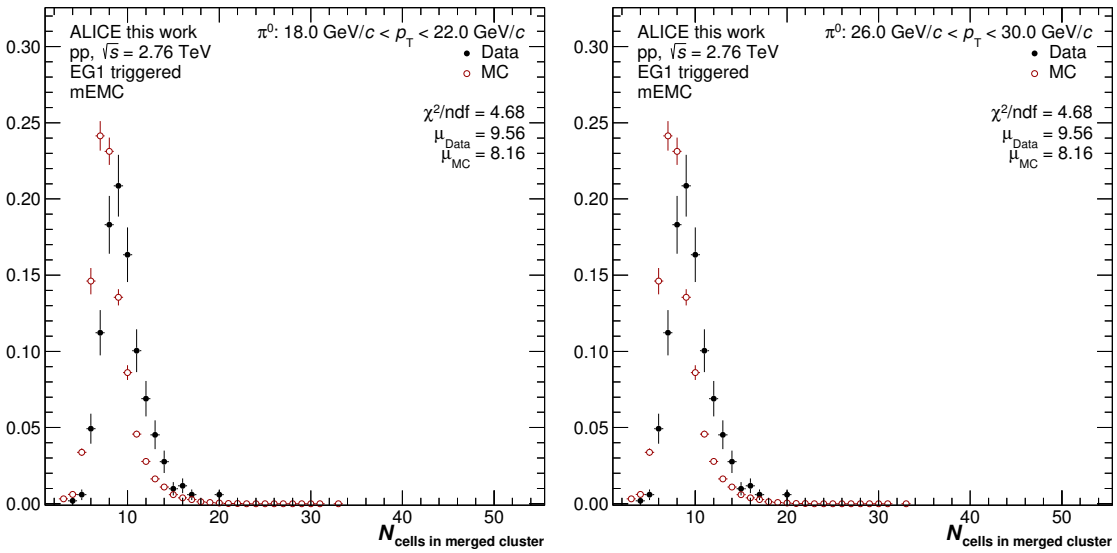

Figure 5.18.: N_{cells} per cluster comparison for data and Monte Carlo for two selected transverse momentum bin for the EG1 trigger in LHC13g.

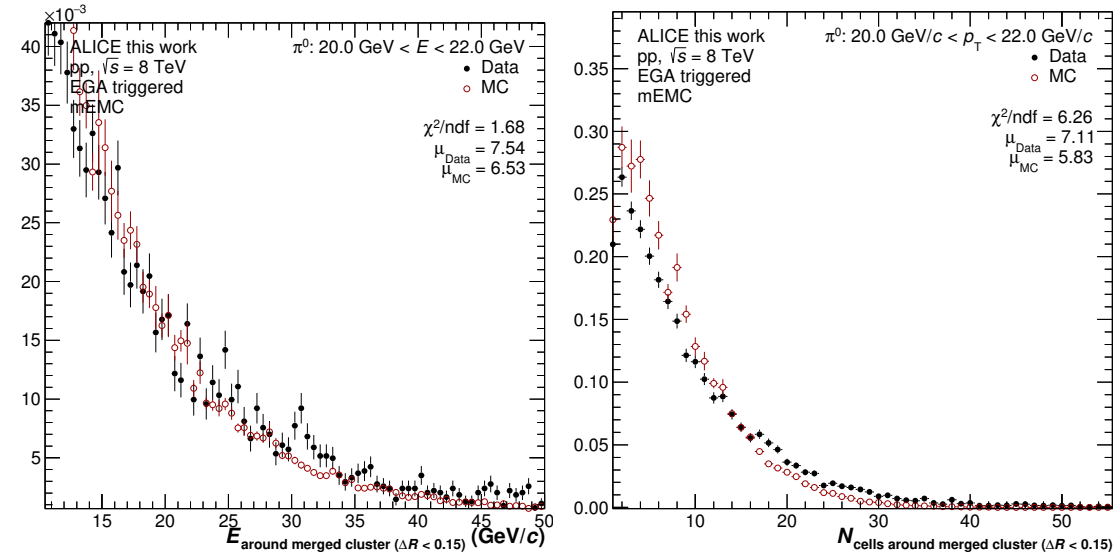

Figure 5.19.: $E_{\text{around merged cluster}}$ (left) and $N_{\text{cells around merged cluster}}$ comparison for data and Monte Carlo for the EGA trigger in the 8 TeV data set for one example energy or transverse momentum slice. Here a cone of $\Delta R < 0.15$ around the cluster has been taken into account for the surroundings.

contribute to the background with about 1.2%. Their contribution was additionally scaled up by up to a factor 2, given by the ratio of fragmentation photons to direct photons according to NLO pQCD calculations [213, 214], to account for prompt photons which are not included in the generator. Lastly, prompt electrons contribute to the contamination about 1%.

The sample of neutral pions, which is obtained in this way also contains π^0 originating from short lived strange particle decays such as the K^0_S, $K^0_L$and Λ. Furthermore, π^0's from material interactions can contribute to the total number of reconstructed pions. None of these secondary pions should be reported in the final invariant cross section or yield as normally their production mechanisms are not considered in the theory calculations.

For the merged cluster analysis, the efficiency and acceptance for the various secondary π^0 contributions has been estimated from the full detector simulations, the respective quantities can be found in Figure 5.21. As the decay length of the strange hadrons varies (see Table 5.3), their reconstruction efficiency, which is folded with the momentum resolution, does as well. For longer

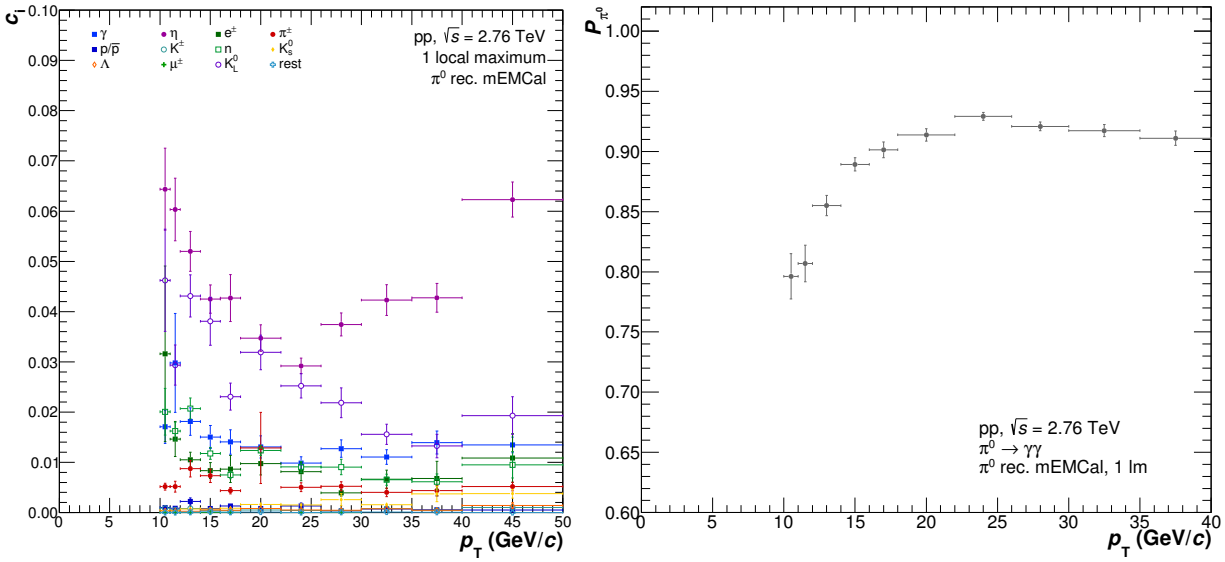

Figure 5.20.: Contamination (c_i) of the neutral pion candidate sample split into the different contributions according to the unmodified simulations (left) and the resulting purity of the neutral pion candidates sample for the weighted average of all triggers with the weights calculated according to Section B.1.1(right). For the purity the contribution from the photons was rescaled in order to account for the prompt photons which are not contained in the simulation.

lived particles this efficiency can even go beyond 1, as the resolution deteriorates due to the wrong assumption for their point of origin. If the statistics in the simulations was not sufficient to extract the respective quantities with reasonable errors, they were fixed to sensible values. Similar to the invariant mass analyses in pp collisions at $\sqrt{s} = 2.76$ TeV the kaon [95,307] and Λ [307] transverse momentum distributions were used as inputs to obtain a data driven decay π^0 spectrum from K^0_S, $K^0_L$and Λ, respectively. However, these distributions had to be extrapolated to higher transverse momenta ($p_T = 100$ GeV/c) using a Tsalis distribution in order to obtain the secondary pion transverse momentum spectrum from the various sources in the full kinematic range of the merged cluster neutral pion measurement. The decay of the strange particles was handled by TGenPhaseSpace for the decay channels given in Table 5.3. Afterwards, they were folded with the respective secondary π^0 efficiency and acceptance. For the secondary pions from material interactions, we fully relied on the full Monte Carlo simulation, which was not possible for the strange hadron decays as their transverse momentum spectra are not well modeled in the considered generators and center-of-mass energies. The final reconstructed yield contained in the merged cluster analysis originating from the different secondary pion sources can be found in Figure 5.22(right) as closed symbols. While the ones estimated purely based on the simulation can be seen as open symbols. Additionally, the fraction with respect to the full sample of reconstructed π^0 in this method is reported on the right of that same figure. The contribution from secondary π^0 from K^0_S decays is of the order of 5-9% and that of the material interactions amounts to about 1.5% beyond 20 GeV/c. The remaining contributions can be neglected. The correction based on the Pythia 6 input spectra would have over predicted these values by 2-4%. In a consequent step, the yield from secondary pions is subtracted, similar to the impurities, prior to the acceptance and efficiency corrections, which are solely based on primary neutral pions.

The geometrical acceptance A is defined as the ratio of π^0 mesons within $|y| < 0.6$, where at least 1 daughter particles is within the fiducial acceptance of the EMCal ($-0.67 < \eta_{\text{calo}} < 0.67$, $1.40 < \varphi_{\text{calo}} < 3.15$), over all π^0 mesons generated in the same rapidity window.

$$A = \frac{N_{\text{meson, } |y|<y_{\text{max}} \text{ with at least one daughter pointing to EMCal}}}{N_{\text{meson, } |y|<y_{\text{max}}}} \tag{5.13}$$

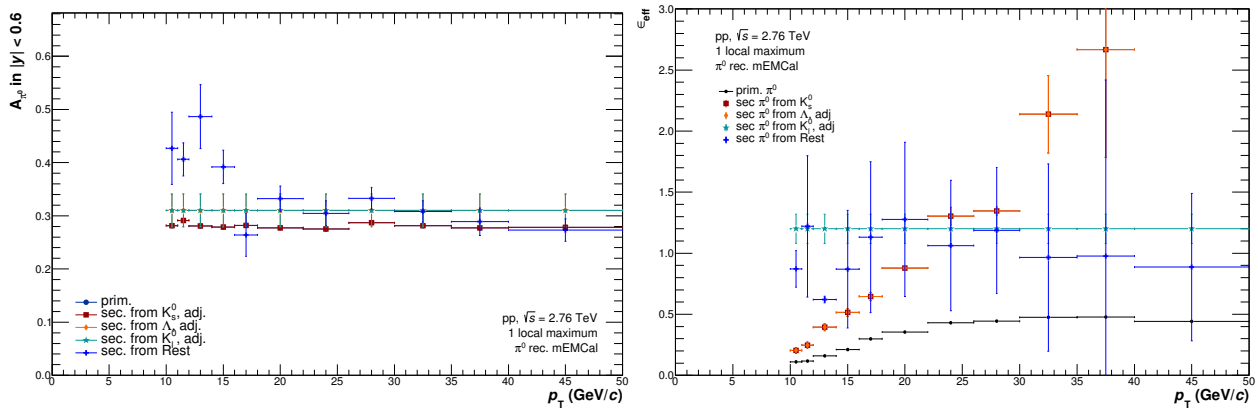

Figure 5.21.: Acceptance (left) and reconstruction efficiency (right) for secondary neutral pions from different sources compared to the respective quantities for the primary pions for the EG1 trigger. Attention: the efficiency correction contains the resolution correction and thus can be larger than 1.

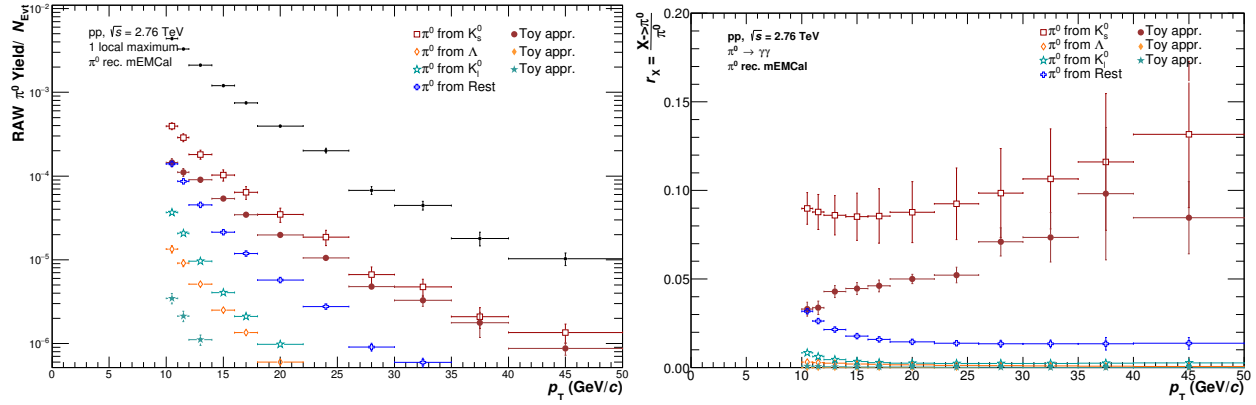

Figure 5.22.: Neutral pion raw yield (black) for the EG1 trigger compared to the secondary yield calculated based on Method A (closed symbols) and Method B (open symbols) (left). The effective correction can be seen on the right in the same color scheme.

Figure 5.23 shows the resulting geometrical acceptance for the π^0 meson. Ideally the acceptance of the meson is a constant, however due to the event weights in the Jet-Jet simulations fluctuations are introduced and the acceptance varies slightly.
In order to estimate the reconstruction efficiency, the same analysis as in real data has been performed on simulated data. Afterwards, it was checked whether these clusters are validated neutral pions. It was calculated by comparing the reconstructed p_T distributions with the generator ones within the given rapidity. By comparing measured and generated p_T of the neutral pion, the p_T resolution (seen in Figure 5.17) is included in the inefficiency correction. Due to the choice of the widest possible signal definition, it is possible to accidentally reconstruct the neutral pion more than once. This can happen in the data and in the simulation and is corrected for by the efficiency as well. At lower transverse momenta, the fraction is about 1%, while it rises at higher transverse momenta to about 2.5%.
As already mentioned, both π^0 decay channels are considered within this analysis technique. Due to the higher efficiency of the $\gamma\gamma$ channel, however, the Dalitz is even further suppressed than its actual branching ratio. The resulting reconstruction efficiency ε_{π^0} is shown in Figure 5.23(left) as a weighted average of the different Jet-Jet simulation samples used within the analysis. It is about 10% at 10 GeV/c and rises to $\sim$ 50% at 40 GeV/c.
As discussed earlier, each of the different categories of reconstructed neutral mesons has its own resolution correction and mean momentum shift. In our analysis, however, we cannot distinguish the different categories in the data and thus need to trust the simulation that the fraction of the categories is correct as well as their respective resolutions. A possible mismatch in these quantities

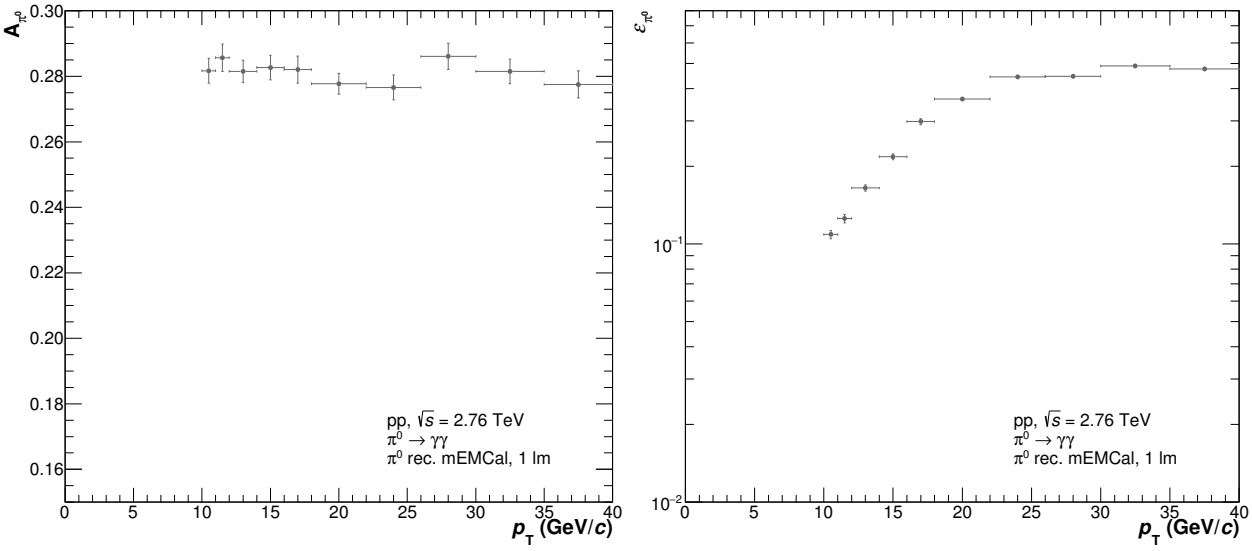

Figure 5.23.: Geometrical acceptance (left) and reconstruction efficiency (right) for π^0 mesons in pp collisions at $\sqrt{s} = 2.76$ TeV versus transverse momentum for the mEMC reconstruction technique. The distributions are combined from the data sets anchored to the different periods with the weights calculated according to their contribution to the final invariant cross section of this reconstruction method.

is taken into account for the systematic uncertainties.
Contrary to the invariant mass analysis techniques involving the EMCal in pp collisions no efficiency bias has been observed by triggering on high momentum particles with the various EMCal triggers due to the higher energy of the clusters considered for this analysis stream as well as the single particle analysis characteristics.
For the final result in pp collisions at $\sqrt{s} = 2.76$ TeV, only the three triggers with the highest thresholds were taken into account for the combination, as the others would not have had enough statistical precision in the desired transverse momentum range. The combination follows the same approach as described for the invariant mass technique. However, the results of different triggers are correlated to an even larger degree with the ρ_{ij}'s ranging from $0.75 - 1$ as almost all systematic uncertainties are originating from the mismatch of the detector description in the simulation which is common for different triggers. The corresponding distribution for the ρ_{ij} and ω_a can be found in Section B.1.1 together with the comparison of the spectra for individual triggers to a fit of the combined spectrum. The individual measurements agree with each other within $5 - 20\%$ with statistical errors ranging from $5 - 40\%$ depending on transverse momentum. Thus, they are considered to be consistent with each other.

5.2. π^0 and η Meson Cross Sections in pp Collisions at $\sqrt{s}$ = 2.76 TeV

5.2.1. Systematic Uncertainties and Combination of Individual Measurements

The systematic uncertainties of the individual measurements (PCM, EMC, PCM-EMC, mEMC) have been evaluated independently of each other by varying the different selection criteria for the photons and mesons. However, as large parts of the systematics are of common origin between PCM, PCM-EMC, EMC and mEMC, they are going to be discussed together in the course of this section. Within Table 5.4, the systematic uncertainties associated with the various measurements in different p_{T} ranges, chosen to reflect the strength of the various methods, are summarized for the neutral pion analyses. While in Table 5.5 and 5.6 the same has been done for the η meson and the η/π^0 ratio, respectively. The systematic uncertainties for all methods in the full p_{T} range can be found in Section B.1.2 split into their various origins. As the measurements obtained with PCM-EMC, EMC and mEMC are a combination of multiple triggers, the systematic uncertainties associated with each method reflect the contribution of different triggered data samples weighted by their statistical uncertainties, as described in the previous sections. The uncertainties for the η/π^0 were evaluated directly on the ratio in order to cancel correlated uncertainties between the π^0 and η measurements. As the PHOS analysis has already been published in [173], its systematics are not discussed.

In the following, the uncertainties associated with the EMC and PCM photon reconstruction are discussed first, then those related to the meson selections. The section is concluded by the discussion of the systematic uncertainties arising from the overall normalization. The same order has been chosen for the summary tables.

EMCal clustering: Within this uncertainty, the mismatch of the description of the clusterization process between data and simulation is quantified. As such, it incorporates the uncertainties arising from the variations of the minimum energy and time on cluster and cell level. Furthermore, it contains the variations of the minimum number of cells as well as the cluster shape parameter σ^2_{long}. The latter is of particular importance for the mEMC reconstruction, since it quantifies the uncertainty of how well the σ^2_{long} distributions of the background are described by the simulations. Thus, this cut has been varied from 0.27 to 0.25 and 0.3 for the mEMC π^0 reconstruction.

For PCM-EMC, the uncertainty ranges from 2.4% at 2.1 GeV/c to 6.2% at 18 GeV/c for the π^0 and from 3.1% at 1.25 GeV/c to 3.6% at 11 GeV/c for the η meson. For EMC, the uncertainty for the π^0 is largest at low p_{T}, namely 4.9%, afterwards it decreases to 2.3% at 3.25 GeV/c, and then rises similarly as PCM-EMC to 4.4% at 18 GeV/c. The uncertainty for the η meson exhibits a similar transverse momentum dependence, as the neutral pion ranging from 2.7% at 3.5 GeV/c to 3.1% at 11 GeV/c. For EMC(PCM-EMC) in case of the η/π^0 a p_{T} independent contribution of 1% from the variation of the cell and cluster time is assumed to cancel out, since it affects clusters from pion and η meson decays in the same way. For mEMC, the uncertainties are slightly larger than those of the di-photon EMC reconstruction as the background description is more important for this technique. They range from 4.6% at 18 GeV/c to 5.9% at 32.5 GeV/c.

EMCal cluster energy calibration: In order to quantify the uncertainty related to the cluster energy calibration, the remaining relative difference between data and simulation in the mass position has been chosen. This difference is on average 0.3% for pp collisions at $\sqrt{s}$ = 2.76 TeV. This leads to an uncertainty on the spectra of about 2%, when taking into account that the spectra approximately fall with p_{T}^{-6}. Furthermore, several variations of the correction of the simulations for the relative energy scale and residual misalignment, as described in Section 4.3.1, have been taken into account. These variations mainly change the underlying mass position correction depending on transverse momentum. To obtain a realistic estimate on the uncertainty associated to this calibration procedure, only correction factors have been considered, for which the neutral pion and eta mass position could be reproduced by the simulation to better than 1.5% over the full p_{T}

p_{T} interval (GeV/c)	1.4–1.6			3.0–3.5			16–20			30–35
Method	PCM	P-E	EMC	PCM	P-E	EMC	P-E	EMC	mEMC	mEMC
EMCal clustering	-	2.4%	4.9%	-	2.1%	2.3%	6.2%	4.4%	4.6%	5.9%
EMCal energy calib.	-	2.0%	4.9%	-	2.1%	2.5%	5.4%	5.5%	4.2%	4.8%
Track matching	-	0.9%	1.8%	-	1.4%	1.7%	6.9%	6.7%	5.4%	6.1%
Secondary track reco.	1.6%	1.1%	-	0.9%	0.8%	-	5.7%	-	-	-
Electron PID	1.3%	0.7%	-	1.5%	0.6%	-	12.7%	-	-	-
PCM photon PID	1.7%	1.4%	-	2.3%	1.1%	-	13.4%	-	-	-
Signal extraction	1.9%	1.5%	2.4%	4.0%	1.9%	1.5%	3.4%	14.1%	-	-
Efficiency	-	2.0%	2.0%	-	3.6%	2.5%	2.1%	2.1%	8.4%	7.1%
Secondary correction	-	-	-	-	-	-	-	-	1.8%	1.8%
Inner material	9.0%	4.5%	-	9.0%	4.5%	-	4.5%	-	-	-
Outer material	-	4.2%	4.2%	-	4.2%	4.2%	4.2%	4.2%	4.2%	4.2%
Trigger norm.+pile-up	0.8%	-	-	0.4%	1.1%	0.5%	7.5%	5.5%	8.0%	8.8%
Tot. sys. uncertainty	9.6%	7.6%	8.9%	10.3%	8.3%	6.5%	24.5%	18.6%	14.9%	15.6%
Stat. uncertainty	2.8%	2.0%	6.5%	5.1%	3.3%	2.8%	14.8%	15.6%	5.7%	11.3%

Table 5.4.: Systematic uncertainty for various sources and methods assigned to the π^0 measurement at different p_{T} intervals. For comparison, the total systematic and the statistical uncertainties are also given. P-E stands for PCM-EMC.

range. As this calibration influences the cluster energy resolution of the EMCal, mainly at low p_{T}, the different detection techniques absorb a mismatch with a different magnitude. This leads to a systematic uncertainty on the neutral pion cross section for the PCM-EMC method ranging from 2.8% at low momenta to 4.4% at higher momenta, while for the EMC it is 5.5% at 1.5 GeV/c and then decreases to 2.5% at 3.25 GeV/c and rises again at high transverse momenta to 5.5%. The systematic uncertainty of the energy calibration for the single cluster neutral pion analysis ranges from 3.9% at 17 GeV/c to 4.5% at 28 GeV/c. For the η meson (η/π^0 ratio), the uncertainties are approximately a factor 1.5 (2) larger at similar p_{T} due to lower photon energies entering at the same meson p_{T}.

Track matching to cluster: Within this uncertainty, the imperfections arising from the propagation of the measured charged particles to the clusters are quantified. This has been done by varying the cluster rejection based on the track matching from tight selections, removing only centrally matched clusters, to rather loose selections, allowing a distance of 2-3 cells depending on φ and η. For the PCM-EMC method also the secondary tracks from the conversion candidates have been propagated to the EMCal surface and the same variations were applied to obtain the systematic uncertainty. The resulting uncertainty on the π^0 measurements is below 2% at low p_{T}, while it increases with increasing meson p_{T} to about 7%. The increase can be explained by the jettier environment around high momentum π^0, which is not fully described by the simulations. For the η meson, these uncertainties are in general larger, ranging between 4.9% and 8.9% due to the worse signal-to-background ratio. In case of the η/π^0 ratio the track matching uncertainty related to the η extraction dominates this systematic uncertainty source.

Secondary track reconstruction: For the reconstruction of photons with the PCM method, a major contribution to the uncertainties arises from the secondary track reconstruction. Its estimates are based on the variation of the minimum p_{T} cuts for the secondary tracks, the TPC found-over-findable clusters selection and restrictions in the φ-acceptance. The latter was only explored for the PCM-EMC reconstruction method requiring that the photons point at least approximately towards the EMCal. This uncertainty depends on the precision of the relative alignment and track matching efficiency between the TPC and ITS in different sectors of the TPC as well as the time dependent variations of the TPC drift velocity and gain. Hence it can vary for different data taking

p_T interval (GeV/c)	1–1.5		3–4			10–12	
Method	PCM	PCM-EMC	PCM	PCM-EMC	EMC	PCM-EMC	EMC
EMCal clustering	-	3.1%	-	3.1%	2.7%	3.6%	3.1%
EMCal energy calib.	-	3.0%	-	3.2%	4.5%	5.0%	6.8%
Track matching	-	8.9%	-	4.9%	5.7%	6.6%	8.8%
Secondary track reco.	3.7%	3.3%	1.6%	3.3%	-	4.1%	-
Electron PID	2.1%	2.5%	2.4%	2.2%	-	5.2%	-
PCM photon PID	3.9%	7.7%	3.9%	7.3%	-	11.2%	-
Signal extraction	6.0%	16.4%	6.0%	8.1%	9.3%	11.8%	3.5%
Efficiency	-	5.0%	-	5.0%	5.7%	5.8%	5.3%
Inner material	9.0%	4.5%	9.0%	4.5%	-	4.5%	-
Outer material	-	4.2%	-	4.2%	4.2%	4.2%	4.2%
Trigger norm.+pile-up	1.8%	-	1.9%	-	2.8%	7.0%	7.2%
Tot. sys. uncertainty	12.3%	22.5%	11.9%	15.5%	14.3%	22.6%	15.5%
Stat. uncertainty	20.4%	43.4%	17.2%	16.7%	10.8%	21.3%	8.9%

Table 5.5.: Systematic uncertainty for various sources and methods assigned to the η measurement at different p_T intervals. For comparison, the total systematic and the statistical uncertainties are also given.

periods and trigger conditions. In case of EMCal triggered, for instance, the reconstructed photons mainly sample the region directly in front of the EMCal. However, in 2013 the ITS had larger inefficiencies in this area, leading to a larger uncertainty for the triggered events. The uncertainties range from 0.8 to 5.7% depending on method and transverse momentum.

Electron PID: Within this category all uncertainties related to the electron identification and contamination rejection for the conversion photons on the level of single legs are summarized. They have been estimated by varying the TPC dE/dx based electron inclusion as well as pion rejection selections. As such, the uncertainties for the π^0 reconstruction are small ($\approx 1\%$) where there is good separation between electron and pions, but increase towards higher momenta up to 12.7%, where electrons and heavier particles cannot be efficiently separated any longer. The same transverse momentum dependence has been observed for the eta meson in both reconstruction techniques. However, the resulting impurities have a larger impact on the reconstructed yield, leading to an error ranging from 2.5% to 5.2% for the PCM-EMC measurement and 2.1% to 2.4% for the PCM measurement.

PCM photon PID: To ascertain the photon identification uncertainty for the PCM photons the selection criteria for the photon quality have been varied. Furthermore, the variation of the Armenteros-Podolanski selections has been taken into account for this contribution. The resulting uncertainties are slightly larger than those associated with the electron PID, but they exhibit a similar p_T dependence. This can be understood by the fact that both selection processes attempt to reduce the contamination, which increases with increasing p_T. Within the η/π^0 ratio, only a small fraction of the uncertainties cancels, due to the different decay kinematics of the two mesons, in particular at high p_T. Thus, this uncertainty is one of the dominant contributions for that measurement.

Signal extraction: For the invariant mass analyses an uncertainty for the yield extraction has been estimated taking into account different integration windows around the fitted mass position as well as different normalization regions of the mixed event background. Additionally, it has been tested, how the signal extraction depends on the signal-to-background ratio by varying the minimum opening angle as well as a mild asymmetry of the decay photons. This led to an uncertainty on the neutral pion extraction ranging from 1.9% to 4.0% for PCM. The small error at low transverse momenta is driven by the excellent momentum resolution of the tracks, which is also reflected in the PCM-EMC uncertainties for the same meson. These range from 1.5% at

p_{T} interval (GeV/c)	1–1.5		3–4			10–12	
Method	PCM	PCM-EMC	PCM	PCM-EMC	EMC	PCM-EMC	EMC
EMCal clustering	-	4.1%	-	4.2%	2.4%	6.0%	2.8%
EMCal energy calib.	-	4.1%	-	4.3%	4.6%	6.6%	7.6%
Track matching	-	8.9%	-	4.9%	5.7%	6.6%	9.0%
Secondary track reco.	3.7%	4.5%	1.6%	4.2%	-	8.1%	-
Electron PID	2.1%	3.3%	2.4%	3.2%	-	7.0%	-
PCM photon PID	3.9%	7.7%	4.0%	6.5%	-	12.7%	-
Signal extraction	6.1%	16.6%	7.0%	9.1%	9.3%	10.5%	8.5%
Efficiency	-	5.4%	-	5.4%	3.8%	7.0%	4.3%
Tot. sys. uncertainty	8.4%	22.5%	8.5%	15.6%	12.6%	23.8%	15.4%
Stat. uncertainty	20.4%	44.1%	17.7%	17.9%	10.9%	22.1%	8.8%

Table 5.6.: Systematic uncertainty for various sources and methods assigned to the η/π^0 measurement at different p_{T} intervals. For comparison, the total systematic and the statistical uncertainties are also given.

low p_{T} to 3.4% at high p_{T}. For the EMC neutral pion extraction a slightly different transverse momentum dependence can be observed. The systematic errors range from 2.4% at low to 1.5% at intermediate and 14.1% at high p_{T}. Its decrease towards higher momenta is explained by the improving energy resolution of the calorimeter. Above 10 GeV/c, however, merging of the two photon clusters sets in, which is not modeled in the simulations to a sufficient extend in this momentum region, therefore leading to larger uncertainties. For the η meson, the uncertainties associated to the signal extraction are generally larger since the signal-to-background ratio is worse and also the mixed event background does not describe the background that well. This is particularly true at low transverse momenta. For PCM the uncertainty is 6%, while it ranges from 16.4% to 8.1% to 11.8% for PCM-EMC. In case of the EMC reconstruction this uncertainty drops from 9.3% at intermediate momenta to 3.5% at high p_{T}, reflecting the improvement of the energy resolution for the calorimeter, as for the η meson the cluster merging would set in only at $\approx$ 35 GeV/c. The signal extraction uncertainties on the two mesons contribute independently to the η/π^0 ratio and hence are added in quadrature.

Efficiency: For pp collisions at $\sqrt{s} = 2.76$ TeV, the systematic uncertainties associated with the efficiency calculation could be checked by comparing the correction factors obtained from different Monte Carlo generators. As such, the input spectra were varied and the effect of these mild changes on the p_{T} resolution has been estimated. For PCM-EMC and EMC, the uncertainties range from 2% to 3.6% depending on the π^0 p_{T}. Within this uncertainty also the modeling of the EMC triggers in the simulation is contained. Thus, they are larger for the η meson, ranging from 5% to 5.8%, where the trigger description plays a larger role. For the η/π^0 ratio the uncertainties related to the trigger simulation largely cancel, while the remaining are added quadratically for both mesons. For the mEMC π^0 reconstruction this uncertainty represents one of the main contributions to the total uncertainty. As in this case, the p_{T} resolution strongly depends on whether the π^0 could be reconstructed with all decay particles contributing to the single cluster or just some of them. To estimate the uncertainty due to a possible imperfection of the modeling of the magnitude of the various contributions to the total yield, the fractions of the respective reconstruction possibilities were varied by 20% each. This led to an uncertainty for the efficiency of 8.4% at mid (18 GeV/c) and 7.1% at high p_{T} (32.5 GeV/c).

Secondary correction: In order to obtain the uncertainty for the secondary π^0 corrections, the parametrized yields for $\mathrm{K}^0_{\mathrm{S}}$ and Λ are varied within the measured uncertainties. However, since the correction factor for EMC and PCM-EMC related to this is only $1-2$% even a variation of 15% on the input yields would lead to a negligible contribution with respect to the other uncertainties. For the mEMC method, on the other hand, the correction is about 5% total and the yield for the $\mathrm{K}^0_{\mathrm{S}}$

and Λ had to be extrapolated to about 5 times the measured maximum p_{T}. Thus, an uncertainty of about 1.8% has been assigned to this correction factor.

Inner material: For the conversion photons the largest source of uncertainty stems from the knowledge of the inner ($R < 180\,\mathrm{cm}$) material of the detector and as such the conversion probability itself. It has been estimated to be 4.5% independently of p_{T} based on detailed comparisons between simulations and data for pp collisions at $\sqrt{s} = 7$ TeV [235, 293, 301]. As such, it affects the PCM mesons measurements with 9% and only contributes 4.5% to the PCM-EMC. This uncertainty cancels for the η/π^0 ratio as both mesons should be affected in the same manor.

Outer material: One of the major contributions to the uncertainties of the EMC related measurements is the uncertainty on the decription of the outer material budget situated in front of EMCal. If the material implemented in the simulations does not reflect reality the absorption rate for photons and the production rate of secondary pions could be biased. In most cases, however, the photon simply converts and at least one of its daughters is reconstructed in the EMCal so that the π^0 will most likely be reconstructed as well, albeit with a degraded p_{T} resolution. With increasing radius of the conversion also the probability to reconstruct π^0's from converted photons increases. In front of the EMCal most of the detector material is closer to the EMCal than 1.5m, namely the TPC outer wall, the TRD and the TOF including their support structures. As the TRD in 2011 and 2013 was only partially installed in front of the EMCal a variation of the EMCal acceptance in φ allows to test also the material implementation of that detector. By comparing the fully corrected π^0 yields in different φ regions a systematic uncertainty of 4.2% has been estimated independent on p_{T}. In this estimate the uncertainty on the material description of the TOF is assumed to be the same as that of the TRD and both contributions are assumed to be independent. It has been assigned to all EMCal related meson measurements and should cancel for the η/π^0 ratio.

Trigger normalization and pile-up: To obtain the uncertainties for the trigger normalization, the fit ranges for the plateau region have been varied (see Figure 4.2). This leads to the rejection factors given in Table 4.4 with the mentioned uncertainties. Afterwards, these uncertainties have been weighted according to their contribution to the final measurement (see Section 5.1.1) to obtain one value for each transverse momentum interval . The uncertainties range between 0.5% and 8.8% and cancel for the η/π^0 ratio as it has been obtained for each trigger class as well and then combined. As only one minimum bias trigger has been used for the PCM measurement no trigger rejection uncertainty has been assigned. However, an uncertainty for the out-of-bunch pile-up correction of $0.8 - 0.4\%$ has been assigned for the π^0 measurement, as described in [173], which increases for the η to about 1.8%. This largely cancels in the η/π^0 ratio and the remaining error can be neglected compared to the other error sources.

The relative statistical and full systematic errors for the individual measurements as a function of transverse momentum can be found in Figure 5.24. While the total systematic errors in the intermediate transverse momentum region are comparable for all invariant mass techniques ($\sim 7 - 10\%$) the statistical errors vary following the dependence seen for ε (see Figure 5.11). The binning in p_{T} for the combined spectrum has been chosen such that the maximum number of measurements are contributing to each transverse momentum slice, while still keeping the slices as narrow as possible.

Since the meson measurements with PHOS, PCM, EMC, PCM-EMC and mEMC are statistically independent and have partly uncorrelated systematic uncertainties, their combination will increase the precision of the respective cross section measurements and particle ratio. For the combination of the different measurements, the same technique has been used as for the combination of the triggers and the full correlation matrix according to the BLUE method has been calculated for each of the spectra measurements and the η/π^0 ratio. To obtain the correlation matrix pairs of measurements have been evaluated to ascertain the fraction of the correlated and uncorrelated part of their systematics with respect to each other. It has been found that the standalone invariant mass measurements with PCM, EMC and PHOS are not correlated with each other, while the

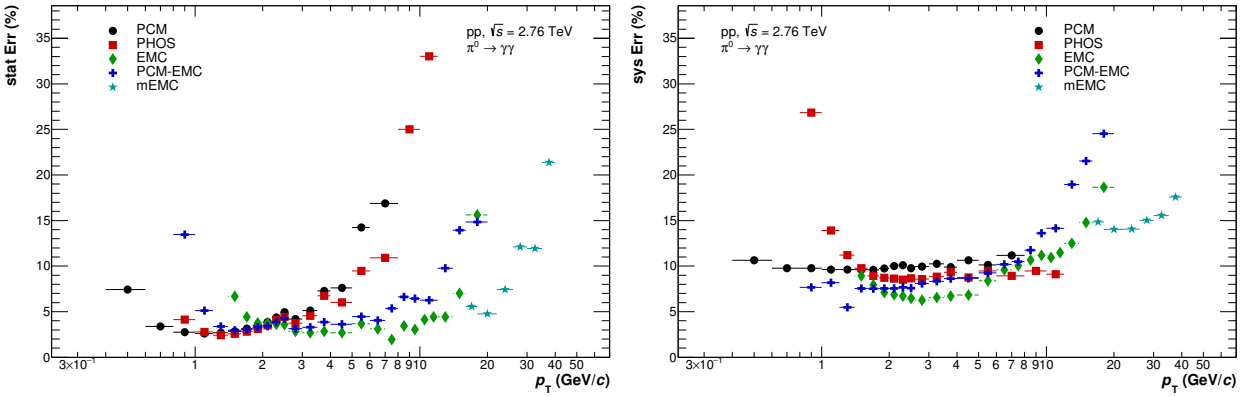

Figure 5.24.: Relative statistical (left) and systematic uncertainties (right) for the neutral pion spectra measured with different reconstruction methods in pp collisions at $\sqrt{s} = 2.76$ TeV as a function of transverse momentum. The respective plots for the η meson spectra and the η/π^0 ratio can be found in Section B.1.3.

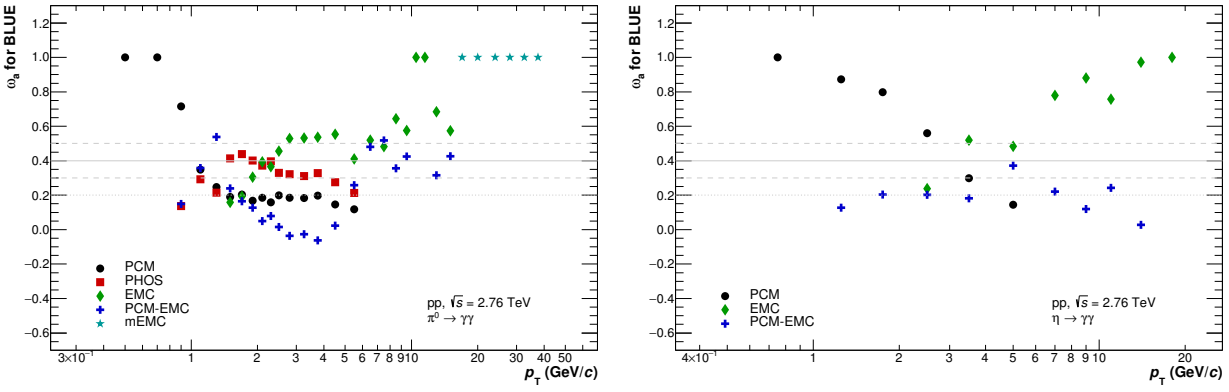

Figure 5.25.: Weights (ω_a) for the individual cross section measurements used in the combination according to the BLUE method [309, 310, 313].

Method	π^0	η	η/π^0
PCM	0.4–8.0	0.5–6.0	0.5–6.0
PHOS	0.8–12.0	n/a	n/a
EMC	1.4–20.0	2.0–20.0	2.0–20.0
PCM-EMC	0.8–20.0	1.0–16.0	1.0–16.0
mEMC	16.0–40.0	n/a	n/a

Table 5.7.: Summary of the p_{T} reach (in GeV/c) of the various reconstruction methods for π^0, η and η/π^0.

Meson	$\mathbf{A_e}$ (pb GeV$^{-2}c^3$)	$\mathbf{T_e}$ (GeV/c)	**A** (pb GeV$^{-2}c^3$)	**T** (GeV/c)	$\mathbf{n_{br}}$
π^0	$(0.79 \pm 0.35) \cdot 10^9$	0.566 ± 0.035	$(74.3 \pm 12.9) \cdot 10^9$	0.441 ± 0.021	3.083 ± 0.027
η	$(18.5 \pm 22.1) \cdot 10^9$	0.149 ± 0.070	$(1.4 \pm 1.0) \cdot 10^9$	0.852 ± 0.136	3.318 ± 0.122

Table 5.8.: Parameters of the two-component model, Equation 5.14 [315, 316], which are used to parametrize the neutral pion and η meson spectra, respectively, for the comparisons to models and among the different methods.

other combinations share part of their systematic uncertainties. This is most apparent among the three EMCal related measurements (EMC, PCM-EMC and mEMC), which share not only the trigger related uncertainties, but also the outer material budget uncertainties and part of the cluster related uncertainties. For the PCM and PCM-EMC results, on the other hand, the largest common uncertainty comes from to the inner material budget. The resulting ω_a for the BLUE method can be found in Figure 5.25 for the spectra measurements versus transverse momentum, while the

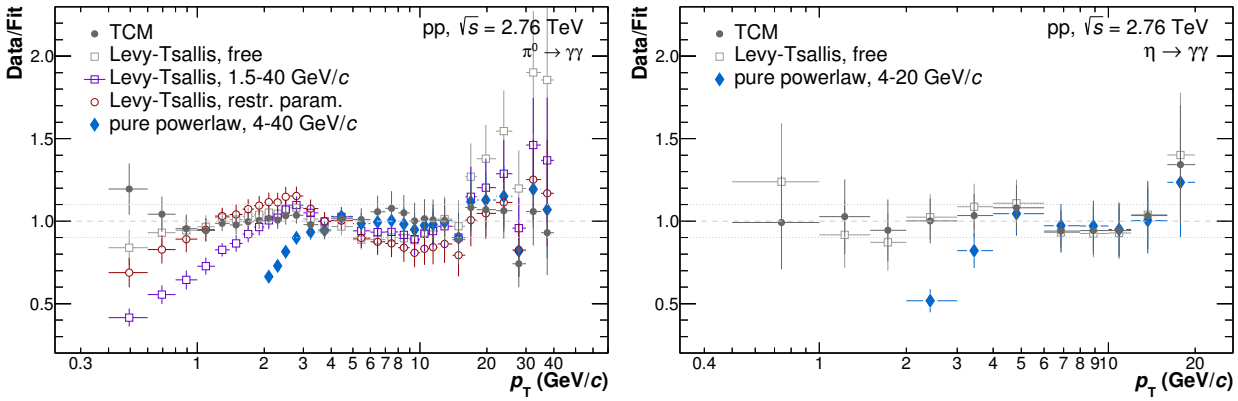

Figure 5.26.: Comparison of the combined neutral pion (left) and eta meson (right) cross section measurement to different fit functions. The ratio to the two-component model (TCM) fit by [315, 316] is shown as closed gray circles, while the ratios of the free Levy-Tsallis fits [308] to the data points are shown as open gray squares. Furthermore, a pure power-law fit to the data above 4 GeV/c is shown as azure diamonds. For the neutral pion the ratio to the fit to the previously published data is shown as red open squares, as well as a free fit only taking into account the data point above 1.5 GeV/c.

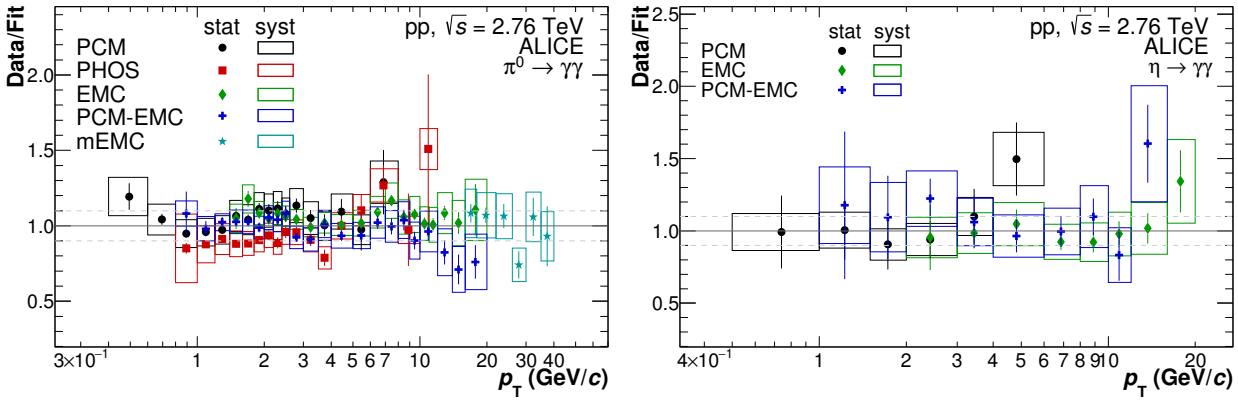

Figure 5.27.: Comparison of the individual measurements in their respective measured transverse momentum ranges relative to the two-component model fits [315, 316] of the final spectra. The final spectra are obtained by combining the individual measurements in the overlapping p_{T} regions with the highest granularity using the full correlation matrix as defined in the BLUE-algorithm [309, 310, 313].

one for the η/π^0 ratio is shown in Figure B.11. For the combination only data points following the same binning are considered. Thus, the PCM and PHOS measurements do not contribute to the final π^0 measurement beyond 6 GeV/c, while their spectra are available beyond that point as seen in Table 5.7 and Figure 5.27. Large ω_a indicate a large contribution to the combined spectrum of the respective method in this transverse momentum bin, while measurements with negative ω_a can be interpreted as highly correlated with at least one other measurement and as such would only reduce the errors and not affect the measured value itself [313]. For most of the transverse momentum slices, at least two data points could be measured except for the lowest and highest momentum points, where only the PCM and mEMC(EMC) method are contributing to the final result for the π^0 and η meson cross section, respectively. Furthermore, the standalone methods tend to carry the larger weight in the combination of the spectra. Mainly, because their statistical errors tend to be better in the respective transverse momentum regions, as it can be seen in Figure 5.24(left).

The combined spectra were fitted with a TCM

$$E\frac{\mathrm{d}^3\sigma}{\mathrm{d}p^3} = A_{\mathrm{e}} \exp\frac{(M - \sqrt{p_{\mathrm{T}}^2 + M^2})}{T_{\mathrm{e}}} + A\left(1 + \frac{p_{\mathrm{T}}^2}{n_{\mathrm{br}} T^2}\right)^{-n_{br}} \tag{5.14}$$

introduced by Bylinkin and Rostovtsev [315, 316], which serves as convenient parametrization of the data without aiming for a physics interpretation. The parameters for the π^0 and η fits are

given in Table 5.8. For both fits the χ^2/n_{dof} values are smaller than 0.5, taking statistical and systematic uncertainties in quadrature. The Levy-Tsallis distribution [308], which could describe the π^0 data in the previously published transverse momentum range [173], fails to describe the extended spectrum. The ratio of the previous fit to the new data can be found in Figure 5.26(left) as red open circles. In general, no Levy-Tsallis parametrization could be found which described the full momentum range to better than 10% in the full transverse momentum region. A simple power-law fit converges and can describe the data if only data points above 4 GeV/c are taken into account for the fit. Then it describes the data starting from 3 GeV/c with an accuracy of $\sim 10\%$. Similar observations have been made for the η meson cross section, where due to its larger systematic and statistical errors, the Levy-Tsallis distribution would suffice as a parameterization, as seen in Figure 5.26(right).
In Figure 5.27 the individual measurements for the π^0 and η meson are compared to the respective two-component model fits. All measurements are shown in the full range available, regardless whether the respective points have been used in the combined result. As already mentioned, the neutral pion spectrum obtained with the PHOS method has already been published in [173], while all the others have either been reanalyzed (PCM) or newly measured (PCM-EMC, EMC, mEMC). The new measurements based on the information provided by the EMCal are consistent with the previously published data for pp collision at $\sqrt{s} = 2.76$ TeV and the combination of all of the results improves the precision of the neutral pions significantly. The figure also demonstrates an approximately fourfold extension of the p_{T} reach of the measurement by using the EMCal.
For the η meson this data represents the first measurement of the cross section for pp collisions at $\sqrt{s} = 2.76$ TeV, spanning from 0.6 GeV/c to 20 GeV/c. The agreement of the different measurement techniques is of the order of $10 - 20\%$ and thus within the statistical errors. Below 2 GeV/c, the measurement is dominated by the PCM reconstruction method, while above 4 GeV/c the EMC measurement dominates the combination. The PCM-EMC measurement contributes about 20% to the measurement, decreasing the uncertainties for nearly all transverse momentum bins. Similar observations can be made for the agreement of the η/π^0 ratio and the contributions of the individual measurements, although the correlation factors are slightly different.

5.2.2. Results

The combined π^0 and η cross sections in pp collisions at $\sqrt{s} = 2.76$ TeV can be seen in Figure 5.28 and the combined η/π^0 ratio in Figure 5.29. On top of the data, the respective two-component model fits by Bylinkin and Rostovtsev [315, 316] (see Table 5.8) are displayed and the ratio of the combined data points to the respective parameterizations is shown in the panels below. The measured cross sections are compared to recent NLO pQCD calculations [318,319] and Pythia 8.2 [317] generator-level simulations using the widely-accepted Monash 2013 tune [320].
In pp collisions, a large fraction of the hadrons at low p_{T} is produced via soft parton interactions and by resonance decays. These processes cannot be described well within the framework of pQCD. In the event-generators they are taken into account, on the other hand. The pQCD calculation for the π^0 [318], which uses the DSS14 fragmentation functions, describe the data better than the calculations using fragmentation functions solely based on lower energy data [173, 321]. Nonetheless, it seems to follow a different shape than the presented data. It overpredicts the data by about 30% at intermediate p_{T} (5 GeV/c < p_{T} < 16 GeV/c), while it is in agreement with the data at higher and lower momenta. The Pyhtia 8.2 calculation describes the data well above 1 GeV/c, but overpredicts it below $p_{\mathrm{T}} = 1$ GeV/c by up to 30% as well. At very high momenta ($p_{\mathrm{T}} > 15$ GeV/c) this Pythia tune tends to underpredict the data by about 10%. However, this slight deviation is covered by the larger uncertainties of the spectrum at higher momenta.
The measured η cross section has been compared to the calculations using the same Pythia 8.2 tune as well as NLO pQCD calculations [319], using the AESSS fragmentation functions. These fragmentation functions, similar to the DSS07 [321] fragmentation functions for the π^0, do not yet

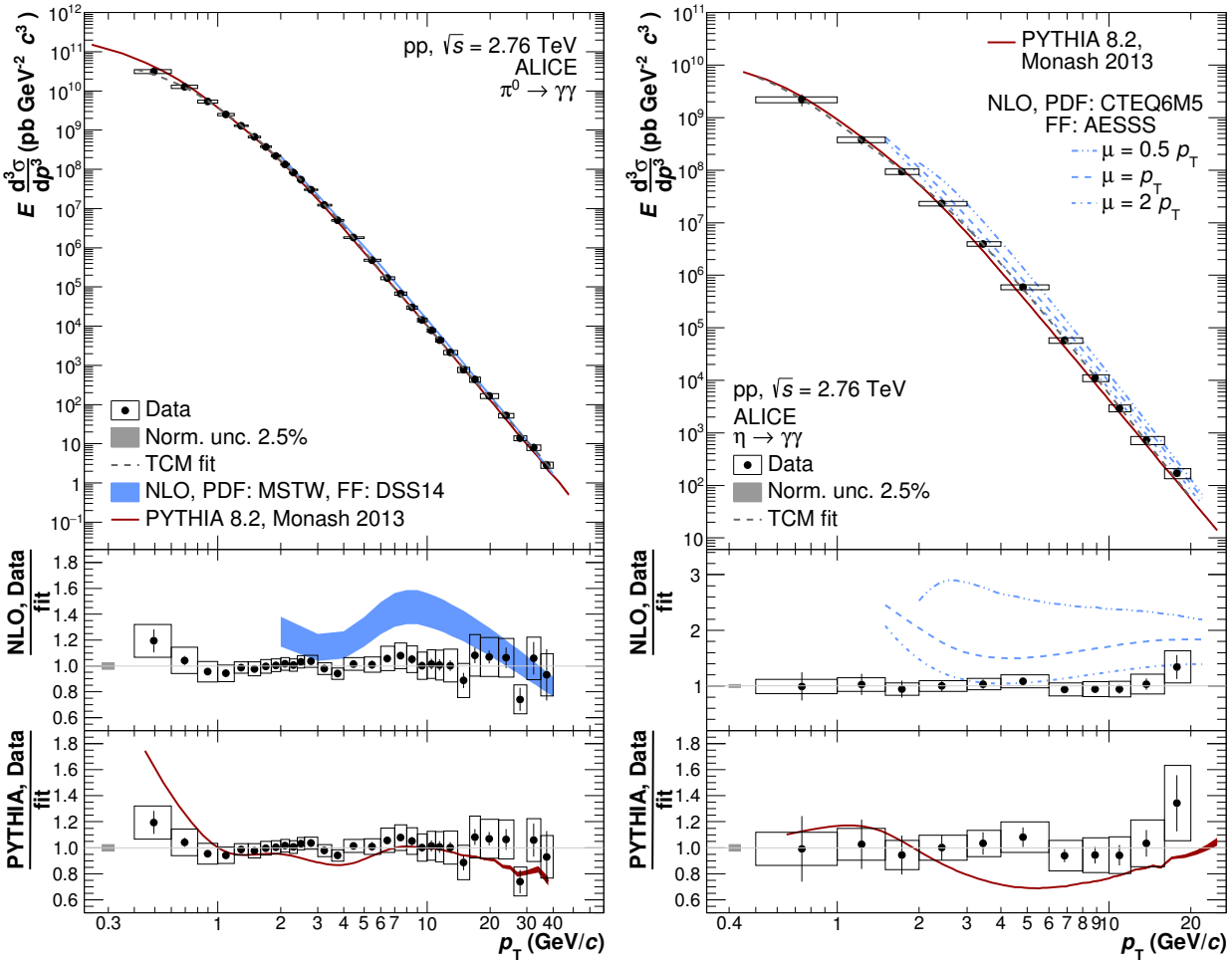

Figure 5.28.: Invariant differential cross section of the π^0 (left, top) and η meson (right, top) for pp collisions at $\sqrt{s} = 2.76$ TeV. The data are compared to Pythia 8.2 [317] generator-level simulations using the Monash 2013 tune as well as recent NLO pQCD calculations [318,319]. The ratios of the data and the calculations to the respective two-component model fits [315,316] to the data are shown in the lower panels. The horizontal error bars denote statistical, the boxes systematic uncertainties.

include data from any of the LHC experiments. Furthermore, they were the first ones to include also the η meson as a final state particle. In order to ascertain the uncertainties of the calculation the authors varied the fragmentation and factorization scale (μ) from $\mu = 0.5p_{\mathrm{T}}$ to $\mu = 2p_{\mathrm{T}}$. At lower energies, the best description of the data point was achieved when choosing the results for $\mu = p_{\mathrm{T}}$. For pp collisions at $\sqrt{s} = 2.76$ TeV, however, only the calculation with μ chosen as $\mu = 2p_{\mathrm{T}}$ can reproduce the data within the uncertainties. For lower values of μ the data are overestimated by up to a factor 2-3. A similar behavior had been seen for the older π^0 predictions, based on the DSS07 fragmentation functions. As such, the inclusion of this η measurement as well as the previously published result at $\sqrt{s} = 7$ TeV in the global fit should improve the fragmentation functions for the η meson significantly and consequently our understanding of the strange versus non-strange fragmentation functions. Even Pythia 8.2 simulations with the Monash 2013 tune perform slightly worse for the η meson than for the π^0, in particular for $p_{\mathrm{T}} > 3$ GeV/c where deviations of up to 1.5σ can be observed. In this region, the data is underestimated by about 20-30%.
When calculation the η/π^0 ratio part of the uncertainties cancel not only for the data but also for the NLO pQCD and Pythia calculations. Thus, even predictions using older fragmentation functions for the π^0 [321] and the η [319], which fail to reproduce the spectra for most of the choices of the fragmentation and factorization scale, are in good agreement with the data as seen in Figure 5.29. Similar statements can be made for the Pythia 8.2 calculations, which can in addition

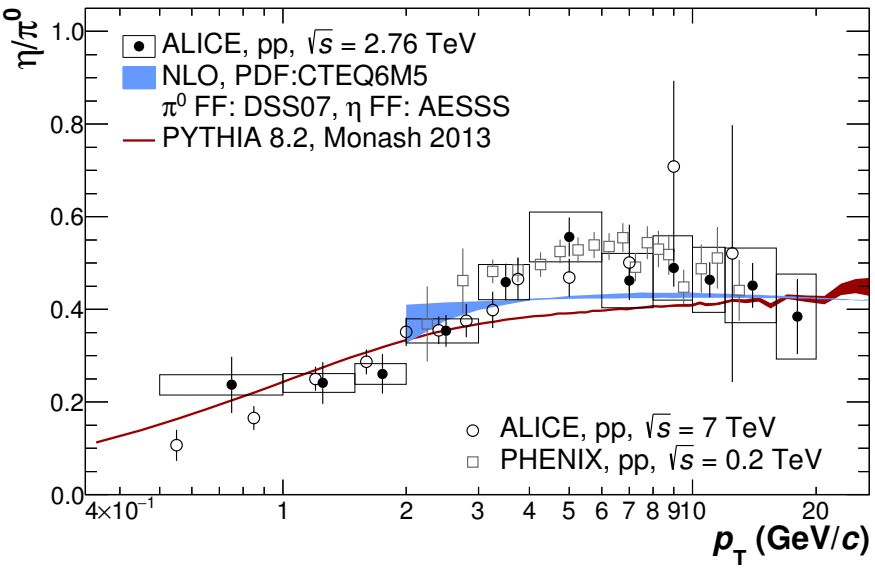

Figure 5.29.: Measured η/π^0 ratio in pp collisions at $\sqrt{s} = 2.76$ TeV compared to NLO pQCD calculations [319,321] and Pythia 8.2 [257] generator-level simulations using the Monash 2013 tune. The horizontal error bars denote statistical, the boxes systematic uncertainties. The data at $\sqrt{s} = 0.2$ TeV [322] and $\sqrt{s} = 7$ TeV [301] are shown with statistical and systematic uncertainties added in quadrature.

reproduce the p_{T}-dependence down to low momenta. However, it also tends to underpredict the ratio above 3 GeV/c by about $20-30\%$, albeit still being in agreement with the data within $1-2\sigma$. The measured η/π^0 ratio is also found to be in agreement with previous measurements in pp collisions at $\sqrt{s} = 0.2$ TeV [322] and $\sqrt{s} = 7$ TeV [301] supporting the assumption that the η/π^0 ratio is collision energy independent. As both mesons exhibit a similar power-law behavior above 4 GeV/c with $n_{\pi^0} = 6.29 \pm 0.02^{\mathrm{stat}} \pm 0.04^{\mathrm{sys}}$ and $n_{\eta} = 6.38 \pm 0.09^{\mathrm{stat}} \pm 0.15^{\mathrm{sys}}$ with χ^2/n_{dof} below 1.8, the ratio flattens above 4 GeV/c at a value of $0.48 \pm 0.02^{\mathrm{stat}} \pm 0.04^{\mathrm{sys}}$. The ratio of the individual power-law fits to the spectra can be seen in Figure 5.26. In this transverse momentum region pQCD should be fully applicable as the contribution from soft parton interactions and resonance decays is close to zero.

The abundance of the neutral pions and eta mesons can be compared to those of other particle species like charged pion, kaons or protons by either looking at their p_{T} differential spectra or their integrated yields and mean transverse momenta. Thus, the measured cross section has been transformed into a yield by multiplying with p_{T} and dividing by the inelastic cross section. The resulting spectra per inelastic collisions are shown in Figure 5.30 together with the ones obtained for the other light flavored hadrons at the same center-of-mass energy [95,162,307,323]. As it can be seen, the neutral and charged pions agree to better than 10% with each other, albeit the neutral pions seem to have a slightly higher yield at intermediate p_{T} (1 GeV/c < p_{T} < 5). Similarly, the neutral and charged kaons agree with each other and show the same spectral shape as the η meson. The total amount, however, seems to be a bit smaller for the η meson ($\sim 80-90\%$) in the measured p_{T} region, which is in accordance with an approximate exponential mass scaling of the total yields. In order to obtain the integrated yields (dN/dy) and mean transverse momentum ($\langle p_{\mathrm{T}} \rangle$) the identified particle spectra have been fitted with a modified Hagedorn function [325].

$$\frac{dN}{dydp_{\mathrm{T}}} = p_{\mathrm{T}}\ A\ \left(\exp\left(-a * p_{\mathrm{T}} - |b| p_{\mathrm{T}}^2\right) + \frac{p_{\mathrm{T}}}{p_0}\right)^{-n} \tag{5.15}$$

Afterwards, the spectra were integrated in the measured transverse momentum region using the measured points and uncertainties, while the fit function was used to estimate the yield in the unmeasured regions. The systematic uncertainties were obtained by moving the data points to their maximum and minimum 1 σ variations of the systematic uncertainties and, afterwards, repeating

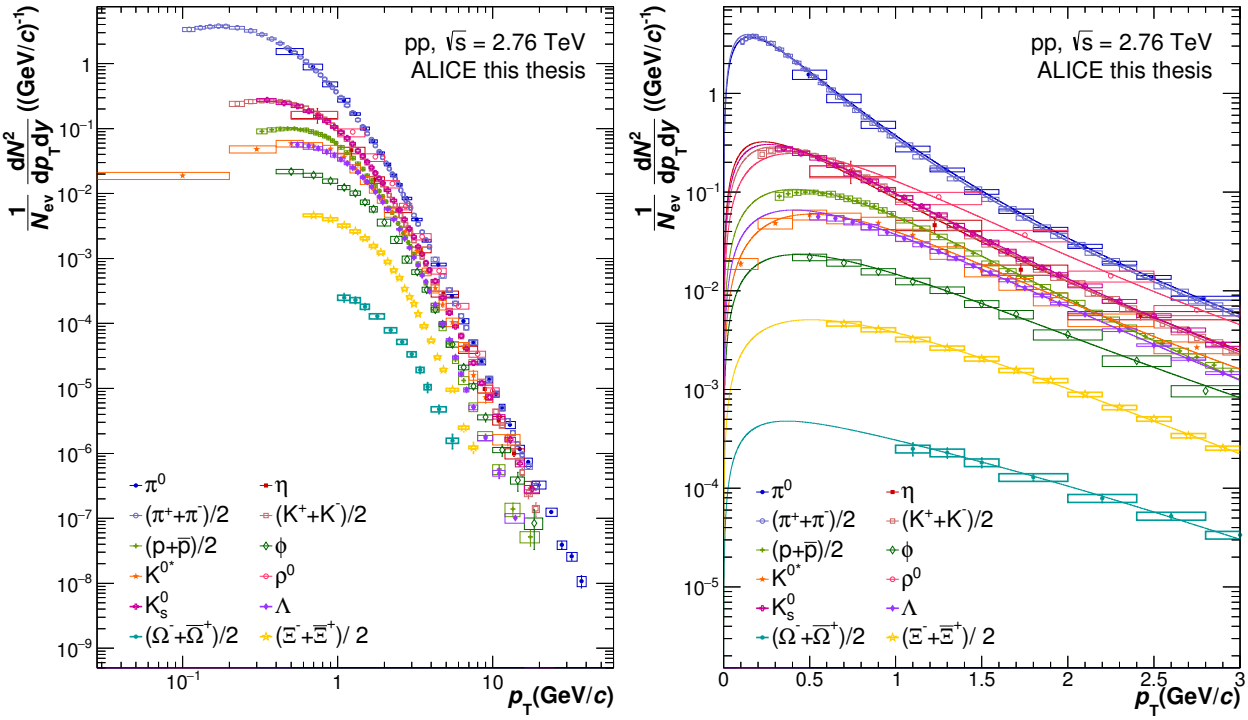

Figure 5.30.: p_T-differential yield for light flavored hadron measured by ALICE in pp collision at $\sqrt{s}$ = 2.76 TeV. The compilation includes the published results of the π^0, η [297], $\pi^{\pm}$, $K^{\pm}$, $p/\bar{p}$ [95], ϕ, K^{*0} [323] and the preliminary results for the K^0_S, Λ [162, 307], Ω, Ξ [162] and ρ^0 [324]. The lines on the right show the modified Hagedorn fits (Equation 5.15) for the various particles in the same color at low transverse momenta. The error bars represent the statistical error, while the systematic errors are indicated by the boxes. The width of the transverse momentum slices is indicated by the width of the systematic error boxes.

the fit using the same functional form. By doing so one can obtain the maximum and minimum yield which is still in accordance with the errors given for each transverse momentum slice. To get an estimate for the extrapolation error in particular at low transverse momenta two different parameterizations were taken into account the Levy-Tsallis [308] and the TCM model [315, 316]. This variation has been kept separate from the other sources of systematic uncertainties as it depends heavily on the choice of functions and might improve in the future. The fits to the spectra using the modified Hagedorn function at low transverse momenta are shown in Figure 5.30(right), while the variations of the fits for the π^0 and η at low momenta are shown in Figure B.12 of Appendix B. The individual parameterizations were optimized such that they reproduce the lowest momentum data points to better than 5% while still describing the full spectrum to better than 10% in order to minimize the extrapolation error. A similar procedure has been followed to obtain the average transverse momenta of the respective particle species, however, in this case the data points were shifted such that they would represent the hardest or softest possible spectrum to obtain the systematic errors. Also here, an additional uncertainty from the choice of the functional from has been taken into account as an independent systematic error. For consistency, all integrated yields and mean p_T values were obtained using the same method. For the ϕ and K^{*0} the values agree within the quoted errors with the published ones [323], even though the error form the functional form is larger with the presented method.

The resulting integrated yields and mean transverse momenta are reported in Table 5.9 and shown as a function of the particle rest mass (M) in Figure 5.31. While the yields fall approximately exponentially as a function of mass the mean transverse momentum ($\langle p_T \rangle$) rises. The latter can be explained by the fact that the pions are more likely to have originated from resonance decays and not directly in the initial hard collisions, thus their spectra are softer. The higher the particle mass,

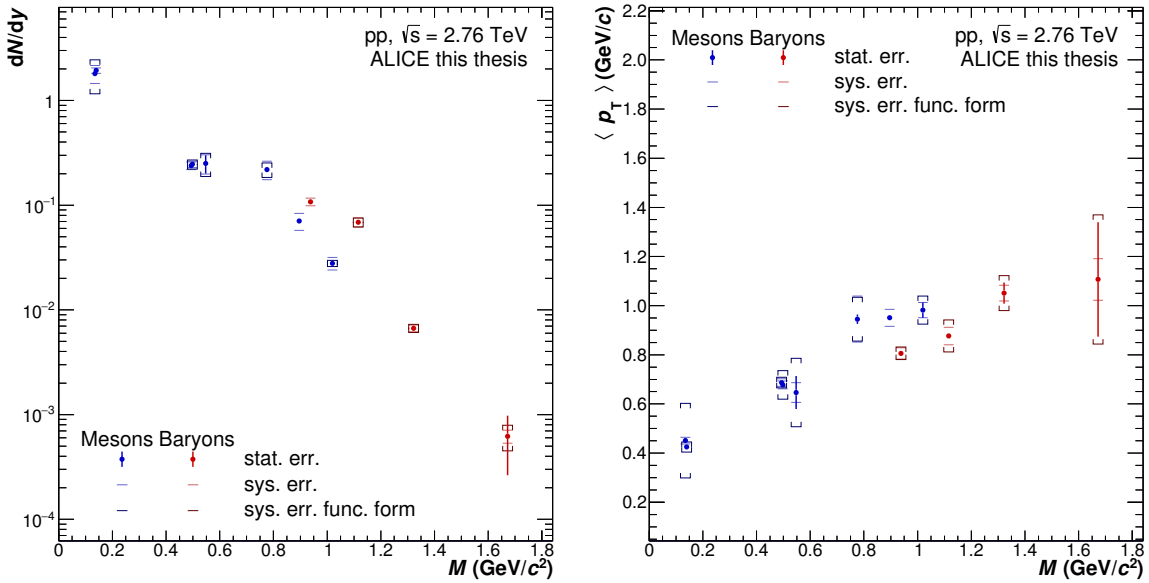

Figure 5.31.: Integrated yield (left) and average transverse momentum (right) as a function of the particle rest mass. The statistical errors are shown as vertical lines while the systematic errors are shown as horizontal lines. An additional error for the choice of the functional form is displayed as brackets.

on the other hand, the more likely it is that they are produced in the collision itself. Furthermore, the baryons and mesons seem to follow a slightly different behavior for the yields and the mean p_{T}. However, this could only be proven if more baryons and mesons would be measured and their systematic uncertainties, in particular those originating from the shape assumption, would be decreased. Furthermore, it can be seen that the average of the π^+ and π^- yield agrees within the systematic errors with that of the π^0. But the central value of the integrated ratio, reported in Table 5.10, is slightly below 1. Based on the naive expectation from the mass scaling and a larger feed down from the resonance decays to the π^0, the ratio was expected to be $\approx 1.05 - 1.10$, which seems to be in contradiction to the measured value, if only the statistical errors are taken into account. If the systematic errors from the extrapolation down to zero momenta, where $\sim 60\%$ of the yield cannot be measured directly for the π^0, are considered as well the basic assumption can no longer be challenged. For the η meson a similar fraction of the yield has been estimated purely based on the fits ($\sim 52\%$), which leads to rather large uncertainties for the integrated η/π^0 ratio of $0.14 \pm 0.03\,^{\mathrm{stat}} \pm 0.04\,^{\mathrm{sys}} \pm 0.06\,^{\mathrm{sys\ f.}}$.
The integrated yields and particle ratios could be used in the future to test the applicability of statistical models like THERMUS [106] or SHARE [107] in small systems as well as basic features of hydrodynamic models in pp collisions ones these calculations become available.

Particle	Mass (GeV/c^2)	dN/dy		ext. (%)	$\langle p_{\mathrm{T}} \rangle$ (GeV/c)	
π^0	0.134977	1.80	$\pm 0.06^{\text{ stat}}$ $\pm 0.35^{\text{ sys}} \pm 0.66^{\text{ sys f.}}$	59	0.451	$\pm 0.008^{\text{ stat}}$ $\pm 0.013^{\text{ sys}} \pm 0.151^{\text{ sys f.}}$
$(\pi^+ + \pi^-)/2$	0.13957	1.9318	$\pm 0.0005^{\text{ stat}}$ $\pm 0.1162^{\text{ sys}} \pm 0.1028^{\text{ sys f.}}$	12	0.4249	$\pm 0.0001^{\text{ stat}}$ $\pm 0.0088^{\text{ sys}} \pm 0.0207^{\text{ sys f.}}$
$(K^+ + K^-)/2$	0.493677	0.2386	$\pm 0.0003^{\text{ stat}}$ $\pm 0.0200^{\text{ sys}} \pm 0.0088^{\text{ sys f.}}$	13	0.6870	$\pm 0.0006^{\text{ stat}}$ $\pm 0.0159^{\text{ sys}} \pm 0.0219^{\text{ sys f.}}$
$\mathrm{K}^0_{\mathrm{S}}$	0.497614	0.246	$\pm 0.001^{\text{ stat}}$ $\pm 0.017^{\text{ sys}} \pm 0.025^{\text{ sys f.}}$	26	0.678	$\pm 0.002^{\text{ stat}}$ $\pm 0.016^{\text{ sys}} \pm 0.058^{\text{ sys f.}}$
η	0.547853	0.25	$\pm 0.05^{\text{ stat}}$ $\pm 0.05^{\text{ sys}} \pm 0.06^{\text{ sys f.}}$	52	0.65	$\pm 0.07^{\text{ stat}}$ $\pm 0.04^{\text{ sys}} \pm 0.14^{\text{ sys f.}}$
ρ^0	0.77549	0.219	$\pm 0.006^{\text{ stat}}$ $\pm 0.044^{\text{ sys}} \pm 0.035^{\text{ sys f.}}$	27	0.95	$\pm 0.02^{\text{ stat}}$ $\pm 0.09^{\text{ sys}} \pm 0.09^{\text{ sys f.}}$
K^{*0}	0.896	0.0705	$\pm 0.0008^{\text{ stat}}$ $\pm 0.0131^{\text{ sys}}$	0	0.950	$\pm 0.006^{\text{ stat}}$ $\pm 0.035^{\text{ sys}} \pm 0.0002^{\text{ sys f.}}$
$(p + \bar{p})/2$	0.938272	0.1076	$\pm 0.0002^{\text{ stat}}$ $\pm 0.0088^{\text{ sys}} \pm 0.0042^{\text{ sys f.}}$	16	0.806	$\pm 0.001^{\text{ stat}}$ $\pm 0.023^{\text{ sys}} \pm 0.026^{\text{ sys f.}}$
ϕ	1.01946	0.028	$\pm 0.001^{\text{ stat}}$ $\pm 0.004^{\text{ sys}} \pm 0.002^{\text{ sys f.}}$	22	0.98	$\pm 0.03^{\text{ stat}}$ $\pm 0.03^{\text{ sys}} \pm 0.057^{\text{ sys f.}}$
$(\Lambda + \bar{\Lambda})/2$	1.11568	0.0687	$\pm 0.0004^{\text{ stat}}$ $\pm 0.0069^{\text{ sys}} \pm 0.0065^{\text{ sys f.}}$	32	0.877	$\pm 0.004^{\text{ stat}}$ $\pm 0.036^{\text{ sys}} \pm 0.065^{\text{ sys f.}}$
$(\Xi^- + \bar{\Xi}^-)/2$	1.32171	0.0067	$\pm 0.0004^{\text{ stat}}$ $\pm 0.0005^{\text{ sys}} \pm 0.0006^{\text{ sys f.}}$	32	1.05	$\pm 0.05^{\text{ stat}}$ $\pm 0.03^{\text{ sys}} \pm 0.07^{\text{ sys f.}}$
$(\Omega^- + \bar{\Omega}^+)/2$	1.67245	0.0006	$\pm 0.0004^{\text{ stat}}$ $\pm 0.00009^{\text{ sys}} \pm 0.0002^{\text{ sys f.}}$	57	1.11	$\pm 0.25^{\text{ stat}}$ $\pm 0.09^{\text{ sys}} \pm 0.26^{\text{ sys f.}}$

Table 5.9.: Integrated particle yields and mean transverse momenta for the measured light flavored particles in pp collisions at $\sqrt{s}$ = 2.76 TeV. The systematic errors have been split in two components: those related to the systematic uncertainties of the measurements themselves (*sys*) and those related to the choice of the functional form of the fit (*sys f.*). Furthermore, the extrapolation fraction of the yield is given in the fourth column.

Particle	Particle Ratio to π^0		Particle Ratio to $(\pi^+ + \pi^-)/2$	
π^0	-		0.93	$\pm 0.03^{\text{stat}}$ $\pm 0.19^{\text{sys}} \pm 0.34^{\text{sys f.}}$
$(\pi^+ + \pi^-)/2$	1.07	$\pm 0.04^{\text{stat}}$ $\pm 0.22^{\text{sys}} \pm 0.39^{\text{sys f.}}$	-	
$(K^+ + K^-)/2$	0.132	$\pm 0.004^{\text{stat}}$ $\pm 0.028^{\text{sys}} \pm 0.048^{\text{sys f.}}$	0.1235	$\pm 0.0001^{\text{stat}}$ $\pm 0.0127^{\text{sys}} \pm 0.0080^{\text{sys f.}}$
K^0_S	0.136	$\pm 0.004^{\text{stat}}$ $\pm 0.028^{\text{sys}} \pm 0.051^{\text{sys f.}}$	0.1274	$\pm 0.0006^{\text{stat}}$ $\pm 0.0119^{\text{sys}} \pm 0.0144^{\text{sys f.}}$
η	0.14	$\pm 0.03^{\text{stat}}$ $\pm 0.04^{\text{sys}} \pm 0.06^{\text{sys f.}}$	0.13	$\pm 0.03^{\text{stat}}$ $\pm 0.03^{\text{sys}} \pm 0.03^{\text{sys f.}}$
ρ^0	0.121	$\pm 0.005^{\text{stat}}$ $\pm 0.034^{\text{sys}} \pm 0.048^{\text{sys f.}}$	0.113	$\pm 0.003^{\text{stat}}$ $\pm 0.024^{\text{sys}} \pm 0.019^{\text{sys f.}}$
K^{0*}	0.039	$\pm 0.001^{\text{stat}}$ $\pm 0.011^{\text{sys}} \pm 0.014^{\text{sys f.}}$	0.0365	$\pm 0.0004^{\text{stat}}$ $\pm 0.0071^{\text{sys}} \pm 0.0020^{\text{sys f.}}$
$(p + \bar{p})/2$	0.060	$\pm 0.002^{\text{stat}}$ $\pm 0.013^{\text{sys}} \pm 0.022^{\text{sys f.}}$	0.0557	$\pm 0.0001^{\text{stat}}$ $\pm 0.0057^{\text{sys}} \pm 0.0037^{\text{sys f.}}$
ϕ	0.0154	$\pm 0.0008^{\text{stat}}$ $\pm 0.0037^{\text{sys}} \pm 0.0056^{\text{sys f.}}$	0.0144	$\pm 0.0006^{\text{stat}}$ $\pm 0.0021^{\text{sys}} \pm 0.0013^{\text{sys f.}}$
$(\Lambda + \bar{\Lambda})/2$	0.038	$\pm 0.001^{\text{stat}}$ $\pm 0.008^{\text{sys}} \pm 0.014^{\text{sys f.}}$	0.0355	$\pm 0.0002^{\text{stat}}$ $\pm 0.0042^{\text{sys}} \pm 0.0039^{\text{sys f.}}$
$(\Xi^- + \bar{\Xi}^-)/2$	0.0037	$\pm 0.0003^{\text{stat}}$ $\pm 0.0008^{\text{sys}} \pm 0.0014^{\text{sys f.}}$	0.0035	$\pm 0.0002^{\text{stat}}$ $\pm 0.0003^{\text{sys}} \pm 0.0004^{\text{sys f.}}$
$(\Omega^- + \bar{\Omega}^+)/2$	0.0003	$\pm 0.0002^{\text{stat}}$ $\pm 0.00008^{\text{sys}} \pm 0.0002^{\text{sys f.}}$	0.0003	$\pm 0.0002^{\text{stat}}$ $\pm 0.00005^{\text{sys}} \pm 0.00009^{\text{sys f.}}$

Table 5.10.: Integrated particle ratio with respect to the neutral or averaged charged pion for pp collisions at $\sqrt{s} = 2.76$ TeV. The systematic errors have been split in two components: those related to the systematic uncertainties of the measurements themselves (*sys*) and those related to the choice of the functional form of the fit (*sys f.*).

5.3. Neutral Pions and Eta Mesons in p–Pb Collisions at $\sqrt{s_{\mathrm{NN}}}$ = 5.02 TeV

5.3.1. Interpolated Reference Spectra for pp Collisions at $\sqrt{s}$ = 5.02 TeV

As there are currently no measured π^0 or η spectra available for pp collisions at $\sqrt{s}$ = 5.02 TeV, the pp reference spectra, which will later be used to calculate the R_{pA}, are calculated based on a p_{T} wise power-law interpolation between the measured spectra at $\sqrt{s}$ = 2.76 TeV (Section 5.2) and the respective measurements at $\sqrt{s}$ = 7 TeV [326] and $\sqrt{s}$ = 8 TeV [327]. To be able to later cancel common systematic error sources among the pp and p–Pb measurements the interpolation has been performed for each reconstruction technique independently. Consequently, also in the interpolation those uncertainties, which are common among the pp measurements at different center-of-mass energies can be neglected, when performing the power-law fits. This leads to a better constrained interpolation function and thus more realistic interpolation errors. For the presented measurements, the inner (4.5%/9%) and outer material budget uncertainties (4.2%) as well as the uncertainties related to the SPD pile-up rejection (< 1%)) could be neglected. These uncertainties will later also cancel in the R_{pA} calculation, while they are added quadratically to the other systematic uncertainties if the interpolated spectra are displayed directly.
As the exponent α of the power-law function

$$f(\sqrt{s}) = A(\sqrt{s})^{\alpha} \tag{5.16}$$

can vary versus transverse momentum, each transverse momentum slice has been fitted independently, with α and A as free parameters. However, due to the fact that the p_{T} slicing at different center-of-mass energies has been optimized according to the statistics in the respective pp data set, none of them fully agrees with each other or with the p–Pb measurement. Thus, as a first step for the interpolation the spectra are fitted with a TCM fit and consecutively rebinned according to that fit. While the respective statistical and systematic errors are interpolated from the original ones at the respective energies using linear interpolation among neighboring transverse momentum slices. To illustrate this procedure, the ratios of the measured π^0 spectra using the PCM-EMC reconstruction method with respect to their fits at $\sqrt{s}$ = 2.76 TeV and $\sqrt{s}$ = 8 TeV are shown in Figure 5.32(colored points). In addition, the ratios of the rebinned spectra are show with gray markers together with the relative interpolated total uncertainties. This procedure does not only allow to smoothen small statistical fluctuations for the measured spectra at the different input energies, but corrects for the differently shifted average transverse momentum at the same time. Which allows to obtain the fully corrected transverse momentum spectra for pp collisions at $\sqrt{s}$ = 5.02 TeV without additional corrections.
An example p_{T} bin of the fits for the combined statistical and uncorrelated systematic errors is shown in Figure 5.33 (left), while the simulated invariant cross sections using Phythia 8.2 Monash as generator can be seen on the right side of the same Figure for a similar transverse momentum slice. In order to estimate the relative statistical and uncorrelated systematic error for each p_{T} bin, pseudo experiments are performed. For each of the input data points at the different energies a Gaussian with the mean of the value and the width of the respective statistical or uncorrelated systematic uncertainty is created. Afterwards, a value is drawn from each distribution independently, which are treated as the new central values at the respective center-of-mass energy. These are then fitted with the power-law and the resulting calculated interpolated point is stored. This procedure is repeated 500 times for each of the uncertainty components and the mean of the resulting distribution represents the central value at that p_{T} if one would only interpolate with the statistical or systematic uncertainty, respectively. The width of the distribution reflects the statistical or uncorrelated systematic uncertainty respectively. As the central values might differ slightly from the combined value, the relative errors are calculated and assigned to the values of the combined fit. In the example plots, the black data points represent the cross section of the

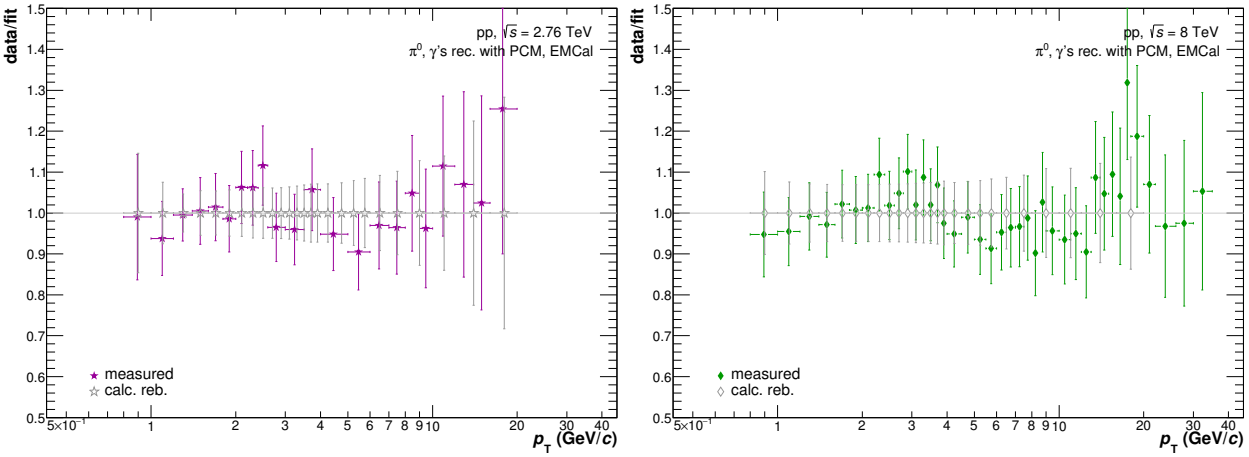

Figure 5.32.: Comparison of original spectra (colored) for the π^0 in pp collisions at $\sqrt{s} = 2.76$ TeV (left) and $\sqrt{s} = 8$ TeV (right) to their respective fits. The rebinned spectra with the respective total uncertainties are shown in gray on each plot.

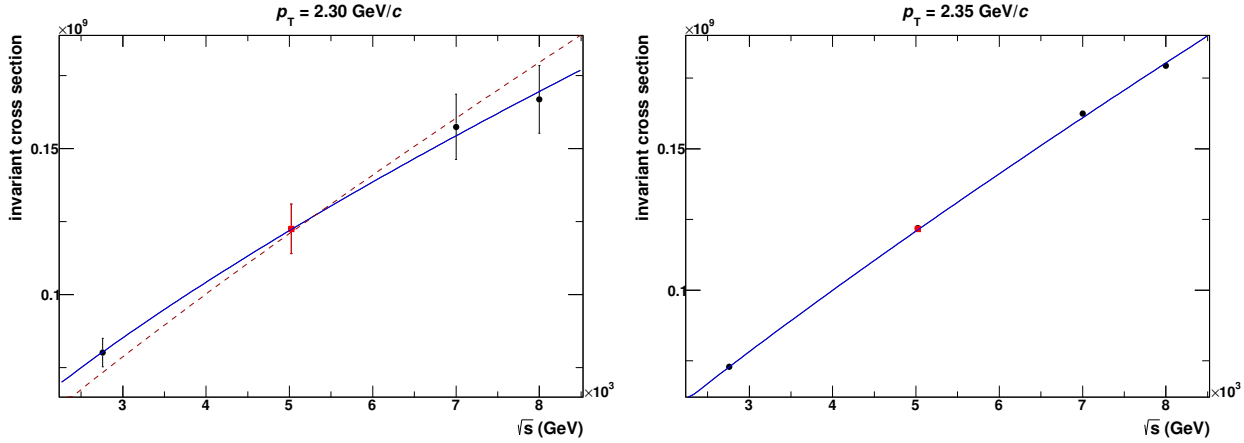

Figure 5.33.: Example of a transverse momentum slice of the cross section measurements of the π^0 to illustrate the interpolation procedure. Left: The interpolation is shown for the measured cross sections (black) with their combined statistical and uncorrelated errors together with the default fit (blue) and the fit using the fixed α from the Pythia 8.2 interpolation (red dashed). Right: The interpolation of the Pythia 8.2 cross sections of the π^0 (black) and their statistical errors, with the default fit to these points (blue). The red points in both plots represent the estimated cross section from the respective fits with their respective errors, estimated based on pseudo experiments with 500 trials.

π^0 in that transverse momentum slice after the rebinning has been performed, while the red data point correspond to the calculated value at $\sqrt{s} = 5.02$ TeV with the respective error estimate. Additionally, the most probable power-law fit using Equation 5.16 to the data points is shown as a blue line.

The statistical and uncorrelated systematic uncertainties for the PCM-EMC measurements entering the interpolation procedure can be found in Figure 5.34 together with the corresponding calculated errors for pp collisions at $\sqrt{s} = 5.02$ TeV as yellow points. The latter have been obtained following the previously outlined procedure. Similar compilations for the EMC and PCM measurements can be found in Appendix B.2.2. The statistical error of the interpolate PCM-EMC π^0 measurement is driven by those related to the respective measurements at $\sqrt{s} = 2.76$ TeV and $\sqrt{s} = 7$ TeV. As these data sets have either the smallest statistics for the minimum bias triggers ($\sqrt{s} = 2.76$ TeV) or a reduced acceptance for the EMCal ($\sqrt{s} = 7$ TeV). As a consequence the statistical error decreases from 11.3% at $p_{\mathrm{T}} = 0.7$ GeV/c to 2.5%-3% at intermediate transverse momenta ($1 - 4$ GeV/c) and afterwards rises nearly linearly to 15% at $p_{\mathrm{T}} = 18$ GeV/c. The uncorrelated systematic error at low momenta is smallest for the data collected at $\sqrt{s} = 2.76$ TeV,

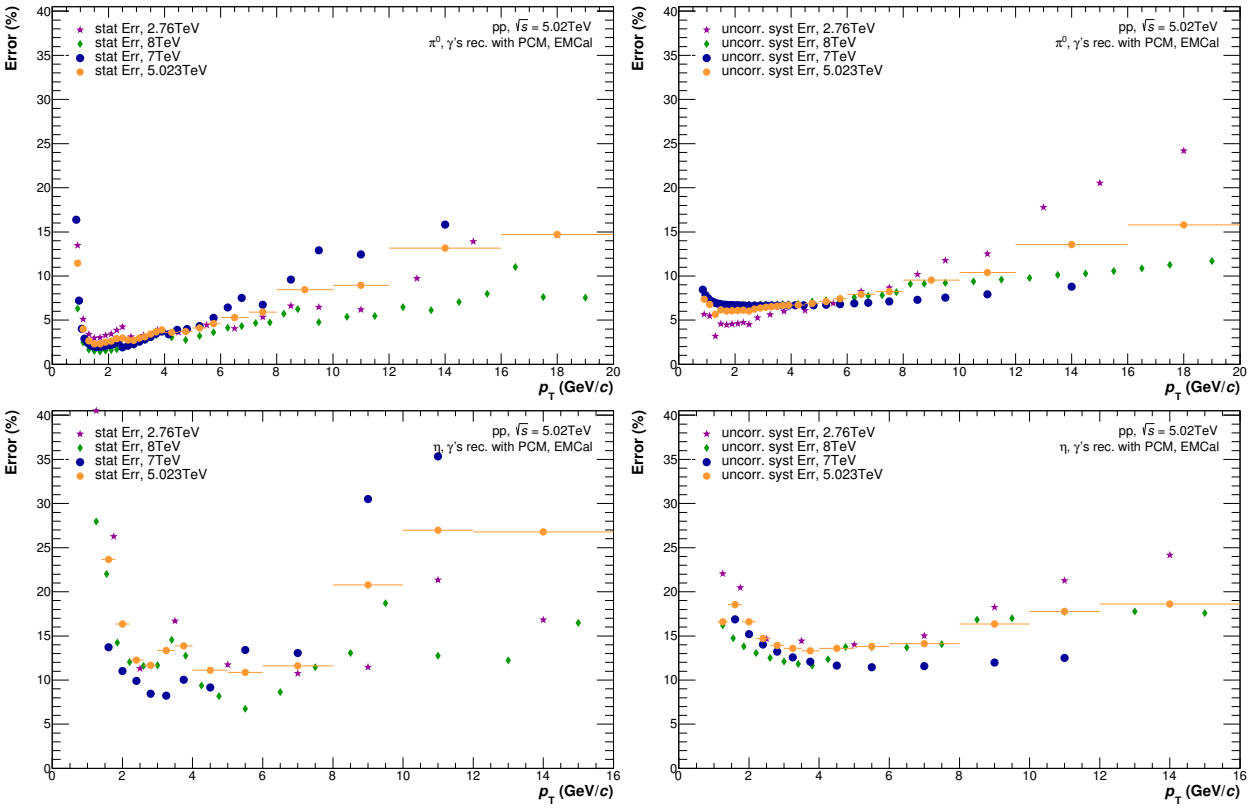

Figure 5.34.: Comparison of the relative statistical (left) and uncorrelated systematic (right) uncertainties of the PCM-EMC neutral meson reconstruction technique for π^0 (upper row) and η (lower row) at the three base energies $\sqrt{s} = 2.76$ TeV (violet), $\sqrt{s} = 7$ TeV (blue) and $\sqrt{s} = 8$ TeV (green) to the interpolated ones at $\sqrt{s} = 5.02$ TeV (yellow).

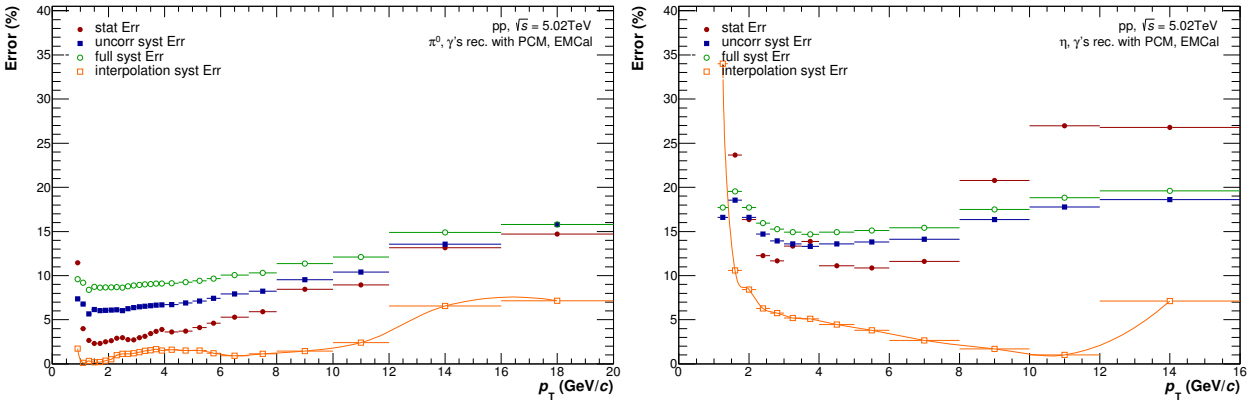

Figure 5.35.: Comparison of the relative error contributions to the interpolated reference spectrum at $\sqrt{s} = 5.02$ TeV for π^0 (left) and η (right) for the PCM-EMC neutral meson reconstruction technique.

while the 7 and 8 TeV data sets seem to be better understood at higher transverse momenta. As a result, the interpolated uncorrelated systematic error stays nearly constant at $6 - 7\%$ from $1 - 5$ GeV/c and then slowly rises to about 15% in the highest transverse momentum slice. For the η, on the other hand, all energies exhibit a similar performance with a statistical uncertainty of about 12% at intermediate transverse momenta and a similarly sized uncorrelated systematic error. In case of the PCM measurements, the resulting statistical uncertainties for pp collisions at $\sqrt{s} = 5.02$ TeV coincide with those of the results at $\sqrt{s} = 8$ TeV, while the systematic errors are closer to those of the measurement at $\sqrt{s} = 2.76$ TeV. The latter is mainly driven by the slightly worse data taking conditions in the 2011 and 2012 data taking campaigns in particular for the

TPC. If it would have been possible to analyze the data collected in 2015 at the correct reference energy of $\sqrt{s} = 5.02$ TeV already, a similar statistical uncertainty would have been expected as shown for the interpolation, as the minimum bias statistics is similar to that of the data collected at $\sqrt{s} = 8$ TeV. For the EMC, the statistical and systematic uncertainties are very similar for different center-of-mass energies, which leads to similar at $\sqrt{s} = 5.02$ TeV as well.
Independently of the already assigned systematic errors originating from the original measurements at different energies, another source of systematics has to be considered, when using an interpolated reference spectrum: the error on the interpolation procedure itself. Even though the interpolation among three different energies to a fourth using a p_{T} wise power-law fit is motivated by the behavior of QCD at high transverse momenta, it cannot be guaranteed to work at low momenta. Thus, to estimate the error, introduced by this assumption, the same interpolation procedure has been performed with input from Pythia 8.2 Monash 2013 calculations for the respective mesons. This has the advantage that the respective calculation at the desired energy of $\sqrt{s} = 5.02$ TeV can be obtained as well and then compared to the interpolated value for each p_{T} slice. The relative deviation between the calculated and interpolated point is then taken into account for the systematic error arising from the interpolation procedure. In addition, the α_{MC} value is stored and the data (with combined errors) are fitted again with this value fixed for α of the power-law fit (red dashed line in Figure 5.33(left)), only leaving the normalization as free parameter. Then again the expected value at $\sqrt{s} = 5.02$ TeV is calculated and the relative difference to the central point purely from data is added in quadrature to the interpolation error as described previously. An overview of the resulting relative errors for pp collisions at $\sqrt{s} = 5.02$ TeV for the PCM-EMC reconstruction technique can be found in Figure 5.35, while those for the PCM and EMC reconstruction can be found in Appendix B.2.2. In general the interpolation error is of the order of 1-2% for the π^0 and 1-5% for the η meson using the PCM-EMC reconstruction technique. However, this uncertainty tends to rise significantly towards the lowest and highest transverse momenta. For the other reconstruction techniques, this uncertainty is slightly larger and can contribute up to 5-7% even at intermediate transverse momenta for PCM, while it contributes about $2 - 3\%$ for the π^0 measurement using the EMC.
Figure 5.36 shows the final interpolated spectrum for the PCM-EMC reconstruction technique with the combined statistical and uncorrelated systematic errors together with the respective spectra at the other center-of-mass energies. The comparison among the different interpolated reference spectra using different inputs can be found in Figure 5.37. For these plots, each of the $\pi^0(\eta)$ interpolations has been performed independently using the all available inputs at different center-of-mass energies for the same reconstruction technique. In order to compare them the same procedure has been applied to the respective fully combined measurements for pp collisions at $\sqrt{s} = 2.76,\ 7$ and 8 TeV and the resulting reference spectra have been fitted with TCM fits (Equation 5.14) to which the individual measurements are then compared. For the reconstruction techniques, like PCM-PHOS and PCM-Dal, where no measurements were available at any pp energy the combined reference spectrum in the correct binning has been chosen and will later be used for the R_{pA} calculation. In general, the agreement of the different interpolated reference spectra is better than 10%. However, the spectra tend to disagree slightly more, deviating up to 20%, towards the edges of the transverse momentum ranges in which the individual measurements can be performed. A similar behavior can be found when looking at the spectra at the inputed center-of-mass energies, like Figure 5.27, which was expected and desired, as most likely similar biases are present in the p–Pb measurements.
The interpolation has additionally been validated through a comparison with the first measurements of the corresponding spectra in pp collisions at $\sqrt{s} = 5.02$ TeV, based on the data collected in 2015 [328]. This comparison can be seen in Figure 5.38 for the π^0 measured with the PCM-EMC and EMC methods. The interpolation is consistent with the measured spectra within the statistical uncertainties of the measurement at $\sqrt{s} = 5.02$ TeV.

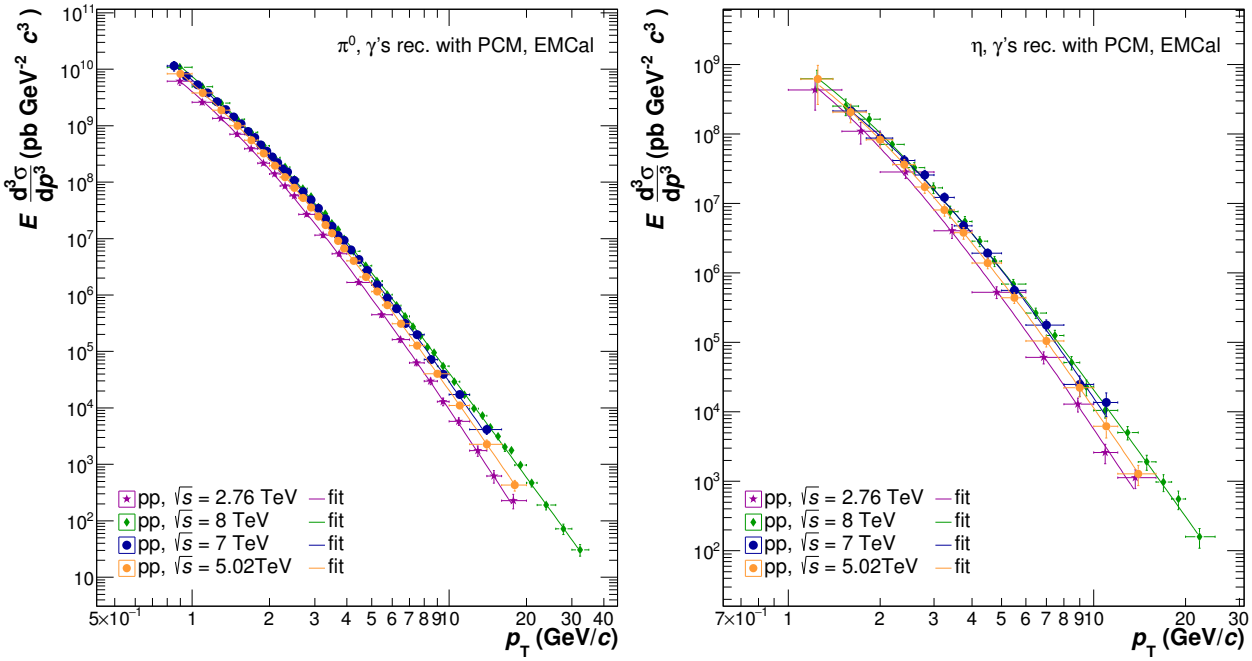

Figure 5.36.: Comparison of cross sections for π^0 (left) and η (right) for all energies measured (interpolated) using PCM-EMC with the calculated reference displayed in the p_T binning of the respective p-Pb spectra.

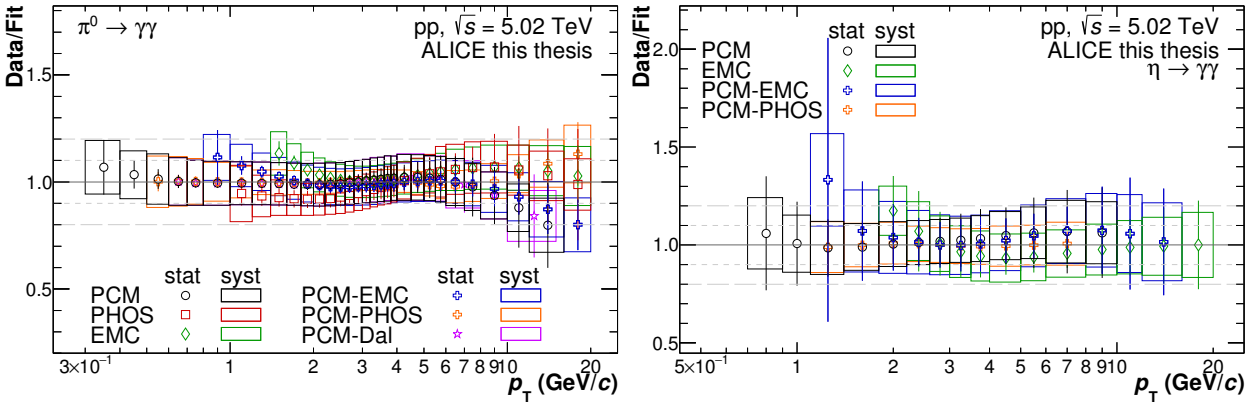

Figure 5.37.: Comparison of the calculated π^0 (left) and η (right) spectra using different reconstruction technique for pp collisions at $\sqrt{s} = 5.02$ TeV. The comparison is done with respect to the fit to the interpolation of the combined results.

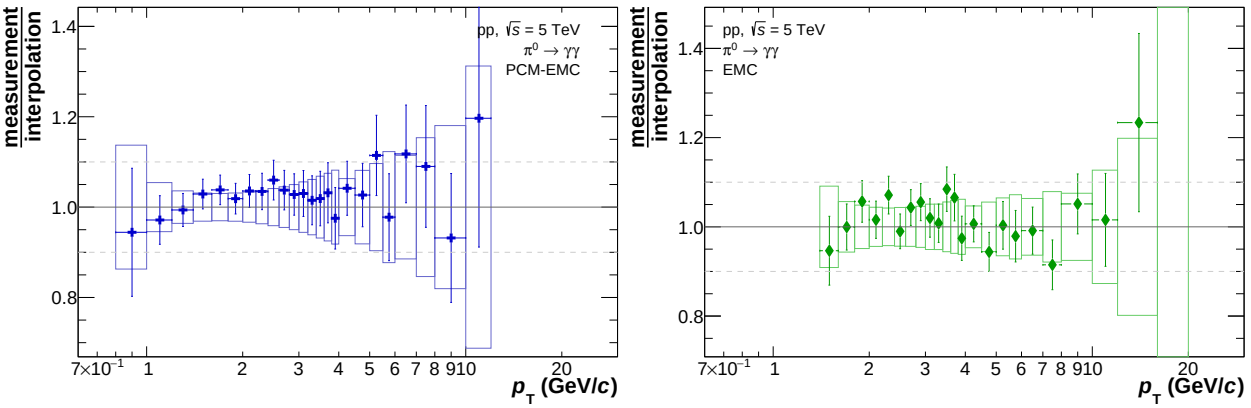

Figure 5.38.: Comparison of the calculated and measured π^0 in spectra in pp collisions at $\sqrt{s} = 5.02$ TeV for the PCM-EMC (left) and EMC (right) reconstruction technique [328]. The error bars indicate the quadratically added statistical error of the measured and calculated reference, while the boxes around unity reflect the uncertainty of the measurement alone.

5.3.2. Systematic Uncertainties and Combination of Individual Measurements

Similar to the analyses carried out for pp collisions at $\sqrt{s} = 2.76$ TeV, the systematic errors have been calculated independently for each of the measurements. While a discussion of the systematic uncertainties of the PCM-Dal [298], PHOS [302] and PCM-PHOS [303] can be found in the respective theses, this chapter will focus on the corresponding uncertainties for the PCM-EMC, PCM and EMC measurements. The latter two had to be reevaluated and refined in the context of this thesis with respect to the previously presented ones [299, 300] to be able to continue with the analyses towards the direct photon extraction in the same data set. As for the previously presented analyses most of the systematic errors have been evaluated by varying the different photon and meson selection criteria and afterwards comparing the fully corrected spectra. In order to suppress the influences of purely statistical fluctuations, however, the resulting differences were only considered if they were significant and passed the Barlow criteria [329]. As this procedure in some cases might still lead to unphysical fluctuations the resulting uncertainties have been smoothed using reasonable functional forms in addition, which reflect the expected behavior of the respective uncertainties.
Although the uncertainties for the EMC, PCM and PCM-EMC have been evaluated independently large parts of these have common origins, which is why they are going to be discussed together once more. The detailed p_{T} dependent uncertainties for each source can be found in Appendix B.2.3. Within the Tables 5.11-5.13, on the other hand, the uncertainties are grouped once more according to their main origin and reported at different transverse momenta highlighting the strength of the different reconstruction techniques. For most systematic uncertainty sources the same grouping has been chosen as for the corresponding uncertainties on the pp measurements at $\sqrt{s} = 2.76$ TeV, thus the emphasize in this section will be on their respective p_{T} behavior. In addition to the uncertainties for the p–Pb measurements, also those related to the interpolated pp reference as well as the R_{pA} are given in the corresponding tables, together with the respective statistical uncertainties for each measurement.
At first, the uncertainties related to the EMC and PCM photon reconstruction in p–Pb will be discussed. Afterwards, the respective uncertainties affecting the meson reconstruction as well as the event selection will be summarized. The detailed discussion on the statistical and systematic uncertainties related to the respective pp reference calculation, however, can be found in the previous section and the number are only reported for comparison and only a short summary is given regarding their transverse momentum dependence and their impact on the R_{pA} uncertainties.
EMCal clustering: In this uncertainty classm the mismatches of the clustering algorithm between data and simulation are summarized. As such, it includes the variations of the minimum energy and time on cluster and cell level, as well as the variations of the number of cells per cluster and the cluster shape parameter σ^2_{long}. The uncertainty on the π^0 spectrum ranges from 1.1% at low transverse momenta for the PCM-EMC reconstruction method to 2% at the highest momenta. If the π^0 is reconstructed with the EMC technique this systematic error ranges from 1.8% at intermediate momenta to about 3.5% at 14 GeV/c. For the η reconstruction, this systematic uncertainty group contributes about twice as much at the same momenta to the total error as for the π^0 while it exhibits a similar transverse momentum dependence. When evaluating this uncertainty on the η/π^0 only a small fraction of the systematic errors among the π^0 and η seems to cancel, which leads to a systematic uncertainties ranging from 3% at 1.5 GeV/c to 6% at 14 GeV/c. While the transverse momentum dependence of the uncertainties is similar to the one seen for pp collisions at $\sqrt{s} = 2.76$ TeV the magnitude differs, due to the quality of the description of the underlying event for pp and p–Pb collision. This leads to slightly larger uncertainties in particular for the η meson in p–Pb collisions.
EMCal cluster energy calibration: The uncertainty related to the cluster energy calibration contains the remaining relative difference between data and simulation regarding the mass position for the respective methods as well as variation of the calibration schemes described in Section 4.3.1.

p_{T} interval (GeV/c)	0.8–1.0		2.4–2.6			6–7			12–16		
Method	PCM	P-E	PCM	P-E	EMC	PCM	P-E	EMC	PCM	P-E	EMC
EMCal clustering	-	1.1%	-	1.1%	1.8%	-	1.3%	2.1%	-	2.0%	3.4%
EMCal energy calib.	-	2.0%	-	2.0%	1.7%	-	2.4%	1.9%	-	4.0%	2.5%
Track matching	-	0.3%	-	0.3%	2.7%	-	0.8%	3.1%	-	3.0%	3.8%
Secondary track reco.	0.6%	0.5%	0.3%	0.5%	-	0.4%	0.7%	-	0.9%	1.0%	-
Electron PID	2.0%	0.5%	1.2%	0.5%	-	1.5%	0.7%	-	8.7%	1.9%	-
PCM photon PID	0.5%	1.6%	0.6%	0.6%	-	1.6%	1.3%	-	5.7%	5.0%	-
Signal extraction	2.7%	5.1%	1.9%	1.4%	1.5%	2.3%	2.2%	1.6%	4.6%	5.7%	5.4%
Efficiency	-	2.0%	-	2.0%	2.0%	-	2.0%	2.0%	-	2.0%	2.0%
Inner material	9.0%	4.5%	9.0%	4.5%	-	9.0%	4.5%	-	9.0%	4.5%	-
Outer material	-	2.8%	-	2.8%	4.2%	-	2.8%	4.2%	-	2.8%	4.2%
Pile-up	1.4%	-	0.6%	-	-	0.5%	-	-	0.7%	-	-
Tot. sys. uncertainty	9.7%	8.1%	9.3%	6.3%	6.2%	9.6%	6.9%	6.5%	14.6%	11.1%	9.2%
Stat. uncertainty	1.2%	6.5%	1.8%	1.4%	1.3%	5.1%	3.8%	2.0%	21.6%	13.3%	6.9%
Uncorr. sys. pp ref	5.0%	7.4%	4.3%	6.0%	6.3%	6.3%	7.9%	8.0%	13.1%	13.5%	10.3%
Interpolation sys. pp ref	0.8%	1.7%	6.7%	1.1%	2.6%	4.2%	0.9%	2.8%	8.1%	6.5%	3.1%
Stat. pp ref	1.9%	11.5%	3.4%	3.0%	2.5%	12.0%	5.3%	2.9%	25.0%	13.2%	8.1%
Tot. sys. unc. R_{pA}	6.3%	9.7%	8.4%	7.1%	8.1%	8.1%	6.5%	9.8%	19.2%	17.9%	13.4%
Stat. unc. R_{pA}	2.3%	13.2%	3.9%	3.3%	2.8%	13.0%	6.5%	3.5%	33.0%	18.7%	10.6%

Table 5.11.: Systematic uncertainty for various sources and methods assigned to the π^0 spectrum measurement at different p_{T} intervals for p–Pb collisions at $\sqrt{s_{\mathrm{NN}}}$ = 5.02 TeV. Furthermore, the uncertainties for the pp reference contributing to the R_{pA} are given. For comparison, the total systematic and the statistical uncertainties are also given for the π^0 spectra and R_{pA}. P-E stands for PCM-EMC.

As it can be seen in Figure 4.13(left) the optimal calibration leads to an agreement of the mass positions, which is better than 0.2(0.4)% on average for both reconstruction techniques of the $\pi^0(\eta)$. Assuming that the spectra fall with approximately $p_{\mathrm{T}}^{-7.2}$, this leads to an uncertainty on the neutral pion and η meson spectrum of 1.4(2.8)% for the neutral pion and η meson, respectively. The variation of the calibration schemes contributes another $1-4\%$ for the π^0 depending on momentum, while this uncertainty ranges from $1.5-10\%$ for the η meson and the η/π^0-ratio, due to the different photon momenta.

Track matching to cluster: As for the same analyses in pp collisions, also the track matching criteria have been varied for the EMC and PCM-EMC meson reconstruction from only rejecting centrally matched clusters to rather loose matching criteria. The rejection of clusters from charged particles is, however, more important for p–Pb collisions as otherwise the signal-to-noise ratio is worse in particular for the EMC reconstruction. While for the PCM-EMC method affects mainly the η meson is affected. Consequently, the uncertainty arising from the variations of the track-matching parameters ranges from 0.3% to 3.0% for the π^0 reconstruction using PCM-EMC and from 2.7% to 3.8% for the π^0 reconstruction using EMC. The η reconstruction using PCM-EMC is particularly affected at the lowest and highest transverse momenta, due to the auto-correlation seen in Figure 4.9, which leads to a third peak like structure between the π^0 and η. As a consequence any mismatch between the simulation and the data regarding the track propagation as well as the track density will have the largest effect on the η meson at very low and very high momenta in this reconstruction technique. The corresponding systematic uncertainty ranges from 4.7% at 1.5 GeV/c to 1.8% at 3.75 GeV/c to 6.2% at 14 GeV/c. In case of the EMC reconstruction, on the other hand, it increases mildly from 4.3% at 3.75 GeV/c to about 5.6% at 14 GeV/c. The respective uncertainties on the η/π^0-ratio are dominated by those of the η meson and are thus

very similar.

Secondary track reconstruction: When reconstructing photons with the PCM method, only a fraction of the secondary track candidates are considered in the secondary vertex calculation. Consequently, the variation of the selection criteria of these tracks has to be considered in the evaluation of the systematic uncertainties. In order to allow for a maximum acceptance and efficiency, the initial cuts were chosen to be very loose and thus the selection criteria could only be tightened. For instance the minimum transverse momentum cut for the secondary tracks has been raised from 50 MeV to at most 125 MeV, which leads to significant signal loses at low transverse momenta, while testing rigorously the response simulation. In addition, the fraction of TPC found-over-findable clusters and the φ-acceptance have been varied. Where the latter is of particular importance for the PCM-EMC reconstruction due to the limited $\eta - \varphi$ coverage of the EMCal. The resulting uncertainties on the π^0 measurements range from 0.6% at very low momenta to 0.3% at intermediate momenta and 1.0% at the highest transverse momenta. For the respective η and η/π^0 measurements, the uncertainties are slightly larger, reaching up to 3.4%, due to the different decay kinematics and consequently a different relative importance of the very low momentum tracks, which tend to be worse described.

Electron PID: Next to the uncertainty on the material within ALICE the PCM reconstruction is most affected by the uncertainties on the rejection of impurities in the electron sample and later the photon sample itself. In order to estimate these the electron identification and contamination rejection criteria based on the TPC $\mathrm{d}E/\mathrm{d}x$ for the single legs of the reconstructed photon candidates have been varied. In the regions, where the electrons and pions can be separated clearly in the TPC, the resulting systematic uncertainty ranges from 1.2% to 0.5%, while it increases in the transverse momentum regions where the Bethe-Bloch curves of these two particle are either crossing or approaching each other. As a consequence this uncertainty becomes dominant at higher transverse momenta reaching values of 8.7% at 14 GeV/c for the PCM reconstruction technique.

PCM photon PID: To further estimate the photon identification uncertainty for the PCM photons the selection criteria have been varied independent of those of the electron. The resulting uncertainties are of similar size and transverse momentum dependence as those related to the electron identification as both are attempting to test the modeling of the impurities in the simulation which increase towards the edges of the measured spectra. As for the electron identification uncertainty, this error is about a factor two larger for the η meson and only a small fraction cancels in the η/π^0-ratio for the respective measurement technique. This uncertainty is one of the dominant error sources for the η/π^0 measurement.

Signal extraction: Similar to the invariant analyses carried out in pp collisions, the systematic uncertainty related to the yield extraction in these reconstruction techniques has been estimated by taking into account different integration windows around the fitted mass position as well as different normalization windows for the mixed event background. Furthermore, the opening angle between the two photons as well as their energy asymmetry has been varied to test the robustness of the signal extraction procedure with respect to the signal-to-noise ratio. To access the dependence of the yield extraction on the choice of the background classification and the respective number of mixed events, the classification regarding the event multiplicity has been changed from the respective photon multiplicities to the track multiplicities and the number of background events was varied. The contribution from the latter variations, however, is negligible as their effects are mitigated by the remaining background subtraction. For the neutral pion, the signal extraction uncertainties tend to be the largest next to those related to the inner and outer material budget. For the PCM reconstruction technique, this uncertainty ranges from 2.7% at 0.9 GeV/c to 1.9% at 2.5 GeV/c to 4.6% at 14 GeV/c due to its excellent transverse momentum resolution of the photons. When reconstructing the π^0 using the EMC method, on the other hand, this source of systematic uncertainties contributes 1.5% at 2.5 GeV/c and then slowly rises to 5.4% at 14 GeV/c. The increasing uncertainty for the EMC method at higher transverse momenta can be attributed to cluster merging above 10 GeV/c in the EMC, which is not optimally modeled in the detector

p_{T} interval (GeV/c)	1.4–1.8		3.5–4			12–16	
Method	PCM	PCM-EMC	PCM	PCM-EMC	EMC	PCM-EMC	EMC
EMCal clustering	-	2.3%	-	2.4%	2.4%	4.4%	3.7%
EMCal energy calib.	-	3.1%	-	3.5%	4.2%	9.3%	6.4%
Track matching	-	4.7%	-	1.8%	4.3%	6.2%	5.6%
Secondary track reco.	0.8%	0.4%	0.5%	2.0%	-	3.4%	-
Electron PID	2.0%	1.7%	1.9%	1.9%	-	6.0%	-
PCM photon PID	2.0%	6.8%	2.3%	3.0%	-	9.4%	-
Signal extraction	2.6%	9.1%	2.9%	4.6%	6.8%	9.0%	9.3%
Efficiency	-	2.0%	-	2.0%	4.0%	2.0 %	4.0%
Inner material	9.0%	4.5%	9.0%	4.5%	-	4.5%	-
Outer material	-	2.8%	-	2.8%	4.2%	2.8%	4.2%
Pile-up	1.1%	-	0.9%	-	-	-	-
Tot. sys. uncertainty	9.9%	14.1%	10.0%	9.6%	11.0%	19.9%	14.4%
Stat. uncertainty	8.0%	12.0%	8.2%	8.4%	9.7%	38.6%	28.6%
Uncorr. sys. pp ref	8.0%	18.5%	6.9%	13.3%	12.8%	18.6%	14.3%
Interpolation sys. pp ref	0.5%	10.6%	2.8%	5.1%	4.7%	7.1%	3.6%
Stat. pp ref	13.7%	23.6%	14.6%	13.9%	11.6%	26.8%	19.8%
Tot. sys. unc. R_{pA}	9.0%	25.0%	8.4%	18.6%	17.0%	27.6%	20.1%
Stat. unc. R_{pA}	15.9%	26.5%	17.1%	16.2%	15.1%	46.9%	26.0%

Table 5.12.: Systematic uncertainty for various sources and methods assigned to the η spectrum measurement at different p_{T} intervals for data taken in p–Pb collisions at $\sqrt{s_{\mathrm{NN}}}$ = 5.02 TeV. Additionally, the uncertainties for the respective pp reference contributing to the R_{pA} are given and or comparison, the total systematic and the statistical uncertainties are also given for the π^0 spectra and R_{pA}.

p_{T} interval (GeV/c)	1.4–1.8		3.5–4			12–16	
Method	PCM	PCM-EMC	PCM	PCM-EMC	EMC	PCM-EMC	EMC
EMCal clustering	-	3.0%	-	3.1%	3.2%	6.0%	5.2%
EMCal energy calib.	-	3.1%	-	3.5%	4.2%	9.3%	6.4%
Track matching	-	4.6%	-	1.8%	4.3%	6.2%	5.6%
Secondary track reco.	0.8%	0.4%	0.5%	2.0%	-	3.4%	-
Electron PID	2.0%	1.7%	1.9%	1.9%	-	6.0%	-
PCM photon PID	2.0%	6.8%	2.3%	3.1%	-	9.6%	-
Signal extraction	3.0%	9.1%	3.3%	4.8%	6.8%	10.7%	10.7%
Efficiency	-	2.8%	-	2.8%	4.5%	2.8%	4.5%
Tot. sys. uncertainty	4.2%	13.4%	4.5%	8.6%	10.6%	20.6%	15.3%
Stat. uncertainty	8.0%	12.0%	8.4%	8.6%	9.8%	40.7%	29.4%

Table 5.13.: Systematic uncertainty for various sources and methods assigned to the η/π^0 measurement at different p_{T} intervals as determined for p–Pb collisions at $\sqrt{s_{\mathrm{NN}}}$ = 5.02 TeV. For comparison, the total systematic and the statistical uncertainties are also given.

simulations and thus leads to larger uncertainties both for the variation of the opening angle and general background subtraction procedure. In case of PCM-EMC, the uncertainty on the neutral pions is largest at the lowest and highest momenta (5.1% and 5.7%) as in both cases mainly very asymmetry decays can be reconstructed. Consequently, also the statistical error on these data points is significant and the distinction between statistical and systematic variations could only

be done to a certain degree in particular for this uncertainty class. In general, however, the signal extraction at higher transverse momenta is less affected by cluster merging when using PCM-EMC and thus the respective systematic uncertainty is smaller. This can be seen as well at intermediate transverse momenta where this methods profits from both the excellent momentum resolution of the PCM photons and the good energy resolution of the EMC photons above 1.5 GeV/c, leading to uncertainties of $1.5 - 2.2\%$. For the η meson the signal extraction uncertainties are in general larger due to the worsened signal-to-background ratio as well as a worse description of the background using event mixing in general. Consequently, the improved peak resolution when including PCM photons improves the signal extraction uncertainties significantly and the respective errors are smallest for PCM, ranging from 2.6% at 1.5 GeV/c to 2.9% at 3.75 GeV/c, followed by the PCM-EMC reconstruction for which this uncertainty contributes 9.1% at 1.5 GeV/c, 4.6% at 3.75 GeV/c and 9% at 14 GeV/c, respectively. For the EMC reconstruction, this uncertainty should decrease with increasing momenta due to the improved energy resolution of the calorimeter as it was observed for pp collisions. Due to the insufficient amount of Monte Carlo simulations, however, this decrease can not be observed, as the correction factors above 10 GeV/c fluctuate too much to clearly distinguish systematic and statistical effects for the yield extraction uncertainty. Thus, a conservative estimate has been chosen, which leads to errors ranging from 6.8% at intermediate p_{T} to 9.3% at 14 GeV/c. When estimating this uncertainty contribution to the η/π^0-ratio, the two mesons contribute independently and their uncertainties are hence added in quadrature.

Efficiency: In order to assess the uncertainty from the transverse momentum resolution correction, which is folded into the efficiency, the correction factors obtained from the two different minimum bias Monte Carlo generators in p–Pb collisions have been compared. As both generators have different p_{T} distributions for the particles of interest, which agree reasonably well with the data in different p_{T} regions. This variation serves as a mild variation of the shape of the underlying distribution leading to a realistic uncertainty of $1-2\%$ for the PCM-EMC and EMC reconstruction techniques. For the PCM reconstruction, this uncertainty is negligible in particular as the simulated spectra have been iteratively altered to match those seen in the data, which in the current simulations is only possible for track based measurements, as described in Section 5.1.1. Within this uncertainty class also the residual difference between the data like efficiency calculation and the validated efficiency is taken into account where necessary, which originates from imperfections of the residual background subtraction due to the long tail on the left side of the invariant mass peaks caused by converted photons for the calorimetric photon reconstruction. Thus, the total systematic uncertainty assigned to the efficiency calculation amounts to 2% on the π^0 spectra measured with PCM-EMC and EMC and 2%(4%) for the η measured with PCM-EMC and EMC, respectively. As it is not obvious that these uncertainties cancel in the η/π^0 ratio they are added in quadrature for the respective measurements.

Secondary correction: As the fraction of secondary pions is relatively small with respect to the primary neutral pions (see Figure 5.8) and the $\mathrm{K}^0_{\mathrm{S}}$ and Λ spectra have been measured with a precision of better than 10% in the same data set, the related systematic uncertainties can be neglected for the neutral pion measurements using the PCM, PCM-EMC and EMC reconstruction techniques.

Inner material: As already discussed for the pp results, the largest uncertainty for the PCM photon reconstruction originates from the precision of the implementation of the material of the inner detectors in the simulations. Currently, this material is know to a precision of 4.5% independent of p_{T}. Which needs to be doubled if both photons are reconstructed using PCM. As both mesons would, however, be affected in the same way this uncertainty cancels in the η/π^0-ratio.

Outer material: In order to estimate the uncertainties related to the material budget description of the outer detectors the same study has been performed as in pp collisions. It has been found that the single EMCal photon uncertainty for regarding this variation is 2.8%, while the same uncertainty of 4.2% independent of p_{T} has been found for analysis involving two photons, which could be reconstructed within the EMCal. This validates the di-photon estimate done for pp

collisions as none of the detector components in the simulations had been changed regarding its material composition. Consequently, an uncertainty of 2.8% and 4.2% has been assigned to the mesons reconstructed with PCM-EMC and EMC, respectively. For the η/π^0 ratio this uncertainty cancels, as both meson would be affected in the same manor.
Pile-up: To estimate the uncertainty on the out-of-bunch pile-up correction for the PCM method, the settings of the statistical background estimate method have been modified such that the highest and lowest possible pile-up contribution would be subtracted from the dca_Z distribution (see Figure 5.10), which would still result in a reasonable dca_Z distribution for primary photons. This procedure led to systematic uncertainty of 2.4% at 0.3 GeV/c for the neutral pion, which decreases rapidly to less than 1% above 1.3 GeV/c. Similar values have been found for this systematic uncertainty on the η meson and they are assumed to largely cancel for the η/π^0-ratio.
Uncertainties on pp reference: The exact method to estimate the statistical and uncorrelated uncertainties of the interpolated pp reference is described in detail in the previous section. While this procedure is rather straight forward for these two uncertainty sources, the error on the interpolation procedure itself depends very much on the assumptions, which are made for the functional form of the interpolation function. Their relative size also depends on the accuracy of the inputed measurements at the different center-of-mass energies and as such can very strongly for different reconstruction techniques. For the PCM reconstruction technique, for instance, this source of systematic error is largest at intermediate momenta, reaching up to 6.7% at 2.5 GeV/c for the neutral pion. While for the other two reconstruction techniques it is smallest at intermediate p_{T} (2-8 GeV/c) and increases only towards the lowest and highest momenta reached by the respective neutral meson reconstruction method. For the η meson all the uncertainties on the interpolated spectrum are in general larger as the respective measurements at lower and higher energies have less relative precision due to the smaller probability of producing an η compared to that of the π^0. When calculating the R_{pA} for the individual techniques and mesons the inner and outer material budget errors do not have to be considered for the R_{pA} error estimates, as such the interpolation errors become one of the dominant systematic error sources in particular for the η meson. Thus, an actual measurement of the respective spectra at the same center-of-mass energy is desirable. As this measurement is not yet available only the most obvious error cancellations could be done (i.e material uncertainties), which could be further improved by varying the selection criteria simultaneously for the pp and p–Pb spectra as soon as they are available.

A comparison among the different measurement techniques regarding their total systematic and statistical uncertainties for the neutral pion spectra is shown in Figure 5.39, while the respective Figures for the remaining measurements can be found in Appendix B.2.4. It can be seen that the statistical uncertainties of the individual measurements for all transverse momentum slices, except those at the edges of the measurable range of the respective methods, are approximately half as large as the respective systematic uncertainties. For most reconstruction methods they are between $1-3\%$ at intermediate momenta, while they rise quickly towards higher and lower momenta. The latter is driven mainly by the acceptance and reconstruction efficiency of the respective methods as all of them investigated approximately the same integrated luminosity. The largest precision for the neutral pion spectra individually is reached with the EMC measurement taking into account both statistical and systematic uncertainties. However, it would still be worse than that of the charged pions [97], which has a total uncertainty of about $5-6\%$ at intermediate transverse momenta, as seen in Figure 5.40(left). If, on the other hand, the partially independent neutral pion measurements are combined using the BLUE method, as described at the end of Section 5.1.1 using the correlation factors shown Figure B.22 the total uncertainty decreases to $3.5-5\%$ between $1.2-8$ GeV/c, making it the most precise identified particle measurement in p–Pb collisions at $\sqrt{s_{\mathrm{NN}}}$ = 5.02 TeV at the LHC in this transverse momentum region. For transverse momenta below 1GeV/c, on the other hand, the charged pion measurement is more precise due to statistical limits for the neutral pions originating from the small reconstruction efficiency and

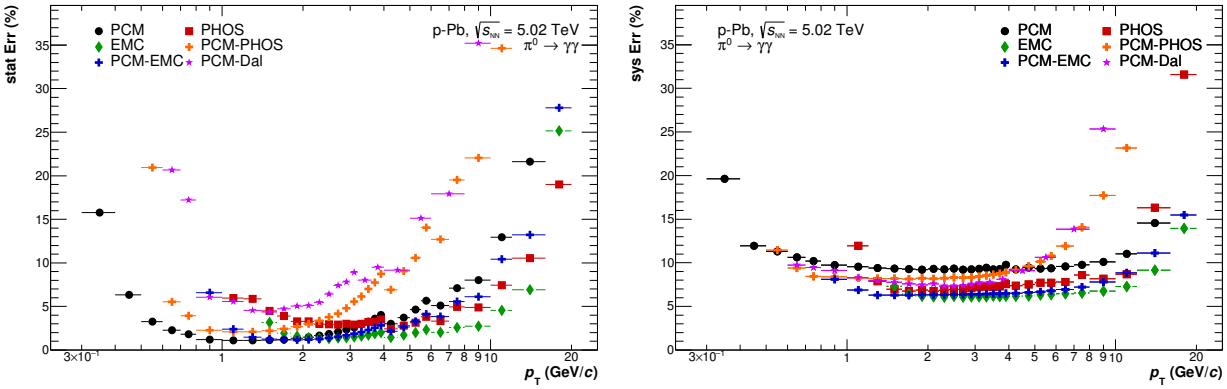

Figure 5.39.: Relative statistical (left) and systematic uncertainties (right) for the π^0 spectra measured with different reconstruction methods in p–Pb collisions at $\sqrt{s_{\mathrm{NN}}} = 5.02$ TeV as a function of transverse momentum.

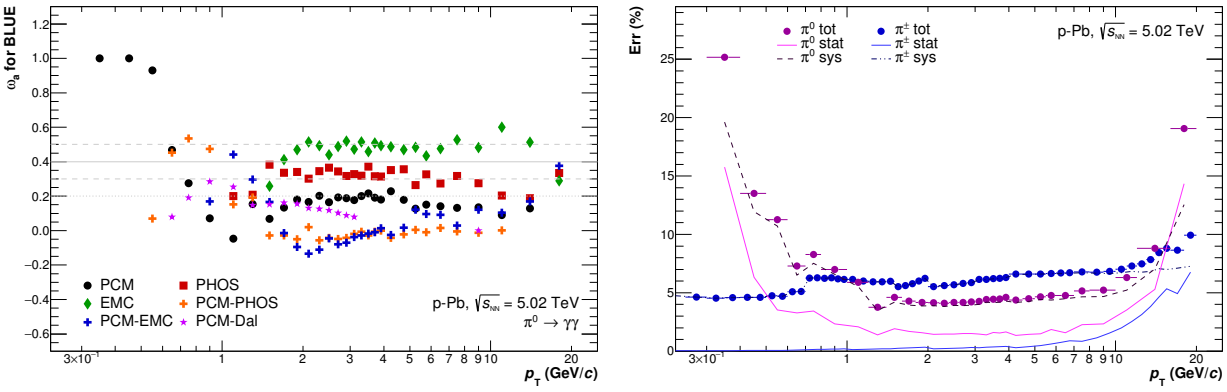

Figure 5.40.: Left: Weights (ω_a) for the invariant yield measurements of neutral pions used in the combination according to the BLUE method [309, 310, 313]. The respective weights for the combination of the other four measurements can be found in Appendix B.2. Right: Total uncertainties for the neutral pion spectrum (violet points) after the combination procedure compared to those of the charged pion measurement [97] (blue points). In addition, the statistical and systematic uncertainties are given separately for each of the measurements as solid and dashed line respectively following the same color scheme.

conversion probability at the respective p_{T}. Similar observation can be made for the R_{pA} of the neutral and charged pions for which the respective comparison can be found in Appendix B.2.4. The R_{pA} measurement benefits in particular from the careful evaluation of the cancellations of the uncertainties for the interpolation procedure and the R_{pA} calculation itself. The uncertainties assigned to the interpolation method itself, on the other hand, are similar among the two different pion measurement, as both are using similar techniques and inputs.
For the η meson invariant yield the statistical and systematic uncertainties are minimal between 1.5 and 7 GeV/c, ranging between $6 - 10\%$ and $9 - 11\%$, respectively, depending on the reconstruction technique, as it can be seen in Figure B.21 of Appendix B.2.4. By combining the four partially independent measurements, however, a total uncertainty of approximately 10% can be achieved as well between $2 - 6$ GeV/c. A significant fraction of this uncertainty is of statistical nature, with errors ranging between 5 and 7% in this transverse momentum region. This could be reduced by either considering in a later measurement the newly collected minimum bias data at the same center-of-mass energy or the respective EMCal triggered data, which have been collected right after the minimum bias data taking in 2013. For the R_{pA} measurement of the η meson larger uncertainties arose from the reference spectrum compared to the respective neutral pion measurement, thus the total error increases in the same transverse momentum region to about 15%. When calculating the η/π^0 ratio, on the other hand, a large fraction of the systematic uncertainties canceled, thus for this measurement the statistical and systematic errors are of similar size and in

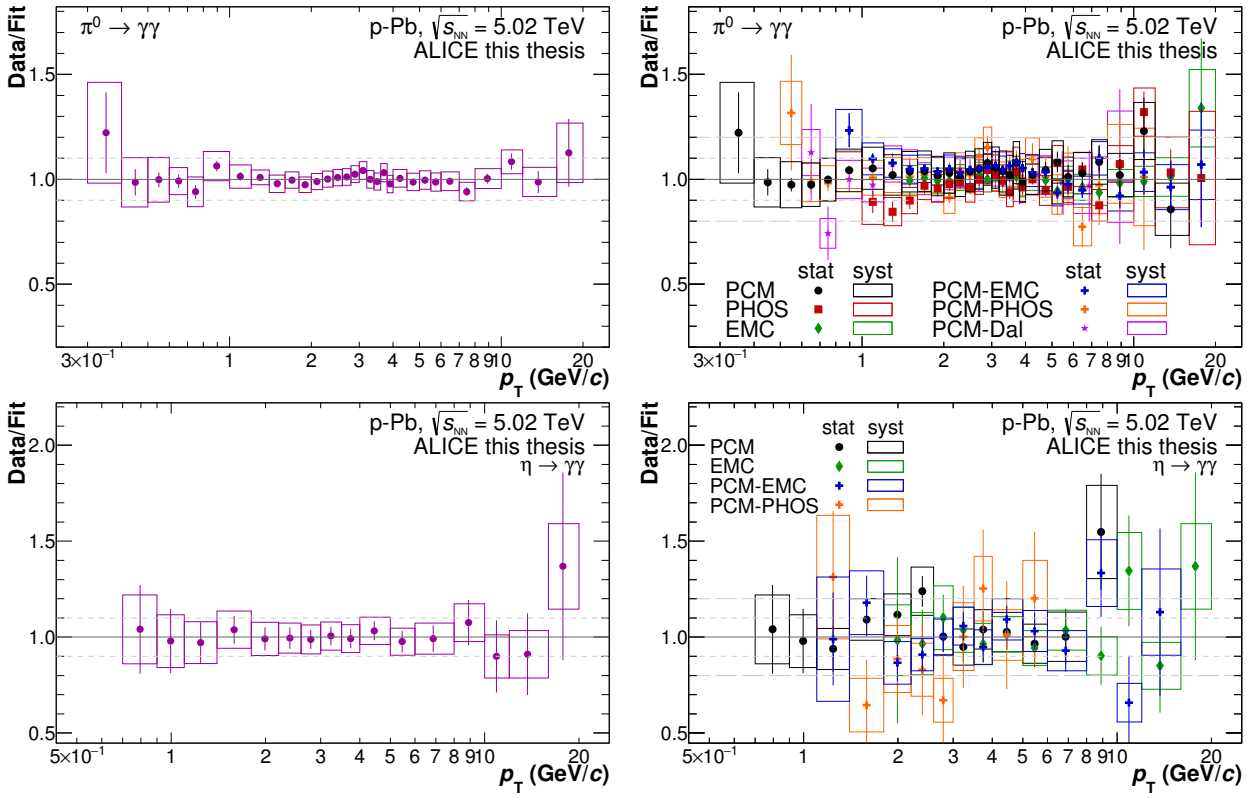

Figure 5.41.: Ratio of the neutral pion (top) and eta meson (bottom) invariant yield measurements in NSD p–Pb collisions at $\sqrt{s_{\mathrm{NN}}}$ = 5.02 TeV to their respective parameterizations using the two-component model fits (Equation 5.14), for which the fit parameters are reported in Table 5.14. The combined measurements are plotted to ascertain the quality of the fit (left). Furthermore, the individual measurements (right) are shown for both observables together with their respective full statistical and systematic uncertainties.

particular towards the lowest and highest momenta the statistical uncertainties dominate.
The final invariant yield measurements for the neutral pion and eta meson are fitted with the TCM function (Equation 5.14) once more and the fit result has been compared to the individual measurements using the various neutral meson reconstruction techniques. These comparison can be found in Figure 5.41. The agreement of the neutral pions among the all measurements, except the PHOS, is better than $1\sigma_{\mathrm{stat}}$. The latter shows about a $1\sigma_{\mathrm{tot}}$ deviation from the remaining individual measurements below 2 GeV/c. This small discrepancy could be explained by a residual mis-calibration of the cluster energy, which has been corrected for in the PCM-PHOS measurement [303] exploiting the same calibration method, which has been presented in this thesis for the EMCal measurements.
For the η meson spectra, the agreement of the individual spectra is slightly worse that that of the neutral pion, in particular at high transverse momenta. Part of these fluctuations unfortunately arises from the limited simulation statistics. Consequently, the statistical uncertainties of the simulations are incorporated in the statistical uncertainties of the respective data points for both mesons.
As for the pp measurement at $\sqrt{s}$ = 2.76 TeV the two-component model fit has been chosen mainly as a convenient parameterization of the data with the additional benefit that the same fit describes the data in pp collisions as well over the full transverse momentum spectrum at all measured energies. The respective parameters for the meson spectra in p–Pb and pp collisions at $\sqrt{s_{\mathrm{NN}}}$ = 5.02 TeV are given in Table 5.14, where the latter were obtained by fitting the interpolated spectrum. For p–Pb collisions additional parameterizations have been evaluated and it has been found that a fit with the modified Hagedorn function (Equation 5.15), would give a similar agreement with the data. The comparison of the different fit functions with the data can

Meson	$\mathbf{A_e}$ ($\mathrm{GeV}^{-2}c^3$)	$\mathbf{T_e}$ (GeV/c)	$\mathbf{A}$ ($\mathrm{GeV}^{-2}c^3$)	$\mathbf{T}$ (GeV/c)	$\mathbf{n_{br}}$
pp, $\sqrt{s} = 5.02$ TeV					
π^0	5.79 ± 0.59	0.1643 ± 0.0079	0.454 ± 0.066	0.629 ± 0.019	3.163 ± 0.018
η	$(2.65 \pm 4.99) \cdot 10^{-4}$	0.9312 ± 0.2622	$(7.46 \pm 2.39) \cdot 10^{-2}$	0.721 ± 0.068	3.105 ± 0.091
p–Pb, $\sqrt{s_{\mathrm{NN}}} = 5.02$ TeV					
π^0	25.85 ± 8.79	0.146 ± 0.018	1.63 ± 0.29	0.664 ± 0.025	3.167 ± 0.026
η	0.67 ± 0.85	0.191 ± 0.100	$(9.64 \pm 5.67) \cdot 10^{-2}$	0.983 ± 0.129	3.301 ± 0.128

Table 5.14.: Parameters of the two-component model, Equation 5.14 [315, 316], which are used to parametrize the neutral pion and η meson spectra, respectively. The values are given for the interpolated reference spectra in pp collisions at $\sqrt{s} = 5.02$ TeV and the respective measurements in p–Pb collisions.

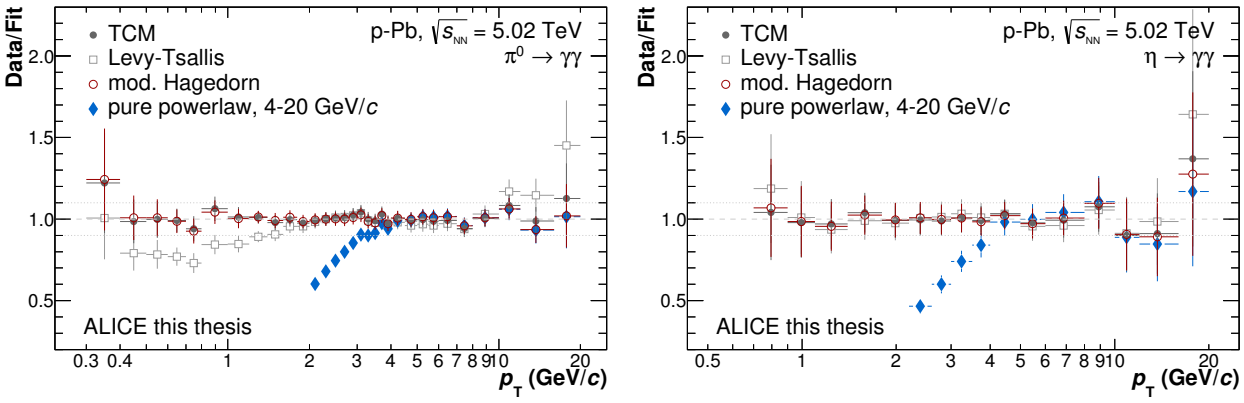

Figure 5.42.: Comparison of the combined neutral pion (left) and eta meson (right) invariant yield measurements in p–Pb collisions at $\sqrt{s_{\mathrm{NN}}} = 5.02$ TeV to different fit functions. The ratio to the two-component model (TCM) fit by [315,316] is shown as closed gray circles, while the ratios of the free Levy-Tsallis fits [308] to the data points are shown as open gray squares. Furthermore, a pure power-law fit to the data above 4 GeV/c is shown as azure diamonds. Additionally, the data have been fitted with a modified Hagedorn fit [325], for which the ratio is shown as open red circles.

be found in Figure 5.42. A fit with a Tsallis distribution fails to describe the neutral pion data, when attempting to fit the full transverse momentum range. It would, however, describe the eta meson spectrum in the measured transverse momentum range. The TCM distribution has been used to correct for the finite bin width and the final spectra are reported at the most probable p_{T}, following the prescription of [304], as it was done for the pp data as well. Also all measured ratios of the spectra have been corrected for this effect. However, the correction in those cases has been done in direction of the yields, as otherwise the ratio would not be possible due to mismatching p_{T} values.

5.3.3. Neutral Meson Transverse Momentum Spectra in p–Pb

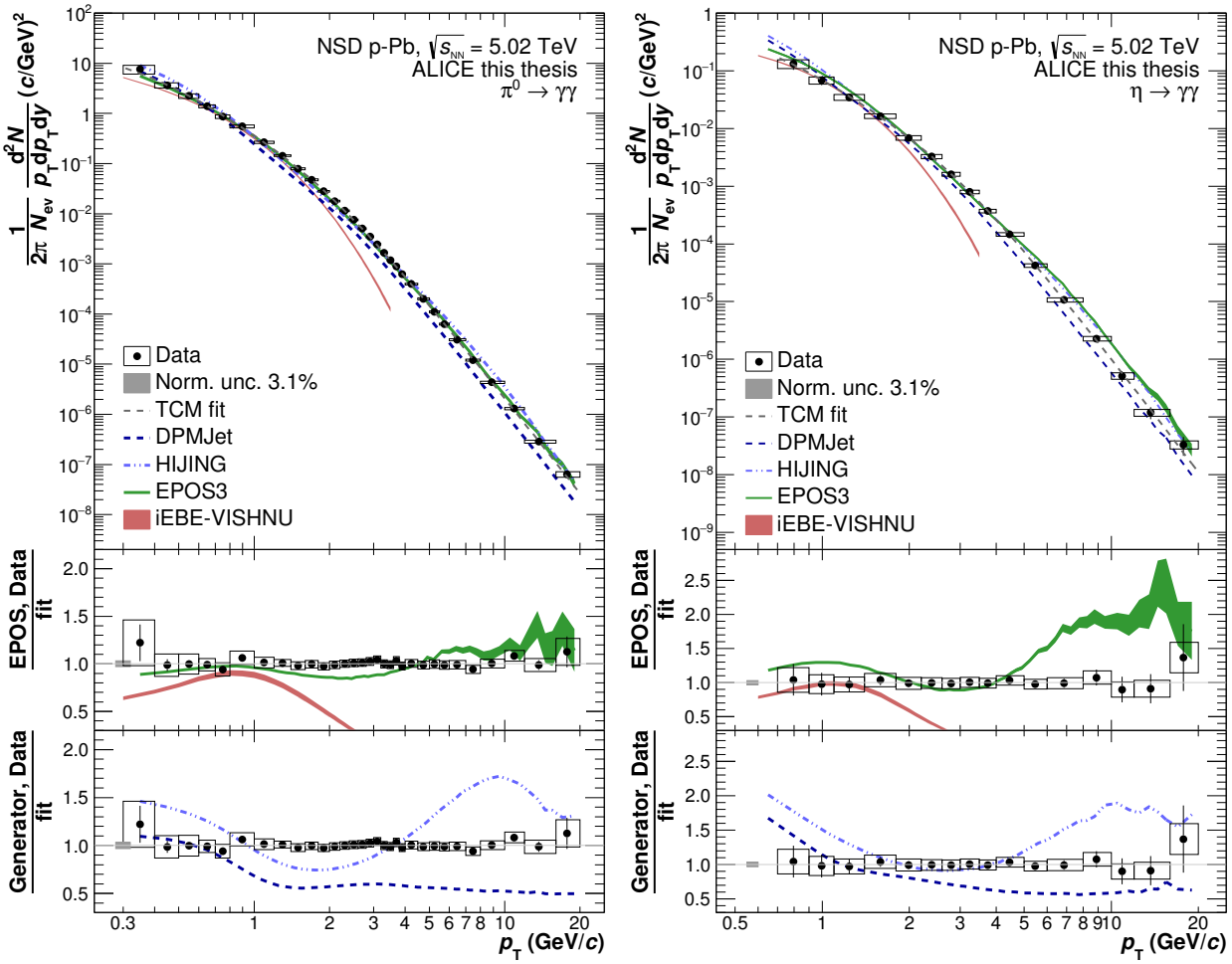

Figure 5.43.: Invariant differential π^0 (left) and η (right) yields produced in NSD p–Pb collision at $\sqrt{s_{NN}}$ = 5.02 TeV. The data are compared to HIJING [260] and DPMJet [259] generator-level simulations as well as recent hydrodynamic model calculations using the iEBE-VISHNU package [103, 330] or the EPOS3 [331] event generator. The ratios of the data and the calculations to the respective two-component model fits [315, 316] to the data are shown in the lower panels. The horizontal error bars denote statistical, the boxes systematic uncertainties. The global normalization uncertainty of 3.1% is not included in the systematic uncertainties and thus displayed as a gray filled box in all ratio plots.

The combined π^0 and η invariant differential yield for p–Pb collisions at $\sqrt{s_{NN}}$ = 5.02 TeV, calculated according to Equation 5.3, normalized to the number of non single-diffractive (NSD) events can be seen in Figure 5.43. For both measurements the statistical uncertainties are displayed as vertical errors bars, whereas the systematic errors are indicated as boxes. As the normalization uncertainty is independent of transverse momentum and particle type it is not included in the displayed boxes but indicated as a solid gray box when comparing the spectra to the theory calculations.

The neutral pion measurement is currently the most precise identified particle measurement at intermediate transverse momenta in p–Pb collisions at $\sqrt{s_{NN}}$ = 5.02 TeV. As such, it will serve as a testing ground for a variety of models, which are trying to understand the interplay of soft and hard processes of particle production in this momentum region. Thus, the measured spectra have been compared to the most common event generators and hydrodynamic models at the moment. The respective comparison of the spectral shapes and the ratios of these to the fit of the measured data points can be found in Figure 5.43 as well.

The comparisons to the event generators, which had been used to obtain the efficiency and acceptance corrections, are shown in the lowest panels. Neither of the two multipurpose generators, which had been tuned to reproduce the RHIC data at low and moderate transverse momenta, can describe the spectra in the full transverse momentum range.
The calculations based on the DPMJet model agree well with the data for $p_{\mathrm{T}} < 1(1.5)$ GeV/c for the neutral pion and η meson respectively. At higher momenta, however, the yield is underestimated by about 40%, while the slope of the spectrum agrees within 10%. This suggests that the model parameters, for instance regarding the percolation and chain fusion, which were necessary to reproduce the low and intermediate momentum hadron measurements at RHIC [332], need to be reoptimized for the new energy regime. This is also supported by the fact that the respective pp measurements differ significantly from the predicted values for LHC energies, as reported by the authors of DPMJet [333].
The HIJING model predictions, on the other hand, oscillate around the measured spectra, overestimating them at low and high transverse momenta by up to 70%, while underestimating the data between 1 and 4 GeV/c by approximately 20% for the neutral pion. As the HIJING model combines pQCD-based calculations for multiple jet production with low p_{T} multi-string phenomenology, it seems likely that the respective parameters determining the cross-over region could be adjusted to reproduce the shape of the neutral pion and η meson spectrum.
A similar oscillation behavior, as for HIJING, can be observed for the EPOS3 [331] event generator as well, although the quantitative agreement is significantly better. This event generator is based on 3D+1 viscous hydrodynamics using flux tube initial conditions, which are generated in the Gribov-Regge multiple scattering framework. The reaction volume is divided into two parts, the core and the corona, which are evolving independently. The core evolution is done using viscous hydrodynamics, while the corona is composed of hadrons from string decays. The respective parameters governing the hydro evolution have been tuned by the authors to reproduce the charged pion and kaon production in none single diffractive p–Pb collisions at the LHC [331]. Consequently, also the neutral pion spectrum is reproduced within $10-20$%. For the η meson, on the other hand, the predictions deviate from the data beyond 4 GeV/c by up to a factor two.
The calculations based on the iEBE-VISHNU package [103, 330] are a combination of a 3D+1 viscous hydrodynamic model coupled to a hadronic cascade model. As starting point of the hydrodynamic evolution, fluctuating initial conditions from a Monte Carlo Glauber model are used. These calculations can only describe the neutral meson spectra up to 1.5(2) GeV/c for the neutral pion and η meson, respectively, as no hard processes are included in the calculations. Figure 5.43 shows that the η meson spectra can be described reasonably well in this transverse momentum region, while the neutral pions are underestimated by up to 30% below 0.6 GeV/c. For momenta above 1.5(2) GeV/c, the calculations deviate strongly as expected. The fact that both models, which incorporate collective effects based on viscous hydrodynamics in their calculations show good agreement at low p_{T}, indicates that even in p–Pb collisions at LHC energies a small quark gluon plasma could be created. This is supported by the observation of elliptic flow in these systems as described in Section 2.3.2.
The combined η/π^0 has been calculated from the individual measurements in each method, which contribute to the η meson spectrum as well. It is presented in Figure 5.44 (right) together with the model predictions, which were already compared to the individual spectra measurements. The η/π^0 ratio increases with p_{T} and reaches a plateau of $0.485 \pm 0.016^{\mathrm{stat}} \pm 0.029^{\mathrm{sys}}$ above a transverse momentum of 4 GeV/c, which agrees very well with the value reported for pp collisions at $\sqrt{s} = 2.76$ TeV. To illustrate the universality of the η/π^0 ratio versus center-of-mass energy and collision system, the data are compared to measurements in p–A (d–A) collisions at lower center-of-mass energies [336, 337] as well as pp collision at LHC energies [297, 301] and the highest center-of-mass energy at RHIC [322] (Figure 5.44 (right)). It has been found that the high p_{T} value is slightly higher than the previously determined world average of p–A (d–A) collisions of 0.4471 ± 0.0075, for which the measurements from FNAL E629 [338], FNAL E706 [339] and FNAL

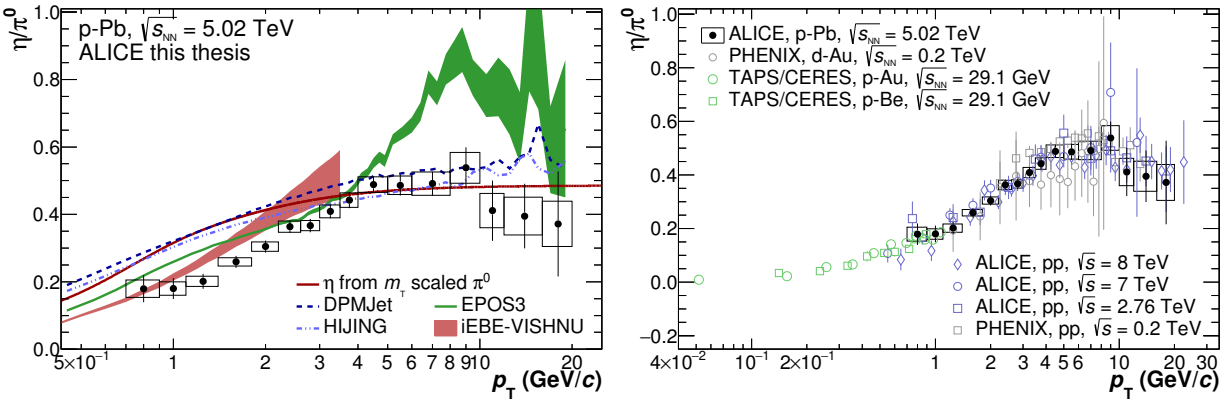

Figure 5.44.: Measured η/π^0 ratio in p–Pb collisions at $\sqrt{s_{\rm NN}} = 5.02$ TeV compared to model calculations based on HIJING [260], DPMJet [259], EPOS3 [331] and iEBE- VISHNU [103]. The horizontal error bars denote statistical, the boxes systematic uncertainties (left). Furthermore, the measured ratio is compared to the η/π^0 ratio obtained by scaling the neutral pion spectrum according to the $m_{\rm T}$-scaling prescription [334, 335]. The data are also compared to measurements in p–A (d–A) collisions at lower energies and the corresponding pp at $\sqrt{s} = 0.2$ TeV [322], $\sqrt{s} = 2.76$ TeV [297], $\sqrt{s} = 7$ TeV [301] and $\sqrt{s} = 8$ TeV [297] (right), for which the statistical and systematic uncertainties have been added in quadrature and are shown as vertical lines. For the p–A measurements the data collected by TAPS/CERES in p–Au and p–Be collisions at $\sqrt{s_{\rm NN}} = 29.1$ GeV [336] and PHENIX in d–Au collisions at $\sqrt{s_{\rm NN}} = 0.2$ TeV [337] have been chosen to highlight the universality of the η/π^0 ratio at different center-of-mass energies.

706 [340] have been considered in addition to those shown in the respective plot. In this compilation the average is, however, driven by the measurement in d–Au collisions at RHIC, due to the comparatively small errors. A similar fit to all available pp and p$\bar{\rm p}$ data points [337, 341–352] including those from ALICE at $\sqrt{s} = 8$ TeV,$\sqrt{s} = 7$ TeV and $\sqrt{s} = 2.76$ TeV yielded a high $p_{\rm T}$ average of 0.5032 ± 0.0069, which is significantly higher than the measured average in p–A collisions. If the presented data for p–Pb collisions are included in the global fit for p–A collisions the value increases to 0.4510 ± 0.0071.

The model calculations for HIJING and DPMJet agree with the measured η/π^0 ratio in the plateau region, even though they did not for the $p_{\rm T}$ differential invariant yield at the corresponding momenta. At lower momenta, however, the data lies significantly below the respective calculations. For the hydro-inspired models on the other hand, the situation is reversed and the data is described within $1 - 2\sigma$ below 3 GeV/c, while EPOS3 in particular overshoots the data by up to a factor two at higher momenta.

In addition to the presented calculations, the eta meson spectrum has been calculated based on the parametrization of the neutral pion using $m_{\rm T}$-scaling [334, 335]. The corresponding η/π^0-ratio has been calculated and is shown as dark red line in Figure 5.44. It reproduces the data above 4 GeV/c by construction, as $m_{\rm T}$-scaling assumes that at high transverse momenta, where $m_{\rm T} \approx p_{\rm T}$, all spectra follow the same power-law behavior, which is supported by the plateau seen in the η/π^0-ratio. However, at lower momenta the data cannot be reproduced by this calculation and most of the data points deviate by more than 1σ from the corresponding $m_{\rm T}$-scaling curve. If all points below 4 GeV/c are taken into account, they deviate by 3.97σ from the calculated $m_{\rm T}$ scaled η spectrum. For the data presented by the PHENIX collaboration, $m_{\rm T}$-scaling seemed to work as their transverse momentum reach is limited at low $p_{\rm T}$.

The assumption, that all heavier particle spectra can be obtained by $m_{\rm T}$-scaling the neutral pion spectrum, is often used when calculating decay photon or electron distributions for the direct photon or heavy flavor electron measurements. In particular for those particles which have not been measured at the respective center-of-energy. As it is apparent, this assumption is rather dangerous at low transverse momenta, where it is observed to be broken, see also [327]. Thus, the largest sources of photons and electrons have to be measured at low momenta to obtain reli-

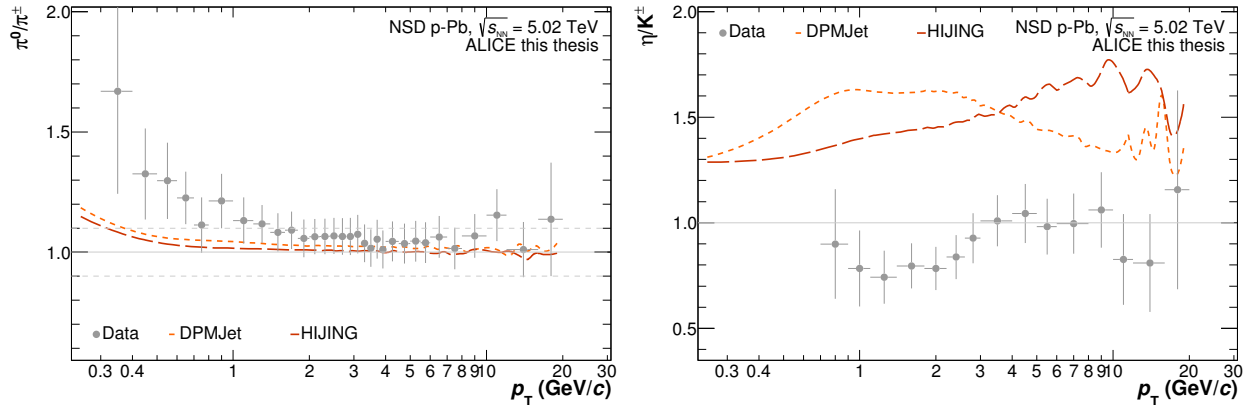

Figure 5.45.: Comparison of the neutral and charged pion differential transverse momentum spectra (left) and the corresponding ratio of the η meson spectra to those of the charged kaons (right). For these comparison the average of the charged spectra [97] has been computed and the quadratically added systematic and statistical uncertainties of the neutral and charged particles are show as vertical error bars. The measured values are compared to those expected from the HIJING and DPMJet simulations, which had been used for the corrections of the neutral meson spectra initially.

able decay photon(electron) distributions. Additionally, the neutral pion spectra are reported as inclusive measurements, which implies that they contain the decays from heavier resonances and other strongly decaying particles, like for instance the η meson decays themselves. As such, the spectrum at lower transverse momenta is enhanced for the neutral pion compared to the spectra of those particles, which have only little contribution from heavier resonance decays. Consequently, at a certain momentum m_{T}-scaling is implicitly broken and should not be applied any longer.
The neutral pion and η meson spectra have also been compared to those of the charged pions and kaons, respectively. The p_{T} differential ratios of the measured spectra are shown in Figure 5.45, together with the corresponding ratios from the HIJING and DPMJet simulations. For these comparisons, the systematic and statistical errors of both measurements were added in quadrature and are indicated as vertical error bars. As it can be seen, the ratio of neutral to charged pions is about 1.05 for $p_{\mathrm{T}} > 1$ GeV/c. Within the uncertainties the ratio agrees, however, with the assumption of charge-symmetric production as well as a small fraction of iso-spin violating decays favoring the decay into neutral pions. The latter is included in the simulations to a different degree as different resonances are considered in the event generators. At momenta below 1 GeV/c the neutral pion production seems to be significantly favored with respect to that of a charged pions and consequently the $\pi^0/\pi^\pm$ increases with decreasing momentum. A fraction of this enhancement is also seen in statistical hadronisation models and is caused partly by the resonance decays and partly by the smaller rest mass of the neutral pions. With the current statistical and systematic uncertainties on the neutral pion measurement in this transverse momentum region, no reliable quantitative statement can be made, though. The comparison of the η meson production with respect to that of the charged kaons, reveals that those two particles are produce in approximately the same quantities and that at lower momenta there are even less η mesons than kaons. From the generators the expected $\eta/\mathrm{K}^\pm$ would have been $1.2 - 1.7$ though, which is not supported by the data. While a simple exponential scaling of the particle production with the particle mass, should lead to an integrated ratio of about $0.92 - 0.94$, which is in better agreement with the data.
An overview of all available identified particle invariant yields for non single diffractive p–Pb collisions at $\sqrt{s_{\mathrm{NN}}} = 5.02$ TeV can be found in Figure 5.46 (left). To ease the comparisons to statistical hadronisation models even further, the integrated yields and mean transverse momenta for each particle have been calculated following the same procedure as outline in Section 5.2.2 for the corresponding measurements in pp collisions at $\sqrt{s} = 2.76$ TeV. The resulting integrated yields and mean transverse momenta are reported in Table 5.15 and shown as a function of the particle rest mass(M) in Figure 5.47. For these estimates, only the light flavored particles have

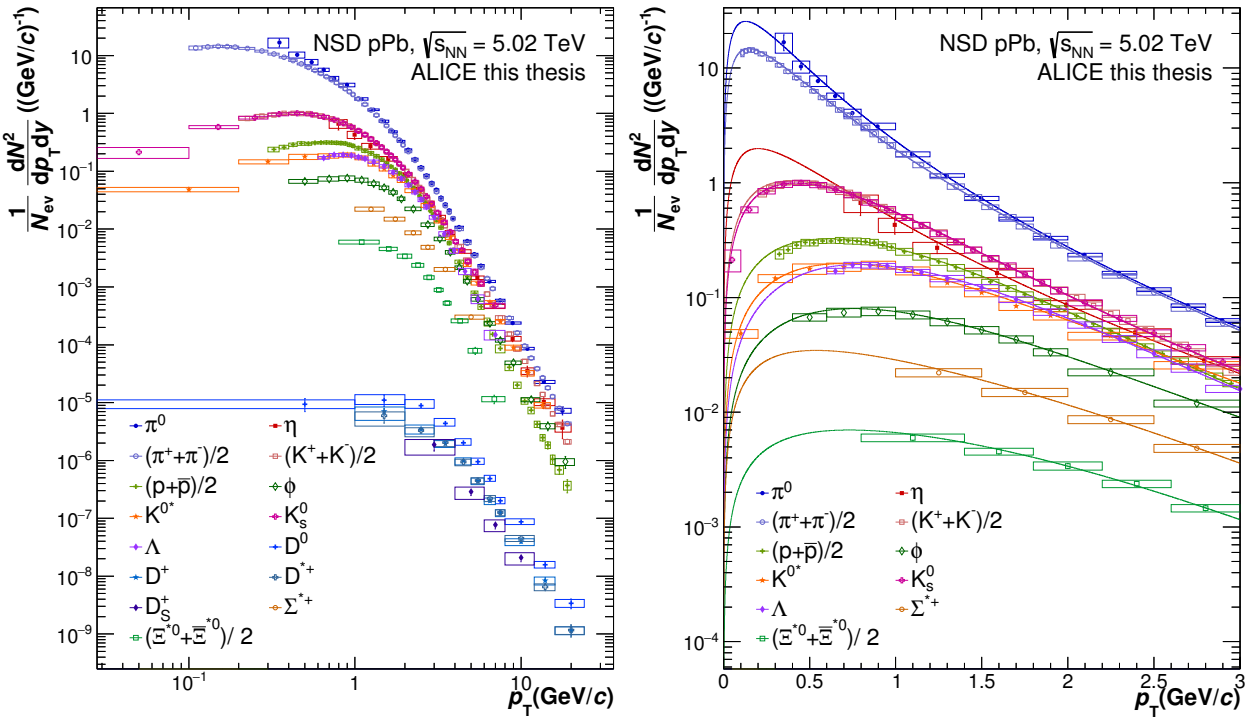

Figure 5.46.: p_T-differential yield for light flavored hadron measured by ALICE in p–Pb collision at $\sqrt{s_{NN}}$ = 5.02 TeV. The compilation includes the presented results of the π^0, η, the published results on the production of the $\pi^{\pm}$, $K^{\pm}$, $p/\bar{p}$ [97], ϕ, K^{*0} [353], Ξ^{*0}, Σ^{*+} [354], D mesons [190, 355] and the preliminary results for the K^0_S, Λ [162]. The lines on the right show the modified Hagedorn fits (Equation 5.15) for the various particles in the same color at low transverse momenta. The vertical error bars represent the statistical error, while the systematic errors are indicated by the boxes. The width of the transverse momentum slices is indicated by the width of the systematic error boxes.

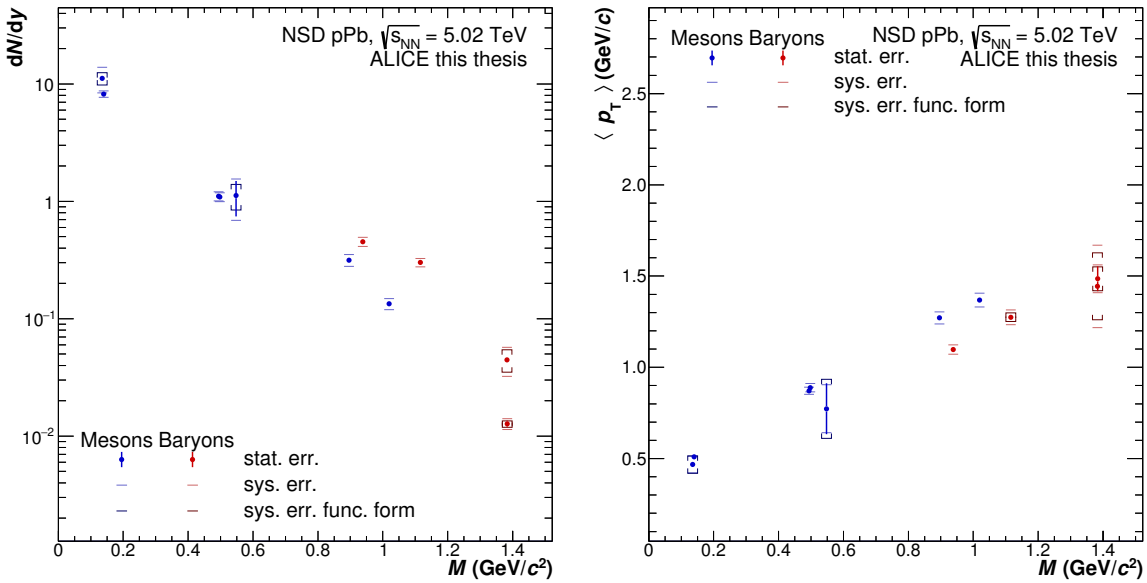

Figure 5.47.: Integrated yield (left) and average transverse momentum (right) as a function of the particle rest mass for NSD p–Pb collisions at $\sqrt{s_{NN}}$ = 5.02 TeV. The statistical errors are shown as vertical lines while the systematic errors are shown as horizontal lines. An additional error for the choice of the functional form is displayed as brackets.

been considered and the values are not reported for the D-mesons.
The plots detailing the fit variations for the π^0 and η meson can be found in Appendix B.3, while the modified Hagedorn fits are displayed in Figure 5.46 (right) at low transverse momenta together with the corresponding measurements. As already observed for pp collisions the integrated yield

Particle	Mass (GeV/c^2)	dN/dy		ext. (%)	$\langle p_{\mathrm{T}} \rangle$ (GeV/c)	
π^0	0.134977	11.2	$\pm 0.5^{\text{ stat}}$ $\pm 2.9^{\text{ sys}} \pm 1.4^{\text{ sys f.}}$	45.1	0.47	$\pm 0.01^{\text{ stat}}$ $\pm 0.05^{\text{ sys}} \pm 0.05^{\text{ sys f.}}$
$(\pi^+ + \pi^-)/2$	0.13957	8.204	$\pm 0.001^{\text{ stat}}$ $\pm 0.514^{\text{ sys}} \pm 0.218^{\text{ sys f.}}$	10.5	0.50899	$\pm 0.00008^{\text{ stat}}$ $\pm 0.01080^{\text{ sys}} \pm 0.01245^{\text{ sys f.}}$
$(K^+ + K^-)/2$	0.493677	1.1066	$\pm 0.0006^{\text{ stat}}$ $\pm 0.0973^{\text{ sys}} \pm 0.0145^{\text{ sys f.}}$	8.60	0.8713	$\pm 0.0003^{\text{ stat}}$ $\pm 0.0197^{\text{ sys}} \pm 0.0101^{\text{ sys f.}}$
$\mathrm{K}^0_{\mathrm{S}}$	0.497614	1.0884	$\pm 0.001^{\text{ stat}}$ $\pm 0.092^{\text{ sys}}$	0.05	0.8886	$\pm 0.0007^{\text{ stat}}$ $\pm 0.0228^{\text{ sys}} \pm 0.0018^{\text{ sys f.}}$
η	0.547853	1.15	$\pm 0.43^{\text{ stat}}$ $\pm 0.46^{\text{ sys}} \pm 0.32^{\text{ sys f.}}$	61.1	0.76	$\pm 0.14^{\text{ stat}}$ $\pm 0.13^{\text{ sys}} \pm 0.18^{\text{ sys f.}}$
K^{*0}	0.896	0.315	$\pm 0.002^{\text{ stat}}$ $\pm 0.038^{\text{ sys}}$	0	1.271	$\pm 0.005^{\text{ stat}}$ $\pm 0.033^{\text{ sys}} \pm 0.0005^{\text{ sys f.}}$
$(p + \bar{p})/2$	0.938272	0.4530	$\pm 0.0003^{\text{ stat}}$ $\pm 0.0398^{\text{ sys}} \pm 0.0046^{\text{ sys f.}}$	9.05	1.09752	$\pm 0.0006^{\text{ stat}}$ $\pm 0.0252^{\text{ sys}} \pm 0.0096^{\text{ sys f.}}$
ϕ	1.01946	0.1340	$\pm 0.0006^{\text{ stat}}$ $\pm 0.0147^{\text{ sys}} \pm 0.0012^{\text{ sys f.}}$	9.92	1.368	$\pm 0.004^{\text{ stat}}$ $\pm 0.038^{\text{ sys}} \pm 0.010^{\text{ sys f.}}$
$(\Lambda + \bar{\Lambda})/2$	1.11568	0.3017	$\pm 0.0007^{\text{ stat}}$ $\pm 0.0250^{\text{ sys}} \pm 0.0072^{\text{ sys f.}}$	19.6	1.274	$\pm 0.002^{\text{ stat}}$ $\pm 0.041^{\text{ sys}} \pm 0.024^{\text{ sys f.}}$
Σ^{*+}	1.3828	0.0447	$\pm 0.0006^{\text{ stat}}$ $\pm 0.0124^{\text{ sys}} \pm 0.0097^{\text{ sys f.}}$	37.7	1.443	$\pm 0.007^{\text{ stat}}$ $\pm 0.226^{\text{ sys}} \pm 0.183^{\text{ sys f.}}$
$(\Xi^{*0} + \bar{\Xi}^{*0})/2$	1.3837	0.0127	$\pm 0.0008^{\text{ stat}}$ $\pm 0.0013^{\text{ sys}} \pm 0.0008^{\text{ sys f.}}$	27.3	1.49	$\pm 0.07^{\text{ stat}}$ $\pm 0.08^{\text{ sys}} \pm 0.07^{\text{ sys f.}}$

Table 5.15.: Integrated particle yields and mean transverse momenta for the measured light flavored particles in NSD p–Pb collisions at $\sqrt{s_{\mathrm{NN}}} = 5.02$ TeV. The systematic errors have been split in two components: those related to the systematic uncertainties of the measurements themselves (*sys*) and those related to the choice of the functional form of the fit (*sys f.*). Furthermore, the extrapolation fraction of the yield is given in the fourth column.

decreases with increasing particle mass, while the mean p_{T} increases following a common function for the meson production. The η meson, however, does not seem to follow this trend, albeit the large uncertainties, would still cover the difference to the naively expected values. Furthermore, as for pp collisions the baryons and mesons seem to follow a different scaling, even though it is not significant yet and more meson measurements at higher masses will be needed to confirm or deny this statement. In addition to the integrated yield, the corresponding integrated particle ratios are reported in Table 5.16, which might be used to test the statistical models without the need to reproduce the absolute numbers. The integrated η/π^0 ratio is found to be $0.103 \pm 0.039^{\text{ stat}} \pm 0.050^{\text{ sys}} \pm 0.031^{\text{ sys f.}}$, which is in agreement with that obtained for pp collisions. The size of the uncertainties is driven by the comparatively large extrapolation fraction of the η meson of 61.1%, which was also seen for the η meson integrated yield and mean p_{T}.
Finally, the p_{T} differential invariant yields of the neutral pions and η mesons obtained for p–Pb collisions at $\sqrt{s_{\mathrm{NN}}} = 5.02$ TeV as well as the interpolated ones for pp collisions at $\sqrt{s} = 5.02$ TeV are compared to next-to-leading order pQCD calculations by Werner Vogelsang [356] and Ilkka Helenius [357, 358]. The calculations are done for different parton distribution functions (PDFs), while always the latest fragmentation functions have been chosen for the respective mesons. The comparisons of the spectra are shown in Figure 5.48, while Figure 5.49 shows the corresponding comparison for the η/π^0 ratio. For each of the distributions, the p–Pb data are shown as solid points, while the interpolated reference is depicted with open symbols. To determine the uncertainties of the pQCD calculations, the renormalization, fragmentation and factorization scales have been varied from $\mu = p_{\mathrm{T}}$ to $\mu = 0.5\ p_{\mathrm{T}}$ and $\mu = 2\ p_{\mathrm{T}}$ to derive the higher and lower bounds, respectively. In case of the η/π^0 ratio, the calculations at the same μ for π^0 and η have been divided through each other, assuming the scale variations are affecting the π^0 and η similarly, and the error has then been estimated based on the η/π^0-ratio variations themselves.

Particle	Particle Ratio to π^0		Particle Ratio to $(\pi^+ + \pi^-)/2$	
π^0	-		1.36	$\pm 0.06^{\text{ stat}}$ $\pm 0.37^{\text{ sys}} \pm 0.17^{\text{ sys f.}}$
$(\pi^+ + \pi^-)/2$	0.74	$\pm 0.03^{\text{ stat}}$ $\pm 0.20^{\text{ sys}} \pm 0.09^{\text{ sys f.}}$	-	
$(K^+ + K^-)/2$	0.100	$\pm 0.004^{\text{ stat}}$ $\pm 0.028^{\text{ sys}} \pm 0.013^{\text{ sys f.}}$	0.13489	$\pm 0.00008^{\text{ stat}}$ $\pm 0.01457^{\text{ sys}} \pm 0.00399^{\text{ sys f.}}$
K^0_S	0.098	$\pm 0.004^{\text{ stat}}$ $\pm 0.027^{\text{ sys}} \pm 0.012^{\text{ sys f.}}$	0.1327	$\pm 0.0001^{\text{ stat}}$ $\pm 0.0140^{\text{ sys}} \pm 0.0035^{\text{ sys f.}}$
η	0.103	$\pm 0.039^{\text{ stat}}$ $\pm 0.050^{\text{ sys}} \pm 0.031^{\text{ sys f.}}$	0.119	$\pm 0.019^{\text{ stat}}$ $\pm 0.047^{\text{ sys}} \pm 0.052^{\text{ sys f.}}$
K^{0*}	0.028	$\pm 0.001^{\text{ stat}}$ $\pm 0.008^{\text{ sys}} \pm 0.004^{\text{ sys f.}}$	0.0385	$\pm 0.0002^{\text{ stat}}$ $\pm 0.0051^{\text{ sys}} \pm 0.0010^{\text{ sys f.}}$
$(p + \bar{p})/2$	0.041	$\pm 0.002^{\text{ stat}}$ $\pm 0.011^{\text{ sys}} \pm 0.005^{\text{ sys f.}}$	0.05522	$\pm 0.00004^{\text{ stat}}$ $\pm 0.00596^{\text{ sys}} \pm 0.00157^{\text{ sys f.}}$
ϕ	0.0120	$\pm 0.0005^{\text{ stat}}$ $\pm 0.0034^{\text{ sys}} \pm 0.0014^{\text{ sys f.}}$	0.01634	$\pm 0.00007^{\text{ stat}}$ $\pm 0.00206^{\text{ sys}} \pm 0.00046^{\text{ sys f.}}$
$(\Lambda + \bar{\Lambda})/2$	0.027	$\pm 0.001^{\text{ stat}}$ $\pm 0.007^{\text{ sys}} \pm 0.003^{\text{ sys f.}}$	0.036775	$\pm 0.00008^{\text{ stat}}$ $\pm 0.00382^{\text{ sys}} \pm 0.00132^{\text{ sys f.}}$
Σ^{*+}	0.0040	$\pm 0.0002^{\text{ stat}}$ $\pm 0.0015^{\text{ sys}} \pm 0.0010^{\text{ sys f.}}$	0.00545	$\pm 0.00007^{\text{ stat}}$ $\pm 0.00155^{\text{ sys}} \pm 0.00119^{\text{ sys f.}}$
$(\Xi^{*0} + \bar{\Xi}^{*0})/2$	0.00114	$\pm 0.00009^{\text{ stat}}$ $\pm 0.00032^{\text{ sys}} \pm 0.00015^{\text{ sys f.}}$	0.0015	$\pm 0.0001^{\text{ stat}}$ $\pm 0.0002^{\text{ sys}} \pm 0.0001^{\text{ sys f.}}$

Table 5.16.: Integrated particle ratio with respect to the neutral or averaged charged pion for NSD p–Pb collisions at $\sqrt{s_{\mathrm{NN}}}$ = 5.02 TeV. The systematic errors have been split in two components: those related to the systematic uncertainties of the measurements themselves (*sys*) and those related to the choice of the functional form of the fit (*sys f.*).

The calculations for pp collisions at $\sqrt{s}$ = 5.02 TeV are based on the older CT10 [359–361] parton distribution functions and use the DSS14 [318] and AESSS [319] fragmentation functions for the π^0 and η meson, respectively. For the neutral pion the calculation using $\mu = p_{\mathrm{T}}$ agrees within 10% with the interpolated reference above p_{T} = 5 GeV/c. Below these momenta, it underestimates the data by about 20%. If the scale variations are considered as well, the calculation and the interpolated data are fully consistent. The agreement is even better than for pp collisions at $\sqrt{s}$ = 2.76 TeV, which could be explained by the use of different PDFs for the latter calculation. For the previous pp comparisons, the MSTW [362] and CTEQQ6M5 [363] had been used for the π^0 and η meson calculations, respectively. For the interpolated η spectrum the calculation with $\mu = p_{\mathrm{T}}$ would not describe the data and overestimates it by $20 - 50\%$, while the same calculation for $\mu = 2\ p_{\mathrm{T}}$ agrees with the interpolated spectrum within 10%. Similar observations have been made for the η meson measurement in pp collisions at $\sqrt{s}$ = 2.76 TeV as well. The agreement for the neutral pions is mostly due to the introduction of the new DSS14 fragmentation functions, which include data from the LHC experiments in the global fit of the fragmentation functions. With older fragmentation functions like DSS07, the agreement would have been on the same level as for the η meson. However, in the DSS14 fragmentation functions the η was not updated. Consequently, it is expected, that once this has been done for the η as well using the same formalism, the calculated spectra will decrease by the same amount, as it was seen for the π^0. The offset in the fragmentation function of the η is also seen in the comparison to the η/π^0 ratio (Figure 5.48), with a high p_{T} value of approximately 0.7.
Within the framework of collinearly-factorized pQCD, effects of the nuclear environment are

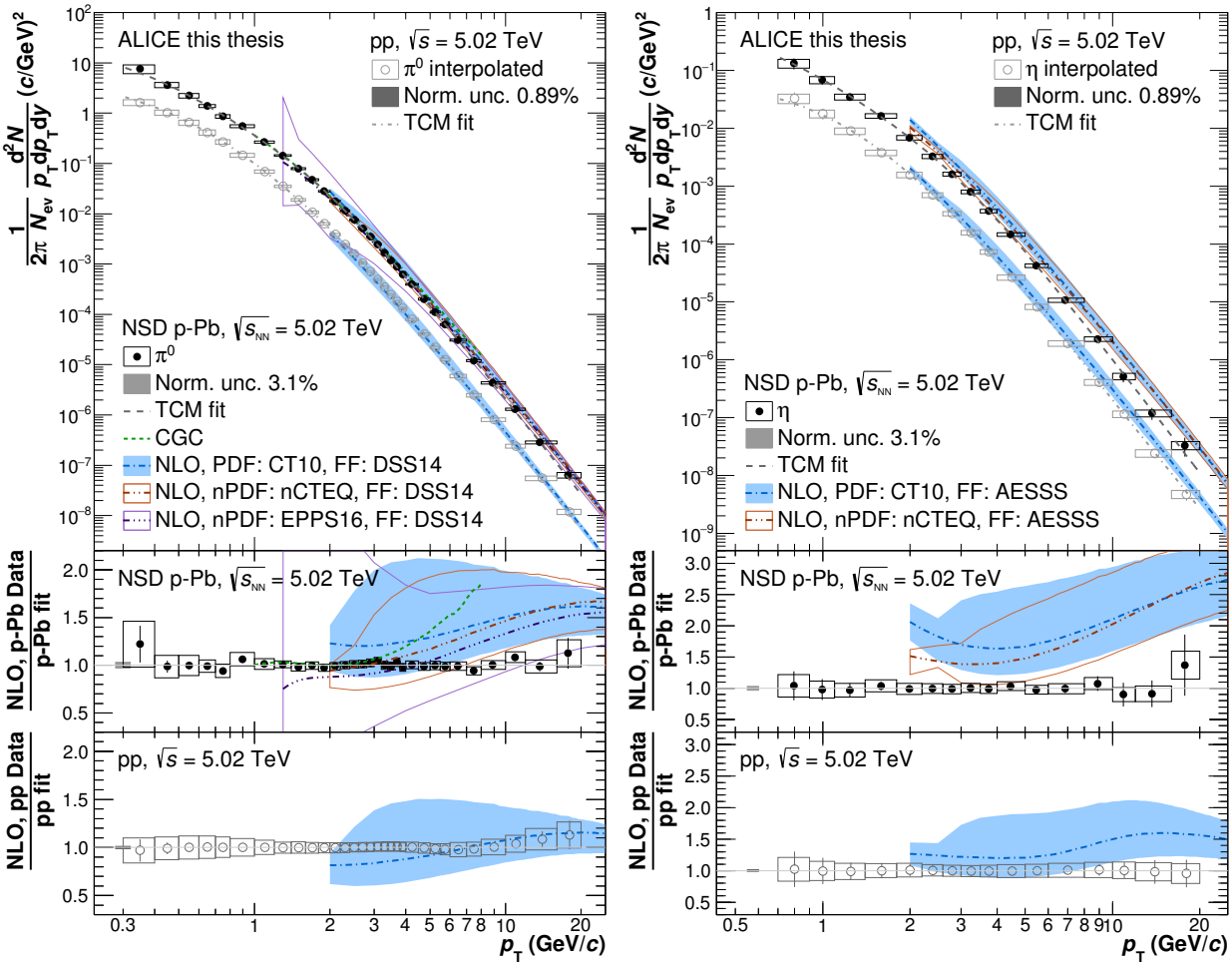

Figure 5.48.: Invariant differential π^0 (left) and η (right) yields produced in NSD p–Pb collision at $\sqrt{s_{\mathrm{NN}}} = 5.02$ TeV, shown as closed dots. Additionally, the interpolated pp reference spectra at $\sqrt{s} = 5.02$ TeV are displayed as open circles with the corresponding statistical and systematic uncertainties. The data are compared next-to-order pQCD calculations from Werner Vogelsang [356] and Ilkka Helenius [357, 358] using the DSS14 [318] and AESSS [319] fragmentation function for the neutral pion and eta meson, respectively. The calculations have been done for different parton distribution functions: CT10 [359–361], nCTEQ15 [364, 365] and EPPS16 [366]. Where necessary, they have been scaled by N_{coll} of 6.9 to be compared to the p–Pb spectra. The neutral pion spectra are also compared to CGC calculations [367]. The ratios of the data and the calculations to the respective two-component model fits [315, 316] to the data are shown in the lower panels. The horizontal error bars denote statistical, the boxes systematic uncertainties. The global normalization uncertainties are not included in the systematic uncertainties and thus displayed as a gray filled box for all ratio plots.

parametrized using nuclear Parton Density Functions (nPDF), which are determined by global fits at next-to-leading order to data from deep inelastic scattering, Drell-Yan and π^0 production. The most commonly used sets at the moment are nCTEQ15 [364, 365] and EPPS16 [366]. The latter evolved from the EPS09 [151, 368] set by including data from the LHC experiments, as well as neutrino scattering measurements. Thus, some of the parameter constrains could be relaxed and it turned out that for the EPS09 version the uncertainties had not been calculated properly and consequently were too small. In order to visualize the effect which the nPDFs have on the respective meson spectra, the calculations for pp collisions using CT10 as a PDF have been scaled with N_{coll} of 6.9. The difference between these scaled calculations and the corresponding ones using the nuclear PDFs is interpreted as being due to shadowing or anti-shadowing, a depletion or enhancement respectively of the parton densities with respect to the free parton. Within the uncertainties, all calculations regardless of the (n)PDF can reproduce the neutral pion invariant yields between 2 and $\approx$ 10 GeV/c. For higher transverse momenta, the calculations start to de-

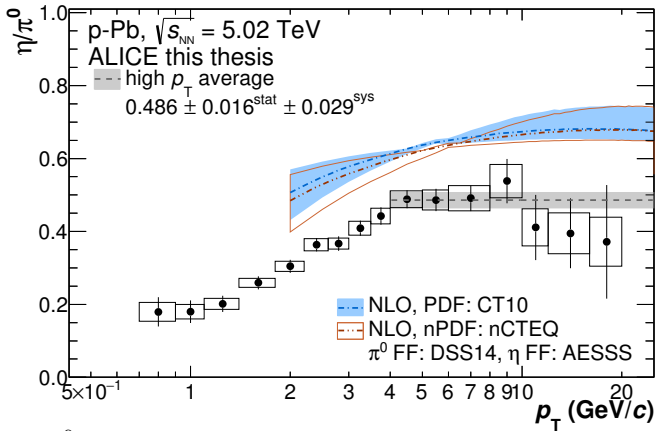

Figure 5.49.: Measured η/π^0 ratio in p–Pb collisions at $\sqrt{s_{\rm NN}}$ = 5.02 TeV compared to NLO pQCD calculations [356] using different PDFs [359–361,364]. In both calculations, the DSS14 [318] and AESSS [319] fragmentation function have been used for the neutral pion and η meson, respectively. The statistical errors are depicted as vertical error bars, while the corresponding systematic uncertainties are shown as empty boxes. Additionally, the high $p_{\rm T}$ average of the measured η/π^0 ratio, $0.485 \pm 0.016^{\rm stat} \pm 0.029^{\rm sys}$, is indicated by the gray dashed line with the corresponding total uncertainty as a band around it.

viate by more 20% from the data. If only the central values are considered for the comparisons, however, the pions are much better described by those calculations including the nuclear PDFs. It can also be seen that the two nuclear PDFs yield different results for the neutral pions in the full transverse momentum range, where the data favors the EPPS16, when considering the full transverse momentum region. For the η meson the calculations perform worse in general, as it would be expected from the comparison for pp collisions. However, the calculation using nCTEQ15 as PDF is still favored by the data even though at high momentum the data is still underestimated by factors of 1.5 to 3.5. The corresponding comparison for the η/π^0ratio among the pp and p–Pb calculations shows, that according to next-to-leading order pQCD calculations the η/π^0ratio is modified below 10 GeV/c, being lower in p–Pb collisions, albeit still being consistent within the respective uncertainties. Unfortunately, no calculations for the η using the EPPS16 nuclear PDFs were available and thus this comparison can not be made for these calculations.
The observation that the η/π^0 ratio flattens above 4 GeV/c for the calculations and the data implies that starting from that point, a power-law fit would yield similar n for both mesons. However, these n might be different for the theoretical predictions and the data, which could explain why at higher transverse momenta the theoretical predictions deviate more from the data in particular for p–Pb collisions. The measured meson spectra have been fitted with a pure power-law distribution above 4 GeV/c with $n_{\pi^0} = 6.110 \pm 0.022^{\rm stat} \pm 0.045^{\rm sys}$ and $n_{\eta} = 6.167 \pm 0.104^{\rm stat} \pm 0.096^{\rm sys}$ with $\chi^2/n_{\rm dof}$ below 0.8. The respective ratios to the data can be seen in Figure 5.42 for the individual fits, for which all uncertainties have been assumed to be uncorrelated versus transverse momentum. Fitting the calculations in the same transverse momentum region as the data yields $n_{\pi^0,\rm CT10} = 6.126 \pm 0.112$, $n_{\pi^0,\rm nCTEQ15} = 6.040 \pm 0.113$ and $n_{\pi^0,\rm EPPS16} = 5.983 \pm 0.26$ for the different calculations. While the η meson calculations are best described by $n_{\eta,\rm CT10} = 6.051 \pm 0.295$ and $n_{\eta,\rm nCTEQ15} = 5.940 \pm 0.122$, respectively. This rather mild change in the power n leads to drastic changes in the spectra at high transverse momenta and explains the observed difference in Figure 5.48.
In addition to the discussed next-to-leading order pQCD calculations, the π^0spectra are compared to calculations using the Color Glass Condensate (CGC) formalism [367,369]. The CGC formalism is an effective theory describing the nuclear environment at low x, where the gluon density is high and non linear processes are expected to play a significant role. As such, it represents an alternative approach to the theoretical description of hadronic structure compared to pQCD. As it can be seen, this approach can describe the neutral pion spectra well up to 4 GeV/c, when using the MV$^\gamma$ initial conditions [370]. The deviation at higher transverse momenta is already present in

the comparison to the pp data at $\sqrt{s} = 7$ TeV [371] and as such was expected.

5.3.4. Neutral Meson Nuclear Modification Factor R_{pA}

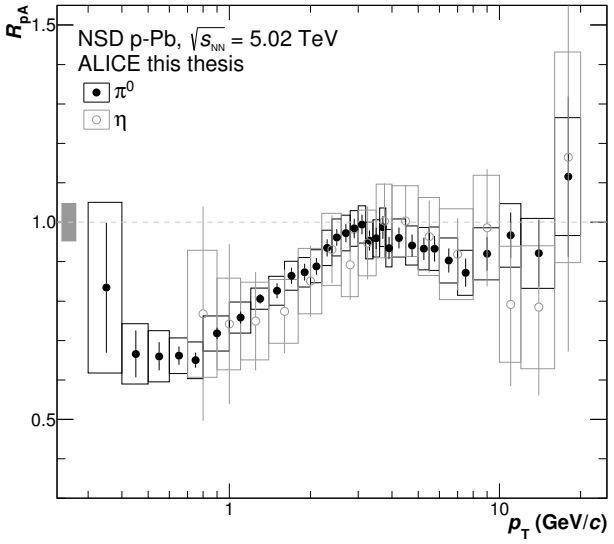

Figure 5.50.: Neutral pion (black circles) and η meson (open gray circles) R_{pA} observed in non single-diffractive p–Pb collisions at $\sqrt{s_{\mathrm{NN}}} = 5.02$ TeV with their corresponding statistical and systematic uncertainties depicted as vertical lines and boxes, respectively. The global uncertainties on the normalization are shown as gray box around unity, as they are common to both measurements. The R_{pA} has been calculated for each individual measurement using the interpolated pp reference for each reconstruction method. The combined R_{pA} is then calculated using the BLUE method.

The nuclear modification factor R_{pA} has been calculated according to

$$R_{\mathrm{pA}} = \frac{\mathrm{d}^2 N^{\mathrm{pA}}/\mathrm{d}y\mathrm{d}p_{\mathrm{T}}}{\langle T_{\mathrm{pA}}\rangle \mathrm{d}^2\sigma^{\mathrm{pp}}/\mathrm{d}y\mathrm{d}p_{\mathrm{T}}}. \tag{5.17}$$

Where $\mathrm{d}^2 N^{\mathrm{pA}}/\mathrm{d}y\mathrm{d}p_{\mathrm{T}}$ corresponds to the invariant yield in p–Pb collisions and $\mathrm{d}^2\sigma^{\mathrm{pp}}/\mathrm{d}y\mathrm{d}p_{\mathrm{T}}$ denotes the interpolated cross section for the correspond meson in pp collisions at the same center-of-mass energy, as already explained for Equation 2.11, the nuclear overlap function is given by $\langle T_{\mathrm{pA}}\rangle$ and corresponds to $\langle T_{\mathrm{pPb}}\rangle = 0.0983 \pm 0.0035$ mb^{-1} [282, 372] at this center-of-mass energy.
In a simplified picture, the nuclear modification factor should be unity at high p_{T} in absence of nuclear effects. As in this scenario a heavy ion collision would be a simple superposition of single pp collisions. It can, however, be modified by multiple effects like the influence of the nuclear PDFs or the formation of an intermediate state, like a hadron gas or quark gluon plasma. The initial motivation for this measurement was, that by measuring this quantity for various identified hadrons in non single-diffractive p–A collisions, where no intermittent state was expected, one might be able to separate the effects from the participation of a single heavy ion in the collision from those related to a possible formation of the quark-gluon-plasma in A–A collisions. Recent measurements at the LHC and RHIC revealed, however, that this picture might be to simplistic as a small QGP may already be formed at least in central p–A collisions.
Figure 5.50 shows the combined R_{pA} for the neutral pion (black circles) and the η meson (gray open circles) with their corresponding statistical and systematic uncertainties depicted as vertical lines and boxes, respectively. While the uncertainties related to the normalization, including those for the nuclear overlap function, are shown as gray filled box as they are common to all measurements at this center-of-mass energy. The combination of the individual measurements has been done using the BLUE method, as described at the end of Section 5.3.2, taking into account the cancellation

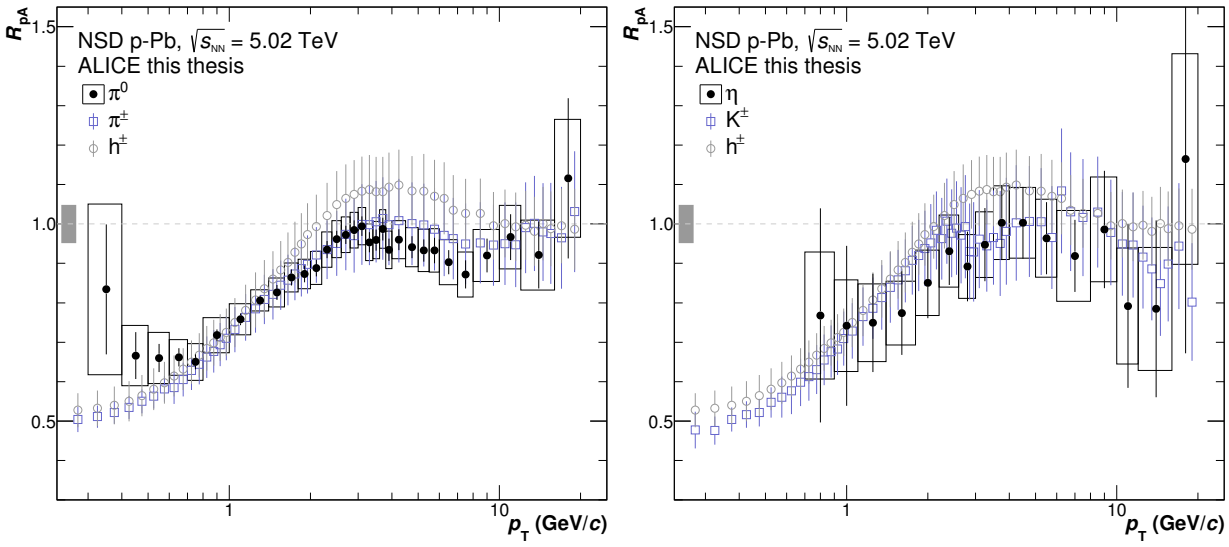

Figure 5.51.: Left: Comparison of the neutral pion R_{pA} (black circles) to the corresponding measurements for unidentified charged hadrons [154] (gray open circles) and charged pions [97] (blue open squares) for p–Pb collisions at $\sqrt{s_{\mathrm{NN}}}$ = 5.02 TeV. Right: Comparison of the eta meson R_{pA} (black circles) to the corresponding measurements for unidentified charged hadrons (gray open circles) and charged kaons [97] (blue open squares) within the same collision system. For the charged particle measurements the total uncertainties are shown as vertical lines. The global uncertainties on the normalization are shown as gray box around unity, as they are common to all measurements.

of p_{T} independent systematic uncertainties, which are common for the calculated pp reference and the p–Pb measurement. The weights of the individual measurement can be found in Figure B.23. The R_{pA} for both mesons is smaller than unity below $p_{\mathrm{T}} = 3$ GeV/c, where a modification of the spectral shape is expected from multiple scattering in the nucleus. This is referred to as Cronin effect and can even lead to an enhancement of the spectra with respect to pp for p–A and A–A collisions. This effect is, however, strongly dependent on the quark mass and number and thus more pronounced for heavier particles and baryons. Above 3 GeV/c the η meson R_{pA} is consistent with unity within its uncertainties. For the neutral pion on the other hand it starts decreasing again and approaches a constant value of approximately 0.9 above 6 GeV/c. Taking into account the normalization uncertainty as well as the individual systematic and statistical uncertainties, however, this deviation from unity cannot yet be considered significant.
The π^0 and η R_{pA} are compared to those of the charged pions and kaons [97] in Figure 5.51. Additionally, the corresponding R_{pA} for the unidentified charged hadrons [154] is shown in both plots. It can be seen that the R_{pA} of the charged and neutral pions agrees within the uncertainties, albeit at higher momenta an offset can be seen, which leads to $\sim 5\%$ higher R_{pA} for the charged pions compared to that of the neutrals. The charged hadron R_{pA} is even larger, as it includes the contribution from the charged kaons and the protons as well, which are enhance at ~ 3 GeV/c due to the Cronin effect, as seen in Figure 2.13. The comparison of the results for the charged kaons, pions and the η meson, reveals a mass ordering at low momenta and a stronger depletion for heavier particles at lower p_{T} is observed. This mass ordering could be interpreted as a sign of collectivity, however, it could also be interpreted in terms of the Cronin-effect. At higher transverse momenta the η meson R_{pA} agrees with that of the charged kaon. Additionally, it can be seen that the R_{pA} of these particles tends to decrease for $p_{\mathrm{T}} > 8$ GeV/c. While this could be an artefact of the large statistical uncertainties of the reference calculations at higher transverse momenta, this trend should be investigated in the higher statistics data set using the measured pp reference. It might lead to a better understanding of the strange quark production in p–A collisions, as the η meson is a superposition of all three light $\mathrm{q\bar{q}}$ pairs, and as such is the lightest meson containing two strange quarks even though the net-strangeness is zero.

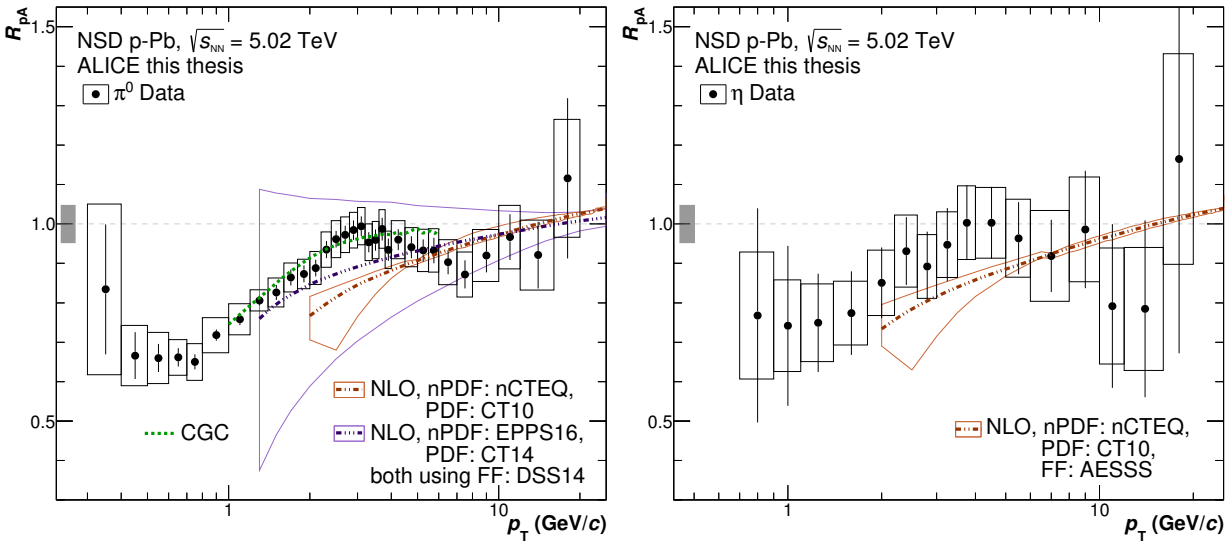

Figure 5.52.: Nuclear modification factor of the neutral pion (left) and η meson (right) in NSD p–Pb collisions at $\sqrt{s_{\mathrm{NN}}} = 5.02$ TeV compared to CGC [367] and NLO pQCD calculations done for two different sets of nuclear PDFs: nCTEQ15 [364,365] and EPPS16 [366]. While statistical and systematic uncertainties of the measurements are shown as vertical line and empty boxes, respectively, the global uncertainties on the normalization is depicted as gray box around unity.

A comparison of the combined neutral pion and eta meson R_{pA} to the NLO pQCD calculations and a CGC calculation can be found in Figure 5.52. The CGC prediction [367] describes the data in the depicted region very well, however, the calculation stops at 6 GeV/c, where the corresponding invariant yield calculation failed to describe the data. The question remains whether it would describe the data beyond that point due to the fact that a similar deviation had been seen in pp collisions for this formalism as well.
To be able to compare the results of the different nuclear PDFs also for the R_{pA} the obtained spectra from Werner Vogelsang [356] scaled by N_{coll} for nCTEQ15 and CT10 have been divide by one other at the same μ and afterwards the remaining variations among the different factorization, fragmentation and renormalization scales are taken as uncertainties of the R_{pA}. This procedure assumes full factorization of the different processes and similar behavior of the scales in different collision systems. Thus, the errors might be too small, while the central values should be correct. The resulting R_{pA} calculations for nCTEQ15 describes the data of both mesons between above 5 GeV/c. The transverse momentum dependence is, however, quite different and the calculation predicts an R_{pA} above unity for momenta above 15 GeV/c. The transverse momentum dependence could already be derived from the different powers of n from the power-law fit to the calculations for the pp and p–A calculations. A similar observation can be made for the corresponding R_{pA} calculation using the EPPS16 nPDFs [357, 358, 366]. The slope of the respective R_{pA} is, however, slightly smaller and thus the central values come closer to the data in particular at lower transverse momenta, where the calculation based on nCTEQ15 underestimated the data by at least a factor $2 - 3$.

6. Direct Photon Analysis

The extraction of direct photons from the large background of decay photons from light mesons and baryons is commonly done using two different techniques:

a) Isolation of the direct photon from other particles in the event by requiring that in a cone of $R < R_{\mathrm{iso}}$ around the photon the total deposited energy by all reconstructed particle does not exceed E_{iso} or

b) statistical subtraction of the decay photons using decay simulations based on the spectra of the measured light flavored particles or tagging methods.

While both analysis techniques are viable approaches to extract the direct photon spectra and correlations, they probe different physics. The main purpose of the isolation analyses is to understand the production of photons in hard collisions, mainly through 2→2 processes like $q + g \rightarrow q + \gamma$ or $\bar{q} + q \rightarrow g + \gamma$. These processes can be calculated using pQCD at next-to-leading order and the measurements help to constrain the parton distribution functions as well as the corresponding fragmentation functions. One of the main concerns in these analyses is, however, the insufficient separation between the photon signal and the surrounding particles for photons below $15 - 20$ GeV/c, as the relative energy difference between the underlying event and the desired probe decreases.
Below these momenta it is more favorable to use the statistical subtraction method for the decay photons or other tagging techniques, which identify the photon as originating from a neutral pion or eta meson decay for instance. In this energy and momentum regime mainly softer processes for the photon production can be accessed. In heavy ion collisions at RHIC and LHC, it is assumed that at low momenta, $p_{\mathrm{T}} < 3$ GeV/c, the production is dominated by the thermal radiation from a quark-gluon plasma or hot hadronic gas (see Section 2.3.4). While it is not clear which production process is the dominant at intermediate momenta (3 GeV/$c < p_{\mathrm{T}} < 10$ GeV/c). Within the experiments, it is unfortunately not possible to distinguish different sources of direct photons and, as discussed, even the distinction between direct and decay photons is not obvious.
The presented direct photon analysis in this thesis is based on the statistical subtraction method in combination with the double ratio method [207], as the main focus is on the extraction of a possible thermal photon signal in pp and p–Pb collisions. The analysis is a direct continuation of the work published in [212] using also other reconstruction techniques for the photons and mesons. The respective Pb–Pb analysis had been carried out as a collaboration between Martin Wilde and myself and is described in detail in [211]. The final results were, however, obtained during the first year of this PHD project and the corresponding paper should be considered a part of the work presented here, although it will not be further discussed in detail.
Within the next chapter, the direct photon reconstruction using three different detection techniques (PCM, PCM-EMC and EMC) will be explained. All of them are based on the double ratio (R_γ) (Equation 2.15) to be able to cancel part of the systematic uncertainties for the photon and meson reconstructions. Consequently, the minimum and maximum transverse momentum reach of the photon measurements in the various techniques has been determined by the transverse momentum reach of the neutral pions, which have been reconstructed using the same analysis method. At first, the procedure to obtain the decay photon spectrum will be explained, which is followed by the description of the corrections needed to obtain a fully corrected inclusive photon spectrum. Afterwards, the combination of these two quantities using the double ratio technique to obtain a direct photon spectrum will be discussed and the corresponding systematic uncertainties will be explained. As the procedure is rather similar for both collision systems, the decay

photon simulation and correction factors for pp collisions at $\sqrt{s} = 2.76$ TeV and p–Pb collision at $\sqrt{s_{\mathrm{NN}}} = 5.02$ TeV will be discussed in parallel. The final results will be discussed in different sections including their systematic uncertainties. The chapter will be concluded by the comparison of the pp, p–Pb and Pb–Pb results for the common reconstruction technique. Furthermore, the results will be compared to the corresponding ones obtained using the PHOS in p–Pb [373] and Pb–Pb collisions [212] as well as NLO pQCD calculations and hydrodynamic calculations.

6.1. Decay Photon Simulation

In order to efficiently simulate the decay photon and electron spectra, the different experiments have developed fast simulations for this specific purpose. These are based on the parametrizations of the measured meson and baryon spectra and usually use the standard particle decay algorithms from Pythia or dedicated decayers to correctly simulate the decay properties of the respective particles. The decay simulations are commonly referred to as cocktail simulations, as they are composed of many different sources and their resulting photon or electron spectra contain particles from various sources and production mechanisms. Within ALICE the decay photon cocktail is implemented in the AliRoot [252] and AliPhysics [253] software packages using the decay algorithms of Pythia 6.4 [255]. Fortunately, no detector response simulation is necessary to correctly generate the decay-photon spectra as later comparisons are done on the level of fully corrected photon spectra, which should be independent of the respective detector response.
Within this thesis only the largest sources of decay photons have been considered in the cocktail simulations. They are listed in Table 6.1 with the considered decays and respective branching ratios as provided by the particle data group [13]. Furthermore, the table contains the references to the measured spectra in the corresponding collision systems to indicate for which particles data have been available. As this list of particles is not exhaustive regarding the photon sources, the experimental definition of the direct photons at low transverse momenta contains also photons from other sources, which have not been simulated in the respective cocktail. It has, however, been ensured that non of these contributions should exceed 0.001% at any momentum and thus can be neglected within the current precision of the measurements. For previous experiments usually only the π^0, η, η' and ω had been considered as decay photon sources, whereas within ALICE also the ϕ, $\rho^{\pm,0}$, Σ^0 and the Δ resonances are contained in the simulations. Also the contributions from K^0_S, K^0_L and Λ have been simulated. Most of the photons originating from these sources are, however, generated through decays of the neutral pions which stemmed from the decay of one of these strange particles. Thus, they are considered secondary photons and have to be dealt with separately. Even more so as they are not necessarily produced at the primary vertex and can thus have different efficiencies depending on the location of the production vertex as well as their momenta. The procedure to correct for these secondary contributions will be explained in Section 6.2.
The largest contribution to the decay photon cocktail are the photons from decays of π^0's ($> 80\%$), followed by those of the η ($\approx 10 - 15\%$), ω ($\approx 2.8\%$) and η' mesons ($\approx 1.4\%$). While the expected direct photon signal at low transverse momenta in pp and p–Pb collisions is of the order of $1 - 5\%$ below 3 GeV/c. Consequently, the invariant differential yields of the neutral pions and η mesons need to be modeled as accurately as possible, basing the parametrizations on the neutral meson data presented in Chapter 5 for the respective collision systems and neutral meson reconstruction techniques. Each of the individually measured π^0 spectra using the different reconstruction techniques in the two collision systems has been parametrized using slightly different parameters in order to be able to cancel possible biases in the R_γ as much as possible, while still smoothing the non-physical statistical fluctuations.
The best possible parametrizations of the individual π^0 spectra have been obtained using a modified Hagedorn function (Equation 5.15), which had already been used to calculate the integrated

particle	mass (MeV)	decay	BR	m_{T} const. C_m	pp	NSD p–Pb
π^0	134.98	$\gamma\gamma$	$9.882 \cdot 10^{-1}$		[297]	this thesis
		$e^+e^-\gamma$	$1.174 \cdot 10^{-2}$			
η	547.85	$\gamma\gamma$	$3.941 \cdot 10^{-1}$		[297]	this thesis
		$\pi^0\gamma\gamma$	$2.560 \cdot 10^{-4}$			
		$\pi^+\pi^-\gamma$	$4.220 \cdot 10^{-2}$			
		$e^+e^-\gamma$	$6.899 \cdot 10^{-3}$			
		$\mu^+\mu^-\gamma$	$3.090 \cdot 10^{-4}$			
η'	957.66	$\rho^0\gamma$	$2.908 \cdot 10^{-1}$	0.40 ± 0.20		
		$\omega\gamma$	$2.746 \cdot 10^{-2}$			
		$\gamma\gamma$	$2.198 \cdot 10^{-2}$			
		$\mu^+\mu^-\gamma$	$1.080 \cdot 10^{-4}$			
ω	782.65	$\pi^0\gamma$	$8.350 \cdot 10^{-2}$	0.85 ± 0.10		
		$\eta\gamma$	$4.600 \cdot 10^{-4}$			
		$\pi^0\pi^0\gamma$	$7.000 \cdot 10^{-5}$			
ρ^0	775.49	$\pi^+\pi^-\gamma$	$9.900 \cdot 10^{-3}$	1.00 ± 0.20	[324]	
		$\pi^0\gamma$	$6.000 \cdot 10^{-4}$			
		$\eta\gamma$	$3.000 \cdot 10^{-4}$			
		$\pi^0\pi^0\gamma$	$4.500 \cdot 10^{-5}$			
ρ^+	775.49	$\pi^+\gamma$	$4.500 \cdot 10^{-4}$	1.00 ± 0.20	*	
ρ^-	775.49	$\pi^-\gamma$	$4.500 \cdot 10^{-4}$	1.00 ± 0.20	*	
ϕ	1019.46	$\eta\gamma$	$1.311 \cdot 10^{-2}$		[323]	[353]
		$\pi^0\gamma$	$1.274 \cdot 10^{-3}$			
		$\pi^+\pi^-\gamma$	$4.100 \cdot 10^{-5}$			
		$\pi^0\pi^0\gamma$	$1.130 \cdot 10^{-4}$			
		$\pi^0\eta\gamma$	$7.300 \cdot 10^{-5}$			
		$\eta'\gamma$	$6.300 \cdot 10^{-5}$			
		$\mu^+\mu^-\gamma$	$1.400 \cdot 10^{-5}$			
Δ^0	1232.00	$n\gamma$	$6.000 \cdot 10^{-3}$	1.00 ± 0.50		
Δ^+	1232.00	$p\gamma$	$6.000 \cdot 10^{-3}$	1.00 ± 0.50		
Σ^0	1192.64	$\Lambda\gamma$	1.000	0.490 ± 0.245		
K_S^0	497.61	$\pi^+\pi^-\gamma$	$1.787 \cdot 10^{-3}$		[95, 307]*	[97, 162]*
		$\gamma\gamma$	$3.000 \cdot 10^{-6}$			
K_L^0	497.61	$\pi^\pm e^\mp\nu\gamma$	$3.988 \cdot 10^{-3}$		[95, 307]*	[97, 162]*
		$\pi^\pm\mu^\mp\nu\gamma$	$4.920 \cdot 10^{-4}$			
		$\pi^+\pi^-\gamma$	$4.200 \cdot 10^{-5}$			
		$\pi^0\gamma\gamma$	$1.000 \cdot 10^{-6}$			
		$\gamma\gamma$	$5.500 \cdot 10^{-4}$			
		$e^+e^-\gamma$	$9.000 \cdot 10^{-6}$			
Λ	1115.68	$n\gamma$	$8.400 \cdot 10^{-4}$		[307]	[162]

Table 6.1.: Meson and Baryon decays which are included in the decay photon simulation together with their corresponding branching ratios [13]. Furthermore, the m_{T} scaling constants at high transverse momentum are given, which have been predicted in [255] or were estimated based on thermal model calculations. In the last two columns the references to the measurements of the respective particles are given, if they are available for the particular collision system and centrality. If a particle had been measured to a better accuracy in a different charge state, the more precise measurement has been used in order to obtain the parametrization, these case are indicated by a * next to the corresponding reference.

yields of the respective mesons. Figure 6.1(left) shows the invariant yield of the neutral pions reconstructed using the PCM-EMC method per minimum bias event as a function of transverse momentum with the corresponding statistical uncertainties together with the respective parametrization used for the decay simulation. Furthermore, the corresponding ratio of the spectrum to the parametrization is shown in the panel below. It can be seen that the chosen functional form describes the data within the statistical uncertainties in the measured region. The same function has also been used to extrapolate the expected yield to higher and lower momenta to allow to measure the direct photons in a larger transverse momentum region than the decay photon of the original neutral pion spectrum would allow. In general, it has been found that to extract the direct photons up to a certain $p_{\mathrm{T,\,max}}$, the neutral pions need to be simulated up to approximately 3 times $p_{\mathrm{T,\,max}}$. In order to obtain the functional form of the η meson yield in both collision systems, a different approach has been followed and the combined η/π^0 ratio has been parametrized and afterwards multiplied with the measured neutral pion yield of the respective reconstruction technique. This procedure reduces the uncertainties on the eta meson yield significantly at higher transverse momenta, as in the η/π^0 ratio part of the uncertainties cancels and consequently the degrees of freedom for the fit in particular at higher momenta are reduced. As presented in the previous chapter, the η/π^0 ratio flattens above 4 GeV/c in pp and p–Pb collisions at all investigated center-of-mass energies. Thus, it seems natural that the ratio of two functions which are each composed of a soft component describing the spectra at low momenta and a hard component describing the particle production at high transverse momenta should be able to fit the measured η/π^0 ratio in the full transverse momentum range. The hard component can be further restricted by requiring that the two spectra follow the same power-law depends above ≈ 4 GeV/c. While the soft component has been chosen to resemble a blast wave function, as for p–Pb collisions a common radial flow component could be present. The resulting empirical function can be written as:

$$\frac{\eta}{\pi^0}(p_{\mathrm{T}}) = \frac{C \cdot \exp\left(\frac{\beta p_{\mathrm{T}} - m_{\mathrm{T}}^{\eta}}{T\sqrt{1-\beta^2}}\right) + N \cdot C_{s/h} \cdot \left(1 + \left(\frac{p_{\mathrm{T}}}{p_0}\right)^2\right)^{-n}}{\exp\left(\frac{\beta p_{\mathrm{T}} - m_{\mathrm{T}}^{\pi^0}}{T\sqrt{1-\beta^2}}\right) + C_{s/h} \cdot \left(1 + \left(\frac{p_{\mathrm{T}}}{p_0}\right)^2\right)^{-n}}, \tag{6.1}$$

where $C_{s/h}$ is a relative normalization between the soft and hard part of the parametrization and N is the constant ratio between the two particle species that is approached at high transverse momenta. The soft component, on the other hand, is determined by a common radial flow velocity β and the kinetic freeze-out temperature T. Even though this functional form is clearly intended to describe the particle production in heavy ion collisions it also yields a good description for lighter collision systems.

The fit to the combined η/π^0 ratio in p–Pb collisions at $\sqrt{s_{\mathrm{NN}}} = 5.02$ TeV can seen in Figure 6.1(right) together with the corresponding ratio of the data points to the fit. The functional form reproduces the measurement within the statistical uncertainties below 8 GeV/c, beyond these momenta the ratio seems to drop in the data, albeit having large statistical uncertainties. Taking into account also other collision systems it has been decided to nonetheless use this parametrization as the last three points seem to fluctuate downwards in the data and no significant deviation from a constant could be observed beyond 4 GeV/c.

For the remaining particles, which have been measured in the different collision systems, the spectra have been parametrized in the available p_{T} range and the functions have been constrained at higher momenta to approximately match the particle ratios observed in the same collisions system at a similar center-of-mass energy. For some of the mesons and baryons, on the other hand, no measurement was available. In those cases m_{T}-scaling was employed using the following formula:

$$E\frac{\mathrm{d}N^X}{\mathrm{d}p^3} = C_{m,X} \cdot f_B(p_{\mathrm{T}}) \left(\sqrt{p_{\mathrm{T}}^2 + m_{0,X}^2}\right). \tag{6.2}$$

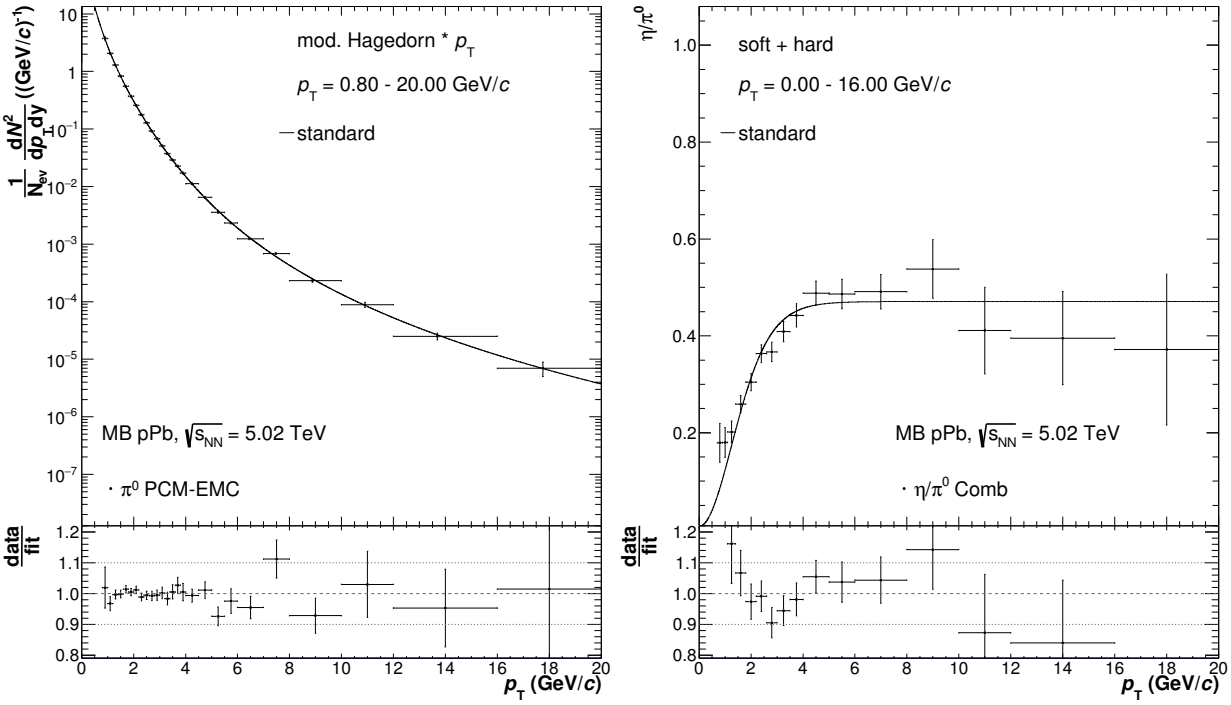

Figure 6.1.: Invariant yield of the neutral pion in minimum bias p–Pb collisions at $\sqrt{s_{\mathrm{NN}}}$ = 5.02 TeV measured with the PCM-EMC neutral meson reconstruction technique (left) together with the corresponding modified hagedorn function (Equation 5.15), which is used as parametrization for the neutral pions using this reconstruction for the decay photon simulation. Additionally, the combined η/π^0ratio for p–Pb collisions at $\sqrt{s_{\mathrm{NN}}}$ = 5.02 TeV (right) together with its parametrization using the fit defined in Equation 6.1. The ratio of the data to the corresponding function is shown in the lower panel. The vertical error bars correspond to the statistical uncertainties of this measurement. The corresponding distributions for the other reconstruction techniques can be found in Appendix C.1.

The factor $C_{m,X}$ represents the relative normalization factor of particle X to the reference particle B at high transverse momenta, which has to be obtained from experimental results and is given in Table 6.1, where necessary. As already explained it has been found that this relation is only approximate and breaks down at low momenta. It should be applicable, however, where $p_{\mathrm{T}} >> m_0$. Furthermore, the scaling should be applied separately for mesons and baryons, as no scaling relation in between mesons and baryons has been observed at RHIC [374,375] or LHC. Consequently, for the mesons the π^0 has been chosen as the base particle, while for the baryons the proton spectrum has been selected as the base parametrization. The scaling properties could be even further improved if the feed-down from heavier strongly decaying particles were to be subtracted from the π^0 and proton spectrum respectively, which has not been done as it would rely too much on the model assumptions of the production of these decays as well.
The p_{T} distributions of the individual mesons and baryons which have been used for the cocktail simulation in p–Pb collisions at $\sqrt{s_{\mathrm{NN}}}$ = 5.02 TeV for the direct photon analysis using the PCM-EMC reconstruction method are shown in Figure 6.2 together with the corresponding particle ratios to the neutral pion spectrum. By construction all particle ratios of the mesons to the neutral pion are flat at high transverse momenta. While they drop significantly for the baryon to neutral pion ratios, as the scaling for the latter was done with respect to the protons.
The resulting decay photon spectra of the different sources can be seen in Figure 6.3 together with their respective relative contribution to the total decay photon cocktail. The cocktail is dominated by the decays of the neutral pion, which contributes between $80 - 90\%$ depending on transverse momentum. The second largest contribution originates, as expected, from the η meson contributing approximately $9 - 16\%$ above a photon momentum of 1 GeV/c. The contributions from heavier mesons, like the ω and η', range between $1.3 - 2.7\%$ and $1.1 - 1.5\%$, respectively.

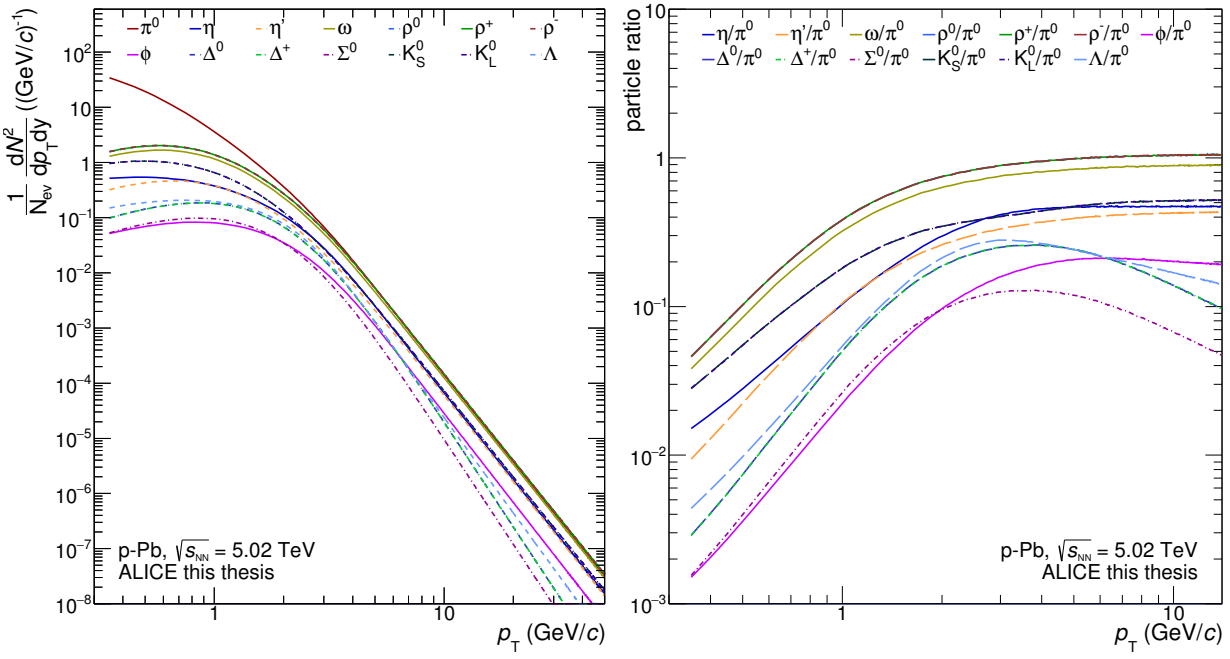

Figure 6.2.: Spectra of all mesons and baryons entering the decay photon simulation (left) as well as their ratios to the neutral pion spectrum for minimum bias p–Pb collisions at $\sqrt{s_{\mathrm{NN}}} = 5.02$ TeV. In these plots the parametrization of the PCM-EMC spectrum has been used for the neutral pions and consequently also for the m_{T}-scaled mesons and the η meson. As the latter is calculated from the fit to the combined η/π^0 ratio multiplied with the neutral pion spectrum parametrization.

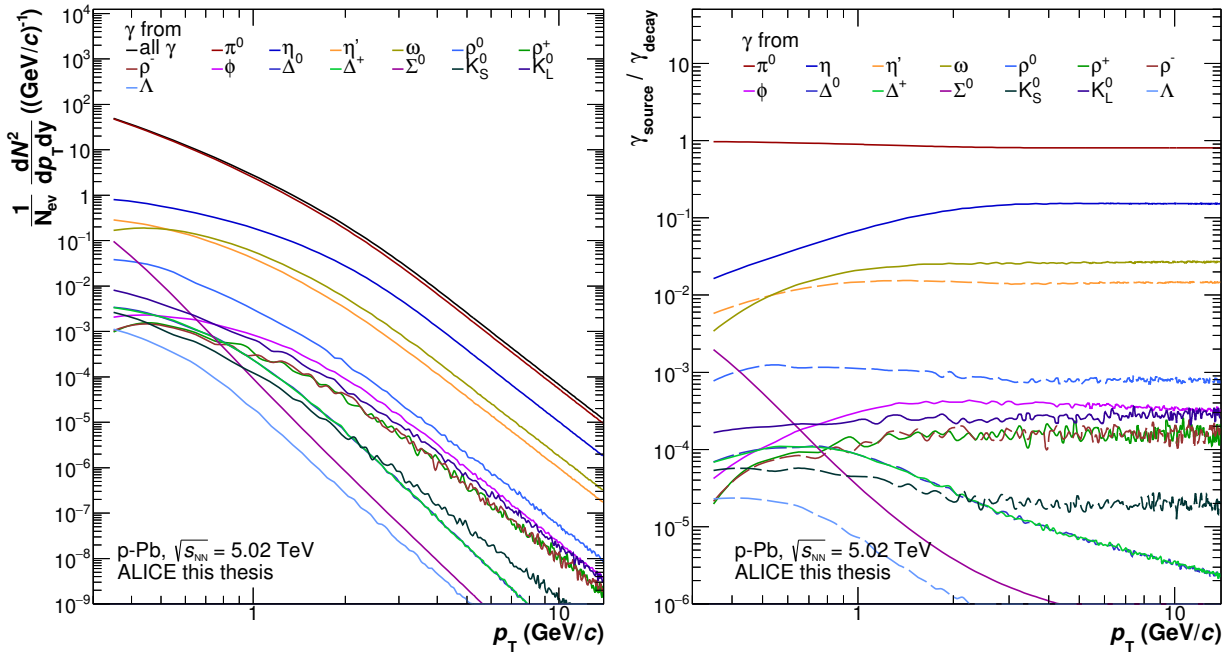

Figure 6.3.: Left: Individual decay photon spectra for p–Pb collision at $\sqrt{s_{\mathrm{NN}}} = 5.02$ TeV using the fit to the PCM-EMC spectrum for the neutral pions and the corresponding m_{T} scaled spectra. Right: Relative contribution of the individual particle decay to the total decay photon spectrum in the same collision system using the same π^0 reconstruction method.

Beyond these contributions, the Σ^0 should be taken into account at very low momenta and the ρ^0 in the full momentum range each of them contributing about 0.1% to the total number of decay photons. The latter two contributions lie, however, well below the current sensitivity limits of the neutral pions themselves. Similar decay photon distributions have been obtained when using the parametrizations of the π^0 reconstructed with the PCM or EMC method as well as the combined neutral pion spectrum. Nonetheless, the individual parametrizations have been used to extract the direct photon signal from the inclusive photon distributions of the individual methods as the spread of the π^0 spectra in certain transverse momentum regions is larger than the expected direct photon signal.
The same procedure has been used to obtain the decay photon cocktail for pp collisions, where once more the neutral pions in their respective reconstruction techniques have been parametrized as well as the combined η/π^0 ratio. Due to the larger statistical uncertainties in particular at low transverse momenta, however, the cocktail is also less constrained in particular for the η meson contribution. The corresponding figures can be found in Appendix C.1. As it is not expected that the particle ratios differ significantly between pp and p–Pb collisions at LHC energies the relative decay photon contributions do neither. At this center-of-mass energy, the ρ contributions can be directly calculated from the respective spectrum [324], which reduces the possible biases on their decay photon distributions and yields a total contribution of the ρ^0 decay photons of 0.08% to the total decay photon spectrum.

6.2. Inclusive and Direct Photon Reconstruction

In order to extract the inclusive photon spectra from the photon candidates obtained in Sections 4.2 and 4.3 using the PCM and EMCal photon reconstruction, respectively, these photon candidates need to be corrected for the contribution from out-of-bunch pile-up, secondary photons from strange particle decays and contaminations from other particles. Furthermore, they need to be corrected for the detector reconstruction efficiency as well as the corresponding energy or momentum resolutions. For the conversion photons, the conversion probability needs to be taken into account in addition. The respective correction factors for pp and p–Pb collisions for the PCM and EMC photon reconstruction techniques will be explained in the following section. In case of the PCM-EMC analysis stream the inclusive photons are purely based on the PCM reconstruction and should ideally coincide with those obtained for the PCM standalone reconstruction. Nonetheless, the respective correction factors are reported for both collision systems, as for instance different data reconstruction streams have been used to obtain the photons for PCM and PCM-EMC for the pp data set, as the EMCal was not read out for all collected events in that data sample. Furthermore, for the p–Pb measurements the HIJING Monte Carlo simulation could only be used for the pure PCM analysis, due to the inclusion of added signals in the respective simulation, which cannot yet be handled properly when using the EMCal information in addition.
If the photons are reconstructed with PCM, the photon candidate sample might contain photons from different events, which are referred to as out-of-bunch pile-up as already explained in Section 5.1.1. As those photons show no significantly different properties from the photons from the triggered event, they cannot be rejected on a particle by particle basis. Thus, the same statistical rejection technique has been applied as for the neutral meson candidates when using the PCM meson reconstruction. For each photon candidate, the distance of closest approach to the primary vertex along the beam axis (dca_Z) has been calculated. The correction is derived as a function of transverse momentum from these distributions afterwards trying to separate the contributions from out-of-bunch photons from those belonging to the triggered event. As for the meson reconstruction the photon candidates are classified according to the amount of ITS hits, which are available on the two legs. The out-of-bunch pile-up contribution is negligible for photon candidates with at least two ITS hits on each leg (category 3). It is the largest, if the photons have been reconstructed

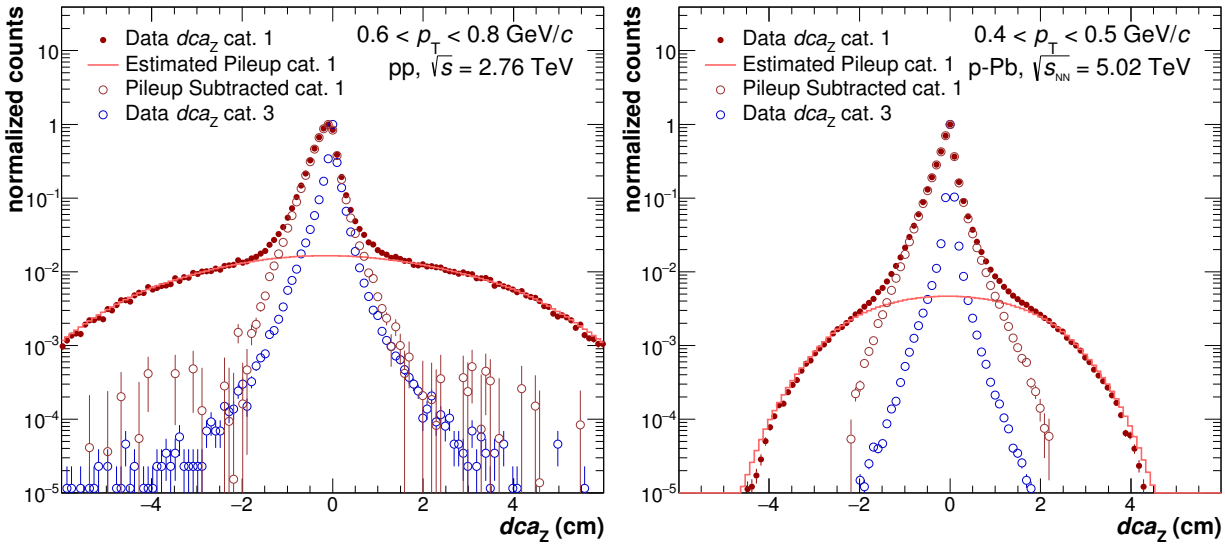

Figure 6.4.: dca_Z distribution for photon candidates with respect to the primary collision vertex in pp collisions at $\sqrt{s} = 2.76$ TeV (left) and p–Pb collisions at $\sqrt{s_{\mathrm{NN}}} = 5.02$ TeV (right) at low transverse momenta. The distributions are shown for two different photon reconstruction categories, where the category 1 photons (red) are reconstructed solely based on the TPC information and photons from category 3 have at least 2 ITS hits on each leg (blue). Furthermore, the estimated background from out-of-bunch pile-up contributing to category 1 is displayed as well as the pile-up subtracted distribution for the same category. The different categories have been normalized such that their maxima agree in order to allow to compare their shapes.

solely based on the TPC information (category 1). Figure 6.4 shows the dca_Z distributions for selected transverse momentum slices in pp and p–Pb collisions for different photon reconstruction categories. The distributions for the photon category 3 reflect the optimal dca_Z distribution for photons, which convert in the lower layers of the ITS for the respective data taking conditions. While the corresponding distribution for the category 1 shows a broader and slightly asymmetric peak on top of a broad Gaussian like structure. The asymmetry in the peak can arise from different resolutions and different ITS coverages for the two halves of the TPC. It is sufficiently well reproduced in the simulations. The additional structure, on the other hand, has been attributed to the out-of-bunch pile-up contributions, similar to the meson analysis. It is approximated using the ROOT [254] internal background estimation routines and the resulting background estimate is shown as well. The same procedure has been repeated for all transverse momentum slices and categories. However, as there is no indication for photons from out-of-bunch pile-up for the categories 2 and 3, these estimates have been neglected, even though the ROOT algorithm would have found a small but non-zero background contribution. The fraction of background photons in category 1 has been weighted with the fraction of photons reconstructed in this category to obtain the final correction factor ($C_{\text{pile-up}}$) for the out-of-bunch pile-up. Furthermore, it has to be taken into account that the dca_Z distribution naturally broadens for photons from strange particle decays, like the $\mathrm{K}^0_{\mathrm{S}}$. Thus, a correction to the estimated out-of-bunch pile-up correction has been derived from the corresponding dca_Z distributions in the simulations.
The final correction factor for the photons used in the inclusive photon spectra for PCM and PCM-EMC are shown in Figure 6.5 for pp and p–Pb collision as a function of transverse momentum. In general, the correction is about 5-6 times larger for the pp data set, as the bunch intensity and in-bunch pile-up probability (μ) were higher than for the p–Pb data taking conditions. Furthermore, it can be seen that the correction decreases with increasing momentum as the fraction of photons reconstructed with ITS information increases. Photons at very low momenta are, however, in more than 55% of the cases reconstructed purely based on the TPC information and thus suffer more from out-of-bunch pile-up. The small difference in the out-of bunch pile-up correction for pp collisions can be attributed to the different reconstruction passes, which are used for the PCM and

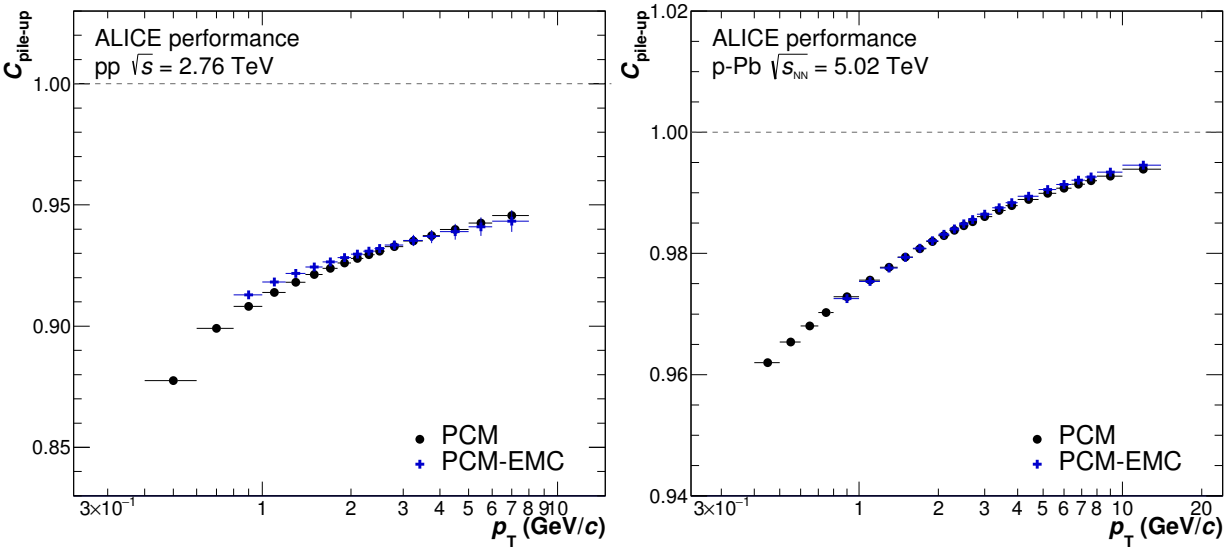

Figure 6.5.: Correction factor ($C_{\text{pile-up}}$) for the of out-of-bunch photon contamination contributing to the photon candidate samples in pp collisions at $\sqrt{s} = 2.76$ TeV (left) and p–Pb collisions at $\sqrt{s_{\text{NN}}} = 5.02$ TeV (right) when reconstructing photons with the PCM photon reconstruction method.

PCM-EMC analyses, respectively. In one case the information from the SDD is included, while it is not in the other one. The pile-up for the PCM reconstruction ranges from 12.5% to 5.5% at high transverse momenta. It is slightly lower for the PCM-EMC analysis for pp collisions at $\sqrt{s} = 2.76$ TeV. For minimum bias p–Pb collisions, on the other hand, the correction factor ranges from 3.5% at 0.45 GeV/c to about 0.5% at 10 GeV/c.

For the photons, which are reconstructed using the EMCal, the contribution from out-of-bunch pile-up is suppressed through rather strict cuts on the timing of the clusters, which leads to an out-of-bunch pile-up contribution of less than 1‰. Thus, it can be neglected within the current statistical uncertainties.

Similar to the neutral pion analyses the photon candidate sample needs to be corrected for secondary photons. These photons are created either by interactions of hadrons with the material or by decays of π^0 from long lived strange particles, like $\mathrm{K}^0_{\mathrm{S}}$, $\mathrm{K}^0_{\mathrm{L}}$ and Λ. The correction procedure follows the same general principle as outlined for the meson reconstruction. Where the contributions arising from the material interactions are taken directly from the general purpose Monte Carlo simulations. Those related to strange particle decays are calculated based on the decay photon cocktail as the amount of strange particles is not correctly described in the general purpose simulations. However, it has to be taken into account that those photons do not necessarily have the same reconstruction efficiencies or momentum resolution as the primary photons as their point of origin does not correspond to the primary vertex. Thus, the photon reconstruction efficiency, resolution and acceptance of the secondary photons from neutral pion decays of the $\mathrm{K}^0_{\mathrm{S}}$, $\mathrm{K}^0_{\mathrm{L}}$ and Λ have been obtained by parameterizing the corresponding quantities from the general purpose simulations. These are afterwards applied to the photon spectra, which have been obtained from the decay photon simulation. Thereafter, the estimated reconstructed secondary photons are subtracted from the photon samples prior to any further corrections.

For the photons reconstructed with PCM, the largest fraction of secondary photons originates from the decays of the $\mathrm{K}^0_{\mathrm{S}}$. It can be seen in the upper row of Figure 6.6 for both collision systems as function of the transverse momentum. Its relative contribution is strongly transverse momentum dependent and ranges from 3.5% at low transverse momenta to about 1(0.5)% at higher momenta for pp and p–Pb collisions, respectively. With increasing momentum more and more photons can be reconstructed including information from the ITS, as the conversion electrons will reach the TPC even if they converted early in the ITS. Thus, the probability to reconstruct photons

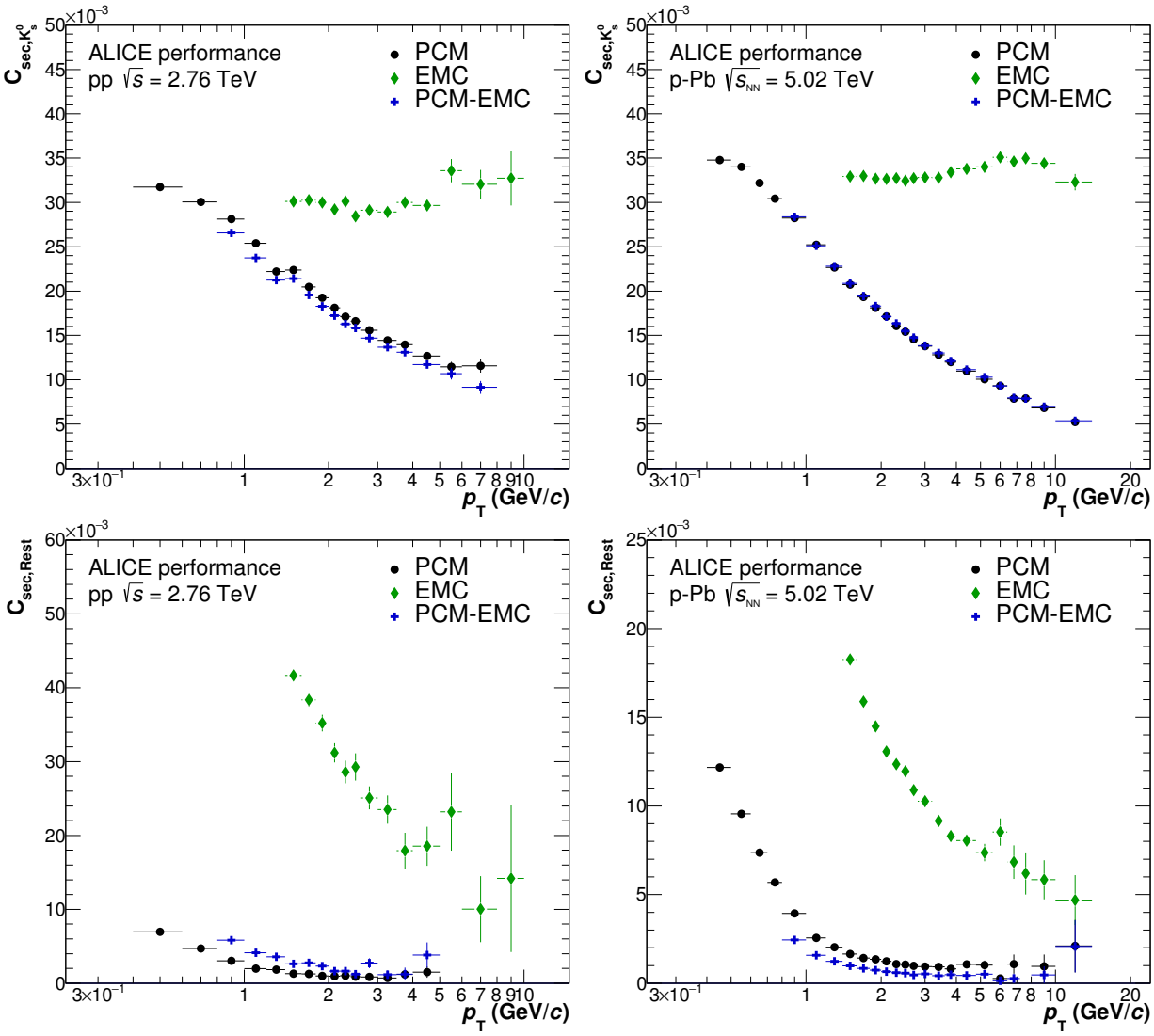

Figure 6.6.: Fraction of secondary photons from decays of neutral pions from K^0_S (top) and interactions of the hadrons with the material (bottom) for the photons reconstructed with the PCM and EMC reconstruction techniques. The fractions are shown for pp (left) and p–Pb collisions (right). In case of the PCM-EMC reconstruction only photons, which have been reconstructed via conversions are considered in the photon sample. However, the data and photon selection criteria or the Monte Carlo simulations, which are be used for the respective analysis, differ slightly in both collision systems from those used for the pure PCM direct photon analysis.

from secondary pion decays decreases. For the photons reconstructed in the EMCal, on the other hand, no such restriction is present and thus the secondary contribution from decays of the K^0_S stays constant at about 3(3.5)% for pp and p–Pb collisions, respectively. The other contribution from secondary strange particle decays for the conversion photons are below 1‰ and can thus be neglected. For the photons reconstructed with the EMCal only the contribution from K^0_L decays needs to be considered in addition. It contributes 0.15% to the total yield of photons, while the contribution from Λ decays is smaller than 0.05%.
The relative contribution of the photons from material interactions for the photons reconstructed with PCM once more depends on the photon selection criteria and the relative abundances of the hadrons with respect to the neutral pion. Consequently, it can vary for the different minimum bias Monte Carlo generators or data reconstruction passes, as it is seen in Figure 6.6 (bottom) when comparing the secondary fractions between PCM and PCM-EMC. Their total magnitude, however, is very similar, regardless of the exact detail of the reconstruction or simulation. It ranges

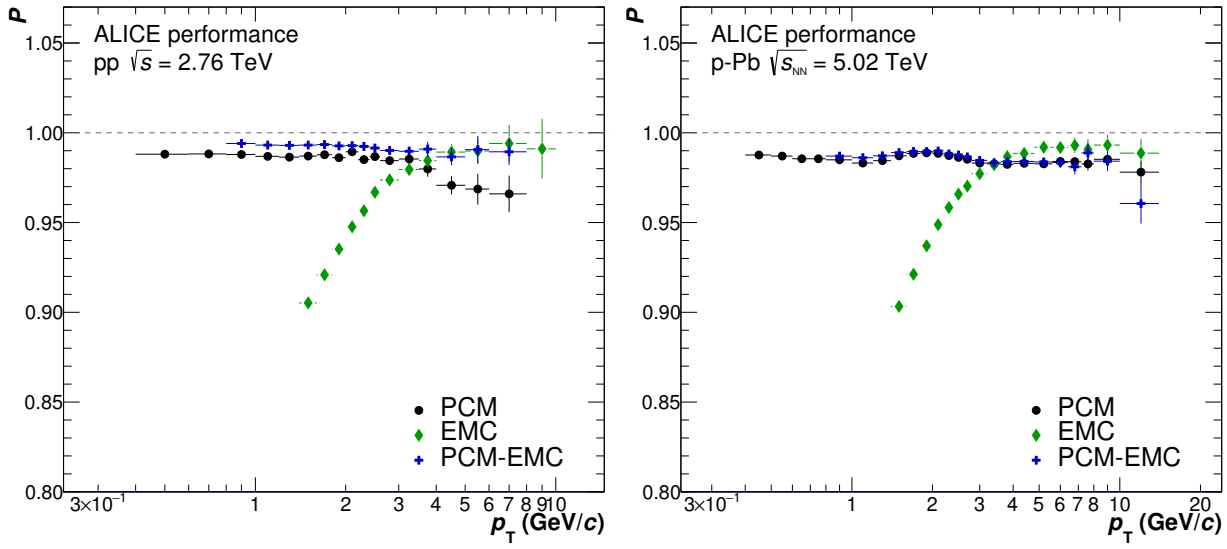

Figure 6.7.: Purity (P) of the reconstructed photon sample for the PCM (PCM-EMC) and EMC photon reconstruction techniques for pp (left) and p–Pb collision (right). In the photon analysis labeled PCM-EMC only the photons reconstructed via conversions are considered for the inclusive photon sample.

from 0.7% to 0.2% for pp collision at $\sqrt{s} = 2.76$ TeV and is slightly larger for p–Pb collisions at $\sqrt{s_{\mathrm{NN}}} = 5.02$ TeV at low transverse momenta ranging from 1.25% to 0.2%. The correction is in general larger for photons reconstructed with the EMCal, where up to 4% of the photons at 1.6 GeV/c need to be subtracted from the raw photon spectrum due to this contribution. This difference in magnitude of the correction can be attributed to the larger amount of material in front of the calorimeter and the deteriorated momentum resolution for these photons.
After the reconstructed photons have been corrected for the out-of-bunch pile-up and secondary photon contributions, which have been obtained, at least partially, in a data-driven way. The remaining impurities are corrected for by relying fully on the general purpose Monte Carlo simulations, which include the full detector response simulation.
The purity of the photon samples has been estimated by the comparing the validated photon candidates with the reconstructed ones. As such, it has been checked for each reconstructed conversion candidate, whether the contributing tracks have been generated by an electron and a positron and whether those originated from the same photon. For the calorimeter photons, on the other hand, a cluster has been considered a validated photon, if it had been created by a photon directly or if an electron from a photon conversion had been registered in the respective cluster. Furthermore, either or had to contribute the largest energy fraction to the corresponding cluster.
The resulting purity estimates (P) can be seen in Figure 6.7 for pp (left) and p–Pb collisions (right) for photons reconstructed with conversions (PCM and PCM-EMC) and for those reconstructed via the electromagnetic calorimeter (EMC). As especially for pp collision $\sqrt{s} = 2.76$ TeV the conversion photon selection criteria were slightly different for the photons entering the PCM and PCM-EMC analyses, respectively, also the purity of the photon sample differs slightly. In addition, different reconstruction conditions have been used for those two analysis streams, see Section 4.1.1. The exclusion of the SDD in the data reconstruction leads to a slightly worsened purity and resolution for the standalone PCM measurement, albeit still being above 98.5% below 3.5 GeV/c. Above 3.5 GeV/c the dE/dx pion rejection cuts have been loosened for the PCM standalone reconstruction and the purity decreases to about 96% for this reconstruction technique, while it stays constant for the PCM-EMC reconstruction, where the rejection had been kept at the same level up to 100 GeV/c (see Table 4.5). For the p–Pb data set, the cuts have been kept the same for both reconstruction techniques which yields similar results for the purity. The only difference between these two reconstruction techniques for p–Pb collisions regarding the PCM photon

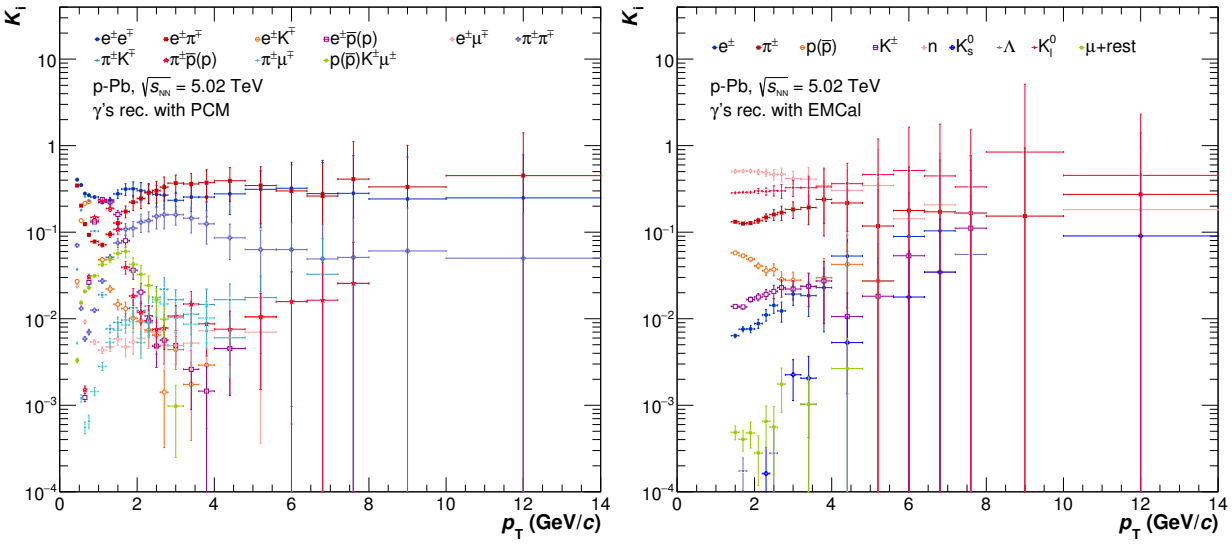

Figure 6.8.: Relative contribution (K_i) of the various identified backgrounds (i) to the total background seen for the photons reconstructed with PCM (left) and EMC (right) for p–Pb collisions at $\sqrt{s_{\mathrm{NN}}} = 5.02$ TeV. The corresponding ones for pp collisions at $\sqrt{s} = 2.76$ TeV can be found in Figure C.5 of Appendix C.2.

reconstruction is the inclusion of the HIJING simulation for the corrections of the PCM standalone measurement. This results in a slightly lower purity estimate and a slightly higher efficiency for the pure PCM reconstruction.

The largest background at low transverse momenta for the chosen PCM selection criteria in p–Pb collision stems from random e^+e^- pairs. These are contributing between $25-45\%$ to the remaining combinatorial background. At higher momenta, however, the contribution from random $e^{\pm}\pi^{\mp}$ pairs increases and it contributes about 45% to the misidentified conversion photon background, as it can be seen in Figure 6.8 (left). Other combinations of electrons with heavier particles, for instance $e^{\pm}\mathrm{K}^{\mp}$ or $e^{\mp}\mathrm{p}/\bar{\mathrm{p}}$, only contribute significantly at certain transverse momenta. In these transverse momentum regions, the Bethe-Bloch curves for the energy loss ($\mathrm{d}E/\mathrm{d}x$) of the corresponding particle species have crossing points with the electron expectation and thus cannot be separated properly any longer from the electron sample. Combinations of two heavier particles, like $\pi^+\pi^-$ or $\pi^{\pm}\mathrm{K}^{\mp}$, are heavily suppressed due to the respective photon selection cuts in q_{T}, χ^2_{red} and ψ_{pair}. The latter two cuts also suppress the contribution from random e^+e^- pairs, significantly. The purity of the calorimetric photon sample (EMC) is significantly worse than that of the converted photons below 3 GeV/c, as seen in Figure 6.7. Above this transverse momentum it is, however, compatible or better than that of the conversion photons. At low transverse momenta, the largest contribution to the impurities arises from neutrons being misidentified as photons. They contribute about $50-60\%$ to the total background, as it can be seen in Figure 6.8 (right). The next largest contribution originates from the direct reconstruction of the $\mathrm{K}^0_{\mathrm{L}}$ in the calorimeter, which contributes about 30% to the total background. It is closely followed by the contamination arising from charged pions (12-20%). At higher momenta, the order of the contributions seems to be inverted with the $\mathrm{K}^0_{\mathrm{L}}$ being the strongest contributor followed by the neutron and charged pion. Unfortunately, the statistics in the simulations for momenta above 5 GeV/c is not sufficient and no clear statement can be made about their absolute magnitude beyond this momentum. The primary electron contamination in the photon sample is negligible for transverse momenta below 6 GeV/c. Above that the electron contribution approaches that of the charged pions and thus has to be taken into account. In particular, as the respective primary electron yield is not well reproduced in the simulations and might need adjustments to match the yields seen in the data. Furthermore, the clusters are corrected for the impurities arising from the direct reconstruction of $\mu^{\pm}$, $\mathrm{K}^{\pm}$, $\mathrm{K}^0_{\mathrm{S}}$, $\mathrm{p}\bar{\mathrm{p}}$, Λ as well as heavier particle contributions. These are, however, contributing less than 5% each

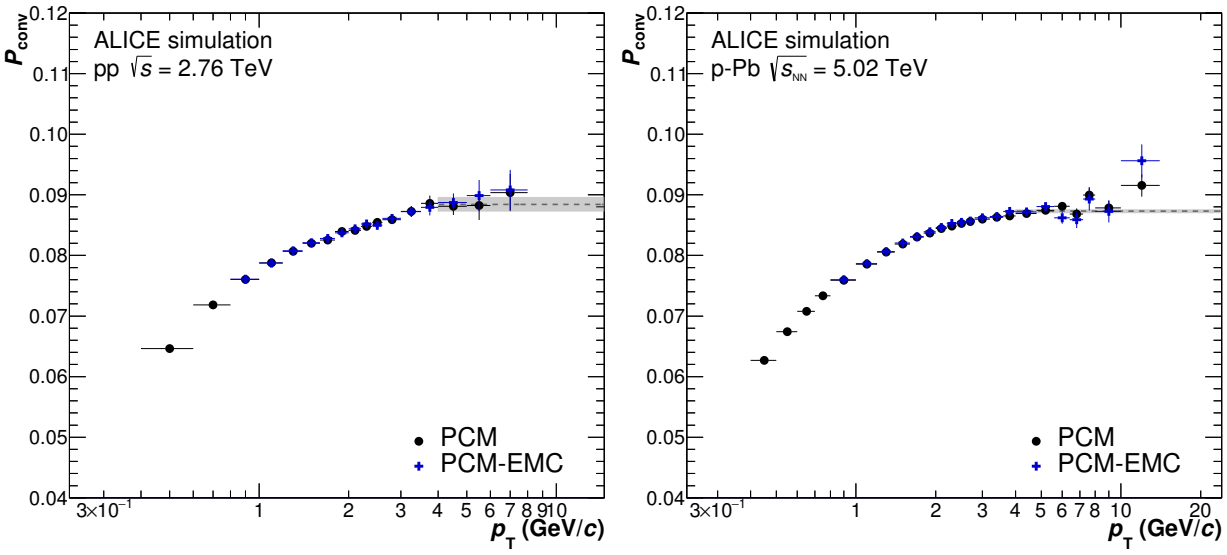

Figure 6.9.: Conversion probability for a photon converting in the ALICE detector within $|\eta_\gamma| < 0.9$ up to $R_{\text{conv}} \leq 250$ cm for pp (left) and p–Pb collisions (right). The dashed line and the corresponding shaded area illustrate the fit to the plateau above 4 GeV/c with its respective uncertainty band.

to the total background. Consequently, their absolute contribution to the reconstructed yield is less than 0.4% even in the lowest transverse momentum slice. For the purity estimates, the direct contributions from the strange particles have not yet been scaled to their correct relative amounts according to the data distributions, which leads to larger systematic uncertainties on the correction factors for the photons reconstructed with the EMCal.
The remaining real primary photon candidates are afterwards corrected for the energy resolution and photon reconstruction efficiency using the same simulations which have been used to obtain the purity estimates. The photon reconstruction efficiency (ε_{rec}) corrects the measured spectra for the loss of photons due to limited reconstruction and detector performance and is usually reported as a function of the true momentum. The conversion probability (P_{conv}) for the PCM photons is, however, not included in this correction factor. It is shown in Figure 6.9 for both collision systems for conversions within $|\eta| < 0.9$ up to $R_{\text{conv}} \leq 250$ cm. If the same photon and electron acceptance criteria are applied this correction factor should be universal. It can only vary if the implementation of the detector material in the simulations has changed or material has been added in the respective data taking period to the detector itself. As neither was the case for the considered data sets the conversion probability is the same in all five general purpose simulations, which are used in the analyses. It only fluctuates slightly due to the processed statistics in the respective analysis streams and simulations. It rises slowly with increasing photon momentum until it reaches a plateau of about 8.73% at 4 GeV/c, indicated by the dashed line in Figure 6.9 with the corresponding fit uncertainties displayed as a gray box. The slope of the increase is determined partially by the minimum electron momentum cut-off set in the analysis, as the electron acceptance corrections are folded into this quantity. The plateau value, on the other hand, will be unaffected by the choice of the minimum electron momentum. Naturally, this quantity also depends on the choice of the minimum conversion radius and accepted photon η and φ of the converted photons. As the latter criteria change the material, which is being sampled.
In order to obtain the corrections for the finite momentum resolution of the detection techniques, Bayesian unfolding has been employed. The corresponding unfolding routines are implemented in the RooUnfold [376] packages, which can be used as an extension to the ROOT package. In the unfolding algorithm a solution to the following equation has to be found:

$$p_{\text{T}}^{\text{rec}} = \mathcal{A} \cdot p_{\text{T}}^{\text{true}}. \tag{6.3}$$

Here $p_{\text{T}}^{\text{rec}}$ refers to the distribution of the measured and consequently smeared transverse momen-

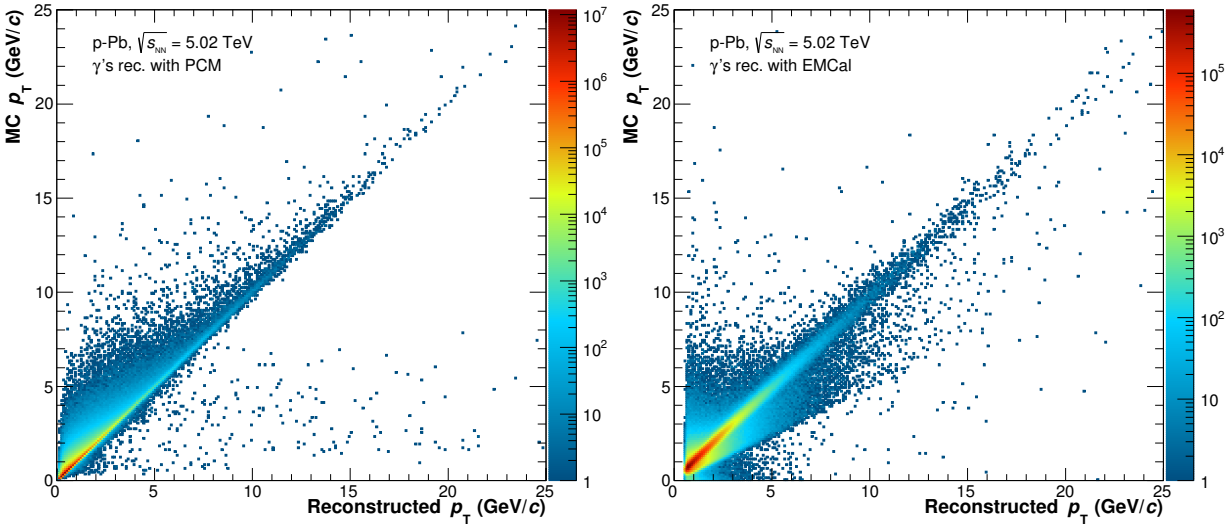

Figure 6.10.: Unnormalized detector response matrices ($\mathcal{A}$) for photons reconstructed via conversions (left) or through the calorimetric measurement in the EMCal (right) for p–Pb collisions at $\sqrt{s_{\mathrm{NN}}} = 5.02$ TeV.

tum, while $p_{\mathrm{T}}^{\mathrm{true}}$ denotes the true distribution of generated transverse momentum values. The relation between those two values is given by the detector response matrix $\mathcal{A}$, which is shown in Figure 6.10 for the PCM and EMC reconstruction techniques for the p–Pb data set. If the response matrix for a certain reconstruction technique is known with infinite precision, the $p_{\mathrm{T}}^{\mathrm{true}}$ an be calculated by an inversion of the matrix $\mathcal{A}$. This inversion may, however, be impossible or largely biased in presence of statistical fluctuations.
This bias can be reduced by the use of the Bayesian theorem [377, 378], which assumes that the conditional probability distribution of a cause (the generated $p_{\mathrm{T}}^{\mathrm{true}}$) in case of measuring an effect (the measured $p_{\mathrm{T}}^{\mathrm{rec}}$) can be expressed as:

$$P(p_{\mathrm{T}}^{\mathrm{true}}|p_{\mathrm{T}}^{\mathrm{rec}}, \mathcal{A}, I) \propto P(p_{\mathrm{T}}^{\mathrm{rec}}|p_{\mathrm{T}}^{\mathrm{true}}, \mathcal{A}, I) P(p_{\mathrm{T}}^{\mathrm{true}}|I). \tag{6.4}$$

According to this assumption the conditional probability is proportional to the product of the likelihoods of the observed data for a given response matrix and true distribution times a certain prior. The prior (I) reflects the knowledge of the true distribution. The final result will consequently depend on the choice of the prior, thus for the unfolding procedure in RooUnfold an iterative approach is being followed using the Monte Carlo photon momentum distribution as the first prior. In the consecutive iterations the unfolded result of the previous iteration will then be used as an updated prior. As the spectral shape of the simulated and real data is similar enough it has been found that 4 iterations will lead to a suitable result. If the number of iterations is chosen to be much larger the spectra will start to follow the statistical fluctuations of the measured data. The results have been cross checked using the Singular Value Decomposition (SVD) unfolding method [379], which is also implemented within the RooUnfold package. Furthermore, an iterative weighting procedure, as for the neutral mesons, has been performed for the inclusive photon spectra in pp collisions at $\sqrt{s} = 2.76$ TeV for which the simulated and real data agree well enough. The differences for the fully correct result between these different resolution correction techniques are of the order of 0.2-0.5%, thus the procedure is considered stable and well controlled and no additional systematic uncertainty beyond the statistical uncertainty arising from the unfolding procedure is considered in the final results. The latter is derived from the square root of the covariance matrix of error propagation matrix which has been obtained during the unfolding procedure.
Finally, the spectra are corrected for the reconstruction efficiency as a function of the true photon momentum, as the unfolding correction has been applied to the raw spectra directly. The respective correction factor ($\varepsilon_{\mathrm{rec}}$) is shown in Figure 6.11 with closed symbols for the three different reconstruction techniques in both collision systems. To estimate the effect of the resolution cor-

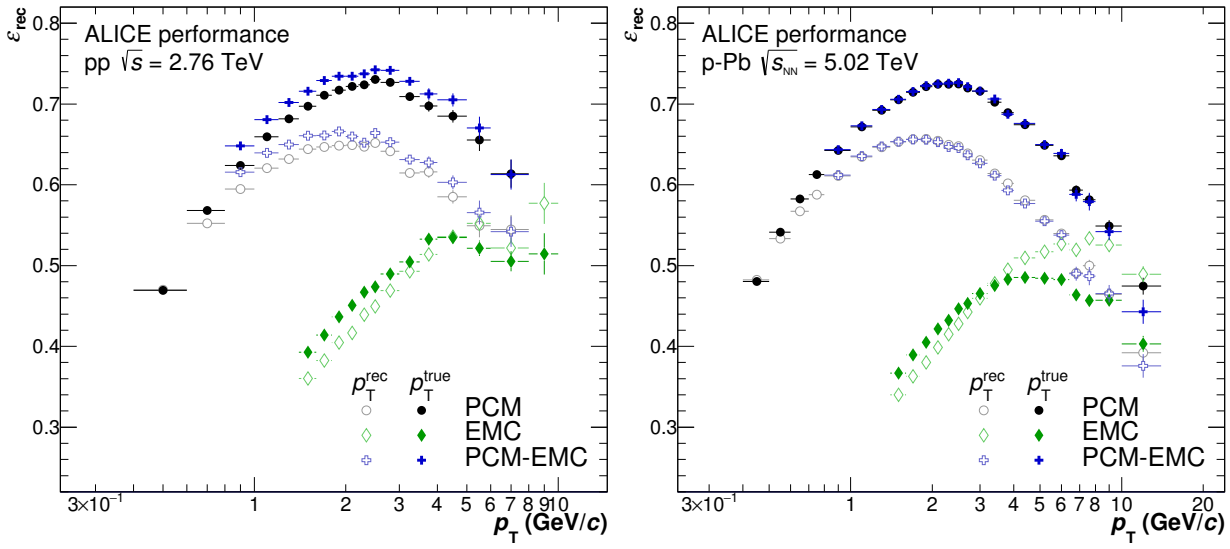

Figure 6.11.: Photon reconstruction efficiency ($\varepsilon_{\mathrm{rec}}$) as a function of the true photon momentum ($p_{\mathrm{T}}^{\mathrm{true}}$, closed symbols) and the reconstructed photon momentum ($p_{\mathrm{T}}^{\mathrm{rec}}$, open symbols) for pp collisions at $\sqrt{s}$ = 2.76 TeV and p–Pb collisions at $\sqrt{s_{\mathrm{NN}}}$ = 5.02 TeV. The reconstruction efficiency is displayed for converted photons (PCM, PCM-EMC) as well as those reconstructed with the EMCal (EMC).

rection, $\varepsilon_{\mathrm{rec}}$ is also shown as function of reconstructed momentum with open symbols. The latter efficiency includes the respective unfolding correction for the transverse momentum resolution.
In general, the $\varepsilon_{\mathrm{rec}}(p_{\mathrm{T}}^{\mathrm{true}})$ is about 20% larger than $\varepsilon_{\mathrm{rec}}(p_{\mathrm{T}}^{\mathrm{rec}})$ for momenta above 2 GeV/c, when considering photons reconstruction with the PCM reconstruction technique. This shift is caused by loss of energy due to radiative processes for the PCM photons. Below 2 GeV/c, the effective correction from the momentum resolution is smaller and the efficiencies are approximately equal for p_{T} of $0.3 - 0.4$ GeV/c. The maximum reconstruction efficiency for PCM photons with the chosen photon and electron selection criteria for the PCM reconstruction in p–Pb collisions is about 73%, whereas it is slightly larger for the pp data set with respective selection criteria. The maximum is reached at about 1.8 GeV/c. The significant drop towards lower momenta is due to the minimum transverse momentum cut-off of the electrons. If the photon converts in the lower ITS layers, a certain minimum electron momentum is needed in order for the electrons to reach the TPC. Additionally, these electrons are very difficult to reconstruct in the TPC as they undergo multiple scattering the detector material and thus might be stopped prior to reaching the minimal track length need to reconstruct the respective electron track. The reconstruction efficiency is even further reduced by the strict selection criteria on the electron PID and photon quality. At higher momenta the reconstruction efficiency decreases due to the strict pion rejection cuts as well as the strict photon quality cuts in q_{T}, χ^2_{red} and ψ_{pair} in order to remove the contamination. Consequently, the efficiency beyond 3 GeV/c drops quickly to about 54% at 10 GeV/c.
For the photons reconstructed in the EMCal, the resolution correction is smaller than that of the PCM photons. It leads to an about 10% higher efficiency for photons with a reconstructed momentum of 1.6 GeV/c. With increasing momentum the effective resolution correction decreases until the clusters from neutral pions start to overlap at about 4 GeV/c. At this point, too much energy might be contained in the reconstructed cluster and the resolution corrections will lead to a lower reconstruction efficiency beyond these momenta. The maximum reconstruction efficiency for the EMCal photons is reached at about 4 GeV/c and amounts to about 50% with the cluster selection criteria chosen for p–Pb collisions. The shape of the reconstruction efficiency is mainly determined through the selection criteria regarding σ^2_{long} and the p_{T} dependent track-matching. These cuts have been optimized to reach a maximum purity instead of the maximum photon reconstruction efficiency, as the latter is usually better reproduced in the simulations.

The full correction formula for the inclusive photon spectrum can be expressed as:

$$N^{\mathrm{corr}}_{\gamma,rec}(p_{\mathrm{T}}) = N^{*}_{\gamma,rec}(p_{\mathrm{T}})\frac{P(p_{\mathrm{T}})}{\varepsilon_{\mathrm{rec}}(p^{\mathrm{rec}}_{\mathrm{T}})P_{\mathrm{conv}}(p_{\mathrm{T}})}. \tag{6.5}$$

Here $N^{*}_{\gamma,rec}(p_{\mathrm{T}})$ corresponds to the pile-up and secondary corrected photon yield as discussed in the course of this section and $P_{\mathrm{conv}}(p_{\mathrm{T}})$ is assumed to be 1 when correcting the photons reconstructed with the EMCal. The fully invariant yield and cross sections can then be calculated as:

$$E\frac{\mathrm{d}^3N}{dp^3} = \frac{1}{2\pi}\frac{1}{p_{\mathrm{T}}}\frac{\mathrm{d}^2N}{\mathrm{d}y\mathrm{d}p_{\mathrm{T}}} = \frac{1}{2\pi}\frac{1}{p_{\mathrm{T}}N_{\mathrm{evt.}}}\frac{N^{\mathrm{corr}}_{\gamma,\mathrm{rec}}}{\Delta y\Delta p_{\mathrm{T}}} \tag{6.6}$$

$$E\frac{\mathrm{d}^3\sigma}{dp^3} = \frac{1}{2\pi}\frac{\sigma_{\mathrm{trig}}}{p_{\mathrm{T}}N_{\mathrm{evt.}}}\frac{N^{\mathrm{corr}}_{\gamma,\mathrm{rec}}}{\Delta y\Delta p_{\mathrm{T}}}. \tag{6.7}$$

The number of events corresponds ($N_{\mathrm{evt.}}$) to the minimum bias triggered events listed in Table 4.2 for the different data taking periods, while σ_{trig} refers to the corresponding cross section of the minimum bias trigger as shown in Table 4.3. The spectra are reported at the center transverse momentum bin contrary to those for the neutral mesons, as no functional form has been found which describes the spectra over the full transverse momentum range.
After having obtained the inclusive photon spectra, the direct photon excess ratio (R_γ) can be calculated according to:

$$R_\gamma(p_{\mathrm{T},\,\gamma}) = \frac{\gamma_{\mathrm{inc}}(p_{\mathrm{T},\,\gamma})}{\gamma_{\mathrm{decay}}(p_{\mathrm{T},\,\gamma})} = \frac{\gamma_{\mathrm{inc}}(p_{\mathrm{T},\,\gamma})/\pi^0(p_{\mathrm{T},\,\pi^0})}{\gamma^{\mathrm{cocktail}}_{\mathrm{decay}}(p_{\mathrm{T},\,\gamma})/\pi^0_{\mathrm{param,\,cocktail}}(p_{\mathrm{T},\,\pi^0})}. \tag{6.8}$$

This ratio is calculated using for each measurement technique using the individual photon and neutral pion spectra, respectively. Furthermore, each of the R_γ measurements uses its own decay photon simulation which is based on the corresponding neutral pion measurement in order to cancel some of the remaining biases, which might be common between the photon and meson measurements. As each of the photon measurements is normalized to the respective neutral pion measurement, possible deviations in the normalization factors, cancel fully as well and it is even possible to reduce some of the uncertainties related to the Monte Carlo corrections.
The neutral pion measurements ($\pi^0(p_{\mathrm{T},\,\pi^0})$) might, however, suffer from rather large statistical fluctuations among neighboring bins, which are not present in the corresponding simulated neutral pion spectrum ($\pi^0_{\mathrm{param,\,cocktail}}(p_{\mathrm{T},\,\pi^0})$). Thus, also the measured neutral spectrum has been fitted with a modified Hagedorn function (Equation 5.15) and the original statistical uncertainties have been assigned to newly obtained spectrum for transverse momentum slice.
In the absence of a direct photon signal the R_γ should be unity, while if is above unity if direct photons are produced in the collision. Nevertheless, statistical or systematic variations might shift the points even below one. The direct photon spectrum can only be calculated for the transverse momentum slices, where an $R_\gamma > 1$ has been measured. In these cases the direct photon spectrum can be calculated through Equation 2.14. Otherwise, only upper limits for the direct photon reconstruction can be given. Thus, before discussing the final results of the different measurements, the corresponding systematic uncertainties will be discussed.

6.3. Systematic Uncertainties

Within this section the systematic uncertainties related to the inclusive photon invariant yield measurements as well as the measurement of the R_γ will be discussed for pp collisions at $\sqrt{s} = 2.76$ TeV and p–Pb collisions at $\sqrt{s_{\rm NN}} = 5.02$ TeV. As for the meson analyses the three different analysis techniques (PCM, PCM-EMC and EMC) will be discussed in parallel, where the underlying cause of the systematics is the same. Once more the uncertainties have been estimated through variations of the selection criteria for the photons and mesons in the different reconstruction techniques and their systematic effect on the inclusive photon spectrum or the R_γ has been quantified directly by comparing the different variations to the final result in that quantify. This procedure has been followed for each transverse momentum slice independent of the neighboring ones. The influence of the statistical fluctuations on the systematic uncertainties estimate has been reduced by using the Barlow criteria [329]. Furthermore, the uncertainties have been equalized among neighboring transverse momentum slice, where necessary. This was done taking guidance from the $p_{\rm T}$ dependence of the underlying cause of the variation.
In order to ease the comparisons with the uncertainties obtained for the respective meson analyses, the same grouping of the uncertainties has been followed as in Sections 5.2.1 and 5.3.2.
It has to be kept in mind that the inclusive photon spectra for the PCM and PCM-EMC reconstruction technique are both based solely on the reconstructed PCM photons, thus they share the majority of the uncertainties as well. However, slightly different data reconstruction conditions have been used for the two analyses in the pp data sample and a different set of simulations for the p–Pb data sample. As such, the uncertainties do not need to be identical in their magnitude, but similar trends should be observed.
The systematic uncertainties for the inclusive photon measurements in pp and p–Pb collisions, respectively, are reported in Table 6.2 and 6.4 for selected transverse slices, while the full $p_{\rm T}$ dependence for the different measurements is shown in Figure C.6 and C.7 of the appendix. In the Table 6.3 and 6.5 the same has been done for the R_γ measurement. In order to get an impression of the statistical precision of the different analysis techniques at the respective momenta, also the statistical errors for the inclusive photons, neutral pions and R_γ are given in the respective tables.
In the following, at first the $p_{\rm T}$ dependent uncertainties for the PCM measurements will be explained. Afterwards, the same will be done for the uncertainties related to the EMCal photon reconstruction. Then, the uncertainties related to the material implementation and pile-up rejection will be discussed. At last, the neutral meson extraction uncertainties as well as those related to the decay photon simulation will be presented, which will only enter for the R_γ systematics. The same order has been followed for the summary tables. The section is concluded by the discussion of the total systematic and statistical uncertainties of the different measurements. In this discussion also the corresponding measurement for the R_γ in p–Pb collisions based on the PHOS will be included. The systematic error components of that measurement are discussed in detail in [373].

Secondary track reconstruction: As already described in previous sections, this category summarizes the uncertainties arising from the secondary track reconstruction and selection. It includes the variations of the minimum $p_{\rm T}$ cuts for the electron as well as those related to the minimum number of clusters in the TPC. For the PCM-EMC R_γ it also includes the variation of the φ acceptance of the conversion photons. For the inclusive photon spectra, this uncertainty is subdominant and amounts to $0.1 - 0.3\%$ depending on $p_{\rm T}$ and collision system. On the level of the R_γ the contribution can rise to up to 8.4% at the maximum or minimum transverse momentum. This is of particular importance for the pp data set, as in that case the statistical fluctuations could not be fully separated from the respective systematic ones.
Electron PID: This uncertainty class contains all uncertainties for the PCM photon selection which are related to the underlying electron selection and pion rejection on the level of the conversion legs. Once more it has been ascertained through the variations of the TPC $\mathrm{d}E/\mathrm{d}x$ selection

criteria. These uncertainties are small in the transverse momentum regions, where there is good separation between the electron and pion line. At higher transverse momenta, however, the uncertainty increases as pions cannot be rejected efficiently any longer. This uncertainty is affected by two competing effects: the modeling of the energy loss in the simulations through GEANT and the relative amounts of the different particle species. Consequently, it can be different even on the photon level for the PCM and PCM-EMC analysis method. For the inclusive photon spectra it ranges from 0.1% to 1.8%. In case of the R_γ however, this uncertainty class can contribute up to 13.4% for the standalone PCM technique at the highest momenta. As the uncertainties of the neutral pion reconstruction contribute as well.

PCM photon PID: The uncertainties related to the photon selection criteria, like the photon quality χ^2_{red}, ψ_{pair} and the Armenteros-Podolanski selection, are summarized within this uncertainty class. As for the meson analysis, they have been estimated by varying these cuts within reasonable limits to test the sensitivity of the inclusive photon spectra and the R_γ with regards to these criteria. In general, the uncertainty ranges from $0.3 - 1.0\%$ at low and intermediate transverse momenta in both collisions systems for the inclusive photon spectra. It increases, however, with increasing momentum due to the increasing contamination from charged pions. The photon quality cuts depend once more on the data reconstruction conditions as well as the particle composition in the simulation and thus can be different for the PCM analysis and the PCM-EMC although in principle the same quantities have been varied. On the level of the R_γ in pp collisions at $\sqrt{s} = 2.76$ TeV, this uncertainty contributes between 1.2 and 3.1%, where the meson and photon statistics is sufficient. At the highest and lowest possible momenta in the respective techniques, it increases rapidly. This behavior can be attributed partially to the fact that in these regions mainly asymmetric neutral meson decays can be reconstructed. Consequently, the photons have either extremely high or low momenta and are thus affected most by the respective photon quality selections. Furthermore, it is rather difficult in these transverse momentum regions to separate the statistical and systematic variations and a more conservative systematics estimate has been chosen. For p–Pb collisions, the uncertainties are slightly smaller at the same transverse momenta, due to the better statistics for the calibration of the tracking and $\mathrm{d}E/\mathrm{d}x$ measurements in the TPC, which leave a smaller fraction of badly reconstructed or fake photons in the sample. The p_{T} dependence, on the other hand, is similar to that seen in pp collisions.

EMCal clustering: This category summarizes the uncertainties related to the clusterization process. They arise from the imperfections of the detector response simulation. Thus, this category incorporates the variations of the minimum cluster and cell energies as well as the variations of the cell and cluster timing. Furthermore, it includes the mismatch of the description of the cluster shape (σ^2_{long}) between the data and the simulation. The shower shape is used to discriminate photonic clusters from those created by merged pions, conversions or other particles. The σ^2_{long} cut had to be tightened for the direct photon analysis with EMC with respect to the one used for the meson analyses, otherwise part of the photons would be counted twice at lower momenta as conversions are included in the signal definition. It is known, however, that the material and thus the fraction of conversions are not understood to the desired level for a direct photon analysis. Consequently, their amount should be reduced as much as possible with the available selection criteria. Unfortunately, by tightening the cut the statistics for the neutral pion at higher momenta has been reduced as well, as the same photon selection criteria are used for the photon and meson calculation in the R_γ. Additionally, it is well known that the cluster shape is not well understood in the simulations for cluster energies between 5 and 10 GeV/c, which leads to larger uncertainties in this transverse momentum region on the level of the inclusive photon. They are, however, partially canceled when looking at the R_γ. For the inclusive photon measurements in the EMCal, this uncertainty class is the largest contributor, ranging from $2.7 - 3.5\%$ for momenta below 5 GeV/c. Above this momentum, the uncertainty rises quickly to about $8 - 8.5\%$ or $10 - 11\%$ for the pp and p–Pb analyses, respectively. The increase is mainly caused by the σ^2_{long} variations. For the PCM-

p_{T} interval (GeV/c)	0.8–1.0		2.0–2.2			6–8		
Method	PCM	PCM-EMC	PCM	PCM-EMC	EMC	PCM	PCM-EMC	EMC
Secondary track reco.	0.3%	0.1%	0.3%	0.1%	-	0.3%	0.1%	-
Electron PID	0.5%	0.1%	0.6%	0.4%	-	1.3%	1.8%	-
PCM photon PID	0.4%	0.9%	0.7%	1.0%	-	2.2%	3.6%	-
EMCal clustering	-	-	-	-	1.1%	-	-	8.3%
EMCal energy calib.	-	-	-	-	1.4%	-	-	2.0%
Track matching	-	-	-	-	0.7%	-	-	0.7%
Efficiency & purity	-	-	-	-	1.5%	-	-	1.5%
Inner material	4.5%	4.5%	4.5%	4.5%	-	4.5%	4.5%	-
Outer material	-	-	-	-	2.8%	-	-	2.8%
Pile-up	1.5%	1.2%	1.1%	0.9%	0.3%	1.5%	0.9%	0.3%
Tot. sys. uncertainty	4.8%	4.7%	4.7%	4.7%	3.7%	5.4%	6.1%	9.2%
Stat. uncertainty	0.3%	0.3%	1.1%	1.4%	0.8%	6.3%	7.6%	4.6%

Table 6.2.: Systematic uncertainties for various sources and methods assigned to the inclusive photon measurement at different p_{T} intervals for pp collisions at $\sqrt{s} = 2.76$ TeV. For comparison, the total systematic and the statistical uncertainties are given in addition.

p_{T} interval (GeV/c)	0.8–1.0		2.0–2.2			6–8		
Method	PCM	PCM-EMC	PCM	PCM-EMC	EMC	PCM	PCM-EMC	EMC
Secondary track reco.	1.2%	7.5%	1.8%	1.3%	-	8.4%	1.3%	-
Electron PID	1.5%	0.8%	2.0%	0.5%	-	13.4%	3.8%	-
PCM photon PID	1.8%	2.9%	2.9%	1.2%	-	11.4%	3.1%	-
EMCal clustering	-	2.5%	-	2.7%	2.5%	-	5.5%	5.7%
EMCal energy calib.	-	2.0%	-	2.1%	2.0%	-	2.6%	2.5%
Track matching	-	5.9%	-	1.6%	0.7%	-	5.7%	1.4%
Efficiency & purity	-	2.0%	-	2.0%	2.5%	-	2.0%	2.5%
Inner material	4.5%	-	4.5%	-	-	4.5%	-	-
Outer material	-	2.8%	-	2.8%	4.2%	-	2.8%	4.2%
Pile-up	1.9%	1.2%	1.1%	0.9%	-	1.7%	0.9%	-
π^0 signal extraction	3.4%	9.8%	4.0%	1.6%	2.4%	4.9%	3.7%	2.4%
Decay photon cocktail	1.7%	1.1%	1.6%	2.3%	2.7%	3.4%	3.1%	2.2%
Tot. sys. uncertainty	6.7%	14.9%	7.4%	6.1%	6.9%	20.9%	11.5%	8.7%
π^0 stat. uncertainty	3.1%	20.3%	5.1%	4.6%	4.0%	22.2%	16.7%	7.3%
γ_{inc} stat. uncertainty	0.3%	0.3%	1.1%	1.4%	0.8%	6.3%	7.6%	4.6%
R_γ stat. uncertainty	3.5%	20.4%	5.5%	5.1%	4.3%	23.1%	18.3%	8.6%

Table 6.3.: Systematic uncertainties for various sources and methods assigned to R_γ measurement at different p_{T} intervals for pp collisions at $\sqrt{s} = 2.76$ TeV. For comparison, the total systematic and the statistical uncertainties are given in addition.

EMC reconstruction, this uncertainty only enters for the R_γ measurement, where it contributes about 2.6%(1.1%) for the pp (p–Pb) analysis at low and intermediate momenta and then increases to a maximum of 5.5% at 7 GeV/c for pp collisions at $\sqrt{s} = 2.76$ TeV. The observed increase for the measurement in p–Pb collisions is significantly smaller and it only reaches 1.5% at 9 GeV/c. In case of the EMC R_γ measurement, on the other hand, this systematic uncertainty contribution ranges from 2.5 to 3.6% for pp and p–Pb collisions at intermediate momenta. It increases towards higher momenta to about $5 - 6$%, where part of the variation seen for the photon is canceled by a simultaneous variation of the neutral pion yields.

p_{T} interval (GeV/c)	0.8–1.0		2.0–2.2			8–10		
Method	PCM	PCM-EMC	PCM	PCM-EMC	EMC	PCM	PCM-EMC	EMC
Secondary track reco.	0.2%	0.2%	0.2%	0.2%	-	0.2%	0.2%	-
Electron PID	0.8%	0.1%	0.9%	0.6%	-	1.8%	1.4%	-
PCM photon PID	0.3%	0.3%	0.4%	0.5%	-	1.9%	2.4%	-
EMCal clustering	-	-	-	-	3.3%	-	-	10.6%
EMCal energy calib.	-	-	-	-	2.6%	-	-	3.4%
Track matching	-	-	-	-	1.2%	-	-	1.0
Efficiency & purity	-	-	-	-	1.5%	-	-	1.5%
Inner material	4.5%	4.5%	4.5%	4.5%	-	4.5%	4.5%	-
Outer material	-	-	-	-	2.8%	-	-	2.8%
Pile-up	0.9%	0.9%	0.6%	0.5%	0.3%	0.6%	0.6%	0.3%
Tot. sys. uncertainty	4.7%	4.6%	4.7%	4.6%	5.4%	5.2%	5.3%	11.6%
Stat. uncertainty	0.1%	0.1%	0.3%	0.3%	0.2%	2.6%	3.4%	1.9%

Table 6.4.: Systematic uncertainties for various sources and methods assigned to the inclusive photon measurement at different p_{T} intervals for minimum bias p–Pb collisions at $\sqrt{s_{\mathrm{NN}}} = 5.02$ TeV. For comparison, the total systematic and the statistical uncertainties are given in addition.

p_{T} interval (GeV/c)	0.8–1.0		2.0–2.2			8–10		
Method	PCM	PCM-EMC	PCM	PCM-EMC	EMC	PCM	PCM-EMC	EMC
Secondary track reco.	0.7%	0.8%	0.2%	0.5%	-	0.4%	1.6%	-
Electron PID	1.7%	1.3%	0.5%	0.3%	-	3.0%	2.2%	-
PCM photon PID	0.6%	2.0%	0.7%	1.1%	-	3.3%	3.4%	-
EMCal clustering	-	1.1%	-	1.1%	3.6%	-	1.5%	5.3%
EMCal energy calib.	-	2.0%	-	2.0%	2.7%	-	2.8%	3.5%
Track matching	-	0.3%	-	0.4%	2.4%	-	1.4%	3.5%
Efficiency & purity	-	2.0%	-	2.0%	2.5%	-	2.0%	2.5%
Inner material	4.5%	-	4.5%	-	-	4.5%	-	-
Outer material	-	2.8%	-	2.8%	4.2%	-	2.8%	4.2%
Pile-up	1.4%	0.9%	0.7%	0.5%	-	0.7%	0.5%	-
π^0 signal extraction	2.7%	5.1%	1.7%	1.3%	3.6%	3.2%	2.7%	3.0%
Decay photon cocktail	1.2%	1.6%	2.3%	1.6%	1.4%	1.6%	1.4%	1.9%
Tot. sys. uncertainty	5.9%	7.3%	5.5%	4.8%	8.0%	7.4%	7.2%	9.0%
π^0 stat. uncertainty	1.1%	6.1%	1.5%	1.2%	1.4%	7.7%	6.0%	3.3%
γ_{inc} stat. uncertainty	0.1%	0.1%	0.3%	0.3%	0.2%	2.6%	3.4%	1.9%
R_γ stat. uncertainty	2.3%	6.4%	2.6%	2.5%	2.6%	8.2%	6.9%	3.8%

Table 6.5.: Systematic uncertainties for various sources and methods assigned to R_γ measurement at different p_{T} intervals for minimum bias p–Pb collisions at $\sqrt{s_{\mathrm{NN}}} = 5.02$ TeV. For comparison, the total systematic and the statistical uncertainties are given in addition.

EMCal cluster energy calibration: In order to quantify the uncertainty related to the cluster energy calibrations, the different calibration functions, described in Section 4.3.1, have been used for the corrections. Afterwards, the relative differences have been estimated on the final inclusive photon spectra and R_γ. These variations led to an uncertainty of about 0.3%-1.5%, which strongly depends on transverse momentum. The p_{T} dependence arises from the fact that the functional form at higher transverse momenta is not well constrained for the calibrations, which are derived purely based on the EMCal information. Another contribution is caused by the remaining mismatch in the neutral pion mass position between the real and simulated data after the corrections have been

applied. For pp collisions at $\sqrt{s} = 2.76$ TeV a remaining offset of about 0.2-0.3% for the neutral pion mass can be observed. This results in an uncertainty on the absolute energy scale of about $1.5-2\%$, when taking into account the steeply falling spectrum of the photons and neutral mesons. It is of similar order for the p–Pb measurement as well, where the difference in the mass positions is smaller, but the spectrum steeper.

Track matching to cluster: This uncertainty quantifies the imperfections arising from the primary and secondary track propagation, which is used to reject clusters mainly originating from charged particles. As for the meson analyses, it has been evaluated by varying the p_{T} dependent track matching criteria for the primary and secondary tracks. These variations have been chosen such that in one case only clusters are rejected, where the track points to the leading cell of the clusters. Whereas, in the other extreme all clusters would be rejected for which a charged particle hits the EMCal surface within a distance of 2-3 cell widths with respect to the center of the leading cell. The resulting uncertainty ranges from 0.7% to 1.2% for the EMC inclusive photon measurement. A similar magnitude is reached on the R_γ at low and intermediate momenta, for the pp analyses. It rises, however, towards lower and higher momenta to up to 5.9% for the PCM-EMC reconstruction of the R_γ. As the track reconstruction is improved by the inclusion of the SDD in the p–Pb data set, the related uncertainties on the R_γ decrease down to 0.3% at low and intermediate momenta for the PCM-EMC reconstruction. For the PCM-EMC reconstruction the track matching uncertainty enters only through the neutral meson reconstruction, and has consequently a smaller effect than for the EMC standalone reconstruction, where it contributes between 2.4 and 3.5% to the total systematic uncertainty of the R_γ.

Efficiency & purity: For the EMCal related measurements, the implications from the choice of the event generator are larger than for the pure PCM measurement. Thus, an additional systematic uncertainty has been introduced to reflect these difficulties. The choice of the generator affects mainly the purity of the EMCal photons an the π^0 reconstruction efficiency, as these depend partially on the underlying event description. The uncertainty has been estimated using different general purpose Monte Carlo event generator for the correction and comparing the final spectra and R_γ result. This leads to a 1.5% p_{T} independent systematic uncertainty on the EMC inclusive photon measurements. While for the R_γ measurements with the PCM-EMC and EMC an uncertainty of 2.0% and 2.5% has been found, irrespective of p_{T}.

Inner material: The largest systematic uncertainty for the conversion photons once more originates from the knowledge of the inner ($R < 180\,\mathrm{cm}$) material of the detector. As already described in Section 5.2.1, it has been estimated to be 4.5% independent of the photon momentum [235,293,301] and has to be taken into account twice, if the neutral pion has been reconstructed with the standalone PCM reconstruction method. Consequently, this uncertainty can be canceled once if the R_γ has been calculated purely based on photons and mesons reconstructed with the PCM method. This leads to a 4.5% uncertainty from this source for the PCM R_γ measurement, same as for the inclusive photon spectrum. If the R_γ is calculated in the hybrid analysis stream, where the inclusive photons are purely reconstructed with PCM but the neutral pion is reconstructed with the PCM-EMC technique, this uncertainty cancels fully. For the standalone EMC reconstruction, the inner material budget uncertainty can be neglected.

Outer material: Within this uncertainty, as for the meson analysis, the mismatches between the implementation of the outer material ($R > 180\,\mathrm{cm}$) in the simulation and the real detector are summarized. As such, mainly the implementation of the material of the TRD and TOF is being tested including their support structures. The outer material budget uncertainty affects only the pure EMC analysis and the R_γ in the PCM-EMC analysis stream. For the photons reconstructed with PCM it can be neglected as they would convert before even reaching the TRD or TOF. As for the neutral meson analysis, it has been estimated by comparing the fully corrected photon and meson spectra in different φ regions. This approach is possible as the TRD was only partly installed for the considered data sets and thus the modeling of this detector in the simulations can be assessed in this manor. The material budget error on the TOF implementation has been

assumed to be of similar size, which leads to a total outer material budget uncertainty of 2.8% for the photons reconstructed in the EMCal. This uncertainty appears to be independent on the photon momentum and does not fully cancel when calculating the R_γ for the EMC method. Thus, for this quantity, an uncertainty of 4.2%, as for the EMC meson analysis, has been assigned.

Pile-up: In order to estimate the uncertainty on the out-of-bunch pile-up correction for photons and mesons reconstructed with the PCM reconstruction technique the settings for the ROOT internal background estimates have been varied. The variations have been chosen such that the respective smallest and largest possible background fraction have been found. These should, however, still describe the distribution seen in Figure 6.4 and 5.10 for the photon and neutral pion, respectively. The latter estimate is only taken into account for the uncertainties on the PCM R_γ. While the uncertainty related to the photon itself enters for the measurements of the inclusive photon and the R_γ measured with the PCM and PCM-EMC reconstruction techniques. Furthermore, an uncertainty of 0.3% has been taken into account for the in-bunch pile-up rejection for the all inclusive photon measurement, regardless of the analysis stream. This uncertainty cancels for the double ratios. The total uncertainty related to the pile-up ranges from 0.9% to 1.9% for the measurements using PCM photons in pp collisions at $\sqrt{s} = 2.76$ TeV, while it contributes between 0.5 and 1.1% for p–Pb collisions at $\sqrt{s_{\mathrm{NN}}} = 5.02$ TeV to the R_γ measurements.

π^0 signal extraction: For the R_γ measurements also the uncertainties arising from the yield extraction of the neutral pion enter in the systematics. For this purpose the same variations as for the respective mesons analysis have been used. The resulting uncertainties depend strongly on the signal-to-background for the different methods as well as the peak resolution and choice of the width of the transverse momentum slice. For the PCM reconstruction the uncertainty ranges from 3.4% at 1 GeV/c to 4.9% at 7 GeV/c for pp collision at $\sqrt{s} = 2.76$ TeV. While it contributes between 1.7% and 3.2% to the R_γ uncertainties for the corresponding p–Pb measurement. For the PCM-EMC R_γ measurement, on the other hand, this uncertainty is dominant at low momenta reaching up to 9.8%(5.1%) for pp (p–Pb) collisions. At intermediate momenta it decreases to 1.6% or 1.3% for pp and p–Pb collisions, respectively. For the highest momenta it increases slightly ones more to 3.7%(2.7%) reflecting the difficulties of the pion extraction due to the higher particle density around a high p_{T} neutral pion in a jet. For the neutral pion reconstruction with the EMC method the signal extraction uncertainties range from 2.4% in pp collisions to about 3% in p–Pb collisions.

Decay photon cocktail: In order to cancel some of the biases seen in the measured spectra of the different analysis techniques, when calculating the R_γ the decay photon cocktail has been calculated separately for each neutral pion spectrum obtained with the different reconstruction techniques (PCM, PCM-EMC, EMC). Each of these spectra is accompanied by its own set of systematic uncertainties. These uncertainties are not taken into account in the default parametrization of the spectrum as they would leave to much freedom for the choice of the functional form as well as the specific parameters of the respective fits. This is of particular importance, as the neutral meson spectra need to be extrapolated into unmeasured transverse momentum regions, where they need to be well constrained using physically meaningful functions. Thus, in order to obtain the systematic uncertainty of the decay photon simulation the measured spectra have been modified within their systematic uncertainties and afterwards parametrized once more using the same functional form. Although this procedure has to be performed for all input spectra, which are used for the cocktail generation, the largest variations in the decay photon cocktail will arise from the modified parametrizations of the neutral pion and eta meson spectra. As these two particles contribute more than 95% of the decay photons. For these two neutral mesons rather large p_{T} independent systematic uncertainties have to be considered, which arise from the inner and outer material budget description. For the R_γ these constant shifts would cancel, however, as the photons and mesons would shift by the same relative amount. Thus, they should not be taken into account for the systematic shifting of the spectra and are taken out from the total systematic uncertainty. The remaining p_{T} dependent systematic uncertainties are then used to shift the measured data points of

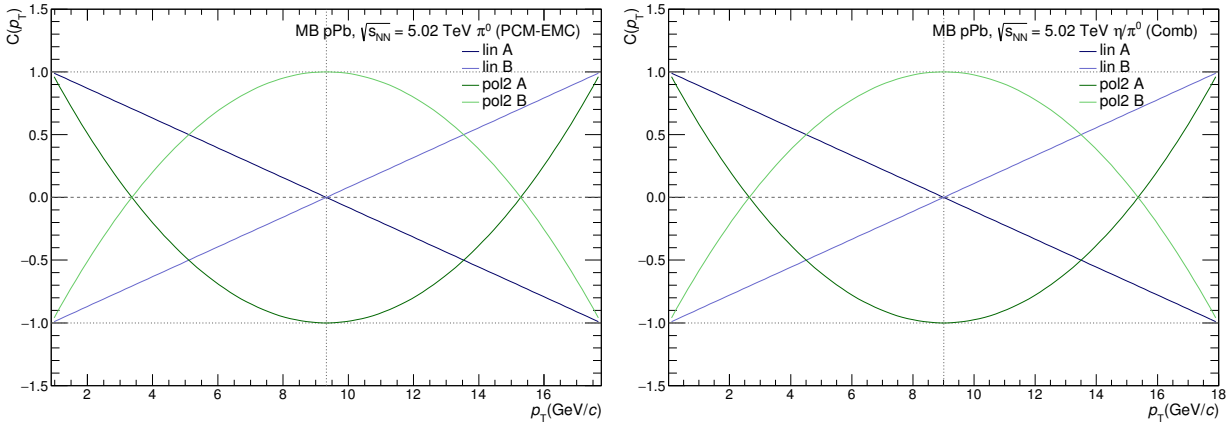

Figure 6.12.: Fraction $C(p_{\mathrm{T}})$ of the systematic uncertainties which is used to shift the central values with their corresponding uncertainties for the neutral pion PCM-EMC measurement (left) and the combined η/π^0 ratio in p–Pb collisions at $\sqrt{s_{\mathrm{NN}}} = 5.02$ TeV.

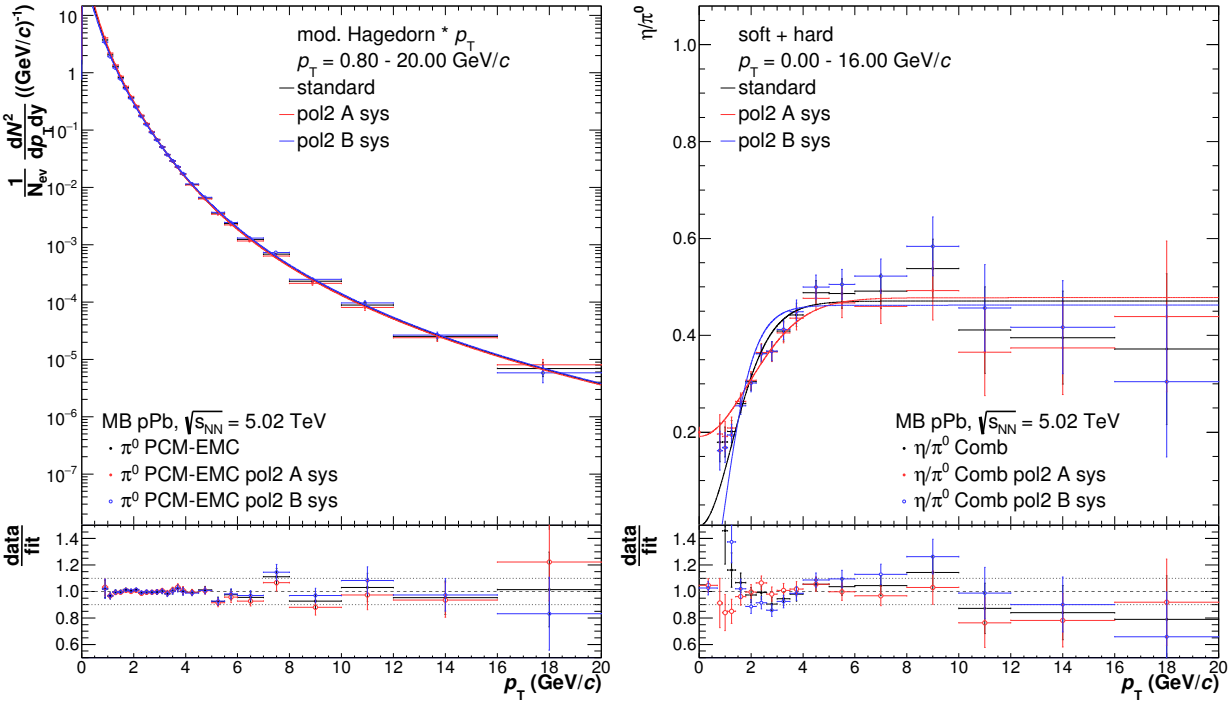

Figure 6.13.: Example of the systematic variations of the neutral pion spectra (left) measured in p–Pb collisions with the PCM-EMC reconstruction technique which enter in the decay photon cocktail systematic uncertainties. The black points show the measured spectra together with their respective parametrization and statistical uncertainties. The red and blue points show the shifted points and the refitted parametrization using the second order polynomial function to shift the data points within their systematic uncertainties. Also the ratio of the newly obtained data to their respective fits is given in the lower panel. The same variation can be seen on the right for the combined η/π^0 ratio following the same color scheme.

the respective spectra to obtain particle spectra with different slopes. For that, the p_{T} dependent systematic uncertainties are multiplied with different p_{T} dependent factors, which are chosen such that they would shift the points by a fraction of the systematic uncertainty. As an example, the factors ($C(p_{\mathrm{T}})$), which are used to shift the neutral pion measurement using PCM-EMC as well as the combined η/π^0 in p–Pb collisions at $\sqrt{s_{\mathrm{NN}}} = 5.02$ TeV are shown in Figure 6.12. In general, two different functional forms have been considered: A linear function (blue), which shifts the data point at the highest transverse momentum up by $1\sigma_{\mathrm{sys}}$, while it shifts the point at the lowest transverse momentum down by $1\sigma_{\mathrm{sys}}$. Furthermore, a second order polynomial function (green) has been taken into account, for which the data points at the highest and lowest momenta are

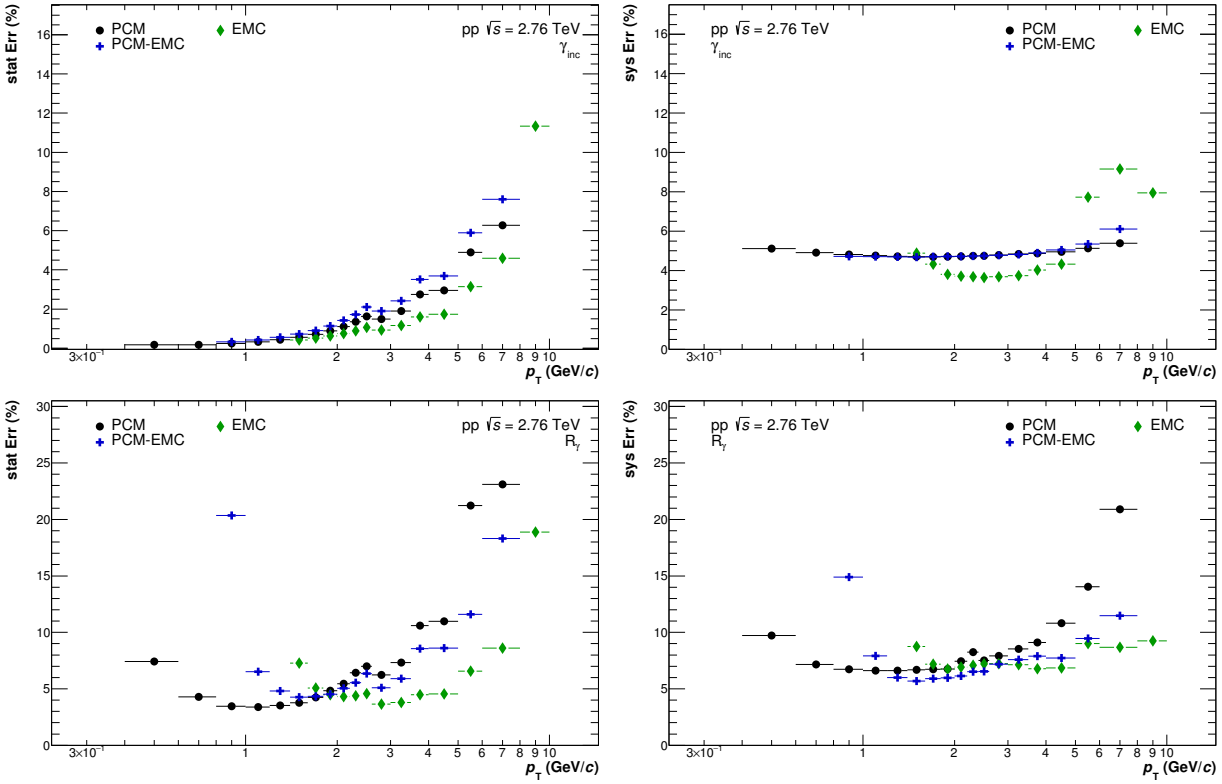

Figure 6.14.: Comparison of the relative statistical (left) and systematic (right) uncertainties related to the inclusive photon spectra (top) and R_γ(bottom) measurements in the different analysis techniques for pp collisions at $\sqrt{s} = 2.76$ TeV.

shifted downwards by $1\sigma_{\text{sys}}$, while in the middle of the measured momentum range the data points are shifted up by $1\sigma_{\text{sys}}$. Also the inverted functions have been considered in the corresponding systematic uncertainties. An example of the shifted data points together with the corresponding variations of the parametrizations for the two second order polynomial variations can be seen in Figure 6.13. In addition to these variations, the m_{T} scaling factors for the unmeasured particles have been varied upwards and downwards by the amount given in Table 6.1. For each variation, all particle spectra parametrizations have been modified in the same manner and a new cocktail has been generated. Afterwards, the results are compared to those using the standard cocktail on the level of the R_γ. The final uncertainties are shown in Figure C.6 and C.7 and the corresponding tables in this section reflect the mean value of the maximum bin-by-bin deviations of the final R_γ results using the different cocktails for each method independently. Their magnitude strongly depends on the magnitude of the p_{T} dependent systematic uncertainties of the underlying neutral pion spectra. In general, the uncertainty for pp collisions is of the order of $1-2\%$ for momenta below 1 GeV/c and then increases quickly to up to 3.5% at intermediate momenta. At higher transverse momenta, it ranges between $2.2-3.4\%$, depending on the reconstruction method. For p–Pb collisions, these uncertainties are in general much lower, as the neutral pions have been measured with a better precision. They range from 1.2% to 2.5% showing a similar transverse momentum behavior as for pp collisions.

The resulting total systematic uncertainties for the invariant inclusive photon yield and R_γ for pp collisions at $\sqrt{s} = 2.76$ TeV for the three analysis methods can be seen in Figure 6.14 as a function of transverse momentum. Furthermore, also the statistical uncertainties for these measurements are displayed in the same format. The statistical uncertainties of the inclusive photon measurements are below 1% for photon momenta below 2 GeV/c. They increase rapidly with increasing momenta, as expected. In the region between 1.5 and 5 GeV/c, all three reconstruction

methods have similar statistical uncertainties, in particular those of the PCM and PCM-EMC reconstruction are nearly equal. Both measurements rely on the photon reconstruction with PCM and only the data reconstruction settings are slightly different. Which makes the photons, which are labeled as PCM-EMC, a subset of those reconstructed for the PCM standalone measurement. They are, however, more precise regarding the tracking as the SDD was included in the reconstruction as well. The total systematic uncertainties of the PCM and PCM-EMC reconstruction techniques are equal as well. Both of them are fully dominated by the material budget uncertainty of 4.5%. The smallest systematic uncertainty for the inclusive photon measurement in pp collisions at $\sqrt{s} = 2.76$ TeV between 1.7 and 5 GeV/c has been obtained for the EMC measurement. It is dominated by the uncertainties arising from the outer material budget. Above these momenta, the EMC systematic uncertainty nearly doubles and to a total of $8 - 9\%$ above 6 GeV/c. While it is theoretically possible to measure the photons in the respective technique to lower momenta, the measurements have been stopped, where no reliable neutral pion measurement in the respective technique could be obtained, ss in this momentum region no R_γ measurement would be possible. The statistical uncertainties of the R_γ measurements are largely driven by those of the neutral pions, as it can be seen in Table 6.3. At low transverse momenta they are partially one order of magnitude larger than those associated with the photon measurement. At the moment, even the statistical uncertainties of the cocktail are partially larger than those related to the photon measurements at these momenta. The latter could, however, be eliminated by generating a larger decay photon sample with the cocktail simulation. The statistical uncertainties arising from the neutral pion measurement, on the other hand, cannot be reduced easily. For momenta above 5 GeV/c also the statistical uncertainty of the photon contributes significantly to the R_γ uncertainties, irrespective of the reconstruction technique. The best statistical precision in this data set for the R_γ has been reached between 0.9 an 5 GeV/c, where it can be measured with a statistical uncertainty of about $3 - 4\%$ in all three techniques. The systematic uncertainty in this region is of the order of $6 - 7\%$ depending on the reconstruction technique. The most precise measurement in this regard originates from the PCM-EMC measurement, as here the systematic uncertainty from the inner material budget cancels fully. Towards higher momenta the calorimeter based techniques show a slightly better performance with respect to the systematic uncertainties.
The corresponding comparisons of the relative uncertainties for the p–Pb measurements can be found in Figure 6.15. For this data set, the statistical uncertainty of the inclusive photon measurements is better than 1% up to transverse momenta of 6 GeV/c. Similar to the uncertainties for the pp data set the PCM statistics is slightly better than that of the PCM-EMC reconstruction, as it also includes the statistical uncertainties of the simulations. The latter is larger for the PCM-EMC reconstruction, as the HIJING simulation has not been used for the corrections, while it was merged with the DPMJET production for the PCM standalone measurement. Once more the systematic uncertainties of these two reconstruction technique are equal, however. The corresponding systematic uncertainty for the EMC measurement is significantly larger than that obtained for pp collisions. Which can be attributed to the larger event activity, which makes it harder to uniquely identify photon clusters. Furthermore, the underlying event description in the simulations is worse than that for pp collisions, which affects the quality of the description of the cluster properties as well as the purity. Thus, it leads to larger uncertainties in particular at higher transverse momenta. Consequently, the best precision for the inclusive photon measurements is reached when reconstructing the photons with the PCM method.
For the R_γ measurement, the statistical precision could be improved to about 2% between 0.8 and 6 GeV/c, through the higher statistics in this data set. This mainly improved the statistical uncertainty for the neutral pion measurement. For the R_γ, also the corresponding PHOS measurement has been performed [373], which has slightly worse statistical uncertainties than those obtained in the course of this thesis. The smallest systematic uncertainties on the R_γ are reached ones more by the PCM-EMC measurement with about $4.8 - 5\%$ between 1 and 7 GeV/c. With the PCM and PHOS reconstruction techniques a systematic uncertainty of about 5.5% could be reached in

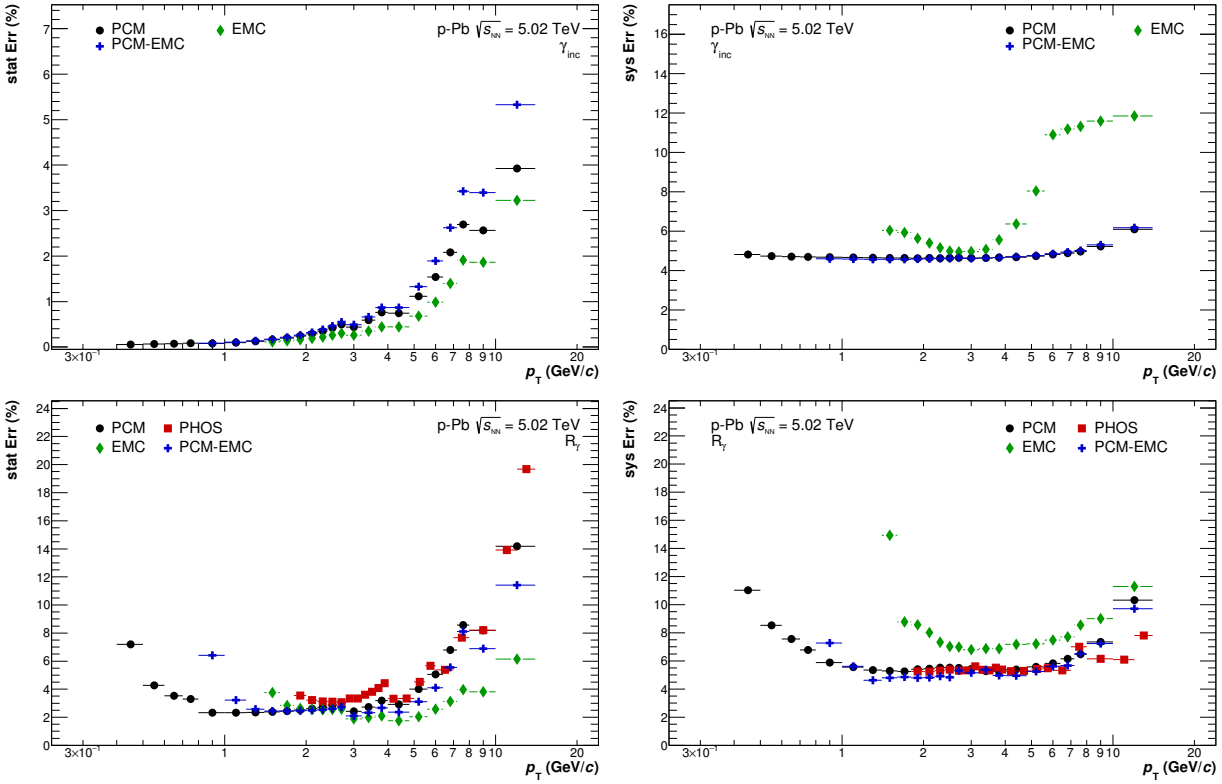

Figure 6.15.: Comparison of the relative statistical (left) and total systematic (right) uncertainties related to the inclusive photon spectra (top) and R_γ measurements in the different analysis techniques for minimum bias p–Pb collisions at $\sqrt{s} = 5.02$ TeV. The uncertainties on the R_γ related to the PHOS measurement have been taken from [373].

the same transverse momentum region. The EMC measurement suffers from a 7% systematic uncertainty between 2.5 and 7 GeV/c. This level of sensitivity is, however, not sufficient to measure an expected direct photon signal of about 3% on top of the decay photon background, with one single reconstruction technique on its own. Thus, only the combination of all available analysis might yield a significant non-zero result.

6.4. Comparison and Combination of the Individual Measurements

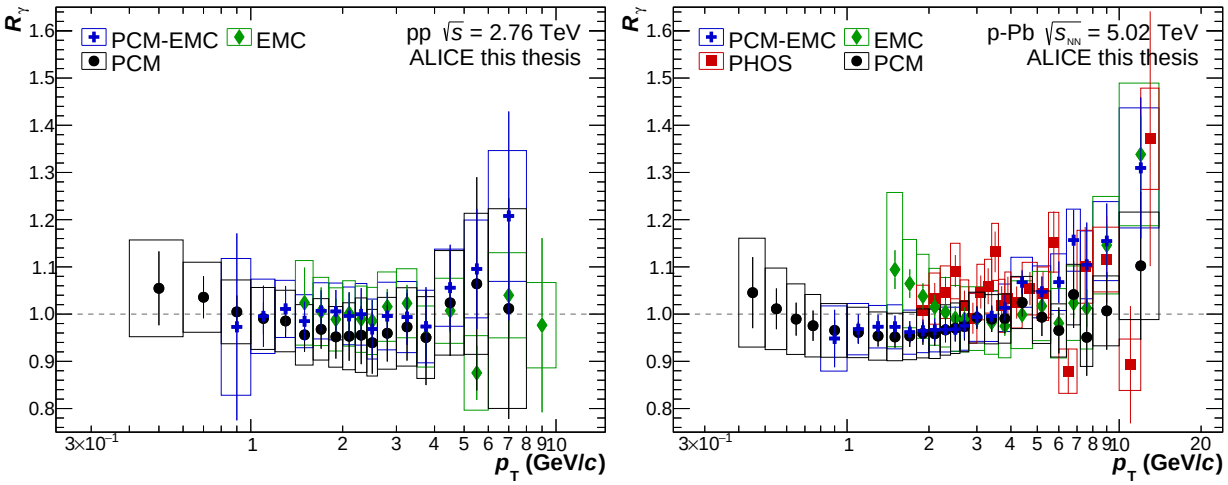

Figure 6.16.: Direct photon excess ratio (R_γ) measured with different reconstruction techniques in pp collisions at $\sqrt{s} = 2.76$ TeV (right) and p–Pb collisions at $\sqrt{s_{\mathrm{NN}}} = 5.02$ TeV (right). For each of the measurements the systematic uncertainties are displayed as boxes with the width of the transverse momentum slice, while the statistical uncertainties are shown as vertical error bars.

The final results for the direct photon excess ratio in the different analysis techniques in pp collisions at $\sqrt{s} = 2.76$ TeV and p–Pb collisions at $\sqrt{s_{\mathrm{NN}}} = 5.02$ TeV can be seen in Figure 6.16. The statistical uncertainties are indicated as error bars, while the systematic uncertainties are displayed as boxes, which reflect the transverse momentum bin width in addition. For the p–Pb measurement also the corresponding result using the PHOS reconstruction [373] is shown in the comparison plot. The latter, unfortunately, does not follow the transverse momentum binning which has been used for the remaining three analysis in the full p_{T} ranges. Thus, the result will only be considered in the combined result between 2 and 3 GeV/c, where the binning coincides among the different measurements. Furthermore, the inclusive photon yield has not been provided either and thus the comparisons in that quantity cannot be done.
The PCM, PCM-EMC and EMC results for pp collisions at $\sqrt{s} = 2.76$ TeV agree with each other within the statistical uncertainties. While the PCM-EMC and EMC measurements are at unity for momenta below 4 GeV/c, there appears to be a nearly p_{T} independent bias for the PCM standalone measurement, which leads to a shift of the R_γ to about 0.96 between 1.5 and 4 GeV/c. Below and above these momenta, no systematic deviation from the remaining measurements and unity can be observed. One of the possible reasons for such a bias could be a bias in the implementation of the material budget of the inner detectors, as this uncertainty cannot be canceled fully for the standalone PCM measurement. However, it is also possible that the deteriorated resolution, due to the lack of the SDD information, causes this shift. In particular the transverse momentum resolution of the neutral pions might not be well enough understood for these reconstruction conditions. Even though these effects should be well within the given uncertainties of the neutral pion measurements, their impact on the direct photon excess ratio can be sizable when calculating the decay photon cocktail. Up to now, no direct or inclusive photon measurement for pp collisions at $\sqrt{s} = 2.76$ TeV using the PHOS reconstruction has been attempted. This is mainly due to the limited statistics in the corresponding data sets and the even smaller acceptance for the PHOS compared to the EMCal.
For the p–Pb sample, the R_γ has been measured in four partially uncorrelated reconstruction techniques and it has been found that these agree within the statistical uncertainties for nearly all considered transverse momentum slices. For momenta below 3 GeV/c, once more a shift below unity is observed for the R_γ measurement using the PCM standalone reconstruction. However, in

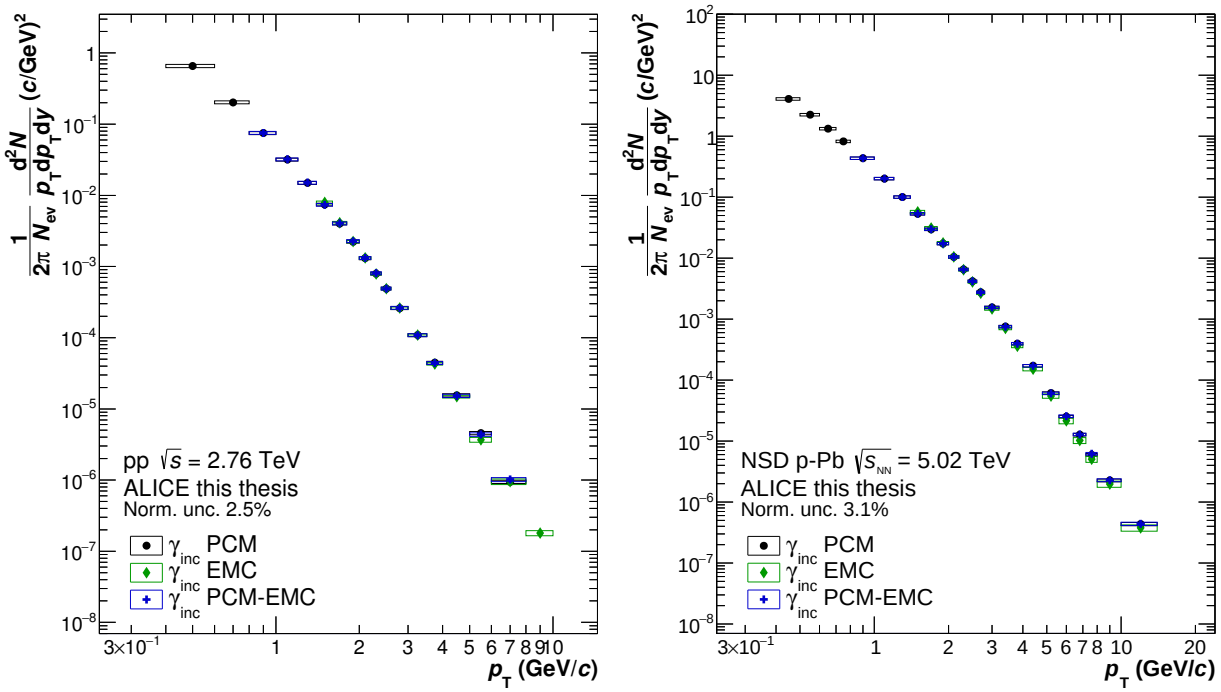

Figure 6.17.: Inclusive photon invariant yield measured with different photon reconstruction techniques in pp collisions at $\sqrt{s}$ = 2.76 TeV (left) and p–Pb collisions at $\sqrt{s_{\mathrm{NN}}}$ = 5.02 TeV (right). For each of the measurements, the systematic uncertainties are displayed as boxes with the width of the transverse momentum slice, while the statistical uncertainties are shown as vertical error bars. The global normalization uncertainties of 2.5% and 3.1% for pp and p–Pb collisions, respectively, have not been included in the systematic error estimates, as they affect all three measurement techniques in the same manner.

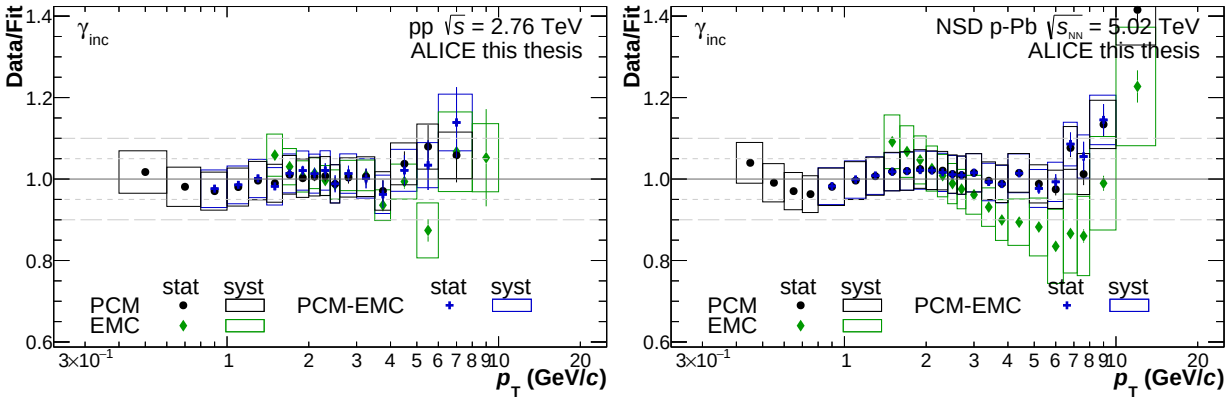

Figure 6.18.: Comparison of the individual inclusive photon spectra to the fit to the combined measurement for pp collisions at $\sqrt{s}$ = 2.76 TeV (left) and p–Pb collisions at $\sqrt{s_{\mathrm{NN}}}$ = 5.02 TeV (right). For each of the measurements, the systematic uncertainties are displayed as boxes with the width of the transverse momentum slice, while the statistical uncertainties are shown as vertical error bars. The corresponding ratio of the combined data points to the respective fits can be found in Figure C.11 of Appendix C.4.

this data set it is observed in the PCM-EMC reconstruction at the same time. This could be an indication that only part of the shift should be attributed to the material budget and at least one additional effect causes the shift. For momenta below 2 GeV/c, an increase in the R_γ is seen for the EMC reconstruction technique. This could be caused by an imperfect description of the neutral pion spectrum for the decay photon cocktail or by a bias due to converted photons in the TRD and TOF material. Although it has been attempted to reduce the latter contributions by tightening the σ^2_{long} selection criteria, it is possible that these cuts are not as effective for the rejection of conversions as for pp collisions. However, the associated systematic uncertainties in this transverse momentum region are rather large for the EMC measurement and thus no significant deviation can be claimed.

The comparison of the inclusive photon spectra for the three analysis techniques presented in this thesis for both collision systems can be seen in Figure 6.17 and the corresponding ratios to the respective combined fits are shown in Figure 6.18. As expected, good agreement has been found among the PCM and PCM-EMC measurements in both collision systems. Both of these techniques rely solely on the photons reconstructed with the PCM method to obtain the inclusive photon spectra. As such, the statistics among these two measurements is highly correlated as well as their systematic uncertainties. The EMC measurement, on the other hand, can be considered as fully uncorrelated. For pp collisions, good agreement among the different inclusive photon measurements has been found and only at the lowest possible momentum in the EMC measurement there seems to be a slight increase with respect to the corresponding measurement in the PCM photon reconstruction. For p–Pb collisions, however, a slightly different slope is seen for the EMC inclusive photon measurement compared to those using the PCM photons. Taking into account the discrepancies in the cluster description between real and simulated data for the EMC measurement, it seems most probable that the largest fraction of the bias is caused by the EMC measurement. This is further supported by the fact that for p–Pb the general event activity is described worse than for pp, which should have a larger impact on the EMC measurement as it might lead to biases in the clusterization process. Additionally, the discrepancy is covered by the larger systematic uncertainties, which had to be assigned to the EMC inclusive photon measurement for p–Pb collisions, as discussed in the previous section.
The individual measurements are combined using the BLUE method [309,310,313], as it was done for the corresponding neutral meson measurements. However, the corresponding correlation factors had to be expanded to also include the correlation among the statistical uncertainties, since the statistical uncertainties of the PCM and PCM-EMC measurements are highly correlated. The assumed correlations fractions (ρ_{ij}) for each pair of measurements i and j for the R_γ measurement in p–Pb collisions can be seen in Figure 6.19. In this figure the statistical correlations are displayed on the left side, while the correlations among the systematic uncertainties of the different measurements can be found on right side. The PHOS measurement is assumed to be fully uncorrelated with the remaining measurement and is thus not included in the respective figures. It can be seen that the statistical correlation is of the order of 40-60% between the PCM and PCM-EMC R_γ measurements, as the largest fraction of the statistical error originates from the neutral meson measurement. These are, however, uncorrelated in their statistics among the two different techniques. The fractions of the correlated systematic uncertainties range from 10%-80% depending on the measurement combinations and are very similar in their p_{T} dependence to the corresponding fractions for the meson measurements.
The resulting weights for the combinations of the direct photon excess ratio for pp and p–Pb collisions can be seen in Figure 6.20, whereas the corresponding ones for the inclusive photon spectra can be found in Appendix C.4. It can be seen that the combined result in both collisions systems is dominated by the PCM standalone measurement below 1 GeV/c, while above these momenta the PCM-EMC and EMC measurements gain in importance. For the pp measurement, the R_γ above 4 GeV/c is completely dominated by the result obtained in the calorimeter, as the other two measurements suffer much more from the low statistics for the respective neutral pion measurements. In particular, as only the minimum bias trigger has been considered for all three reconstruction techniques. For p–Pb collisions, on the other hand, the weight of the PCM and EMC is approximately the same for transverse momenta above 6 GeV/c. Below that the PCM and PCM-EMC measurements contribute about 40% each to the final measurement for the transverse momentum bins, where both measurements could be obtained. Between 2 and 3 GeV/c also the PHOS R_γ could be used in the combination. This was not possible for the remaining transverse momentum slices due to a different choice of the respective bin widths. In this region, the same weight is given to the PCM, PCM-EMC and PHOS measurements, while the EMC R_γ measurements contributes only marginally due to its larger systematic uncertainties.

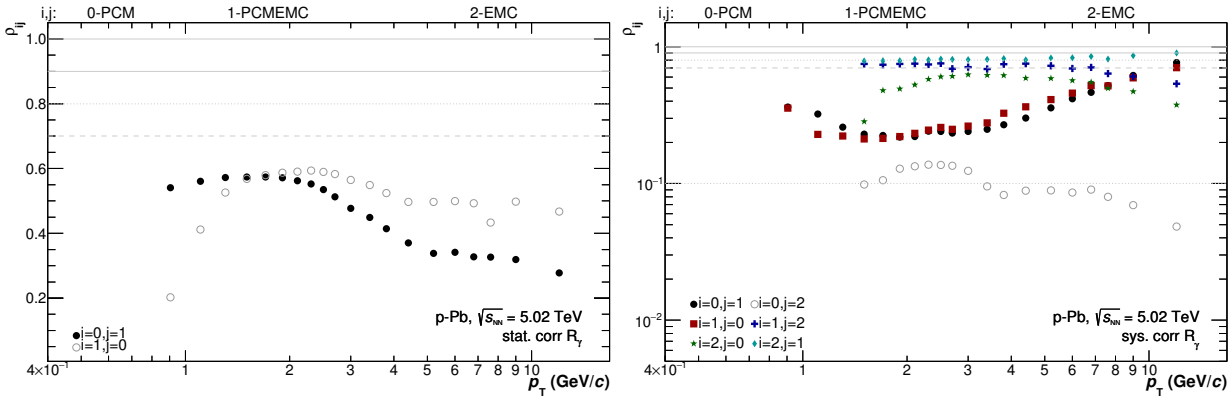

Figure 6.19.: Correlation fractions (ρ_{ij}) for each pair of measurements i and j for the R_γ in p–Pb collisions at $\sqrt{s_{\mathrm{NN}}} = 5.02$ TeV. The correlation among the statistical uncertainties is shown on the left side, while the corresponding one for the systematic uncertainties is shown on the right side. Similar plots for the R_γ in pp collisions at $\sqrt{s} = 2.76$ TeV as well as the inclusive photon spectra can be found in Appendix C.4.

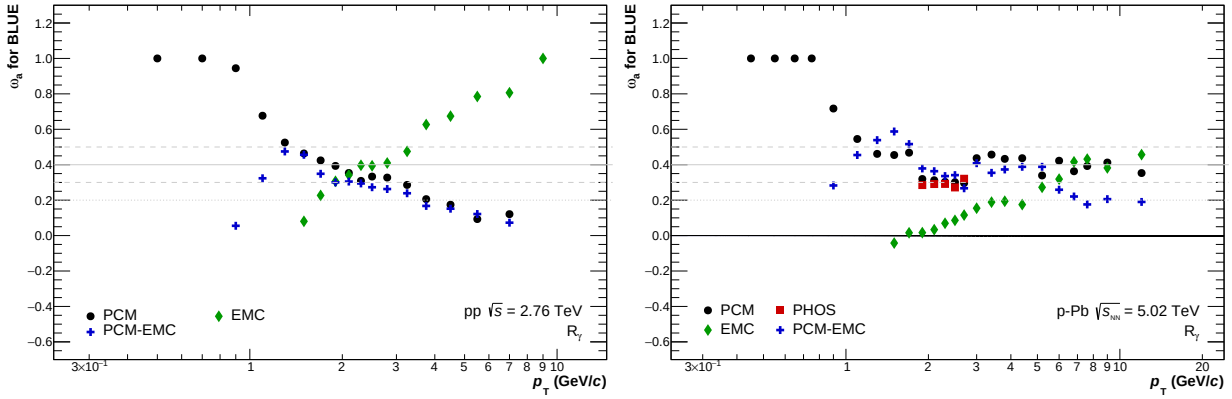

Figure 6.20.: Weights (ω_a) for the individual R_γ measurements in pp (left) and p–Pb collisions (right), which are used in the combinations according to the BLUE method [309,310,313] for the respective collision systems.

The final combined results on the R_γ for minimum bias pp collisions at $\sqrt{s} = 2.76$ TeV and p–Pb collisions at $\sqrt{s_{\mathrm{NN}}} = 5.02$ TeV can be seen in Figure 6.21. The respective relative statistical, systematic and total uncertainties are displayed in Figure 6.22. Through the combination of the individual pp measurements it is possible to reach a total uncertainty below 7% between 1 and 5 GeV/c. In this region, the total uncertainty is driven mainly by the systematic uncertainties, which do not exceed 6% at these transverse momenta. Consequently, a significant direct photon signal could only be extracted from this data set, if it exceeds $7\% - 8\%$. Such an excess is, however, not expected for minimum bias pp collisions, which is confirmed by the measured R_γ. The R_γ is found to be consistent with unity within the statistical uncertainties over the full transverse momentum range covered by the measurement.
For the p–Pb measurement, on the other hand, the statistical uncertainties between 1 and 6 GeV/c could be reduced to less than 2% and the corresponding systematic uncertainties do not exceed 4% in the same transverse momentum range. Thus, it should be possible to extract a direct photon signal, if it is larger than 5% above the decay photon background in the corresponding transverse momentum range. However, no significant excess for p–Pb collisions has been found for $p_{\mathrm{T}} < 4$ GeV/c. For transverse momenta between 0.8 and 2 GeV/c, the most probable values are even below unity and do not agree with unity within the statistical uncertainties. As already discussed this could be attributed to a mismatch either in the tracking or the material budget description in the simulated data, which affects mainly the conversion photons. For momenta below 0.8 GeV/c, the statistical uncertainty increases and the neutral pions can no longer be reconstructed with a sufficient precision. Consequently, it will be interesting to see whether the increase of the R_γ at these momenta remains for the higher statistics data, which have been

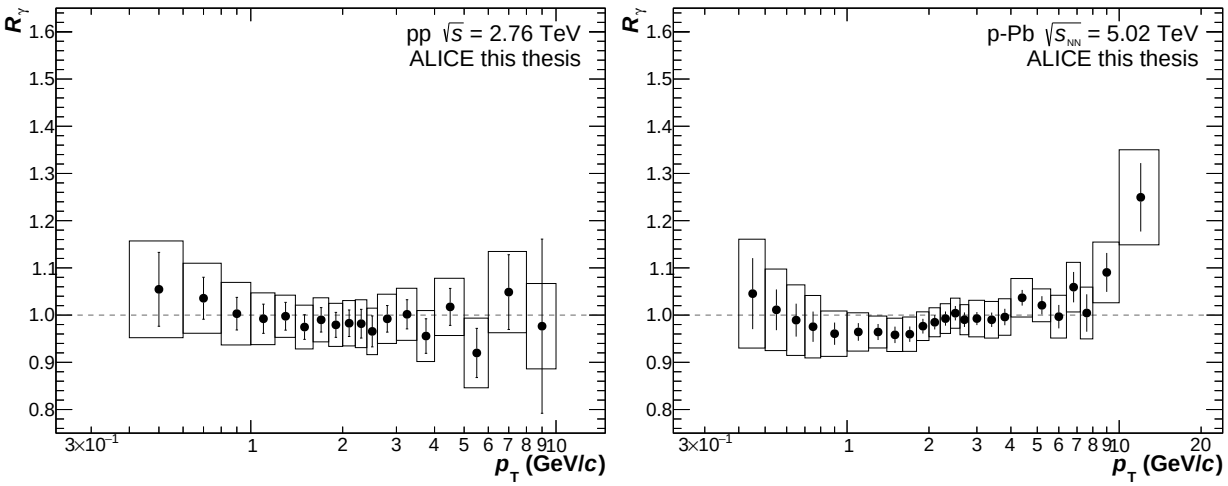

Figure 6.21.: Combined direct photon excess ratio (R_γ) measured in minimum bias pp collisions at $\sqrt{s}$ = 2.76 TeV (left) and p–Pb collisions at $\sqrt{s_{\rm NN}}$ = 5.02 TeV (right).

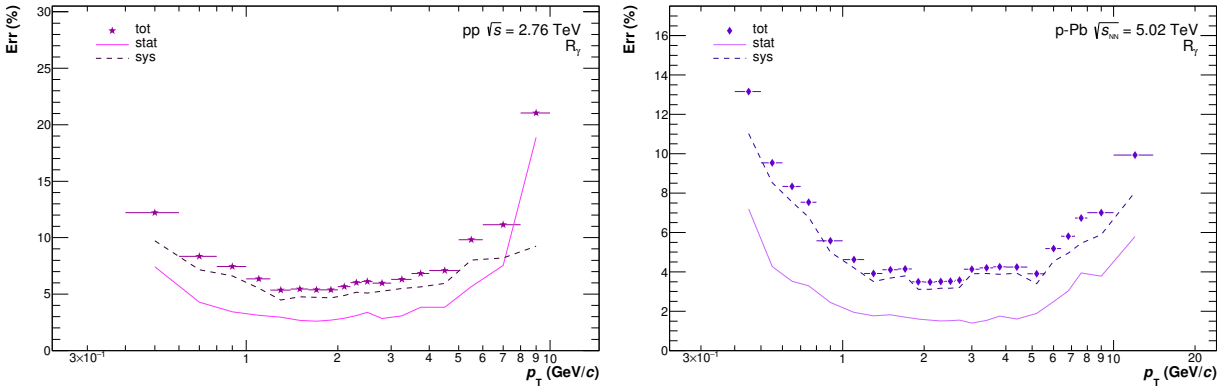

Figure 6.22.: Total uncertainties for the R_γ measurement in pp (left) and p–Pb collisions (right) after the combination of the 3(4) partially independent measurements. In addition, the statistical and systematic uncertainties are given separately for each of the measurements as solid and dashed lines, respectively.

collected in 2016. At high transverse momenta, an excess of the direct photons with respect to the decay photons can be observed and the corresponding direct photon spectrum can be calculated. For transverse momenta below 6 GeV/c, only upper limits can be provided for the direct photon production in p–Pb collisions at $\sqrt{s_{\rm NN}}$ = 5.02 TeV.

6.5. Direct Photons Measurements at LHC energies

The obtained direct photon excess ratio for pp collisions at $\sqrt{s}$ = 2.76 TeV has been compared to two direct photon next-to-leading order pQCD calculations using different PDFs and fragmentation functions (FF) in Figure 6.23. As only the direct photon contribution can be calculated within the framework of next-to-leading order pQCD, the decay photon spectrum has been taken from the same decay photon simulation, which has been used for the experimental measurements. In order to reduce the uncertainties at higher momenta, however, the combined neutral pion spectrum has been used to obtain the pion parametrization. The remaining inputs are the same as for the experimental measurements. The excess ratio for the NLO pQCD calculation can then be calculated as:

$$R_{\gamma,\mathrm{pQCD}}(p_{\mathrm{T}}) = 1 + \left(N_{\mathrm{coll}} \cdot \frac{\gamma_{\mathrm{dir,\ NLO}}(p_{\mathrm{T}})}{\gamma_{\mathrm{decay,\ cocktail}}(p_{\mathrm{T}})} \right). \tag{6.9}$$

For pp collisions $N_{\rm coll}$ is assumed to be 1, while it has to be considered when comparing these calculations to measurement obtained from p–Pb and Pb–Pb collisions. For p–Pb collisions the calculations were scaled by $N_{\rm coll}$ = 6.9 in accordance with the calculated value at $\sqrt{s_{\rm NN}}$ = 5.02 TeV

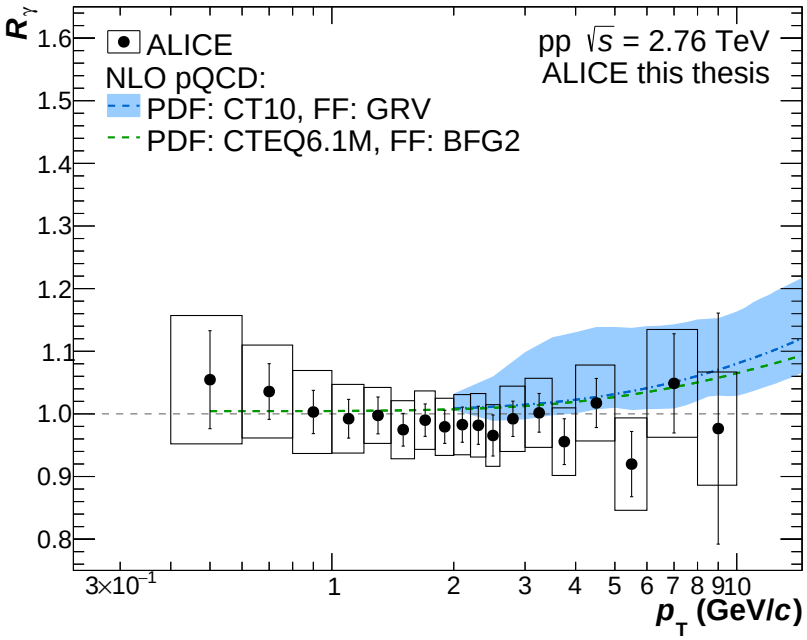

Figure 6.23.: Comparison of the direct photon excess ratio (R_γ) for pp collisions at $\sqrt{s} = 2.76$ TeV and the corresponding next-to-leading order pQCD calculations for the direct photons. The calculations have been done by Werner Vogelsang [356] and Jean-Francois Paquet [202] using the CT10 [359–361] and CTEQ6.1M [380] parton distribution functions as input for the respective calculations. In addition, different fragmentation function have been chosen by the authors: GRV [381] and BFG2 [382]. Both combinations describe the data on the direct photon production at lower center-of-mass energies with similar precision, however [383] and thus can be considered adequate.

from the Glauber Monte-Carlo simulations [384]. The uncertainties of the NLO pQCD calculations are given through a simultaneous variation of the fragmentation, factorization and renormalization scales from the $\mu = p_{\mathrm{T}}$ to $\mu = 0.5p_{\mathrm{T}}$ and $\mu = 2p_{\mathrm{T}}$, respectively. They are depicted as a band in the corresponding figure for the calculation from Werner Vogelsang [356] using the CT10 parton distribution functions [359–361] together with GRV fragmentation function [381]. For the calculation from Jean-Francois Paquet [202], no uncertainties have been provided. This calculation has been extended towards lower momenta using a bootstrapping techniques, which assumes that the shape of the direct photon production spectra is the same for different μ and only the absolutes yields change. With this technique it is possible to go to lower momenta by increasing μ gradually to $\mu = 3, 4, 5, \ldots p_{\mathrm{T}}$ and afterwards renormalizing the corresponding calculations to the one obtained for $\mu = p_{\mathrm{T}}$. For this calculation, a different set of PDFs and fragmentation functions has been chosen [380, 382], which can lead to small differences at higher transverse momenta. Both combinations, however, describe the results on the direct photon at lower center-of-mass energies equally well. The same is observed for pp collisions at $\sqrt{s} = 2.76$ TeV, where according to the pQCD calculations, only an excess of less than 1% below 3 GeV/c would be expected. For momenta above 7 GeV/c, however, an enhancement of $7 - 10\%$ is expected. The measured points, albeit consistent with 1, would also support such a small excess at higher momenta within the uncertainties.

From the measured R_γ it is possible to derive upper limits on the p_{T} differential direct photon production in pp collisions at $\sqrt{s} = 2.76$ TeV. The direct photon signal at a certain momentum can be calculated according to:

$$\gamma_{\mathrm{dir}} = \left(1 - \frac{1}{R_\gamma}\right) \cdot \gamma_{\mathrm{inc}} \tag{6.10}$$

Combined with the large systematic and statistical uncertainties, the size of the signal is, however, to small and the upper limits will be at least 1 order of magnitude higher that the actually expected signal. The upper limits are defined as a 95% confidence level of the corresponding data point tak-

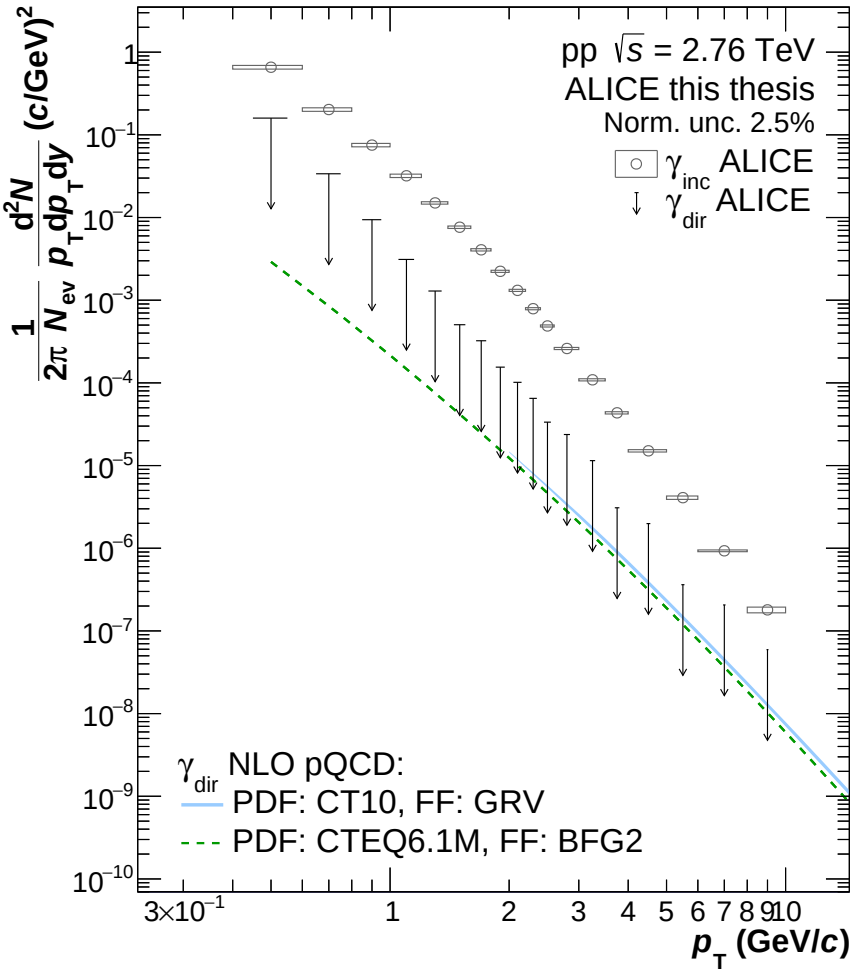

Figure 6.24.: Comparison of the upper limits on the direct photon production in pp collisions at $\sqrt{s}$ = 2.76 TeV with the corresponding NLO pQCD provided by Werner Vogelsang [356](light blue) and Jean-Francois Paquet [202] (green). The depicted arrows correspond to upper limits with a 95% confidence level. Furthermore, the measured inclusive photon spectrum at the same collision energy is shown as open gray dots. The global normalization uncertainty of 2.5% is not included in the systematic uncertainties or upper limits.

ing into account the uncertainties of the corresponding inclusive photon measurement in addition. They are displayed as arrows in Figure 6.24 together with the corresponding expectations from the next-to leading order calculations and the corresponding inclusive photon measurement. With the current precision of the data it is unfortunately not possible the challenge the theory calculations. It has to be mentioned, that the calculation by J.F. Paquet had been used in the previous Pb–Pb publication [212] in order to subtract the hard photon component from the measured direct photon spectra in Pb–Pb at $\sqrt{s_{\rm NN}}$ = 2.76 TeV. This hard component should ideally be measured in pp collisions at the same energy and thus would correspond to the presented measurement. With the current uncertainties the measured data do not provide an improvement of the these assumptions, however. The comparison to the obtained inclusive photon spectrum shows, that for most transverse momentum slice the direct photon spectrum will be at least 1 order of magnitude smaller that that of the inclusive measurement, as expected.
The comparison of the combined R_γ result for NSD p–Pb collisions at $\sqrt{s_{\rm NN}}$ = 5.02 TeV to various theory calculations is shown in Figure 6.25. To understand the effect of the modification caused by the presence of a Pb nucleus in the collision, three different next-to-leading order pQCD calculations are compared to the measured data, where each of them uses a different (nuclear) parton distribution function, but the same fragmentation function for the photons. The direct

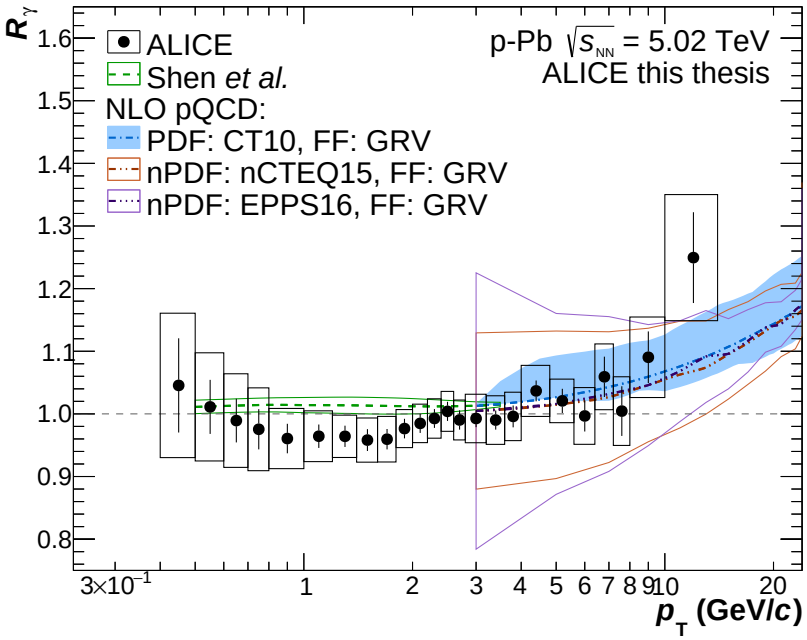

Figure 6.25.: Comparison of the measured direct photon excess ratio to various theory predictions for non-single diffractive p–Pb collisions at $\sqrt{s_{\mathrm{NN}}} = 5.02$ TeV. The data are compared to three different next-to-leading order calculations using different (n)PDFs [359–361, 365, 366]. The latter have been provided by Werner Vogelsang [356, 385] and Hendrik Poppenborg [386]. Furthermore, they are compared to a recent hydro calculation by Chun Shen *et al.* [103] at lower transverse momenta.

photon excess ratio for the theory calculations is once more obtained according to Equation 6.9 using the decay photon cocktail provided by ALICE. The latter is based on the combined neutral pion measurement and the corresponding combined η/π^0 ratio, which are presented in Section 5.3.3. The uncertainties of the theory calculations are given once more by the simultaneous variations of the factorization, fragmentation and renormalization scales. Only the latest nPDF sets [365, 366] have been chosen for the comparison to the data, while the pure pp calculation relies once more on the CT10 PDF [359–361]. It can be seen that all three calculations describe the excess of direct photons above the decay photon at higher momenta, regardless of the choice of the (n)PDF. The differences are mainly reflected in the uncertainties, which are significantly larger for the calculations using the two calculations using the nPDFs. For the central values of the calculations, the differences are smaller than $1-2\%$, which are not distinguishable within the current statistical and systematic uncertainties of the experimental data.
Additionally, the data are compared to a recent hydro calculation by Chun Shen *et al.* [103], which predicts an excess yield of $2-3\%$ in minimum bias collisions below 3 GeV/c. Unfortunately, the measured data are shifted below unity by an unresolved experimental bias in this transverse momentum region and no clear statement can be made, whether such a signal is observed or not. However, even if the bias would not have been present the current precision of the data would not have allowed to exclude a signal of 2%. The same calculation also predicts a small but non-zero anisotropic flow for 0-5% central p–Pb collisions at the same center-of-mass energy with an excess yield of about 2-5% at low transverse momenta. With the newly collected high statistics data for p–Pb collisions at $\sqrt{s_{\mathrm{NN}}} = 5.02$ TeV from 2016 and the sensitivity reached in this thesis, it might be possible to extract the direct photon yield in these collisions or at least constrain the theory expectations.
The measured R_γ for NSD p–Pb collision at $\sqrt{s_{\mathrm{NN}}} = 5.02$ TeV allows the partial extraction of a direct photon spectrum for transverse momenta above 6 GeV/c, while in the remaining transverse momentum range only upper limits with a confidence level of 95% can be provided. The data points and corresponding upper limits are compared to the theory calculations for the direct photon spectra in Figure 6.26. The same calculations as for the R_γ are depicted for the spectra as

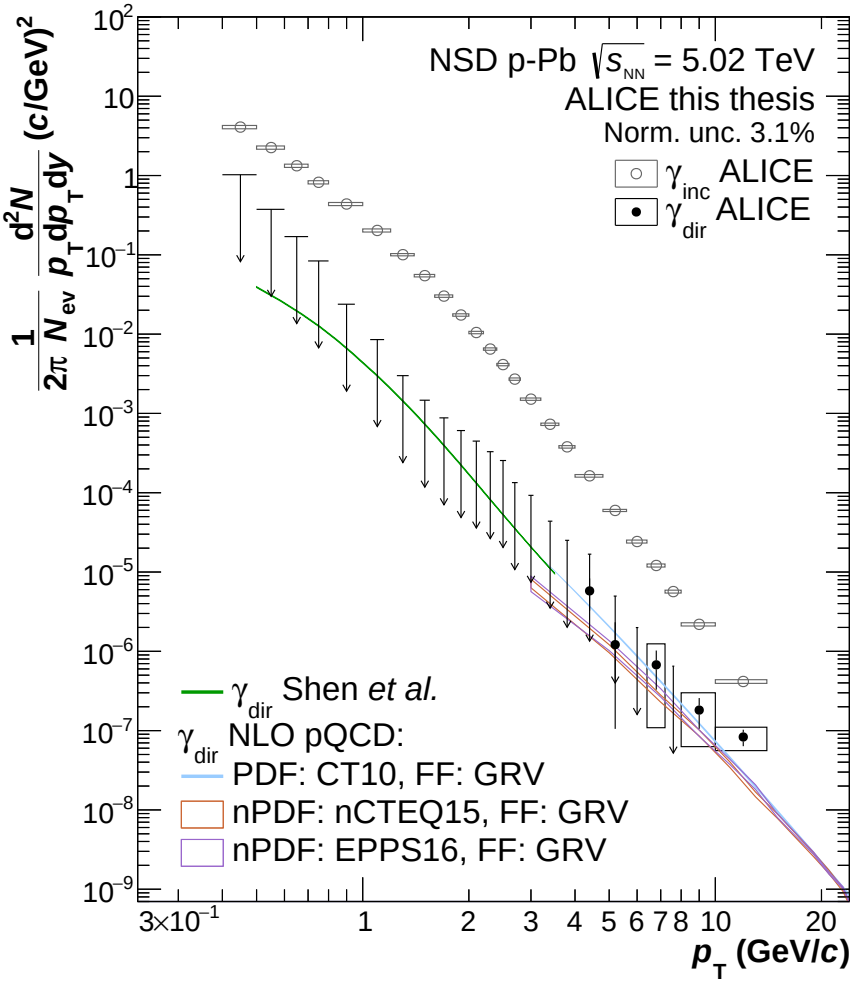

Figure 6.26.: Comparison of the direct photon invariant yield measured in NSD p–Pb collisions at $\sqrt{s_{\mathrm{NN}}} = 5.02$ TeV to theoretical predictions based on hydrodynamic models [103] at low transverse momenta and NLO pQCD calculations for momenta above 3 GeV/c [385, 386]. Furthermore, the obtained upper limits according to a 95% confidence limit are shown as arrows. If only a statistically significant data point could be obtained, this is indicated via the display of a dot on the corresponding upper limits. Additionally, the invariant yield of the measured inclusive photons is shown as open gray dots. The global normalization uncertainty of 3.5% has not been considered for the upper limits or in the systematic uncertainties.

well. Furthermore, the inclusive photon invariant yield is shown in the same figure as open gray dots. It can be seen that for the highest transverse momenta, the data points are underestimated by the next-to-leading order calculations by about a factor 2, while they agree with the data points and upper limits at lower momenta. For data points, where the R_γ would have been above unity, if only the statistical uncertainties would have been considered, the most probable yield according to the statistical uncertainties is depicted as a point without a systematic uncertainty box. Instead the corresponding upper limit is drawn as an arrow for these data points in addition. As expected for the R_γ measurement, none of the theory predictions can be validated or excluded at lower momenta, due to the even larger uncertainties on the direct photon spectrum. The increase of the uncertainties arises from the inclusion of the corresponding inclusive photon uncertainties for the direct photon ones as well.

The comparison to the inclusive photon spectrum indicates a different slope of the inclusive and direct photons for momenta above $7 - 8$ GeV/c. To confirm this observation, it will be necessary to include the calorimetric triggered data samples for p–Pb collisions, which had been collected in 2013, in the corresponding analyses as well. This should improve the statistical uncertainties above 7 GeV/c by at least a factor $2 - 5$ depending on the measurement technique. Furthermore, the combination would benefit from the inclusion of the PHOS measurement in the full momentum

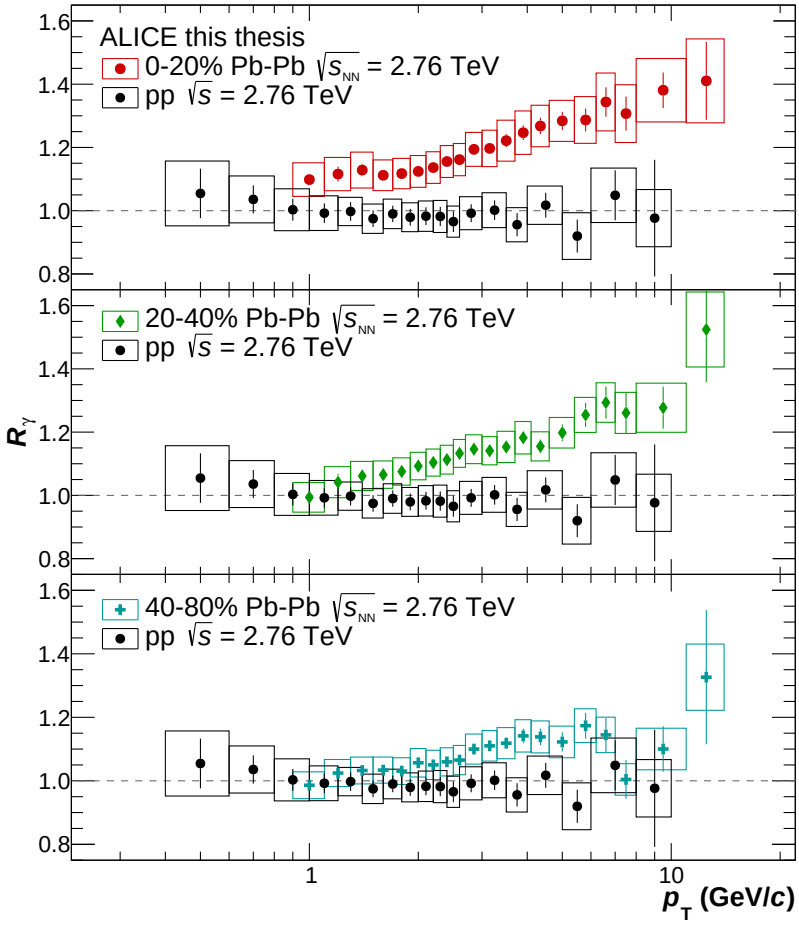

Figure 6.27.: Comparison of the direct photon excess ratio for Pb–Pb collision at $\sqrt{s_{\mathrm{NN}}} = 2.76$ TeV in different centrality classes [212] to the corresponding measurement in pp collisions at $\sqrt{s} = 2.76$ TeV.

region.
Finally, the pp results on the R_γ at $\sqrt{s} = 2.76$ TeV are compared to the published Pb–Pb results [212] in Figure 6.27. The latter had been published after the first year of the PHD as a result of a cooperation with Martin Wilde. For the Pb–Pb results, no data from EMCal related measurements had been available yet, thus the combination relied fully on the independent PCM and PHOS results in the three different centrality classes. It can be seen that the low momentum excess increases when going to more and more central events, while for the corresponding pp no excess is seen at any transverse momentum. For momenta above $5 - 7$ GeV/c, no effects from the quark gluon plasma should be seen any longer in the direct photon spectrum for Pb–Pb collisions and thus a possible excess seen in pp collisions is expected to scale with N_{coll}. However, the large statistical uncertainties in the pp data set do not allow a direct comparison between the high p_{T} pp and Pb–Pb data, yet on the level of the N_{coll} scaled R_γ.
Instead, the scaled upper limits for pp collisions are superimposed to the corresponding direct photon spectra measurements in Pb–Pb in Figure 6.28. It can be seen that even for momenta above 5 GeV/c the precision of the pp data does not yet suffice to confirm the expected N_{coll} scaling behavior. Once more it might be possible to improve the pp measurement in this transverse momentum region by including either the corresponding PHOS measurement, once it becomes available, or the triggered EMCal data sets. For the latter mainly the PCM-EMC would benefit from the improved statistics, whereas it is not yet clear to which momenta the EMC standalone measurement should be pursued, when taking into account the onset of cluster merging in the EMCal. However, for momenta above $12 - 15$ GeV/c, an isolated photon analysis should be feasible within ALICE and it could be tried to match the different kinds of analyses in this region,

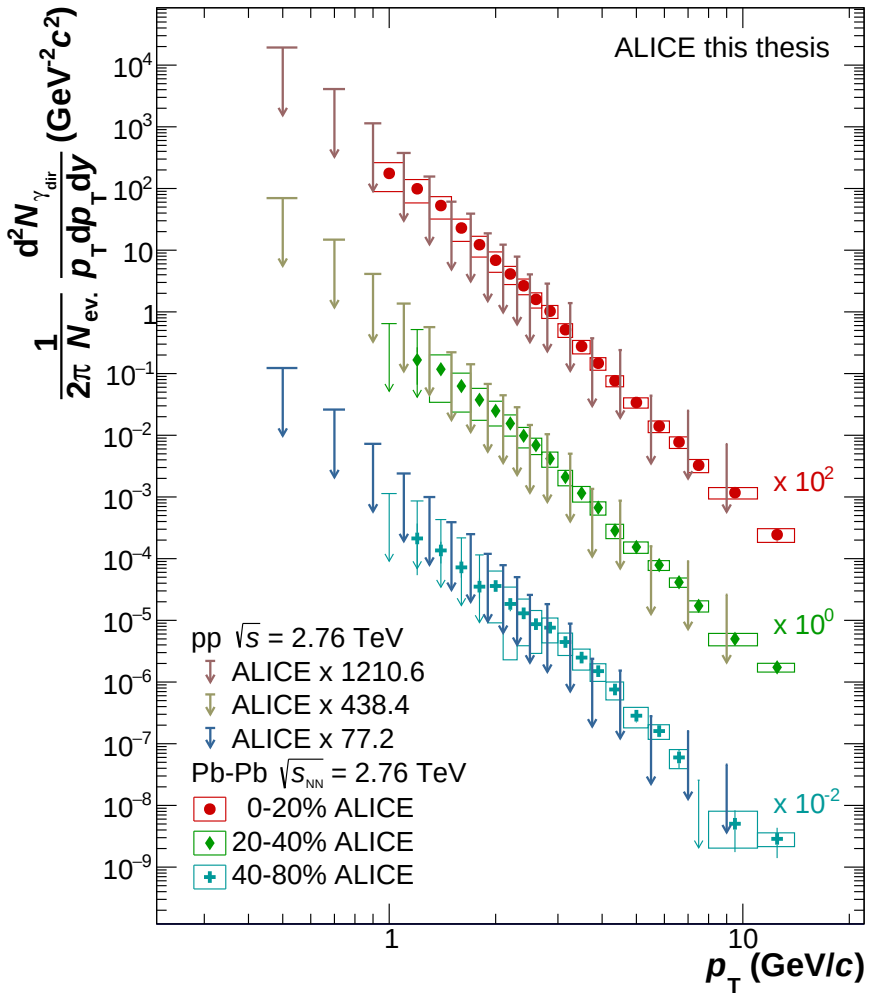

Figure 6.28.: Comparison of the N_{coll}-scaled upper limits for the direct photon spectrum in pp collision at $\sqrt{s} = 2.76$ TeV to the corresponding Pb–Pb spectra at $\sqrt{s_{\mathrm{NN}}} = 2.76$ TeV for the $0-20\%$, $20-40\%$ and $40-80\%$ central events [212]. The vertical lines indicate the statistical uncertainties, while the systematic uncertainties are displayed as boxes with the width of the corresponding p_{T} slice. The vertical arrows indicate the upper limits. If only a statistically significant data point could be obtained, this is indicated via the display of a dot on the corresponding upper limit. For visibility the most central and most peripheral spectra have been scaled by 100 and 0.01, respectively. The global normalization uncertainties are not considered in this plot. However, they do not exceed 5% and can thus be neglected for the presented comparison.

albeit part of the fragmentation photons might be excluded in case of the isolated photon analysis.

7. Summary

In this thesis, the measurements of direct photons and light neutral mesons have been presented for minimum bias pp collisions at $\sqrt{s} = 2.76$ TeV and p–Pb collisions at $\sqrt{s_{\mathrm{NN}}} = 5.02$ TeV.
Direct photons are an intriguing probe of the quark-gluon-plasma and the subsequent hot hadron gas phase. In particular, as they should leave the respective medium without interacting with it, once they have been produced. However, these photons are embedded in a large background originating from the decay of light mesons and baryons into photons. The by far largest contributors to this background are the neutral pions and eta mesons. Thus, in order to extract the direct photons a thorough understanding of the light neutral meson production in the same collision system is required. This is of particular importance for pp and p–Pb collisions, where the excess of photons is expected to be of the order of a few percent even at high transverse momenta. The analyzed data has been collected by the ALICE experiment at the LHC at CERN in the beginning of 2011 and 2013, respectively.
Within ALICE, photons can be reconstructed either through their energy deposit in one of the electromagnetic calorimeters, EMCal and PHOS, or via the conversion photon reconstruction (PCM). For the latter the electrons originating from conversions in the inner layers of the detector are reconstructed using the tracking information from the ITS and TPC and then paired to photon candidates. Based on these photons the π^0 and η meson are reconstructed statistically using the invariant mass technique. In this thesis the pure PCM and EMC meson analyses have been pursued, which rely on pairs of photons reconstructed with the same photon reconstruction technique. Furthermore, a hybrid analysis using one photon from the EMCal and one from the conversions has been developed (PCM-EMC). The latter combines the excellent momentum resolution of the conversions with the higher statistics of the calorimetric measurement. Hence, it combines the advantages of the two standalone techniques, in particular when using the EMCal triggered data sets. For $p_{\mathrm{T}} > 20$ GeV/c it is not possible any longer to separate the two photons from a neutral pion decay in the EMCal. Thus, to extend the measurements to higher p_{T} a new reconstruction technique has been developed, which relies on the characteristic shape of the π^0 energy deposition in the EMCal. It has been shown that this reconstruction technique can be pursued reliably up to $p_{\mathrm{T}} = 40$ GeV/c in the pp data set at $\sqrt{s} = 2.76$ TeV, whereas for other data sets with higher statistics for the EMCal triggers, this analysis could be extended to up to 100 GeV/c.
Using the PCM-EMC reconstruction it was possible to devise an independent relative energy-position correction for the EMCal, which reduces the energy-scale uncertainty to $0.2 - 0.3\%$ in the measured transverse momentum region. The same technique could also be used to further calibrate the PHOS, as it can be seen in [303] using the same calibration framework.
Exploiting the full photon reconstruction and triggering capabilities of the ALICE detector system, the neutral pion differential invariant cross section could be measured in pp collisions at $\sqrt{s} = 2.76$ TeV for transverse momenta of $0.4 < p_{\mathrm{T}} < 40$ GeV/c with a minimum total uncertainty of about $5-6\%$ between $1-6$ GeV/c and $15-20\%$ total uncertainties between $20-35$ GeV/c. Furthermore, the η meson cross section has been measured at the same energy between $0.6 < p_{\mathrm{T}} < 20$ GeV/c. Above 4 GeV/c these spectra are found to exhibit a similar power-law behavior with an exponent of about $n \approx 6.3$. The spectra have been compared to next-to-leading order calculations using the latest parton distribution and fragmentation functions. These differ from the data by about 30% for the π^0 and between 30-50% for the η meson. The comparisons to generator-level simulations with PYTHIA 8.2, on the other hand, yield an agreement better than 10-30% to the data for nearly all transverse momenta. For the η the theory uncertainties are significantly larger

than those of the corresponding neutral pion calculation, as the fragmentation functions have not been updated through the inclusion of experimental data from the LHC. Therefore, the presented η measurement will serve as an important constraint to further understand the fragmentation of the gluons and quarks to particles, which include at least one strange quark in the final state.
For p–Pb collisions the neutral pion spectrum could be measured for transverse momenta of $0.3 - 20$ GeV/c with a total uncertainty better than 5% between $1.2 - 10$ GeV/c. Hence, it is the most precise identified particle measurement in p–Pb collisions at $\sqrt{s_{\mathrm{NN}}} = 5.02$ TeV. In this collision system the η meson p_{T} differential invariant yield could be measured between 0.7 and 20 GeV/c. Once more the spectra follow a power-law behavior above 4 GeV/c with $n \approx 6.1$. A comparison of the results to next-to-leading order pQCD calculations using different (nuclear) PDFs, reveals that within the current model uncertainties no clear preference for a certain (n)PDF can be derived from the data, although the inclusion of the nuclear effects yields a slightly better description of the data. The newly obtained precision for the neutral pion measurement will also help to further understand the interplay between the hard and soft part of the collisions and will thus serve as a valuable input for tuning the multipurpose event generators for p–Pb collisions, which currently fail to reproduce the measured data.
The spectra measured in p–Pb collisions are compared to the corresponding interpolated pp reference spectra. For that purpose the nuclear modification factor R_{pA} has been calculated for both mesons. It has been found that both mesons might be suppressed in p–Pb collisions above 4 GeV/c. For the neutral pion this suppression is of the order of $5 - 10$ %. No other light meson shows such a strong suppression with similar uncertainties in minimum bias p–Pb collisions. The influence of the initial state effects on the R_{pA}, has been studied through a comparison with various models, which only include cold-nuclear matter effects. It has been found, that a fraction of the observed suppression, can be explained by the these effects. Thus, it will be interesting to see whether the suppression is also seen for the higher statistics data sample from 2016 using the same reconstruction techniques. This measurement will, however, also benefit from a measured pp reference as well as the application of the single cluster analysis for p–Pb collisions by which this measurement could be extended to significantly higher transverse momenta. If the suppression remains or proves to be even larger, this would be an indication for the production of a Quark-Gluon plasma in minimum bias p–Pb collisions.
Another key observation, for the discovery of the creation of a quark-gluon-plasma in heavy-ion collisions, was the collective expansion of the medium and thus the collective motion of a large fraction of the produced particles in a central heavy-ion collision. However, recent results from the LHC experiments on various observables in high-multiplicity p–Pb and pp collisions also indicate collective behavior in these collision systems. It has been found that also the neutral pion and η meson spectrum are better reproduced by the theoretical models at low transverse momenta, if these models include a hydrodynamic evolution of the event. Additionally, an indication of a mass ordering is also present in the comparison of the different nuclear modification factors at low transverse momenta.
In addition to the p_{T} differential measurements for pp and p–Pb collisions also the integrated neutral pion and eta yield are presented as well as the mean transverse momentum. They are compared to the results for other particle species and it has been found that the integrated yield decreases as a function of the particle mass, while the mean transverse momentum increases. These results can be used to test the applicability of statistical models, like THERMUS [106] or SHARE [107], for small collisions systems where thermal and chemical equilibrium might not be reached yet.
As a result of the in-depth understanding of the detectors, which has been reached for the neutral meson measurements, the direct photon spectra for pp and p–Pb collisions could be extracted using three partially independent reconstruction techniques. The direct photon extraction has been done following the statistical subtraction method for which the decay-photon background is subtracted from the inclusive-photon measurement. The decay photon background has been estimated using

a decay photon simulation, which is based on the measured hadron spectra. It is dominated by the photons from the π^0 and η decays, which are well constrained by the presented measurements. The only expected source of direct photons in pp collisions are originating from the initial interactions of the colliding nucleons. They are commonly referred to as prompt photons and their excess over the decay photons below 30 GeV/c is less than 10%. The corresponding measurement of the excess ratio (R_γ) in pp collisions at $\sqrt{s} = 2.76$ TeV is consistent with unity in the full transverse momentum range, thus upper limits on the direct photon production in this collision system could be extracted. Within the uncertainties, other sources of direct photon production can not be excluded. As this measurement is still dominated by the statistical uncertainties of the $R_\gamma$measurements, it has to be performed for pp collision at other LHC center-of-mass energies for which higher statistics minimum bias data sets are available, only then will it be possible to determine whether no other source contribute to the direct photon production cross section in pp collisions.

For p–Pb collisions, on the other hand, it is not clear which photon sources should be contributing to the direct photon spectrum, as a small quark-gluon plasma could be produced in these collisions. However, the predicted excess thermal photon yield for $p_{\mathrm{T}} < 3$ GeV/c does not exceed 2-3%. At higher momenta a clear excess of about 10% at 10 GeV/c should be seen, however, as the prompt photon contribution increases with increasing energy and is expected to scale with the number of collision. The measured R_γ for non-single diffractive p–Pb collisions at $\sqrt{s_{\mathrm{NN}}} = 5.02$ TeV clearly exceeds unity for momenta above 6 GeV/c and thus a direct photon spectrum can be measured. The obtained data points are in agreement with the expectations from next-to-leading order calculations using different (n)PDFs. Below 6 GeV/c no significant excess photon yield is observed and thus only upper limits can be provided. The upper limits do, however, not exclude a thermal photon production at low transverse momenta of the order of $2 - 3\%$ as it would have been predicted by Shen et al. [103].

For central p–Pb collisions the expected direct photon signal at low transverse momenta increases. Thus, the application of the presented techniques to $0 - 5\%$ p–Pb collisions, assuming similar uncertainties, could further the understanding of the source of the collective behavior seen in p–Pb. The same techniques should also be tested in Pb–Pb collisions to further improve the uncertainties for these measurements as well and provide an independent measurement of the previously obtained results.

A. Acronyms and Technical Terms

ACORDE	ALICE cosmic ray detector
ADC	analog-to-digital converter
AGS	Alternating Gradient Synchrotron
ALICE	A Large Ion Collider Experiment
AOD	Analysis Object Data
ATLAS	A Toroidal LHC Apparatus
BLUE	Best Linear Unbiased Estimate
BNL	Brockhaven National Laboratory
CCMF	Conv-Calo mass fit
CCRF	Conv-Calo ratio fit
CERN	European Organization for Nuclear Research
CGC	Color Glass Condensate
CMF	Calo mass fit
CMS	Compact Muon Solenoid experiment
CPV	Charged-Particle-Veto
CRF	Calo ratio fit
CTP	Central Trigger Processor
DAQ	Data Acquisition
DCA	distance of closest approach
DCal	Di-jet Calorimeter
DGLAP	Dokshitzer–Gribov–Lipatov–Altarelli–Parisi
DIS	Deep Inelastic Scattering
DPM	Dual Parton Model
EM	electromagnetic
EMCal	Electromagnetic Calorimeter
ESD	Event Summary Data
FEE	Front End Electronics

FF	Fragmentation Functions
FMD	Forward Multiplicity Detector
FPGA	Field Programmable Gate Array
GTU	Global Tracking Unit
HLT	High Level Trigger
HMPID	High Momentum Particle Identification Detector
INEL	Inelastic
ISR	Intersecting Storage Rings
ITS	Inner Tracking System
JETPHOX	JETPHOX
L0	level-0
L1	level-1
L3	High Energy Physics Experiment at LEP
LEP	Large Electron Positron Collider
LHA	Les Houches Accord
LHC	Large Hadron Collider
LHCb	LHC beauty experiment
LHEF	Les Houches Event Files
LO	Leading Order
LQCD	Lattice QCD
LS	long shutdown
LTU	Local Trigger Unit
MRPC	Multigap Resistive Plate Chamber
MTR	Muon trigger
MWPC	multi-wire-proportional chamber
NLO	Next-to-Leading Order
NNLO	Next-to-Next-to Leading Order
nPDF	nuclear Parton Density Functions
NSD	non single-diffractive
PCA	point of closest approach
PCM	Photon Conversion Method

PDF	Parton Distribution Function
PHENIX	Pioneering High Energy Nuclear Interactions eXperiment
PHOS	Photon Spectrometer
PID	particle identification
PMD	Photon Multiplicity Detector
pQCD	perturbative QCD
QA	quality assurance
QCD	Quantum Chromodynamics
QED	Quantum Electrodynamics
QFT	Quantum Field Theory
QFD	Quantum Flavordynamics
QGP	Quark-Gluon Plasma
RHIC	Relativistic Heavy Ion Collider
RICH	Ring Imaging Cherenkov detector
rms	root mean square
SD	single-diffractive
SDD	Silicon Drift Detector
SDM	Symmetric Decay Method
SHM	Statistical Hadronisation Model
SM	Standard Model
SONIC	Super hybrid mOdel simulatioN for relativistic heavy-Ion Collisions
SPD	Silicon Pixel Detector
SPS	Super Proton Synchrotron
SSD	Silicon Strip Detector
STAR	Solenoidal Tracker At RHIC
SVD	Singular Value Decomposition
TCM	two-component model
TZERO	Timing and Trigger detector at ALICE
TOF	Time-Of-Flight detector
TPC	Time Projection Chamber
TR	transition radiation

TRD	Transition Radiation Detector
TRG	Trigger System
TRU	Trigger Region Unit
V^0	Unknown Particle
VZERO	V0 detector
ZDC	Zero Degree Calorimeter
ZEM	Zero Degree Electromagnetic Calorimeter
ZN	Zero Degree Neutron Calorimeter
ZP	Zero Degree Proton Calorimeter

B. Additional Neutral Meson Plots

B.1. π^0 and η in pp Collisions at $\sqrt{s}$ = 2.76 TeV

B.1.1. Combination of Different Triggers

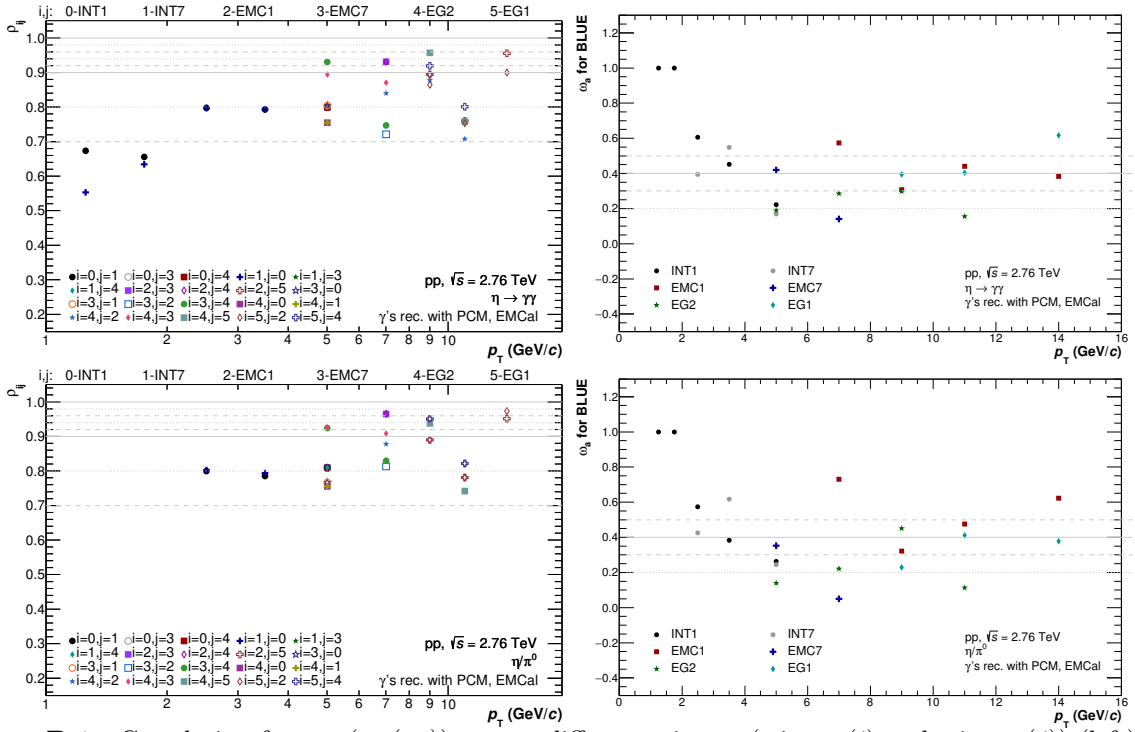

Figure B.1.: Correlation factors ($\rho_{ij}(p_{\mathrm{T}})$) among different triggers (trigger (i) and trigger (j)) (left) and resulting weights for different triggers (right) for the eta meson spectra (top) and η/π^0 (bottom) using the PCM-EMC neutral meson reconstruction for pp collisions at $\sqrt{s} = 2.76$ TeV.

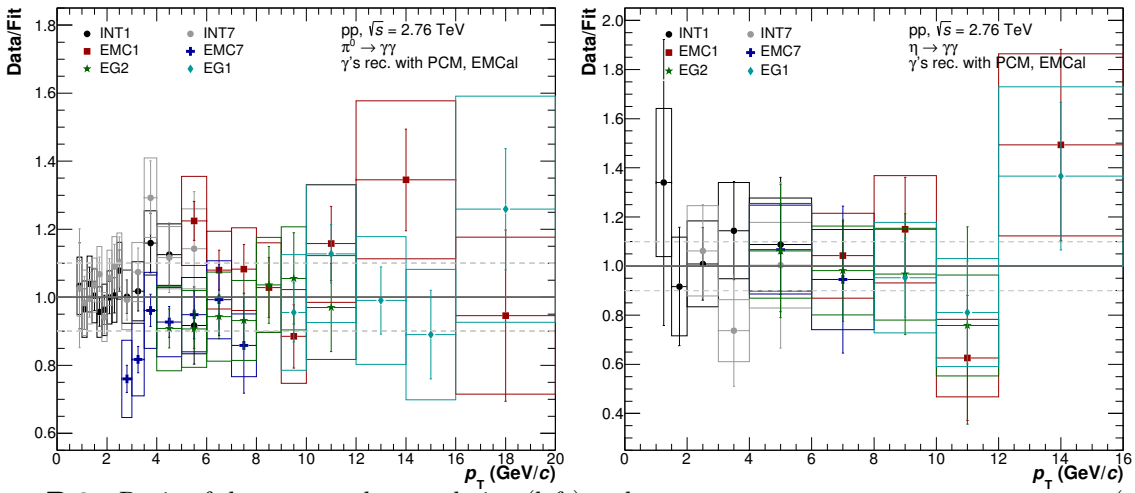

Figure B.2.: Ratio of the measured neutral pion (left) and eta meson transverse momentum spectra (right) for individual triggers measured with PCM-EMC compared to a Bylinkin fit to the respective combined spectrum for pp collisions at $\sqrt{s} = 2.76$ TeV.

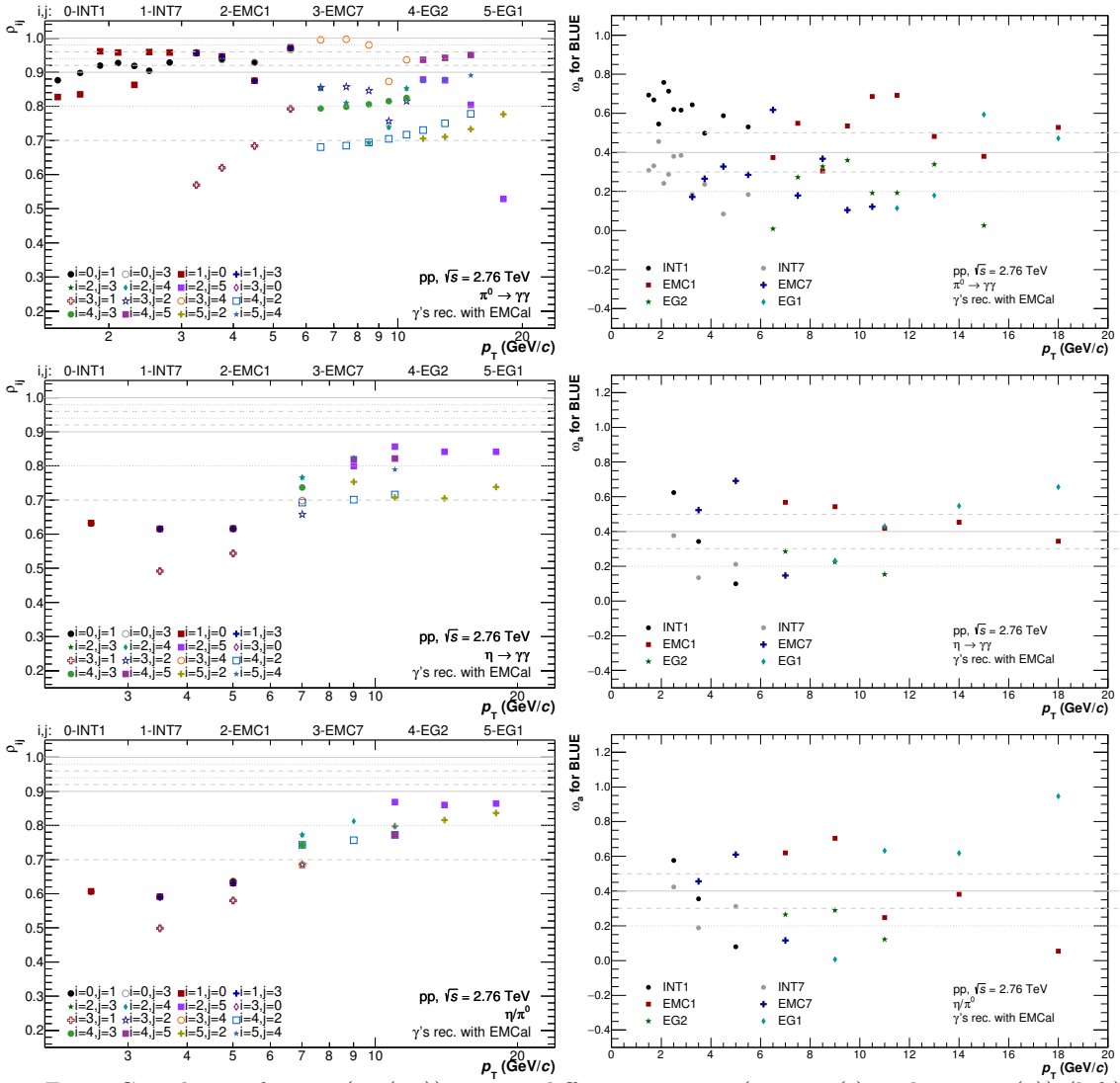

Figure B.3.: Correlation factors ($\rho_{ij}(p_{\mathrm{T}})$) among different triggers (trigger (i) and trigger (j)) (left) and resulting weights for different triggers (right) for the neutral pion (top) and eta meson spectra (middle) and η/π^0 (bottom) using the EMC neutral meson reconstruction for pp collisions at $\sqrt{s} = 2.76$ TeV.

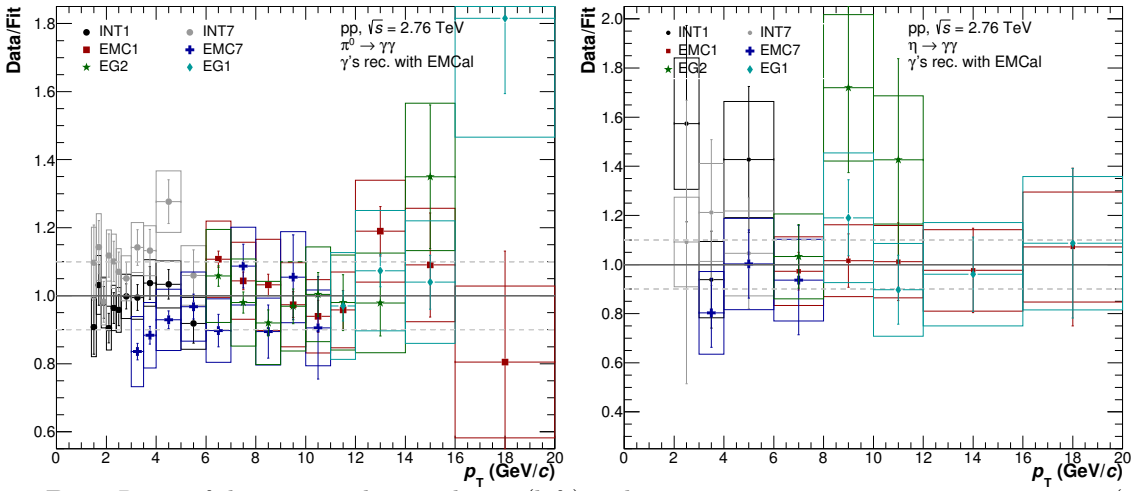

Figure B.4.: Ratio of the measured neutral pion (left) and eta meson transverse momentum spectra (right) for individual triggers measured with EMC compared to a Bylinkin fit to the respective combined spectrum for pp collisions at $\sqrt{s} = 2.76$ TeV.

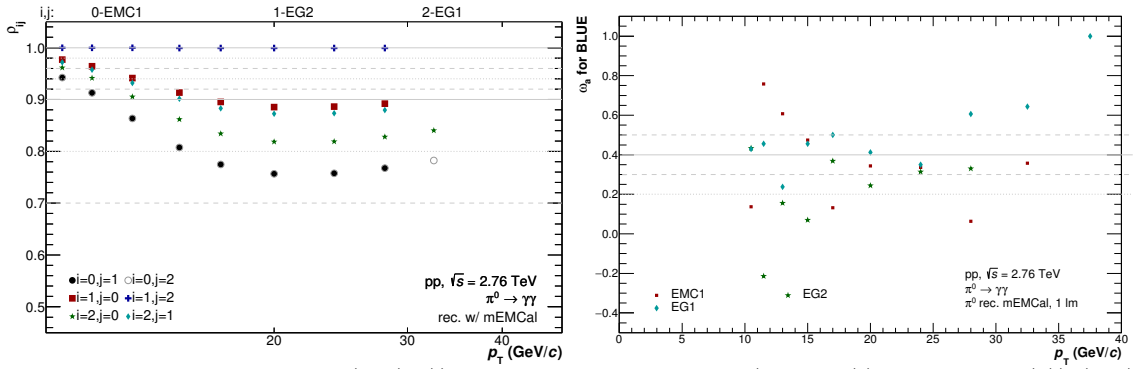

Figure B.5.: Correlation factors ($\rho_{ij}(p_T)$) among different triggers (trigger (i) and trigger (j)) (left) and resulting weights for different triggers (right) for the neutral pion spectra using the mEMC neutral meson reconstruction technique for pp collisions at $\sqrt{s} = 2.76$ TeV.

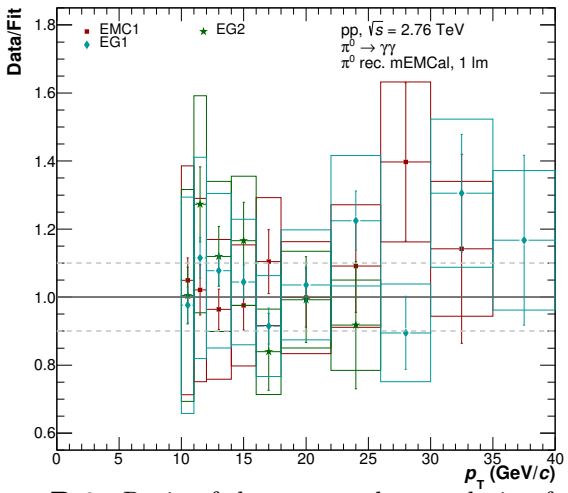

Figure B.6.: Ratio of the measured neutral pion for individual triggers measured with mEMC compared to a Bylinkin fit to the respective combined spectrum for pp collisions at $\sqrt{s} = 2.76$ TeV.

B.1.2. Systematic Uncertainties

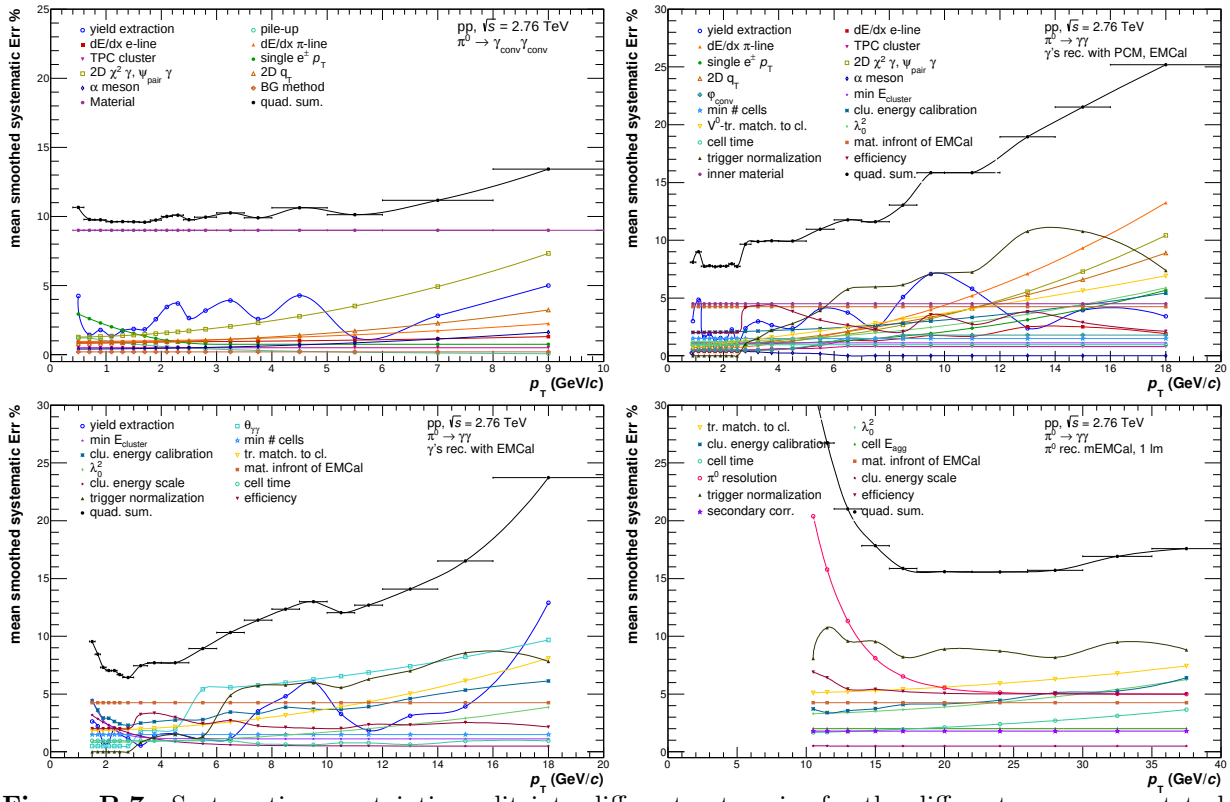

Figure B.7.: Systematic uncertainties split into different categories for the different measurement techniques of the neutral pion for pp collisions at $\sqrt{s} = 2.76$ TeV.

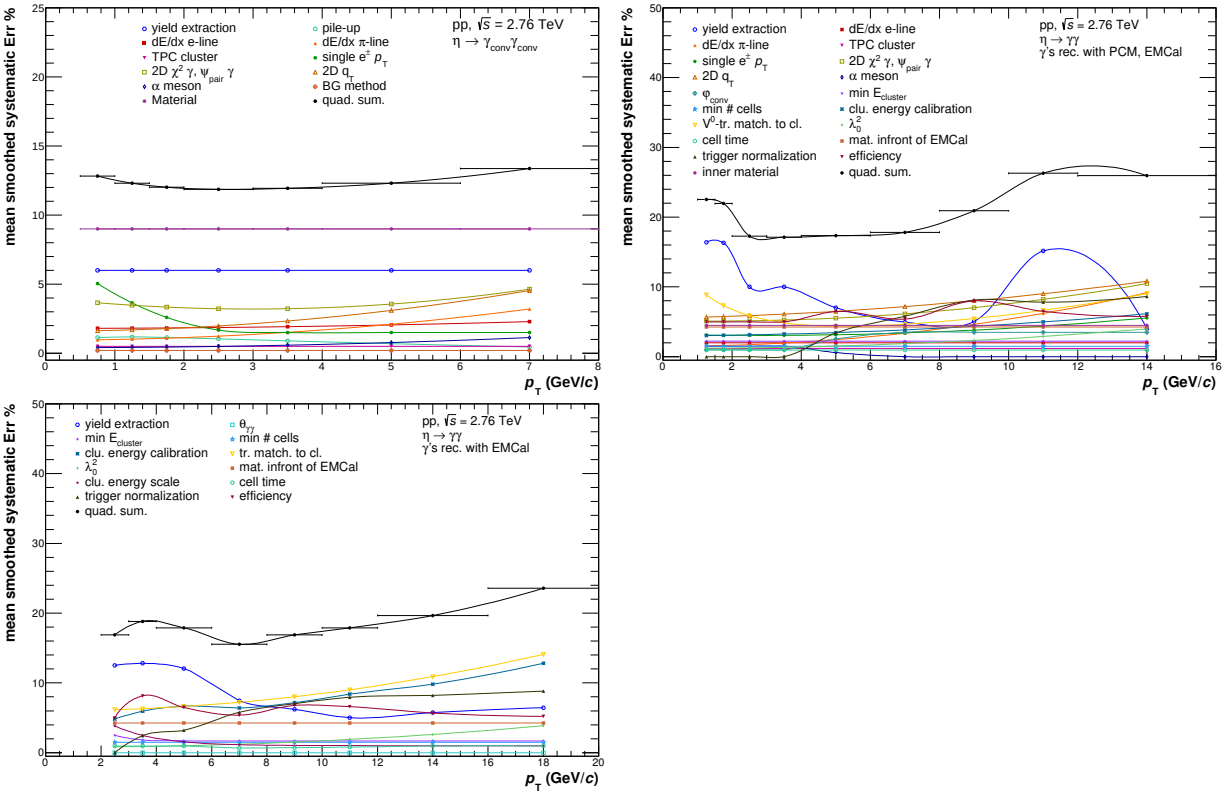

Figure B.8.: Systematic uncertainties split into different categories for the different measurement techniques of the eta meson for pp collisions at $\sqrt{s} = 2.76$ TeV.

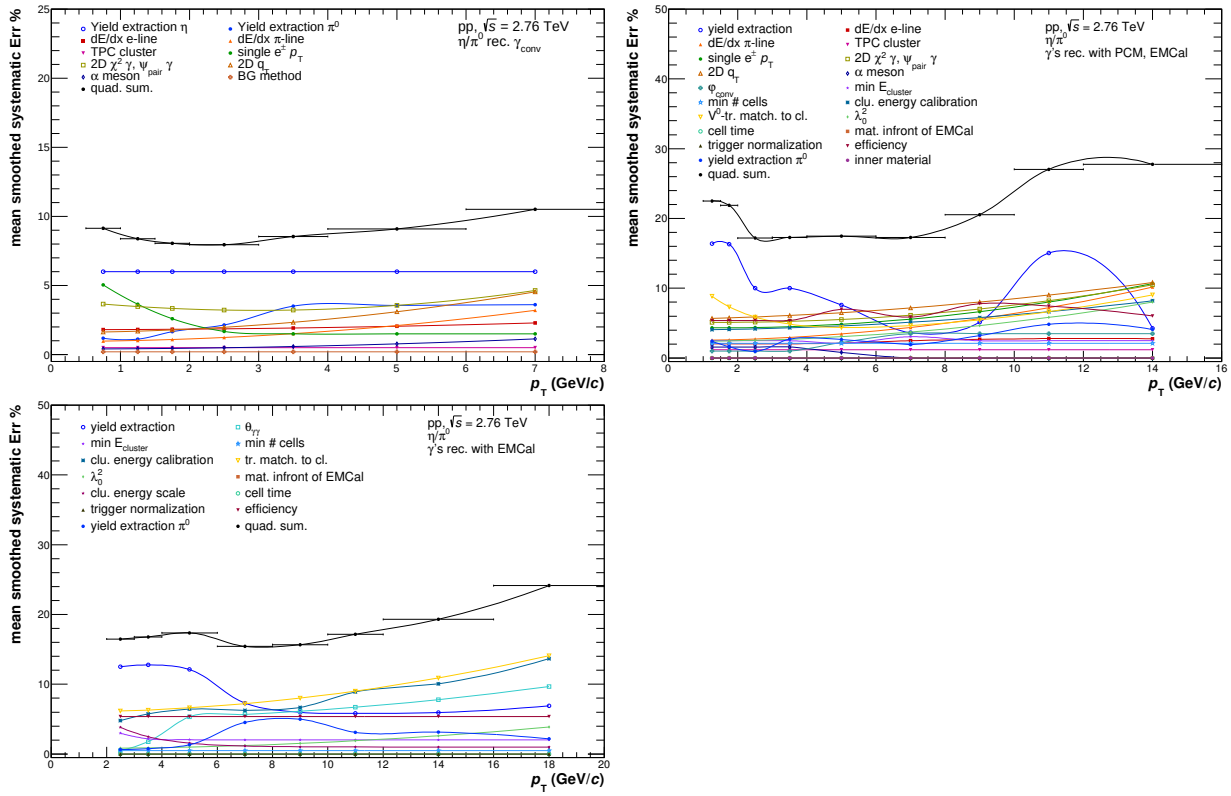

Figure B.9.: Systematic uncertainties split into different categories for the different measurement techniques of the η/π^0 ratio for pp collisions at $\sqrt{s} = 2.76$ TeV.

B.1.3. Combination of Individual Measurements

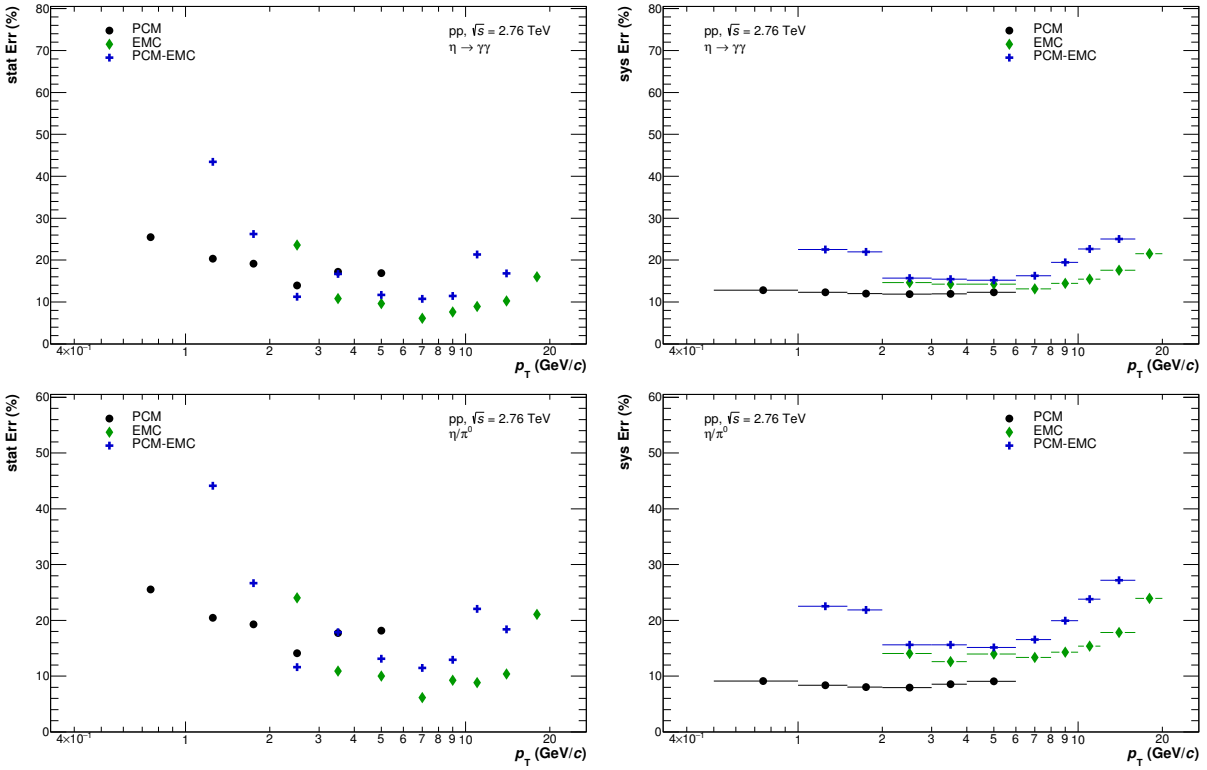

Figure B.10.: Relative statistical (left) and systematic uncertainties (right) for the η meson spectra (top) and the η/π^0 ratio (bottom) measured with different reconstruction methods in pp collisions at $\sqrt{s} = 2.76$ TeV as a function of transverse momentum.

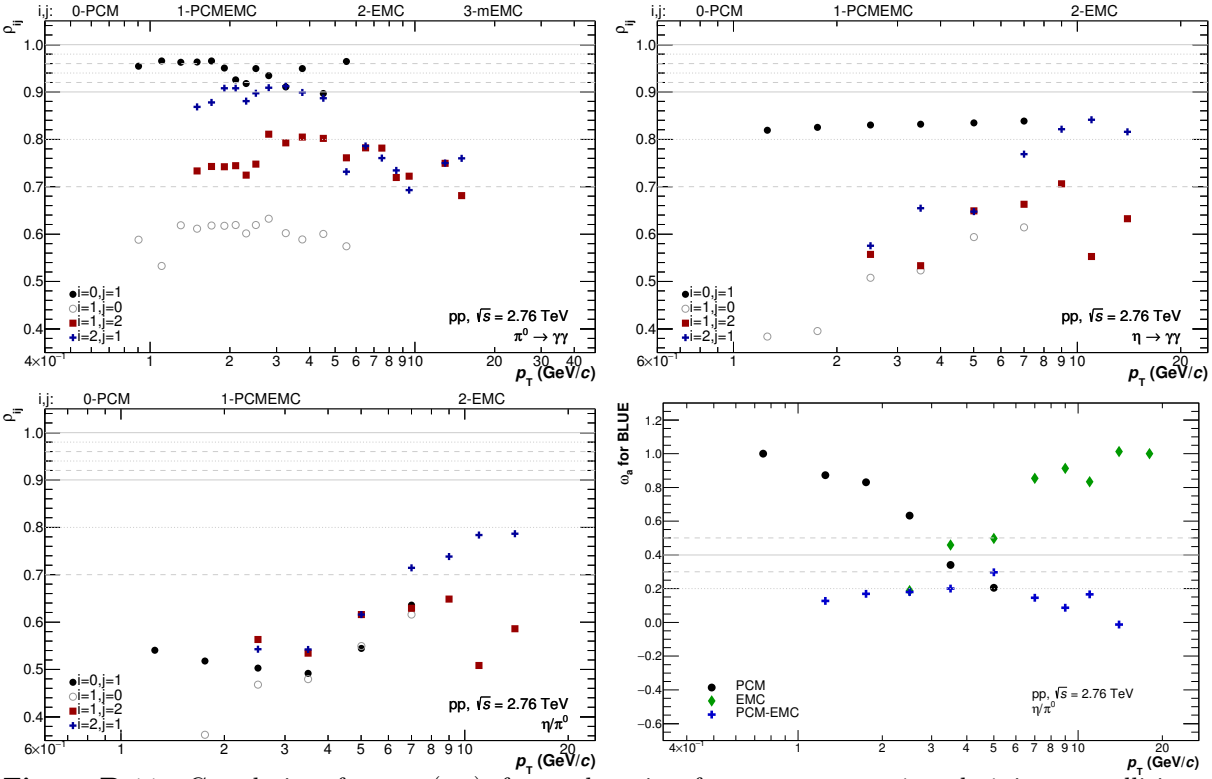

Figure B.11.: Correlation factors (ρ_{ij}) for each pair of measurements i and j in pp collisions at $\sqrt{s} = 2.76$ TeV for different observables. Furthermore, the resulting weights are shown for the η/π^0 while the remaining weights can be found in Figure 5.25.

B.1.4. Fits for Integrated Yield Calculations

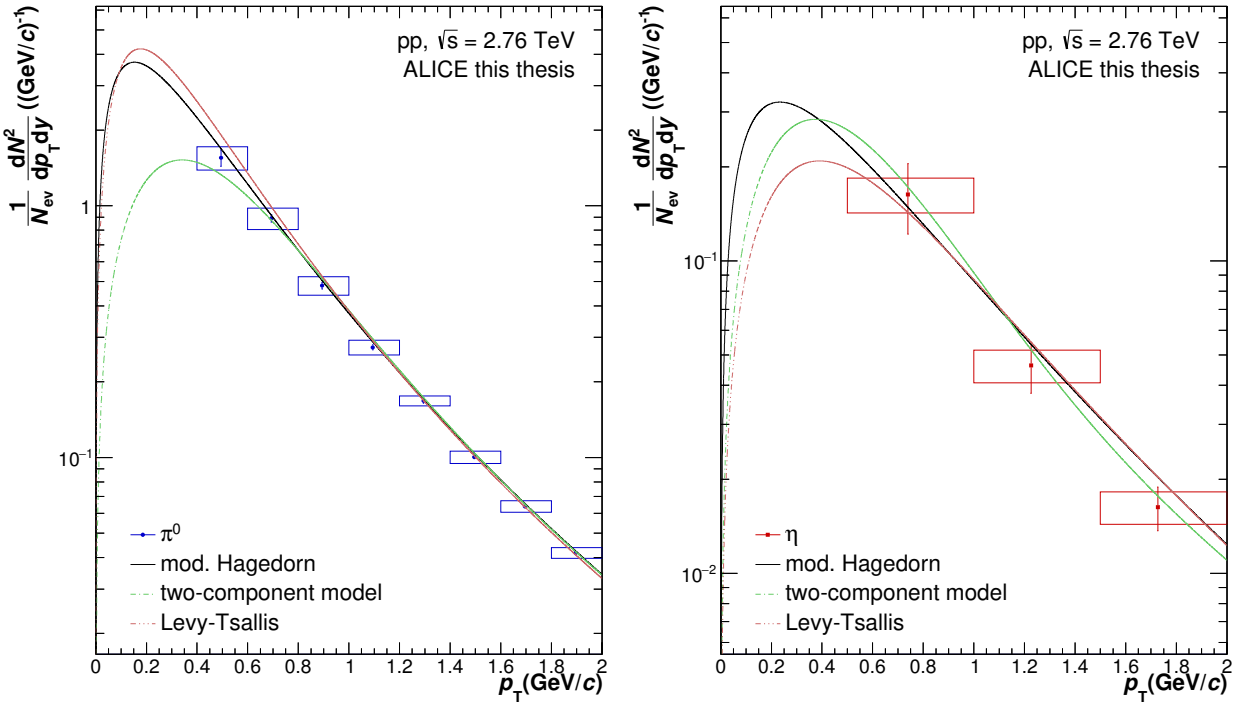

Figure B.12.: p_T differential yields for the neutral pion (left) and η meson (right) at low momenta, compared to the three different parameterizations used to estimate the uncertainties on the integrated yields.

B.2. π^0 and η in p–Pb Collisions at $\sqrt{s_{\mathrm{NN}}}$ = 5.02 TeV

B.2.1. Invariant Mass Distributions for p–Pb Collisions

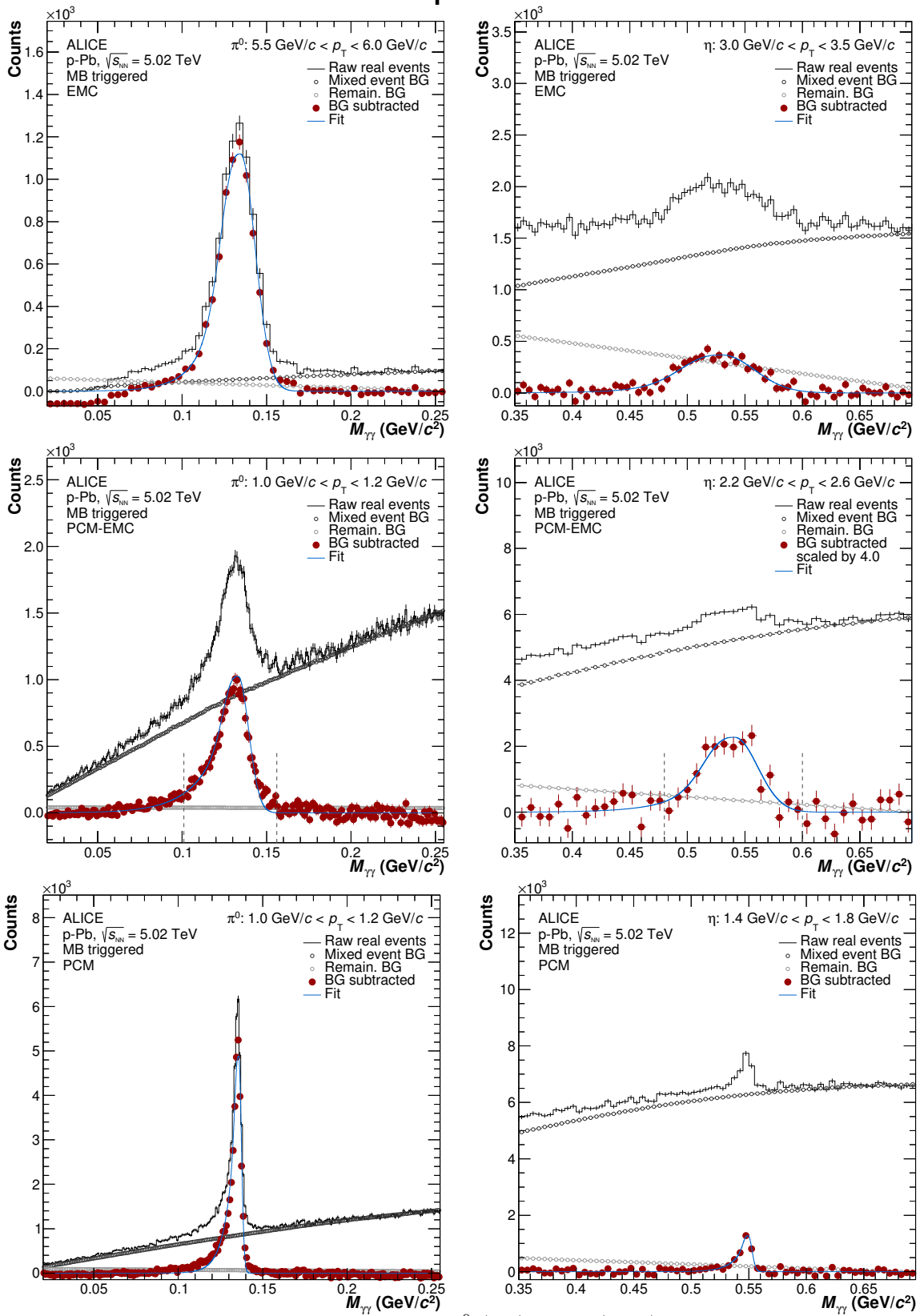

Figure B.13.: Invariant mass distributions in the π^0 (left) and η (right) peak region for INT7 triggered p–Pb events at $\sqrt{s_{\mathrm{NN}}} = 5.02$ TeV for the different photon combinations EMC (top panels), PCM-EMC (middle panels) and PCM (lower panels).

B.2.2. Interpolated pp Reference Spectra at $\sqrt{s}$ = 5.02 TeV

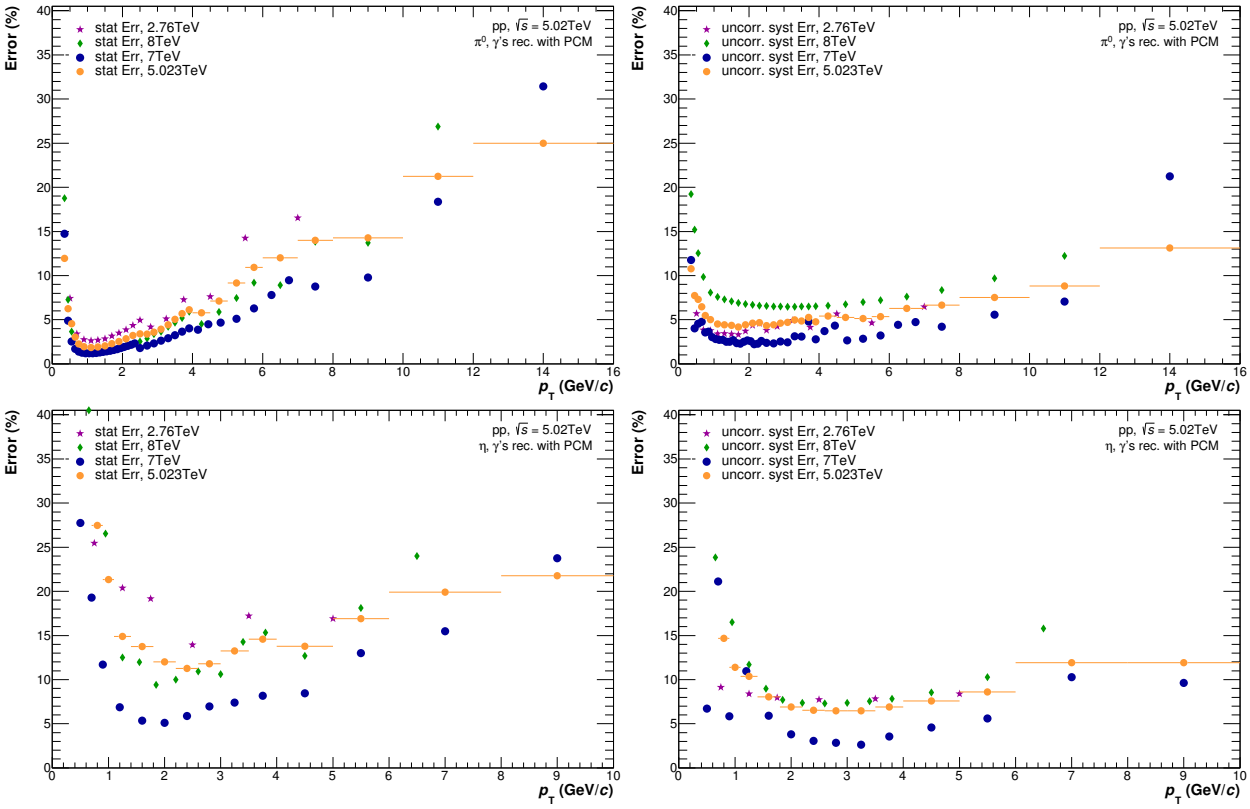

Figure B.14.: Comparison of the relative statistical (left) and uncorrelated systematic (right) uncertainties of the PCM neutral meson reconstruction technique for π^0 (top) and η (bottom) at the three base energies $\sqrt{s}$ = 2.76 TeV (violet), $\sqrt{s}$ = 7 TeV (blue) and $\sqrt{s}$ = 8 TeV (green) to the interpolated ones at $\sqrt{s}$ = 5.02 TeV (yellow).

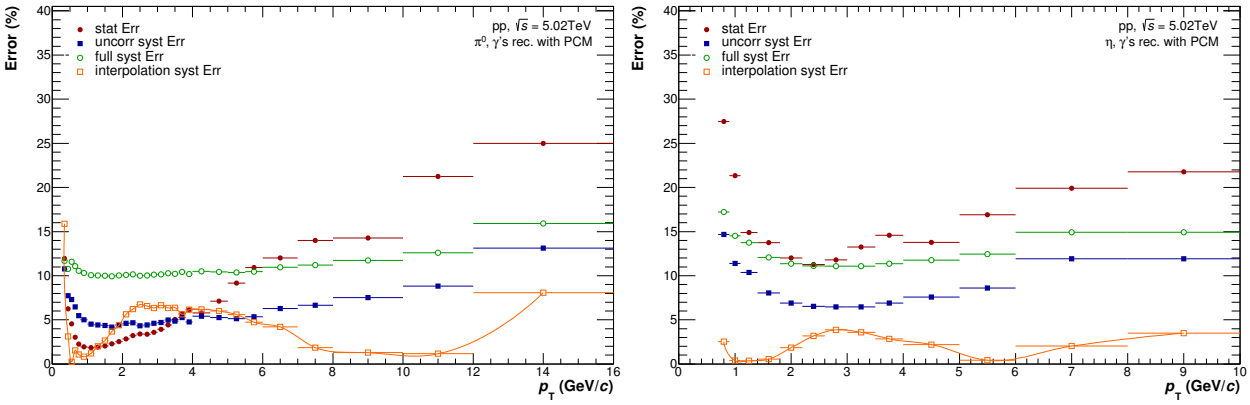

Figure B.15.: Comparison of the relative error contributions for π^0 (left) and η (right) at $\sqrt{s}$ = 5.02 TeV for the PCM neutral meson reconstruction technique.

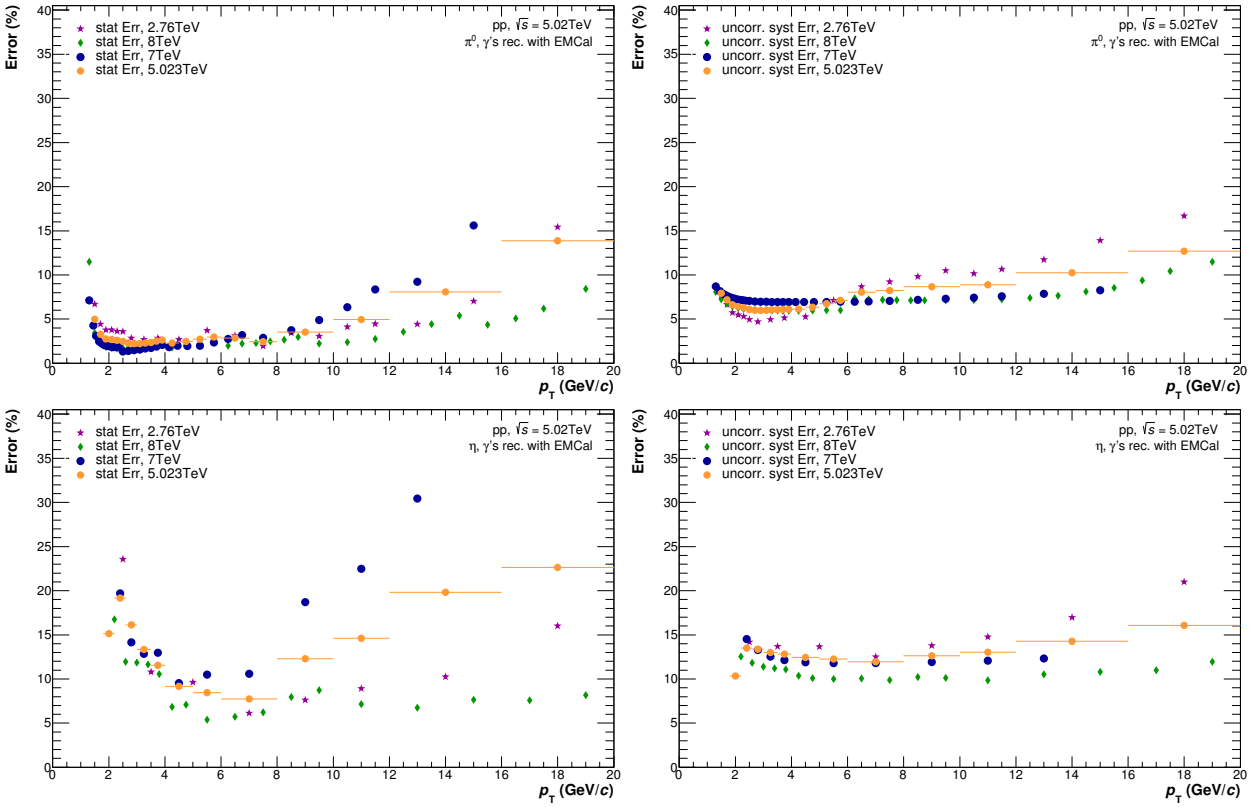

Figure B.16.: Comparison of the relative statistical (left) and uncorrelated systematic (right) uncertainties of the EMC neutral meson reconstruction technique for π^0 (top) and η (bottom) at the three base energies $\sqrt{s} = 2.76$ TeV (violet), $\sqrt{s} = 7$ TeV (blue) and $\sqrt{s} = 8$ TeV (green) to the interpolated ones at $\sqrt{s} = 5.02$ TeV (yellow).

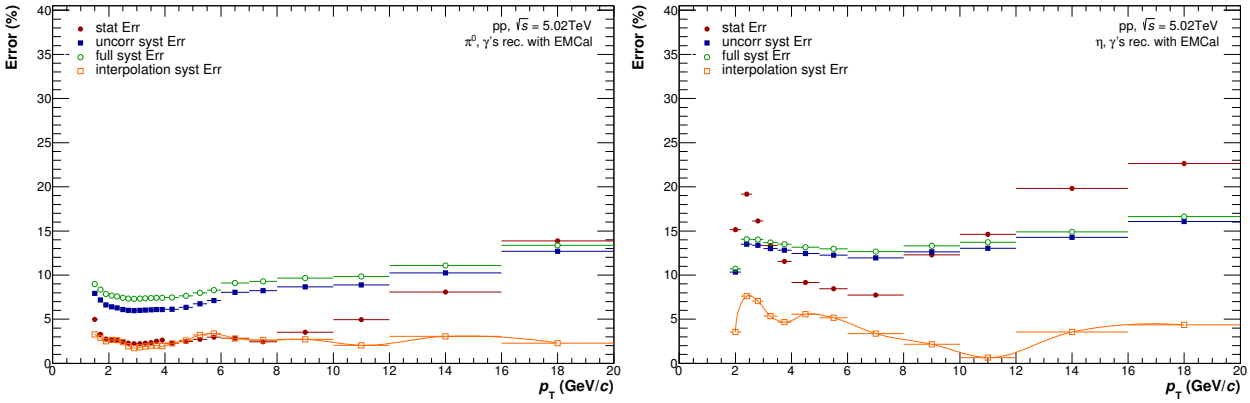

Figure B.17.: Comparison of the relative error contributions for π^0 (left) and η (right) at $\sqrt{s} = 5.02$ TeV for the EMC neutral meson reconstruction technique.

B.2.3. Systematic Uncertainties

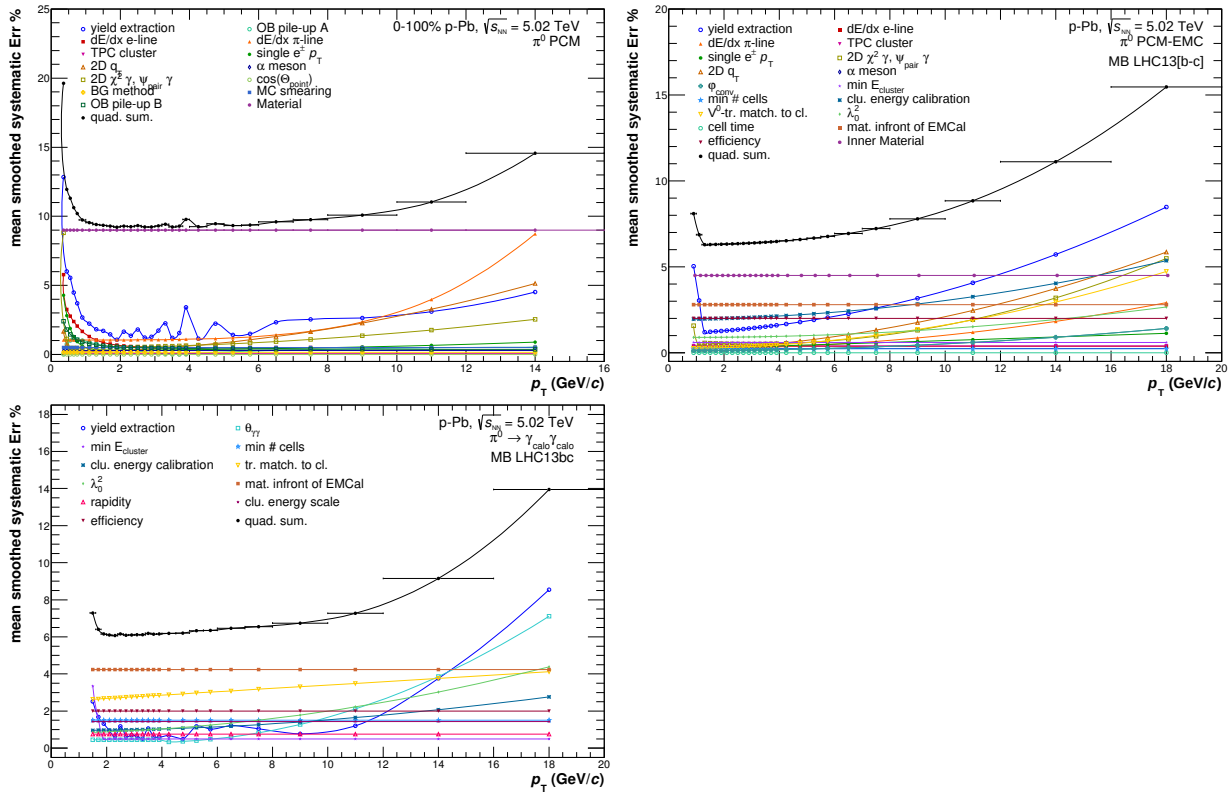

Figure B.18.: Systematic uncertainties split into different categories for the different measurement techniques of the neutral pion for p–Pb collisions at $\sqrt{s_{\mathrm{NN}}} = 5.02$ TeV.

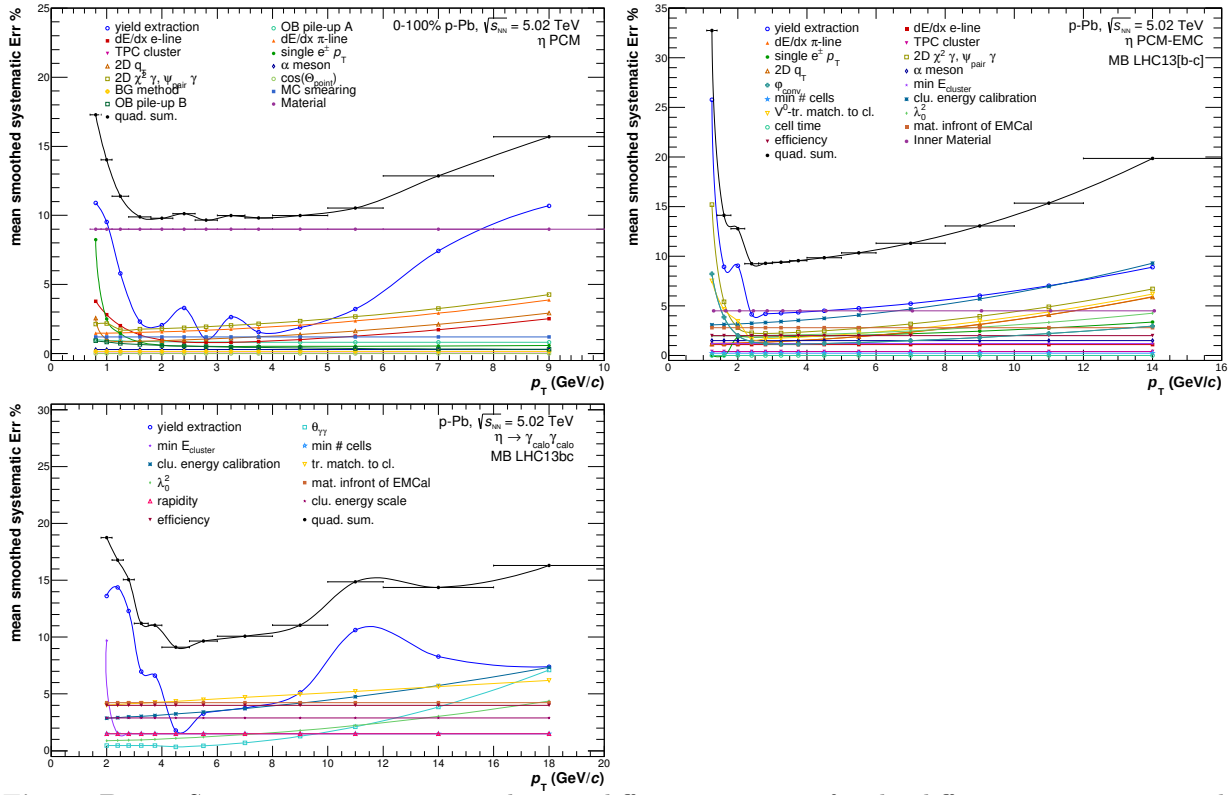

Figure B.19.: Systematic uncertainties split into different categories for the different measurement techniques of the eta meson for p–Pb collisions at $\sqrt{s_{\mathrm{NN}}} = 5.02$ TeV.

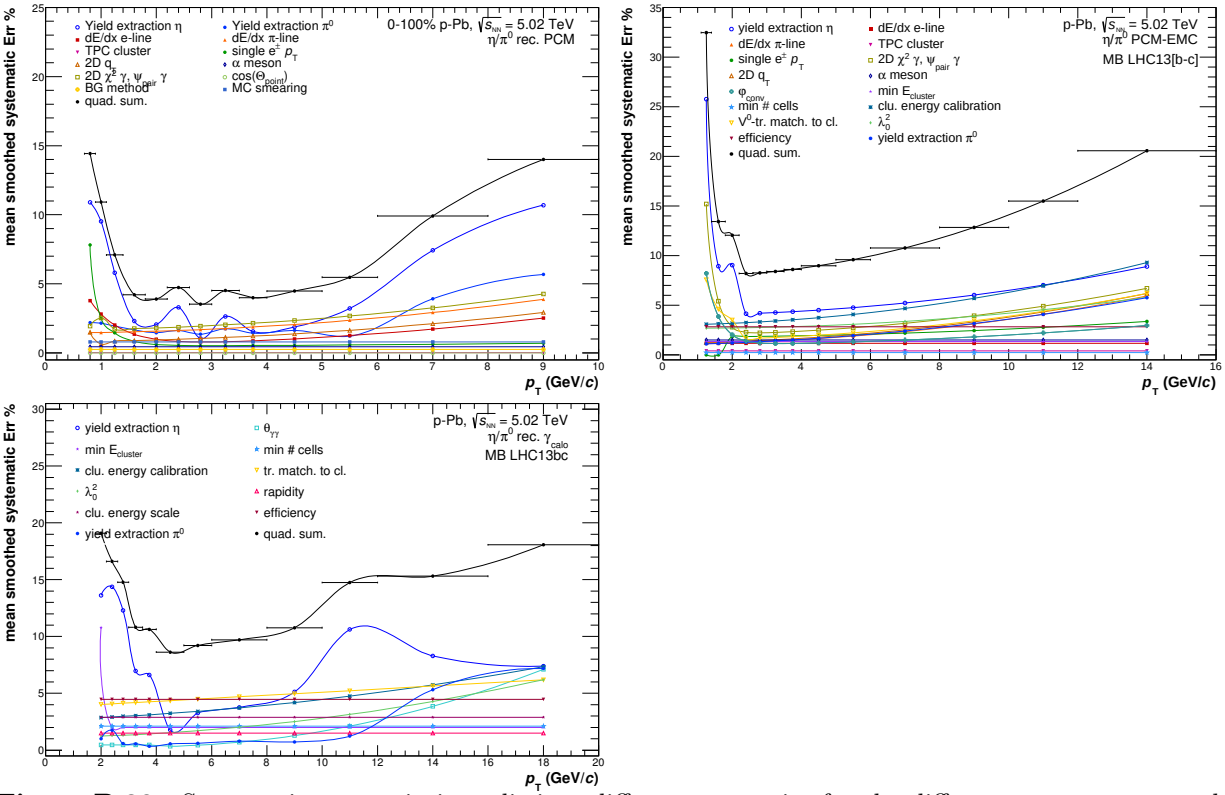

Figure B.20.: Systematic uncertainties split into different categories for the different measurement techniques of the η/π^0 ratio for p–Pb collisions at $\sqrt{s_{\mathrm{NN}}} = 5.02$ TeV.

B.2.4. Combination of Individual Measurements

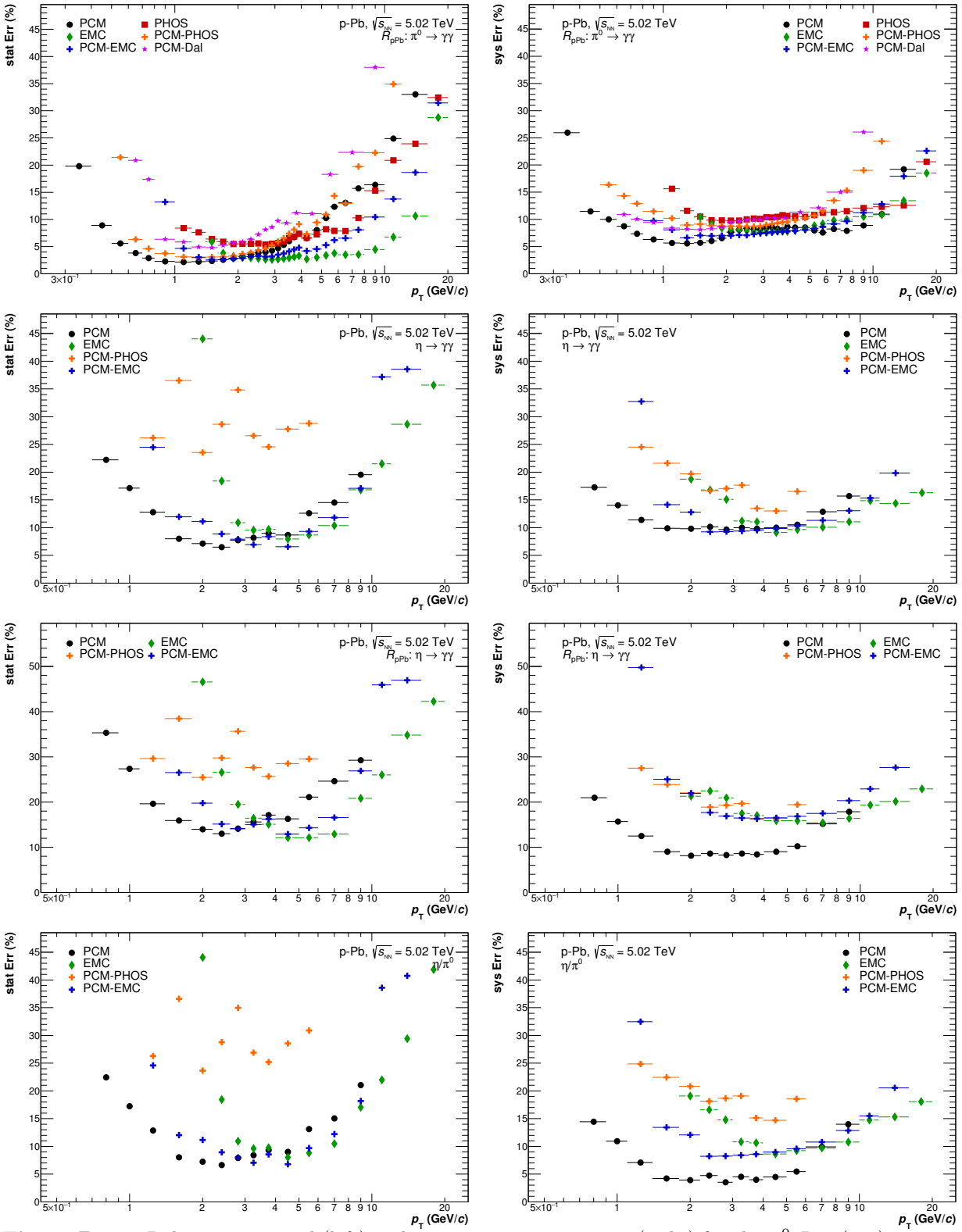

Figure B.21.: Relative statistical (left) and systematic uncertainties (right) for the π^0 R_{pA} (top), η meson spectrum (upper middle) and R_{pA} (lower middle) as well as the η/π^0 ratio (bottom) measured with different reconstruction methods in p–Pb collisions at $\sqrt{s_{\mathrm{NN}}} = 5.02$ TeV.

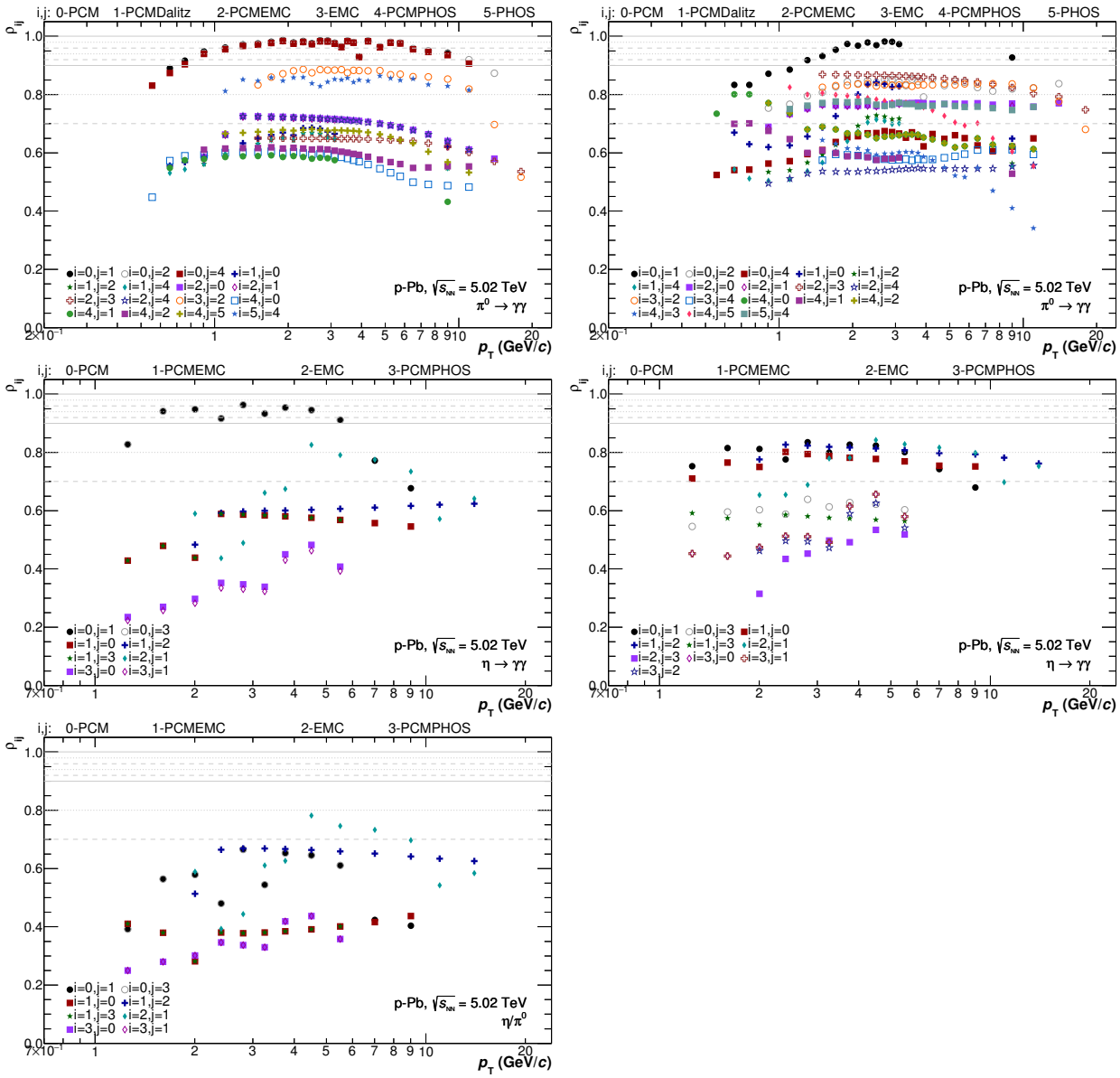

Figure B.22.: Correlation factors (ρ_{ij}) for each pair of measurements i and j in p–Pb collisions at $\sqrt{s_{\mathrm{NN}}} = 5.02$ TeV for different observables. Top: π^0 transverse momentum spectrum (left) and R_{pA} (right). Middle: η transverse momentum spectrum (left) and R_{pA} (right). Bottom: η/π^0.

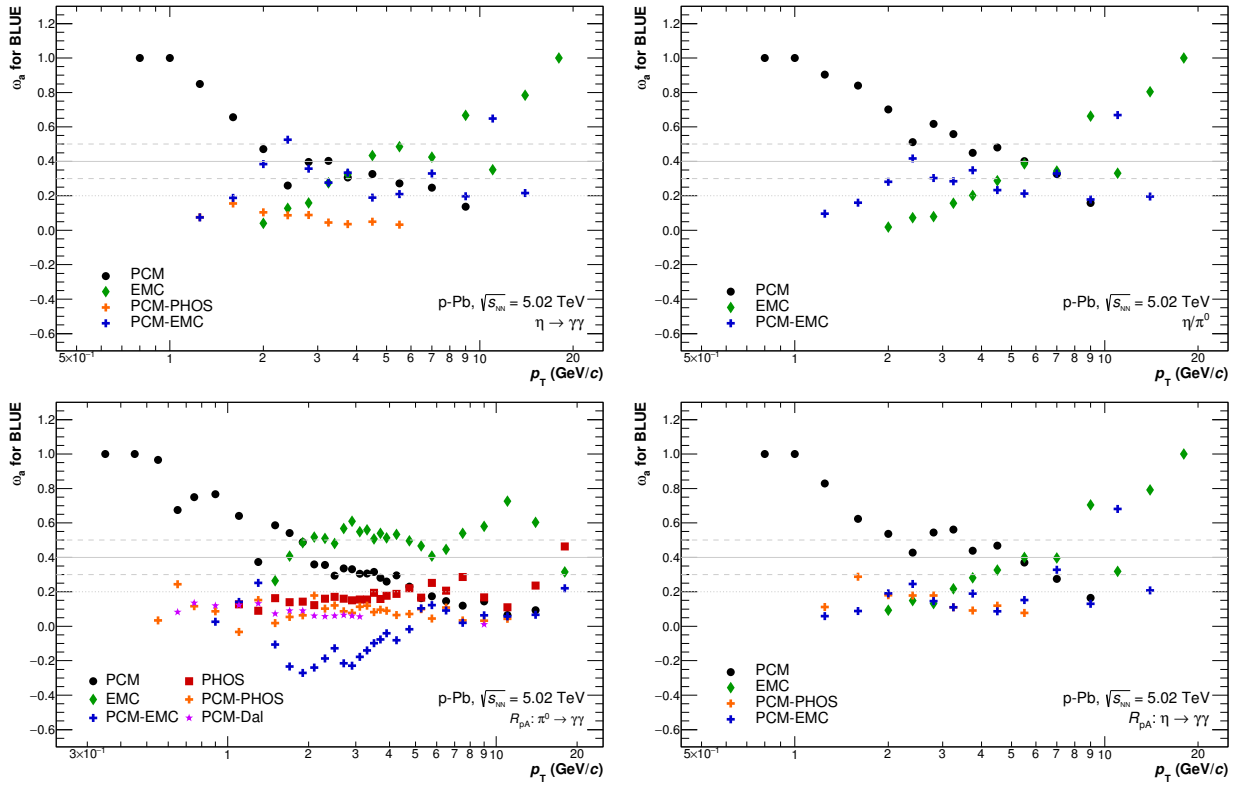

Figure B.23.: Weights (ω_a) of the individual measurements for the η meson invariant yield measurement (top, left) as well as for the η/π^0 ratio (top, right) and the R_{pA} of π^0 (bottom, right) and η (bottom, right) used in the combination according to the BLUE method [309, 310, 313].

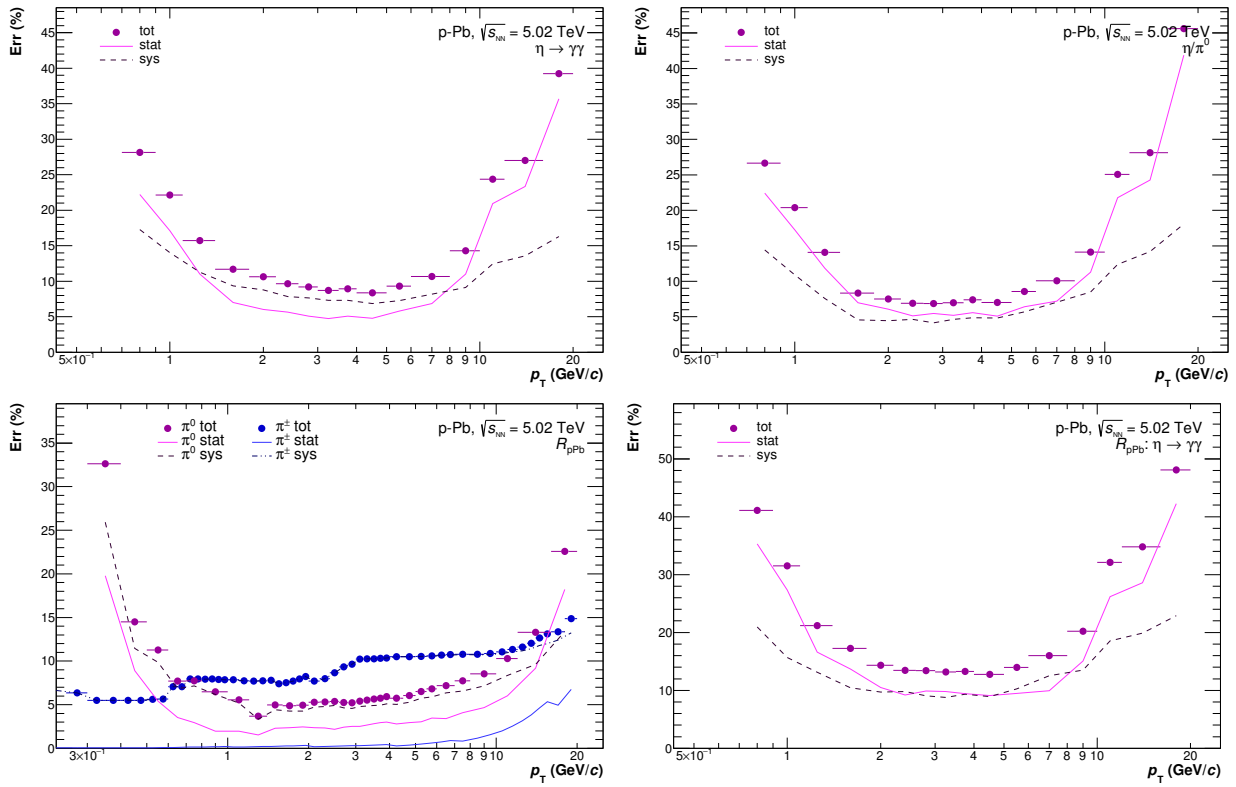

Figure B.24.: Overview of the relative total, systematic and statistical uncertainties of the η spectrum (top, left), η/π^0 ratio (top, right) and the R_{pA}'s for the π^0 (bottom, left) and η (bottom, right). Additionally, the corresponding uncertainties of the charged pion R_{pA} are depicted in the bottom left plot in blue.

B.3. Integrated Yield

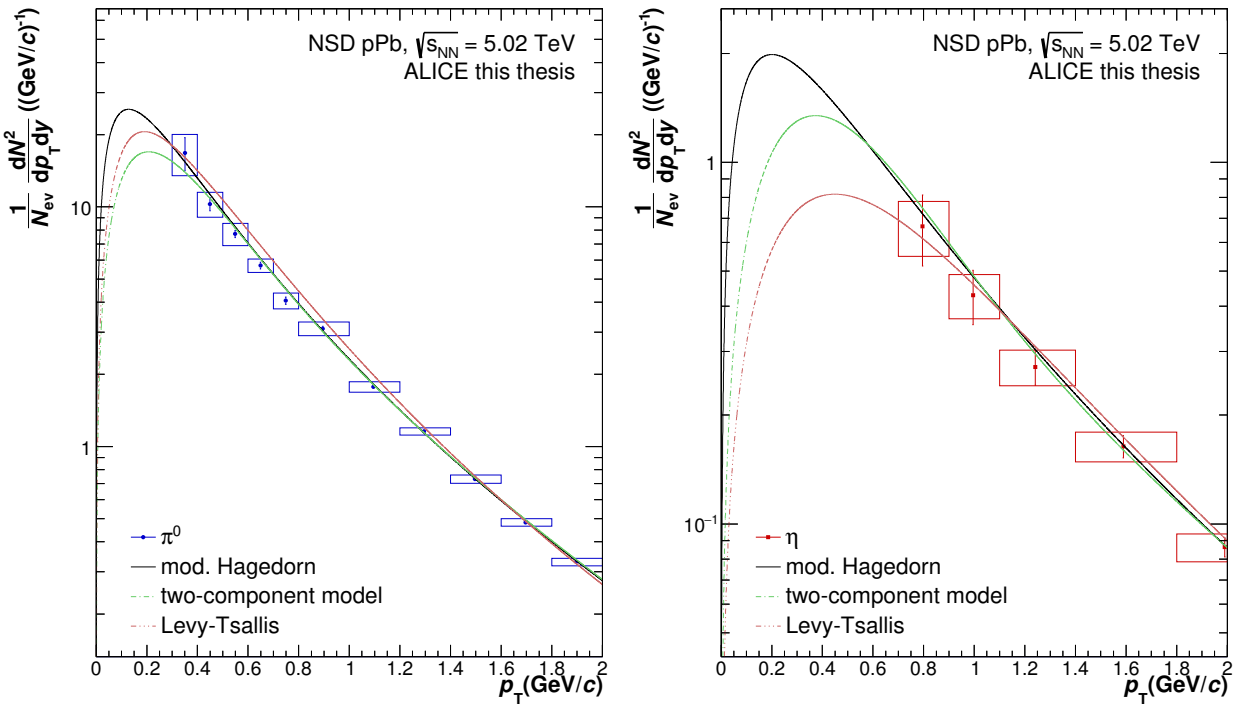

Figure B.25.: p_T differential yields for the neutral pion (left) and η meson (right) at low momenta, compared to the three different parameterizations used to estimate the integrated yields and mean transverse momenta including their uncertainties.

C. Additional Direct Photon Plots

C.1. Decay Photon Cocktail for pp Collisions at $\sqrt{s}$ = 2.76 TeV and p–Pb Collisions at $\sqrt{s_{\mathrm{NN}}}$ = 5.02 TeV

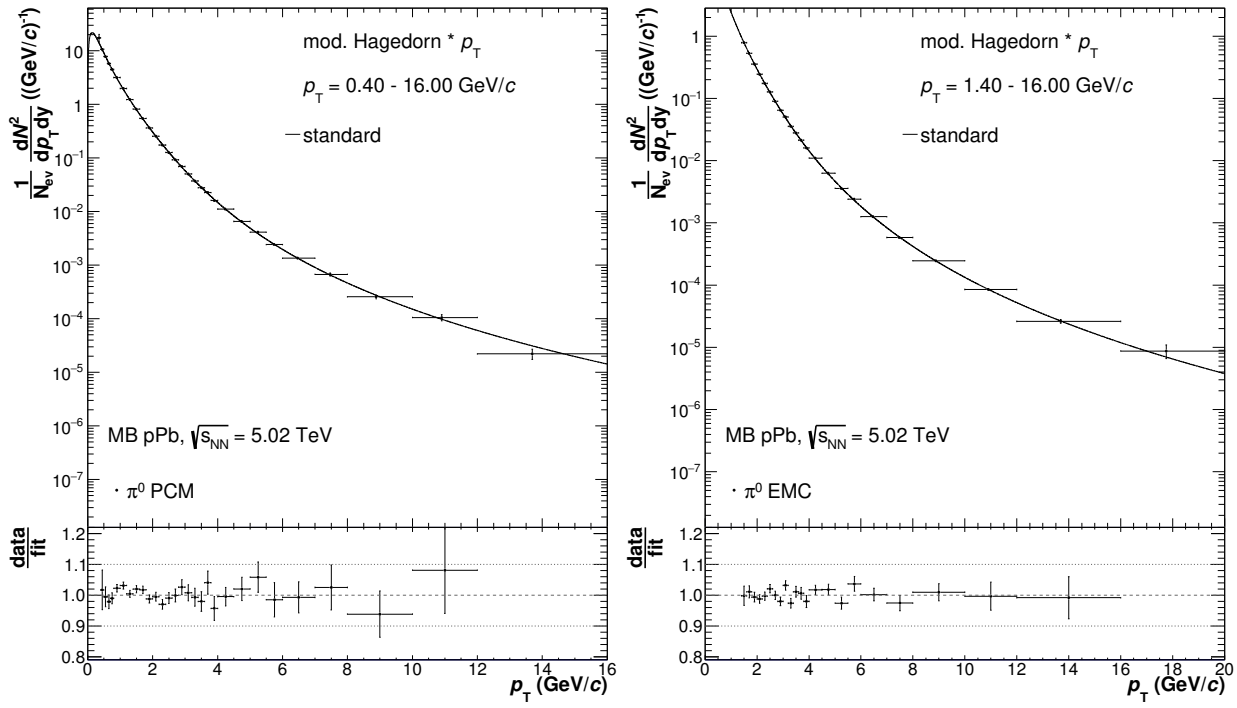

Figure C.1.: Invariant yield of the neutral pion in minimum bias p–Pb collisions at $\sqrt{s_{\mathrm{NN}}} = 5.02$ TeV measured with the PCM(left) and EMC(right) neutral meson reconstruction technique together with the corresponding modified hagedorn functions (Equation 5.15), which are used as parametrizations for respective reconstruction techniques in the decay photon simulations. The ratio of the data to the corresponding function is shown in the lower panel. The vertical error bars correspond to the statistical uncertainties of the measurements.

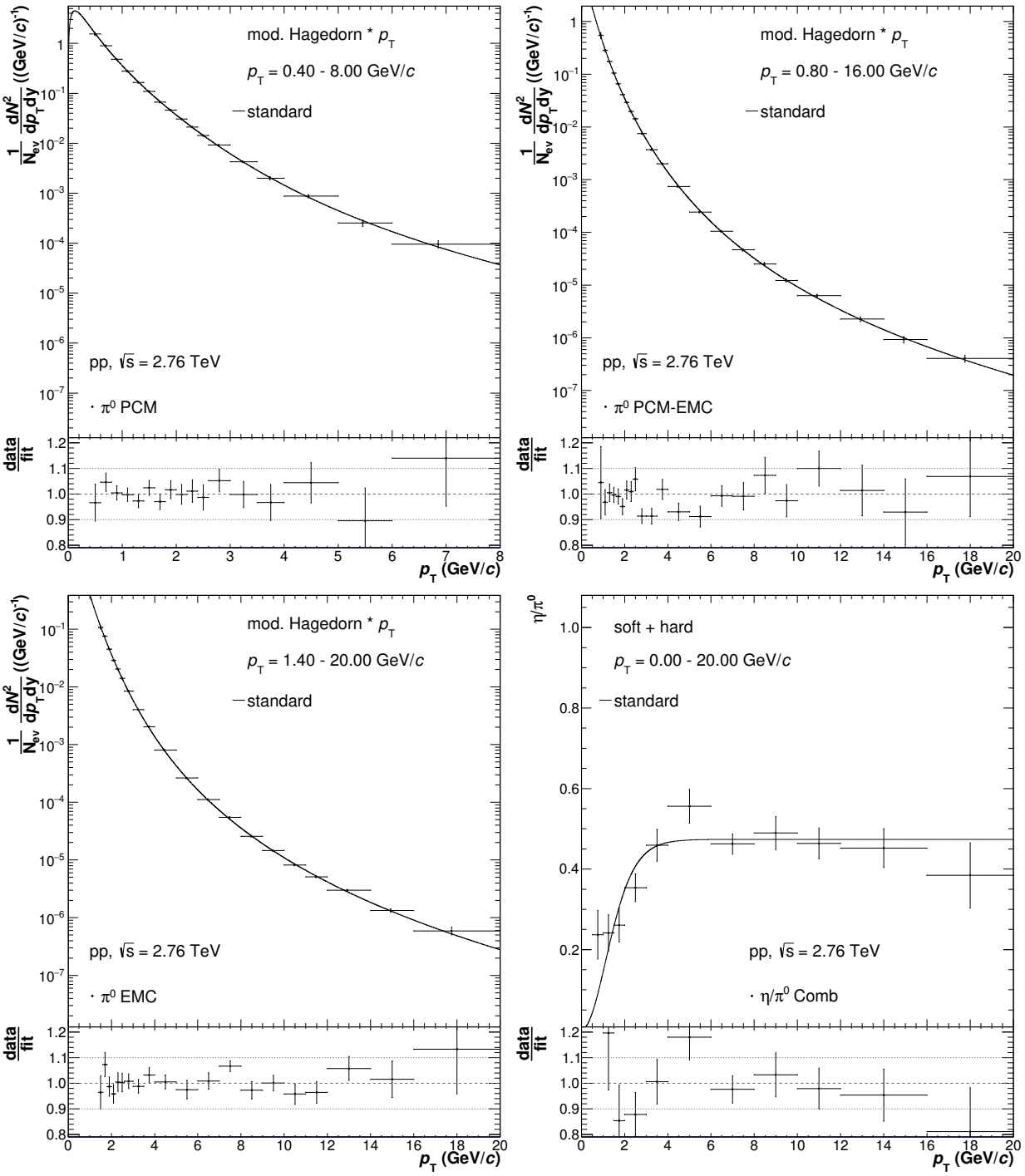

Figure C.2.: Invariant yield of the neutral pion in minimum bias pp collisions at $\sqrt{s} = 2.76$ TeV measured with the PCM(top, left), PCM-EMC(top, right) and EMC(bottom, left) neutral meson reconstruction technique. They are displayed together with their corresponding modified hagedorn fits (Equation 5.15), which are used as parametrizations for the neutral pions for the respective decay photon simulations. Furthermore, the combined η/π^0ratio (bottom, right) for pp collisions at $\sqrt{s} = 2.76$ TeV is shown together with its parametrization using the fit defined in Equation 6.1. The ratio of the data to the corresponding functions are shown in the lower panels. The vertical error bars correspond to the statistical uncertainties of the measurements.

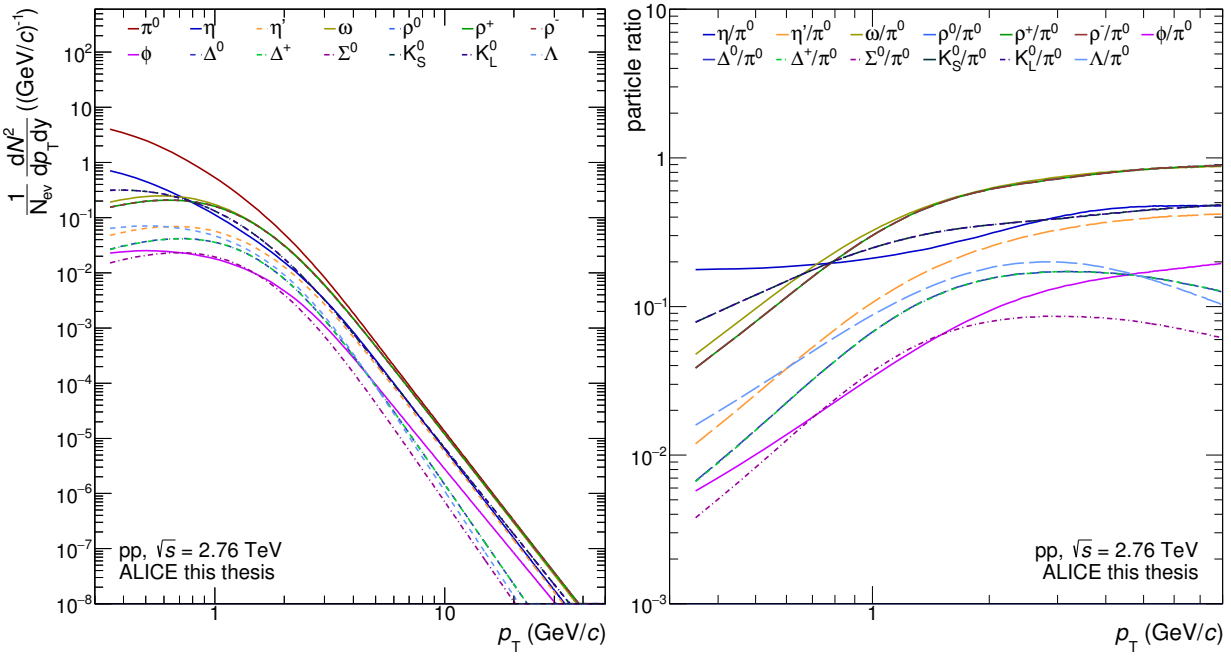

Figure C.3.: Spectra of all mesons and baryons entering the decay photon simulation (left) as well as their ratios to the neutral pion spectrum in pp collision at $\sqrt{s} = 2.76$ TeV. In these plots the parametrization of the PCM spectrum has been used for the neutral pions and consequently also for the m_{T}-scaled mesons and the η meson. The latter is calculated from the fit to the combined η/π^0 ratio multiplied with the neutral pion spectrum parametrization.

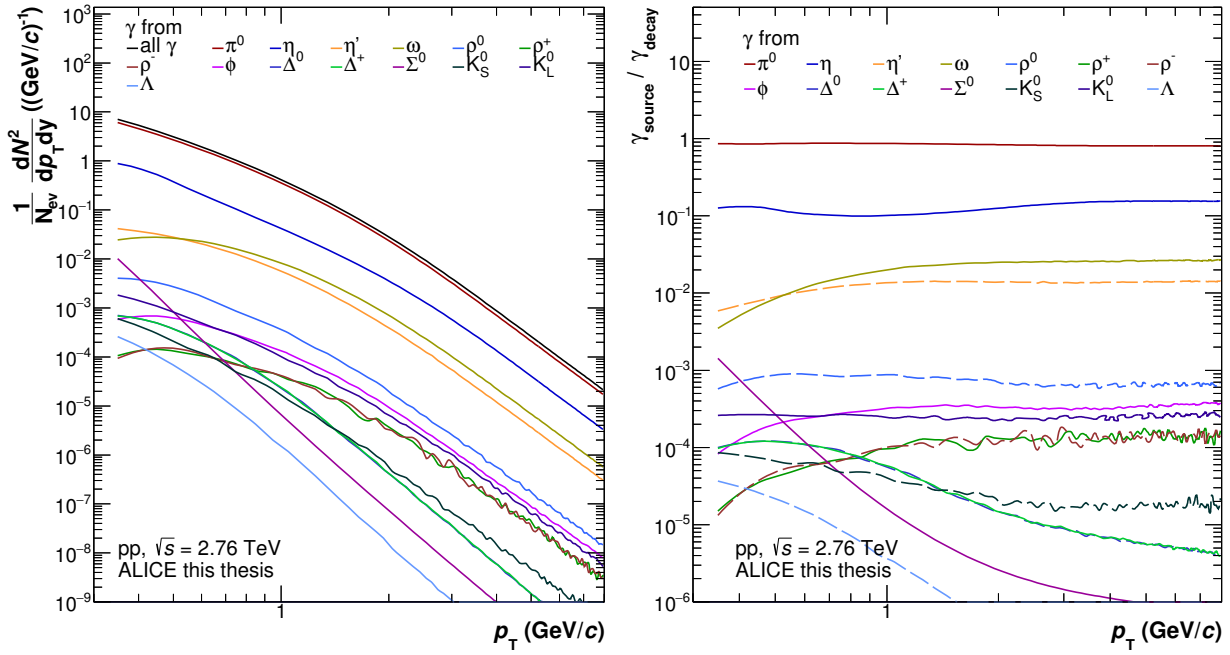

Figure C.4.: Left: Individual decay photon spectra for pp collision at $\sqrt{s} = 2.76$ TeV using the fit to the PCM spectrum for the neutral pions and the corresponding m_{T} scaled spectra. Right: Relative contribution of the individual particle decays to the total decay photon spectrum in the same collision system using the same π^0 reconstruction method.

C.2. Photon Spectra Corrections

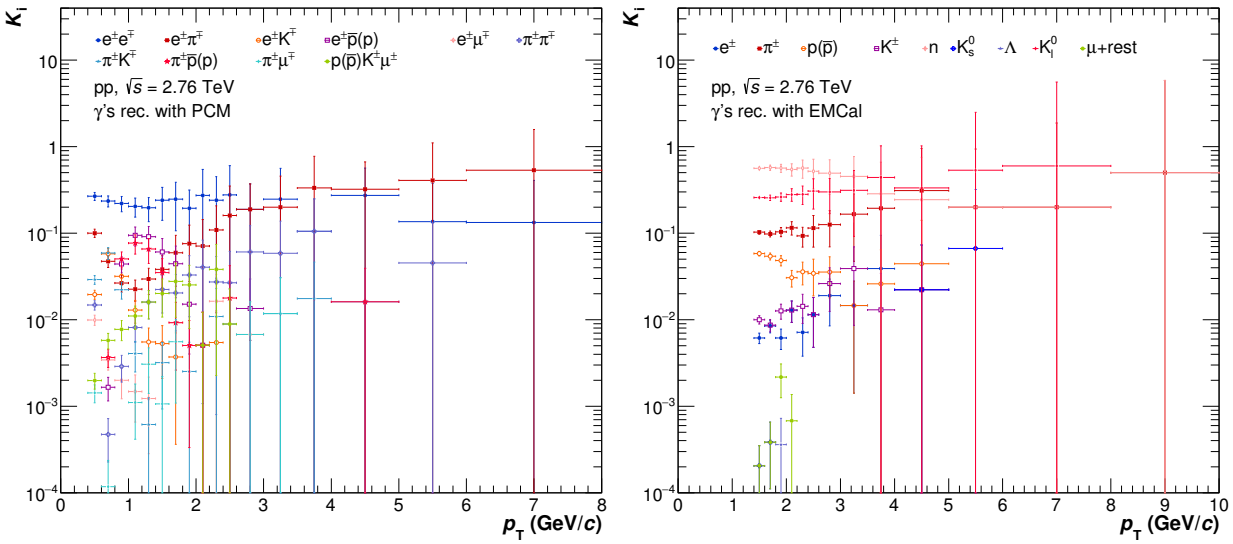

Figure C.5.: Relative contribution (K_i) of the various identified backgrounds (i) to the total background seen for the photons reconstructed with PCM (left) and EMC (right) for pp collisions at $\sqrt{s} = 2.76$ TeV.

C.3. Systematic Uncertainties

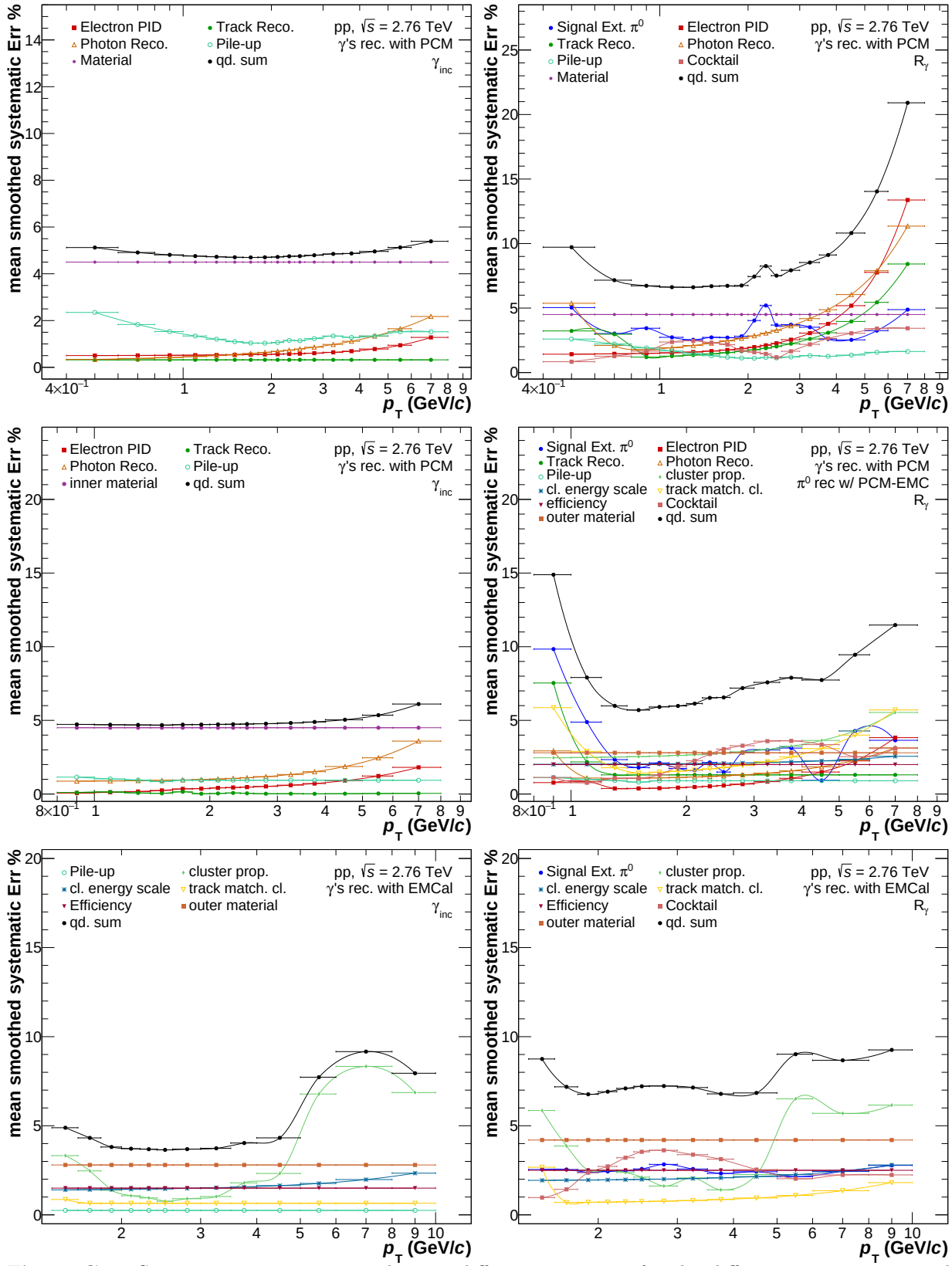

Figure C.6.: Systematic uncertainties split into different categories for the different measurement techniques: PCM (top), PCM-EMC (middle), EMC (bottom). The uncertainties are reported for the inclusive photon invariant yield measurement (left) as well as the R_γ (right) for pp collisions at $\sqrt{s} = 2.76$ TeV.

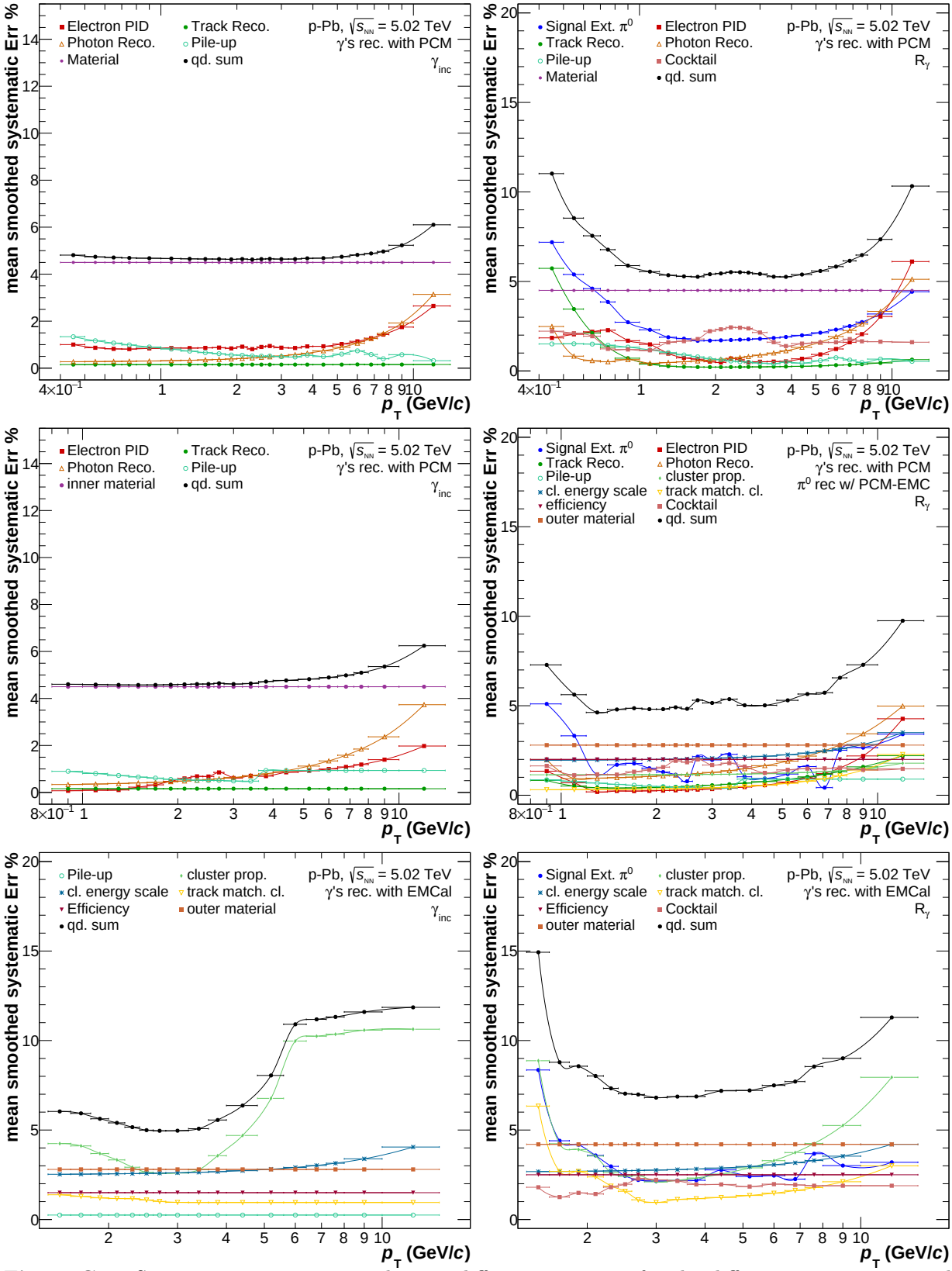

Figure C.7.: Systematic uncertainties split into different categories for the different measurement techniques: PCM (top), PCM-EMC (middle), EMC (bottom). The uncertainties are reported for the inclusive photon invariant yield measurement (left) as well as the R_γ (right) for p–Pb collisions at $\sqrt{s_{\mathrm{NN}}} = 5.02$ TeV.

C.4. Combination of Individual Measurements

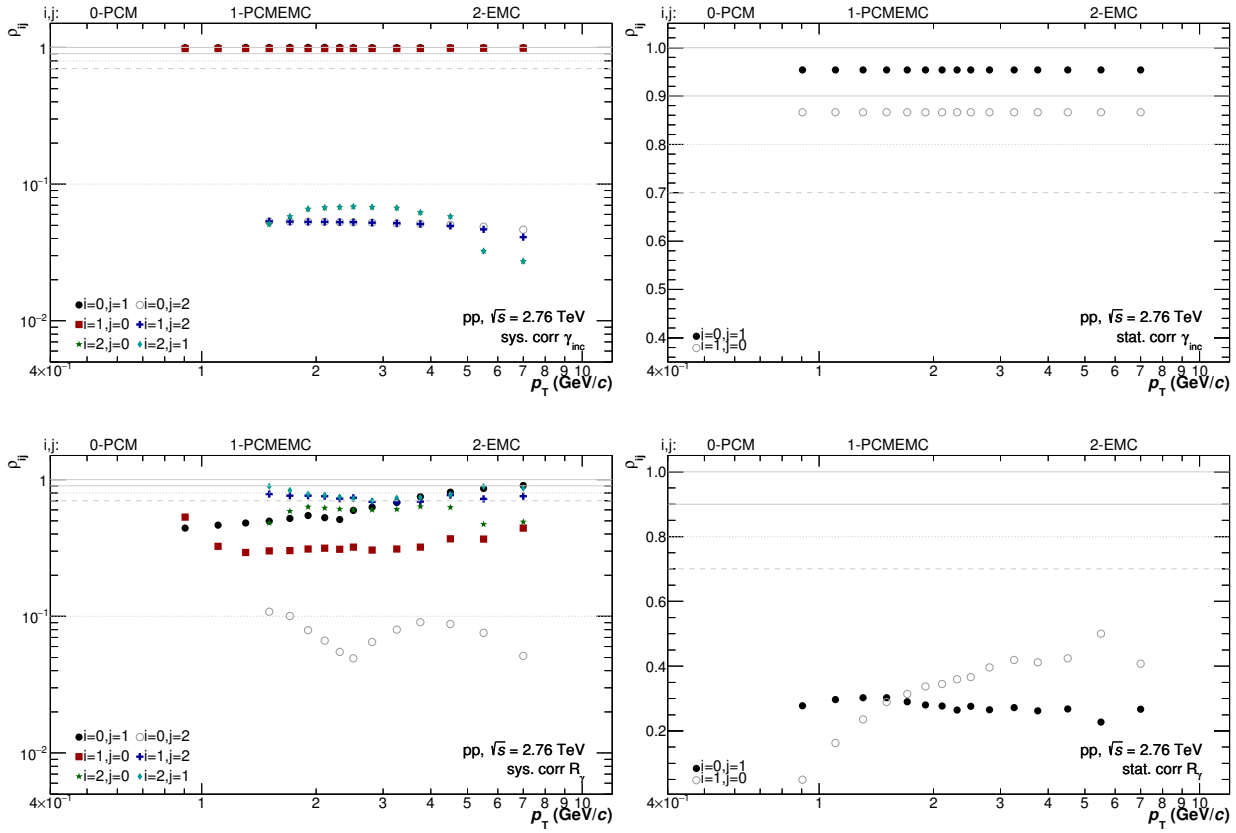

Figure C.8.: Correlation fractions among the systematic (left) and statistical (right) uncertainties for a pair of measurement i and j for the inclusive photon (top) and R_γ (bottom) measurements in pp collisions at $\sqrt{s} = 2.76$ TeV.

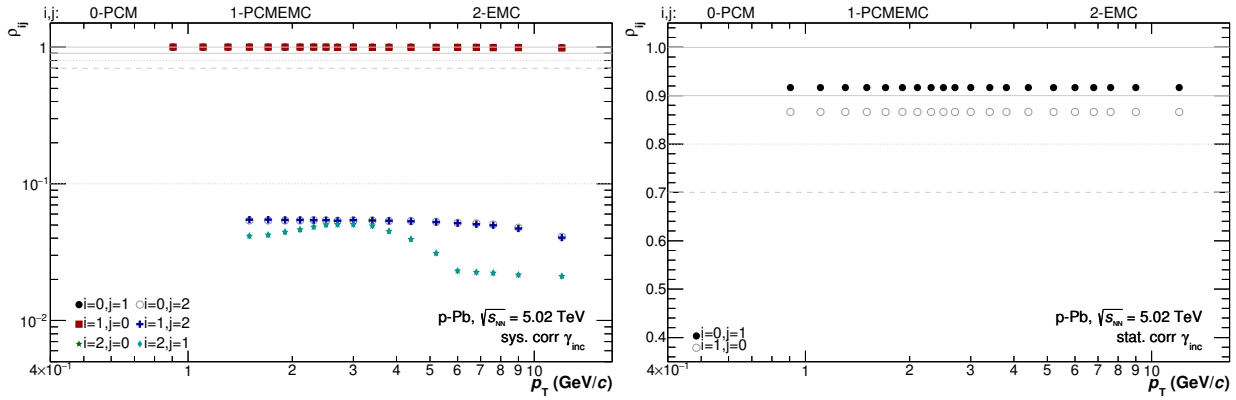

Figure C.9.: Correlation fractions among the systematic (left) and statistical (right) uncertainties for a pair of measurement i and j for the inclusive photon measurements in p–Pb collisions at $\sqrt{s_{\mathrm{NN}}} = 5.02$ TeV.

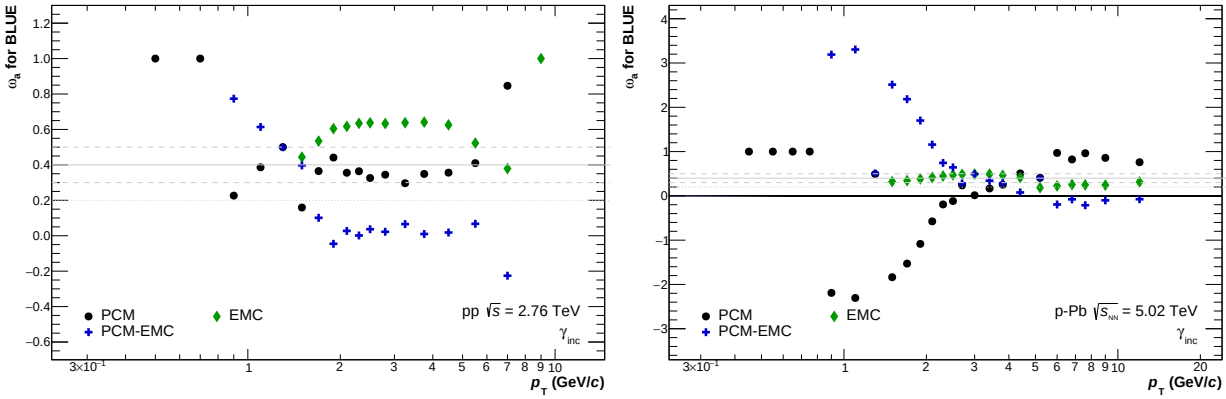

Figure C.10.: Weight of the individual inclusive photon measurements in pp (left) and p–Pb (right) collisions usind in the combination according to the BLUE method.

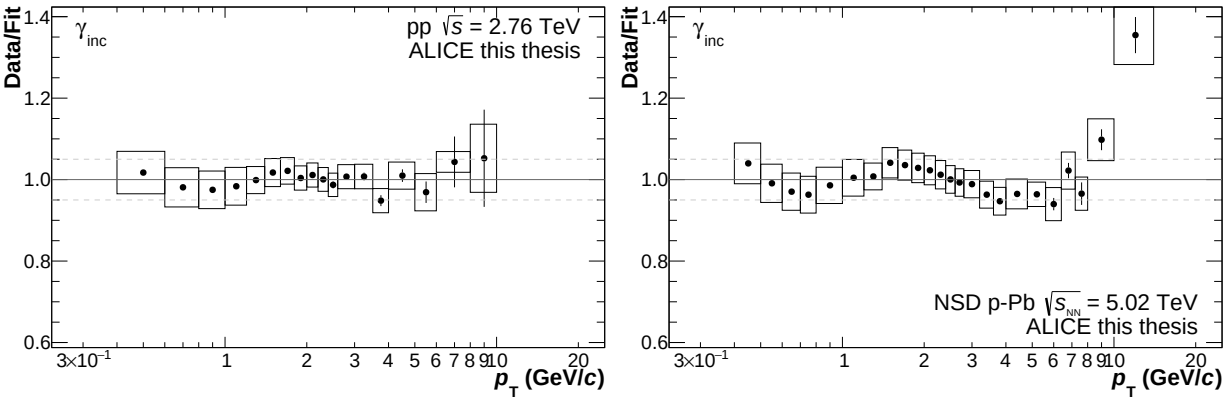

Figure C.11.: Comparison of the combined inclusive photon yield in pp (left) and p–Pb (right) collisions to their respective Tsallis fits.

D. List of Publications

- The full list of 128 papers can be found at: https://inspirehep.net/search?ln=en&ln=en&p=a+F.Bock.1
- 127 publications with the ALICE collaboration since 2012 (status 15.09.2017)
- Lead author in 10 internal documents, a list of which can be provided on request.
- Significant contributions have been made to the following publications:
  If not otherwise specified in [], I am a lead author.
- The ones which are subject of this thesis are highlighted by a bold reference index.

[1] *Neutral pion and η meson production in proton-proton collisions at $\sqrt{s} = 0.9$ TeV and $\sqrt{s} = 7$ TeV*, ALICE Collaboration, PLB **717** (2012) 162-172 (100 citations); [*Lead analyzer*]

[2] *Performance of the ALICE Experiment at the CERN LHC*, ALICE Collaboration, Int.J.Mod.Phys. A**29** (2014) 1430044 (271 citations); [*Contributions to the chapters on gamma reconstruction and secondary vertexing*]

[3] *Neutral pion production at midrapidity in pp and Pb-Pb collisions at $\sqrt{s_{NN}} = 2.76$ TeV*, ALICE Collaboration, EPJ C **74** (2014) no.10, 3108 (52 citations)

[4] *Direct photon production in Pb-Pb collisions at $\sqrt{s_{NN}} = 2.76$ TeV*, ALICE Collaboration, PLB **754** (2016) 235-248 (67 citations)

[5] *Impact of residual contamination on inclusive and direct photon flow*, F. Bock et al., J.Phys. G **44** (2017) no.2, 025106 (1 citation)

[6] *Production of π^0 and η mesons up to high transverse momentum in pp collisions at 2.76 TeV*, ALICE Collaboration, EPJ C **77** (2017) no.5, 339 (3 citations)

[7] *π^0 and η meson production in proton-proton collisions at $\sqrt{s} = 8$ TeV*, ALICE Collaboration, *arXiv:1708.08745* [*development of the analysis techniques used in [6] and applied to other energy, as well as analysis contributions*]

Bibliography

[1] S. Glashow, "Partial Symmetries of Weak Interactions", *Nucl.Phys.* **22** (1961) 579–588.

[2] A. Salam, "Weak and Electromagnetic Interactions", *Conf.Proc.* **C680519** (1968)a 367–377.

[3] A. Salam, "Fundamental Theory of Matter: A Survey of Results and Methods.", in "Contempory Physics: Trieste Symposium", vol. 19, p. 3. International Atomic Energy Agency, June 1968b.

[4] S. Weinberg, "A Model of Leptons", *Phys.Rev.Lett.* **19** (1967) 1264–1266.

[5] V. Mathieu, N. Kochelev, and V. Vento, "The Physics of Glueballs", *Int. J. Mod. Phys.* **E18** (2009) 1–49, arXiv:0810.4453.

[6] **BaBar Collaboration**, J. P. Lees *et al.*, "Dalitz plot analyses of $J/\psi \to \pi^+\pi^-\pi^0$, $J/\psi \to K^+K^-\pi^0$, and $J/\psi \to K^0_S K^\pm\pi^\mp$ produced via e^+e^- annihilation with initial-state radiation", arXiv:1702.01551.

[7] **Belle Collaboration**, S. K. Choi *et al.*, "Observation of a narrow charmonium - like state in exclusive $B^\pm \to K^\pm\pi^+\pi^-$ J/ ψ decays", *Phys. Rev. Lett.* **91** (2003) 262001, arXiv:hep-ex/0309032.

[8] R. L. Jaffe, "Multi-Quark Hadrons. 1. The Phenomenology of (2 Quark 2 anti-Quark) Mesons", *Phys. Rev.* **D15** (1977)a 267.

[9] R. L. Jaffe, "Multi-Quark Hadrons. 2. Methods", *Phys. Rev.* **D15** (1977)b 281.

[10] R. F. Lebed, R. E. Mitchell, and E. S. Swanson, "Heavy-Quark QCD Exotica", arXiv:1610.04528.

[11] D. Diakonov, V. Petrov, and M. V. Polyakov, "Exotic anti-decuplet of baryons: Prediction from chiral solitons", *Z. Phys.* **A359** (1997) 305–314, arXiv:hep-ph/9703373.

[12] S. L. Olsen, "Multiquark Hadrons", in "12th International Conference on Hypernuclear and Strange Particle Physics (HYP 2015) Sendai, Japan, September 7-12, 2015". 2016. arXiv:1611.01277.

[13] **Particle Data Group**, C. Patrignani *et al.*, "Review of Particle Physics", *Chin. Phys.* **C40** (2016), no. 10, 100001.

[14] D. d'Enterria, "α_s review (2016)", in "51st Rencontres de Moriond on QCD and High Energy Interactions La Thuile, Italy, March 19-26, 2016". 2016. arXiv:1606.04772.

[15] **CMS Collaboration**, V. Khachatryan *et al.*, "Constraints on parton distribution functions and extraction of the strong coupling constant from the inclusive jet cross section in pp collisions at $\sqrt{s} = 7$ TeV", *Eur. Phys. J.* **C75** (2015)a, no. 6, 288, arXiv:1410.6765.

[16] **CMS Collaboration**, V. Khachatryan *et al.*, "Measurement of the inclusive 3-jet production differential cross section in proton–proton collisions at 7 TeV and determination of the strong coupling constant in the TeV range", *Eur. Phys. J.* **C75** (2015)b, no. 5, 186, arXiv:1412.1633.

[17] J. C. Collins and D. E. Soper, "Parton Distribution and Decay Functions", *Nucl. Phys.* **B194** (1982) 445–492.

[18] P. Skands, "Introduction to QCD", in "Proceedings, Theoretical Advanced Study Institute in Elementary Particle Physics: Searching for New Physics at Small and Large Scales (TASI 2012): Boulder, Colorado, June 4-29, 2012", pp. 341–420. 2013. arXiv:1207.2389.

[19] **NuTeV Collaboration**, D. Mason *et al.*, "Measurement of the Nucleon Strange-Antistrange Asymmetry at Next-to-Leading Order in QCD from NuTeV Dimuon Data", *Phys. Rev. Lett.* **99** (2007) 192001.

[20] A. Cooper-Sarkar, "What did HERA teach us about the structure of the proton?", *J. Phys.* **G39** (2012) 093001, arXiv:1206.0894.

[21] **ZEUS Collaboration, H1 Collaboration**, H. Abramowicz *et al.*, "Combination of measurements of inclusive deep inelastic $e^{\pm}p$ scattering cross sections and QCD analysis of HERA data", *Eur. Phys. J.* **C75** (2015), no. 12, 580, arXiv:1506.06042.

[22] S. Alekhin, K. Melnikov, and F. Petriello, "Fixed target Drell-Yan data and NNLO QCD fits of parton distribution functions", *Phys. Rev.* **D74** (2006) 054033, arXiv:hep-ph/0606237.

[23] E. G. de Oliveira, A. D. Martin, and M. G. Ryskin, "Drell-Yan as a probe of small x partons at the LHC", *Eur. Phys. J.* **C72** (2012) 2069, arXiv:1205.6108.

[24] V. N. Gribov and L. N. Lipatov, "Deep inelastic e p scattering in perturbation theory", *Sov. J. Nucl. Phys.* **15** (1972) 438–450, [Yad. Fiz.15,781(1972)].

[25] Y. L. Dokshitzer, "Calculation of the Structure Functions for Deep Inelastic Scattering and e+ e- Annihilation by Perturbation Theory in Quantum Chromodynamics.", *Sov. Phys. JETP* **46** (1977) 641–653, [Zh. Eksp. Teor. Fiz.73,1216(1977)].

[26] G. Altarelli and G. Parisi, "Asymptotic Freedom in Parton Language", *Nucl. Phys.* **B126** (1977) 298–318.

[27] T. Eichten, H. Faissner, F. Hasert, S. Kabe, W. Krenz, *et al.*, "Measurement of the neutrino - nucleon anti-neutrino - nucleon total cross-sections", *Phys.Lett.* **B46** (1973) 274–280.

[28] **E598 Collaboration**, J. Aubert *et al.*, "Experimental Observation of a Heavy Particle J", *Phys.Rev.Lett.* **33** (1974) 1404–1406.

[29] **SLAC-SP-017 Collaboration**, J. Augustin *et al.*, "Discovery of a Narrow Resonance in e^+ e^- Annihilation", *Phys.Rev.Lett.* **33** (1974) 1406–1408.

[30] C. Rubbia, "Experimental Observation of the Intermediate Vector Bosons W^+, W^-, and Z^0", *Rev.Mod.Phys.* **57** (1985) 699–722.

[31] **CDF Collaboration**, F. Abe *et al.*, "Observation of top quark production in $\bar{p}p$ collisions", *Phys.Rev.Lett.* **74** (1995) 2626–2631, arXiv:hep-ex/9503002.

[32] **D0 Collaboration**, S. Abachi *et al.*, "Observation of the top quark", *Phys.Rev.Lett.* **74** (1995) 2632–2637, arXiv:hep-ex/9503003.

[33] **DONUT Collaboration**, K. Kodama *et al.*, "Observation of tau neutrino interactions", *Phys.Lett.* **B504** (2001) 218–224, arXiv:hep-ex/0012035.

[34] **ATLAS Collaboration**, G. Aad *et al.*, "Observation of a new particle in the search for the Standard Model Higgs boson with the ATLAS detector at the LHC", *Phys. Lett.* **B716** (2012) 1–29, arXiv:1207.7214.

[35] **CMS Collaboration**, S. Chatrchyan *et al.*, "Observation of a new boson at a mass of 125 GeV with the CMS experiment at the LHC", *Phys. Lett.* **B716** (2012) 30–61, arXiv:1207.7235.

[36] F. Englert and R. Brout, "Broken Symmetry and the Mass of Gauge Vector Mesons", *Phys.Rev.Lett.* **13** (1964) 321–323.

[37] P. W. Higgs, "Broken symmetries, massless particles and gauge fields", *Phys.Lett.* **12** (1964)a 132–133.

[38] P. W. Higgs, "Broken Symmetries and the Masses of Gauge Bosons", *Phys.Rev.Lett.* **13** (1964)b 508–509.

[39] G. Guralnik, C. Hagen, and T. Kibble, "Global Conservation Laws and Massless Particles", *Phys.Rev.Lett.* **13** (1964) 585–587.

[40] P. W. Higgs, "Spontaneous Symmetry Breakdown without Massless Bosons", *Phys.Rev.* **145** (1966) 1156–1163.

[41] T. Kibble, "Symmetry breaking in non-abelian gauge theories", *Phys.Rev.* **155** (1967) 1554–1561.

[42] **ALEPH Collaboration, CDF Collaboration, D0 Collaboration, DELPHI Collaboration, L3 Collaboration, OPAL Collaboration, SLD Collaboration, LEP Electroweak Working Group, Tevatron Electroweak Working Group, SLD Electroweak and Heavy Flavour Groups**, "Precision Electroweak Measurements and Constraints on the Standard Model", arXiv:1012.2367.

[43] **LEP Working Group for Higgs boson searches, ALEPH Collaboration, DELPHI Collaboration, L3 Collaboration, OPAL Collaboration**, R. Barate *et al.*, "Search for the standard model Higgs boson at LEP", *Phys.Lett.* **B565** (2003) 61–75, arXiv:hep-ex/0306033.

[44] **CDF Collaboration**, T. Aaltonen *et al.*, "Measurement of Particle Production and Inclusive Differential Cross Sections in p anti-p Collisions at $\sqrt{s} = 1.96$ TeV", *Phys.Rev.* **D79** (2009) 112005, arXiv:0904.1098.

[45] **D0 Collaboration**, V. M. Abazov *et al.*, "Combined search for the standard model Higgs boson decaying to $b\bar{b}$ using the D0 Run II data set", *Phys.Rev.Lett.* **109** (2012) 121802, arXiv:1207.6631.

[46] **CDF Collaboration**, T. Aaltonen *et al.*, "Combined search for the standard model Higgs boson decaying to a bb pair using the full CDF data set", *Phys.Rev.Lett.* **109** (2012)a 111802, arXiv:1207.1707.

[47] **CDF Collaboration, D0 Collaboration**, T. Aaltonen *et al.*, "Evidence for a particle produced in association with weak bosons and decaying to a bottom-antibottom quark pair in Higgs boson searches at the Tevatron", *Phys.Rev.Lett.* **109** (2012)b 071804, arXiv:1207.6436.

[48] **ATLAS Collaboration**, G. Aad *et al.*, "Combined search for the Standard Model Higgs boson using up to 4.9 fb^{-1} of pp collision data at $\sqrt{s} = 7$ TeV with the ATLAS detector at the LHC", *Phys.Lett.* **B710** (2012) 49–66, arXiv:1202.1408.

[49] **ATLAS Collaboration, CMS Collaboration**, G. Aad *et al.*, "Combined Measurement of the Higgs Boson Mass in pp Collisions at $\sqrt{s} = 7$ and 8 TeV with the ATLAS and CMS Experiments", *Phys. Rev. Lett.* **114** (2015) 191803, arXiv:1503.07589.

[50] **ATLAS Collaboration, CMS Collaboration**, G. Aad *et al.*, "Measurements of the Higgs boson production and decay rates and constraints on its couplings from a combined ATLAS and CMS analysis of the LHC pp collision data at $\sqrt{s} = 7$ and 8 TeV", *JHEP* **08** (2016) 045, arXiv:1606.02266.

[51] **CMS Collaboration**, V. Khachatryan *et al.*, "Constraints on the spin-parity and anomalous HVV couplings of the Higgs boson in proton collisions at 7 and 8 TeV", *Phys. Rev.* **D92** (2015), no. 1, 012004, arXiv:1411.3441.

[52] **CMS Collaboration**, V. Khachatryan *et al.*, "Combined search for anomalous pseudoscalar HVV couplings in VH(H $\to b\bar{b}$) production and H $\to$ VV decay", *Phys. Lett.* **B759** (2016) 672–696, arXiv:1602.04305.

[53] **ATLAS Collaboration**, G. Aad *et al.*, "Evidence for the spin-0 nature of the Higgs boson using ATLAS data", *Phys. Lett.* **B726** (2013) 120–144, arXiv:1307.1432.

[54] e. Sarkar, S., e. Satz, H., and e. Sinha, B., "The physics of the quark-gluon plasma", *Lect.Notes Phys.* **785** (2010) 1–369.

[55] L. D. McLerran and B. Svetitsky, "A Monte Carlo Study of SU(2) Yang-Mills Theory at Finite Temperature", *Phys. Lett.* **B98** (1981)a 195, [,283(1980)].

[56] L. D. McLerran and B. Svetitsky, "Quark Liberation at High Temperature: A Monte Carlo Study of SU(2) Gauge Theory", *Phys. Rev.* **D24** (1981)b 450.

[57] J. Kuti, J. Polonyi, and K. Szlachanyi, "Monte Carlo Study of SU(2) Gauge Theory at Finite Temperature", *Phys. Lett.* **B98** (1981) 199, [,287(1980)].

[58] F. Karsch and E. Laermann, "Susceptibilities, the specific heat and a cumulant in two flavor QCD", *Phys. Rev.* **D50** (1994) 6954–6962, arXiv:hep-lat/9406008.

[59] Z. Fodor and S. D. Katz, "Lattice determination of the critical point of QCD at finite T and mu", *JHEP* **03** (2002) 014, arXiv:hep-lat/0106002.

[60] M. D'Elia and M.-P. Lombardo, "Finite density QCD via imaginary chemical potential", *Phys. Rev.* **D67** (2003) 014505, arXiv:hep-lat/0209146.

[61] C. R. Allton, S. Ejiri, S. J. Hands, O. Kaczmarek, F. Karsch, E. Laermann, and C. Schmidt, "The Equation of state for two flavor QCD at nonzero chemical potential", *Phys. Rev.* **D68** (2003) 014507, arXiv:hep-lat/0305007.

[62] P. Braun-Munzinger and J. Stachel, "The quest for the quark–gluon plasma", *Nature* **448** (2007), no. 7151, 302–309.

[63] C. Wong, "Introduction to high-energy heavy-ion collisions", World Scientific Pub Co Inc, 1995.

[64] R. J. Fries and B. Müller, "Heavy ions at LHC: Theoretical issues", *Eur.Phys.J.* **C34** (2004) S279–S285, arXiv:nucl-th/0307043.

[65] Y. Aoki, S. Borsanyi, S. Durr, Z. Fodor, S. D. Katz, *et al.*, "The QCD transition temperature: results with physical masses in the continuum limit II.", *JHEP* **0906** (2009) 088, arXiv:0903.4155.

[66] M. Cheng, N. H. Christ, S. Datta, J. van der Heide, C. Jung, *et al.*, "The Transition temperature in QCD", *Phys.Rev.* **D74** (2006) 054507, arXiv:hep-lat/0608013.

[67] S. Borsanyi, G. Endrodi, Z. Fodor, A. Jakovac, S. D. Katz, S. Krieg, C. Ratti, and K. K. Szabo, "The QCD equation of state with dynamical quarks", *JHEP* **11** (2010) 077, arXiv:1007.2580.

[68] **HotQCD Collaboration**, A. Bazavov *et al.*, "Equation of state in (2+1)-flavor QCD", *Phys. Rev.* **D90** (2014) 094503, arXiv:1407.6387.

[69] P. Braun-Munzinger, K. Redlich, and J. Stachel, "Particle production in heavy ion collisions", arXiv:nucl-th/0304013.

[70] E. V. Shuryak, "Quark-Gluon Plasma and Hadronic Production of Leptons, Photons and Psions", *Phys. Lett.* **B78** (1978) 150, [Yad. Fiz.28,796(1978)].

[71] M. L. Miller, K. Reygers, S. J. Sanders, and P. Steinberg, "Glauber modeling in high energy nuclear collisions", *Ann.Rev.Nucl.Part.Sci.* **57** (2007) 205–243, arXiv:nucl-ex/0701025.

[72] **ALICE Collaboration**, J. Adam *et al.*, "Centrality dependence of particle production in p-Pb collisions at $\sqrt{s_{\rm NN}}$= 5.02 TeV", *Phys. Rev.* **C91** (2015), no. 6, 064905, arXiv:1412.6828.

[73] B. Müller, J. Schukraft, and B. Wysłouch, "First Results from Pb+Pb Collisions at the LHC", *Ann. Rev. Nucl. Part. Sci.* **62** (2012) 361–386, arXiv:1202.3233.

[74] e. Armesto, N., e. Borghini, N., e. Jeon, S., e. Wiedemann, U.A., S. Abreu, *et al.*, "Heavy Ion Collisions at the LHC - Last Call for Predictions", *J.Phys.* **G35** (2008) 054001, arXiv:0711.0974.

[75] **ALICE Collaboration**, B. Abelev *et al.*, "Charged-particle multiplicity density at mid-rapidity in central Pb–Pb collisions at $\sqrt{s_{\rm NN}}$ = 2.76 TeV", *Phys.Rev.Lett.* **105** (2010) 252301, arXiv:1011.3916.

[76] **ATLAS Collaboration**, G. Aad *et al.*, "Measurement of the centrality dependence of the charged particle pseudorapidity distribution in lead-lead collisions at $\sqrt{s_{\rm NN}}$ = 2.76 TeV with the ATLAS detector", *Phys.Lett.* **B710** (2012) 363–382, arXiv:1108.6027.

[77] **CMS Collaboration**, S. Chatrchyan *et al.*, "Dependence on pseudorapidity and centrality of charged hadron production in PbPb collisions at a nucleon-nucleon centre-of-mass energy of 2.76 TeV", *JHEP* **1108** (2011) 141, arXiv:1107.4800.

[78] **ALICE Collaboration**, J. Adam *et al.*, "Centrality dependence of the charged-particle multiplicity density at midrapidity in Pb–Pb collisions at $\sqrt{s_{\rm NN}}$ = 5.02 TeV", *Phys. Rev. Lett.* **116** (2016), no. 22, 222302, arXiv:1512.06104.

[79] J. Bjorken, "Highly Relativistic Nucleus-Nucleus Collisions: The Central Rapidity Region", *Phys.Rev.* **D27** (1983) 140–151.

[80] **CMS Collaboration**, K. Krajczar, "Charged hadron multiplicity and transverse energy densities in Pb Pb collisions from CMS", *J.Phys.* **G38** (2011) 124041.

[81] **ALICE Collaboration**, J. Adam *et al.*, "Measurement of transverse energy at midrapidity in Pb–Pb collisions at $\sqrt{s_{\rm NN}}$ = 2.76 TeV", *Phys. Rev.* **C94** (2016), no. 3, 034903, arXiv:1603.04775.

[82] B. Back, M. Baker, M. Ballintijn, D. Barton, B. Becker, *et al.*, "The PHOBOS perspective on discoveries at RHIC", *Nucl.Phys.* **A757** (2005) 28–101, arXiv:nucl-ex/0410022.

[83] **BRAHMS Collaboration**, I. Arsene *et al.*, "Quark gluon plasma and color glass condensate at RHIC? The Perspective from the BRAHMS experiment", *Nucl.Phys.* **A757** (2005) 1–27, arXiv:nucl-ex/0410020.

[84] **PHENIX Collaboration**, K. Adcox *et al.*, "Formation of dense partonic matter in relativistic nucleus-nucleus collisions at RHIC: Experimental evaluation by the PHENIX collaboration", *Nucl.Phys.* **A757** (2005) 184–283, arXiv:nucl-ex/0410003.

[85] **STAR Collaboration**, J. Adams *et al.*, "Experimental and theoretical challenges in the search for the quark gluon plasma: The STAR Collaboration's critical assessment of the evidence from RHIC collisions", *Nucl.Phys.* **A757** (2005) 102–183, arXiv:nucl-ex/0501009.

[86] A. Baran, W. Broniowski, and W. Florkowski, "Description of the particle ratios and transverse momentum spectra for various centralities at RHIC in a single freezeout model", *Acta Phys. Polon.* **B35** (2004) 779–798, arXiv:nucl-th/0305075.

[87] F. Becattini, M. Gazdzicki, A. Keranen, J. Manninen, and R. Stock, "Chemical equilibrium in nucleus nucleus collisions at relativistic energies", *Phys. Rev.* **C69** (2004) 024905, arXiv:hep-ph/0310049.

[88] F. Becattini, "An Introduction to the Statistical Hadronization Model", arXiv:0901.3643.

[89] C. Shen, U. Heinz, P. Huovinen, and H. Song, "Radial and elliptic flow in Pb+Pb collisions at the Large Hadron Collider from viscous hydrodynamic", *Phys.Rev.* **C84** (2011) 044903, arXiv:1105.3226.

[90] G. Kestin and U. W. Heinz, "Hydrodynamic radial and elliptic flow in heavy-ion collisions from AGS to LHC energies", *Eur.Phys.J.* **C61** (2009) 545–552, arXiv:0806.4539.

[91] S. A. Voloshin, A. M. Poskanzer, and R. Snellings, "Collective phenomena in non-central nuclear collisions", arXiv:0809.2949.

[92] R. Snellings, "Elliptic Flow: A Brief Review", *New J.Phys.* **13** (2011) 055008, arXiv:1102.3010.

[93] E. Schnedermann, J. Sollfrank, and U. W. Heinz, "Thermal phenomenology of hadrons from 200 A/GeV S+S collisions", *Phys.Rev.* **C48** (1993) 2462–2475, arXiv:nucl-th/9307020.

[94] M. Floris, "Identified particles in pp and Pb–Pb collisions at LHC energies with the ALICE detector", *J.Phys.* **G38** (2011) 124025, arXiv:1108.3257.

[95] **ALICE Collaboration**, B. B. Abelev *et al.*, "Production of charged pions, kaons and protons at large transverse momenta in pp and Pb–Pb collisions at $\sqrt{s_{\rm NN}}$ =2.76 TeV", *Phys. Lett.* **B736** (2014)a 196–207, arXiv:1401.1250.

[96] **ALICE Collaboration**, B. B. Abelev *et al.*, "Multi-strange baryon production at mid-rapidity in Pb–Pb collisions at $\sqrt{s_{\rm NN}}$ = 2.76 TeV", *Phys. Lett.* **B728** (2014)b 216–227, arXiv:1307.5543, [Corrigendum: Phys. Lett.B734,409(2014)].

[97] **ALICE Collaboration**, J. Adam *et al.*, "Multiplicity dependence of charged pion, kaon, and (anti)proton production at large transverse momentum in p-Pb collisions at $\sqrt{s_{\rm NN}}$ = 5.02 TeV", *Phys. Lett.* **B760** (2016)a 720–735, arXiv:1601.03658.

[98] **ALICE Collaboration**, J. Adam *et al.*, "Multi-strange baryon production in p-Pb collisions at $\sqrt{s_{\rm NN}} = 5.02$ TeV", *Phys. Lett.* **B758** (2016)b 389–401, arXiv:1512.07227.

[99] **ALICE Collaboration**, B. B. Abelev *et al.*, "Multiplicity Dependence of Pion, Kaon, Proton and Lambda Production in p-Pb Collisions at $\sqrt{s_{\rm NN}} = 5.02$ TeV", *Phys. Lett.* **B728** (2014) 25–38, arXiv:1307.6796.

[100] **ALICE Collaboration**, B. Abelev *et al.*, "Pion, Kaon, and Proton Production in Central Pb–Pb Collisions at $\sqrt{s_{\rm NN}} = 2.76$ TeV", *Phys. Rev. Lett.* **109** (2012) 252301, arXiv:1208.1974.

[101] M. Bleicher, E. Zabrodin, C. Spieles, S. Bass, C. Ernst, *et al.*, "Relativistic hadron hadron collisions in the ultrarelativistic quantum molecular dynamics model", *J.Phys.* **G25** (1999) 1859–1896, arXiv:hep-ph/9909407.

[102] S. Bass, M. Belkacem, M. Bleicher, M. Brandstetter, L. Bravina, *et al.*, "Microscopic models for ultrarelativistic heavy ion collisions", *Prog.Part.Nucl.Phys.* **41** (1998) 255–369, arXiv:nucl-th/9803035.

[103] C. Shen, J.-F. Paquet, G. S. Denicol, S. Jeon, and C. Gale, "Collectivity and electromagnetic radiation in small systems", *Phys. Rev.* **C95** (2017) 014906, arXiv:1609.02590.

[104] C. Shen, J. F. Paquet, G. S. Denicol, S. Jeon, and C. Gale, "Thermal photon radiation in high multiplicity p+Pb collisions at the Large Hadron Collider", *Phys. Rev. Lett.* **116** (2016), no. 7, 072301, arXiv:1504.07989.

[105] M. Floris, "Hadron yields and the phase diagram of strongly interacting matter", *Nucl. Phys.* **A931** (2014) 103–112, arXiv:1408.6403.

[106] S. Wheaton and J. Cleymans, "THERMUS: A Thermal model package for ROOT", *Comput. Phys. Commun.* **180** (2009) 84–106, arXiv:hep-ph/0407174.

[107] M. Petrán, J. Letessier, V. Petráček, and J. Rafelski, "Hadron production and quark-gluon plasma hadronization in Pb–Pb collisions at $\sqrt{s_{\rm NN}} = 2.76$ TeV", *Phys. Rev.* **C88** (2013), no. 3, 034907, arXiv:1303.2098.

[108] I. Kraus, J. Cleymans, H. Oeschler, and K. Redlich, "Particle production in p-p collisions and prediction for LHC energy", *Phys.Rev.* **C79** (2009) 014901, arXiv:0808.0611.

[109] F. Becattini, P. Castorina, J. Manninen, and H. Satz, "The Thermal Production of Strange and Non-Strange Hadrons in e^+e^- Collisions", *Eur. Phys. J.* **C56** (2008) 493–510, arXiv:0805.0964.

[110] Y. Pan and S. Pratt, "Baryon Annihilation in Heavy Ion Collisions", arXiv:1210.1577.

[111] A. Andronic, P. Braun-Munzinger, and J. Stachel, "Thermal hadron production in relativistic nuclear collisions: The Hadron mass spectrum, the horn, and the QCD phase transition", *Phys.Lett.* **B673** (2009) 142–145, arXiv:0812.1186.

[112] F. Becattini, P. Castorina, A. Milov, and H. Satz, "A Comparative analysis of statistical hadron production", *Eur.Phys.J.* **C66** (2010) 377–386, arXiv:0911.3026.

[113] J.-Y. Ollitrault, "Anisotropy as a signature of transverse collective flow", *Phys.Rev.* **D46** (1992) 229–245.

[114] S. Voloshin and Y. Zhang, "Flow study in relativistic nuclear collisions by Fourier expansion of Azimuthal particle distributions", *Z.Phys.* **C70** (1996) 665–672, arXiv:hep-ph/9407282.

[115] I. Selyuzhenkov, "Charged particle directed flow in Pb–Pb collisions at $\sqrt{s_{\rm NN}} = 2.76$ TeV measured with ALICE at the LHC", *J.Phys.* **G38** (2011) 124167, arXiv:1106.5425.

[116] **ALICE Collaboration**, K. Aamodt *et al.*, "Elliptic flow of charged particles in Pb–Pb collisions at 2.76 TeV", *Phys. Rev. Lett.* **105** (2010) 252302, arXiv:1011.3914.

[117] **ALICE Collaboration**, K. Aamodt *et al.*, "Harmonic decomposition of two-particle angular correlations in Pb–Pb collisions at $\sqrt{s_{\rm NN}} = 2.76$ TeV", *Phys.Lett.* **B708** (2012) 249–264, arXiv:1109.2501.

[118] **ALICE Collaboration**, B. B. Abelev *et al.*, "Multiparticle azimuthal correlations in p -Pb and Pb–Pb collisions at the CERN Large Hadron Collider", *Phys. Rev.* **C90** (2014), no. 5, 054901, arXiv:1406.2474.

[119] **ATLAS Collaboration**, G. Aad *et al.*, "Measurement of flow harmonics with multi-particle cumulants in Pb+Pb collisions at $\sqrt{s_{\rm NN}} = 2.76$ TeV with the ATLAS detector", *Eur. Phys. J.* **C74** (2014), no. 11, 3157, arXiv:1408.4342.

[120] **ALICE Collaboration**, J. Adam *et al.*, "Correlated event-by-event fluctuations of flow harmonics in Pb–Pb collisions at $\sqrt{s_{\rm NN}} = 2.76$ TeV", *Phys. Rev. Lett.* **117** (2016) 182301, arXiv:1604.07663.

[121] **ALICE Collaboration**, J. Adam *et al.*, "Flow dominance and factorization of transverse momentum correlations in Pb–Pb collisions at the LHC", arXiv:1702.02665.

[122] **ALICE Collaboration**, K. Aamodt *et al.*, "Higher harmonic anisotropic flow measurements of charged particles in Pb–Pb collisions at $\sqrt{s_{\rm NN}} = 2.76$ TeV", *Phys.Rev.Lett.* **107** (2011) 032301, arXiv:1105.3865.

[123] **ALICE Collaboration**, B. B. Abelev *et al.*, "Elliptic flow of identified hadrons in Pb–Pb collisions at $\sqrt{s_{\rm NN}} = 2.76$ TeV", *JHEP* **06** (2015) 190, arXiv:1405.4632.

[124] U. Heinz, C. Shen, and H.-C. Song, "The viscosity of quark-gluon plasma at RHIC and the LHC", *AIP Conf.Proc.* **1441** (2012) 766–770, arXiv:1108.5323.

[125] **ALICE Collaboration**, B. B. Abelev *et al.*, "Azimuthal anisotropy of D meson production in Pb–Pb collisions at $\sqrt{s_{\rm NN}} = 2.76$ TeV", *Phys. Rev.* **C90** (2014), no. 3, 034904, arXiv:1405.2001.

[126] W. Horowitz and M. Gyulassy, "Quenching and Tomography from RHIC to LHC", *J.Phys.* **G38** (2011) 124114, arXiv:1107.2136.

[127] W. Alberico, A. Beraudo, A. De Pace, A. Molinari, M. Monteno, *et al.*, "Heavy-flavour spectra in high energy nucleus-nucleus collisions", *Eur.Phys.J.* **C71** (2011) 1666, arXiv:1101.6008.

[128] P. Gossiaux, R. Bierkandt, and J. Aichelin, "Tomography of a quark gluon plasma at RHIC and LHC energies", *Phys.Rev.* **C79** (2009) 044906, arXiv:0901.0946.

[129] P. Gossiaux, J. Aichelin, T. Gousset, and V. Guiho, "Competition of Heavy Quark Radiative and Collisional Energy Loss in Deconfined Matter", *J.Phys.* **G37** (2010) 094019, arXiv:1001.4166.

[130] H. van Hees, V. Greco, and R. Rapp, "Heavy-quark probes of the quark-gluon plasma at RHIC", *Phys.Rev.* **C73** (2006) 034913, arXiv:nucl-th/0508055.

[131] O. Fochler, J. Uphoff, Z. Xu, and C. Greiner, "Jet quenching and elliptic flow at RHIC and LHC within a pQCD-based partonic transport model", *J.Phys.* **G38** (2011) 124152, arXiv:1107.0130.

[132] B. Müller and J. L. Nagle, "Results from the relativistic heavy ion collider", *Ann.Rev.Nucl.Part.Sci.* **56** (2006) 93–135, arXiv:nucl-th/0602029.

[133] **CMS Collaboration**, S. Chatrchyan *et al.*, "Centrality dependence of dihadron correlations and azimuthal anisotropy harmonics in PbPb collisions at $\sqrt{s_{\mathrm{NN}}} = 2.76$ TeV", *Eur.Phys.J.* **C72** (2012) 2012, arXiv:1201.3158.

[134] **CMS Collaboration**, S. Chatrchyan *et al.*, "Measurement of higher-order harmonic azimuthal anisotropy in PbPb collisions at $\sqrt{s_{\mathrm{NN}}} = 2.76$ TeV", *Phys. Rev.* **C89** (2014), no. 4, 044906, arXiv:1310.8651.

[135] J. Jia, "Measurement of elliptic and higher order flow from ATLAS experiment at the LHC", *J.Phys.* **G38** (2011) 124012, arXiv:1107.1468.

[136] **PHENIX Collaboration**, A. Adare *et al.*, "Measurements of Higher-Order Flow Harmonics in Au+Au Collisions at $\sqrt{s_{\mathrm{NN}}} = 200$ GeV", arXiv:1105.3928.

[137] **PHENIX Collaboration**, A. Adare *et al.*, "Measurements of Higher-Order Flow Harmonics in Au+Au Collisions at $\sqrt{s_{\mathrm{NN}}} = 200$ GeV", *Phys.Rev.Lett.* **107** (2011)b 252301, arXiv:1105.3928.

[138] **STAR Collaboration**, P. Sorensen, "Higher Flow Harmonics in Heavy Ion Collisions from STAR", *J.Phys.* **G38** (2011) 124029, arXiv:1110.0737.

[139] S. Voloshin, "Anisotropic flow", *Nucl.Phys.* **A715** (2003) 379–388, arXiv:nucl-ex/0210014.

[140] R. J. Fries, B. Müller, C. Nonaka, and S. A. Bass, "Hadronization in heavy ion collisions: Recombination and fragmentation of partons", *Phys.Rev.Lett.* **90** (2003)a 202303, arXiv:nucl-th/0301087.

[141] R. J. Fries, B. Müller, C. Nonaka, and S. A. Bass, "Hadron production in heavy ion collisions: Fragmentation and recombination from a dense parton phase", *Phys.Rev.* **C68** (2003)b 044902, arXiv:nucl-th/0306027.

[142] V. Greco, C. Ko, and P. Levai, "Parton coalescence at RHIC", *Phys.Rev.* **C68** (2003) 034904, arXiv:nucl-th/0305024.

[143] **PHENIX Collaboration**, A. Adare *et al.*, "Scaling properties of azimuthal anisotropy in Au+Au and Cu+Cu collisions at $\sqrt{s_{\mathrm{NN}}} = 200$ GeV", *Phys.Rev.Lett.* **98** (2007) 162301, arXiv:nucl-ex/0608033.

[144] **CMS Collaboration**, V. Khachatryan *et al.*, "Evidence for collectivity in pp collisions at the LHC", *Phys. Lett.* **B765** (2017) 193–220, arXiv:1606.06198.

[145] **ATLAS Collaboration**, M. Aaboud *et al.*, "Measurements of long-range azimuthal anisotropies and associated Fourier coefficients for *pp* collisions at $\sqrt{s} = 5.02$ and 13 TeV and *p*+Pb collisions at $\sqrt{s_{\rm NN}}$=5.02 TeV with the ATLAS detector", arXiv:1609.06213.

[146] C. Aidala *et al.*, "Measurement of long-range angular correlations and azimuthal anisotropies in high-multiplicity *p*+Au collisions at $\sqrt{s_{\rm NN}} = 200$ GeV", arXiv:1609.02894.

[147] M. Habich, J. L. Nagle, and P. Romatschke, "Particle spectra and HBT radii for simulated central nuclear collisions of C + C, Al + Al, Cu + Cu, Au + Au, and Pb + Pb from $\sqrt{s} = 62.4$ - 2760 GeV", *Eur. Phys. J.* **C75** (2015), no. 1, 15, arXiv:1409.0040.

[148] **ALICE Collaboration**, B. B. Abelev *et al.*, "Long-range angular correlations of π, K and p in p-Pb collisions at $\sqrt{s_{\rm NN}} = 5.02$ TeV", *Phys. Lett.* **B726** (2013) 164–177, arXiv:1307.3237.

[149] B. Schenke, S. Schlichting, P. Tribedy, and R. Venugopalan, "Mass ordering of spectra from fragmentation of saturated gluon states in high multiplicity proton-proton collisions", *Phys. Rev. Lett.* **117** (2016), no. 16, 162301, arXiv:1607.02496.

[150] J. Cronin, H. J. Frisch, M. Shochet, J. Boymond, R. Mermod, *et al.*, "Production of Hadrons with Large Transverse Momentum at 200 GeV, 300 GeV, and 400 GeV", *Phys.Rev.* **D11** (1975) 3105.

[151] K. Eskola, H. Paukkunen, and C. Salgado, "EPS09: A New Generation of NLO and LO Nuclear Parton Distribution Functions", *JHEP* **0904** (2009) 065, arXiv:0902.4154.

[152] R. Baier, Y. L. Dokshitzer, A. H. Mueller, and D. Schiff, "Radiative energy loss of high-energy partons traversing an expanding QCD plasma", *Phys.Rev.* **C58** (1998) 1706–1713, arXiv:hep-ph/9803473.

[153] R. Baier, Y. L. Dokshitzer, S. Peigne, and D. Schiff, "Induced gluon radiation in a QCD medium", *Phys.Lett.* **B345** (1995) 277–286, arXiv:hep-ph/9411409.

[154] **ALICE Collaboration**, B. B. Abelev *et al.*, "Transverse momentum dependence of inclusive primary charged-particle production in p-Pb collisions at $\sqrt{s_{\rm NN}} = 5.02$ TeV", *Eur. Phys. J.* **C74** (2014), no. 9, 3054, arXiv:1405.2737.

[155] **CMS Collaboration**, V. Khachatryan *et al.*, "Charged-particle nuclear modification factors in PbPb and pPb collisions at $\sqrt{s_{\rm NN}} = 5.02$ TeV", *JHEP* **04** (2017) 039, arXiv:1611.01664.

[156] **ATLAS Collaboration**, G. Aad *et al.*, "Transverse momentum, rapidity, and centrality dependence of inclusive charged-particle production in $\sqrt{s_{\rm NN}}$=5.02 TeV *p* + Pb collisions measured by the ATLAS experiment", *Phys. Lett.* **B763** (2016) 313–336, arXiv:1605.06436.

[157] **ALICE Collaboration**, B. Abelev *et al.*, "Centrality Dependence of Charged Particle Production at Large Transverse Momentum in Pb–Pb Collisions at $\sqrt{s_{\rm NN}} = 2.76$ TeV", arXiv:1208.2711.

[158] **CMS Collaboration**, S. Chatrchyan *et al.*, "Study of high-p_T charged particle suppression in PbPb compared to pp collisions at $\sqrt{s_{\rm NN}}$ =2.76 TeV", *Eur.Phys.J.* **C72** (2012)a 1945, arXiv:1202.2554.

[159] **CMS Collaboration**, S. Chatrchyan *et al.*, "Measurement of isolated photon production in pp and PbPb collisions at $\sqrt{s_{\rm NN}} = 2.76$ TeV", *Phys.Lett.* **B710** (2012)b 256–277, arXiv:1201.3093.

[160] **CMS Collaboration**, S. Chatrchyan *et al.*, "Study of Z boson production in PbPb collisions at nucleon-nucleon centre of mass energy $\sqrt{s_{\rm NN}}$= 2.76 TeV", *Phys.Rev.Lett.* **106** (2011) 212301, arXiv:1102.5435.

[161] **CMS Collaboration**, S. Chatrchyan *et al.*, "Study of W boson production in PbPb and pp collisions at $\sqrt{s_{\rm NN}}$ = 2.76 TeV", *Phys.Lett.* **B715** (2012) 66–87, arXiv:1205.6334.

[162] **ALICE Collaboration**, D. Colella, "Strangeness production in p-Pb and Pb–Pb collisions with ALICE at LHC", *J. Phys. Conf. Ser.* **779** (2017), no. 1, 012043, arXiv:1609.06900.

[163] **ALICE Collaboration**, B. B. Abelev *et al.*, "K^0_S and Λ production in Pb–Pb collisions at $\sqrt{s_{\rm NN}}$ = 2.76 TeV", *Phys. Rev. Lett.* **111** (2013) 222301, arXiv:1307.5530.

[164] **ALICE Collaboration**, J. Adam *et al.*, "Transverse momentum dependence of D-meson production in Pb–Pb collisions at $\sqrt{\rm s_{NN}}$ = 2.76 TeV", *JHEP* **03** (2016) 081, arXiv:1509.06888.

[165] **ALICE Collaboration**, K. Aamodt *et al.*, "Suppression of Charged Particle Production at Large Transverse Momentum in Central Pb–Pb Collisions at $\sqrt{s_{\rm NN}}$ = 2.76 TeV", *Phys.Lett.* **B696** (2011) 30–39, arXiv:1012.1004.

[166] **ATLAS Collaboration**, G. Aad *et al.*, "Measurement of charged-particle spectra in Pb+Pb collisions at $\sqrt{s_{\rm NN}}$ = 2.76 TeV with the ATLAS detector at the LHC", *JHEP* **09** (2015) 050, arXiv:1504.04337.

[167] **PHENIX Collaboration**, A. Adare *et al.*, "Suppression pattern of neutral pions at high transverse momentum in Au+Au collisions at $\sqrt{s_{\rm NN}}$ = 200 GeV and constraints on medium transport coefficients", *Phys. Rev. Lett.* **101** (2008) 232301, arXiv:0801.4020.

[168] **PHENIX Collaboration**, S. Adler *et al.*, "Centrality dependence of direct photon production in $\sqrt{s_{\rm NN}}$ = 200 GeV Au + Au collisions", *Phys.Rev.Lett.* **94** (2005) 232301, arXiv:nucl-ex/0503003.

[169] **PHENIX Collaboration**, T. Isobe, "Systematic study of high-p(T) direct photon production with the PHENIX experiment at RHIC", *J. Phys.* **G34** (2007) S1015–1018, arXiv:nucl-ex/0701040.

[170] **ATLAS Collaboration**, G. Aad *et al.*, "Centrality, rapidity and transverse momentum dependence of isolated prompt photon production in lead-lead collisions at $\sqrt{s_{\rm NN}}$ = 2.76 TeV measured with the ATLAS detector", *Phys. Rev.* **C93** (2016), no. 3, 034914, arXiv:1506.08552.

[171] **ATLAS Collaboration**, G. Aad *et al.*, "Measurement of the production and lepton charge asymmetry of W bosons in Pb+Pb collisions at $\sqrt{s_{\rm NN}}$ = 2.76 TeV with the ATLAS detector", *Eur. Phys. J.* **C75** (2015), no. 1, 23, arXiv:1408.4674.

[172] **ATLAS Collaboration**, G. Aad *et al.*, "Measurement of Z boson Production in Pb+Pb Collisions at $\sqrt{s_{\rm NN}}$=2.76 TeV with the ATLAS Detector", arXiv:1210.6486.

[173] **ALICE Collaboration**, B. B. Abelev *et al.*, "Neutral pion production at midrapidity in pp and Pb–Pb collisions at $\sqrt{s_{\rm NN}}$ = 2.76 TeV", *Eur. Phys. J.* **C74** (2014), no. 10, 3108, arXiv:1405.3794.

[174] **ALICE Collaboration**, B. B. Abelev *et al.*, "$K^*(892)^0$ and $\phi(1020)$ production in Pb–Pb collisions at $\sqrt{s_{\rm NN}}$ = 2.76 TeV", *Phys. Rev.* **C91** (2015) 024609, arXiv:1404.0495.

[175] **ALICE Collaboration**, J. Adam *et al.*, "Measurement of D_s^+ production and nuclear modification factor in Pb–Pb collisions at $\sqrt{s_{NN}} = 2.76$ TeV", *JHEP* **03** (2016) 082, arXiv:1509.07287.

[176] **ALICE Collaboration**, B. Abelev *et al.*, "J/ψ suppression at forward rapidity in Pb–Pb collisions at $\sqrt{s_{NN}} = 2.76$ TeV", *Phys. Rev. Lett.* **109** (2012) 072301, arXiv:1202.1383.

[177] **ALICE Collaboration**, B. B. Abelev *et al.*, "Centrality, rapidity and transverse momentum dependence of J/ψ suppression in Pb–Pb collisions at $\sqrt{s_{NN}}$=2.76 TeV", *Phys. Lett.* **B734** (2014)a 314–327, arXiv:1311.0214.

[178] **ALICE Collaboration**, B. B. Abelev *et al.*, "Suppression of $\Upsilon(1S)$ at forward rapidity in Pb–Pb collisions at $\sqrt{s_{NN}} = 2.76$ TeV", *Phys. Lett.* **B738** (2014)b 361–372, arXiv:1405.4493.

[179] **ALICE Collaboration**, J. Adam *et al.*, "Inclusive, prompt and non-prompt J/ψ production at mid-rapidity in Pb–Pb collisions at $\sqrt{s_{NN}} = 2.76$ TeV", *JHEP* **07** (2015) 051, arXiv:1504.07151.

[180] **CMS Collaboration**, S. Chatrchyan *et al.*, "Indications of suppression of excited Υ states in PbPb collisions at $\sqrt{s_{NN}} = 2.76$ TeV", *Phys. Rev. Lett.* **107** (2011) 052302, arXiv:1105.4894.

[181] **CMS Collaboration**, S. Chatrchyan *et al.*, "Suppression of non-prompt J/psi, prompt J/psi, and Y(1S) in PbPb collisions at $\sqrt{s_{NN}} = 2.76$ TeV", *JHEP* **1205** (2012)a 063, arXiv:1201.5069.

[182] **CMS Collaboration**, S. Chatrchyan *et al.*, "Observation of sequential Upsilon suppression in PbPb collisions", *Phys. Rev. Lett.* **109** (2012)b 222301, arXiv:1208.2826.

[183] **CMS Collaboration**, A. M. Sirunyan *et al.*, "Relative modification of prompt ψ(2S) and J/ψ yields from pp to PbPb collisions at $\sqrt{s_{NN}} = 5.02$ TeV", *Submitted to: Phys. Rev. Lett.*, 2016 arXiv:1611.01438.

[184] **ALICE Collaboration**, B. Abelev *et al.*, "Measurement of charged jet suppression in Pb–Pb collisions at $\sqrt{s_{NN}} = 2.76$ TeV", *JHEP* **03** (2014) 013, arXiv:1311.0633.

[185] **ALICE Collaboration**, J. Adam *et al.*, "Measurement of jet suppression in central Pb–Pb collisions at $\sqrt{s_{NN}} = 2.76$ TeV", *Phys. Lett.* **B746** (2015) 1–14, arXiv:1502.01689.

[186] **CMS Collaboration**, V. Khachatryan *et al.*, "Measurement of inclusive jet cross-sections in pp and PbPb collisions at $\sqrt{s_{NN}}$=2.76 TeV", *Submitted to: Phys. Rev. C*, 2016 arXiv:1609.05383.

[187] **ATLAS Collaboration**, G. Aad *et al.*, "Measurements of the Nuclear Modification Factor for Jets in Pb+Pb Collisions at $\sqrt{s_{NN}}$ =2.76 TeV with the ATLAS Detector", *Phys. Rev. Lett.* **114** (2015), no. 7, 072302, arXiv:1411.2357.

[188] Y. L. Dokshitzer, V. A. Khoze, and S. Troian, "On specific QCD properties of heavy quark fragmentation ('dead cone')", *J.Phys.* **G17** (1991) 1602–1604.

[189] **ALICE Collaboration**, J. Adam *et al.*, "ϕ-meson production at forward rapidity in p-Pb collisions at $\sqrt{s_{NN}} = 5.02$ TeV and in pp collisions at $\sqrt{s} = 2.76$ TeV", arXiv:1506.09206.

[190] **ALICE Collaboration**, B. B. Abelev *et al.*, "Measurement of prompt D-meson production in $p - Pb$ collisions at $\sqrt{s_{NN}} = 5.02$ TeV", *Phys. Rev. Lett.* **113** (2014), no. 23, 232301, arXiv:1405.3452.

[191] **ALICE Collaboration**, J. Adam *et al.*, "Rapidity and transverse-momentum dependence of the inclusive J/ψ nuclear modification factor in p-Pb collisions at $\sqrt{s_{\rm NN}} = 5.02$ TeV", *JHEP* **06** (2015) 055, arXiv:1503.07179.

[192] **ALICE Collaboration**, B. B. Abelev *et al.*, "J/ψ production and nuclear effects in p-Pb collisions at $\sqrt{s_{\rm NN}} = 5.02$ TeV", *JHEP* **02** (2014) 073, arXiv:1308.6726.

[193] **ALICE Collaboration**, J. Adam *et al.*, "Centrality dependence of inclusive J/ψ production in p-Pb collisions at $\sqrt{s_{\rm NN}} = 5.02$ TeV", *JHEP* **11** (2015) 127, arXiv:1506.08808.

[194] **ALICE Collaboration**, B. B. Abelev *et al.*, "Suppression of ψ(2S) production in p-Pb collisions at $\sqrt{s_{\rm NN}} = 5.02$ TeV", *JHEP* **12** (2014) 073, arXiv:1405.3796.

[195] **ALICE Collaboration**, B. B. Abelev *et al.*, "Production of inclusive Υ(1S) and Υ(2S) in p-Pb collisions at $\sqrt{s_{\rm NN}} = 5.02$ TeV", *Phys. Lett.* **B740** (2015) 105–117, arXiv:1410.2234.

[196] **CMS Collaboration**, V. Khachatryan *et al.*, "Measurement of inclusive jet production and nuclear modifications in pPb collisions at $\sqrt{s_{\rm NN}} = 5.02$ TeV", *Eur. Phys. J.* **C76** (2016), no. 7, 372, arXiv:1601.02001.

[197] **ALICE Collaboration**, J. Adam *et al.*, "Centrality dependence of charged jet production in p–Pb collisions at $\sqrt{s_{\rm NN}} = 5.02$ TeV", *Eur. Phys. J.* **C76** (2016), no. 5, 271, arXiv:1603.03402.

[198] **ATLAS Collaboration**, G. Aad *et al.*, "Centrality and rapidity dependence of inclusive jet production in $\sqrt{s_{\rm NN}} = 5.02$ TeV proton-lead collisions with the ATLAS detector", *Phys. Lett.* **B748** (2015) 392–413, arXiv:1412.4092.

[199] **ALICE Collaboration**, J. Adam *et al.*, "*D*-meson production in *p*-Pb collisions at $\sqrt{s_{\rm NN}}$ =5.02 TeV and in pp collisions at $\sqrt{s}$ =7 TeV", *Phys. Rev.* **C94** (2016), no. 5, 054908, arXiv:1605.07569.

[200] **CMS Collaboration**, S. Chatrchyan *et al.*, "Studies of jet quenching using isolated-photon+jet correlations in PbPb and *pp* collisions at $\sqrt{s_{\rm NN}} = 2.76$ TeV", *Phys. Lett.* **B718** (2013) 773–794, arXiv:1205.0206.

[201] S. Turbide, C. Gale, S. Jeon, and G. D. Moore, "Energy loss of leading hadrons and direct photon production in evolving quark-gluon plasma", *Phys.Rev.* **C72** (2005) 014906, arXiv:hep-ph/0502248.

[202] J.-F. Paquet, C. Shen, G. S. Denicol, M. Luzum, B. Schenke, S. Jeon, and C. Gale, "Production of photons in relativistic heavy-ion collisions", *Phys. Rev.* **C93** (2016), no. 4, 044906, arXiv:1509.06738.

[203] R. Chatterjee, H. Holopainen, T. Renk, and K. J. Eskola, "Collision centrality and τ_0 dependence of the emission of thermal photons from fluctuating initial state in ideal hydrodynamic calculation", *Phys. Rev.* **C85** (2012) 064910, arXiv:1204.2249.

[204] R. Chatterjee, H. Holopainen, I. Helenius, T. Renk, and K. J. Eskola, "Elliptic flow of thermal photons from event-by-event hydrodynamic model", *Phys. Rev.* **C88** (2013) 034901, arXiv:1305.6443.

[205] O. Linnyk, V. Konchakovski, T. Steinert, W. Cassing, and E. L. Bratkovskaya, "Hadronic and partonic sources of direct photons in relativistic heavy-ion collisions", *Phys. Rev.* **C92** (2015), no. 5, 054914, arXiv:1504.05699.

[206] C. Shen, U. W. Heinz, J.-F. Paquet, and C. Gale, "Thermal photons as a quark-gluon plasma thermometer reexamined", *Phys. Rev.* **C89** (2014), no. 4, 044910, arXiv:1308.2440.

[207] **WA98**, M. M. Aggarwal *et al.*, "Direct photon production in 158-A-GeV Pb-208 + Pb-208 collisions", arXiv:nucl-ex/0006007.

[208] P. Khandai, P. Shukla, and V. Singh, "Meson spectra and m_T scaling in $p+p$, d+Au, and Au + Au collisions at $\sqrt{s_{\rm NN}} = 200$ GeV", *Phys.Rev.* **C84** (2011) 054904, arXiv:1110.3929.

[209] **STAR Collaboration**, B. Abelev *et al.*, "Inclusive π^0, η, and direct photon production at high transverse momentum in $p+p$ and d+Au collisions at $\sqrt{s_{\rm NN}} = 200$ GeV", *Phys.Rev.* **C81** (2010) 064904, arXiv:0912.3838.

[210] **ALICE**, M. Wilde, "Measurement of Direct Photons in pp and Pb-Pb Collisions with ALICE", *Nucl. Phys.* **A904-905** (2013) 573c–576c, arXiv:1210.5958.

[211] M. Wilde, "Measurement of Direct Photons in pp and Pb–Pb Collisions with Conversion Pairs", PhD thesis, U. Munster, 2015. http://inspirehep.net/record/1503863/files/CERN-THESIS-2015-338.pdf

[212] **ALICE Collaboration**, J. Adam *et al.*, "Direct photon production in Pb–Pb collisions at $\sqrt{s_{\rm NN}} = 2.76$ TeV", *Phys. Lett.* **B754** (2016) 235–248, arXiv:1509.07324.

[213] L. E. Gordon and W. Vogelsang, "Polarized and unpolarized prompt photon production beyond the leading order", *Phys. Rev.* **D48** (1993) 3136–3159.

[214] W. Vogelsang and M. R. Whalley, "A Compilation of data on single and double prompt photon production in hadron hadron interactions", *J. Phys.* **G23** (1997) A1–A69.

[215] M. Klasen, C. Klein-Bösing, F. König, and J. P. Wessels, "How robust is a thermal photon interpretation of the ALICE low-$p_{\rm T}$ data?", *JHEP* **10** (2013) 119, arXiv:1307.7034.

[216] H. van Hees, M. He, and R. Rapp, "Pseudo-critical enhancement of thermal photons in relativistic heavy-ion collisions?", *Nucl. Phys.* **A933** (2015) 256–271, arXiv:1404.2846.

[217] **PHENIX Collaboration**, A. Adare *et al.*, "Enhanced production of direct photons in Au+Au collisions at $\sqrt{s_{\rm NN}} = 200$ GeV and implications for the initial temperature", *Phys.Rev.Lett.* **104** (2010) 132301, arXiv:0804.4168.

[218] J.-F. Paquet, C. Shen, G. Denicol, M. Luzum, B. Schenke, S. Jeon, and C. Gale, "Thermal and prompt photons at RHIC and the LHC", *Nucl. Phys.* **A956** (2016) 409–412.

[219] C. Shen, "Electromagnetic Radiation from QCD Matter: Theory Overview", *Nucl. Phys.* **A956** (2016) 184–191, arXiv:1601.02563.

[220] I. Iatrakis, E. Kiritsis, C. Shen, and D.-L. Yang, "Holographic Photon Production and Anisotropic Flow", in "8th International Conference on Hard and Electromagnetic Probes of High-energy Nuclear Collisions: Hard Probes 2016 (HP2016) Wuhan, Hubei, China, September 23-27, 2016". 2016a. arXiv:1612.05114.

[221] I. Iatrakis, E. Kiritsis, C. Shen, and D.-L. Yang, "Direct-Photon Spectra and Anisotropic Flow in Heavy Ion Collisions from Holography", in "12th Conference on Quark Confinement and the Hadron Spectrum (Confinement XII) Thessaloniki, Greece, August 28-September 4, 2016". 2016b. arXiv:1611.04848.

[222] O. Linnyk, E. L. Bratkovskaya, and W. Cassing, "Effective QCD and transport description of dilepton and photon production in heavy-ion collisions and elementary processes", *Prog. Part. Nucl. Phys.* **87** (2016) 50–115, arXiv:1512.08126.

[223] **STAR Collaboration**, L. Adamczyk *et al.*, "Direct virtual photon production in Au+Au collisions at $\sqrt{s_{\rm NN}} = 200$ GeV", arXiv:1607.01447.

[224] **PHENIX Collaboration**, A. Adare *et al.*, "Observation of direct-photon collective flow in $\sqrt{s_{\rm NN}} = 200$ GeV Au+Au collisions", *Phys. Rev. Lett.* **109** (2012) 122302, arXiv:1105.4126.

[225] **PHENIX Collaboration**, A. Adare *et al.*, "Azimuthally anisotropic emission of low-momentum direct photons in Au+Au collisions at $\sqrt{s_{\rm NN}} = 200$ GeV", *Phys. Rev.* **C94** (2016), no. 6, 064901, arXiv:1509.07758.

[226] **ALICE Collaboration**, D. Lohner, "Measurement of Direct-Photon Elliptic Flow in Pb-Pb Collisions at $\sqrt{s_{\rm NN}} = 2.76$ TeV", *J. Phys. Conf. Ser.* **446** (2013) 012028, arXiv:1212.3995.

[227] D. Lohner, "Anisotropic flow of direct photons in Pb-Pb collisions at 2.76 TeV per nucleon", PhD thesis, Heidelberg U., 2013-09-16. http://inspirehep.net/record/1296412/files/245328385_CERN-THESIS-2013-158.pdf

[228] **PHENIX Collaboration**, A. Adare *et al.*, "Direct photon production in d+Au collisions at $\sqrt{s_{\rm NN}} = 200$ GeV", *Phys. Rev.* **C87** (2013) 054907, arXiv:1208.1234.

[229] e. Evans, L. and e. Bryant, P., "LHC Machine", *JINST* **3** (2008) S08001.

[230] J. Jowett and C. Carli, "The LHC as a proton nucleus collider", *Conf. Proc.* **C060626** (2006) 550–552, [,550(2006)].

[231] J. M. Jowett, "The LHC as a Nucleus-Nucleus Collider", *J. Phys.* **G35** (2008) 104028, arXiv:0807.1397.

[232] C. De Melis, "The CERN accelerator complex. Complexe des accélérateurs du CERN", Jul 2016, General Photo.

[233] "ALICE webpage". http://aliceinfo.cern.ch/

[234] **ALICE Collaboration**, K. Aamodt *et al.*, "The ALICE experiment at the CERN LHC", *JINST* **3** (2008) S08002.

[235] **ALICE Collaboration**, B. B. Abelev *et al.*, "Performance of the ALICE Experiment at the CERN LHC", *Int. J. Mod. Phys.* **A29** (2014) 1430044, arXiv:1402.4476.

[236] **ALICE EMCal Collaboration**, U. Abeysekara *et al.*, "ALICE EMCal Physics Performance Report", arXiv:1008.0413.

[237] J. Allen *et al.*, "ALICE DCal: An Addendum to the EMCal Technical Design Report Di-Jet and Hadron-Jet correlation measurements in ALICE", Tech. Rep. CERN-LHCC-2010-011. ALICE-TDR-14-add-1, Jun 2010.

[238] **ALICE Collaboration**, G. Dellacasa *et al.*, "ALICE technical design report of the inner tracking system (ITS)", 1999.

[239] **ALICE Collaboration**, K. Aamodt *et al.*, "Alignment of the ALICE Inner Tracking System with cosmic-ray tracks", *JINST* **5** (2010) P03003, arXiv:1001.0502.

[240] **ALICE Collaboration**, G. Dellacasa *et al.*, "ALICE: Technical design report of the time projection chamber", 2000.

[241] J. Alme, Y. Andres, H. Appelshauser, S. Bablok, N. Bialas, *et al.*, "The ALICE TPC, a large 3-dimensional tracking device with fast readout for ultra-high multiplicity events", *Nucl.Instrum.Meth.* **A622** (2010) 316–367, arXiv:1001.1950.

[242] **STAR Collaboration**, H. Agakishiev *et al.*, "Observation of the antimatter helium-4 nucleus", *Nature* **473** (2011) 353, arXiv:1103.3312.

[243] **ALICE Collaboration**, "ALICE Transition-Radiation Detector (TRD): Technical Design Report", tech. rep., CERN/LHCC/2001–21, 2001.

[244] **ALICE Collaboration**, G. Dellacasa *et al.*, "ALICE technical design report of the time-of-flight system (TOF)", 2000.

[245] **ALICE Collaboration**, S. Beole *et al.*, "ALICE technical design report: Detector for high momentum PID", 1998.

[246] **ALICE Collaboration**, G. Dellacasa *et al.*, "ALICE technical design report of the photon spectrometer (PHOS)", 1999.

[247] G. Conesa, H. Delagrange, J. Diaz, M. Ippolitov, Y. Kharlov, *et al.*, "Performance of the ALICE photon spectrometer PHOS", *Nucl.Instrum.Meth.* **A537** (2005) 363–367.

[248] **ALICE Collaboration**, P. Cortese *et al.*, "ALICE electromagnetic calorimeter technical design report", 2008.

[249] R. Bramm, T. Kollegger, C. Loizides, and R. Stock, "The Physics of ALICE HLT trigger modes", arXiv:hep-ex/0212050.

[250] **ALICE Collaboration**, "ALICE Trigger, Data Acquisition, High Level Trigger, Control System: Technical Design Report", tech. rep., CERN/LHCC-2003-062, ALICE TDR 010, 2004.

[251] **ALICE Collaboration**, B. Abelev *et al.*, "Centrality determination of Pb–Pb collisions at $\sqrt{s_{\rm NN}} = 2.76$ TeV with ALICE", *Phys. Rev.* **C88** (2013), no. 4, 044909, arXiv:1301.4361.

[252] **ALICE Collaboration**, "AliRoot". a.
http://git.cern.ch/pub/AliRoot

[253] "AliPhysics". b.
http://git.cern.ch/pub/AliPhysics

[254] "ROOT webpage".
http://root.cern.ch/

[255] T. Sjöstrand, S. Mrenna, and P. Z. Skands, "PYTHIA 6.4 Physics and Manual", *JHEP* **0605** (2006) 026, arXiv:hep-ph/0603175.

[256] T. Sjöstrand, "PYTHIA 8 Status Report", arXiv:0809.0303.

[257] T. Sjöstrand, S. Mrenna, and P. Z. Skands, "A Brief Introduction to PYTHIA 8.1", *Comput.Phys.Commun.* **178** (2008) 852–867, arXiv:0710.3820.

[258] R. Engel, "Phojet manual", *University of Siegen preprint*, 1995 95–05.

[259] S. Roesler, R. Engel, and J. Ranft, "The Monte Carlo event generator DPMJET-III", in "Advanced Monte Carlo for radiation physics, particle transport simulation and applications. Proceedings, Conference, MC2000, Lisbon, Portugal, October 23-26, 2000", pp. 1033–1038. 2000. arXiv:hep-ph/0012252.

[260] X.-N. Wang and M. Gyulassy, "HIJING: A Monte Carlo model for multiple jet production in p p, p A and A A collisions", *Phys.Rev.* **D44** (1991) 3501–3516.

[261] Z.-W. Lin, C. M. Ko, B.-A. Li, B. Zhang, and S. Pal, "A Multi-phase transport model for relativistic heavy ion collisions", *Phys.Rev.* **C72** (2005) 064901, arXiv:nucl-th/0411110.

[262] M. Dobbs and J. B. Hansen, "The HepMC C++ Monte Carlo event record for High Energy Physics", *Comput. Phys. Commun.* **134** (2001) 41–46.

[263] R. Brun, F. Bruyant, M. Maire, A. McPherson, and P. Zanarini, "GEANT3", 1987.

[264] **GEANT4**, S. Agostinelli *et al.*, "GEANT4: A Simulation toolkit", *Nucl.Instrum.Meth.* **A506** (2003) 250–303.

[265] A. Fasso, A. Ferrari, S. Roesler, P. Sala, F. Ballarini, *et al.*, "The Physics models of FLUKA: Status and recent developments", *eConf* **C0303241** (2003) MOMT005, arXiv:hep-ph/0306267.

[266] I. Bird, "Computing for the Large Hadron Collider", *Ann. Rev. Nucl. Part. Sci.* **61** (2011) 99–118.

[267] L. Robertson, "Computing Services for LHC: From Clusters to Grids", in "From the web to the grid and beyond: Computing paradigms driven by high-energy physics", R. Brun, F. Carminati, and G. G. Carminati, eds., pp. 69–89.

[268] R. Frühwirth, "Application of kalman filtering to track and vertex fitting", *Nuclear Instruments and Methods in Physics Research Section A: Accelerators, Spectrometers, Detectors and Associated Equipment* **262** (1987), no. 2–3, 444 – 450.

[269] **ALICE Collaboration**, E. Alessandro, G *et al.*, "ALICE: Physics performance report, volume II", *J.Phys.* **G32** (2006) 1295–2040.

[270] **ALICE EMCal Collaboration**, O. Bourrion *et al.*, "The ALICE EMCal L1 trigger first year of operation experience", *JINST* **8** (2013) C01013, arXiv:1210.8078.

[271] S. van der Meer, "Calibration of the Effective Beam Height in the ISR", 1968.

[272] **ALICE Collaboration**, B. Abelev *et al.*, "Measurement of inelastic, single- and double-diffraction cross sections in proton–proton collisions at the LHC with ALICE", *Eur. Phys. J. C*, 2012 arXiv:1208.4968.

[273] **ALICE Collaboration**, "ALICE luminosity determination for pp collisions at $\sqrt{s} = 5$ TeV", Jul 2016.

[274] S. Tripathy, "Inelastic Normalization Factors for pp collisions at $\sqrt{s}$= 5.02, 8, and 13 TeV", June 2017. internal report.
https://aliceinfo.cern.ch/Notes/sites/aliceinfo.cern.ch.Notes/files/notes/analysis/stripath/2017-Jun-14-analysis_note-INEL_norm.pdf

[275] R. Engel, J. Ranft, and S. Roesler, "Hard diffraction in hadron hadron interactions and in photoproduction", *Phys.Rev.* **D52** (1995) 1459–1468, arXiv:hep-ph/9502319.

[276] "The Coordinated Theoretical-Experimental Project on QCD". http://www.phys.psu.edu/~cteq/

[277] P. Collins, "An Introduction to Regge Theory and High-Energy Physics", Cambridge University Press, 1977.

[278] B. Andersson, S. Mohanty, and F. Söderberg, "Recent developments in the Lund model", arXiv:hep-ph/0212122.

[279] **Particle Data Group**, K. Nakamura *et al.*, "Review of particle physics", *J.Phys.* **G37** (2010) 075021.

[280] A. Capella, U. Sukhatme, C.-I. Tan, and J. Tran Thanh Van, "Dual parton model", *Phys.Rept.* **236** (1994) 225–329.

[281] R. K. Ellis, W. J. Stirling, and B. Webber, "QCD and collider physics", Cambridge University Press, 1996.

[282] **ALICE Collaboration**, B. Abelev *et al.*, "Pseudorapidity density of charged particles in p + Pb collisions at $\sqrt{s_{\rm NN}} = 5.02$ TeV", *Phys. Rev. Lett.* **110** (2013), no. 3, 032301, arXiv:1210.3615.

[283] J. Ranft, "The Dual parton model at cosmic ray energies", *Phys. Rev.* **D51** (1995) 64–84.

[284] J. Ranft, "DPMJET version II.5: Sampling of hadron hadron, hadron - nucleus and nucleus-nucleus interactions at accelerator and cosmic ray energies according to the two component dual parton model: Code manual", arXiv:hep-ph/9911232.

[285] R. Engel, J. Ranft, and S. Roesler, "Photoproduction off nuclei and point - like photon interactions 1. Cross-sections and nuclear shadowing", *Phys. Rev.* **D55** (1997) 6957–6967, arXiv:hep-ph/9610281.

[286] S. Roesler, R. Engel, and J. Ranft, "Photoproduction off nuclei: Particle and jet production", *Phys. Rev.* **D57** (1998) 2889–2902.

[287] P. Aurenche, F. W. Bopp, A. Capella, J. Kwiecinski, M. Maire, J. Ranft, and J. Tran Thanh Van, "Multiparticle production in a two component dual parton model", *Phys. Rev.* **D45** (1992) 92–105.

[288] S. Yu. Shmakov, V. V. Uzhinsky, and A. M. Zadorozhnyi, "DIAGEN: Generator of inelastic nucleus-nucleus interaction diagrams", *Comput. Phys. Commun.* **51** (1988) 125–135.

[289] B. Andersson, G. Gustafson, and B. Nilsson-Almqvist, "A Model for Low $p_{\rm T}$ Hadronic Reactions, with Generalizations to Hadron - Nucleus and Nucleus-Nucleus Collisions", *Nucl.Phys.* **B281** (1987) 289.

[290] B. Nilsson-Almqvist and E. Stenlund, "Interactions Between Hadrons and Nuclei: The Lund Monte Carlo, Fritiof Version 1.6", *Comput.Phys.Commun.* **43** (1987) 387.

[291] F. Bock, "ALICE Capabilities for Studying Photon Physics with the Conversion Method at LHC Energies", Bachelor's thesis, University of Heidelberg, June 2010. http://www.physi.uni-heidelberg.de//Publications/Bock-Bachelorthesis.pdf

[292] K. Koch, "Measurement of π^0 and η mesons with photon conversions in ALICE in proton-proton collisions at $\sqrt{s}$ = 0.9, 2.76, 7 TeV", PhD thesis, University of Heidelberg, February 2012.
http://www.ub.uni-heidelberg.de/archiv/13113

[293] F. Bock, "Neutral Pion and Eta Meson Production in pp and Pb–Pb Collisions at the LHC with the ALICE Detector", Master's thesis, University Heidelberg, December 2012.
http://www.physi.uni-heidelberg.de//Publications/Bock-Masterthesis.pdf

[294] J. Podolanski and R. Armenteros, "Analysis of V-events", *Phil. Mag.* **7** (1954).

[295] T. Awes, F. Obenshain, F. Plasil, S. Saini, S. Sorensen, and G. Young, "A simple method of shower localization and identification in laterally segmented calorimeters", *Nucl.Instrum.Method* **A311** (1992), no. 1, 130–138.

[296] **ALICE Collaboration**, J. Adam *et al.*, "Measurement of the production of high-p_{T} electrons from heavy-flavour hadron decays in Pb-Pb collisions at $\sqrt{s_{\mathrm{NN}}}$ = 2.76 TeV", arXiv:1609.07104.

[297] **ALICE Collaboration**, S. Acharya *et al.*, "Production of π^0 and η mesons up to high transverse momentum in pp collisions at 2.76 TeV", *Eur. Phys. J.* **C77** (2017), no. 5, 339, arXiv:1702.00917.

[298] P. G. Zamora, "Measurement of the π^0 meson properties through its Dalitz decay channel in pp and p-pPb collisions with the ALICE experiment at the LHC", PhD thesis, Madrid, CIEMAT, 2016.
http://inspirehep.net/record/1503580/files/Thesis-2016-Zamora.pdf

[299] A. Passfeld, "Neutral meson measurement via photon conversions in p-Pb collisions at $\sqrt{s_{\mathrm{NN}}}$ = 5.02 TeV with ALICE at the LHC", Octorber 2015. internal report.
https://aliceinfo.cern.ch/Notes/sites/aliceinfo.cern.ch.Notes/files/notes/analysis/apassfel/2015-Oct-13-analysis_note-AnalysisNote_Pi0inpPb_v5.pdf

[300] M. Sas, "Neutral mesons & direct photon flow", Master's thesis, Utrecht University, August 2016.
https://dspace.library.uu.nl/handle/1874/337631

[301] **ALICE Collaboration**, B. Abelev *et al.*, "Neutral pion and η meson production in proton-proton collisions at $\sqrt{s}$ = 0.9 TeV and $\sqrt{s}$ = 7 TeV", *Phys.Lett.* **B717** (2012) 162–172, arXiv:1205.5724.

[302] T. Okubo, "Neutral pion measurement in p-Pb collisions at $\sqrt{s_{\mathrm{NN}}}$ = 5.02 TeV", PhD thesis, Hiroshima University, January 2017.
http://cds.cern.ch/record/2255065

[303] L. Lamers, "Neutral Meson Reconstruction with the ALICE Detector", Bachelor's thesis, August 2017.
https://twiki.cern.ch/twiki/pub/ALICE/GammaConvTheses/Bachelor_Lizette_Lamers_PCMPHOS_pPb.pdf

[304] G. D. Lafferty and T. R. Wyatt, "Where to stick your data points: The treatment of measurements within wide bins", *Nucl.Instrum.Meth.* **A355** (1995) 541–547.

[305] G. I. Kopylov, "Like particle correlations as a tool to study the multiple production mechanism", *Phys. Lett.* **B50** (1974) 472–474.

[306] **ALICE Collaboration**, K. Koch, "π^0 and η measurement with photon conversions in ALICE in proton-proton collisions at $\sqrt{s} = 7$ TeV", *Nucl.Phys.* **A855** (2011) 281–284, arXiv:1103.2217.

[307] S. Schuchmann, "Modification of K^0_s and $\Lambda(\overline{\Lambda})$ transverse momentum spectra in Pb-Pb collisions at $\sqrt{s_{\rm NN}} = 2.76$ TeV with ALICE", PhD thesis, Frankfurt U., 2015-04-14. http://inspirehep.net/record/1429481/files/fulltext_6cIw6W.pdf

[308] C. Tsallis, "Possible generalization of Boltzmann-Gibbs statistics", *J. Statist. Phys.* **52** (1988) 479–487.

[309] L. Lyons, D. Gibaut, and P. Clifford, "How to Combine Correlated Estimates of a Single Physical Quantity", *Nucl.Instrum.Meth.* **A270** (1988) 110.

[310] A. Valassi, "Combining correlated measurements of several different physical quantities", *Nucl.Instrum.Meth.* **A500** (2003) 391–405.

[311] L. Lyons, "Statistics for nuclear and particle physicists", Cambridge, Uk: Univ. Pr., 1986.

[312] R. J. Barlow, "Statistics: a guide to the use of statistical methods in the physical sciences", John Wiley & Sons, 1989.

[313] A. Valassi and R. Chierici, "Information and treatment of unknown correlations in the combination of measurements using the BLUE method", *Eur.Phys.J.* **C74** (2014) 2717, arXiv:1307.4003.

[314] **CDF, D0, Top Averaging Group**, L. Demortier, R. Hall, R. Hughes, B. Klima, R. Roser, and M. Strovink, "Combining the top quark mass results for Run 1 from CDF and D0", 1999.

[315] A. A. Bylinkin and A. A. Rostovtsev, "Role of quarks in hadroproduction in high energy collisions", *Nucl. Phys.* **B888** (2014) 65–74, arXiv:1404.7302.

[316] A. A. Bylinkin and M. G. Ryskin, "Secondary hadron distributions in two component model", *Phys. Rev.* **D90** (2014), no. 1, 017501, arXiv:1404.4739.

[317] T. Sjöstrand, S. Ask, J. R. Christiansen, R. Corke, N. Desai, P. Ilten, S. Mrenna, S. Prestel, C. O. Rasmussen, and P. Z. Skands, "An Introduction to PYTHIA 8.2", *Comput. Phys. Commun.* **191** (2015) 159–177, arXiv:1410.3012.

[318] D. de Florian, R. Sassot, M. Epele, R. J. Hernández-Pinto, and M. Stratmann, "Parton-to-pion fragmentation reloaded", *Phys. Rev.* **D91** (2015), no. 1, 014035, arXiv:1410.6027.

[319] C. A. Aidala, F. Ellinghaus, R. Sassot, J. P. Seele, and M. Stratmann, "Global analysis of fragmentation functions for η mesons", *Phys. Rev.* **D83** (2011) 034002, arXiv:1009.6145.

[320] P. Skands, S. Carrazza, and J. Rojo, "Tuning PYTHIA 8.1: the Monash 2013 Tune", *Eur. Phys. J.* **C74** (2014), no. 8, 3024, arXiv:1404.5630.

[321] D. de Florian, R. Sassot, and M. Stratmann, "Global analysis of fragmentation functions for pions and kaons and their uncertainties", *Phys.Rev.* **D75** (2007) 114010, arXiv:hep-ph/0703242.

[322] **PHENIX Collaboration**, A. Adare *et al.*, "Cross section and double helicity asymmetry for η mesons and their comparison to neutral pion production in p+p collisions at $sqrts = 200GeV$", *Phys. Rev.* **D83** (2011) 032001, arXiv:1009.6224.

[323] **ALICE Collaboration**, J. Adam *et al.*, "K$^*(892)^0$ and $\phi(1020)$ meson production at high transverse momentum in pp and Pb-Pb collisions at $\sqrt{s_{\rm NN}} = 2.76$ TeV", *Phys. Rev.* **C95** (2017), no. 6, 064606, arXiv:1702.00555.

[324] **ALICE Collaboration**, V. G. Riabov, "Resonance production in ALICE", *J. Phys. Conf. Ser.* **798** (2017), no. 1, 012054.

[325] R. Hagedorn *Riv. Nuovo Cim. 6N10, 1*, 1983.

[326] N. Schmidt, "Neutral meson and direct photon measurements using the photon conversion method with ALICE in pp collisions at $\sqrt{s}$=7 TeV", December 2016. internal report. https://aliceinfo.cern.ch/Notes/sites/aliceinfo.cern.ch.Notes/files/notes/analysis/nschmidt/2016-Dec-08-analysis_note-aliceNoteMesonPhotonPCM7TeV_v0.pdf

[327] **ALICE Collaboration**, S. Acharya *et al.*, "π^0 and η meson production in proton-proton collisions at $\sqrt{s} = 8$ TeV", arXiv:1708.08745.

[328] N. Schmidt, "Neutral meson measurements with EMCal and PCM-EMCal in ALICE in pp collisions at $\sqrt{s} = 5$ TeV", September 2017. internal report. https://aliceinfo.cern.ch/Notes/sites/aliceinfo.cern.ch.Notes/files/notes/analysis/nschmidt/2017-Sep-05-analysis_note-aliceNoteMesonPCMCalo5TeV_v0.1.pdf

[329] R. Barlow, "Systematic errors: Facts and fictions", in "Advanced Statistical Techniques in Particle Physics. Proceedings, Conference, Durham, UK, March 18-22, 2002", pp. 134–144. 2002. arXiv:hep-ex/0207026.

[330] C. Shen, Z. Qiu, H. Song, J. Bernhard, S. Bass, and U. Heinz, "The iEBE-VISHNU code package for relativistic heavy-ion collisions", *Comput. Phys. Commun.* **199** (2016) 61–85, arXiv:1409.8164.

[331] K. Werner, B. Guiot, I. Karpenko, and T. Pierog, "Analysing radial flow features in p-Pb and p-p collisions at several TeV by studying identified particle production in EPOS3", *Phys. Rev.* **C89** (2014), no. 6, 064903, arXiv:1312.1233.

[332] F. W. Bopp, J. Ranft, R. Engel, and S. Roesler, "RHIC data and the multichain Monte Carlo DPMJET-3", in "Ultra-relativistic nucleus-nucleus collisions. Proceedings, 17th International Conference, Quark Matter 2004, Oakland, USA, January 11-17, 2004". 2004. arXiv:hep-ph/0403084.

[333] F. Bopp and J. Ranft, "Inclusive distributions in p-p collisions at LHC energies compared with an adjusted DPMJET-III model with chain fusion", in "Proceedings, 3rd International Workshop on Multiple Partonic Interactions at the LHC (MPI@LHC 2011): Hamburg, Germany, 21-25 Nov 2011", pp. 41–49. 2011. arXiv:1110.6403.

[334] M. Bourquin and J. M. Gaillard, "A Simple Phenomenological Description of Hadron Production", *Nucl. Phys.* **B114** (1976) 334–364.

[335] J. Schaffner-Bielich, D. Kharzeev, L. D. McLerran, and R. Venugopalan, "Generalized scaling of the transverse mass spectrum at the relativistic heavy ion collider", *Nucl. Phys.* **A705** (2002) 494–507, arXiv:nucl-th/0108048.

[336] G. Agakishiev *et al.*, "Neutral meson production in p Be and p Au collisions at 450-GeV beam energy", *Eur. Phys. J.* **C4** (1998) 249–257.

[337] **PHENIX Collaboration**, S. Adler *et al.*, "High transverse momentum η meson production in p^+p, d^+ Au and Au+Au collisions at $\sqrt{s_{\rm NN}} = 200$ GeV", *Phys.Rev.* **C75** (2007) 024909, arXiv:nucl-ex/0611006.

[338] J. Povlis *et al.*, "Nuclear Enhancement of π^0 and eta mesons Produced at Large Transverse Momenta", *Phys. Rev. Lett.* **51** (1983) 967.

[339] **Fermilab E706 Collaboration**, G. Alverson *et al.*, "Production of direct photons and neutral mesons at large transverse momenta by π^- and p beams at 500-GeV/c", *Phys. Rev.* **D48** (1993) 5–28.

[340] **Fermilab E706 Collaboration**, L. Apanasevich *et al.*, "Production of π^0 and eta mesons at large transverse momenta in pi- p and pi- Be interactions at 515-GeV/c", *Phys. Rev.* **D69** (2004) 032003, arXiv:hep-ex/0308022.

[341] G. J. Donaldson *et al.*, "Inclusive eta Production at Large Transverse Momenta", *Phys. Rev. Lett.* **40** (1978) 684.

[342] **WA70 Collaboration**, M. Bonesini *et al.*, "High Transverse Momentum η Production in π^-p, π^+p and pp Interactions at 280-GeV/c", *Z. Phys.* **C42** (1989) 527.

[343] **CERN-Lausanne-Michigan-Rockefeller, UA6 Collaboration**, J. Antille *et al.*, "A Measurement of the Inclusive π^0 and η Production Cross-sections at High $p_{\rm T}$ in $p\bar{p}$ and pp Collisions at $\sqrt{s} = 24.3$-GeV", *Phys. Lett.* **B194** (1987) 568.

[344] M. Aguilar-Benitez *et al.*, "Inclusive particle production in 400-GeV/c p p interactions", *Z. Phys.* **C50** (1991) 405–426.

[345] E. Amaldi *et al.*, "Inclusive eta production in pp collisions at ISR energies", *Nucl. Phys.* **B158** (1979) 1–10.

[346] C. Kourkoumelis *et al.*, "Inclusive π^0 production at very large $p_{\rm T}$ at the ISR", *Phys. Lett.* **84B** (1979)a 271–276.

[347] C. Kourkoumelis *et al.*, "Inclusive η production at high $p_{\rm T}$ at the ISR", *Phys. Lett.* **84B** (1979)b 277–280.

[348] **Fermilab E706 Collaboration**, L. Apanasevich *et al.*, "Production of π^0 and eta mesons at large transverse momenta in pp and p Be interactions at 530-GeV/c and 800-GeV/c", *Phys. Rev.* **D68** (2003) 052001, arXiv:hep-ex/0204031.

[349] **Axial Field Spectrometer Collaboration**, T. Akesson *et al.*, "A comparison of direct photon, π^0, and eta production in p anti-p and pp interactions at the CERN ISR", *Phys. Lett.* **158B** (1985) 282–288.

[350] **Axial Field Spectrometer Collaboration**, T. Akesson *et al.*, "Inclusive η Production at Low Transverse Momentum in 63-GeV pp Collisions at the CERN Intersecting Storage Rings", *Phys. Lett.* **B178** (1986) 447.

[351] **Axial Field Spectrometer Collaboration**, T. Akesson *et al.*, "Production of π^0 and η at 11-degrees in pp Collisions at $\sqrt{s} = 63$-GeV", *Z. Phys.* **C18** (1983) 5.

[352] **UA2, Bern-CERN-Copenhagen-Orsay-Pavia-Saclay Collaboration**, M. Banner *et al.*, "Inclusive Particle Production in the Transverse Momentum Range Between 0.25-GeV/c and 40-GeV/c at the CERN S $p\bar{p}$ S Collider", *Z. Phys.* **C27** (1985) 329.

[353] **ALICE Collaboration**, J. Adam *et al.*, "Production of K* (892)^0 and ϕ (1020) in p–Pb collisions at $\sqrt{s_{\rm NN}} = 5.02$ TeV", *Eur. Phys. J.* **C76** (2016), no. 5, 245, arXiv:1601.07868.

[354] **ALICE Collaboration**, D. Adamova *et al.*, "Production of $\Sigma(1385)^{\pm}$ and $\Xi(1530)^0$ in p-Pb collisions at $\sqrt{s_{\rm NN}} = 5.02$ TeV", *Eur. Phys. J.* **C77** (2017), no. 6, 389, arXiv:1701.07797.

[355] **ALICE Collaboration**, J. Adam *et al.*, "Measurement of azimuthal correlations of D mesons and charged particles in pp collisions at $\sqrt{s} = 7$ TeV and p-Pb collisions at $\sqrt{s_{\rm NN}} = 5.02$ TeV", *Eur. Phys. J.* **C77** (2017), no. 4, 245, arXiv:1605.06963.

[356] B. Jager, A. Schafer, M. Stratmann, and W. Vogelsang, "Next-to-leading order QCD corrections to high p(T) pion production in longitudinally polarized pp collisions", *Phys. Rev.* **D67** (2003) 054005, arXiv:hep-ph/0211007.

[357] I. Helenius, K. J. Eskola, H. Honkanen, and C. A. Salgado, "Impact-Parameter Dependent Nuclear Parton Distribution Functions: EPS09s and EKS98s and Their Applications in Nuclear Hard Processes", *JHEP* **07** (2012) 073, arXiv:1205.5359.

[358] D. d'Enterria, K. J. Eskola, I. Helenius, and H. Paukkunen, "Confronting current NLO parton fragmentation functions with inclusive charged-particle spectra at hadron colliders", *Nucl. Phys.* **B883** (2014) 615–628, arXiv:1311.1415.

[359] H.-L. Lai, M. Guzzi, J. Huston, Z. Li, P. M. Nadolsky, J. Pumplin, and C. P. Yuan, "New parton distributions for collider physics", *Phys. Rev.* **D82** (2010) 074024, arXiv:1007.2241.

[360] J. Gao, M. Guzzi, J. Huston, H.-L. Lai, Z. Li, P. Nadolsky, J. Pumplin, D. Stump, and C. P. Yuan, "CT10 next-to-next-to-leading order global analysis of QCD", *Phys. Rev.* **D89** (2014), no. 3, 033009, arXiv:1302.6246.

[361] M. Guzzi, P. Nadolsky, E. Berger, H.-L. Lai, F. Olness, and C. P. Yuan, "CT10 parton distributions and other developments in the global QCD analysis", arXiv:1101.0561.

[362] A. D. Martin, W. J. Stirling, R. S. Thorne, and G. Watt, "Parton distributions for the LHC", *Eur. Phys. J.* **C63** (2009) 189–285, arXiv:0901.0002.

[363] W. K. Tung, H. L. Lai, A. Belyaev, J. Pumplin, D. Stump, and C. P. Yuan, "Heavy Quark Mass Effects in Deep Inelastic Scattering and Global QCD Analysis", *JHEP* **02** (2007) 053, arXiv:hep-ph/0611254.

[364] A. Kusina, K. Kovařik, T. Ježo, D. B. Clark, F. I. Olness, I. Schienbein, and J. Y. Yu, "Update on nCTEQ PDFs: nuclear PDF uncertainties and LHC applications", *PoS* **DIS2014** (2014) 047, arXiv:1408.1114.

[365] K. Kovarik *et al.*, "nCTEQ15 - Global analysis of nuclear parton distributions with uncertainties in the CTEQ framework", *Phys. Rev.* **D93** (2016), no. 8, 085037, arXiv:1509.00792.

[366] K. J. Eskola, P. Paakkinen, H. Paukkunen, and C. A. Salgado, "EPPS16: Nuclear parton distributions with LHC data", *Eur. Phys. J.* **C77** (2017), no. 3, 163, arXiv:1612.05741.

[367] T. Lappi and H. Mäntysaari, "Single inclusive particle production at high energy from HERA data to proton-nucleus collisions", *Phys. Rev.* **D88** (2013) 114020, arXiv:1309.6963.

[368] K. J. Eskola, H. Paukkunen, and C. A. Salgado, "EPS09 - Nuclear PDFs and Their Uncertainties at NLO", *Nucl. Phys.* **A830** (2009) 599C–602C, arXiv:0906.4231.

[369] F. Gelis, "Color Glass Condensate and Glasma", *Int. J. Mod. Phys.* **A28** (2013) 1330001, arXiv:1211.3327.

[370] J. L. Albacete, N. Armesto, J. G. Milhano, P. Quiroga-Arias, and C. A. Salgado, "AAMQS: A non-linear QCD analysis of new HERA data at small-x including heavy quarks", *Eur. Phys. J.* **C71** (2011) 1705, arXiv:1012.4408.

[371] **ALICE Collaboration**, A. Marín, "Neutral meson production in pp and Pb–Pb collisions measured by ALICE at the LHC", *Nucl. Phys.* **A931** (2014) 438–443, arXiv:1408.2765.

[372] **ALICE Collaboration**, B. Abelev *et al.*, "Transverse Momentum Distribution and Nuclear Modification Factor of Charged Particles in p-Pb Collisions at $\sqrt{s_{\mathrm{NN}}} = 5.02$ TeV", arXiv:1210.4520.

[373] D. Peressounko, "Direct and isolated photons in p-Pb collisions measured with PHOS", April 2017. internal report. https://aliceinfo.cern.ch/Notes/sites/aliceinfo.cern.ch.Notes/files/notes/analysis/prsnko/2017-Apr-04-analysis_note-pPb_GammaTagging.pdf

[374] **STAR Collaboration**, B. I. Abelev *et al.*, "Strange particle production in p+p collisions at $\sqrt{s} = 200$ GeV", *Phys. Rev.* **C75** (2007) 064901, arXiv:nucl-ex/0607033.

[375] **PHENIX Collaboration**, A. Adare *et al.*, "Measurement of neutral mesons in p+p collisions at $\sqrt{s}$= 200 GeV and scaling properties of hadron production", *Phys. Rev.* **D83** (2011) 052004, arXiv:1005.3674.

[376] T. Adye, "Unfolding algorithms and tests using RooUnfold", in "Proceedings, PHYSTAT 2011 Workshop on Statistical Issues Related to Discovery Claims in Search Experiments and Unfolding, CERN,Geneva, Switzerland 17-20 January 2011", pp. 313–318, CERN. CERN, Geneva, 2011. arXiv:1105.1160.

[377] R. Bayes, "An essay toward solving a problem in the doctrine of chances", *Phil. Trans. Roy. Soc. Lond.* **53** (1764) 370–418.

[378] G. D'Agostini, "A Multidimensional unfolding method based on Bayes' theorem", *Nucl. Instrum. Meth.* **A362** (1995) 487–498.

[379] A. Hocker and V. Kartvelishvili, "SVD approach to data unfolding", *Nucl. Instrum. Meth.* **A372** (1996) 469–481, arXiv:hep-ph/9509307.

[380] D. Stump, J. Huston, J. Pumplin, W.-K. Tung, H. L. Lai, S. Kuhlmann, and J. F. Owens, "Inclusive jet production, parton distributions, and the search for new physics", *JHEP* **10** (2003) 046, arXiv:hep-ph/0303013.

[381] M. Gluck, E. Reya, and A. Vogt, "Parton fragmentation into photons beyond the leading order", *Phys. Rev.* **D48** (1993) 116, [Erratum: Phys. Rev.D51,1427(1995)].

[382] L. Bourhis, M. Fontannaz, and J. P. Guillet, "Quarks and gluon fragmentation functions into photons", *Eur. Phys. J.* **C2** (1998) 529–537, arXiv:hep-ph/9704447.

[383] T. Kaufmann, A. Mukherjee, and W. Vogelsang, "Access to Photon Fragmentation Functions in Hadronic Jet Production", *Phys. Rev.* **D93** (2016), no. 11, 114021, arXiv:1604.07175.

[384] D. G. d'Enterria, "Hard scattering cross-sections at LHC in the Glauber approach: From pp to pA and AA collisions", arXiv:nucl-ex/0302016.

[385] W. Vogelsang, "Private communication", 2017.

[386] H. Poppenborg, "Private communication", 2017.

Acknowledgements

My greatest dept is to Prof. Dr. Johanna Stachel, for supporting me since 2009 and giving me the opportunity to carry out my doctoral thesis within her group.
Moreover, I would like to express my deepest gratitude to Dr. Constantin Loizides for his guidance as well as never ending enthusiasm and encouragement during the past 5 years. I value your knowledge and friendship equally much.
Additionally, I would like to thank Prof. Dr. Stefanie Hansmann-Menzemer for reading and evaluating this thesis.
I wish to express my gratitude to Daniel Mühlheim, Nicolas Schmidt, Lucia Leardini, Mike Sas, Lucas Altenkämper, Martin Wilde and the whole conversion group for all the support and discussions, which I enjoyed very much and which helped me grow as a researcher.
I would also like to express my gratitude to my theory colleagues: Charles Gale, Jean-Francois Paquet, Chun Shen and Werner Vogelsang, who had the never ending patience to teach me about their research and provide me the needed inputs form their side for this thesis.
In addition I would like to thank to all people from my various working groups. Be it at CERN, at LBL or virtually in the PWGGA. Thanks for supporting me and providing a kind and challenging working environment.
Furthermore, I would like to thank the people who read and corrected the thesis and lend me their support during the past few month. I hope I can return the favor at some point!
Last but certainly not least, I want to thank my family and friends. Marta, Redmer, Sabrina, Leticia, Stefania, Alessandra and many more, thanks for being there for me, when I needed you and for the countless hours we spend enjoying each others company. You kept me going!
Thanks to all of you!

Ein ganz besonderer Dank gilt jedoch meiner Familie, darum formuliere ich ihn auf Deutsch, damit sie ihn alle verstehen können.
Mutti und Vati, ich bin euch so unendlich dankbar für eure niemals endende Unterstützung, ob nun moralischer oder finanzieller Natur. Ihr beide habt einen wahnsinnig grossen Anteil daran, dass ich es bis zu diesem Punkt in meinem Leben geschafft habe und ich werde euch das nie vergessen. Franziksa danke, dass du mich so lange bei Verstand gehalten hast! Ich kann mir vorstellen, dass dir das nicht immer leicht gefallen ist. Aber du hast einen fantastischen Job geleistet durch deinen positive Art und unsere wundervolle geschwisterliche Beziehung. Simon ich kann dir nicht genug danken für deine unendliche Geduld mit mir und meinen verrückten Arbeitszeiten. Ich hoffe inständig, dass ich deine Geduld mit mir nie wieder so auf die Probe stellen muss!
Ich habe noch so viele andere Dinge für die ich euch allen dankbar bin. Eines allerdings macht mich traurig, dass nicht mehr alle meine wundervollen Grosseltern den heutigen Tag mit mir verbringen können. Ihr habt einen riesigen Teil dazu beigetragen, wer ich heute bin und wer ich in Zukunft sein möchte und ich werde euch dafür für immer dankbar sein und an euch denken! Darum ist diese Arbeit vor Allem euch gewidmet. Ihr habt mir gezeigt, dass egal wie schwierig die Umstände sind, man immer nach seinem besten Selbst streben sollte. Ihr habt mir beigebracht, dass Probleme nicht dafür da sind , sich ihnen geschlagen zu geben, sondern sich ihnen zu stellen und sie zu bewältigen!
Vielen Lieben Dank euch Allen!

Erklärung

Ich versichere, dass ich diese Arbeit selbständig verfasst habe und keine anderen als die angegebenen Quellen und Hilfsmittel benutzt habe.

Heidelberg, den 18.9.2017 Unterschrift: .....
Friederike Bock